New Directions in Civil Engineering

Series Editor
W. F. CHEN
Purdue University

Zdeněk P. Bažant and Jaime Planas
Fracture and Size Effect in Concrete and Other Quasibrittle Materials

W.F. Chen and Seung-Eock Kim
LRFD Steel Design Using Advanced Analysis

W.F. Chen and E.M. Lui
Stability Design of Steel Frames

W.F. Chen and K.H. Mossallam
Concrete Buildings: Analysis for Safe Construction

W.F. Chen and S. Toma
Advanced Analysis of Steel Frames: Theory, Software, and Applications

W.F. Chen and Shouji Toma
Analysis and Software of Cylindrical Members

Y.K. Cheung and L.G. Tham
Finite Strip Method

Hsai-Yang Fang
Introduction to Environmental Geotechnology

Yuhshi Fukumoto and George C. Lee
Stability and Ductility of Steel Structures under Cyclic Loading

Ajaya Kumar Gupta
Response Spectrum Method in Seismic Analysis and Design of Structures

C.S. Krishnamoorthy and S. Rajeev
Artificial Intelligence and Expert Systems for Engineers

Boris A. Krylov
Cold Weather Concreting

Pavel Marek, Milan Guštar and Thalia Anagnos
Simulation-Based Reliability Assessment for Structural Engineers

N.S. Trahair
Flexural-Torsional Buckling of Structures

Jan G.M. van Mier
Fracture Processes of Concrete

S. Vigneswaran and C. Visvanathan
Water Treatment Processes: Simple Options

FRACTURE AND SIZE EFFECT in Concrete and Other Quasibrittle Materials

Zdeněk P. Bažant
Walter P. Murphy Professor of Civil Engineering
and Materials Science
Northwestern University
Evanston, Illinois

Jaime Planas
Professor of Materials Science
E.T.S. Ingenieros de Caminos, Canales y Puertos
Universidad Politécnica de Madrid
Madrid, Spain

CRC Press
Boca Raton Boston London New York Washington, D.C.

Library of Congress Cataloging-in-Publication Data

Bažant, Z. P.
Fracture and size effect in concrete and other quasibrittle materials / Zdeněk P. Bažant and Jamie Planas.
p. cm.
Includes bibliographical references and index.
ISBN 0-8493-8284-X (alk. paper)
1. Concrete--Fracture,. 2. Fracture mechanics. 3. Elastic analysis (Engineering) I. Planas, Jaime. II. Title. III. Series.
TA440.B377 1997
620.1'.30426—dc21
for Library of Congress 97-26399
CIP

International Standard Book Number 0-8493-8284-X
Library of Congress Card Number 97-26399
Printed in the United States of America 2 3 4 5 6 7 8 9 0
Printed on acid-free paper

Preface

Our book is intended to serve as both a textbook for graduate level courses in engineering and a reference volume for engineers and scientists. We assume that the reader has the background of the B.S. level mechanics courses in the departments of civil, mechanical, or aerospace engineering. Aside from synthesizing the main results already available in the literature, our book also contains some new research results not yet published and many original derivations.

The subject of our book is important to structural, geotechnical, mechanical, aerospace, nuclear, and petroleum engineering, as well as materials science and geophysics. In our exposition of this subject, we try to proceed from simple to complex, from special to general. We try to be as concise as possible and use the lowest level of mathematics necessary to treat the subject clearly and accurately. We include the derivations or proofs of all the important results, as well as their physical justifications. We also include a large number of fully worked out examples and an abundance of exercise problems, the harder ones with hints. Our hope is that the reader will gain from the book true understanding rather than mere knowledge of the facts.

A special feature of our book is the theory of scaling of the failure loads of structures, and particularly the size effect on the strength of structures. We present a systematic exposition of this currently hot subject, which has gained prominence in current research. It has been only two decades that the classical model of size effect, based on Weibull-type statistical theory of random material strength, was found to be inadequate in the case of quasibrittle materials. Since then, a large body of results has been accumulated and is scattered throughout many periodicals and proceedings. We attempt to bring it together in a single volume. In treating the size effect, we try to be comprehensive, dealing even with aspects such as statistical and fractal, which are not normally addressed in the books on fracture mechanics.

Another special feature of our book is the emphasis on quasibrittle materials. These include concrete, which is our primary concern, as well as rocks, toughened ceramics, composites of various types, ice, and other materials. Owing to our concern with the size effect and with quasibrittle fracture, much of the treatment of fracture mechanics in our book is different from the classical treatises, which were concerned primarily with metals.

In its scope, our book is considerably larger than the subject matter of a single semester-length course. A graduate level course on fracture of concrete, with proper treatment of the size effect and coverage relevant also to other quasibrittle materials, may have the following contents: Chapter 1, highlights of Chapters 2, 3, and 4, then a thorough presentation of the main parts of Chapters 5, 6, 7, and 8, parts of Chapters 9 and 12, and closing with mere comments on Chapters 10, 11, and 13. A quarter-length course obviously requires a more reduced coverage.

The book can also serve as a text for a basic course on fracture mechanics. In that case, the course consists of a thorough coverage of Section 1.1 and Chapters 2, 3, 4, 5, and 7.

Furthermore, the book can be used as a text for a course on the scaling of fracture (i.e., the size effect), as a follow-up to the aforementioned basic course on fracture mechanics (or to courses on fracture mechanics based on other books). In that case, the coverage of this second course may be as follows: the rest of Chapters 1 and 5, a thorough exposition of Chapter 6, the rest of Chapters 7 and 8, much of Chapter 9, followed by highlights only of Chapter 10, bits of Chapter 11, and a thorough coverage of Chapter 12.

Chapters 13 and 14, the detailed coverage of which is not included in the foregoing course outlines, represent extensions important for computational modeling of fracture and size effect in structures. They alone can represent a short course, or they can be appended to the course on fracture of concrete or the course on scaling of fracture, although at the expense of the depth of coverage of the preceding chapters.

We were stimulated to write this book by our teaching of various courses on fracture mechanics, damage, localization, material instabilities, and scaling.[1] Our collaboration on this book began already in 1990, but had to proceed with many interruptions, due to extensive other commitments and duties. Most of the book was written between 1992 and 1995.

Our book draws heavily from research projects at Northwestern University funded by the Office of Naval Research, National Science Foundation, Air Force Office of Scientific Research, Waterways Experiment Station of the U.S. Army Corps of Engineers, Argonne National Laboratory, Department of Energy, and Sandia National Laboratories, as well as from research projects at the Universidad Politécnica de Madrid, funded by Dirección General de Investigación Científica y Técnica (Spain) and Comisión Interministerial de Ciencia y Tecnología (Spain). We are grateful to these agencies for their support.

The first author wishes to express his thanks to his father, Zdeněk J. Bažant, Professor Emeritus of Foundation Engineering at the Czech Technical University (ČVUT) in Prague, and to his grandfather Zdeněk Bažant, late Professor of Structural Mechanics at ČVUT, for having excited his interest in structural mechanics and engineering; to his colleagues and research assistants, for many stimulating discussions; and to Northwestern University, for providing an environment conducive to scholarly inquiry. He also wishes to thank his wife Iva for her moral support and understanding. Thanks are further due to Carol Surma, Robin Ford, Valerie Reed and Arlene Jackson, secretaries at Northwestern University, for their expert and devoted secretarial assistance.

The second author wishes to express his thanks to his mother María Rosselló, and to his sisters Joana María and María for their continuous encouragement. He also wishes to thank his wife Diana for her patience and moral support. He further expresses his thanks to Manuel Elices, professor and head of Department of Materials Science, for his continued teaching and support and for allowing the author to devote so much time to his work on this book; to assistant professor Gustavo V. Guinea for his stimulating discussions and friendly support; to Claudio Rocco, visiting scientist on leave from the Universidad de la Plata (Argentina), for providing test results and pictures for the section on the Brazilian test; to Gonzalo Ruiz, assistant professor, for providing test results and figures for the section on minimum reinforcement; and to all the colleagues, research students and personnel in the Department of Material Science, for their help in carrying out other duties which suffered from the author's withdrawal to his writing of the book.

Z.P.B. and J.P.
Evanston and Madrid
April, 1997

[1] In the case of the first author: The course on Fracture of Concrete, introduced at Northwestern University in 1988, and intensive short courses on these subjects taught at Politecnico di Milano (1981, 1993, 1997), Swiss Federal Institute of Technology, Lausanne (1987, 1989, 1994), Ecole Normale Supérieure de Cachan, France (1992), and Lulea University, Sweden (1994). In the case of the second author: The undergraduate courses on Fracture Mechanics and Continuum Mechanics and the doctoral-level courses of Physics of Continuum Media and Advanced Fracture Mechanics at the Universidad Politécnica de Madrid, and intensive short courses on Fracture Mechanics taught at Universidad Politécnica and at Universidad Carlos III in Madrid (1994, 1995), and at Universidad de la Plata, Argentina (1995).

Vector and Tensor Notation

In this book, both component and compact form are used for representation of vectors and tensors. Component notation is standard, since cartesian reference axes are used in general. For the compact notation that is used in several chapters to simplify the expressions, the following conventions are used:

1. Geometric vectors are bold faced lower case roman latin letters: e.g., $\mathbf{n}, \mathbf{t}, \mathbf{m}$.
2. Microplane or, in general, microscopic vectors are denoted by a superimposed arrow, thus $\vec{n}, \vec{\varepsilon}, \vec{\sigma}$.
3. Except for a few greek boldmath for classical stresses and strains ($\boldsymbol{\sigma}$ and $\boldsymbol{\varepsilon}$), second-order tensors are represented as bold face upper case roman latin letters, such as $\mathbf{E}, \mathbf{N}, \mathbf{M}, \mathbf{A}$, etc.
4. Fourth-order tensors are represented as bold faced upper case *italic* latin letters, such as $\boldsymbol{E}, \boldsymbol{C}, \boldsymbol{B}$, etc.
5. The transformation of a vector by a second-order tensor into another vector is represented by simple juxtaposition: $\mathbf{t} = \boldsymbol{\sigma}\mathbf{n}$ or $\mathbf{t} = \mathbf{T}\mathbf{n}$.
6. The transformation of a second-order tensor by a fourth-order tensor into another second-order tensor is represented by simple juxtaposition as well: $\boldsymbol{\sigma} = \boldsymbol{E}\boldsymbol{\varepsilon}$, $\boldsymbol{\varepsilon} = \boldsymbol{C}\boldsymbol{\sigma}$ or $\mathbf{H} = \boldsymbol{D}\mathbf{N}$, etc.
7. The inner-product of two vectors or two second-rank tensors is represented by a dot, e.g., $\vec{n}\cdot\vec{m}$, $\mathbf{n}\cdot\mathbf{m}$, $\vec{\sigma}\cdot\delta\vec{\varepsilon}$, $\boldsymbol{\sigma}\cdot\delta\boldsymbol{\varepsilon}$, $\mathbf{T}\cdot\dot{\mathbf{F}}$, etc. Accordingly, the expression $\mathbf{T}\cdot\boldsymbol{C}\mathbf{S}$ represents the inner product of the second order tensors $\mathbf{T}$ and $\mathbf{E} = \boldsymbol{C}\mathbf{S}$, the latter being the transformed by the fourth-order tensor $\boldsymbol{C}$ of the second-order tensor $\mathbf{S}$.

About the Authors

Born and educated in Prague, Dr. Zdeněk P. Bažant became in 1973 professor at Northwestern University, was named in 1990 to the distinguished W.P. Murphy Chair, and served during 1981-87 as Director (founding) of the Center for Concrete and Geomaterials. He has authored over 370 refereed journal articles and published books on Stability of Structures (1991), Concrete at High Temperatures (1996) and Creep of Concrete (1966). He served as Editor (in Chief) of ASCE Journal of Engineering Mechanics (1988-94), and is Regional Editor of the International Journal of Fracture and member of many other editorial boards. He was founding president of IA-FraMCoS, president of the Society of Engineering Science, and chairman of IA-SMiRT Division H. He has chaired many technical committees in ASCE, RILEM and ACI. He is a Registered Structural Engineer in Illinois. He has been staff consultant to Argonne National Laboratory and consulted for many firms and institutes. His awards include the Prager Medal from SES; Newmark Medal, Huber Prize and T.Y. Lin Award from ASCE; RILEM Medal; Humboldt Award; an honorary doctorate from ČVUT, Prague; Guggenheim, Kajima, JSPS, NATO and Ford Foundation Fellowships; Meritorious Paper Award from the Structural Engineering Association; Best Engineering Book of the Year Award from AAP; Medal of Merit from the Czech Society of Mechanichs; Gold Medal from the Building Research Institute of Spain; Honorary Memberships in the last two and in the Czech Society of Civil Engineers, and others. He is a Fellow of the American Academy of Mechanics, ASME, ASCE, RILEM and ACI. In 1996 he was elected to the National Academy of Engineering.

Dr. Jaime Planas received his degree in civil engineering in 1974 from the Universidad de Santander, Spain. He received his Ph.D. degree from the Universidad Politécnica de Madrid, Spain, in 1997. His doctoral thesis was awarded the Entrecanales Prize to the best thesis in soil mechanics and the Extraordinary Prize of the Polytechnical University of Madrid. He joined the Department of Materials Science of the Universidad Politécnica de Madrid, first as a lecturer (1975-77), later as assistant professor (1978-1988) and in 1989 he became professor. He teaches, or has taught, general physics, materials science, continuum mechanics, fracture mechanics and constitutive equations to students of civil engineering and of materials engineering. He conducted research on low temperature (-170 °C) mechanical properties of engineering materials and on fracture mechanics applied to materials for civil engineering. Since 1983 his main interest focused on fracture of concrete and quasibrittle materials. In this field, he actively participated in various RILEM and ESIS Technical Committees and published over 50 research papers and several reviews.

The authors in Segovia, Spain, in 1992. In the background, the aqueduct of Segovia, build by the Romans two thousand years ago.

Mému zesnulému dědečkovi Zdeňkovi, otci Zdeňkovi a matce Štěpánce, kteří pěstovali moji touhu o poznání, a ženě Ivě, která jí podporovala.[1]
Zdeněk P. Bažant

A mon pare i ma mare, a les meves germanes, i a la meva dona, amb el meu amor i les meves gràcies, ara i sempre.[2]
Jaime Planas

[1] To my late grandfather Zdeněk, father Zdeněk, and mother Štěpánka who nurtured my desire for knowledge, and my wife Iva who supported it.

[2] To my father and mother, to my sisters, and to my wife, with my love and my thanks, now and ever.

Dr. Zdeněk Bažant, one of the persons to whom this book is dedicated, was born on November 25, 1879, in Prostějov and died on September 1, 1954, in Nové Město na Moravě (both now in the Czech Republic). He was professor of structural mechanics and strength of materials at the Czech Technical University in Prague (ČVUT) and a member of the Czechoslovak Academy of Sciences. He was twice elected the rector (president) of ČVUT. He authored several books and many research articles in Czech, English, French, and German.

Contents

1

Why Fracture Mechanics?

Fracture mechanics is a failure theory that

1. determines material failure by *energy* criteria, possibly in conjunction with strength (or yield) criteria, and
2. considers failure to be *propagating* throughout the structure rather than simultaneous throughout the entire failure zone or surface.

While fracture mechanics has already been generally accepted in failure analysis of metal structures, especially in aerospace, naval, and nuclear engineering, its advent in the field of concrete structures is new. Therefore, after briefly outlining the history of this discipline, we will attempt in this introductory chapter to spell out the reasons for adopting the fracture mechanics approach and will focus especially on the structural size effect – the main reason for introducing fracture mechanics into the design of concrete structures.

1.1 Historical Perspective

Concrete structures are, of course, full of cracks. Failure of concrete structures typically involves stable growth of large cracking zones and the formation of large fractures before the maximum load is reached. So why has not the design of concrete structures been based on fracture mechanics, a theory whose principles have been available since the 1950s? Have concrete engineers been guilty of ignorance?

Not really. The forms of fracture mechanics that were available until recently were applicable only to homogeneous brittle materials, such as glass or to homogeneous typical structural metals. The question of applicability of these classical theories to concrete was explored long ago, beginning with Kaplan (1961) and others, but the answer was negative (e.g., Kesler, Naus and Lott 1972). Now, we understand that the reason for the negative answer was that the physical processes occurring in concrete fracture are very different from those taking place in the fracture of the aforementioned materials and, especially, that the material internal length scale for these fracture processes is much larger for concrete than for most materials. A form of fracture mechanics that can be applied to this kind of fracture has appeared only during the late 1970s and the 1980s.

Concrete design has already seen two revolutions. The first, which made the technology of concrete structures possible, was the development of the elastic no-tension analysis during 1900-1930. The second revolution, based on a theory conceived chiefly during the 1930s, was the introduction of plastic limit analysis during 1940-1970. There are now good reasons to believe that introduction of fracture mechanics into the design of concrete structures might be the third revolution. The theory, formulated mostly after 1980, finally appears to be ripe.

1.1.1 Classical Linear Theory

The stimulus for fracture mechanics was provided by a classical paper of Inglis (1913), who obtained the elastic solution for stresses at the vertex of an ellipsoidal cavity in an infinite solid and observed that, as the ellipse approaches a line crack (i.e., as the shorter axis tends to zero), the stress at the vertex of the ellipse tends to infinity (Fig. 1.1.1). Noting this fact, Griffith (1921, 1924) concluded that, in presence of a crack, the stress value cannot be used as a criterion of failure since the stress at the tip of a sharp crack in an elastic continuum is infinite no matter how small the applied load (Fig. 1.1.1b).

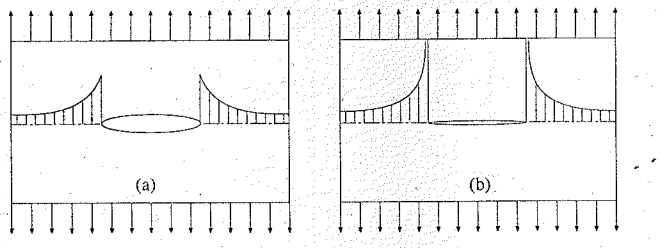

Figure 1.1.1 The stress at the ellipse vertices is finite in an elastic plate with an elliptical hole (a); but the stress concentration tends to infinity as the ellipse shrinks to a crack (b).

This led him to propose an energy criterion of failure, which serves as the basis of the classical linear elastic fracture mechanics (LEFM) or of the more general elastic fracture mechanics (EFM, in which linearity is not required). According to this criterion, which may be viewed as a statement of the principle of balance of energy, the crack will propagate if the energy *available* to extend the crack by a unit surface area equals the energy *required* to do so. Griffith took this energy to be equal to $2\gamma_s$, where γ_s is the specific surface energy of the elastic solid, representing the energy that must be supplied to break the bonds in the material microstructure and, thus, create a unit area of new surface.

Soon, however, it was realized that the energy actually required for unit crack propagation is much larger than this value, due to the fact that cracks in most materials are not smooth and straight but rough and tortuous, and are accompanied by microcracking, frictional slip, and plasticity in a sizable zone around the fracture tip. For this reason, the solid state specific surface energy $2\gamma_s$ was replaced by a more general *crack growth resistance,* $\mathcal{R}$, which, in the simplest approximation, is a constant. The determination of $\mathcal{R}$ has been, and still is, a basic problem in experimental fracture mechanics. The other essential problem of LEFM is the determination, for a given structure, of the energy available to advance the crack by a unit area. Today, this magnitude is called the *energy release rate,* and is usually called $\mathcal{G}$ (note that the rate is with respect to crack length, not time).

The early Griffith work was considered of a rather academic nature because it could only explain the failure of very brittle materials such as glass. Research in this field was not intensely pursued until the 1940s. The development of elastic fracture mechanics essentially occurred during 1940-1970, stimulated by some perplexing failures of metal structures (e.g., the fracture splitting of the hulls of the "Liberty" ships in the U.S. Navy during World War II). During this period, a good deal of theoretical, numerical, and experimental work was accomplished to bring LEFM to its present state of mature scientific discipline.

In a highly schematic vision, the essence of the theoretical work consisted in generalizing Griffith's ideas, which he had worked out only for a particular case, to any situation of geometry and loading, and to link the energy release rate $\mathcal{G}$ (a structural, or global, quantity) to the elastic stress and strain fields. The essence of the experimental work consisted in setting up test methods to measure the crack growth resistance $\mathcal{R}$. In the energetic approach, the last theoretical step was the discovery of the J-integral by Rice (1968a,b). It gave a key that closed, on very general grounds, the circle relating the energy release rate to the stress and strain fields close to the crack tip for any elastic material, linear or not, and supplied a logical tool to analyze fracture for more general nonlinear behaviors. Today, it is one of the cornerstones of elastoplastic fracture mechanics, the branch of fracture mechanics dealing with fracture of ductile materials.

The second major achievement in the theoretical foundation of LEFM was due to Irwin (1957), who introduced the concept of the stress intensity factor K as a parameter for the intensity of stresses close to the crack tip and related it to the energy release rate. Irwin's approach had the enormous advantage that the stress intensity factors are additive, while Griffith's energy release rates were not. However, his approach was limited to linear elasticity, while the concept of energy release rate was not.

1.1.2 Classical Nonlinear Theories

LEFM, which is expounded in Chapters 2–4, provides the basic tool today for the analysis of many structural problems dealing with crack growth, such as safety in presence of flaws, fatigue crack growth, stress corrosion cracking, and so on. However, soon after the introduction of the fracture mechanics concepts, it became evident that LEFM yielded good predictions only when fracture was very brittle, which meant that most of the structure had to remain elastic up to the initiation of fracture. This was not the case for many practical situations, in particular, for tough steels which were able to develop large plastic zones near the crack tip before tearing off. The studies of Irwin, Kies and Smith (1958) identified the size of the yielding zone at the crack tip as the source of the misfit. Then, various nonlinear fracture mechanics theories were developed, more or less in parallel. Apart from elastoplastic fracture mechanics (essentially based on extensions of the J-integral concept, and outside the scope of this book), two major descriptions were developed: equivalent elastic crack models and cohesive crack models.

In the equivalent crack models, which will be presented in detail in Chapters 5 and6, the nonlinear zone is approximately simulated by stating that its effect is to decrease the stiffness of the body, which is approximately the same as increasing the crack length while keeping everything else elastic. This longer crack is called the effective or equivalent crack. Its treatment is similar to LEFM except that some rules have to be added to express how the equivalent crack extends under increased forces. In this context, Irwin (1958) in general terms, and more clearly Krafft, Sullivan and Boyle (1961), proposed the so-called R-curve (resistance curve) concept, in which the crack growth resistance $\mathcal{R}$ is not constant but varies with the crack length in a manner empirically determined in advance. This simple concept still remains a valuable tool provided that the shape of the R-curve is correctly estimated, taking the structure geometry into account.

For concrete, the equivalent crack models proposed by Jenq and Shah (1985a,b) and Bažant and co-workers are among the most extended and have led to test recommendations for fracture properties of concrete (see Chapters 5 and 6). The 1980s have also witnessed a rise of interest in the size effect, as one principal consequence of fracture mechanics. A simple approximate formula for the effect of structure size on the nominal strength of structures has been developed (Bažant 1984a) and later exploited, not only for the predictions of failures of structures, but also as the basis of test recommendations for the determination of nonlinear fracture properties, including the fracture energy, the length of the fracture process zone, and the R-curve. This R-curve concept has also been applied to ceramics and rocks with some success, although until recently it has not been recognized that the R-curves are not a true material property but depend on geometry.

The cohesive crack models, which are discussed in detail in Chapter 7, were developed to simulate the nonlinear material behavior near the crack tip. In these models, the crack is assumed to extend and to open while still transferring stress from one face to the other. The first cohesive model was proposed by Barenblatt (1959, 1962) with the aim to relate the macroscopic crack growth resistance to the atomic binding energy, while relieving the stress singularity (infinite stress was hard to accept for many scientists). Barenblatt simulated the interatomic forces by introducing distributed cohesive stresses on the newly formed crack surfaces, depending on the separation between the crack faces. The distribution of these cohesive atomic forces was to be calculated so that the stress singularity would disappear and the stresses would remain bounded everywhere. Barenblatt postulated that the cohesive forces were operative on only a small region near the crack tip, and assumed that the shape of the crack profile in this zone was independent of the body size and shape. Balancing the external work supplied to the crack tip zone —which he showed to coincide with Griffith's $\mathcal{G}$— against the work of the cohesive forces —which was $2\gamma_s$ by definition— he was able to recover the Griffith's results while eliminating the uncomfortable stress singularity.

Dugdale (1960) formulated a model of a line crack with a cohesive zone with constant cohesive stress (yield stress). Although formally close to Barenblatt's, this model was intended to represent a completely different physical situation: macroscopic plasticity rather than microscopic atomic interactions. Both models share a convenient feature: the stress singularity is removed. Although very simplified, Dugdale's approach to plasticity gave a good description of ductile fracture for not too large plastic zone sizes. However, it was not intended to describe fracture itself and, in Dugdale's formulation, the plastic zone extended forever without any actual crack extension.

More elaborate cohesive crack models have been proposed with various names (Dugdale-Barenblatt models, fictitious crack models, bridged crack models, cracks with closing pressures, etc.). Such models

include specific stress-crack opening relations simulating complete fracture (with a vanishing transferred stress for large enough crack openings) to simulate various physically different fracture mechanisms: crazing in polymers (which must take viscoelastic strains into account, see Chapter 11), fiber and crack bridging in ceramics, and frictional aggregate interlock and crack overlapping in concrete. All these models share common features; in particular, a generic model can be formulated such that all of them become particular cases, and the mathematical and numerical tools are the same (Elices and Planas 1989).

However, the fictitious crack model proposed by Hillerborg for concrete (Hillerborg, Modéer and Petersson 1976) merits special comment . In general, all the foregoing fracture mechanics theories require a preexisting crack to analyze the failure of a structure or component. If there is no crack, neither LEFM nor EFM, equivalent crack models or classical cohesive crack models, can be applied. This is not so with Hillerborg's fictitious crack model. It is a cohesive crack in the classical sense described above, but it is more than that because it includes crack initiation rules for any situation (even if there is no precrack). This means that it can be applied to initially uncracked concrete structures and describe all the fracture processes from no crack at all to complete structural breakage. It provides a continuous link between the classical strength-based analysis of structures and the energy-based classical fracture mechanics: cohesive cracks start to open as dictated by a strength criterion that naturally and smoothly evolves towards an energetic criterion for large cracks. We will discuss this model in detail in Chapter 7.

1.1.3 Continuum-Based Theories

The foregoing description is, at least for concrete, only half of the story: the half dealing with researchers interested in discovering when and how a preexisting crack-like flaw or defect would grow. The other half deals with structural engineers wanting to describe the crack formation and growth from an initially flaw-free structure (in a macroscopic sense). The first finite element approaches to that problem consisted in reducing to zero the stiffness of the elements in which the tensile strength was reached (Rashid 1968). Later, more sophisticated models were used with progressive failure of the elements (progressive softening) and, starting with the work of Kachanov (1958), there was a great proliferation of continuum damage mechanics models with internal variables describing softening.

However, even though some results were very promising, it later became apparent that numerical analysis using these continuum models with softening yielded results strongly dependent on the size of the elements of the finite element mesh (see the next section for details). To overcome this difficulty while keeping the continuum mechanics formulation —which seems more convenient for structural analysis— Bažant developed the crack band model in which the crack was simulated by a fracture band of a fixed thickness (a material property) and the strain was uniformly distributed across the band (Bažant 1976, 1982; Bažant and Cedolin 1979, 1980; Bažant and Oh 1983a; Rots et al. 1985). This approximation, analyzed in depth in Chapter 8, was initially rivalling Hillerborg's model, but it soon became apparent that they were numerically equivalent (Elices and Planas 1989).

Since the 1980s, a great effort, initiated by Bažant (1984b) with the imbricate continuum, was devoted to develop softening continuum models that can give a consistent general description of fracture processes without further particular hypotheses regarding when and how the fracture starts and develops. In the nonlocal continuum approach, discussed in Chapter 13, the nonlinear response at a point is governed not only by the evolution of the strain at that point but also by the evolution of the strains at other points in the neighborhood of that point. These models, which probably constitute the most general approach to fracture, evolved from the early nonlocal elastic continua (Eringen 1965, 1966; Kröner 1967) to nonlocal continua in which the nonlocal variables are internal irreversible variables such as damage or inelastic strain (Pijaudier-Cabot and Bažant 1987; Bažant and Lin 1988a,b). Higher-order continuum models, in which the response at a point depends on the strain tensor and on higher order gradients (which include Cosserat continua) are related to the nonlocal model and are also intended to handle fracture in a continuum framework (e.g., de Borst and Mühlhaus 1991). However, the numerical difficulties associated with using generalized continuum models make these models available for practical use to only a few research groups. Moreover, sound theoretical analysis concerning convergence and uniqueness is still lacking, which keeps these models somewhat provisional. Nevertheless, the generalizing power of these models is undeniable and they can provide a firm basis to extend some simpler and well accepted models. It has been recently shown, for example, that the cohesive crack models arise as rigorous solutions of a certain class of nonlocal models (Planas, Elices and Guinea 1993).

1.1.4 Trends in Fracture of Quasibrittle Materials

The research activity in fracture mechanics of quasibrittle materials —concrete, rocks, ceramics, composites, ice, and some polymers— experienced a burst of activity during the 1980s. Much research effort was —and still is— devoted to refine the foregoing models, to improve the analytical and numerical tools required to handle the models, to develop experimental methods to measure the parameters entering the various theories, and to relate the macroscopic fracture behavior to the microstructural features of the materials. In this respect, idealized models reflecting the heterogeneous nature of concrete have been developed to help understanding of the macroscopic behavior (see Chapter 14 for details). Extensive bibliographies and historical reviews of concrete fracture mechanics have recently appeared in the reports of various committees (Wittmann 1983; Elfgren 1989; ACI Committee 446 1992).

Recently, it is being recognized that fractures of concrete and of modern toughened ceramics exhibit strong similarities. Their exploitation should benefit both disciplines. In fact, the way to toughen ceramics is to make them behave more like concrete, especially reinforced concrete.

At present, we are entering a period in which introduction of fracture mechanics into concrete design is becoming possible (see Chapter 10). This will help achieve more uniform safety margins, especially for structures of different sizes. This, in turn, will improve economy as well as structure reliability. It will make it possible to introduce new designs and utilize new concrete materials. Fracture mechanics will no doubt be especially important for high-strength concrete structures, fiber-reinforced concrete structures, concrete structures of unusually large sizes, and other novel structures. Applications of fracture mechanics are most urgent for structures such as concrete dams and nuclear reactor vessels or containments, for which the safety concerns are particularly high and the consequences of a potential disaster enormous.

One of the simplest ways to incorporate fracture mechanics into design practice is through the size effect, or modification of structural strength with the size of the structure. The analysis of size effect starts later in this chapter and permeates most of the book.

1.2 Reasons for Fracture Mechanics Approach

Since concrete structures have been designed and successfully built according to codes that totally ignore fracture mechanics theory, it might seem unnecessary to change the current practice. Nevertheless, there are five compelling reasons for doing so.

Reason 1: Energy required for crack formation must be taken into account.

Reason 2: The results of the structural analysis must be objective.

Reason 3: The structural analysis must agree with the absence of yield plateau from the load-deflection diagram.

Reason 4: The structural analysis must adequately compute the energy absorption capability and ductility.

Reason 5: The structural analysis must capture the size effect.

Let us examine these reasons in more detail.

1.2.1 Energy Required for Crack Formation

From the strictly physical viewpoint, it must be recognized that while crack initiation may depend on stress, the actual formation of cracks requires a certain energy —the fracture energy. Hence, energy criteria should be used. This reason might suffice to a physicist, but not to a designer, at least at a first glance. There are, however, more practical reasons for taking the fracture mechanics approach.

1.2.2 Objectivity of Analysis

A physical theory must be objective, in the sense that the results of calculations made with it must not depend on subjective aspects such as the choice of coordinates, the choice of mesh, etc. If a theory is found

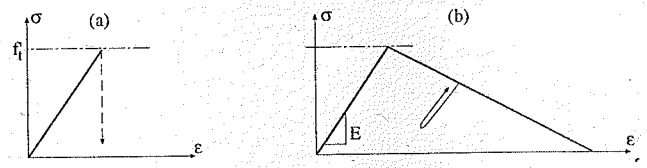

Figure 1.2.1 Softening stress-strain curves in smeared cracking models: (a) step softening; (b) progressive softening (from ACI Committee 446 1992).

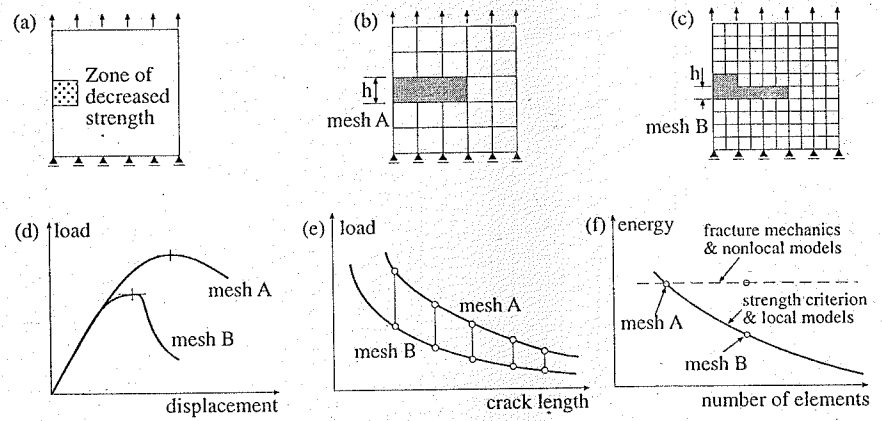

Figure 1.2.2 Illustration of lack of mesh-objectivity in classical smeared crack models (adapted from ACI Committee 446 1992).

to be unobjective, it must be rejected. There is no need to even compare it to experiments. Objectivity comes ahead of experimental verification.

A powerful, widely used approach to finite element analysis of concrete cracking is the concept of smeared cracking, introduced by Rashid (1968), which does not utilize fracture mechanics. According to this concept, the stress in a finite element is limited by the tensile strength of the material, f_t'. After the strength limit is reached, the stress in the finite element must decrease. In the initial practice, the stress was assumed to drop suddenly to zero, but it was soon realized that better and more realistic results are usually obtained if the stress is reduced gradually, i.e., the material is assumed to exhibit gradual strain softening (Scanlon 1971; Lin and Scordelis 1975); see Fig. 1.2.1. The concept of sudden or gradual strain-softening, though, proved to be a mixed blessing. After this concept had been implemented in large finite element codes and widely applied, it was discovered that the convergence properties are incorrect and the calculation results are unobjective as they significantly depend on the analyst's choice of the mesh (Bažant 1976, 1983; Bažant and Cedolin 1979, 1980, 1983; Bažant and Oh 1983a; Darwin 1985; Rots et al. 1985).

This problem, known as spurious mesh sensitivity, can be illustrated, for example, by the rectangular panel in Fig. 1.2.2a, which is subjected to a uniform vertical displacement at the top boundary. A small region near the center of the left side is assumed to have a slightly smaller strength than the rest of the panel, and consequently a smeared crack band starts growing from left to right. The solution is obtained by incremental loading with two finite element meshes of very different mesh sizes, as shown (Fig 1.2.2b,c). Stability check indicates that cracking must always localize in this problem into a band of single-element width at the cracking front. Typical numerical results for this as well as other similar problems are illustrated in Fig. 1.2.2d–f. In the load-deflection diagram (Fig. 1.2.2d), one can see that the

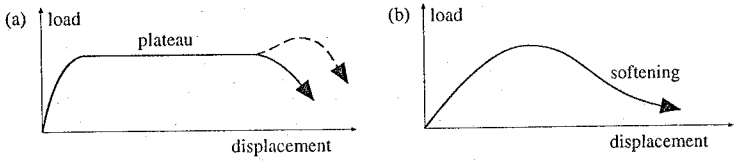

Figure 1.2.3 Load-deflection curves with and without yielding plateau (adapted from ACI Committee 446 1992).

peak load as well as the post-peak softening strongly depends on the mesh size, the peak load being roughly proportional to $h^{-1/2}$ where h is the element size. Plotting the load vs. the length of the crack band, one again finds large differences (Fig. 1.2.2e). The energy that is dissipated due to cracking decreases with the refinement of the mesh (Fig. 1.2.2f), and converges to zero as $h \to 0$, which is, of course, physically unacceptable.

The only way to avoid the foregoing manifestations of unobjectivity is some form of fracture mechanics or nonlocal model. By specifying the energy dissipated by cracking per unit length of the crack or the crack band, the overall energy dissipation is forced to be independent of the element subdivision (see the horizontal dashed line in Fig. 1.2.2f), and so is the maximum load.

1.2.3 Lack of Yield Plateau

Based on load-deflection diagrams, one may distinguish two basic types of structural failure: plastic and brittle. The typical characteristic of plastic failure is that the structure develops a single-degree-of-freedom mechanism such that the failure in various parts of the structure proceeds simultaneously, in proportion to a single parameter. Such failures are manifested by the existence of a long yield plateau on the load-deflection diagram (Fig. 1.2.3a). If the load-deflection diagram lacks such a plateau, the failure is not plastic but brittle (Fig. 1.2.3b) . When there are nosignificant geometric effects (such as the P–Δ effect in buckling), the absence of a plateau implies the existence of softening in the material due to fracture, cracking, or other damage. This further implies that the failure process cannot develop a single-degree-of-freedom mechanism but consists of propagation of the failure zones throughout the structure. The failure is nonsimultaneous and propagating.

To illustrate such behavior, consider the punching shear failure of a slab (Fig. 1.2.4). The typical (approximate) distributions of tensile stress σ along the failure surface are drawn in the figure. If the material is plastic, the cross-section gradually plasticizes until all its points are at the yield limit (Fig. 1.2.4b). However, if the material exhibits strain softening, then the stress peak moves across the failure zone, leaving a reduced stress (strain softening) in its wake (Fig. 1.2.4c,d). The stress reduction in the wake is mild if the structure is small, in which case the plastic limit analysis is not too far off (Fig. 1.2.4c). If the structure is large, however, the stress profile develops a steep stress drop behind the peak-stress point, and then the limit analysis solutions grossly overestimate the failure load (Fig. 1.2.4d).

1.2.4 Energy Absorption Capability and Ductility

The area under the entire load-deflection diagram represents the energy that the structure will absorb during failure. Consideration of this energy is important, especially for dynamic loading, and determines the ductility of the structure. Plastic limit analysis can give no information on the post-peak decline of the load and the energy dissipated in this process. According to plasticity, the load is constant after the peak, and the energy absorption theoretically unlimited. So some form of fracture mechanics is inevitable.

1.2.5 Size Effect

The size effect is, for design engineers, the most compelling reason for adopting fracture mechanics. Therefore, we discuss it more thoroughly now, and we will return to it in considerable detail in future

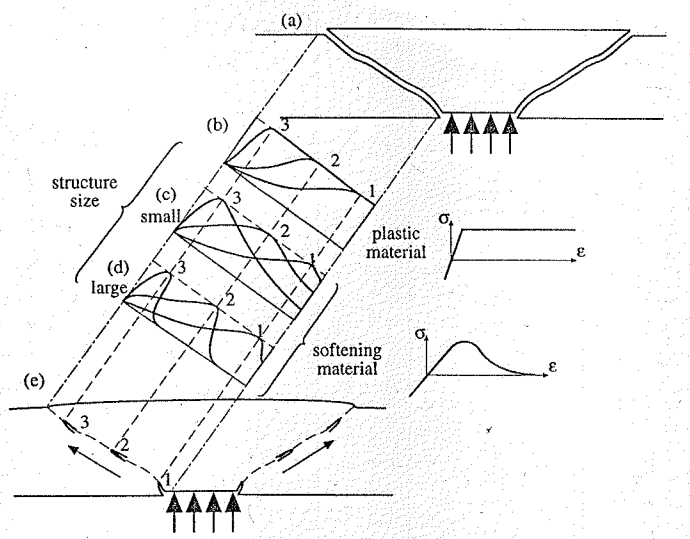

Figure 1.2.4 Influence of the structure size on the length of the yielding plateau in a punched slab (from ACI Committee 446 1992).

chapters. By general convention, the load capacity predicted by plastic limit analysis or any (deterministic) theory in which the material failure criterion is expressed in terms of stress or strain (or both) are said to exhibit no size effect. The size effect represents the deviation from such a prediction, i.e., the size effect on the structural strength is the deviation, engendered by a change of structure size, of the actual load capacity of a structure from the load capacity predicted by plastic limit analysis (or any theory based on critical stresses or strains).

The size effect is rigorously defined through a comparison of geometrically similar structures of different sizes. It is conveniently characterized in terms of the nominal strength, σ_{Nu}, representing the value of the nominal stress, σ_N, at maximum (ultimate) load, P_u. The nominal stress, which serves as a load parameter, may, but need not, represent any actual stress in the structure and may be defined simply as $\sigma_N = P/bD$ when the similarity is two-dimensional or as P/D^2 when the similarity is three-dimensional; b = thickness of a two-dimensional structure, and D = characteristic dimension of the structure, which may be chosen as any dimension, e.g., the depth of the beam, or the span, or half of the span, since only the relative values of σ_N matter. The nominal strength is then $\sigma_{Nu} = P_u/bD$ or P_u/D^2 (see Section 1.4.1 for more details).

According to the classical failure theories, such as the elastic analysis with allowable stress, plastic limit analysis, or any other theory that uses some type of a strength limit or failure surface in terms of stress or strain (e.g., viscoelasticity, viscoplasticity), σ_{Nu} is constant, i.e., independent of the structure size, for any given geometry, *notched or not*. We can, for example, illustrate it by considering the elastic and plastic formulas for the strength of beams in bending shear and torsion. These formulas are found to be of the same form except for a multiplicative factor. Thus, if we plot $\log \sigma_{Nu}$ vs. $\log D$, we find the failure states, according to strength or yield criteria, to be always given by a horizontal line (dashed line in Fig. 1.2.5). So, the failures according to the strength or yield criteria exhibit no size effect.

By contrast, failures governed by linear elastic fracture mechanics exhibit a rather strong size effect, which in Fig. 1.2.5 is described by the inclined dashed line of slope $-1/2$, as we shall justify in Chapter 2. The reality for concrete structures is a transitional behavior illustrated by the solid curve in Fig. 1.2.5. This curve approaches a horizontal line for the strength criterion if the structure is very small, and an inclined straight line of slope $-1/2$ if the structure is very large.

There is another size effect that calls for the use of fracture mechanics. It is the size effect on ductility

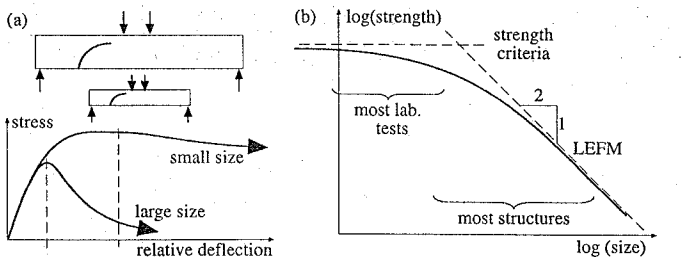

Figure 1.2.5 Size effects: (a) on the curves of nominal stress vs. relative deflection, and (b) on the strength in a bilogarithmic plot (adapted from ACI Committee 446 1992).

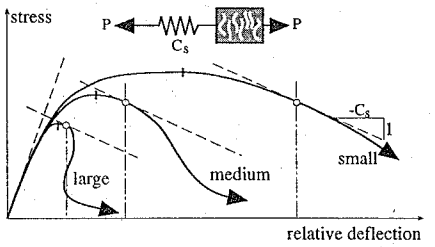

Figure 1.2.6 Size effect on the structural ductility (adapted from ACI Committee 446 1992).

of the structure, which is the opposite of brittleness, and may be characterized by the deformation at which the structure fails under a given type of loading. For loading in which the load is controlled, structures fail (i.e., become unstable) at their maximum load, while for loading in which the displacement is controlled, structures fail in their post-peak, strain-softening range. In a plot of σ_N vs. the deflection, the failure point is characterized by a tangent (dashed line in Fig. 1.2.6) of a certain constant inverse slope $-C_s$ where C_s is the compliance of the loading device (see e.g., Bažant and Cedolin 1991, Sec. 13.2). Geometrically similar structures of different sizes typically yield load-deflection curves of the type shown in Fig. 1.2.6. As illustrated, failure occurs closer to the peak as the size increases. This effect is again generally predicted by fracture mechanics, and is due to the fact that in a larger structure more strain energy is available to drive the propagation of the failure zone.

The well-known effect of structure size or member size on crack spacing and crack width is, to a large extent, also explicable by fracture mechanics. It may also be noted that the spurious effect of mesh size (Reason 2, Section 1.2.2) can be regarded as a consequence of the structural size effect.

1.3 Sources of Size Effect on Structural Strength

There are six different size effects that may cause the nominal strength to depend on structure size:

I. Boundary layer effect, also known as the wall effect. This effect is due to the fact that the concrete layer adjacent to the walls of the formwork has inevitably a smaller relative content of large aggregate pieces and a larger relative content of cement and mortar than the interior of the member. Therefore, the surface layer, whose thickness is independent of the structure size and is of the same order of magnitude as the maximum aggregate size, has different properties. The size effect is due to the fact that in a smaller member, the surface layer occupies a large portion of

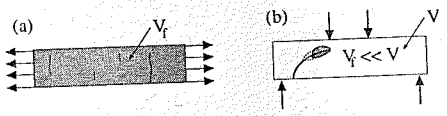

Figure 1.3.1 The essence of the difference between statistical and fracture size effect (adapted from ACI Committee 446 1992).

the cross-section, while in a large member, it occupies a small part of the cross-section. In most situations, this type of size effect does not seem to be very strong. A second type of boundary layer effect arises because, under normal stress parallel to the surface, the mismatch between the elastic properties of aggregate and mortar matrix causes transverse stresses in the interior, while at the surface these stresses are zero. A third type of boundary layer size effect arises from the Poisson effect (lateral expansion) causing the surface layer to nearly be in plane stress, while the interior is nearly in plane strain. This causes the singular stress field at the termination of the crack front edge at the surface to be different from that at the interior points of the crack front edge (Bažant and Estenssoro 1979). A direct consequence of this, easily observable in fatigue crack growth in metals, is that the termination of the front edge of a propagating crack cannot be orthogonal to the surface. The second and third types exist even if the composition of the boundary layer and the interior is the same.

2. *Diffusion phenomena*, such as heat conduction or pore water transfer. Their size effect is due to the fact that the diffusion half-times (i.e., half-times of cooling, heating, drying, etc.) are proportional to the square of the size of the structure. At the same time, the diffusion process changes the material properties and produces residual stresses which in turn produce inelastic strains and cracking. For example, drying may produce tensile cracking in the surface layer of the concrete member. Due to different drying times and different stored energies, the extent and density of cracking may be rather different in small and large members, thus engendering a different response. For long-time failures, it is important that drying causes a change in concrete creep properties, that creep relaxes these stresses, and that in thick members the drying happens much slower than in thin members.
3. *Hydration heat* or other phenomena associated with chemical reactions. This effect is related to the previous one in that the half-time of dissipation of the hydration heat produced in a concrete member is proportional to the square or the thickness (size) of the member. Therefore, thicker members heat to higher temperatures, a well-known problem in concrete construction. Again, the nonuniform temperature rise may cause cracking, induce drying, and significantly alter the material properties.
4. *Statistical size effect*, which is caused by the randomness of material strength and has traditionally been believed to explain most size effects in concrete structures. The theory of this size effect, originated by Weibull (1939), is based on the model of a chain. The failure load of a chain is determined by the minimum value of the strength of the links in the chain, and the statistical size effect is due to the fact that the longer the chain, the smaller is the strength value that is likely to be encountered in the chain. This explanation, which certainly applies to the size effect observed in the failure of a long concrete bar under tension (Fig. 1.3.1), is described by Weibull's weakest-link statistics. However, as we will see in Chapter 12, on closer scrutiny, this explanation is found to be inapplicable to most types of failures of reinforced concrete structures. In contrast to metallic and other structures, which fail at the initiation of a macroscopic crack (i.e., as soon as a microscopic flaw or crack reaches macroscopic dimensions), concrete structures fail only after a large stable growth of cracking zones or fractures. The stable crack growth causes large stress redistributions and a release of stored energy, which, in turn, causes a much stronger size effect, dominating over any possible statistical size effect. At the same time, the mechanics of failure restricts the possible locations of the decisive crack growth at the moment of failure to a very small zone. This causes the random strength values outside this zone to become irrelevant, thus suppressing the statistical size effect. We will also see that some recent experiments on diagonal shear failure of reinforced concrete beams contradict the prediction of the statistical theory.

5. *Fracture mechanics size effect*, due to the release of stored energy of the structure into the fracture front. This is the most important source of size-effect, and will be examined in more detail in the next section and thoroughly in the remainder of the book.
6. *Fractal nature of crack surfaces.* If fractality played a significant role in the process of formation of new crack surface, it would modify the fracture mechanics size effect. However, such a role is not indicated by recent studies (Chapter 12 and Bažant 1997d). Probably this size effect is only a hypothetical conjecture.

In practical testing, the first 3 sources of size effect can be, for the most part, eliminated if the structures of different sizes are geometrically similar in two rather than three dimensions, with the same thickness for all the sizes. Source 1 becomes negligible for sufficiently thick structures. Source 2 is negligible if the specimen is sealed and is at constant temperature. Source 3 is significant only for very massive structures. The statistical size effect is always present, but its effect is relatively unimportant when the fracture size effect is important. Let us now give a simple explanation of this last and dominant size effect.

1.4 Quantification of Fracture Mechanics Size Effect

In the classical theories based on plasticity or limit analysis, the strength of geometrically similar structures is independent of the structure size. As already pointed out, however, concrete structures and, in general, structures made of brittle or quasibrittle materials, do not follow this trend. In this section we first define what is understood by strength and size of a structural element and then examine how the strength depends on the size. We finally give a simple justification of Bažant's size effect law. The experimental evidence supporting the existence of size effect will be presented in the next section.

1.4.1 Nominal Stress and Nominal Strength

The size effect is understood as the dependence of the structure strength on the structure size. The strength is conventionally defined as the value of the so-called *nominal stress* at the peak load. The nominal stress is a load parameter defined as proportional to the load divided by a typical cross-sectional area:

$$\sigma_N = c_N \frac{P}{bD} \quad \text{for } 2D \text{ similarity}, \qquad \sigma_N = c_N \frac{P}{D^2} \quad \text{for } 3D \text{ similarity} \tag{1.4.1}$$

in which P = applied load, b = thickness of a two-dimensional structure (which, for certain reasons, in experiments should be preferably chosen the same for all structure sizes); D = characteristic dimension of the structure or specimen; and c_N = coefficient introduced for convenience, which can be chosen as $c_N = 1$, if desired. For $P = P_u$ = maximum load, Eq. (1.4.1) gives the nominal strength, σ_{Nu}.

Coefficient c_N can be chosen to make Eq. (1.4.1) coincide with the formula for the stress in a certain particular point of a structure, calculated according to a certain particular theory. For example, consider the simply supported beam of span S and depth h, loaded at mid-span by load P, as shown in Fig. 1.4.1a. Now we may choose, for example, σ_N to coincide with the elastic bending formula for the maximum normal stress in the beam (Fig. 1.4.1b), and the beam depth as the characteristic dimension ($D = h$), in which case we have

$$\sigma_N = \frac{3PS}{2bh^2} = c_N \frac{P}{bD}, \text{ with } c_N = 1.5\frac{S}{h} \tag{1.4.2}$$

It appears that c_N depends on the span-to-depth ratio which can vary for various beams. It is thus important to note that the size effect may be consistently defined only by considering geometrically similar specimens or structures of different sizes, with geometrically similar notches or initial cracks. Without geometric similarity, the size effect would be contaminated by the effects of varying structure shape. With this restriction (most often implicitly assumed), coefficient c_N is constant because, for geometrically similar structures, S/h is constant by definition.

The foregoing definition of σ_N is not the only one possible. Alternatively, we may choose σ_N to

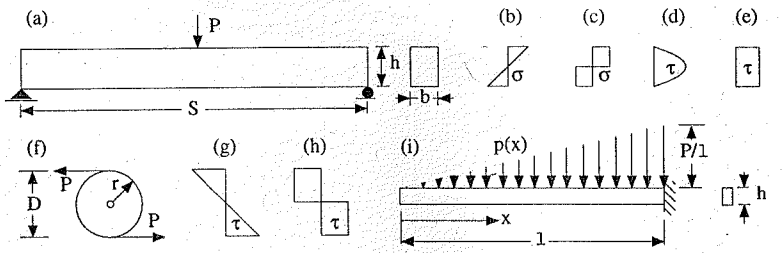

Figure 1.4.1 (a) Three-point bent beam. (b) Elastic stress distribution. (c) Plastic stress distribution. (d) Elastic shear stress distribution. (e) Plastic shear stress distribution. (f) Shaft subjected to torsion. (g) Elastic shear stress distribution. (h) Plastic shear stress distribution. (i) Cantilever beam with linearly distributed load.

coincide with the plastic bending formula for the maximum stress (Fig. 1.4.1c), in which case we have

$$\sigma_N = \frac{PS}{bh^2} = c_N \frac{P}{bD}\ , \text{ with } c_N = \frac{S}{h}\ (= \text{ constant}) \tag{1.4.3}$$

Alternatively, we may choose as the characteristic dimension the beam span instead of the beam depth ($D = S$), in which case we have

$$\sigma_N = \frac{3PS}{2bh^2} = c_N \frac{P}{bD}\ , \text{ with } c_N = 1.5\frac{S^2}{h^2}\ (= \text{ constant}) \tag{1.4.4}$$

We may also choose σ_N to coincide with the formula for the maximum shear stress near the support according to the elastic bending theory (Fig. 1.4.1d), in which case we have, with $D = h$,

$$\sigma_N = \frac{3P}{4bh} = c_N \frac{P}{bD}\ , \text{ with } c_N = 0.75\ (= \text{ constant}) \tag{1.4.5}$$

Alternatively, using the span as the characteristic dimension ($D = S$), we may write

$$\sigma_N = \frac{3P}{4bh} = c_N \frac{P}{bD}\ , \text{ with } c_N = \frac{3S}{4h}\ (= \text{ constant}) \tag{1.4.6}$$

All the above formulae are valid definitions of the nominal strength for three-point bent beams, although the first one (1.4.2) is the most generally used (and that used throughout this book). Other examples are given next.

Example 1.4.1 Consider torsion of a circular shaft of radius r, loaded by torque $T = 2Pr$ where P is the force couple shown in Fig. 1.4.1f. Using σ_N to coincide with the elastic formula for the maximum shear stress, we may write, taking $D = 2r =$ diameter,

$$\sigma_N = \frac{4P}{\pi r^2} = \frac{16P}{\pi D^2} = c_N \frac{P}{D^2}\ , \text{ with } c_N = \frac{16}{\pi}\ (= \text{ constant}) \tag{1.4.7}$$

If, instead, we chose the radius as the characteristic dimension ($D = r$), we may write

$$\sigma_N = \frac{4P}{\pi r^2} = c_N \frac{P}{D^2}\ , \text{ with } c_N = \frac{4}{\pi}\ (= \text{ constant}) \tag{1.4.8}$$

Note that in this case we have a three-dimensional similarity. □

Example 1.4.2 Consider the cantilever of span ℓ and cross-section depth h shown in Fig. 1.4.1i, which is loaded by distributed load $p(x)$ increasing linearly from the cantilever end. We chose the value of the distributed load at the fixed end to be denoted as P/ℓ (ℓ is used to achieve the correct dimension). Now,

choosing σ_N to coincide with the elastic bending formula for the maximum stress, and the characteristic dimension to coincide with the beam depth ($D = h$), we may write

$$\sigma_N = \frac{P\ell}{bh^2} = c_N \frac{P}{bD}\ , \text{ with } c_N = \frac{\ell}{h}\ (=\text{constant}) \tag{1.4.9}$$

which is again of the same form. □

To sum up, the nominal stress can be defined by the simple equation (1.4.1) regardless of the complexity of structure shape and material behavior, and can be used as a load parameter having the dimension of stress.

1.4.2 Size Effect Equations

With the foregoing definitions, the size effect consists in the variation of the nominal strength σ_{Nu} with size D. There are various possible plots showing special aspects of the size effect, but the most widely used is the bilogarithmic plot already shown in Fig. 1.2.5 in which $\log \sigma_{Nu}$ is plotted vs. $\log D$. As previously discussed in Section 1.2.5, the strength theory (based on yield or strength criteria) predicts no size effect (horizontal dashed line in Fig. 1.2.5b); this is the kind of response assumed in most engineering approaches and codes (see Chapter 10 for a detailed discussion about the need of including the size effect in the codes.) On the other extreme, we have the purely brittle behavior of structures that fail by crack instability at a fixed crack-to-size ratio (relative crack length). In the next chapter, after presenting the essentials of linear elastic fracture mechanics (LEFM) we will see that the size effect in such a case is shown in the plot of Fig. 1.2.5b as an inclined line of slope -1/2. The actual size effect behavior is best described by a transitional curve having the two straight lines as asymptotes, as sketched in Fig. 1.2.5b.

The simplest size effect law satisfying this condition was derived by Bažant (1984a) under very mild assumptions which apply, approximately, to a large number of practical cases. Bažant's size effect equation brings into play the energy required for crack growth as shown in the next paragraph, where a short derivation is presented. However, the final expression can be written (without explicitly showing the fracture energy term) as a function depending on only two parameters as

$$\sigma_{Nu} = \frac{Bf'_t}{\sqrt{1 + D/D_0}} \tag{1.4.10}$$

where f'_t is the tensile strength of the material, introduced only for dimensional purposes, B is a dimensionless constant, and D_0 is a constant with the dimension of length. Both B and D_0 depend on the fracture properties of the material and on the geometry (shape) of the structure, but not on the structure size. Simple derivations of this size effect law are given next.

1.4.3 Simple Explanation of Fracture Mechanics Size Effect

Consider a uniformly stressed panel as shown in Fig. 1.4.2. Imagine first that fracture proceeds as the formation of a crack band (or fracture band) of thickness h_f across the central section of the panel. Now, the extension of the crack band by a unit length will require a certain amount of energy that, per unit thickness of the specimen, is called *fracture energy* and is denoted as G_f. The value of G_f may be considered, for the present purposes, approximately a material constant. To determine the load required to propagate the band, an energy balance condition must be imposed by writing that the energy available is equal to the energy required for band extension.

To do so, one writes that the strain energy released from the structure at constant σ_N (which is the condition of maximum load) is used to further propagate the crack band. As an approximation, we may assume that the presence of a crack band of thickness h_f reduces the strain energy density in the band and cross-hatched area from $\sigma_N^2/2E$ (for the intact panel) to zero (E = elastic modulus of material). The cross-hatched area is limited by two lines of some empirical slope k. When the crack band extends by Δa at no boundary displacements, the additional strain energy that is released comes from the densely cross-hatched strip of horizontal dimension Δa (Fig. 1.4.2a). If the failure modes are geometrically similar, as

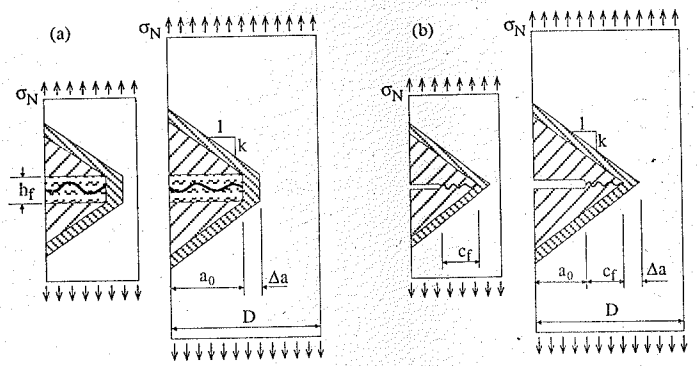

Figure 1.4.2 Sketches for explaining size effect: (a) blunt crack band, (b) slit-like process zone (adapted from ACI Committee 446 1992).

is usually the case, then the larger the panel, the longer is the crack band at failure. Consequently, the area of the densely cross-hatched strip for a larger panel is also larger. Therefore, in a larger structure, more energy is released from the strip by the same extension of the crack band. This is the source of size effect.

Quantitatively, the energy released per unit panel thickness is given by the area of the densely cross-hatched region $h_f\Delta a + 2ka_0\Delta a$ times the thickness, times the energy density of the intact panel $\sigma_N^2/2E$. Therefore, the release of energy from the aforementioned strip (at constant boundary displacement) is $b(h_f\Delta a + 2ka_0\Delta a)\sigma_N^2/2E$, where b is the panel thickness. This must be equal to the energy required to create the fracture, which is $G_f b\Delta a$.Therefore,

$$b(h_f\Delta a + 2ka_0\,\Delta a)\frac{\sigma_N^2}{2E} = G_f\, b\Delta a \tag{1.4.11}$$

Solving for the nominal stress, one obtains the size effect law (1.4.10) in which

$$Bf_t' = \sqrt{\frac{2G_fE}{h_f}} = \text{constant}, \quad \text{and} \quad D_0 = \frac{h_fD}{2ka_0} = \text{constant}. \tag{1.4.12}$$

Note that D_0 depends on the structure shape through the constant k but is independent of the structure size if the structures are geometrically similar (D/a_0 = constant); f_t' = tensile strength, introduced for convenience; and h_f = width of the fracture band front, which is treated here approximately as a constant, independent of structure size.

Lest one might get the impression that this explanation of size effect works only for a crack band but not for a sharp line crack, consider the similar panels of different sizes with line cracks as shown in Fig. 1.4.2b. In concrete, there is always a sizable fracture process zone ahead of the tip of a continuous crack, of some finite length which may, in the crudest approximation, be considered constant. Over the length of this zone, the transverse normal stress gradually drops from f_t' to 0. Because of the presence of this zone, the elastically equivalent crack length that causes the release of strain energy from the adjacent material is longer than the continuous crack length, a_0, by a distance c_f which can be assumed to be approximately a material constant.

When the crack extends by length Δa, the fracture process zone travels with the crack tip, and the area from which additional strain energy is released consists of the strips of horizontal dimension Δa that are densely cross-hatched in Fig. 1.4.2b. Following the same procedure as before for the crack band, we see that the area of the zone from which energy is released is $2k(a_0 + c_f)\Delta a$. So the total energy release is $b2k(a_0 + c_f)\Delta a\sigma_N^2/2E$, which must be equated to the energy required for crack extension, $bG_f\Delta a$, thus delivering the equation

$$b2k(a_0 + c_f)\Delta a\frac{\sigma_N^2}{2E} = G_f b\Delta a \tag{1.4.13}$$

Solving for σ_N, one again obtains the size effect law in (1.4.10) in which now

$$Bf_t' = \sqrt{\frac{G_fE}{kc_f}} = \text{constant}, \quad \text{and} \quad D_0 = c_f\frac{D}{a_0} = \text{constant}. \tag{1.4.14}$$

The foregoing equations are only approximate in their details, because of the simplifying assumptions in determining the structural energy release. However, their structure is correct. The same form is obtained using simplified theories for other geometries (e.g., bending). The fine-tuned equations require the use of more sophisticated fracture mechanics concepts, and their presentation will be deferred until Chapter 6.

As will be shown in Chapter 9, Eq. (1.4.10) can also be derived, in a completely general way, by dimensional analysis and similitude arguments (Bažant 1984a). This general derivation rests on two basic hypotheses: (1) the propagation of a fracture or crack band requires an approximately constant energy supply (the fracture energy, G_f) per unit area of fracture plane , and (2) the energy released by the structure due to the propagation of the fracture or crack band is a function of both the fracture length and the size of the fracture process zone at the fracture front.

Applications of Eq. (1.4.10) to brittle failures of concrete structures rest on two additional hypotheses: (3) the failure modes of geometrically similar structures of different sizes are also geometrically similar (e.g., a diagonal shear crack has at failure about the same slope and the same relative length), and (4) the structure does not fail at crack initiation (which is really a requirement of good design).

These hypotheses are never perfectly fulfilled, so it must be kept in mind that Eq. (1.4.10) is approximate, valid only within a size range of about 1:20 for most structures (for a broader size range, a more complicated formula would be required). This size range is sufficient for most practical purposes, but for some structures the range of interest extends beyond the applicability range. This is so because a sufficiently large change of structure size may alter the failure mode and thus render Eq. (1.4.10) inapplicable beyond that size; this happens, for example, for the brazilian split-cylinder tests. The analysis of such 'anomalous' size effect will be deferred until Chapter 9.

Exercises

1.1 In fracture mechanics manuals, it is customary to use for σ_N the maximum tensile stress computed elastically for an unnotched specimen. Express σ_N for a beam in terms of the maximum bending moment M, the beam depth D, and the central moment of inertia of the cross-section I. (Answer: $\sigma_N = MD/2I$)

1.2 Determine σ_N as in the previous exercise for a hollow cylindrical bar of outer diameter D and inner diameter αD ($\alpha < 1$) subjected to a torsional moment M_T. (Answer: $\sigma_N = 16M_T/[\pi D^3(1-\alpha^4)]$)

1.3 With the same criteria as in the previous exercises, determine σ_N for a circular bar of diameter D subjected to simultaneous tension and torsion; let P be the tensile force and $M_T = \beta PD$ the torque, where β is some dimensionless constant. Give the coefficient c_N corresponding to Eq. (1.4.1). Hint: use Mohr's circle to find the maximum tensile stress.

1.4 Results from the literature were analyzed by the authors using a characteristic specimen dimension D and a nominal stress σ_N defined with $c_N = 1$. The results for the best fit of Bf_t' and D_0 were 1.15 MPa and 322 mm, respectively. To compare with other results, you want to use a nominal stress defined using the same characteristic size D, but a constant $\hat{c}_N = 2.5$. What would the values of the best-fit constants (say $\hat{B}f_t'$ and $\hat{D}_0$) in this case. (Answer: $\hat{B}f_t' = 2.88$ MPa, $\hat{D}_0 = 322$ mm.)

1.5 Generalize the previous exercise and prove that if, for a particular selection of c_N and D, the size effect parameters are Bf_t and D_0, for a different selection $\hat{c}_N$ and $\hat{D}$ (where $\hat{D}/D$ = constant), their value is $\hat{B}f_t' = (\hat{c}_N/c_N)Bf_t'$ and $\hat{D}_0 = (\hat{D}/D)D_0$.

1.6 Find the relationship between h_f and c_f that make identical Eqs. (1.4.12) and (1.4.14).

Table 1.5.1 Summary of size effect test series.

Series	Material	Specimen type[a]	a_0/D	S/D	b (mm)	c_N	Reference
A1–A6	concrete	SEN-TPB	1/3	4	76.2	6	Walsh 1972
B1	concrete	SEN-TPB	1/6	2.5	38.1	3.75	Bažant and Pfeiffer 1987
B2	concrete	DEN-EC	1/6	—	38.1	1	Ibid.
B3	concrete	DEN-T	1/6	—	19.1	1	Ibid.
B4	concrete	DEN-S	1/6	—	38.1	1	Bažant and Pfeiffer 1986
C1	mortar	SEN-TPB	1/6	2.5	38.1	3.75	Bažant and Pfeiffer 1987
C2	mortar	DEN-EC	1/6	—	38.1	1	Ibid.
C3	mortar	DEN-T	1/6	—	19.1	1	Ibid.
C4	mortar	DEN-S	1/6	—	38.1	1	Bažant and Pfeiffer 1986
D1	HSC	SEN-TPB	1/3	2.5	38.1	3.75	Gettu, Bažant and Karr 1990
E1	marble	SEN-TPB	0.5	4	30	6	Fathy 1992
E2	granite	SEN-TPB	0.5	4	30	6	Ibid.
F1	limestone	SEN-TPB	0.4	4	13	6	Bažant, Gettu and Kazemi 1991
G1	SiO_2	SEN-TPB	0.2[b]	4	$= D$	6	McKinney and Rice 1981[c]
G2	SiC CN-137	SEN-TPB	0.2	4	$= D$	6	Ibid.
G3	SiC CN-163	SEN-TPB	0.2	4	$= D$	6	Ibid.
H1–2	concrete	DP	—	—	—	0.4	Marti 1989
I1	microcon.	BPO	—	—	—	$4/\pi$	Bažant and Şener 1988
J1	mortar	UPT	—	—	—	0.75	Bažant, Şener and Prat 1988
J2	R. mortar	RPT	—	—	—	0.75	Ibid.
K1	R. mortar	LRB-UB	—	—	—	0.5	Bažant and Kazemi 1991
K2	R. mortar	LRB-AB	—	—	—	0.5	Ibid.
L1	microcon.	PS	—	—	—	$1/\pi$	Bažant and Cao 1987

[a] See specimen types in Fig. 1.5.1.

[b] Variable. Results have been reduced to a fixed $a_0/D = 0.2$.

[c] See also Bažant and Kazemi 1990b.

1.5 Experimental Evidence for Size Effect

The size effect law proposed by Bažant (Eq. (1.4.10)) has been verified by a large number of experimental data, for both notched fracture specimens and unnotched structures. We will postpone a full discussion of the implications of size effect for structural analysis until Chapter 10, but we will review the evidence now.

Results from 23 test series, among those available, are briefly examined in the following, corresponding to various authors, materials, and specimens. The essentials of the specimen characteristics are summarized in Table 1.5.1 and Fig. 1.5.1. In particular, the coefficient c_N corresponding to Eq. (1.4.1) to each series of experiments is included in Table 1.5.1. Some characteristics of the materials, together with the size range and the best fits for Bf_t' and D_0, are summarized in Table 1.5.2, where the sources of the data are also displayed. Further details of the tests are given in the following; however, detailed descriptions are not given; they can be obtained from the referenced sources.

Since various fitting procedures have been used in the literature to get the optimal fit of the size effect law to the experimental data, a unified procedure has been used in this book. In this procedure the nonlinear regression is directly performed on the data presented as a bilogarithmic diagram (see Chapter 6 for a discussion of the fitting procedures). To do so, we call $v = \ln \sigma_{Nu}$, and take v to be the variable whose quadratic error is to be minimized with the following approximating equation —equivalent to (1.4.10):

$$v = \ln(Bf_t') - 0.5 \ln\left(1 + \frac{D}{D_0}\right) \tag{1.5.1}$$

The optimal fits for Bf_t' and D_0 were calculated using a standard Levenberg-Marquardt algorithm. The values of Bf_t' and D_0 with their standard errors are given in Table 1.5.2.

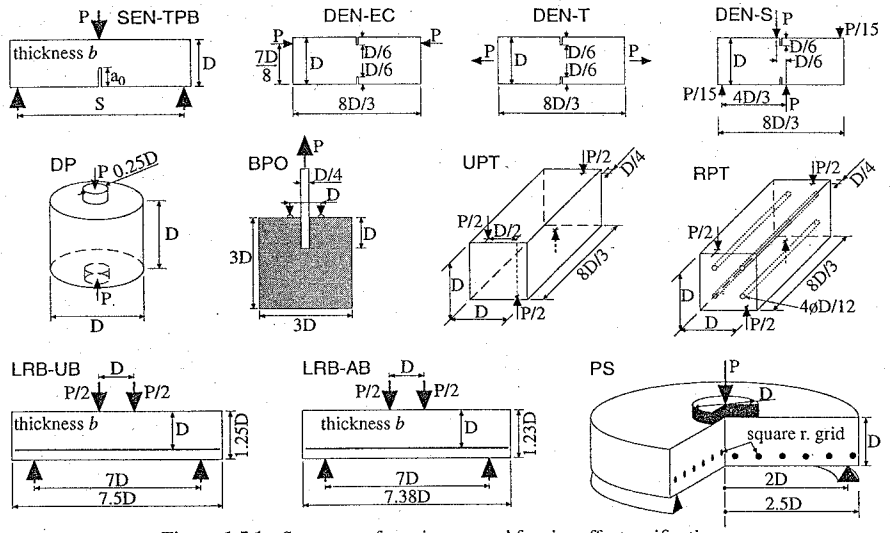

Figure 1.5.1 Summary of specimens used for size effect verification.

Table 1.5.2 Essential data of size effect tests

Series	Material	d_a[a] (mm)	Strength[b] (MPa)	Elastic Modulus (GPa)	Size Range (mm)	Bf_t' (MPa)	D_0 (mm)
A1	concrete	12.7	23.1	n.a.	76–381	4.5 ± 0.9	36 ± 17
A2	concrete	12.7	35.4	n.a.	76–381	2.8 ± 0.5	157 ± 99
A3	concrete	12.7	14.3	n.a.	76–381	3.2 ± 2.1	34 ± 52
A4	concrete	12.7	15.6	n.a.	76–381	1.7 ± 0.3	126 ± 78
A5	concrete	12.7	46.8	n.a.	76–381	2.9 ± 0.4	212 ± 114
A6	concrete	12.7	32.7	n.a.	76–381	4.1 ± 0.7	55 ± 23
B1	concrete	12.7	34.1	n.a.	76–305	6.0 ± 0.3	60 ± 10
B2	concrete	12.7	37.4	n.a.	76–305	3.9 ± 0.2	54 ± 10
B3	concrete	12.7	29.1	n.a.	76–152	2.7 ± 0.1	184 ± 38
B4	concrete	12.7	39.7	n.a.	76–305	4.6 ± 0.1	719 ± 130
C1	mortar	4.83	48.4	n.a.	76–305	14 ± 4	7.7 ± 4.4
C2	mortar	4.83	48.1	n.a.	76–305	6.6 ± 1.3	10 ± 5
C3	mortar	4.83	46.4	n.a.	76–152	3.3 ± 0.1	95 ± 17
C4	mortar	4.83	49.0	n.a.	76–305	5.9 ± 0.2	190 ± 25
D1	HSC	9.5	96.0	n.a.	38–152	32 ± 8	19 ± 11
E1	marble	4	7.7[c]	36	12.5–100	3.7 ± 0.2	47 ± 10
E2	granite	2	12.3[c]	39	12.5–100	5.1 ± 0.2	35 ± 5
F1	limestone	1.5	3.45[c]	30.5	13–102	3.3 ± 0.1	45 ± 6
G1	SiO_2	0.02	—	58	5–32	17 ± 3	2.6 ± 1.2
G2	SiC CN-137	2	—	130	7–37	36 ± 4	101 ± 157
G3	SiC CN-163	2	—	140	7–37	35 ± 3	7.3 ± 2.2
H1	concrete	9.5	33.3	n.a.	76–610	2.7 ± 0.1	352 ± 63
H2	concrete	9.5	23.6	n.a.	76–1219	1.95 ± 0.05	601 ± 83
I1	microcon.	6.35	45.8	13–51	45.9	36 ± 14	6 ± 6
J1	mortar	4.83	43.7	n.a.	38–152	5.4 ± 0.3	37 ± 6
J2	mortar	4.83	43.6	n.a.	38–152	6.2 ± 2.1	23 ± 20
K1	mortar	4.83	46.8	n.a.	41–163	2.2 ± 0.1	151 ± 40
K2	mortar	4.83	46.2	n.a.	21–330	4.6 ± 1	11 ± 6
L1	microcon.	6.35	na	48–53	25–102	10.3 ± 1.3	178 ± 178

[a] Maximum aggregate or grain size.

[b] Compressive unless otherwise stated.

[c] Splitting tensile strength.

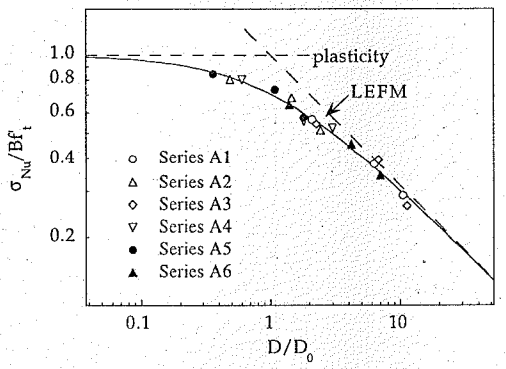

Figure 1.5.2 Size effect results of Walsh (1972).

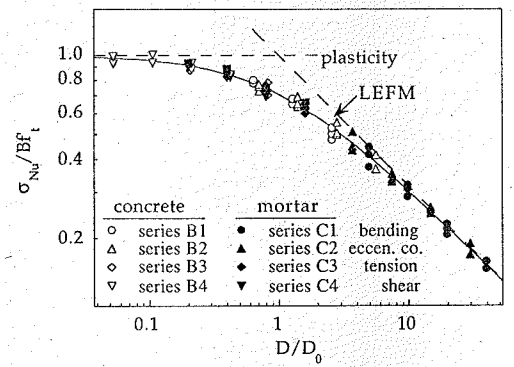

Figure 1.5.3 Size effect results of Bažant and Pfeiffer (1986, 1987).

1.5.1 Structures with Notches or Cracks

The size effect law was originally verified (Bažant 1983, 1984a) by comparisons with the tests of Walsh (1972), whose results are summarized in Fig.1.5.2. Walsh used single-edge-notched beams in three-point bending (SEN-TPB, see Table 1.5.1 and Fig. 1.5.1, test series A1–6). Walsh was apparently first to plot the test results as $\log \sigma_{Nu}$ vs. $\log D$, but did not try to describe this plot mathematically or generalize it. Walsh's classical tests, however, were of limited range, too short for the scatter obtained, and included only one type of fracture specimen, and so the comparisons were not completely conclusive.

A stronger experimental verification was presented by Bažant and Pfeiffer (1986, 1987), covering a broader size range and four very different types of specimens : SEN-TPB, double-edge-notched in eccentric compression (DEN-EC), double-edge notch in eccentric compression (DEN-EC), and double-edge notch in shear (DEN-S); see Table 1.5.1 and Fig. 1.5.1, test series B1–4 and C1–4. The research included tests on concrete (series B1–4) and on mortar (series C1–4). The test results and their optimum fits by the size effect law are shown in Fig. 1.5.3. Obviously, the comparison provides a strong justification for the size effect law (for statistical comparisons, see the original paper). The data points in Fig. 1.5.3 refer to individual tests.

An experimental size effect study of high strength concrete has been conducted by Gettu, Bažant and Karr (1990), using SEN-TPB. The results are shown in Fig. 1.5.4, again in comparison with the optimum fits by the size effect law and its asymptotes.

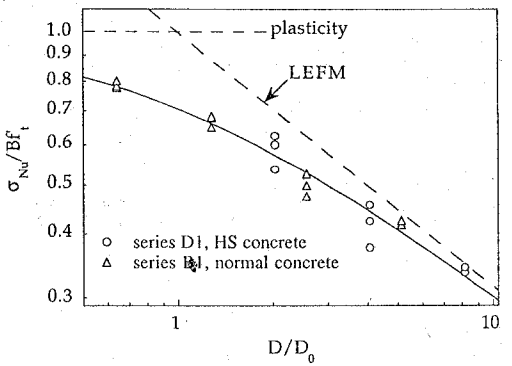

Figure 1.5.4 Size effect results of Gettu, Bažant and Karr (1990). Results of Bažant and Pfeiffer (1987) for ordinary concrete are also included for comparison.

For concrete, the foregoing results have been complemented by the extensive size effect data for SEN-TPB specimens published by Bažant and Gettu (1992). These tests (as well as similar tests of fracture of limestone by Bažant, Bai and Gettu 1993), however, also included a systematic investigation of the effect of the loading rate, and, therefore, the presentation of these data is better postponed to Chapter 11. Further, it has been shown (Bažant, Kim and Pfeiffer 1986) that the size effect law agrees well with the results of the size effect tests by Jenq and Shah (1985a,b), although a good fitting was not possible because the size range was too limited compared to the scatter obtained.

The ability of the size effect law (1.4.10) to describe the strength variation of notched specimens in materials other than concrete has been investigated, too, particularly for rocks and ceramics. Moving from coarser grained rocks to ceramics, Fathy (1992) tested marble and granite; Bažant, Gettu and Kazemi (1991) limestone; and McKinney and Rice (1981) slip-cast fused silica (SiO_2) and nitridized silicon carbide (SiC CN-137 and SiC CN-137). Fig. 1.5.5 summarizes their test results. It can be seen that the size effect law describes the various results acceptably well.

Recent experimental data indicate a similar degree of agreement for composites and for ice. Bažant, Daniel and Li (1996) tested in tension both single- and double-edge notched specimens of highly orthotropic carbon-epoxy fiber laminates and they found good agreement with the size effect law for a 1:8 range of sizes. Adamson et al. (1995) and Mulmule, Dempsey and Adamson (1995) performed various series of tests on sea ice using various specimen geometries. In one of the series, square plates with a notch subjected to opening forces at the notch mouth were tested with a size ratio of 1:160 (the specimens ranged from 0.5 to 80 m in size). This is the test series of wider size range known to date. The results showed a very good agreement with the size effect law.

1.5.2 Structures Without Notches or Cracks

Extensive tests have been carried out to verify (1.4.10) for various types of failure of unnotched concrete structures. Good agreement of (1.4.10) with test results has been demonstrated for:

1. Double-punch tests of cylinders (Marti 1989).
2. Pullout failure of bars (Bažant and Şener 1988), pullout of studded anchors (Eligehausen and Ožbolt 1990), and bond splices (Şener 1992).
3. Failures of unreinforced pipes (Gustafsson and Hillerborg 1985; Bažant and Cao 1986).
4. Torsional failure of beams (Bažant, Şener and Prat 1988).
5. Diagonal shear failure of longitudinally reinforced beams without or with stirrups, unprestressed or prestressed (Bažant and Kim 1984; Bažant and Sun 1987; Bažant and Kazemi 1991).
6. Punching shear failure of slabs (Bažant and Cao 1987).

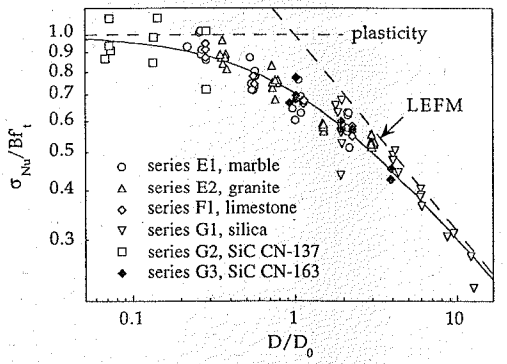

Figure 1.5.5 Size effect results for various kinds of rocks and ceramics (Fathy 1992; Bažant, Gettu and Kazemi 1991; McKinney and Rice 1981).

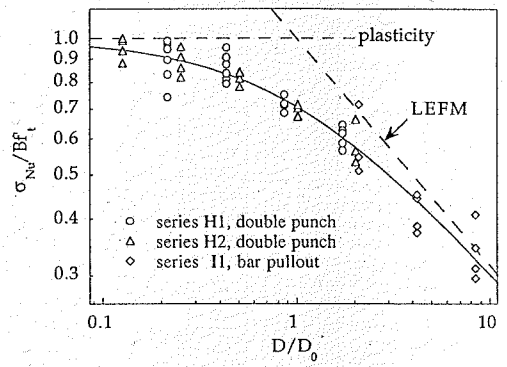

Figure 1.5.6 Size effect in double punch tests (Marti 1989) and bar pullout (Bažant and Şener 1988).

A sample of the results, which can be regarded as an additional verification of applicability of fracture mechanics to brittle failures of concrete structures, are shown in Figs. 1.5.6 and 1.5.7.

As further evidence of applicability of fracture mechanics, Fig. 1.5.8 shows, for the punching shear failure, that the post-peak load drop becomes steeper and larger as the size increases. This is because, in a larger specimen, there is (for the same σ_N) more energy to be released into a unit crack extension. The load must be reduced since the fracture extension dissipates the same amount of energy.

The existing test data on concrete specimens with regular-size aggregate reported in the literature also offer evidence of size effect, and the need for a fracture mechanics based explanation has been pointed out by various researchers, beginning with Reinhardt (1981a, 1981b). The data from the literature are generally found to agree with Fig. 1.2.5b although often the evidence is not very strong because the data exhibit very large statistical scatter and the size range is insufficient.

Due to large scatter and size range limitation, about equally good fits can often be obtained with other theories of size effect, e.g., Weibull's statistical theory. However, the measured size effect curves in the Figs. 1.5.2–1.5.7 do not agree with the Weibull-type statistical theory. This theory gives a straight line of slope –1/6 for two-dimensional similarities and –1/4 for two-dimensional similarity, which are significantly smaller than seen in the figures.

Much of the scatter probably stems from the fact that the test specimens of various sizes were not geometrically similar. Theoretical adjustments must, therefore, be made for the factors of shape before

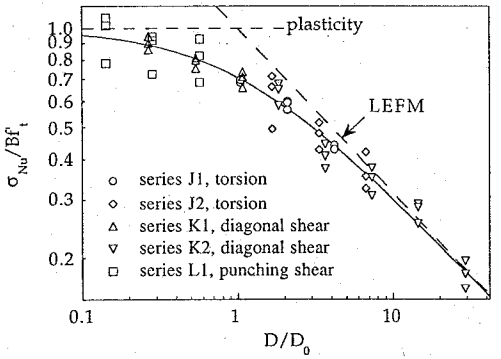

Figure 1.5.7 Size effect in torsion for plain (J1) and reinforced (J2) concrete prisms (Bažant, Şener and Prat 1988); diagonal shear failure of longitudinally reinforced beams for unanchored (K1) and anchored (K2) bars (Bažant and Kazemi 1991); and punching shear of slabs (Bažant and Cao 1987).

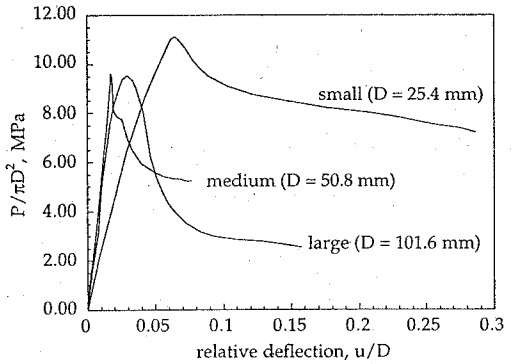

Figure 1.5.8 Size effect on the load-deflection curve in punching of slabs (adapted from Bažant and Cao 1987; series L1 in Tables 1.5.1 and 1.5.2).

the comparison with (1.4.10) can be made and, since the exact theory is not known, such adjustments introduce additional errors, manifested as scatter.

Exercises

1.7 In the plastic limit ($D/D_0 \ll 1$), the nominal strength is given by Bf'_t. Determine the largest size for which Bažant's size effect law differs from the plastic limit less than 5%. Hint: use the approximation $(1+x)^{-1/2} \approx 1 - x/2$ for $x \ll 1$.

1.8 Apply the result of the preceding exercise to the tests in Tables 1.5.1 and 1.5.2. Decide, for each test series, whether specimens of such size can be representative of the material. Hint: compare the specimen size with the maximum aggregate or grain size.

1.9 In the LEFM limit ($D/D_0 \gg 1$), the nominal strength is given by $Bf'_t\sqrt{D_0/D}$. Determine the smallest size for which Bažant's size effect law differs from the LEFM limit less than 5%. Hint: use the approximation $(1+x)^{-1/2} \approx 1 - x/2$ for $x \ll 1$.

1.10 Apply the result of the preceding exercise to the tests in Tables 1.5.1 and 1.5.2. Decide, for each test series, whether specimens of such size can be manufactured for laboratory testing.

1.11 We say that one structure is more brittle than another when its situation on the $\log \sigma_{Nu}$ vs. $\log D$ size effect plot is closer to LEFM limit. If (and only if) two structures are geometrically identical but made of different materials, the difference in the brittleness is entirely due to the difference in material brittleness. Decide which are the more brittle materials in the following tests (defined in Tables 1.5.1 and 1.5.2 and Figs. 1.5.1–1.5.7): (a) Concrete in series B1–4 and mortar in series C1–4; (b) Marble in series E1 and granite in series E2; (c) Concrete in series H1 and concrete in series H2; (c) ceramic materials in series G1, G2, and G3.

2

Essentials of LEFM

Linear elastic fracture mechanics (LEFM) is the basic theory of fracture, originated by Griffith (1921, 1924) and completed in its essential aspects by Irwin (1957, 1958) and Rice (1968a,b).

LEFM is a highly simplified, yet sophisticated, theory, that deals with sharp cracks in elastic bodies. As we shall see, LEFM is applicable to any material as long as certain conditions are met. These conditions are related to the basic ideal situation analyzed in LEFM in which all the material is elastic except in a vanishingly small region (a point) at the crack tip. In fact, the stresses near the crack tip are so high that some kind of inelasticity must take place in the immediate neighborhood of the crack tip; however, if the size of the inelastic zone is small relative to linear the dimensions of the body (including the size of the crack itself), the disturbance introduced by this small inelastic region is also small and, in the limit, LEFM is verified exactly.

Thus, LEFM is the basic theoretical reference to describe the behavior of any material with cracks, even if, as it happens for concrete, the geometry and dimensions of structures built in practice do not allow direct use of LEFM.

This and the next two chapters give an overall view of the mathematical theory of LEFM with some straightforward applications to idealized cases. They are not intended as a substitute for handbooks or treatises on LEFM. Their objective is to simplify the access of the reader to the concepts required in the remaining chapters and, at the same time, to provide in this book a self-contained presentation, so that recourse to external references be minimized.

This introductory chapter gives a short account of the most essential concepts in LEFM. Section 2.1 develops the energetic approach to fracture —the Griffith approach. It introduces the concept of energy release rate $\mathcal{G}$, representing the energy available for fracture, and the fracture energy or crack resisting force $\mathcal{R}$, representing the energy required for fracture. Also included in this section are the basic expressions for $\mathcal{G}$, and some techniques to describe fracture processes (Section 2.1). The systematic analysis of the techniques available to compute $\mathcal{G}$ and to measure $\mathcal{R}$ is deferred until the next chapter.

Section 2.2 introduces the concept of stress intensity factor K_I based on a simple example and describes the general properties of the stresses and displacements near the crack tip (the formal derivation of such properties is skipped in this introductory chapter and postponed until Chapter 4). It also shows that the energetic approach and the approach based on K_I —Irwin's approach— are equivalent, and rewrites the crack growth criterion in terms of the stress intensity factor. The presentation of the methods to compute stress intensity factors and other related quantities is postponed until the next chapter.

The final Section 2.3 deduces the size effect laws for classical plasticity and for LEFM. As explained in the previous Chapter, these are the reference laws for any nonlinear fracture model, and are extensively used for comparison with experimental as well as theoretical nonlinear size effects in the remainder of the book.

2.1 Energy Release Rate and Fracture Energy

Formation of a crack in an elastic solid initially subjected to uniform uniaxial tension disrupts the trajectories of the maximum principal stress in the manner depicted in Fig. 2.1.1a. This indicates that stress concentrations must arise near the crack tip. They were calculated by Inglis (1913) as the limit case of his solution for an elliptical hole.

From Inglis's solution, Griffith (1921, 1924) noted that the strength criterion cannot be applied because the stress at the tip of a sharp crack is infinite no matter how small the load is (Fig. 2.1.1b). He further concluded that the formation of a crack necessitates a certain energy per unit area of the crack plane,

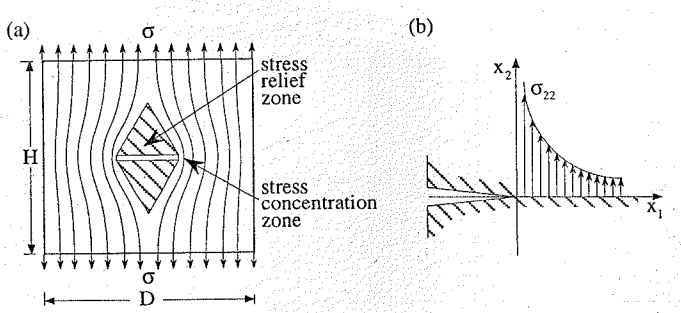

Figure 2.1.1 (a) Disruption of the trajectories of maximum principal stress by a crack; (b) singular distribution of normal stress ahead of the crack tip (adapted from ACI Committee 446 1992).

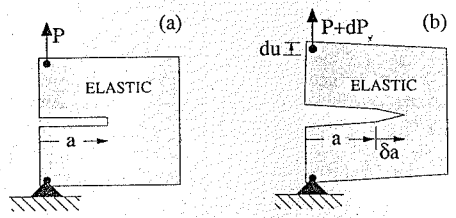

Figure 2.1.2 Crack growth in a cracked specimen: (a) initial situation; (b) co-planar crack growth upon further loading.

which is a material property, provided the structure is so large that the crack tip region in which the fracture process takes place is negligible. However, more general approaches accept that the specific energy required for crack growth may depend on the cracking history instead of being a constant. In such cases, the energy required for a unit advance of the crack is called the crack growth resistance, $\mathcal{R}$.

The basic problem in fracture mechanics is to find the amount of energy available for crack growth and to compare it to the energy required to extend the crack. Although conceptually simple, the problem is far from trivial and deserves a detailed analysis.

2.1.1 The General Energy Balance

Consider a plane structure of thickness b in which a preexisting straight crack of length a is present (Fig. 2.1.2). Assume that upon quasi-static loading, a certain load level is attained at which the crack advances an elemental length δa in its own plane, sweeping an element of area $\delta A = b\,\delta a$. The energy $\delta\mathcal{W}^F$ required to do so is the increment of area times the crack growth resistance:

$$\delta\mathcal{W}^F = \mathcal{R}\,b\,\delta a \tag{2.1.1}$$

Alternative notations found in the literature for the crack growth resistance $\mathcal{R}$ are G_R when it is history-dependent, and G_c and G_{Ic} (critical energy release rate) when it is a material property not dependent on the cracking history. In this book, we use G_f for the latter case because this is the most widespread notation in the field of concrete fracture. G_f is called the *specific fracture energy*, or fracture energy, for short. In Section 2.1.5 we will justify that the only case consistent with the hypotheses of elastic fracture, where the inelastic zone is negligibly small, is that of $\mathcal{R} = \text{constant} = G_f$.

The total energy supply to the structure is the external work, which, in the infinitesimal process under consideration, is denoted as $\delta\mathcal{W}$. From this total supply, a part is stored in the structure as elastic energy, $\delta\mathcal{U}$. The remainder is left to drive other processes and to generate kinetic energy $\delta\mathcal{K}$. When the only energy-consuming process is fracture, and the process is quasi-static ($\delta\mathcal{K} = 0$), this remainder is the

available energy for fracture, or elemental energy release $\delta\mathcal{W}^R$:

$$\delta\mathcal{W}^R = \delta\mathcal{W} - \delta\mathcal{U} \tag{2.1.2}$$

Although Eq. (2.1.2) may be directly handled in many cases (as done by Griffith 1921), it is often more convenient to work with specific energies (energies per unit area of crack growth). The specific available energy, usually called the energy release rate, $\mathcal{G}$, is thus defined so that

$$\mathcal{G}\,b\,\delta a = \delta\mathcal{W}^R = \delta\mathcal{W} - \delta\mathcal{U} \tag{2.1.3}$$

The essential advantage of using $\mathcal{G}$ is that, as it will turn out in the next paragraph, $\mathcal{G}$ is a *state function*. This means that $\mathcal{G}$ depends on the instantaneous geometry and boundary conditions, but not on how they vary in the actual fracture process, or on how they have been attained.

The balance of energy requires that, in a quasi-static process,

$$\mathcal{G}\,\delta a = \mathcal{R}\,\delta a \qquad \text{for quasi-static growth} \tag{2.1.4}$$

and in a more general incipiently dynamic situation (initial kinetic energy $\mathcal{K} = 0$, kinetic energy increase $\delta\mathcal{K} \geq 0$),

$$\mathcal{G}\,\delta a = \mathcal{R}\,\delta a + \delta\mathcal{K}/b \tag{2.1.5}$$

Since $\delta\mathcal{K} \geq 0$ (because initially $\mathcal{K} = 0$ and always $\mathcal{K} \geq 0$), the equations may be made to hold in any circumstance (as they should, the balance of energy being a universal law, the first law of thermodynamics) if the following fracture criterion is met:

$$\text{if } \mathcal{G} < \mathcal{R} \text{ then } \delta a = 0 \text{ and } \delta\mathcal{K} = 0 \quad \text{No crack growth (stable)} \tag{2.1.6}$$

$$\text{if } \mathcal{G} = \mathcal{R} \text{ then } \delta a \geq 0 \text{ and } \delta\mathcal{K} = 0 \quad \text{Quasi-static growth possible} \tag{2.1.7}$$

$$\text{if } \mathcal{G} > \mathcal{R} \text{ then } \delta a > 0 \text{ and } \delta\mathcal{K} > 0 \quad \text{Dynamic growth (unstable)} \tag{2.1.8}$$

This system of conditions summarizes what seems obvious: If the energy available is less than that required, then the crack cannot grow (and the structure is stable). If the energy available equals the required energy, then the crack can grow statically, i.e., with negligible inertia forces (and the structure can be stable or unstable depending on the variation of $\mathcal{G} - \mathcal{R}$ with displacements). If the energy available exceeds that required, then the structure is unstable and the crack will run dynamically (the excess energy being turned into kinetic energy).

The central problems of elastic fracture mechanics are to measure the crack growth resistance, $\mathcal{R}$, for particular materials and situations, on one hand, and to calculate the energy release rate $\mathcal{G}$, on the other. This latter problem may be handled in various equivalent ways, the bases of which are explored next.

2.1.2 Elastic Potentials and Energy Release Rate

Consider the plane elastic specimen in Fig. 2.1.2, in which the crack length a can take any value. Let P be the load and u the load-point displacement. By definition, the elementary work is

$$\delta\mathcal{W} = P\delta u \tag{2.1.9}$$

for any incremental process. For an equilibrium situation and given any crack length a, there is a unique relationship between the equilibrium force and the displacement (which can be calculated by solving the elastic problem). So we can write

$$P = P(u, a) \tag{2.1.10}$$

where $P(u, a)$ can be determined by elastic equilibrium analysis of the structure. Based on the corresponding elastic solution, the stored (elastic) strain energy can also be calculated for any u and a:

$$\mathcal{U} = \mathcal{U}(u, a) \tag{2.1.11}$$

Consider, then, that the elastic body with a crack of length a is subjected, in a static manner, to displacement δu, with *no crack growth.* In this situation, all the work is stored as strain energy, so that

$$\delta\mathcal{W} - [\delta\mathcal{U}]_a = 0 \tag{2.1.12}$$

where subscript a indicates that the crack length remains constant in this process.

Consider now a general process where both u and a are allowed to vary. Then, Eq. (2.1.3), which is the definition of $\mathcal{G}$, can be written as

$$\mathcal{G}\, b\, \delta a = P(u,a)\delta u - \left\{ \left[\frac{\partial \mathcal{U}(u,a)}{\partial u}\right]_a \delta u + \left[\frac{\partial \mathcal{U}(u,a)}{\partial a}\right]_u \delta a \right\} \tag{2.1.13}$$

Considering equilibrium variation at $\delta a = 0$, one obtains the well-known second Castigliano's theorem:

$$P(u,a) = \left[\frac{\partial \mathcal{U}(u,a)}{\partial u}\right]_a \tag{2.1.14}$$

So the first two terms in (2.1.13) in an equilibrium process cancel and we get

$$\mathcal{G} = \mathcal{G}(u,a) = -\frac{1}{b}\left[\frac{\partial \mathcal{U}(u,a)}{\partial a}\right]_u \tag{2.1.15}$$

This basic result shows that the energy release rate $\mathcal{G}$ is indeed a state function, because it depends only on the instantaneous boundary conditions and geometry (in this case uniquely defined by u and a).

Sometimes one may prefer to use the equilibrium load P rather than the equilibrium displacement u as an independent variable. In such case, it is preferable to introduce a dual elastic potential, the complementary energy $\mathcal{U}^*$, defined as

$$\mathcal{U}^* = P\,u - \mathcal{U} \tag{2.1.16}$$

Substituting $\mathcal{U}$ from this equation in the expression for the available energy (2.1.2), together with the expression (2.1.9) for the elemental work, one gets for the elemental energy release

$$\delta\mathcal{W}^R = \delta\mathcal{W} - \delta\mathcal{U} = P\delta u - \delta(Pu - \mathcal{U}^*) = \delta\mathcal{U}^* - u\,\delta P \tag{2.1.17}$$

Writing the complementary energy and the displacement as functions of the applied load and the crack length

$$u = u(P,a)\,, \qquad \mathcal{U}^* = \mathcal{U}^*(P,a) \tag{2.1.18}$$

and considering an equilibrium process in which both P and a are allowed to vary, Eq. (2.1.17) yields

$$\mathcal{G}\, b\, \delta a = -u(P,a)\delta P + \left\{ \left[\frac{\partial \mathcal{U}^*(P,a)}{\partial P}\right]_a \delta P + \left[\frac{\partial \mathcal{U}^*(P,a)}{\partial a}\right]_P \delta a \right\} \tag{2.1.19}$$

Considering equilibrium variation at $\delta a = 0$, one gets the well-known first Castigliano's theorem

$$u(P,a) = \left[\frac{\partial \mathcal{U}^*(P,a)}{\partial P}\right]_a \tag{2.1.20}$$

So the first two terms in (2.1.19) cancel and we have

$$\mathcal{G} = \mathcal{G}(P,a) = \frac{1}{b}\left[\frac{\partial \mathcal{U}^*(P,a)}{\partial a}\right]_P \tag{2.1.21}$$

The couple of equations (2.1.20) and (2.1.21) are strictly equivalent to the couple (2.1.14) and (2.1.15). Indeed, in this single-point-load problem there are 4 mechanical variables, namely, P, u, a, and $\mathcal{G}$, but only two of them are independent variables (Elices 1987). The choice of the independent variables is arbitrary, and is usually done depending on the boundary conditions and the available data.

Remark: Under isothermal conditions (slow loading, slow crack growth), $\mathcal{U}$ represents the Helmholtz's free energy of the structure and $\mathcal{U}^*$ its Gibbs' free energy. Under isentropic (or adiabatic) conditions (rapid loading, rapid growth), $\mathcal{U}$ represents the internal (total) energy of the structure and $\mathcal{U}^*$ represents the enthalpy (see e.g., Bažant and Cedolin 1991, Sec. 10.1).

Other potentials can be used to perform the foregoing analysis. For example, the potential energy Π of the structure-load system, defined as $\Pi = \mathcal{U} - W_a(u)$, where $W_a(u) = \int_0^u P_a(u')\,du'$ is the work of the applied load $P_a(u)$, which is assumed to be defined independently of the structure. The energy release rate is easily expressed in terms of the potential energy as

$$\mathcal{G} = \mathcal{G}(u,a) = -\frac{1}{b}\left[\frac{\partial \Pi(u,a)}{\partial a}\right]_u \tag{2.1.22}$$

Same as for the strain energy, a dual potential can be defined for the potential energy, the complementary potential energy Π^* of the structure-load system, defined as $\Pi^* = \mathcal{U}^* - W_a^*(P)$, where $W_a(P) = \int_0^P u(P')\,dP'$ is the complementary work of the applied load (which is 0 for dead loads). The energy release rate is easily expressed in terms of the complementary potential energy as

$$\mathcal{G} = \mathcal{G}(P,a) = \frac{1}{b}\left[\frac{\partial \Pi^*(P,a)}{\partial a}\right]_P \tag{2.1.23}$$

In this book, the potential energy and complementary potential energy of the structure-load system will not be used. △

The foregoing results may seem too particular because no distributed loads were considered. This limitation may be overcome in most practical cases by defining *generalized forces and displacements.* A generalized force Q and its associated generalized displacement q are defined in such a way that the external work $\delta\mathcal{W}$ may be written as

$$\delta\mathcal{W} = Q\,\delta q \tag{2.1.24}$$

With this definition, all the foregoing expressions hold as long as one interprets P as a generalized force and u as its generalized displacement.

There are many well known cases of generalized forces used in engineering. For example: the generalized displacement associated with a torque is the angular rotation; the generalized displacement associated with a pressure acting inside a cavity is the volume variation of the cavity.

Example 2.1.1 To illustrate the application of the above equations, consider a long-arm double cantilever beam (DCB) specimen subjected to constant moments M as depicted in Fig. 2.1.3a. Assume further that the material is linear elastic, and that the arms are slender enough for the classical theory of bending to apply. With these hypotheses, the elastic or complementary energy per unit length of the beam is known from the theory of strength of materials (e.g., Timoshenko 1956):

$$\frac{d\mathcal{U}}{dx} = \frac{d\mathcal{U}^*}{dx} = \frac{M^2}{2EI} \tag{2.1.25}$$

where x is the coordinate of a cross-section along the beam axis, E the elastic modulus, and I the inertia moment of the cross-section of the beam. We thus compute the elastic or complementary energy of the specimen as the energy of two pure bent cantilever beams of length a:

$$\mathcal{U} = \mathcal{U}^* = 2a\frac{M^2}{2EI}, \tag{2.1.26}$$

and compute the energy release rate by direct application of (2.1.21)

$$\mathcal{G} = \frac{M^2}{bEI}, \tag{2.1.27}$$

with M taking the place of P. □

Example 2.1.2 As another example, consider the double cantilever specimen in Fig. 2.1.3b. The bending moment distribution for the upper arm, $M = Px$, is also shown in this figure. Within the

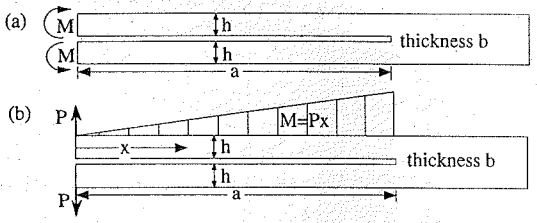

Figure 2.1.3 Long double cantilever beam specimen subjected to (a) pure bending, and (b) opening end forces.

classical beam theory (neglecting shear), the corresponding complementary energy per unit length of one arm is given now, according to (2.1.25), by $d\mathcal{U}^*/dx = P^2x^2/2EI$. The total complementary energy is obtained by integration along both arms of the specimen

$$\mathcal{U}^* = 2\frac{P^2}{2EI}\int_0^a x^2\,dx = \frac{P^2a^3}{3EI} \tag{2.1.28}$$

With this, Equations (2.1.20) and (2.1.21) provide expressions for the relative displacement between the load points, u, and for the energy release rate $\mathcal{G}$

$$u = \frac{2Pa^3}{3EI} = \frac{8Pa^3}{Ebh^3}, \qquad \mathcal{G} = \frac{P^2a^2}{bEI} = \frac{12P^2a^2}{Eb^2h^3} \tag{2.1.29}$$

in which we set $I = bh^3/12$. Except for a factor 2, the first expression for u in the previous equation is very well known in the field of strength of materials. The factor 2 comes from the relative displacement of the forces (working displacement) being twice the deflection of one beam. □

2.1.3 The Linear Elastic Case and the Compliance Variation

The foregoing general results are greatly simplified in the particular, yet essential, case of linear elasticity, because of the linear relationship between u and P at constant a. This may be written as

$$u = C(a)\,P \tag{2.1.30}$$

where $C(a)$ is the (secant) compliance for a crack length a. After substituting u from Eq. (2.1.30) into Eq. (2.1.20), it immediately follows by integration that the complementary energy must be

$$\mathcal{U}^* = \frac{1}{2}C(a)P^2. \tag{2.1.31}$$

Substitution of this expression into Eq. (2.1.21) gives the following result for the energy release rate:

$$\mathcal{G}(P,a) = \frac{P^2}{2b}\frac{dC(a)}{da} \equiv \frac{P^2}{2b}C'(a), \tag{2.1.32}$$

where, in the second expression, the first derivative of the compliance has been briefly denoted as $C'(a)$.

In the foregoing derivation, (P,a) were taken as independent variables. But one can equally well use (u,a) as independent variables. Substituting P from Eq. (2.1.32) into Eq. (2.1.14), it follows by immediate integration that the elastic energy must be

$$\mathcal{U}(u,a) = \frac{u^2}{2C(a)} \tag{2.1.33}$$

Henceforth, from Eq. (2.1.21), the energy release rate is found to be

$$\mathcal{G}(u,a) = \frac{u^2}{2bC^2(a)}\frac{dC(a)}{da} \equiv \frac{u^2}{2bC^2(a)}C'(a) \tag{2.1.34}$$

which, in view of (2.1.30), turns out to be identical to the previous Eq. (2.1.32), as it must.

At this point it is worth to recall the well-known fact that, in linear elasticity, the elastic energy and the complementary energy always take the same value (although they are conceptually different, as graphically shown in the next subsection). In the case of a single point load, it is sometimes useful to rewrite Eqs. (2.1.31) and (2.1.33) in the form

$$\mathcal{U} = \mathcal{U}^* = \frac{1}{2}P\,u \tag{2.1.35}$$

Example 2.1.3 Consider again the pure bent DCB in Fig. 2.1.3a with the same hypotheses as stated in the previous section. Taking M as the generalized force, the relative rotation θ of the arm ends is the corresponding generalized displacement. Since the rotation of each beam end is $\theta/2$, and such rotation has an expression well known from the strength of materials: $\theta/2 = aM/EI$. Therefore, the generalized compliance is

$$C = \frac{\theta}{M} = \frac{2a}{EI} \tag{2.1.36}$$

The use of (2.1.32) leads again to Eq. (2.1.27) for $\mathcal{G}$. □

Example 2.1.4 Consider again the long-arm DCB specimen of Fig. 2.1.3b subjected to loads P at the arm tips. In this case, the deflection of each arm is well known to be $u_1 = Pa^3/3EI$. Thus the displacement over which the loads P work is $u = 2u_1 = 2Pa^3/3EI$, from which it follows that

$$C = \frac{2a^3}{3EI} \tag{2.1.37}$$

Using (2.1.32) again yields the result (2.1.29). □

Example 2.1.5 Consider the center cracked panel depicted in Fig. 2.1.1a. Let the dimensions of the panel —width, height, thickness— be, respectively, D, H, and b; and assume a central crack of total length $2a$. (Note: it is customary to use $2a$ instead of a for the crack length for this kind of internal cracks; this requires special care when differentiating with respect to crack length, see below.) A detailed elastic analysis (Chapter 4) delivers the relative displacement of the upper and lower edges of the panel as a function of the crack size. For small cracks ($2a \ll D$, $2a \ll H$) and plane stress, this displacement turns out to be

$$u = \frac{\sigma H}{E}\left(1 + \frac{2\pi a^2}{DH}\right) = \frac{PH}{BDE}\left(1 + \frac{2\pi a^2}{DH}\right) \tag{2.1.38}$$

where we wrote that the resultant load is $P = \sigma BD$. From the last expression we get $C = u/P$ and using (2.1.32) with a replaced by $2a$, we get

$$\mathcal{G} = \frac{P^2}{2B}\frac{dC}{d(2a)} = \frac{P^2\pi a}{B^2D^2E} = \frac{\sigma^2}{E}\pi a \tag{2.1.39}$$

This is one of the most celebrated Griffith's results (although Griffith, obtained it in a different way). □

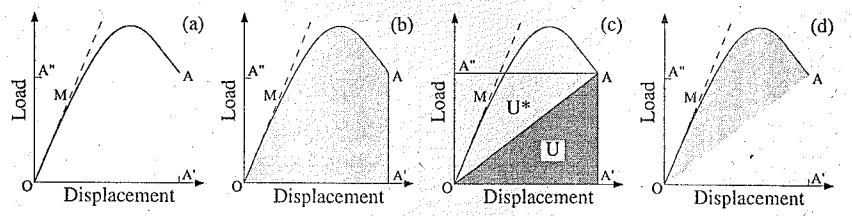

Figure 2.1.4 (a) Quasi-static load-displacement curve. (b) Area representing the total work supply. (c) Areas representing elastic strain energy and complementary energy. (d) Area representing energy supply for fracture and energy dissipated in fracture.

2.1.4 Graphical Representation of Fracture Processes

The energetic equations allow graphical interpretation which, in many instances, supply vivid pictures helpful for problem-solving and explaining. A loading process of a specimen or structure is sometimes best followed on a load-displacement plot. In the case of a single load P, the displacement to consider is the load-point displacement u. Let the plot of a *quasi-static* P-u curve for a given specimen be as shown in Fig. 2.1.4a. The work supplied to the specimen from the beginning of the loading, point O, up to point A, is the integral of $P\,du$, which is equal to the area $OMAA'O$ shown in Fig. 2.1.4b. The area that complements this to rectangle $OA''AA'$ is the integral of $u\,dP$, and is called the complementary work.

If all of the material remains linear elastic except for a zone of negligible volume along the crack path, the (elastic) strain energy $\mathcal{U}$ is represented by the area of the triangle OAA' in Fig. 2.1.4c. The complementary energy $\mathcal{U}^*$ is the area of the triangle OAA'' which complements OAA' to the rectangle $OA'AA''$, of area Pu.

The energy supplied for fracture is the difference between the work and the fracture energy, hence, the area $OMAO$ in Fig. 2.1.4d (it is also the difference between the complementary energy and the complementary work). If the curve shown corresponds to an actual quasi-static fracture process, then the energy supplied for fracture must coincide with the energy consumed by fracture; hence, the area $OMAO$ in Fig. 2.1.4d is also the energy consumed in fracture.

An equilibrium fracture process from point A, where the crack length was a, to a nearby point B, where the crack length has increased by Δa, may be represented as shown in Fig. 2.1.5a. The energy release available for fracture is the area of triangle OAB. This area coincides, except for second-order small terms, with those corresponding to the *virtual* (nonequilibrium) processes represented in Figs. 2.1.5b, c, and d, respectively, corresponding to constant displacement, constant load, and arbitrary $\Delta P/\Delta u$. The energy release rate $\mathcal{G}$ is the limit of the ratio of the area of *any* of the shaded triangles to the crack extension. This shows, again, that $\mathcal{G}$ is path independent, hence, a state function. When Fig. 2.1.5b is used, Eq. (2.1.15) is obtained. When Fig. 2.1.5c is used, Eq. (2.1.21) is obtained. Both turn out to be identical to Eq.(2.1.32) as the reader may easily check. For example, taking the shaded triangle in Fig. 2.1.5c, we express the fracture energy as

$$\mathcal{G}\,b\,\Delta a = \text{area}(OAB'') = \frac{1}{2}P\,(\overline{AB''}) = \frac{1}{2}P[PC(a+\Delta a) - PC(a)] = \frac{1}{2}P^2C'(a)\Delta a \quad (2.1.40)$$

from which Eq. (2.1.32) immediately follows.

As previously stated, only two of the four variables P, u, a, and $\mathcal{G}$ can be taken as independent variables. Any pair of them may be used to define the entire fracture process. However, it is useful to take conjugate variable pairs, as is customary in thermodynamics, because then the areas in the graphical representation have direct energetic interpretations. One of such pair is the P-u representation just analyzed. The other is the $\mathcal{G}$-a representation. This representation has the advantage that $\mathcal{G}$ is the "driving force" for crack growth which is directly related to the material property $\mathcal{R}$, the "resisting force".

If one then imagines a plot of a loading process in a $\mathcal{G}$-a plane, such as that in Fig. 2.1.6a, one finds that OM is a loading at constant crack length under increasing $\mathcal{G}$. At point M, the crack starts to increase under increasing $\mathcal{G}$ up to point A. The total energy released is the integral of $\mathcal{G}\,da$, equal, henceforth,

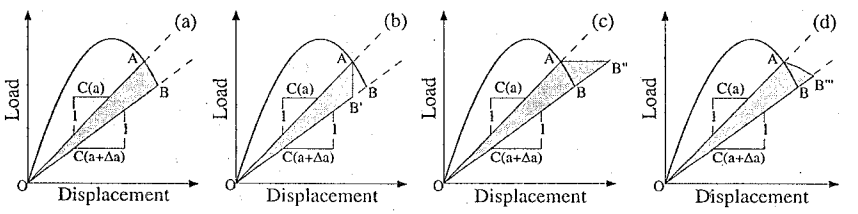

Figure 2.1.5 (a) Actual (equilibrium) incremental fracture process. (b-d) Virtual (nonequilibrium) incremental fracture processes: (b) At constant displacement; (c) at constant load; and (d) at arbitrary $\Delta P/\Delta u$.

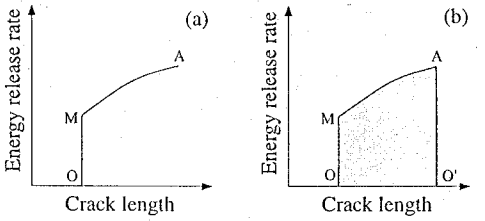

Figure 2.1.6 (a) Loading path in a $\mathcal{G} - a$ plot. (b) Area representing the total energy supply for fracture and the energy dissipated in fracture.

to the area $OMAO'O$ in Fig. 2.1.6b. Moreover, if the process is an actual quasi-static (equilibrium) process, this coincides with the total fracture energy.

Furthermore, the instantaneous $\mathcal{G}$ on the MA portion, where the crack is actually growing, must coincide with the instantaneous fracture energy which, in this example, is not constant. This is an example of the so-called R-curve behavior, a short for resistance curve behavior, in which the crack growth resistance increases with the crack extension (Chapter 5). In Section 2.1.6 we argue that this is not a kind of behavior consistent with the hypotheses of LEFM, which really imply that the crack growth resistance must be a constant.

2.1.5 Rice's J-Integral

One of the most famous equations in fracture mechanics is the J-integral, due to J. Rice (1968a). Although in its original derivation, the J-integral was not directly related to $\mathcal{G}$, soon after that Rice (1968b) realized that J was equal to $\mathcal{G}$. In the following paragraphs we introduce the J-integral as a particular form of expressing the energy release rate.

In deriving the J integral, the general expression (2.1.3) is used, together with a particular way of expressing the work and the elastic energy and a particular virtual process. To start fixing the main concepts, we first notice that although we have been continuously referring to a given body, any part of a body is another body in mechanical terms. Henceforth, all the equations used so far may be used for any subbody. In a plane case, we can take any contour Γ surrounding the crack tip to define a subbody and apply to it the energy balance equations —in particular Eq. (2.1.3)— to find $\mathcal{G}$. This is what is done in the derivation that follows.

The derivation of the J-integral is done in many books in an Eulerian framework, where the axes and the contour Γ move with the crack tip. It is important to realize that ours use the Lagrangian coordinates (coordinates of material points in the initial state), and then the reference subbody defines a closed system. If that were not the case, the flow (transport) terms would have to be included in the energy balance equations.

In the plane case, the elemental external work $\delta\mathcal{W}$ is (for stress-free crack surfaces) just the work done

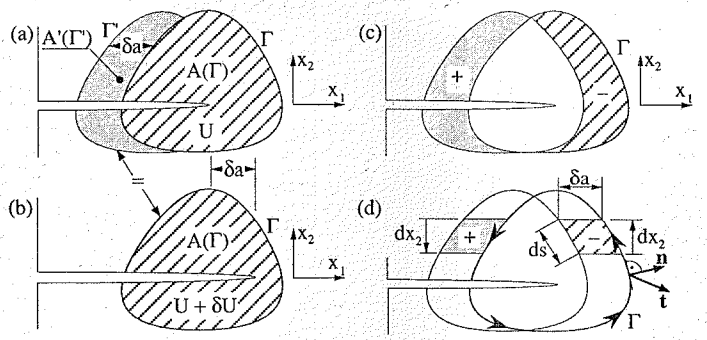

Figure 2.1.7 Determination of the variation of elastic energy by the J-integral.

by the surface tractions on the boundary Γ:

$$\delta \mathcal{W} = b \int_\Gamma t_i \delta u_i \, ds \tag{2.1.41}$$

where ds is the differential of arc-length along the contour Γ, t_i the components of the surface traction vectors acting on this boundary, and u_i the components of the displacement vector (summation is implied by repeated indices).

We write the elastic energy $\mathcal{U}$ as the integral of the elastic (or strain) energy density, $\overline{U}$, throughout the volume of the subbody defined by Γ, which, for a plane case reads

$$\mathcal{U} = b \int_{\mathcal{A}(\Gamma)} \overline{U} \, dA \tag{2.1.42}$$

where $\mathcal{A}(\Gamma)$ stands for the plane area of the subbody.

Substitution of the above equations (2.1.41) and (2.1.42) into Eq. (2.1.3) leads to:

$$\mathcal{G} \, \delta a = \int_\Gamma t_i \delta u_i \, ds - \delta \left[\int_{\mathcal{A}(\Gamma)} \overline{U} \, dA \right] \tag{2.1.43}$$

The next step is to evaluate the variations δ in any virtual elemental process. To obtain the J-integral expression, we select a virtual process in which we translate all the fields (displacement, stress, energy density) a distance δa parallel to the crack, while extending the crack by this same amount. The variation of the displacement of a given material point, situated at (x_1, x_2) due to the translation is easily obtained:

$$\delta u_i(x_1, x_2) = u_i(x_1 - \delta a, x_2) - u_i(x_1, x_2) = -u_{i,1}(x_1, x_2) \delta a \tag{2.1.44}$$

where $u_{i,1}$ stands for $\partial u_i / \partial x_1$.

The other variation to be computed is that of the elastic energy — the integral in Eq. (2.1.43). It may be evaluated in various ways. Direct analytical treatment using an expression for the elastic energy density similar to the previous equation (2.1.44) is straightforward. However, the solution may be obtained in a much more physical (and graphical) way as follows: Let the cross-hatched area shown in Fig. 2.1.7a be the subbody $\mathcal{A}(\Gamma)$ defined by the contour Γ in its initial situation. When the crack is extended and the fields are translated by δa, the subbody reaches a state as defined in Fig. 2.1.7b. Because, by construction, the fields in part (b) of the figure are those in part (a) translated, the final energy of the subbody $\mathcal{A}(\Gamma)$ coincides with the initial energy of a subbody $\mathcal{A}'(\Gamma')$ defined by a contour Γ' obtained by displacing Γ a distance δa towards the left, as shown in Fig. 2.1.7a by a lightly shaded area partially hidden by $\mathcal{A}(\Gamma)$. Therefore, the *variation* of $\mathcal{U}$ between the initial and final states, is equal to the *difference* of

initial energies between the two bodies $\mathcal{A}'(\Gamma')$ and $\mathcal{A}(\Gamma)$:

$$\delta \mathcal{U} = \mathcal{U}[\mathcal{A}'(\Gamma')] - \mathcal{U}[\mathcal{A}(\Gamma)] \tag{2.1.45}$$

and, graphically, this energy reduces to the energy contained in the two crescents shown in Fig. 2.1.7c, positive for the lightly shaded part (on the left) and negative for the cross-hatched part (on the right). The result may be expressed as a contour integral using the infinitesimal surface elements and the contour orientation depicted in Fig. 2.1.7d:

$$\delta \mathcal{U} = b \delta \left[\int_{\mathcal{A}(\Gamma)} \overline{U} \, dA \right] = -b \int_\Gamma \overline{U} \, dx_2 \; \delta a \tag{2.1.46}$$

Substitution of this result and that in Eq. (2.1.44) for δu_i in Eq. (2.1.44), finally leads to the following expression for the energy release rate:

$$\mathcal{G} = \int_\Gamma (\overline{U} \, dx_2 - t_i \, u_{i,1} ds) \tag{2.1.47}$$

The integral expression in the right hand member is Rice's J-integral. This integral can be computed (i.e., it is defined) whenever all points on contour Γ are elastic, even in situations where elastic fracture mechanics does not apply. However, the J-integral is equal to the energy release rate, $\mathcal{G}$, only if (1) the nonelastic zone reduces to a point in the interior of Γ, (2) the crack faces are traction-free, and (3) the crack is plane and extends in its own plane.

The J-integral as written in 2.1.47 is —because the factor dx_2 must take the proper sign— an *oriented* line integral. It must be performed anti-clockwise, from the lower to the upper face of the crack, to give the correct result. This need may be avoided by realizing that the sign is correctly captured if one writes $dx_2 = n_1 ds$ where n_1 is the component along the crack line of the unit outward normal to the contour, and ds is the unoriented arc-length differential. The J-integral may then be written as an unoriented contour integral with positive arc-length differential. (This is, in fact, equivalent to considering the line integral as a surface integral per unit thickness, where $ds = dA/b$ is the lateral area per unit thickness.) The resulting expression is

$$J = \int_\Gamma (\overline{U} \, n_1 - t_i \, u_{i,1}) ds \tag{2.1.48}$$

Although the J-integral can be analytically evaluated in only very few cases (one of which is shown in the forthcoming example), it is a very powerful theoretical tool.

Example 2.1.6 Consider again the pure bent DCB in Fig. 2.1.3a with the same hypotheses as stated in the preceding section. Let us compute the J integral following the path $ABCDEF$ shown in Fig. 2.1.8. Since $n_1 = 0$ and $t_i = 0$ along BC and DE, the contribution of these two segments to the J integral is zero. So is the contribution from CD if one assumes that this segment is far enough from the crack tip to be stress free. Therefore, only the segments AB and AF contribute to the integral. Moreover, their contribution is identical, by symmetry arguments. If we call σ the bending stress, which is the normal stress σ_{11} in the direction of the arm axis and the only nonzero component of the stress tensor, we have (along FE, for example): (1) $n_1 = -1$; (2) $\overline{U} = \sigma^2/2E$; (3) $t_1 = -\sigma$ (note the sign); and (4) $u_{1,1} = \varepsilon_{11} = \sigma/E$. Thus

$$J = \frac{1}{2E} \int_E^F \sigma^2 ds$$

Using $\sigma = Mz/2I$ where z is measured from the center line and $ds = dz$, Eq. (2.1.27) for $\mathcal{G}$ is readily recovered. □

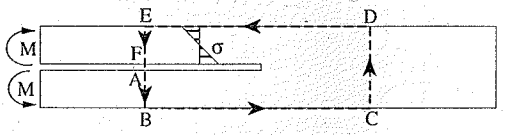

Figure 2.1.8 Integration path (dashed line) used to compute J in the pure bending DCB.

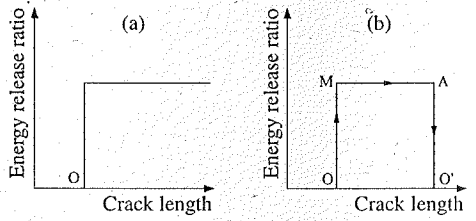

Figure 2.1.9 (a) In true LEFM, crack growth must take place under constant $\mathcal{G}$. (b) A loading-cracking-unloading process in a LEFM specimen.

2.1.6 Fracture Criterion and Fracture Energy

In true LEFM, in which nonlinear behavior and fracture occur at a single mathematical point at the crack tip, the crack must grow statically under constant $\mathcal{G}$, because the material has no memory of the previous loading. This implies that the crack growth resistance is a constant: $\mathcal{R} = G_f$. So the quasi-static loading path in a $\mathcal{G}$-a plot is a step function as depicted in Fig. 2.1.9a.

When the LEFM limit is applicable, a loading-cracking-unloading path in the $\mathcal{G}$-a plot looks as shown in Fig. 2.1.9b. Along the segment OM, $\mathcal{G}$ increases while the crack retains its initial length a_0. Along MA, the crack grows under constant $\mathcal{G} = G_f$. If at point A the specimen is unloaded, the crack will not heal, and so the unloading AO' will take place at constant crack length $a = a_1$ down to zero load.

This process may be also plotted in a P-u plot, a much more usual way of plotting experimental results. In such a plot, the constant crack length segments OM and AO' become constant compliance lines, i.e., straight lines through the origin. The MA segment is an iso-$\mathcal{G}$ curve corresponding to $\mathcal{G} = G_f$, the equation of which is obtained by eliminating the crack length a from equations 2.1.21 and 2.1.22:

$$u = C(a)\, P \tag{2.1.49}$$

$$G_f = \frac{P^2}{2b} C'(a) \tag{2.1.50}$$

The resulting P-u plot for the process shown in Fig. 2.1.9b typically looks as shown in Fig. 2.1.10a, with negative slope for the iso-$\mathcal{G}$ curve. However, there exist certain geometries where the iso-$\mathcal{G}$ curves display positive slope as depicted in Fig. 2.1.10b.

Example 2.1.7 A DCB specimen similar to that in Fig. 2.1.3b has a thickness $b = 10$ mm, width $2h = 20$ mm, and initial crack length $a_0 = 80$ mm, with $E = 300$ GPa and $G_f = 100$ N/m. We want to describe the evolution of the crack by means of the $\mathcal{G}(a)$ and $P(u)$ curves in a quasi-static test in which the displacement is monotonically increased until the crack doubles its initial length and then is decreased until complete unloading.

The $\mathcal{G}(a)$ curve is immediate (Fig. 2.1.11a): the crack length is constant and equal to $a_0 = 80$ mm while $\mathcal{G}$ is increasing up to $G_f = 100$ N/m (segment OM); from this point on, the fracture energy is kept constant at 100 N/m until the crack reaches 160 mm (point A) where unloading begins at constant crack length down to O'.

To follow the $P(u)$ process we use the approximate results for u and $\mathcal{G}$ from Examples 2.1.2 and 2.1.4.

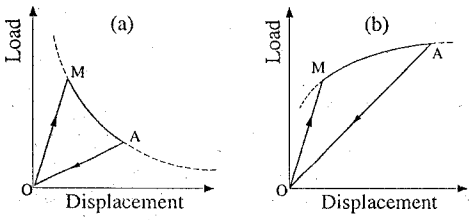

Figure 2.1.10 P-u plot of a loading-cracking-unloading in LEFM: (a) For a typical structure where iso-$\mathcal{G}$ curves display downwards slope; (b) for more exotic structures or loadings the slope of the iso-$\mathcal{G}$ curves may be positive.

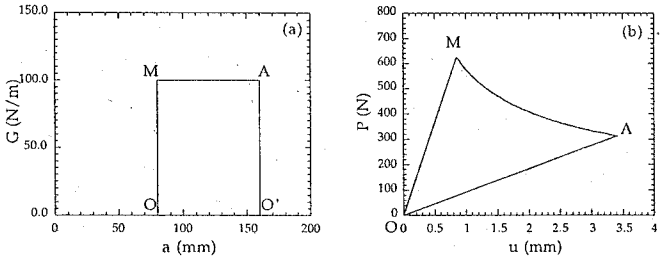

Figure 2.1.11 Process experienced by the DCB specimen in Example 2.1.7; (a) $\mathcal{G}$–a; (b) P–u diagram.

Initially, $a = a_0 = 80$ mm, and the load grows proportionally to the displacement following the first of (2.1.29) with $a = a_0$:

$$u = \frac{8Pa_0^3}{Ebh^3} \quad \Rightarrow \quad P(\text{N}) = 732.4\; u(\text{mm}) \tag{2.1.51}$$

where the dimensions in parentheses indicate the units for the load and the displacement.

Point M corresponds to $\mathcal{G} = G_f$ with $a = a_0$; the load P_M at which this condition is met is obtained from the second of (2.1.29):

$$G_f = \frac{12P_M^2 a_0^2}{Eb^2h^3} \quad \Rightarrow \quad P_M = 625 \text{ N} \tag{2.1.52}$$

corresponding to a displacement u_M that, according to (2.1.51), is given by $u_M = 0.8533$ mm. From this point on, the crack will grow and the displacement and load will evolve following Eqs. (2.1.29) with $G = G_f$. The results are:

$$P(\text{N}) = 625\,\frac{a_0}{a} \quad \text{and} \quad u(\text{mm}) = 0.8533\,\frac{a^2}{a_0^2} \tag{2.1.53}$$

which are the parametric equations of the P–u curve during the process MA in Fig. 2.1.11a. The cartesian equation is obtained by eliminating a from the foregoing equations. The result is $P = P_M\sqrt{u_M/u}$ or $P(\text{N}) = 577.4\; u^{-1/2}(\text{mm}^{-1/2})$.

Values P_A and u_A at the unloading point A are obtained by setting $a = a_A = 2a_0$ in the parametric equations (2.1.53) with the result $P_A = 312.5$ N and $u_A = 3.413$ mm. The unloading branch then follows as a linear equation down to the origin, i. e., $P = P_A u/u_A$ or $P(\text{N}) = 91.55\; u(\text{mm})$. Figure 2.1.11b shows the curve followed in the P–u diagram. □

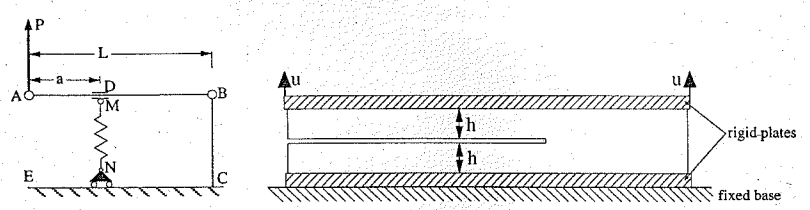

Figure 2.1.12 Illustrations for exercises 2.1 (left) and 2.8 (right).

Exercises

2.1 Consider the mechanism in Fig. 2.1.12 consisting of two rigid bars AB and BC joined by a hinge at B, and a spring MN of constant k. The spring is connected to bar AB by a frictional slider D and to the rigid support EC by a rolling support. Let L be the known length of bar AB, a the position of the slider on this bar, P the vertical load applied at point A, and u the vertical displacement of point A. (a) Find the elastic energy of the system as a function of u and a. (b) Find the load as a function of u and a. (c) Find the energy available to displace the slider a unit length, called $\mathcal{G}$ by analogy with crack growth. (d) Show that $\mathcal{G}$ is no more than the component along AB of the force that the spring exerts on the slider. (e) Show that the slider tends to move towards point B whatever the direction of the load P.

2.2 Give a detailed proof of Eqs. (2.1.20) and (2.1.21).

2.3 Derive the equivalent of equation (2.1.3) for the energy release rate in circular cracks of growing radius a in an axisymmetric stress field. (Answer: $2\pi a\mathcal{G}\,\delta a = \delta\mathcal{W}^R$.)

2.4 Show that the generalized displacement associated with the resultant force of a uniform traction distribution is the average displacement in the direction of the tractions over the area of their application. (Hint: write $t_i = \sigma e_i$, where σ is a variable stress and e_i is a fixed unit vector.)

2.5 To simulate rock fracture in the laboratory, a very large panel of thickness b with a relatively small crack of length $2a$ is tested by injecting a fluid into the crack. From Inglis (1913) results it is known that under pressure p the straight crack adopts an elliptical shape, with minor axis $c = 2pa/E'$, where the effective modulus E' is equal to the Young modulus E for generalized plane stress and equal to $E/(1-\nu^2)$ for plane strain, with $\nu =$ Poisson's ratio. (a) Find the complementary energy as a function of p and a. (b) Find the energy release rate for this case (note that a is the half crack length, not the crack length).

2.6 To test the fracture behavior of rock, a large 50-mm-thick slab will be tested in a laboratory by injecting a fluid into a central crack of initial length $2a_0 = 100$mm. Let p be the fluid pressure and V the volume expansion of the crack. In the assumption of full linear elastic behavior with $G_f = 20$ N/m, find and plot the p-V and $\mathcal{G}$-a curves the panel experiences when it is subjected to a controlled-volume injection until the crack grows up to 1000 mm, after which it is unloaded to zero pressure. Use effective elastic modulus $E' = 60$ MPa in the expression for $\mathcal{G}$ obtained in exercise 2.5.

2.7 For the panel of exercise 2.6, find and plot the p-V and $\mathcal{G}$-a curves for a test in which the crack extends from 100 mm to 1000 mm under volume expansion control and then the panel is unloaded. Assume that resistance to crack growth varies with crack extension Δa in the form

$$\mathcal{R} = 2G_f\left[1 - \frac{\Delta a}{2\lambda}\right] \qquad \text{for} \qquad 0 \le \Delta a \le \lambda \tag{2.1.54}$$

$$\mathcal{R} = G_f \qquad \text{for} \qquad \Delta a > \lambda \tag{2.1.55}$$

where $G_f = 100$ N/m and $\lambda = 276$ mm. Find the peak pressure and the maximum increase in volume. Use an effective elastic modulus $E' = 60$ GPa.

2.8 Find the J integral for an infinite strip, of thickness b and width $2h$, with a symmetric semi-infinite crack subjected to imposed zero displacements on its lower face and constant vertical displacement u on its upper face (Fig. 2.1.12; Rice 1968a). Assume linear elasticity and plane strain with known elastic modulus E and Poisson's ratio ν.

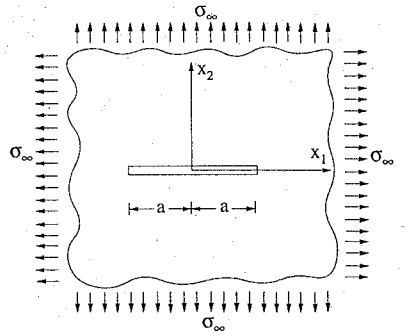

Figure 2.2.1 Center cracked infinite panel subjected to remote equiaxial tension.

2.9 A double cantilever beam specimen with arm depths $h = 10$ mm, thickness $b = 10$ mm, and initial crack length $a_0 = 50$ mm, is made of a material with a fracture energy $G_f = 180$ J/m^2 and an elastic modulus $E = 250$ GPa. The specimen is tested at a controlled displacement rate so that the load goes through the maximum and then decreases, at still increasing displacement, down to 25% of the peak load. When this point is reached, the specimen is completely unloaded. Assuming that LEFM and the beam theory apply, find the $P(u)$ and $G(a)$ curves. Give the equations of the different arcs and the coordinates of the characteristic points.

2.2 LEFM and Stress Intensity Factor

It was a great achievement of Irwin to reformulate LEFM problem in terms of the stress states in the material close to the crack tip rather than energetically and prove that this, so-called local, approach was essentially equivalent to the Griffith energetic (or global) approach.

The essential fact is that when a body contains a crack, a strong stress concentration develops around the crack tip. If the behavior of the material is isotropic and linear elastic except in a vanishingly small fracture process zone, it happens that this stress concentration has the same distribution close to the crack tip whatever the size, shape, and specific boundary conditions of the body. Only the intensity of the stress concentration varies. For the same intensity, the stresses around and close to the crack tip are identical.

To prove this assertion and to be able to solve problems for cracked structures of interest in engineering, mathematical tools specially suited to handle problems of elastic bodies with cracks were developed in the theory of elasticity. However, a user of LEFM (even a proficient one) does not need to make use of the sophisticated mathematical formalisms required to prove the most general properties of the elastic fields in cracked bodies. Therefore, in this section we present the most important results regarding linear elastic bodies with cracks. Chapter 4 gives the mathematical treatment and derivation of these results, intended only for those readers who wish to understand the sources of LEFM in greater depth.

We also restrict the analysis to the so-called *mode I*, by far the most often encountered mode in engineering practice. This is the mode where the crack lies in a plane of geometrical and loading symmetry of the structure and, therefore, no shear stresses act on the crack plane. The shear loading modes (II and III) and the fracture criteria associated with them will be analyzed in Chapter 4.

2.2.1 The Center Cracked Infinite Panel and the Near-Tip Fields

Consider a crack of length $2a$ in a two-dimensional infinite linear elastic isotropic solid, subjected to uniform normal stress σ_∞ at infinity in all directions (Fig. 2.2.1). The solution of this problem was obtained by Griffith (1921), as a particular solution of the panel with an elliptical hole obtained by Inglis (1913), and is derived in full in Chapter 4. Using the central axes shown in Fig. 2.2.1, the normal stresses

σ_{22} along the uncracked part of the crack plane ($x_2 = 0, x_1^2 - a^2 > 0$) are expressed as:

$$\sigma_{22} = \sigma_\infty \frac{|x_1|}{\sqrt{x_1^2 - a^2}} \tag{2.2.1}$$

This result shows that the stresses tend to infinity when the crack tips are approached from the solid. So the stress field has a singularity at the crack tip. In order to determine the asymptotic near-tip stress field, we write the stresses as a function of the distance r to the right crack tip, that is, replacing $x_1 - a$ with r (and x_1 with $r + a$, and $x_1 + a$ with $r + 2a$). Then, setting $x_1^2 - a^2 = (x_1 + a)(x_1 - a)$, we get for σ_{22} the following asymptotic approximation:

$$\sigma_{22} = \frac{\sigma_\infty \sqrt{a}}{\sqrt{2r}} \left[1 + \frac{3r}{4a} - \frac{5r^2}{32a^2} + ...\right] \tag{2.2.2}$$

where the factor in square brackets shows the first three terms of the Taylor series expansion of $(1 + r/a)/\sqrt{1 + r/2a}$. This factor obviously tends to 1 for $r \ll a$. It is now customary to denote

$$K_I = \sigma_\infty \sqrt{\pi a} \tag{2.2.3}$$

and call it the stress intensity factor (Subscript I refers to the opening mode of fracture, or mode I, to be distinguished from the shear modes II and III whose discussion is deferred to Chapter 4). The near-tip ($r/a \to 0$) expression for σ_{22} now becomes

$$\sigma_{22} = \frac{K_I}{\sqrt{2\pi r}} \tag{2.2.4}$$

which shows that the stress displays a singularity of order $r^{-1/2}$ at the crack tip.

For the normal displacements u_2 along the crack faces ($x_1^2 - a^2 < 0$), the elastic solution delivers

$$u_2^{\pm} = \pm \frac{2\sigma_\infty}{E'} \sqrt{a^2 - x_1^2} \tag{2.2.5}$$

where u_2^+ and u_2^- are, respectively, the vertical displacement of the upper and lower faces of the crack, and E' is the effective elastic modulus defined as

$$\begin{aligned} E' &= E && \text{for plane stress} \\ E' &= E/(1 - \nu^2) && \text{for plane strain} \end{aligned} \tag{2.2.6}$$

The crack opening w is the jump in displacement between the faces of the crack, $w = u_2^+ - u_2^-$, and is obtained from Eq. (2.2.5) as

$$w = \frac{4\sigma_\infty}{E'} \sqrt{a^2 - x_1^2} \tag{2.2.7}$$

To see how the crack opening behaves in the neighborhood of the crack tip, we rewrite the last equation as a function of the distance r from the right crack tip (now $r = a - x_1$) and substitute $\sigma_\infty = K_I/\sqrt{\pi a}$ to get

$$w = \frac{8}{\sqrt{2\pi} E'} K_I \sqrt{r} \left[1 - \frac{r}{4a} - \frac{r^2}{32a^2} + ...\right] \tag{2.2.8}$$

where the factor in the square brackets shows the first three terms of the Taylor series expansion of $\sqrt{1 - r/2a}$. Thus, the near-tip ($r \ll a$) expression for the crack opening w is

$$w = \frac{8}{\sqrt{2\pi} E'} K_I \sqrt{r} \tag{2.2.9}$$

which shows that the profile of the deformed crack is parabolic (more precisely, a parabola of the second degree with its axis coincident with the crack line.)

Although the above near-tip results made use of a quite particular case, they remain valid for all the mode I loading cases. This will be further discussed next.

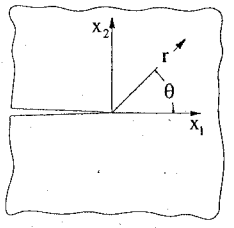

Figure 2.2.2 Axes for near crack tip field description.

2.2.2 The General Near-Tip Fields and Stress Intensity Factors

The results of the previous section may be generalized to any mode I loaded crack using various mathematical formulations described in Chapter 4 to come. The analysis shows that the stresses $\sigma_{ij}(r, \theta)$ at any distance r of the crack tip may be written as are given by

$$\sigma_{ij}(r, \theta) = \frac{K_I}{\sqrt{2\pi r}} S_{ij}(r, \theta) \tag{2.2.10}$$

where K_I is the mode I stress intensity factor proportional to the load, and functions $S_{ij}(r, \theta)$ of polar coordinates (r, θ) —Fig. 2.2.2— are regular everywhere, except at load points, other crack tips and reentrant corners. These functions are dimensionless, and thus independent of structure size and load, but they depend on the geometry of the structure and of the loading . When the crack tip is approached ($r \to 0$), the general near-tip expression may be written as

$$\sigma_{ij}(r, \theta) = \frac{K_I}{\sqrt{2\pi r}} S_{ij}^I(\theta) \tag{2.2.11}$$

where K_I is proportional to the load and the dimensionless functions $S_{ij}^I(\theta) = S_{ij}(0, \theta)$ are independent of geometry and the same for all mode I situations. They are given in Section 4.3.2, Eqs. (4.3.18)–(4.3.19).

This result means that two different linear elastic cracked bodies (different sizes, shapes, and material) subjected to mode I loading have identical stress distribution close and around the crack tip if the values of the stress intensity factors K_I are the same for both of them.

When r is not very small, the expression (2.2.11) represents the first term (the dominant one) of the series expansion in powers of r of the general expression (2.2.10). To illustrate this, the general power series expansion for the σ_{22} stress component along the crack plane, which is analogous to that for the center cracked panel, Eq. (2.2.2), is

$$\sigma_{22} = \frac{K_I}{\sqrt{2\pi r}} \left[1 + \beta_1 \frac{r}{D} + \beta_2 \frac{r^2}{D^2} + ... + \beta_m \frac{r^m}{D^m} + ...\right] \tag{2.2.12}$$

where D is a characteristic dimension of the structure (which may be, but in general need not be, chosen as the crack length a, as it was for the center-cracked panel). The dimensionless coefficients β_m, depend on the details of geometry and loading.

In the case of the center-cracked panel subjected to equiaxial remote stress, the series expansion is given by Eq. (2.2.2). For this geometry the first term is dominant, with error under within 3%, at distances $r \leq 0.04a$. For other geometries, the first term of the above series is identical, but the subsequent terms may differ appreciably (Wilson 1966; Knott 1973). However, if the size of the fracture process zone is much less than the K_I-dominated zone (a few percent of the crack size, in general) the remaining terms can be neglected and LEFM holds. If the fracture zone is too large, some inelastic fracture theory must be introduced. This is the case for concrete in most practical situations, and the main concern of this book.

Similar conclusions are reached if the displacement field around the crack tip is analyzed. The general

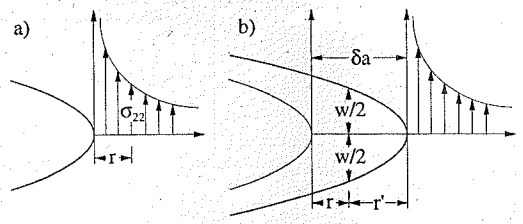

Figure 2.2.3 Near-tip stresses and crack openings in crack propagation: (a) initial situation, (b) after crack advanced an amount δa.

solution using polar coordinates at the crack tip is of the form

$$u_i(r,\theta) = \frac{K_I}{E'}\sqrt{\frac{8r}{\pi}}\,D_i(r,\theta) \tag{2.2.13}$$

where the dimensionless functions $D_i(r,\theta)$ are regular and depend on the geometry and loading. The near-tip distribution for $r \to 0$, however, is geometry independent:

$$u_i = \frac{K_I}{E'}\sqrt{\frac{8r}{\pi}}\,D_i^I(\theta) \tag{2.2.14}$$

The dimensionless functions $D_i^I(\theta) = D_i(0,\theta)$ are given in Section 4.3.2, Eq. (4.3.20).

An important consequence of Eq. (2.2.13) is the expression of the crack opening profile. The upper crack face corresponds to $\theta = \pi$ and the lower crack face to $\theta = -\pi$, so we can write $w = u_2(r,\pi) - u_2(r,-\pi)$. Thus, using (2.2.13) and expanding the resulting expression in power series of r we get an expression similar to Eq. (2.2.8) for the center cracked panel:

$$w = \frac{8}{\sqrt{2\pi}E'}K_I\sqrt{r}\left[1 + \gamma_1\frac{r}{D} + \gamma_2\frac{r^2}{D^2} + \ldots + \gamma_m\frac{r^m}{D^m} + \ldots\right] \tag{2.2.15}$$

where D is the characteristic dimension of the structure previously introduced in Eq. (2.2.12), and the dimensionless coefficients γ_m depend again on the geometry of structure and loading. It can be proved (see Chapter 4) that they are related to coefficients β_m of the stress expansion as follows:

$$\gamma_m = \frac{(-1)^m}{2m+1}\beta_m \tag{2.2.16}$$

2.2.3 Relationship Between K_I and $\mathcal{G}$

Since the asymptotic near-tip stress field is unique, and since the rate of energy flow into the crack tip must depend only on this field, there must exist a unique relationship between the energy release rate $\mathcal{G}$, and the stress intensity factor K_I. There are various ways to derive it. The simplest is to calculate the work of stress during the opening of a short slit ahead of the crack. We consider Mode I and imagine the crack tip to be advanced by an infinitesimal distance δa in the direction of axis x_1 (Fig. 2.2.3a,b). Let A and B be the initial and final state. We use the procedure illustrated in Fig. 2.2.4, where the initial stress state A has been preserved by introducing a line slit of length δa ahead of the preexisting crack, but keeping it closed by means of external surface tractions equal to the stresses existing in the actual state A (Fig. 2.2.4a). The final state B is then reached by reducing these stresses proportionally down to zero. In doing so, the intermediate states are such as the one depicted in Fig. 2.2.4b, in which the surface traction (closing tractions) are reduced to $\tau\sigma_{22}^A$, where τ is a scalar load parameter varying from 1 in the initial state A to 0 in the final state B (Fig. 2.2.4d). The crack openings in the intermediate states must vary linearly with τ because the structure is elastic, and so they must be proportional to $(1-\tau)$ and,

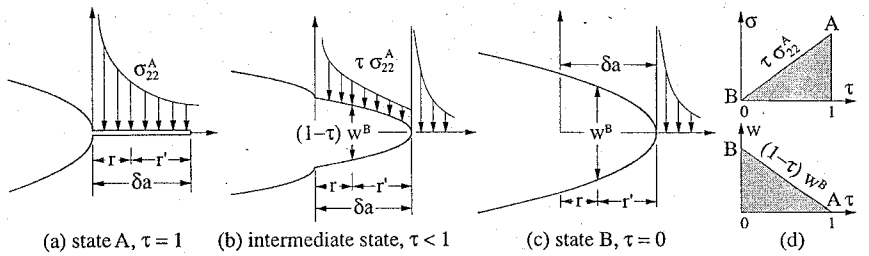

(a) state A, $\tau = 1$ (b) intermediate state, $\tau < 1$ (c) state B, $\tau = 0$ (d)

Figure 2.2.4 Proportional release of the closing tractions are used to compute the energy release rate.

therefore, equal to $(1-\tau)w^B$ (Fig. 2.2.4d). Since the remote boundaries are assumed clamped, the only energy supply in going from the initial to the final state is the work done by the closing surface tractions. The elemental work per unit area at a given location on the crack surface when the crack opens dw under tractions σ_{22} is $-\sigma_{22}dw$, the minus sign coming from the different orientation of σ_{22} (closing) and dw (opening). Using this for an elemental intermediate step in which the load factor τ varies by $d\tau$, the work (external energy supply) per unit surface of the slit turns out to be

$$d\left(\frac{d\mathcal{W}}{b\,da}\right) = -(\tau\sigma_{22}^A)d[(1-\tau)\,w^B] = -\tau\sigma_{22}^A(-d\tau\,w^B) \tag{2.2.17}$$

where b is the thickness of the body. Integration yields the total work per unit surface done by the surface tractions in passing from state A to B:

$$\frac{d\mathcal{W}_{A-B}}{b\,da} = \sigma_{22}^A\,w^B\int_1^0 \tau d\tau = -\frac{1}{2}\sigma_{22}^A\,w^B \tag{2.2.18}$$

Therefore, the total external work supply — thus also the elastic energy variation at clamped boundaries — is obtained by integration of the previous equation with respect to r:

$$\mathcal{U}_B - \mathcal{U}_A = \mathcal{W}_{A-B} = -\frac{1}{2}\,b\int_0^{\delta a}\sigma_{22}^A\,w^B\,dr \tag{2.2.19}$$

Since δa is vanishingly small, one may now use the near-tip field expressions (2.2.4) and (2.2.9),

$$\sigma_{22}^A = \frac{K_I^A}{\sqrt{2\pi r}} \quad ; \quad w^B = \sqrt{\frac{32}{\pi}}\frac{K_I^B}{E'}\sqrt{\delta a - r} \tag{2.2.20}$$

After substitution into Eq. (2.2.19), this leads to

$$\delta\mathcal{U} = \mathcal{U}_B - \mathcal{U}_A = -b\frac{2K_I^AK_I^B}{\pi E'}\int_0^{\delta a}\sqrt{\frac{\delta a - r}{r}}dr = -b\frac{K_I^AK_I^B}{E'}\,\delta a \tag{2.2.21}$$

in which the integration has been performed by means of the substitution $r = \delta a\,\sin^2 t$. Noting that under fixed boundary conditions $\mathcal{G}b\delta a = -\delta\mathcal{U}$, and that $K_I^B \to K_I^A = K_I$ for $\delta a \to 0$, we obtain the celebrated Irwin's result:

$$\mathcal{G} = \frac{K_I^2}{E'} \tag{2.2.22}$$

This shows that Griffith's and Irwin's approaches are equivalent, and allows us to discuss fracture criteria.

2.2.4 Local Fracture Criterion for Mode I: K_{Ic}.

Mode I is quite simple. Since the stress state of the material surrounding a very small fracture process zone —the crack tip— is uniquely determined by K_I, the crack will propagate when this stress intensity

factor reaches a certain critical value K_{Ic}, called fracture toughness. K_{Ic} for the given material may be determined performing a fracture test and determining the K_I value that provoked failure. Because the energy fracture criterion must also hold, and indeed does according to the fundamental relationship (2.2.22), K_{Ic} is related to the fracture energy G_f by

$$K_{Ic} = \sqrt{E' G_f} \tag{2.2.23}$$

With this definition, the local fracture criterion for pure mode I may be stated in analogy to the energy criterion: indexfracture criterion!in local approach

$$\text{if} \quad K_I < K_{Ic} \quad \text{then:} \quad \text{No crack growth (stable)} \tag{2.2.24}$$

$$\text{if} \quad K_I = K_{Ic} \quad \text{then:} \quad \text{Quasi-static growth possible} \tag{2.2.25}$$

$$\text{if} \quad K_I > K_{Ic} \quad \text{then:} \quad \text{Dynamic growth (unstable)} \tag{2.2.26}$$

For loadings that are not pure mode I, the problem becomes more difficult because, in general, an initially straight crack kinks upon fracture and the criteria must give not only the loading combination that produces the fracture, but also the kink direction. This is still an open problem today, and the interested reader may find a summary of the most widely used criteria in Chapter 4. For most of the discussions in this book, LEFM mode I fracture is all that is needed.

Exercises

2.10 Estimate the strength of a large plate under uniaxial tensile stress if it contains through cracks of up to 10 mm. The plate is made of a brittle steel with $K_{Ic} = 60$ MPa$\sqrt{\text{m}}$.

2.11 Assuming plane stress and applicability of beam theory, find the expression for the stress intensity factor (mode I) of a double cantilever beam specimen of thickness b, arm length a, and arm depth h subjected to two opposite bending moments M (see Fig. 2.1.3).

2.12 Determine the stress intensity factor of the center-cracked panel subjected to internal pressure, described in exercise 2.5 (a) Use Irwin's relationship, (b) use the near-tip expansion for the crack opening.

2.13 To test the fracture behavior of rock, a large 50-mm-thick panel of this material will be tested in a laboratory by injecting a fluid into a central crack of initial length $2a_0 = 100$mm. Let p be the fluid pressure and V the volume expansion of the crack. Assuming linear elastic behavior with $K_{Ic} = 35$ kPa$\sqrt{\text{m}}$, find and plot the p-V and K-a curves the panel would experience if it were subjected to a controlled volume injection until the crack grew up to 1000 mm, and was then unloaded to zero pressure. Use Inglis result given in exercise 2.5 and an effective elastic modulus $E' = 60$ MPa in the determination of the volume increase.

2.14 Find the stress intensity factor for the infinite strip of exercise 2.8.

2.15 Check that the coefficients of the near-tip power expansions for σ_{22} and w for the center cracked panel subjected to remote equiaxial stress satisfy the relationship (2.2.16).

2.3 Size Effect in Plasticity and in LEFM

Scaling laws are the most fundamental aspect of every physical theory. As discussed in Chapter 1, the problem of scaling law and size effect in the theories of structural failure has received considerable attention, particularly with regard to distributed damage and nonlinear fracture behavior. The necessity of using theories that correctly predict the size effect was emphasized in Section 1.2.5 and the basis for the general analysis together with some simple size effect derivations and examples was presented in Section 1.4. It was shown that for plasticity theory (and for allowable-stress analysis, too) no size effect was predicted, but that for LEFM the nominal structural strength decreased with increasing size as $D^{-1/2}$. The main objective of the present section is to derive these properties from the basic theories.

To do so, we first study the implications of limit analysis for size effect. Then we set up the general forms that the expressions for K_I and $\mathcal{G}$ must take, and derive the size effect for LEFM. We end the section

with a brief discussion of the effect of structure size on the strength of structures containing relatively very small flaws whose size is independent of the size of the structure.

We remember from Section 1.4 that, unless otherwise stated, the size effect is defined by comparing geometrically similar structures of different sizes (in the case of notched or fractured structures, the geometric similarity, of course, means that the notches or initial traction-free cracks are also geometrically similar). In this section, our interest is in analyzing the effect of the size on the nominal strength σ_{Nu} which was defined in Section 1.4.1. We recall that its general form for plane problems is

$$\sigma_{Nu} = c_N \frac{P_u}{bD} \tag{2.3.1}$$

where c_N depends only on geometrical ratios and thus is a constant for geometrically similar structures.

We also recall from Section 1.4 that, since any two consistently defined nominal stresses are related by a constant factor, the general trend of the size effect is independent of the exact choices for c_N and D. However, for quantitative analysis and, specially, for comparison of results from various sources, it is useful to make a consistent choice throughout.

2.3.1 Size Effect for Failures Characterized by Plasticity, Strength, or Allowable Stress

Consider a family of geometrically similar structures subjected to proportional loading characterized by the nominal stress σ_N. Assume that the response of the material can be fully described by a certain constitutive equation relating the stress and strain tensors. No restrictions other than rate independence are imposed on this relation. It may be linear or nonlinear elastic, elasto-plastic, or of some other more sophisticated kind. The point is that the constitutive equation and fracture criterion contain parameters which either are dimensionless (hardening exponents, strain thresholds, etc.) or have the dimension of stress (elastic moduli, yield stresses), but do not contain any parameter with dimension of length. In other words, no characteristic size exists.

Consider a reference structure of size D and a scaled geometrically similar structure of size $D' = \lambda D$. Assume that for the reference structure (that of size D) the stress at an arbitrary point of coordinates (x_1, x_2) for a given load characterized by σ_N is given by $\sigma_{ij}(\sigma_N, x_1, x_2)$. This stress distribution satisfies the equilibrium equations and the traction-imposed boundary conditions. Considering the scaled structure, it turns out that if the stresses at homologous points of coordinates $x_1' = \lambda x_1$ and $x_2' = \lambda x_2$ is taken to be identical to those for the reference structure, then this state corresponds to the actual solution for the second structure. This correspondence may be analytically stated as:

$$\sigma'_{ij}(\sigma_N, x_1', x_2') = \sigma_{ij}(\sigma_N, x_1, x_2) \quad \text{with } x_1' = \lambda x_1 \text{ and } x_2' = \lambda x_2 \tag{2.3.2}$$

Then, it is easy to prove that, with this condition, (1) the traction-imposed boundary conditions are automatically satisfied because of the similitude (the imposed surface tractions at the boundary are identical at homologous points); (2) the equilibrium conditions $\sigma_{ij,j} = 0$ are also trivially verified; (3) the constitutive equation is also satisfied if the strain fields are related by an equation similar to (2.3.2):

$$\varepsilon'_{ij}(\sigma_N, x_1', x_2') = \varepsilon_{ij}(\sigma_N, x_1, x_2) \quad \text{with } x_1' = \lambda x_1 \text{ and } x_2' = \lambda x_2 \tag{2.3.3}$$

where ε_{ij} and ε'_{ij} are the strain tensors for the structures of sizes D and D', respectively; and (4) the last equation is verified if the similitude law for the displacements is given by

$$u_i'(\sigma_N, x_1', x_2') = \lambda u_i(\sigma_N, x_1, x_2) \quad \text{with } x_1' = \lambda x_1 \text{ and } x_2' = \lambda x_2 \tag{2.3.4}$$

which is proven as follows:

$$\varepsilon'_{ij}(\sigma_N, x_1', x_2') = \frac{1}{2}\left(\frac{\partial u_i'}{\partial x_j'} + \frac{\partial u_j'}{\partial x_i'}\right) = \frac{1}{2}\left(\frac{\lambda \partial u_i}{\partial(\lambda x_j)} + \frac{\lambda \partial u_j}{\partial(\lambda x_i)}\right) =$$

$$= \varepsilon_{ij}(\sigma_N, x_1, x_2) \quad \text{with } x_1' = \lambda x_1 \text{ and } x_2' = \lambda x_2 \tag{2.3.5}$$

Therefore, the laws of similitude (2.3.2) and (2.3.3) just state that for a given nominal stress σ_N, the stresses and strains at homologous points of two geometrically similar structures are identical. This implies, in particular, that the stress and strain maxima and minima also occur at homologous points.

If failure is assumed to occur when the stress, strain, or, in general, a certain function of the two $\Phi(\sigma_{ij}, \varepsilon_{ij})$ reaches a critical value, i.e., when:

$$\Phi(\sigma_{ij}, \varepsilon_{ij}) = \Phi_c \tag{2.3.6}$$

where Φ_c is a given critical or allowable value, then the two similar structures will fail at the same nominal stress. Thus, for theories such as plasticity or elasticity with strength limit or allowable stress, the nominal strength of two similar structures of sizes D and D' is identical:

$$\sigma'_{Nu} = \sigma_{Nu} \tag{2.3.7}$$

In such a case we say that there is no size effect.

The foregoing result may be also obtained from dimensional analysis. Indeed in this kind of problem, the external load at fracture is completely determined by σ_{Nu}, D and a number of geometrical ratios γ_i (those defining the shape, for example, the span-to-depth ratio). The material response is determined by a certain critical or allowable stress σ_c and a number of dimensionless ratios μ_i (the hardening exponent, strain parameters, and ratios of elastic modulus to the allowable stress, E/σ_c, for example). With these variables, the only dimensionally correct expression for the nominal strength is

$$\sigma_{Nu} = \sigma_c \phi(\gamma_i, \mu_i) \tag{2.3.8}$$

where $\phi(\gamma_i, \mu_i)$ is a dimensionless function. Since the arguments γ_i are geometrical ratios that remain constant for geometrically similar structures, and since the μ_i are constants for a given material, (2.3.7) follows.

2.3.2 General Forms of the Expressions for K_I and $\mathcal{G}$

Since crack growth in LEFM is defined by the condition $\mathcal{G} = G_f$ or $K_I = K_{Ic}$, we need to know the structure of the equations for K_I and $\mathcal{G}$ if we want to investigate the influence of the size. And since size effect is one of the main topics of this book, it is also convenient to define the conventional forms of the equations we are going to use so that the size D is made explicit. Systematization of the presentation of the existing results also requires using general mathematical forms of the equations for K_I and $\mathcal{G}$, so that a single experimental or numerical result may be used for any similar specimen or structure.

To determine the general form, we consider a family of geometrically similar structures subjected to the same type of loading (for example, the center cracked panel in Fig. 2.1.1 or the DCB specimens in Fig. 2.1.3). Let D be a characteristic dimension (for example, the panel width or the arm depth in the DCB specimen), all the remaining dimensions being proportional (for example, the height-to-width ratio of the panel and the total length-to-depth ratio for the DCB), except for the crack-to-depth ratio a/D, which is free to vary. The purpose of the analysis is to obtain the general expression for $\mathcal{G}$ and K_I showing explicitly the dependence on the variables P (or σ_N), D and $\alpha = a/D$. Let us first elaborate the examples:

Example 2.3.1 For the center cracked panel with a short crack ($\alpha = a/D \ll 1$) the expression for the stress intensity factor (2.2.3) can be written in either of the two following forms:

$$K_I = \sigma_N \sqrt{D} \sqrt{\pi\alpha} = \frac{P}{b\sqrt{D}} \sqrt{\pi\alpha} \tag{2.3.9}$$

where we set $\sigma_N = \sigma = P/bD$, and b is the panel thickness. □

Example 2.3.2 For the DCB specimen of Fig. 2.1.3b, we take the approximate expression (2.1.29), substitute it into Irwin's relationship (2.2.22) (assuming plane stress, $E' = E$), and then we get

$$K_I = \sigma_N \sqrt{D} 2\alpha\sqrt{3} = \frac{P}{b\sqrt{D}} 2\alpha\sqrt{3} \tag{2.3.10}$$

where we substituted $D = h$, $\sigma_N = P/bD$. □

The resemblance of the expressions for the these two simple cases is evident. They only differ in the factors depending on α ($\sqrt{\pi\alpha}$ for the panel and $2\alpha\sqrt{3}$ for the DCB specimen). This result is general. Indeed, because the response is linear elastic, the stress intensity factor must be proportional to the force per unit thickness P/b. Since the stress intensity factor must have dimensions of Force×Length$^{-3/2}$ and must depend on the relative crack depth α, the only possible forms of the expression based on P and σ_N are:

$$K_I = \frac{P}{b\sqrt{D}} \hat{k}(\alpha) = \sigma_N \sqrt{D}\, k(\alpha) \tag{2.3.11}$$

where $\hat{k}(\alpha)$ and $k(\alpha)$ are dimensionless functions, $\alpha = a/D$ is the relative crack depth, and $k(\alpha) = \hat{k}(\alpha)/c_N$. The convention of using 'hatted' k for expressions based on P and plain k for expressions based on σ_N will be retained throughout the book.

The general forms for the energy release rate $\mathcal{G}$ may be obtained directly from the foregoing by using Irwin's relationship (2.2.22). They are

$$\mathcal{G} = \frac{P^2}{b^2 D E'} \hat{g}(\alpha) \quad \text{or} \quad \mathcal{G} = \frac{\sigma_N^2}{E'} D\, g(\alpha) \tag{2.3.12}$$

where

$$\hat{g}(\alpha) = \hat{k}^2(\alpha) \quad \text{and} \quad g(\alpha) = \frac{1}{c_N^2} \hat{g}(\alpha) = k^2(\alpha) \tag{2.3.13}$$

In what follows, we systematically use the forms (2.3.11) and (2.3.12). Other equivalent forms can be found in the literature, as discussed latter.

Another simple argument leading to (2.3.12) is to note that the complementary energy of the structure must be expressible as $\mathcal{U}^* = 2\overline{U} V f(\alpha)$, where $\overline{U} = \sigma_N^2/2E'$ is a nominal energy density, $V = bD^2$ is the volume of the structure and $f(alpha)$ is a dimensionless function. Then $\mathcal{G} = \partial\mathcal{U}^*/b\partial a = (\partial\mathcal{U}^*/\partial\alpha)/bD = (\sigma_N^2/E')Df'(\alpha)$. Setting $g(\alpha) = f'(\alpha)$, one gets Eq. (2.3.12).

2.3.3 Size Effect in LEFM

Consider now a family of geometrically similar plane cracked structures loaded in mode I. Let a_0 be the initial crack length and $\alpha_0 = 0/D$ the initial relative crack length. From (2.3.11), the crack growth condition, $K = K_{Ic}$ is fulfilled when σ_N reaches a value σ_{Ni} (initiation stress) given by

$$\sigma_{Ni} = \frac{K_{Ic}}{\sqrt{D} k(\alpha_0)} \tag{2.3.14}$$

After reaching this point, the crack will grow and the nominal stress will vary to keep $K_I = K_{Ic}$, i.e.,

$$\sigma_N = \frac{K_{Ic}}{\sqrt{D} k(\alpha)} \quad \text{for} \quad \alpha > \alpha_0 \tag{2.3.15}$$

Obviously, if $k(\alpha)$ increases with α, then σ_N decreases after the crack starts to grow and the peak load coincides with the onset of crack growth. If, on the other hand, $k(\alpha)$ decreases with α, then σ_N increases after the crack starts to grow and, eventually, reaches a maximum when $k(\alpha)$ reaches a minimum. The first case corresponds to the so-called *positive geometries* (Planas and Elices 1989a) and for them

$$\sigma_{Nu} = \sigma_{Ni} = \frac{K_{Ic}}{\sqrt{D} k(\alpha_0)} \quad \text{if} \quad k'(\alpha_0) > 0 \tag{2.3.16}$$

where $k'(\alpha_0)$ stands for the derivative of $k(\alpha)$ at $\alpha = \alpha_0$. For negative geometries, the peak load occurs when the crack length reaches a value α_M for which $k(\alpha)$ goes through a minimum, thus,

$$\sigma_{Nu} = \frac{K_{Ic}}{\sqrt{D} k(\alpha_M)} \quad \text{if} \quad k'(\alpha_0) > 0 \quad k(\alpha_M) = \text{minimum} \tag{2.3.17}$$

In any case, since both α_0 and α_M are constant for geometrically similar structures, it turns out that the nominal strength is always inversely proportional to the square root of the size. Hence, for similar precracked structures of sizes D_1 and $D = \lambda D_1$, the nominal strengths are related by

$$\sigma_{Nu} = \sigma_{Nu_1}\sqrt{\frac{D_1}{D}} = \lambda^{-1/2}\sigma_{Nu_1} \propto D^{-1/2} \tag{2.3.18}$$

Thus, it has been generally proved that geometrically similar structures following LEFM exhibit the inverse square root size effect.

2.3.4 Structures Failing at Very Small Cracks Whose Size is a Material Property

The foregoing size-effect analysis applies always to structures in which the crack length at maximum load is proportional to the size of the structure. This kind of size effect, however, differs from that found in normal kinds of metallic and other structures which become unstable and fail (or must be assumed to fail) before a small flaw, represented by a microcrack, can become a macrocrack of significant length compared to the structure size.

If the crack is small compared to the distances over which the stresses vary appreciably (let's call them microcracks, for short), it is easy to show (see the superposition method to compute K_I in the next chapter) that the stress intensity factor always takes the form

$$K_I = k_0\sigma\sqrt{a} \tag{2.3.19}$$

where σ is the stress normal to the microcrack plane at the microcrack location computed as if no microcrack existed in the structure; a is the half-length or radius (for a pennyshape) of the microcrack and k_0 a constant depending on the exact shape and location of the crack (but not on microcrack or structure size). Consider now two structures that are similar (which means macro-geometrically similar) and contain identical microcracks in homologous positions. Since we have proved in Section 2.3.1 that the stresses at homologous positions are identical, it follows that the microcrack at a specific site starts to grow in both structures at the same nominal stress level. If one further assumes that *global failure follows immediately after one of the cracks starts to grow,* it turns out that the two structures will fail at the same nominal stress level. Hence, in this type of similitude no size effect is present because, in fact, it is equivalent to analysis based on allowable-stress or strength criterion (in which the allowable stress or strength varies from microcrack site to microcrack site).

However, getting similar structures with identical distribution of microcracks is practically impossible, so actual structures are macroscopically similar but microscopically random. Then the strength of the structure can be defined only on statistical (probabilistic) grounds, and a size effect appears because the probability of getting larger flaws in the more highly stressed regions of the structure increases with the structure size. The analysis of this kind of size effect will be deferred until Chapter 12, where we prove that the statistical size effect vanishes asymptotically when macrocracks or notches exist at the start of failure in the body (see also the short discussion in Section 1.3).

With respect to quasibrittle materials, and particularly concrete, it is important to note that they contain plenty of microcracks, but failure does not happen as soon as one of these microcracks starts to grow. It only occurs after many microcracks have grown and coalesced to form a macroscopic fracture process zone. This is a feature that makes the classical statistical theory of strength inapplicable to these materials.

Exercises

2.16 Show that the stress intensity factor for a penny shaped crack of radius a coaxial to a cylindrical bar of diameter D subjected to uniaxial stress σ must take the form (2.3.11). What is the form if K_I is written in terms of the axial load $P = \sigma\pi D^2/4$?

2.17 Find the general forms for the energy release rate of a penny shaped crack of radius a coaxial to a cylindrical bar of diameter D subjected to uniaxial stress σ.

2.18 In most handbooks on stress intensity factors, K_I is written in the form $K_I = Y\sigma\sqrt{\pi a}$ where a is the crack length, σ a characteristic stress, and Y a dimensionless factor depending only on geometrical ratios, in particular on the relative notch depth a/D where D is a characteristic linear dimension of the body. Rewrite this in the form (2.3.11) and find the relationship between Y and $k(\alpha)$.

2.19 Write the stress intensity factor of the DCB specimen of Fig. 2.1.3b in terms of the relative displacement u of the load-points. Show that the general form of K_I for imposed displacement must be $K_I = (Eu/\sqrt{D})\tilde{k}(\alpha)$ where E is the elastic modulus, u the displacement, D a characteristic dimension of the body, $\alpha = a/D$ the relative crack depth, and $\tilde{k}(\alpha)$ a nondimensional function.

2.20 To analyze the behavior of a large structure with cracks, which is assumed to behave in an essentially linear elastic manner, a reduced scale model is built at a 1/10 scale. The model is tested so that the stresses at homologous points are identical in both model and reality, and we require the full scale and reduced models to break at the same stress level. Determine the scale factors for (a) loads, (b) toughness, and (c) fracture energy.

3

Determination of LEFM Parameters

The application of LEFM to practical problems requires knowledge of the stress intensity factors or the energy release rates for the actual geometry and type of loading. In many cases one further needs the evolution of K_I with crack length. The selection of the method adequate to treat a particular problem depends very much on external inputs: economical importance of the problem; time available for analysis; bibliographical, analytical, numerical, and experimental facilities available to the analyst.

Fracture mechanics literature contains a vast number of closed form solutions of various elastic bodies with cracks. If the problem at hand can be approximated by one of the cases in the handbooks or papers, the problem is solved with ease. Section 3.1.1 briefly shows the use of closed form solutions from the handbooks. Quite often the problem does not coincide with any of the cases of the handbook, but can be obtained by superposition of other cases. The superposition may range from simple two-state cases to continuous weighted superposition in the sense of Green's function. Section 3.1.2 illustrates by some examples the use of the superposition method.

Close to the handbook cases solved with ease are the cases where the elastic energy release rate can be analytically calculated using the energetic approaches of Section 2.1, together with adequate simplifying assumptions. The stress intensity factor, usually mode I intensity factor, then follows from Irwin's relationship $K_I = \sqrt{E'\mathcal{G}}$. Section 3.2 illustrates some of the available approximations.

When no closed-form solutions are available, other strategies are at hand for the analyst to choose. The first one is to try to find an analytical solution. This is a highly specialized mathematical task out of the reach of most engineering practitioners and researchers. It can be accomplished by one of the formal approaches described in Chapter 4, and is outside the scope of this book.

When all the analytical treatments fail — because Green's functions are not available for the geometry of interest, for example — one may resort to numerical methods, an expedient that is getting increasingly easy to handle, increasingly reliable, and becoming readily accessible to engineers (Section 3.3.1). Alternatively, the stress intensity factor of reduced-scale elastic specimens can be experimentally measured in various ways (Section 3.3.2).

Application of LEFM to practical cases requires the fracture parameters of the given materials to be known, too. The main aspects of the determination of K_{Ic} and G_f are presented in Section 3.4.

An aspect often involved in fracture problems is the determination of displacements and similar variables such as crack volume or crack opening profile. Section 3.5 shows how these displacements can be calculated when closed form expressions for the stress intensity factor as a function of crack length are known. As a corollary, the stress intensity due to a point load on the crack faces is determined from the expressions of the crack opening profile and stress intensity factor for another arbitrary loading —an expression known as Bueckner's (1970) weight function.

3.1 Setting up Solutions from Closed-Form Expressions

3.1.1 Closed-Form Solutions from Handbooks

A large number of solutions for stress intensity factors have been collected in handbooks (Sih 1973; Rooke and Cartwright 1976; Tada, Paris and Irwin 1985; Murakami 1987). The energy release rates are not included in these handbooks because the expressions for K_I are simpler, and the expressions for $\mathcal{G}$ are very easily obtained from those for K_I using Irwin's equation.

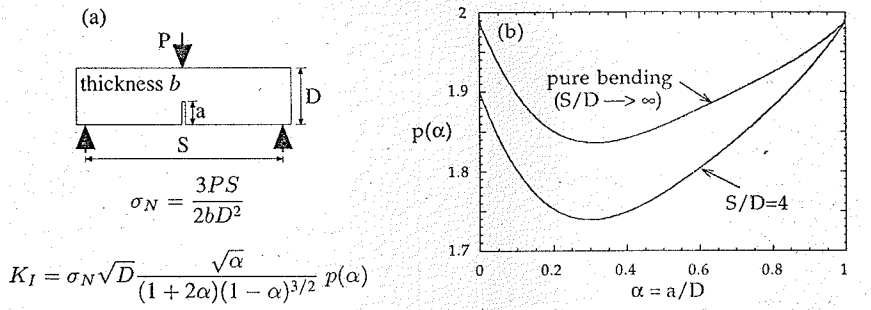

Figure 3.1.1 Notched beam in three-point bending. (a) Definition of geometry and expression for K_I; (b) variation of the shape factor $p(\alpha)$.

A few of the collected solutions are exact. Most of them are empirical fits of approximate but accurate numerical results. In a few cases no analytical expressions are given, but a graphical representation of the results is provided. In most cases of complex analytical expressions, a graphical representation is provided as well as the closed-form expression. Different fits, with different ranges of applicability and different accuracies, may be available for a given case, a point that must never be overlooked.

In this book, we write the expressions for K_I in the form (2.3.11) because of our interest in the size effect. This is to be taken into account when comparisons are made with handbooks in which the prototype expression for a stress intensity factor is taken to be that for a center cracked infinite panel, so most handbooks use the form $K_I = \sigma_N\sqrt{\pi a}F(\alpha)$, where $F(\alpha)$ is a dimensionless function of the relative crack length. Comparing this with (2.3.11), it turns out that the relationship between $k(\alpha)$ and $F(\alpha)$ is $k(\alpha) = \sqrt{\pi\alpha}F(\alpha)$.

Example 3.1.1 For a single-edge cracked beam subjected to three-point bending (Fig. 3.1.1a), the expression for K_I depends mildly on the shear force magnitude near the central cross-section, i.e., on the span-to-depth ratio. Fig. 3.1.1b shows a plot of $k(\alpha)$ for the limiting case of pure bending (formally equivalent to $S/D \to \infty$) and for the case $S/D = 4$ (a standard ASTM testing geometry). Analytical approximate expressions for these two cases were produced by Tada, Paris and Irwin (1973), for pure bending, and by Srawley (1976), for $S/D = 4$. Recently, Pastor et al. (1995) produced expressions accurate within 0.5% for any a/D. The latter expressions have the advantage over the former that their structure is identical (additionally, they correct a 4% error that crept in the Srawley formula in the limit of short cracks). With the definition of σ_N shown in Fig. 3.1.1, the shape factor takes the form

$$k_{S/D} = \sqrt{\alpha}\,\frac{p_{S/D}(\alpha)}{(1+2\alpha)(1-\alpha)^{3/2}} \tag{3.1.1}$$

where $p_r(\alpha)$ is a fourth degree polynomial in α. The expression of the polynomials for $S/D = 4$ and ∞ (pure bending) are

$$p_4(\alpha) = 1.900 - \alpha\left[-0.089 + 0.603(1\text{–}\alpha) - 0.441(1-\alpha)^2 + 1.223(1-\alpha)^3\right] \tag{3.1.2}$$

$$p_\infty(\alpha) = 1.989 - \alpha(1\text{–}\alpha)\left[0.448 - 0.458(1-\alpha) + 1.226(1-\alpha)^2\right] \tag{3.1.3}$$

Note that for very short cracks ($\alpha \to 0$) the shape factors $k(\alpha)$ behave as $c_0\sqrt{\pi\alpha}$, where c_0 is a constant close to 1.12. For very deep cracks ($\alpha \to 1$), $k(\alpha) \propto c_1(1-\alpha)^{-3/2}$, where c_1 is a constant close to 2/3. This is the general trend for specimens in which the resultant force over the crack plane is zero. □

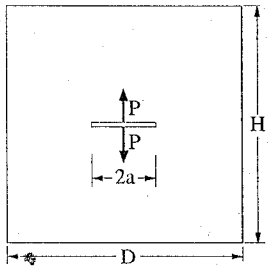

Figure 3.1.2 Center crack loaded by symmetric concentrated forces.

Example 3.1.2 The stress intensity factor for the center cracked panel of Fig. 2.1.1 was obtained numerically by Isida (1973) with very high accuracy for $H \gg D$. These results may be approximated within 0.1% by the Feddersen-Tada expression (Feddersen 1966; Tada, Paris and Irwin (1973))

$$K_I = \sigma\sqrt{D}k(\alpha), \qquad k(\alpha) = \sqrt{\frac{\pi\alpha}{\cos\pi\alpha}}\,(1 - 0.1\alpha^2 + 0.96\alpha^4) \tag{3.1.4}$$

In this case, the behavior for short cracks coincides with that for an infinite panel, $k(\alpha) \to \sqrt{\pi\alpha}$; for long cracks ($\alpha \to 0.5$), $k(\alpha) \to c_2(1-2\alpha)^{-1/2}$ where c_2 is a constant very close to 1. □

Example 3.1.3 The stress intensity factors for cracks with concentrated loads applied on the crack faces display a completely different type of dependence on the crack length. The simplest case is that of a center-cracked infinite panel loaded with two equal and opposite forces at the centers of the crack faces (Fig. 3.1.2, with a/H and $a/D \ll 1$). The stress intensity factor is then written as

$$K_I = \frac{P}{b\sqrt{\pi a}} \tag{3.1.5}$$

which shows that for a given load P the stress intensity factor *decreases* as the crack length increases. It is obvious, however, that this decrease cannot be indefinite for a real (finite) plate. Indeed, based on numerical results by Newman (1971), Tada, Paris and Irwin (1973) proposed the following modified formula for a finite panel of width D and height $H = 2D$:

$$K_I = \frac{P}{b\sqrt{D}}\hat{k}(a/D), \qquad \hat{k}(\alpha) = \frac{1 - 0.5\alpha + 0.957\alpha^2 - 0.16\alpha^3}{\sqrt{\pi\alpha(1-2\alpha)}} \tag{3.1.6}$$

with error less than 0.3% for any a/D. Note that for a relatively small crack length ($a/D \to 0$), this expression coincides with that for the infinite panel. On the other hand, for large cracks ($a/D \to 0.5$), $\hat{k}(\alpha) \to c_2(1-2\alpha)^{-1/2}$, which coincides with the previous example if one sets $\sigma_N = P/bD$. □

3.1.2 Superposition Methods

One of the advantages of LEFM is that the solutions for different loading cases are additive in stresses, strains, and displacements. Since stress intensity factors are nothing but parameters of the stress field, the stress intensity factors are also additive. This explains why Irwin's local approach is more popular than Griffith's global approach, even though they are generally equivalent. The energy release rates are not additive (although they are square-root additive); however, special care must be taken in problems in which geometrical nonlinearities arise. Such is generally the case when the resultant mode I stress intensity factor at any of the crack tips becomes negative. This implies interpenetration of the faces of the crack which is in reality impossible; instead, there is partial closing of the crack with face-to-face compression, which is a nonlinear phenomenon.

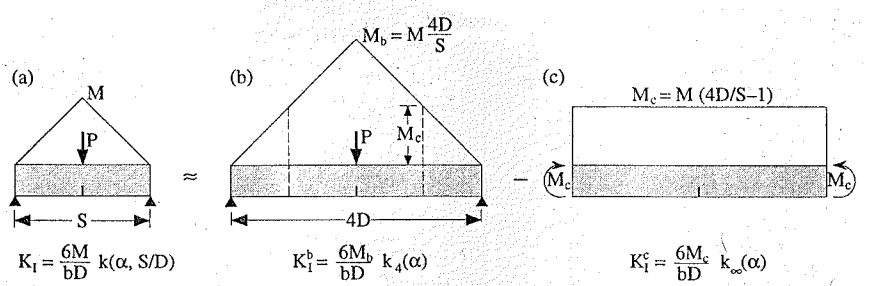

Figure 3.1.3 Load decomposition in three-point bent beams.

The literature is replete with problems solvable by superposition. Many cases are quite obvious: the actual loading often is just a superposition of various simpler loadings for which the stress intensity factors are known. This is the case for eccentric tension or compression of cracked strips which are solved by superposition of a pure tension or compression state and a pure bending state. Sometimes the simple states are not so obvious, as the following example shows.

Example 3.1.4 To obtain the stress intensity factor of a single-edge cracked specimen subjected to three-point bending for arbitrary span-to-depth ratio, Guinea (1990) and Pastor et al. (1995) used the approximate superposition illustrated in Fig. 3.1.3. In this approximation, the solutions for $S/D = 4$ (Fig. 3.1.3b) and for pure bending (Fig. 3.1.3c) are superposed so that the resulting bending moment distribution over the central part is the same as that for the actual beam (Fig. 3.1.3a). The result may be written as:

$$k_{S/D}(\alpha) = k_\infty(\alpha) + \frac{4D}{S}[k_4(\alpha) - k_\infty(\alpha)] \tag{3.1.7}$$

where $k_4(\alpha)$ and $k_\infty(\alpha)$ are the solutions for $S/D = 4$ and ∞ given in the example 3.1.1. Rearranging, the final expression turns out to be of the form (3.1.1) with $p_{S/D}(\alpha)$ given by

$$p_{S/D}(\alpha) = p_\infty(\alpha) + \frac{4D}{S}[p_4(\alpha) - p_\infty(\alpha)] \tag{3.1.8}$$

with $p_4(\alpha)$ and $p_\infty(\alpha)$ given by (3.1.2) and (3.1.3). This solution was checked against existing results in the literature for $S/D = 8$ (Brown and Srawley 1966) and finite element results using very small singular quarter-node elements for $S/D = 8$ and 2.5 (Pastor et al. 1995). The results coincided within 1%. □

A particularly important class of superposition is that in which the effect of remotely applied stresses is first reduced to the effect of a stress distribution over the crack faces and then the stress intensity factor, due to this stress distribution, is obtained by integration of the stress intensity factor due to a point load at an arbitrary location on the crack faces. Let us illustrate these steps by examples; first the reduction to a case with stresses on the crack faces.

Example 3.1.5 Consider a center-cracked panel subjected to remote uniaxial stress σ. We may decompose the whole elastic solution (Fig. 3.1.4a) as the solution for an *uncracked* panel (Fig. 3.1.4b) and the solution for a cracked panel with the faces of the cracks subjected to stresses identical but opposite to those in the uncracked panel (Fig. 3.1.4c). In this way, the remote boundary conditions are satisfied, as well as the boundary conditions on the crack face. Of course, the stress intensity factor for load case (b) is zero (there is no singularity in an uncracked panel) so that one finds that the stress intensity factors of cases (a) and (c) are identical. This particular example proves that the stress intensity factor for a center-cracked panel subjected to remote uniaxial stress σ is identical to that corresponding to a center-cracked panel with the crack subjected to internal pressure $p = \sigma$. □

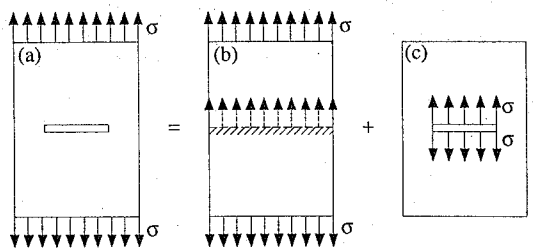

Figure 3.1.4 Solution for a cracked panel expressed as superposition of the solution for an uncracked panel and the solution for a loaded crack with no remote stresses.

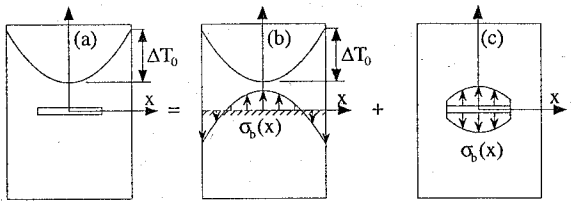

Figure 3.1.5 Superposition used to analyze thermally induced stress intensity factors.

Even if the foregoing examples may seem very simple, the basic procedure is always the same. In particular, this is the most usual method when internal stresses build up due to thermal or moisture gradients. In those cases, the internal stress distribution is first computed for the body without crack (but with non-uniform temperature or moisture distribution), and then equal and opposite stresses are applied on the crack faces (while keeping uniform temperature).

Example 3.1.6 Consider a long center-cracked panel with free ends subjected to heating on both its sides. Assume that at a given instant the temperature profile is parabolic across the section: $\Delta T = \Delta T_0(2x/D)^2$ (Fig. 3.1.5a). We decompose this state in the state shown in Fig. 3.1.5b, with thermal gradient and no crack, and the state shown in Fig. 3.1.5c, with no thermal gradient and stresses on the crack faces equal and opposite to those in case (b). The stresses in case (b) may be estimated in the classical way by assuming that initially plane sections remain plane. If we call β the coefficient of linear thermal expansion, the result for the stress distribution along the crack plane is

$$\sigma^b = \frac{1}{3}\beta E \Delta T_0 \left[1 - 2\left(\frac{2x}{D}\right)^2\right] \tag{3.1.9}$$

Except for a change in sign, this is the stress distribution to be applied on the crack faces in state (c). As in the previous example, the stress intensity factor for the original state (a) is equal to that for state (c) because in state (b) there is no crack and thus there is no stress singularity. □

Once the equivalent problem with stresses on the crack faces has been obtained, the problem remains of finding the stress intensity factor for this case. This may be done directly if the so-called *Green function* for the problem is known. The Green function is no more than the expression for the stress intensity factor engendered by a unit point load applied at any location on the crack face.

To be systematic, we write the stress intensity factor generated by a load-pair P_x located at point x on

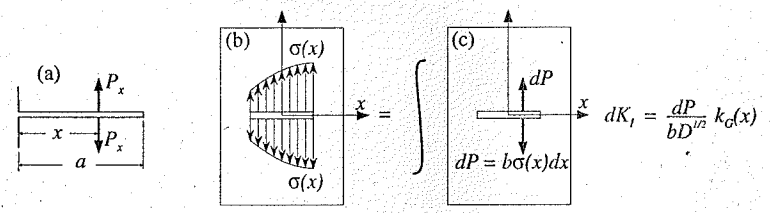

Figure 3.1.6 Superposition based on Green's function: (a) Base problem; (b) general problem for a center cracked panel; (c) Superposition corresponding to the general problem.

the crack faces (Fig. 3.1.6a) in the form

$$K_I = \frac{P_x}{b\sqrt{D}} k_G(\alpha, x/D) \tag{3.1.10}$$

where $k_G(\alpha, x/D)$ is the dimensionless Green function (the Green's function with dimensions includes the factor $1/b\sqrt{D}$). If k_G is known, the stress intensity factor generated by an arbitrary stress distribution over the crack faces is easily obtained by integration, as shown in the following example (which can easily be generalized to other more complex situations).

Example 3.1.7 Consider the center-cracked panel subjected to a known normal stress distribution over the crack faces, symmetric with respect to the crack plane (Fig. 3.1.6b). Let the stress at relative distance x/D from the crack center be $\sigma(x/D)$. If we subdivide the crack into infinitesimal length elements dx, the element at x contributes with an elemental concentrated load $dP_x = b\,\sigma(x/D)$. According to (3.1.10) this produces an infinitesimal stress intensity factor $dK_I = (\sigma(x/D)/\sqrt{D}) k_G(\alpha, x/D)\ dx$. Now, adding up the contributions from all the elements we get

$$K_I = \int dK_I = \frac{1}{\sqrt{D}} \int_{-a}^{a} \sigma(x/D) k_G(\alpha, x/D)\ dx \tag{3.1.11}$$

or, with the change $x/D = u$

$$K_I = \sqrt{D} \int_{-\alpha}^{\alpha} \sigma(u)\ k_G(\alpha, u)\ du \tag{3.1.12}$$

To check this approximation, let us consider the previous Examples 3.1.5 and 3.1.6 for the limiting case $\alpha = a/D \ll 1$. In such a limit, the plate may be considered to be infinite, and the function $k_G(\alpha, u)$, with $u = x/D$, simplifies to

$$k_G(\alpha, u) = \frac{1}{\sqrt{\pi\alpha}} \frac{\alpha + u}{\sqrt{\alpha^2 - u^2}} \tag{3.1.13}$$

Substitution of this expression into (3.1.12) gives

$$K_I = \sqrt{D}\ \frac{1}{\sqrt{\pi\alpha}} \int_{-\alpha}^{\alpha} \sigma(u)\ \frac{\alpha + u}{\sqrt{\alpha^2 - u^2}}\ du \tag{3.1.14}$$

For the case of uniform tension $\sigma(u) = \sigma =$ constant, the integration readily delivers the well-known result $K_I = \sigma\sqrt{\pi a}$ (in the integral, set $u = \alpha \sin t$, $du = \alpha \cos t\ dt$). For the case of the parabolic distribution of temperature in Example 3.1.6 we notice that since we are considering $a/D \ll 1$, and since $x \leq a$, then the term $2(2x/D)^2$ in (3.1.9) is also negligible. Thus, the stress intensity factor for this case is just $K_I = \beta E \Delta T_0 \sqrt{\pi a}/3$. □

The function $m_G = K_I/P_x = k_G(\alpha, x/D)/\sqrt{D}$ is called the weight function, of which k_G is a dimensionless version. Finding the weight function for a particular case is a difficult problem of elasticity theory, which will be briefly outlined in Section 3.5.5. For a systematic approach to the weight function method, see Wu and Carlsson (1991).

Exercises

3.1 A long strip of width $D = 400$ mm is subjected to variable uniaxial stress with peaks of 14 MPa. In these conditions, edge cracks may be assumed to grow due to fatigue, and the designer wants the strip not to fail before the fatigue cracks are clearly visible. Determine the required toughness (K_{Ic}) if the crack length at which the strip fails must be (a) at least 10 mm, (b) at least 50 mm. Give also the values of the fracture energy if the material is a steel ($E' \approx 200$ GPa).

3.2 In a long strip of width $D = 300$ mm, the expected peak stress (uniaxial) is 30 MPa. If there exist welding flaws which resemble a center crack, determine the maximum flaw size allowable if the fracture toughness is 96 MPa$\sqrt{\text{m}}$ and (a) the strength safety factor is 1; (b) the strength safety factor is 2. (Hint: make a first estimate of a assuming $a/D \ll 1$, and then iterate until 1% accuracy of the result.)

3.3 Estimate the stress intensity factor for eccentric tension in a single-edge cracked strip. Let P be the load, D and b the strip width and thickness, and e the eccentricity (positive towards the cracked side). Write the results as (a) $(P/b\sqrt{D})k(\alpha)$; (b) $\sigma_N\sqrt{D}k(\alpha)$, with σ_N equal to the mean remote tensile stress; (c) same, but with σ_N equal to the maximum remote tensile stress; show that in this latter case, the shape function $k(\alpha)$ for very short cracks tends to the same value as that for a semi-infinite plate with an edge crack.

3.4 A thin slit of length $2c$ is machined in a large panel of thickness b made of a brittle material. A flat jack of identical length is inserted into the slit and pressure is applied to it until a crack propagates symmetrically. Determine the stress intensity factor at the crack tips for arbitrary crack length $2a$ and jack pressure p. Show that when $a \gg c$, the stress intensity factor approaches that corresponding to a center crack loaded at its center by a pair of forces equal to the jack force.

3.5 In the pressurized panel of the previous exercise, plot the evolution of the pressure in the jack vs. the crack length for quasi-static crack growth. Assume that the initial slit behaves as a crack, and that the fracture toughness K_{Ic} is known. (Hint: plot $p\sqrt{c}/K_{Ic}$ vs a/c.)

3.6 A large panel has a center crack of length $2a$ subjected to a symmetric internal pressure distribution which takes the value p_0 at the crack center and decreases linearly to zero at the crack tips. Determine the stress intensity factor.

3.7 Show that if a center crack in a large panel is subjected to an arbitrary symmetric pressure distribution of the type $p = p_0\phi(x/a)$, where $\phi(x/a)$ is a dimensionless function of the relative coordinate x/a along the crack, the resulting stress intensity factor is always of the form $K_I = kp_0\sqrt{\pi a}$ where k is a constant.

3.2 Approximate Energy-Based Methods

Building on the results of Section 2.1, let us now review the techniques that provide approximate solutions for $\mathcal{G}$ in a number of cases. The presentation is not intended to be exhaustive. Its purpose is twofold: to give at least a minimum of insight on how to obtain the energy release rate, and to provide a number of simple equations for $\mathcal{G}$ which can be used in solving typical fracture problems.

The section covers first the simplified approaches to truly linear problems, relying only on simple mechanics of materials. After that, a certain geometrically nonlinear case is briefly analyzed: the extension of a surface delamination crack due to buckling under compression.

3.2.1 Examples Approximately Solvable by Bending Theory

In Section 2.1 we already presented the DCB specimen as an example of structures in which the energy release rates may be approximately calculated by bending theory (Fig. 2.1.3). The energy release rates of

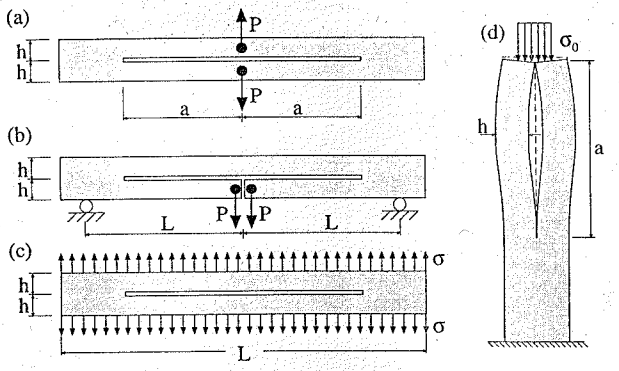

Figure 3.2.1 Structures with energy release rate approximately solvable by beam theory.

the beams or structures shown in Fig. 3.2.1 can also be solved in this way if they are slender and the cracks are assumed to grow straight ahead. The solutions are asymptotically exact as the slenderness tends to infinity.

The approximation, which has already been used in Examples 2.1.1–2.1.4, consists of using the classical beam theory to determine the load-point displacement and the elastic energy for the arms at both sides of the crack, assuming fixed ends at the crack root sections. Two basic approaches may be used. In the first, the bending moment distribution is computed; then the energy per unit length of beam, $M^2/2EI$, is integrated to find the total elastic energy or the complementary energy and the energy release rate is determined by differentiation with respect to crack length according to Eqs. (2.1.15) or (2.1.21). This procedure was illustrated in Examples 2.1.1 and 2.1.2. The second approach is to compute first the compliance and use Eq. (2.1.32) to determine the energy release rate in the manner in Examples 2.1.3 and 2.1.4.

All the structures shown in Fig. 3.2.1 can be solved in either way, although some structures are statically indeterminate and then the redundant forces must be solved first. Care should be taken regarding the value of the crack length in these structures, which is a when a single crack tip exists, but Na when N crack tips are present. Hence, partial derivatives must be with respect to Na to obtain the energy release rate per crack tip.

3.2.2 Approximation by Stress Relief Zone

Consider the center cracked panel of Fig. 3.2.2a subjected to remote stress σ_∞ perpendicular to the crack plane, and assume that the crack length is much less than the remaining dimensions of the plate. The principal stress trajectories in Fig. 2.1.1a reveal that the formation of a crack causes stress relief in the shaded, approximately triangular regions next to the crack. As an approximation, one may suppose the stress relief region to be limited by lines of some constant slope k (Fig. 3.2.2a), called the "stress diffusion" lines, and further assume that under constant boundary displacements the stresses inside the stress relief region drop to zero while *remaining unchanged outside*. Based on this assumption, the total loss of strain energy due to the formation of a crack of length $2a$ at controlled (fixed) boundary displacements is $\Delta\mathcal{U} = -2ka^2b(\sigma_\infty^2/2E)$ where $\sigma_\infty^2/2E$ is the initial strain energy density. Writing that $\sigma_\infty = Eu/L$ where u and L are the panel elongation and length, we can rewrite the loss of strain energy as $\Delta\mathcal{U} = -2ka^2bE(u^2/2L^2)$ and, therefore, the energy release rate per crack tip is

$$\mathcal{G} = -\frac{1}{b}\left[\frac{\partial(\Delta\mathcal{U})}{2\partial a}\right]_u = 2kaE\frac{u^2}{L^2} = 2ka\frac{\sigma_\infty^2}{E} \tag{3.2.1}$$

where in reaching the last equality we assume that after crack formation the relationship $\sigma_\infty = Eu/L$ is still approximately valid, an assumption that we will show to hold later.

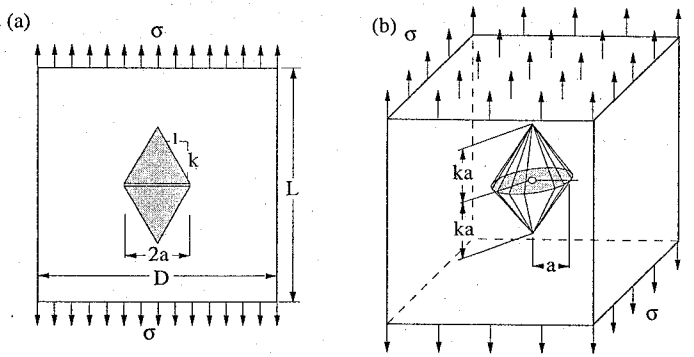

Figure 3.2.2 Approximate zones of stress relief: (a) for a center cracked panel, (b) for a penny-shaped crack.

The foregoing approximate result is in exact agreement with Griffith solution (1924) if one assumes that $k = \pi/2 = 1.571$. Even if k is unknown, the form of this equation obtained by the stress relief argument is correct. If the stress relief zone is assumed to be a circle of radius a passing through the crack tips, the result also happens to be exact. The same is true when the zone is taken as a rectangle of width $2a$ and height $\pi a/2$, or any geometrical figure whose area is πa^2.

For the penny-shaped crack in an infinite elastic space subject to remote tension σ_∞ (Fig. 3.2.2b), the stress relief region may be taken to consist of two cones of base πa^2 and height ka. Therefore, $\Delta\mathcal{U} = -2\frac{1}{3}\pi a^2 ka(\sigma_\infty^2/2E) = -\frac{12}{3}\pi ka^3 Eu^2/L^2)$. Also, $\mathcal{G} = -[\partial\Delta\mathcal{U}/\partial(\pi a^2)]_u = -[\partial\Delta\mathcal{U}/\partial a]_u/2\pi a$, i.e.,

$$\mathcal{G} = \frac{k\sigma_\infty^2 a}{2E} = \frac{k\sigma_\infty^2 a}{2E} \tag{3.2.2}$$

Again, this equation is of the correct form and is in exact agreement with the analytical result (Sneddon 1946) if one assumes that $k = 8/\pi$. The exact value also results if the stress relief zone is assumed to be a rotational ellipsoid of minor semiaxes a, a and $8a/\pi$ or any geometrical figure whose volume is $16a^3/3$.

The approximate method of stress relief zones can be applied in diverse situations for a quick estimate of $\mathcal{G}$. The value of k depends on geometry and its order of magnitude is 1 (except in the case of high orthotropy). The error in intuitive estimations of k can be substantial; however, the form of the equation obtained for $\mathcal{G}$ is correct.

There is a dichotomy in the method of stress relief zone which one must be aware of. Since the stress relief zone in Fig. 3.2.2 does not reach the top and bottom boundaries, the stress σ at top and bottom can remain constant and equal to σ_∞. Since there is a continuous zone of constant stress $\sigma = \sigma_\infty$ connecting the top and bottom boundaries, the displacements at top and bottom also remain constant during the crack extension at constant σ_∞.

However, from Eq. (2.1.32), it follows that a non-zero $\mathcal{G}$ implies an increase of the compliance due to the presence of the crack. This, in turn, implies that the stress cannot remain constant while the crack extends at constant displacement. The variation of compliance due to crack extension may be obtained from Eq. (3.2.1) and from this the stress variations at constant displacement may be inferred. Let D be the width of the panel, L its length, u the relative displacement between the top and bottom boundaries. The resultant load and initial (uncracked) compliance then are:

$$P = \sigma_\infty bD \tag{3.2.3}$$

$$C_0 = \frac{L}{bDE} \tag{3.2.4}$$

Inserting the foregoing expression for P into Eq. (2.1.32) (taking care to change the total crack length

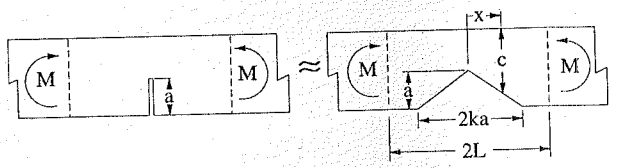

Figure 3.2.3 Herrmann's approximation.

a to $2a$) and equating the result to Eq. (3.2.1), one easily finds

$$\frac{dC(a)}{da} = \frac{8ka}{bD^2E} \tag{3.2.5}$$

which integrates to

$$C(a) = C_0 + \frac{4ka^2}{bD^2E} \tag{3.2.6}$$

From this, one sees that the variation of compliance contains the factor $(a/D)^2$ whose absolute value tends to vanish when the size of the panel is much larger than the crack length. The remote stress drop due to crack extension at constant displacement is also shown to vanish as $(a/D)^2$. Indeed, by differentiating the relation $u = C(a)P$ one finds the first-order approximation for the remote stress drop as

$$\Delta\sigma_\infty(u,a) \approx -\sigma_\infty(u,0)\frac{4ka^2}{LD} \tag{3.2.7}$$

where the higher order terms in $4ka^2/LD$ have been neglected.

Henceforth, the initial contradiction between the hypotheses of both constant remote stress and displacement exists at the theoretical level, but is resolved at the approximation level because it has been proved *a posteriori* that, in this case, the stress drop is vanishingly small when the crack is small relative to the size of the panel.

3.2.3 Herrmann's Approximate Method to Obtain $\mathcal{G}$ by Beam Theory

A remarkably simple method for close approximation of $\mathcal{G}$ in notched beams was discovered by Kienzler and Herrmann (1986) and Herrmann and Sosa (1986). The method was derived from a certain unproven hypothesis (postulate) regarding the energy release when the thickness of the fracture band is increased. Bažant found a different derivation of this method (Bažant 1990a) which is simpler and at the same time indicates that the hypothesis used by Herrmann et al. might not be exact but merely a good approximation. Also, Herrmann's method relies on more sophisticated concepts (material forces) which are elegant but seem more complicated than necessary to obtain the result. An even a simpler method of deriving Bažant's and Herrmann's results has been recently developed by Planas and Elices (1991d). This last will be presented now.

The method consists of approximating the cracked beam by a triangularly notched beam as shown in Fig. 3.2.3, and calculating its energy in the frame of the strength of materials theory (bent beam of variable inertia.)

Let k be the slope of the sides of the triangular notch, to be determined empirically. Let b and D be, respectively, the thickness, and depth of the unnotched beam, and let M be the constant bending moment over a central portion of the beam of length $2L \geq 2ka$. With the axis shown in Fig. 3.2.3, the complementary energy of the central portion is

$$\mathcal{U}^* = M^2 \int_0^{ka} \frac{1}{EI(c)}\,dx + (L-ka)\frac{M^2}{EI_1} \tag{3.2.8}$$

where EI_1 is the bending stiffness of the unnotched beam and $EI(c)$ is the bending stiffness when the

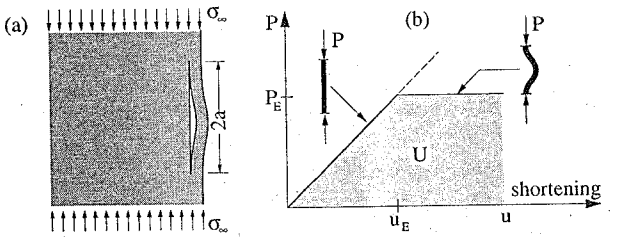

Figure 3.2.4 (a) Buckling of a subsurface layer. (b) Load-displacement curve for a buckling beam.

depth has been reduced to c,

$$c = D - a + \frac{x}{k} \tag{3.2.9}$$

Applying Eq. (2.1.21) to Eq. (3.2.8), one finds:

$$b\,\mathcal{G} = M^2 \int_0^{ka} \frac{\partial}{\partial c}\left(\frac{1}{EI(c)}\right)\frac{\partial c}{\partial a}\,dx + M^2\frac{1}{EI(D)}k - k\frac{M^2}{EI_1} \tag{3.2.10}$$

where, since $I(D) = I_1$, the second and third terms cancel out. Moreover, from Eq. (3.2.9), $\partial c/\partial a = -k\,\partial c/\partial x$. Integration now delivers Herrmann's result

$$\mathcal{G} = \frac{k}{b}\left(\frac{1}{EI_2} - \frac{1}{EI_1}\right)M^2 \tag{3.2.11}$$

where EI_2 is the bending stiffness of the central (notched) section.

When the remote flexural stress $\sigma_f = MD/2I_1$ is used as a measure of the load, and the expressions of the inertia moments for rectangular cross-section are substituted, the previous equation reads

$$\mathcal{G} = \frac{kD\sigma_f^2}{3E}\left[\left(\frac{D}{D-a}\right)^3 - 1\right] \tag{3.2.12}$$

According to Kienzler and Herrmann (1986, Figs. 3 and 4), this compares (for $k = 1$) very well with accurate solutions from handbooks. However, it appears that the agreement would be even better for some value $k \neq 1$ (Bažant 1990a). For very shallow notches, this method requires rather large k-value (about 4) to accurately fit the results. But in this case, the approximation by a beam of variable thickness is poor.

The results of Herrmann and Sosa (1986) for double-edge-notched and center-cracked specimens may also be obtained using the Planas and Elices expedient of approximating the crack by a triangular notch (coinciding with the shaded areas in Fig. 3.2.2a for the center cracked panel), and performing a classical analysis with the assumption that the cross-sections remain plane.

3.2.4 Subsurface Cracking in Compression by Buckling

A slightly exceptional case in LEFM is that shown in Fig. 3.2.4a, where a subsurface (delamination) crack may grow due to buckling of the layer above it, induced by a remotely applied compressive stress σ_∞. In this case the computation of $\mathcal{G}$ must take into account the geometrical nonlinearity implied in buckling.

To do this, one computes the elastic energy of a buckled beam, $\mathcal{U}_b$, as the work supply when no dissipative processes take place. This coincides with the area swept by the P-u curve, where P is the compressive load applied to the beam and u is the beam shortening. When h, b, and $2a$ are, respectively, the depth, thickness, and length of the beam, the P-u curve coincides with the straight line $P = bhEu/2a$ for loads below Euler's buckling load P_E and is horizontal ($P = P_E$) for further displacements (Fig. 3.2.4). The

area under the curve $\mathcal{U}_b$ is

$$\mathcal{U}_b = P_E\, u - \frac{1}{2} P_E\, u_E = 2abh\sigma_E \left(\frac{u}{2a} - \frac{\sigma_E}{2E}\right) \tag{3.2.13}$$

where $\sigma_E = P_E/bh$ is the buckling stress, which, for fixed ends and rectangular cross-section, is

$$\sigma_E = \frac{\pi^2 h^2}{12a^2} E \tag{3.2.14}$$

The fundamental simplification in our problem consists of assuming that the displacement of the ends of the buckling layer of length $2a$ is imposed by the deformation of the surrounding material which stays at stress level σ_∞. So we have

$$u = 2a\frac{\sigma_\infty}{E} \tag{3.2.15}$$

and, after substitution into Eq. (3.2.13), the strain energy of the buckled layer is

$$\mathcal{U}_b = abh\frac{\sigma_E}{E}(2\sigma_\infty - \sigma_E) \tag{3.2.16}$$

The energy $\mathcal{U}$ of the whole system is $\mathcal{U}_b$ plus the strain energy of the surrounding material, which is the strain energy density $\sigma_\infty^2/2E$ times the surrounding volume, equal, in turn, to the total (constant) volume of the body V minus the volume of the buckling layer $2abh$. The resulting expression is

$$\mathcal{U} = (V - 2abh)\frac{\sigma_\infty^2}{2E} + abh\frac{\sigma_E}{E}(2\sigma_\infty - \sigma_E) = V\frac{\sigma_\infty^2}{2E} - 2abh\frac{(\sigma_\infty - \sigma_E)^2}{2E} \tag{3.2.17}$$

From this, the expression for $\mathcal{G}$ follows at once using Eq. (2.1.15) with the condition, following from the simplifications used in the derivation, that σ_∞ remains constant at constant displacement. After inserting Eq. (3.2.14) and differentiating with respect to a, one gets the following expression for the energy release rate:

$$\mathcal{G} = -\frac{1}{b}\left[\frac{\partial \mathcal{U}}{2\partial a}\right]_u = \frac{h}{E}\left[\sigma_\infty^2 + \frac{\pi^2 h^2}{6a^2}\sigma_\infty E - \frac{\pi^4 h^4}{48a^4} E^2\right] \tag{3.2.18}$$

This result captures some, but not all, of the important aspects of the problem of delamination in layered composites (Sallam and Simitses 1985, 1987; Yin, Sallam, and Simitses 1986).

3.3 Numerical and Experimental Procedures to Obtain K_I and $\mathcal{G}$

In many practical problems there is no analytical solution for the energy release rate, and one must resort to experimental or numerical approximations. While experimental procedures have been extensively used in the past, modern computers have made the numerical procedures relatively easy. In this section we give only a brief sketch of the available methods for the case in which the propagation direction is known.

3.3.1 Numerical Procedures

There are various numerical approaches to solving linear elastic fracture problems. For our purposes, the best classification is based on commercial availability. Special purpose computer programs, which make use of special properties of the fields in plane elasticity (see Chapter 4) and are usually usually not available commercially, may be very accurate, but are generally restricted to research by specialists. This is the case of the so-called boundary collocation, in which special power expansions of the unknowns are used for a particular problem and the coefficients of the expansion are determined so that the boundary conditions be satisfied only in some average sense.

Restricting attention to commercial programs, we may distinguish between special purpose programs and general purpose programs. Special purpose programs are specifically designed to deal with cracks and determine stress intensity factors, so that the user may access to post-process routines that will readily

compute the stress intensity factor from a basic numerical solution. General purpose programs are those available to solve general elasticity problems, which can be used, with special strategies, to solve fracture problems. With the general purpose programs, two basic strategies may be used: (1) incremental stiffness method, and (2) near-tip field fitting.

The incremental stiffness method essentially consists of determining the compliance for two different, but close, crack lengths $a - \Delta a$ and $a + \Delta a$. Then the energy release rate G is estimated as

$$\mathcal{G} \approx \frac{P^2}{2b}\,\frac{C(a + \Delta a) - C(a - \Delta a)}{2\Delta a} \tag{3.3.1}$$

Any finite element, finite difference, or boundary element code may be used to produce the two compliance values for two close crack lengths. Numerical resolution and mesh refinement limit the accuracy of this procedure. In very general terms, there are two possible approaches: (1) use only one mesh and simulate crack extension by freeing one node, so that the crack extends by one element, or (2) modify the mesh for the second calculation in which the node at the crack tip is displaced by Δa. The first method is easy to use and does not require modification of the global stiffness matrix, but requires a fine mesh so that the numerical differentiation in (3.3.1) gives accurate results. The second method decouples the crack extension from the mesh size, but requires partial recalculation of the stiffness matrix.

Example 3.3.1 A commercial finite element code was used to analyze a single-edge cracked beam in three-point bending, with a span-to-depth ratio $S/D = 4$ (Guinea 1990). Half the beam was discretized so that 100 equally sized elements were placed along the crack plane. The crack length was varied by changing the boundary conditions along the nodes in the crack plane, from opening displacement prevented (no crack at this node) to load free (crack at this node). Computations were performed in plane stress with $D = 1$, $b = 1$, and $E = 1$, for a load $P = 1$ (in arbitrary, but consistent, units). Although, the purpose of the computations was other than determining K_I, the results can be used to examine the accuracy of the differential stiffness method.

Consider, for example, the case $a = 0.5D$. The displacements computed for crack lengths $a_1 = 0.49D$ $a_2 = 0.51D$ were, respectively, 57.261 and 61.663, numerically identical to the compliance values (because $P = 1$). The energy release rate is then evaluated from (3.3.1) as $\mathcal{G} \approx (1^2/2)(61.663 - 57.261)/0.02 = 110.1$ in appropriate units. Now, since we always write $\mathcal{G} = (P/bD)\hat{g}(\alpha)$, it turns out that in our calculation the numerical value of $\mathcal{G}$ (with its arbitrary units) coincides with the dimensionless value of $\hat{g}(0.5)$. Therefore, $\hat{g}(0.5) \approx 110$. The stress intensity factor follows from Irwin's equation as $K_I = \sqrt{E'\mathcal{G}} \approx \sqrt{110} = 10.5$. Now, since we write $K_I = \sigma_N\sqrt{D}k(\alpha)$, we may easily find $k(0.5)$ upon noting that for a span-to-depth ratio of 4, $\sigma_N = 6P/bD$. The result is $k(0.5) \approx 10.5/6 = 1.75$. This value is to be compared with that given by equations (3.1.1) and (3.1.2) (or Fig. 3.1.1) which give $k(0.5) = 1.77$. Thus, the numerical estimate turns out to be about 1.2% lower than the more accurate value. □

The near-tip field fitting consists of making use of the known near-tip behavior of the stress and displacement or crack opening fields to make an estimate for K_I. It can make use, for example, of the stress distribution ahead of the crack tip, which is known to behave as $\sigma_{22} = K_I/\sqrt{2\pi r}$, where σ_{22} is the stress normal to the crack plane, and r is the distance to the crack tip. This means that a plot of $\sigma_{22}\sqrt{2\pi r}$ vs. r should tend to K_I as r approaches zero. It is also possible to use the displacement field, particularly the crack opening, which is known to behave as $w = 8K_I\sqrt{r}/E'\sqrt{2\pi}$. Therefore, the limit of $wE'\sqrt{2\pi}/8\sqrt{r}$ as $r \to 0$ is also K_I.

Example 3.3.2 The results of the nodal reactions along the uncracked ligament, or the crack opening distribution, may be used to make a near-tip field fit. We use $K_I = \lim_{r\to 0}\sigma_{22}\sqrt{2\pi r}$, and agree to write $K_I = \sigma_N\sqrt{D}k(\alpha)$ and for a given value of α, we define

$$\kappa(r) = \frac{\sigma_{22}}{\sigma_N}\sqrt{2\pi\frac{r}{D}} \tag{3.3.2}$$

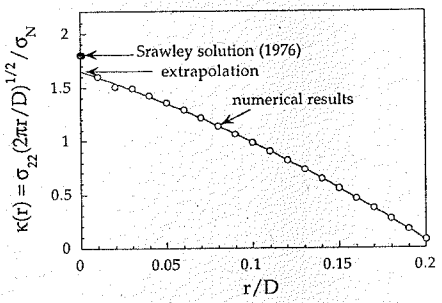

Figure 3.3.1 Plot of normal stresses times $\sqrt{r}$ vs. r (r =distance to crack tip). Extrapolation to zero gives the dimensionless stress intensity factor.

then $k(\alpha) = \lim_{r\to 0} \kappa(r)$. Plotting the nodal values of κ_n vs. the distance to the crack tip, and extrapolating to zero, we get an estimate of $k(\alpha)$. This was used in the finite element computations described in the previous example (now for $a/D = 0.5$). The nodal normal stresses were obtained as $\sigma_{22_n} \approx R_n/bh$, where R_n is the nodal reaction and h the width of the elements. From this, the nodal values of κ were obtained and plotted as shown in Fig. 3.3.1. The extrapolated value gives $k(0.5) \approx 1.65$. This value differs by 7% from the more accurate value $k(0.5) = 1.77$ obtained from equations (3.1.1) and (3.1.2) (or Fig. 3.1.1). □

The foregoing examples show two of the ways to determine K_I and $\mathcal{G}$ from numerical results. The determination of K_I from the crack opening profile is left as one of the exercises. The general experience is that the differential stiffness method is more accurate for a given mesh size. This is probably due to the cancellation of constant errors in the differentiation process. However this method requires two computations, while the near-tip field fitting requires only one, although this is really not a problem with the kind of computers available today.

Getting good results (less than 5% error) with near-tip analysis requires extremely fine meshes, because of the difficulty in representing the crack tip singularity with ordinary finite elements. Indeed, careful studies of convergence by Wilson (1971) and Oglesby and Lamackey (1972) showed that the near-tip approximate solution may not converge to the analytical solution whatever the mesh refinement. To solve this problem, one needs special elements whose shape functions include a $r^{-1/2}$ singular term.

Various singular finite elements have been developed (see, e.g., Aliabadi and Rooke 1991), but most of them incorporate special shape function and require specially designed finite element codes. A remarkable exception is the so-called quarter-node isoparametric element (Barsoum 1975, 1976; Henshell and Shaw 1975). In this formulation, a standard 8-node isoparametric quadrilateral element is collapsed, as shown in Fig. 3.3.2a, to a triangular quarter-point element. The vertex corresponding to the collapsed nodes 1–7–8 becomes the singular point, and a $r^{-1/2}$ singularity is achieved by placing nodes 2 and 6 at a quarter (from the singular vertex) of the radial sides of the triangle. These elements are placed in a rosette around the crack tip as shown in Fig. 3.3.2b.

The stress intensity factor may be evaluated from the displacement fields of any of the elements, but most usually K_I is obtained from the values of the crack opening evaluated at the two nodes along the crack faces. With this method, values of K_I accurate within a few percent may be obtained without much mesh refinement. However, recent recommendations by ESIS Technical Committee 8 (1991) suggest, again, that best results for stress intensity factors are obtained if energetic approaches based on the determination of $\mathcal{G}$ are used instead of near-tip fields.

The differential stiffness method is not the only way to determine $\mathcal{G}$. The J-integral and other path-independent integral expressions may be (and have been) used to determine the energy release rate. This has the advantage that the evaluation of J is made using values of the fields at points far from the crack tip, where the errors are expected to be smaller. It also avoids numerical differentiation, and a single

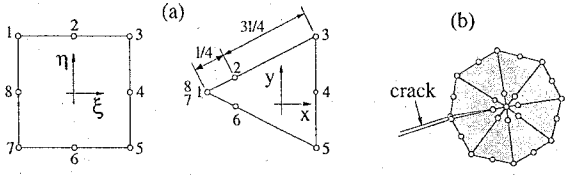

Figure 3.3.2 (a) Collapsing of an 8-node quadratic isoparametric element into a singular quarter-node element. (b) Rosette of singular finite elements at a crack tip.

computation is enough. It requires, however, special postprocessing routines, both in finite elements codes and in boundary element codes.

Although finite element codes dominate the market, commercial codes based on boundary elements have recently become available. They yield K_I-values of much higher accuracy than finite element codes. The main advantage of this kind of formulation is that only the boundary of the elements must be modeled, so that the number of degrees of freedom is greatly reduced. This is, of course, achieved at the cost of larger complexity of the code, especially the postprocessing. In particular, handling cracks may require special formulations and special postprocessing which are outside the scope of this book (for details, see Aliabadi and Rooke 1991).

3.3.2 Experimental Procedures

Experimental procedures to determine the stress intensity factor were often used with some intensity in the past, when numerical calculations were of limited availability. All the methods relied on measuring some features of the displacement fields of elastic specimens, and relating them to the energy release rate or to the stress intensity factor.

The simplest method, which is generally used in laboratory environments, uses the experimental version of the differential stiffness method. It is implemented by measuring the compliance of a specimen for various crack depths and determining $\mathcal{G}$ from $\mathcal{G} = (P^2/2b)dC/da$. In principle, two tests with two slightly different crack lengths are enough to get a result for a given crack length. However, experimental accuracies being always very limited, it is usually better to make a larger number of tests over a finite range, fit a smooth curve to these results, and then perform the differentiation. Because the experimental accuracy in obtaining the compliance is rarely better than 1%, this method is not very reliable unless the compliance variation due to the growth of the crack is a sufficiently large fraction of the total compliance. This excludes large specimens or structures with tiny cracks (or, generally speaking, small relative crack depths). In some test setups, a further source of error is that, in order to have a good control of the geometry, cracks are substituted by cut slits (notches). In this case, the notch width must be much less than any relevant dimension of the specimen (crack length, remaining ligament length, distance of applied loads from the crack tip, etc.).

Other methods rely on the analysis of the properties of the strain or displacement fields close to the crack tip. These include: strain gauge techniques, photoelastic techniques, interferometric techniques, and the caustics method.

The strain gauge technique measures the strain and stress at a set of points around the crack tip by means of bonded electrical strain gauges. In the photoelastic technique, the shear strain field around the crack is measured in a specimen made of a photoelastic polymer. In the interferometric techniques, the displacement field (usually the component normal to the crack plane) is mapped by interferometry. From the experimental results of stress, shear-strain, or displacement vs. the distance to the crack tip, near-tip fitting techniques similar to those sketched for numerical methods are used to infer the value of the stress intensity factor.

The principle of the caustics method is different of the former in that it uses the out-of-plane displacements to find the stress intensity factor. Due to Poisson effect, a depression of the surface of the specimen is produced around the crack tip. If the surface is polished, a mirror with a profile determined by the elastic

field is produced. When a beam of light impinges normally over this mirror, the reflected rays produce a bright kidney-shaped spot whose size is related to the stress intensity factor. If transparent specimens are used, transmitted light can be used and then the specimen acts as a lens with a profile determined by the elastic field.

In all these techniques, it is essential to guarantee that the plastic zone is small compared to the size of the region over which the stresses, strains, or displacements are measured. If notches, instead of cracks, are used (which is usual in photoelastic techniques), corrections are required to take into account the finite radius at the tip.

For details of the experimental techniques, see Smith and Kobayashi 1993.

3.4 Experimental determination of K_{Ic} and G_f

When a crack in a laboratory specimen may be guaranteed to behave in a linear elastic way, the experimental determination of K_{Ic} or G_f is conceptually easy. The simplest way is to use a specimen in which the crack growth initiation coincides with the peak load (all the standard specimens belong to this category). In this case, one simply loads the specimen up to failure and records the peak load P_u. If LEFM conditions are fulfilled, the value of the stress intensity factor for this load coincides with K_{Ic}:

$$K_{Ic} = K_{Iu} = \frac{P_u}{b\sqrt{D}} k(\alpha) \tag{3.4.1}$$

where $\alpha = a/D$ is the relative crack length at the beginning of the test.

The difficulties in this kind of testing arise at two different levels: (1) Specimen preparation (precracking), and (2) verification of LEFM conditions. These aspects are well defined for metals in most national standards, particularly in ASTM E 399. The crack is grown from a normalized starter notch by fatigue under controlled conditions. The LEFM conditions are verified in two ways. First, the nonlinearity of the load displacement curve before peak is limited (an ideally brittle material is completely linear up to failure). This is done as shown in Fig. 3.4.1a by defining a kind of conventional (load) elastic limit P_5 for which the secant stiffness is 95% of the initial tangent stiffness. Deviation from linearity is acceptable if either the peak load occurs before the elastic limit or the ratio P_u/P_5 is less than 1.1 (see the standards for details).

Apart from this direct verification of linearity, there is a further condition which verifies that the specimen thickness and size are large enough for the nonlinear zone at fracture to be negligible (for engineering purposes). Since the standard specimens are designed so that their thickness is one-half of their width or depth ($b = 0.5D$) and the crack length is close to half the depth ($\alpha \approx 0.5D$), the thickness and size conditions are expressed in a single condition:

$$b \geq 2.5 \left(\frac{K_{Ic}}{\sigma_c}\right)^2 \tag{3.4.2}$$

where σ_c is a conventional flow stress (usually a value between the conventional 0.2% proof stress and the tensile strength). The origin of the foregoing equation is discussed in detail in the next chapter. Here, it is enough to say that the factor $(K_{Ic}/\sigma_c)^2$ is proportional to the size of the plastic zone, so the equation really places a limit on the extent of the plastic zone relative to the specimen size.

For materials other than metals, the situation is more complex. Cracks in polymers and structural ceramics cannot easily be grown using cyclic loading. For polymers, cracking by forcing a razor blade into the notch root has been chosen by ASTM standards (ASTM 1991). For fine ceramics, no standards are yet available, and round robins are being performed to compare toughness test results on specimens with different kinds of notches and cracks, as that promoted by ESIS TC 6 (Pastor 1993; Primas and Gstrein 1994). Specifications for the minimum size required for LEFM to apply have been set for polymers, and are similar to those previously stated for metals. No agreed limitations have been set yet for ceramics.

For concrete, it is generally accepted today that the sizes required for LEFM to apply are really huge (several meters or even tens of meter). Therefore, special purpose tests taking into account the nonlinear

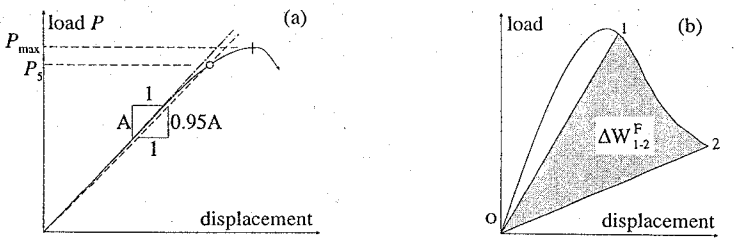

Figure 3.4.1 Experimental determination of fracture properties: (a) Load-displacement curves and definition of the conventional limit P_5 (After ASTM E 399, simplified); (b) determination of G_f from experiment.

fracture behavior of concrete have been set. They will be analyzed in the following chapters, where nonlinear models are introduced.

For any material, nonstandard tests may also be used to determine the fracture properties of the material, whenever the size of the specimen is large enough for LEFM to apply. One such method, based on an energetic analysis, consists of performing a stable test (controlling the displacement rather than the applied load) and simultaneously measuring the load, P, the load point displacement, u, and the crack length, a. Let the $P-u$ curve be known between the points 1 and 2 at which the crack lengths were measured to be, respectively, a_1 and a_2 (Fig. 3.4.1b). Then, according to Section 2.1.4, the energy consumed in fracture between points 1 and 2, $\Delta\mathcal{W}^F_{1-2}$, is the area of the curvilinear triangle $O12$, while the area of the newly formed crack is $b(a_2 - a_1)$; hence,

$$G_f = \frac{\Delta\mathcal{W}^F_{1-2}}{b(a_2 - a_1)} \tag{3.4.3}$$

The accuracy of the result depends on the accuracy of the individual measurements, which may be controlled to some extent by adequate experimental design, but it also depends on the degree of accuracy of the hypotheses underlying the equation above. The method becomes inaccurate, even invalid, if the inelastic zone ahead of the crack tip is so large that the hypothesis of negligible inelastic zone is no longer acceptable.

Determination of how large the inelastic zone is, relative to the specimen dimensions, and how large its size must be to stay reasonably close to LEFM is, to a great extent, one of the objectives of the various inelastic fracture mechanics approaches that will be analyzed in the remaining chapters. At this stage, we only list the most obvious conditions that the experimental outputs should fulfill:

1. Deviation from linearity prior to the peak load should be small. This applies to specimens where the iso-$\mathcal{G}$ curves are monotonically decreasing as in Fig. 2.1.10a. The more rounded the peak, the farther the behavior is from LEFM. Quantitative criteria to ensure prepeak linearity can be formulated, similar to those previously given by ASTM E 399.
2. The $P-u$ curve after the peak should be an iso-$\mathcal{G}$ curve. The most direct way to check this point is to take various arcs 1-2, 2-3, 3-4, and so on, and calculate a value of G_f for each of these arcs. They should be equal if LEFM applies.
3. When unloading is performed, the unloading curve should be straight and unload to the origin. Deviation from this behavior indicates deviation from LEFM.

Exercises

3.8 Find the expression for the energy release rate of the structure in (a) Fig. 3.2.1a, (b) Fig. 3.2.1c.

3.9 A brittle material may contain planar voids. If these voids are similar to penny-shaped cracks, determine the maximum diameter of the voids which allow the material to be used up to 90 percent of its elastic limit. Complementary tests delivered values of 55 MPa for the yield strength and 16 kJ/m^2 for the fracture energy.

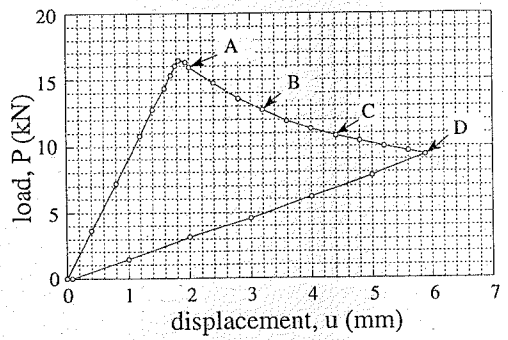

Figure 3.4.2 Test output in an experimental determination of G_f.

3.10 Use the triangular notch approximation of Planas and Elices to get the energy release rate of a center-cracked panel such as that depicted in Fig. 3.2.2. Show that for the limiting case $a/D \to 0$ the expression coincides with that obtained from the stress relief zone approximation in Section 3.2.2.

3.11 The results of the finite element calculation of Guinea (described in example 3.3.1) gave, for $a/D = 0.5$, the crack opening profile near the crack tip included in the table below, where r and w are, respectively, the distance to the crack tip and the crack opening (in appropriate length units; remember that in the computation $b = D = 1$, $P = 1$, $E = 1$ and plane stress was used). (a) Show that $K_I = \lim_{r\to 0} wE'\sqrt{\pi/32r}$. (b) Plot $wE\sqrt{\pi/32r}$ vs. r and get an estimate of K_I for the computed case. (c) For the usual definition of σ_N shown in Fig. 3.1.1, determine from the previous result an estimate of the shape factor $k(0.5)$. (d) Evaluate the error of the estimate in comparison with the more precise equations of example 3.1.1.

r	0.01	0.02	0.03	0.04	0.05	0.06	0.07	0.08	0.09
w	3.1669	4.5816	5.7928	6.8123	7.7424	8.6050	9.4201	10.198	10.947

3.12 Compliance tests have been performed on single-edge crack specimens of 25 mm thickness and 50 mm depth made of a material with an elastic modulus of $E = 3$ GPa. Nine specimens with crack lengths ranging between 23 and 27 mm were subjected to the same load, $P = 500$ N, and their displacement was measured. The results are shown in the following table. Give an estimate of the energy release rate, in J/m^2, for a specimen of this particular shape, size, and material with a crack length of 25 mm, for any load, P expressed in N.

a (mm)	23.1	23.6	23.9	24.4	24.9	25.6	25.8	26.5	27.0
u (μm)	270	291	289	310	317	347	348	369	397

3.13 A specimen geometrically similar to that in the preceding exercise has been loaded up to crack initiation. The specimen had a thickness of 10 mm and a depth of 100 mm, with an initial crack of 50 mm. The load at which the crack started to grow was 17.5 kN. Additional testing provided for the elastic modulus of that material, the value $E = 100$ GPa. Estimate the fracture energy under the assumption that LEFM applies.

3.14 A double-cantilever beam specimen subjected to opposite point loads at the ends of its arms has been tested under displacement control. The specimen thickness was 50 mm and the arm depth 30 mm. The resulting load-displacement curve is shown in Fig. 3.4.2b. If the initial crack length was 150 mm, (a) give an estimate of the elastic modulus of the material. (b) Give an estimate of G_f using the peak load value and the initial crack length. (c) Give estimates of the crack length at points A, B, C, and D. (d) Give average values of the crack growth resistance over arcs AB, BC, and DE. (e) Decide whether LEFM is a reasonably good approximation, and, if it is, give a final estimate for G_f.

3.5 Calculation of Displacements from K_I-Expressions

3.5.1 Calculation of the Displacement

The procedure to obtain the displacement from the expression of K_I as a function of the crack depth is, in fact, the reverse of that used in Section 2.1 to obtain $\mathcal{G}$ from the expression of the compliance. To obtain the compliance (from which the displacement follows trivially), we couple (2.1.32) with Irwin's relationship (2.2.22) to get

$$\frac{1}{2b}P^2\frac{dC(a)}{da} = \frac{K_I^2}{E'} \tag{3.5.1}$$

This provides the basic equation to solve for the compliance, which may be simplified by using the general expression (2.3.11) for K_I:

$$\frac{dC(a)}{da} = \frac{2}{bDE'}\hat{k}^2(\alpha) \tag{3.5.2}$$

This equation may be integrated between the limits for no crack, for which the compliance is C_0, and an arbitrary crack length a:

$$C(a) = C_0 + \frac{2}{bDE'}\int_0^a \hat{k}^2(\alpha)da = C_0 + \frac{2}{bE'}\int_0^{a/D} \hat{k}^2(\alpha)\, d\alpha \tag{3.5.3}$$

where the second expression follows by setting $da = D\, d\alpha$.

Thus, setting $u = CP$, the displacement can be written as

$$u = \frac{P}{bE'}\hat{v}(\alpha), \qquad \alpha = \frac{a}{D} \tag{3.5.4}$$

The dimensionless function $\hat{v}(\alpha)$ is given by

$$\hat{v}(\alpha) = \hat{v}_0 + \hat{v}^c(\alpha), \qquad \hat{v}_0 = u_0\frac{bE'}{P}, \qquad \hat{v}^c(\alpha) = 2\int_0^\alpha \hat{k}^2(\alpha')\, d\alpha' \tag{3.5.5}$$

in which u_0 is the elastic displacement of the structure in the absence of crack and $\hat{v}^c(\alpha)$ is the additional displacement due to the crack.

Often the displacement is expressed in terms of the nominal strength $\sigma_N = c_N P/bD$ instead of the load P. Making the substitution and taking into account the definitions of functions $\hat{k}(\alpha)$ and $k(\alpha)$ given in and below (2.3.11), one gets

$$u = \frac{\sigma_N}{E'}Dv(\alpha), \qquad \alpha = \frac{a}{D} \tag{3.5.6}$$

The dimensionless function $v(\alpha)$ is given by

$$v(\alpha) = v_0 + v^c(\alpha), \qquad v_0 = u_0\frac{E'}{\sigma_N D}, \qquad v^c(\alpha) = 2\int_0^\alpha k^2(\alpha')\, d\alpha' \tag{3.5.7}$$

in which, again, u_0 is the elastic displacement the structure would experiment if uncracked. Note that the equations are formally the same as before, except that the functions labeled by hats (which we always use with P) are replaced by functions without hats, representing variables expressed in terms of σ_N.

Example 3.5.1 Consider a large plate with a very short edge crack ($a \ll D$) subjected to remote stress σ (Fig. 3.5.1). The approximate expression of the stress intensity factor is $K_I = 1.1215\sigma\sqrt{\pi a}$, which may be rewritten as $K_I = \sigma\sqrt{D}1.1215\sqrt{\pi\alpha}$. Therefore, taking $\sigma_N = \sigma$ we have

$$k(\alpha) = 1.1215\sqrt{\pi\alpha} \tag{3.5.8}$$

Thus, from the last equation of (3.5.7), we get

$$v^c(\alpha) = 2 \times 1.258\pi\int_0^\alpha \alpha'\, d\alpha' = 1.258\pi\alpha^2 \tag{3.5.9}$$

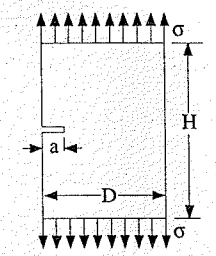

Figure 3.5.1 Single-edge cracked panel subjected to remote uniaxial stress.

Since the displacement for an uncracked panel is $u_0 = \sigma H/E$, the second equation of (3.5.7) gives $v_0 = H/D$. Therefore, the total displacement is

$$u = \frac{\sigma_N}{E'} D \left(\frac{H}{D} + 1.258\pi\alpha^2 \right) \tag{3.5.10}$$

Identical results are obtained if calculations are done in terms of the resultant load $P = \sigma b D$. □

The foregoing expressions hold for a single-tipped crack, and a stands for the total crack length. For the center cracked panel, or more generally for internal cracks, where the total crack length is customarily represented by $2a$, the matters become a little more complex in the case of loadings that are not symmetric with respect to the axis normal to the crack. In such a case, the energy release rates are different at one and the other tip. This means that in reality $\partial \mathcal{U}^*/\partial a = \mathcal{G}^+ + \mathcal{G}^-$ where the superscripts + and − refer to the right and left tips, respectively. Therefore, we must also distinguish the stress intensity factors K_I^+ and K_I^- and their associated shape factors $k^+(\alpha)$ and $k^-(\alpha)$. A development strictly parallel to the previous one for a single-tipped crack leads to identical expressions for the displacement, except that function $v^c(\alpha)$ is now given by

$$v^c(\alpha) = 2 \int_0^\alpha \left[k^{+^2}(\alpha') + k^{-^2}(\alpha') \right] d\alpha' \tag{3.5.11}$$

and similarly for the functions with hats. This shows that, for symmetric loadings ($k^+ = k^- = k$), the double-tip case reduces to the single-tip one just by replacing $d\alpha$ by $2d\alpha$. But for nonsymmetric loading, the expression is quite different.

3.5.2 Compliances, Energy Release Rate, and Stress Intensity Factor for a System of Loads

To calculate arbitrary displacements from K_I expressions, it is convenient to establish a more general framework in which a system of independent forces P_i ($i = 1, \ldots, n$) is assumed to act on a cracked elastic body. Let the displacement of the load-point i in the direction of P_i be u_i. The displacements may be written as linear functions of the loads:

$$u_i = \sum_{j=1}^{n} C_{ij}(a) P_j \qquad i = 1, \ldots, n \tag{3.5.12}$$

where $C_{ij}(a)$ are the elements of the compliance matrix (which depend upon the crack length a). As a consequence of the reciprocity theorem, the compliance matrix is symmetric: $C_{ij} = C_{ji}$.

The elastic and complementary energies are equal, and are given by $\mathcal{U} = \mathcal{U}^* = \sum_{i=1}^n P_i u_i/2$. Substituting (3.5.12), the complementary energy is obtained as

$$\mathcal{U}^* = \frac{1}{2} \sum_{i=1}^{n} \sum_{j=1}^{n} C_{ij}(a) P_i P_j \tag{3.5.13}$$

From this expression and (2.1.21), we obtain the following expression for the energy release rate:

$$\mathcal{G} = \frac{1}{2b} \sum_{i=1}^{n} \sum_{j=1}^{n} P_i P_j \frac{dC_{ij}(a)}{da} \tag{3.5.14}$$

For a general system of loads, this equation is the equivalent of (2.1.34) .

For the stress intensity factor, we may apply the superposition principle and write

$$K_I = \sum_{i=1}^{n} K_{Ii} = \frac{1}{b\sqrt{D}} \sum_{i=1}^{n} P_i \, \hat{k}_i(\alpha) \tag{3.5.15}$$

where $K_{Ii} = (P_i/b\sqrt{D})\hat{k}_i(\alpha)$ is the stress intensity factor due to P_i alone. Now, according to Irwin's equation, $\mathcal{G} = K_I^2/E'$, and so

$$\frac{1}{2b} \sum_{i=1}^{n} \sum_{j=1}^{n} \frac{dC_{ij}(a)}{da} P_i P_j = \frac{1}{b^2 D E'} \sum_{i=1}^{n} \sum_{j=1}^{n} \hat{k}_i(\alpha) \hat{k}_j(\alpha) P_i P_j \tag{3.5.16}$$

The values of the P_is are arbitrary. So for the equality to hold for any P_i, the coefficients of the products $P_i P_j$ on both sides of the equation must be identical. We thus find that

$$\frac{dC_{ij}(a)}{da} = \frac{2}{bDE'} \hat{k}_i(\alpha) \hat{k}_j(\alpha) \qquad (i, j = 1, \ldots, n) \tag{3.5.17}$$

which is the generalization of (3.5.2) to any system of forces. This equation can be integrated in the same way as before, to obtain

$$C_{ij}(a) = C_{ij_0} + \frac{2}{bE'} \int_0^{a/D} \hat{k}_i(\alpha) \hat{k}_j(\alpha) d\alpha \qquad (i, j = 1, \ldots, n) \tag{3.5.18}$$

where C_{ij_0} is the component of the compliance matrix for the uncracked body ($a = 0$). This equation provides the means of obtaining the displacements u_j at various points caused by only one force, say P_1 (all the remaining forces being zero). The result is, obviously, $u_j = C_{j1} P_1$.

The foregoing equation can be recast in terms of the full expression of the stress intensity factor, by setting that $\hat{k}(\alpha) = b\sqrt{D}\, K_{Ii}/P_i$ and thus

$$C_{ij}(a) = C_{ij_0} + \frac{2b}{E'} \int_0^a \frac{K_{Ii} K_{Ij}}{P_i P_j} da \qquad (i, j = 1, \ldots, n) \tag{3.5.19}$$

which does not require a particular form of expressing the stress intensity factor, and can be directly used when P_i are generalized forces rather than point loads.

Note, again, that in the foregoing expressions a stands for the total crack length, and the energy release rates correspond to a single crack tip. For the center cracked panel, the two crack tips must be made explicit, as previously done for the single force loading, Eq. (3.5.11). The general expression for multiple loading is:

$$C_{ij}(a) = C_{ij_0} + \frac{2}{bE'} \int_0^{a/D} \left[\hat{k}_i^+(\alpha) \hat{k}_j^+(\alpha) + \hat{k}_i^-(\alpha) \hat{k}_j^-(\alpha) \right] d\alpha \qquad i, j = 1, \ldots, n \tag{3.5.20}$$

where $\hat{k}_i^+(\alpha)$ and $\hat{k}_i^-(\alpha)$ are the shape factors for the stress intensity factor created by load P_i at the right and at the left crack tips, respectively.

3.5.3 Calculation of the Crack Mouth Opening Displacement

As an important application of the foregoing general result, let us calculate the expression for the crack mouth opening displacement (CMOD), which we denote as w_M (Fig. 3.5.2). Aside from the actual load P, we also consider a virtual loading P_M consisting in a pair of forces at the crack mouth working

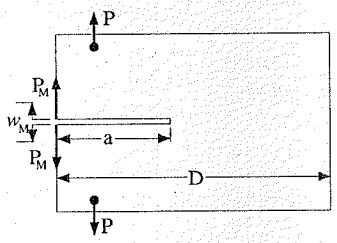

Figure 3.5.2 Crack mouth opening w_M, applied load P, and crack mouth load P_M.

through w_M. In the previous expressions we now have $n = 2$, and we set $P_1 \equiv P$, $P_2 \equiv P_M$, $u_1 \equiv u$, $u_2 \equiv w_M$, $C_{11}(a) \equiv C(a)$, and $C_{12}(a) \equiv C_M(a)$ so that we write the displacements as

$$u = C(a)\,P + C_M(a)\,P_M \tag{3.5.21}$$

$$w_M = C_M(a)\,P + C_{MM}(a)\,P_M \tag{3.5.22}$$

We also set $\hat{k}_1(\alpha) \equiv \hat{k}(\alpha)$ and $\hat{k}_2(\alpha) \equiv \hat{k}_M(\alpha)$ for the shape factors corresponding to forces P and P_M. Noting that $C_{M0} \equiv C_{120} = 0$ (because when the crack length is zero, the crack opening is also zero), the cross-compliance for the CMOD, $C_M(a)$, follows from (3.5.18):

$$C_M(a) = \frac{2}{bE'}\int_0^{a/D} \hat{k}(\alpha)\hat{k}_M(\alpha)d\alpha \tag{3.5.23}$$

Thus, according to (3.5.22), the crack mouth opening displacement when the structure is loaded by P alone is

$$w_M = \frac{P}{bE'}\hat{v}_M(\alpha)\,, \quad \hat{v}_M(\alpha) = 2\int_0^{\alpha} \hat{k}(\alpha')\hat{k}_M(\alpha')d\alpha' \tag{3.5.24}$$

Again, this can be expressed in terms of σ_N instead of P; the result is

$$w_M = \frac{\sigma_N}{E'}Dv_M(\alpha)\,, \quad v_M(\alpha) = 2\int_0^{\alpha} k(\alpha')\hat{k}_M(\alpha')d\alpha' \tag{3.5.25}$$

where we notice again that the expression is identical to the previous one except that the hat is removed for $k(\alpha)$ (but not for $\hat{k}_M(\alpha)$).

Example 3.5.2 Consider again the plate of Fig. 3.5.1. When a pair of loads P_M is applied to the crack mouth (as shown in Fig. 3.5.2), the corresponding stress intensity factor is expressed as $K_I = 2.594P_M/b\sqrt{\pi a}$ (Ouchterlony 1975; also Tada, Paris and Irwin 1985). This can be rewritten as $K_I = (P_M/b\sqrt{D})2.594/\sqrt{\pi\alpha}$. Therefore, the shape function $\hat{k}_M(\alpha)$ is

$$\hat{k}_M(\alpha) = \frac{2.594}{\sqrt{\pi\alpha}} \tag{3.5.26}$$

Substituting this and (3.5.8) into (3.5.25) we get the CMOD:

$$w_M = \frac{\sigma}{E'}D2\int_0^{\alpha} 2.909\,d\alpha' = 5.818\frac{\sigma}{E'}D\alpha = 5.818\frac{\sigma}{E'}a \tag{3.5.27}$$

which is the expression found, for example, in Tada, Paris and Irwin (1985). □

3.5.4 Calculation of the Volume of the Crack

A further interesting application of the general relation (3.5.18) is the determination of the volume of the opened crack. To this end, we must consider a loading which is work-conjugate to volume, i.e., such that the work is expressible as the product of the conjugate generalized force with the variation of crack volume dV. Such a loading is a uniform internal pressure p over the crack faces; then p and V are conjugate variables and can be used directly in the energetic expressions. It is now necessary to adjust (3.5.18), because the dimensions of the variables are different. This is fairly easy and is left to the reader as an exercise. Here we execute a simple trick to be able to use (3.5.18) as it is: we define a generalized force P_V from p, and its associated displacement $u_v \propto V$ so that $P_V u_V = pV$ and the dimensions be those of force and length:

$$P_V = pbD \quad \text{and} \quad u_V = \frac{V}{bD} \tag{3.5.28}$$

(Note that the crack length a must *not* appear in the definition of P_v and u_V.) Working now as in our calculation of the CMOD, we have $n = 2$, and set $P_1 \equiv P$, $P_2 \equiv P_V$, $u_1 \equiv u$, $u_2 \equiv u_V$, $C_{11}(a) \equiv C(a)$, and $C_{12}(a) \equiv C_V(a)$. So we may write the displacements as

$$u = C(a)\,P + C_V(a)\,P_V \tag{3.5.29}$$

$$u_v = C_V(a)\,P + C_{VV}(a)\,P_V \tag{3.5.30}$$

We also set $\hat{k}_1(\alpha) \equiv \hat{k}(\alpha)$ for the shape factor corresponding to force P, and $\hat{k}_2(\alpha) \equiv \hat{k}_V(\alpha)$ for the one corresponding to the internal pressure — in which the stress intensity factor must be written in the form $K_I = (P_V/b\sqrt{D})\hat{k}_V(\alpha)$. Thus, the cross-compliance for u_V, $C_V(a)$, follows from (3.5.18) with $C_{V0} \equiv C_{120} = 0$ (because when the crack length is zero, the crack volume is also zero):

$$C_V(a) = \frac{2}{bE'}\int_0^{a/D} \hat{k}(\alpha)\hat{k}_V(\alpha)d\alpha \tag{3.5.31}$$

The crack volume follows from (3.5.30) and (3.5.28):

$$V = bDu_V = bDC_V P = \frac{PD}{E'}\hat{v}_V(\alpha) \tag{3.5.32}$$

where

$$\hat{v}_V(\alpha) = 2\int_0^{\alpha} \hat{k}(\alpha')\hat{k}_V(\alpha')d\alpha' \tag{3.5.33}$$

If we write V in terms of σ_N instead of P, we get

$$V = \frac{\sigma_N}{E'}bD^2 v_V(\alpha)\,, \quad v_V(\alpha) = 2\int_0^{\alpha} k(\alpha')k_V(\alpha')d\alpha' \tag{3.5.34}$$

where $k(\alpha')$ is the shape factor defined in (2.3.11) and $k_V(\alpha')$ is defined so that the stress intensity factor created by a uniform pressure inside the crack is written as $K_I = p\sqrt{D}k_V(\alpha)$.

Example 3.5.3 Consider again the plate of Fig. 3.5.1. When a uniform pressure p is applied to the crack faces, the superposition sketched in Fig. 3.5.3 shows that the stress intensity factor is identical to that corresponding to a remote uniaxial stress $\sigma = p$. The corresponding stress intensity factor is $K_I = 1.1215p\sqrt{\pi a}$, and so the shape function $k_V(\alpha)$ is

$$k_V(\alpha) = 1.1215\sqrt{\pi\alpha} \tag{3.5.35}$$

Substituting this and (3.5.8) in (3.5.34), we get the crack volume:

$$V = \frac{\sigma}{E'}bD^2 2\int_0^{\alpha} 1.258\pi\alpha'\,d\alpha' = \frac{\sigma}{E'}bD^2\alpha^2 = \frac{\sigma}{E'}1.258\pi ba^2 \tag{3.5.36}$$

where we wrote $D\alpha = a$. □

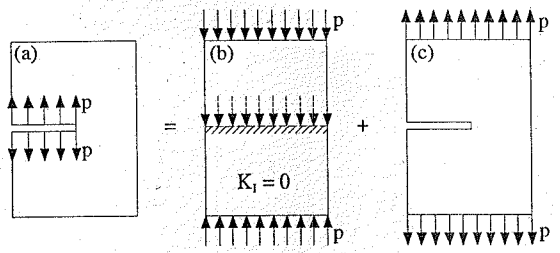

Figure 3.5.3 Stress intensity factors for internal pressure p and remote uniaxial stress p are identical.

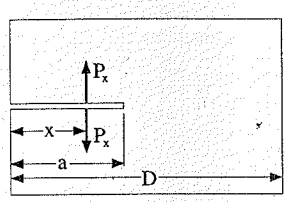

Figure 3.5.4 Virtual loading used in the computation of the crack opening profile.

For an internal crack of length $2a$, the results are similar, except that the shape factors at both tips of the crack appear explicitly, as in previous sections. Then the expression for $v_V(\alpha)$ in (3.5.34) must be replaced by

$$v_V(\alpha) = 2\int_0^\alpha \left[k^+(\alpha')k_V^+(\alpha') + k^+(\alpha')k_V^-(\alpha')\right] d\alpha' \tag{3.5.37}$$

3.5.5 Calculation of the Crack Opening Profile

To obtain the crack opening profile from K_I expressions, we need to know the stress intensity factor produced by a pair of point loads at an arbitrary position x along the crack. Let P_x be the magnitude of the loads located at x (Fig 3.5.4). The displacement conjugate of the pair P_x is the crack opening at point x, $w(x)$. The stress intensity factor may be written as in (3.1.10), where now it is essential to remark that when the point loads are applied on the uncracked part of the crack plane (i.e., when $x > a$) they do not generate any stress intensity factor at the crack tip, so that we can write

$$k_G(\alpha, x/D) = 0 \qquad \text{for} \quad x > a \ (\text{or } x/D > \alpha) \tag{3.5.38}$$

Then we proceed as we did in calculating the CMOD. We first write the displacements as

$$u = C(a)\,P + C_x(a)\,P_x \tag{3.5.39}$$

$$w(x) = C_x(a)\,P + C_{xx}(a)\,P_x \tag{3.5.40}$$

The compliance $C_x \equiv C_{12}$ is obtained from (3.5.18) with $\hat{k}_1(\alpha) = \hat{k}(\alpha)$, $\hat{k}_2(\alpha) = k_G(\alpha, x/D)$, and $C_{120} = 0$:

$$C_x(a) = \frac{2}{bE'}\int_0^{a/D} \hat{k}(\alpha)k_G(\alpha, x/D)d\alpha \tag{3.5.41}$$

Now, taking into account (3.5.38) and (3.5.40), the crack opening profile is obtained as

$$w(x,a) = \frac{P}{bE'}\hat{v}_x(\alpha)\,, \qquad \hat{v}_x(\alpha) = 2\int_{x/D}^\alpha \hat{k}(\alpha')k_G(\alpha', x/D)d\alpha' \tag{3.5.42}$$

where it is understood that this equation is valid for $x \le a$, and that, obviously, $w(x,a) = 0$ for $x \ge a$. The foregoing equation can be rewritten in terms of σ_N as

$$w(x,a) = \frac{\sigma_N}{E'}Dv_x(\alpha)\,, \qquad v_x(\alpha) = 2\int_{x/D}^\alpha k(\alpha')k_G(\alpha', x/D)d\alpha' \tag{3.5.43}$$

where, again, $k(\alpha)$ is defined in (2.3.11).

For an internal crack for which a is the half crack length, the previous adjustment for two crack tips must be performed again. The result is identical to (3.5.43) except that $v(\alpha)$ is now replaced by

$$v_x(\alpha) = 2\int_{x/D}^\alpha \left[k^+(\alpha')k_G^+(\alpha', x/D) + k^-(\alpha')k_G^-(\alpha', x/D)\right] d\alpha' \tag{3.5.44}$$

Example 3.5.4 Consider the center cracked panel of Fig. 2.1.1 subjected to remote uniaxial stress σ, and assume the crack to be very small relative to the dimensions of the panel. To obtain the crack opening profile we use the stress intensity factor for a pair of point loads on the crack faces introduced in Example 3.1.7 (Fig. 3.1.6c), with $k_G^+(\alpha, x/D)$ given Eq. (3.1.13). Because of the symmetry, the shape factor for the tip on the left is $k_G^-(\alpha, x/D) = k_G^+(\alpha, -x/D)$. Introducing this and $k^+(\alpha) = k^-(\alpha) = \sqrt{\pi\alpha}$ into (3.5.44), and substituting the result in the first of (3.5.43), we get

$$w(x,a) = \frac{\sigma}{E'}D\int_{x/D}^\alpha \frac{4\alpha'}{\sqrt{\alpha'^2 - (x/D)^2}}d\alpha' = \frac{4\sigma}{E'}\sqrt{a^2 - x^2} \tag{3.5.45}$$

which does coincide with the solution obtained by the complete elastic analysis of the problem; see Section 2.2.1. □

3.5.6 Bueckner's Expression for the Weight Function

Bueckner (1970) devised a procedure to obtain the weight function $k_G(\alpha, x/D)$ from the solution for the stress intensity factor and crack opening profile for arbitrary loading. This is the method exploited in the book by Wu and Carlsson (1991). Here it suffices to exploit (3.5.42) for demonstrating the simplest version of Bueckner's result. Differentiating that equation with respect to a (and keeping in mind that $\alpha = a/D$), we get:

$$\frac{\partial w(x,a)}{\partial a} = \frac{\sigma_N}{E'}D\frac{\partial \hat{v}_x(\alpha)}{\partial \alpha}\frac{1}{D} = \frac{\sigma_N}{E'}2k(\alpha)k_G(\alpha, x/D) = \frac{2K_I}{E'\sqrt{D}}k_G(\alpha, x/D) \tag{3.5.46}$$

where in the last expression we substituted (2.3.11), i.e., $K_I = \sigma_N\sqrt{D}k(\alpha)$. Solving for $k_G(\alpha, x/D)$, we get

$$k_G(\alpha, x/D) = \frac{E'\sqrt{D}}{K_I(a)}\frac{\partial w(x,a)}{2\partial a} \tag{3.5.47}$$

The arguments a and x have been made explicit for clarity. Note that, compared to the expressions in other texts, our analysis is limited to pure mode I (structures and loadings symmetric with respect to the crack plane), and so the half crack opening $w/2$ is equal to half the displacement of the upper face, which is the usual variable included in the weight function expressions. We use the crack opening rather than the displacement of one crack face because in the following chapters the crack opening is the essential variable.

Consider now the center-cracked panel. Since it has two crack tips, we cannot get both weight functions from a single loading. This is clear from (3.5.44) where two unknowns are present, namely $k_G^+(\alpha, x/D)$ and $k_G^-(\alpha, x/D)$. In particular, from the solution for a symmetric loading for which $\hat{k}_s^+(\alpha) = \hat{k}_s^-(\alpha) =$

$\hat{k}_s(\alpha)$, we can find only the symmetric part of the weight function. Indeed, proceeding as before, we get

$$k_G^+(a/D, x/D) + k_G^-(a/D, x/D) = \frac{E'\sqrt{D}}{K_{Is}(a)} \frac{\partial w_s(x,a)}{2\partial a} \tag{3.5.48}$$

where subscript s indicates that the loading corresponding to this solution must be symmetric. The symmetric part of k_G is all that is needed to obtain further crack opening profiles for other symmetric loadings. To obtain the complete expression for the right and left weight functions, we also need to solve the antisymmetric case, for which $\hat{k}_a^+(\alpha) = -\hat{k}_a^-(\alpha)$. If this solution is available, it is easy to find the antisymmetric part as

$$k_G^+(a/D, x/D) - k_G^-(a/D, x/D) = \frac{E'bD}{P_a \hat{k}_a^+(a/D)} \frac{\partial w_a(x,a)}{2\partial a} = \frac{E'\sqrt{D}}{K_{Ia}^+(a)} \frac{\partial w_a(x,a)}{2\partial a} \tag{3.5.49}$$

where subscript a refers to antisymmetric loading. Combining (3.5.49) and (3.5.48), one can easily obtain the expression for the weight functions corresponding to both crack tips.

Exercises

3.15 The stress intensity factor for a center cracked strip of width D, with a crack of length $2a$ subjected to remote uniaxial stress, may be approximated by the Feddersen-Tada expression (3.1.4) within 0.1%. Write the equation for the additional compliance of the strip due to the crack. Take two terms of the series expansion of the integrand in powers of a/D, calculate the additional compliance, and estimate the values a/D for which this result is accurate within 2%.

3.16 For the panel in Exercise 3.4, find the volume of hydraulic fluid injected into the jack for given crack length $2a$ and pressure p, assuming the fluid to be incompressible. Hints: Define $P = 2pbc$ and $u = V/2bc$. Watch the integration limits. Integrate by parts twice.

3.17 Find the volume of a centrally located crack in a large panel subjected to equal and opposite normal forces at the crack center.

3.18 Find the crack opening profile of a centrally located crack in a large panel subjected to equal and opposite normal forces at the crack center. Note the logarithmic singularity at $x = 0$.

4

Advanced Aspects of LEFM

In this chapter, we summarize some advanced topics in LEFM that were not covered in depth in the preceding chapters. First, we present the theoretical framework to analytically handle plane elasticity problems with cracks. Emphasis is put on the understanding of various methods of solution, such as the complex potentials (expounded in Section 4.1), Westergaard stress functions (presented in Section 4.2), and Airy stress functions (developed as exercises). The presentation does not aim at complete, formal presentations (for this purpose, see, e.g., England 1971). Neither it aims at teaching the skills to obtain the solution from scratch. It only aims at facilitating insight into the use of complex potentials and Westergaard stress functions to obtain stress and displacement fields. As a basic example, these methods are applied to the analysis of the infinite center-cracked panel.

The complex potentials are next used to analyze the near-tip fields (Section 4.3). The in-plane case, involving fracture modes I (pure opening) and II (in-plane shear), is discussed first. Then the formalism to handle the antiplane case of mode III (antiplane shear) is introduced and the general antiplane stress and displacement near-tip fields are obtained.

The next topic covered is that of the path-independent integrals, of which the J–integral is the most important. Section 4.4 shows formally that Rice's J–integral is path-independent under certain assumptions; it introduces a further path-independent integral for the LEFM case which is based on the reciprocity theorem and is used to provide another derivation of Irwin's relation. Finally, other path independent integrals are briefly discussed (I–, J_k–, L–, and M–integrals).

The last section deals with the topic of mixed mode fracture in LEFM. The existing fracture criteria are briefly described, with emphasis put on the single-parameter models, especially the maximum principal stress criterion (Erdogan and Sih 1963).

4.1 Complex Variable Formulation of Plane Elasticity Problems

4.1.1 Navier's Equations for the Plane Elastic Problem

We take axes x_1, x_2 lying in the plane of the structure, and axis x_3 perpendicular to it. Plane states always require $\sigma_{13} = \sigma_{23} = 0$, while $\sigma_{33} = 0$ in generalized plane stress, and $\varepsilon_{33} = 0$ in plane strain.

Restricting attention to the in-plane components of vectors and tensors (i.e., restricting indices to values 1 and 2), the equilibrium equation for negligible body forces are reduced to state that the 2D divergence of the stress tensor must vanish:

$$\sigma_{ij,j} = 0 \tag{4.1.1}$$

where subscript $_{,j}$ implies partial derivative with respect to the corresponding cartesian coordinate (i.e., $f_{,j} = \partial f/\partial x_j$). Repeated indices imply summation over $i = 1, 2$.

The plane version of Hooke's law may be reduced to (see, for example, Malvern 1969):

$$\sigma_{ij} = \lambda' \varepsilon_{kk} \delta_{ij} + 2G\varepsilon_{ij} \tag{4.1.2}$$

where G is the shear modulus and λ' is an effective plane Lamé constant. These elastic constants can be written as

$$G = \frac{E}{2(1+\nu)}, \qquad \lambda' = \frac{E'\nu'}{(1-\nu'^2)} \tag{4.1.3}$$

and $\sigma_\infty = K_{IN}/\sqrt{\pi a_0}$ in (7.5.25) and (7.5.26) and take the limits for $a_0 \to \infty$. The first terms of Maclaurin's series expansion of $\sec x$ and $ln(1+x)$ are $1 + x^2/2 + \cdots$, and $x + \cdots$, respectively.]

7.23 Consider a Dugdale model for the asymptotic limit of large crack in large body. (a) Use (7.5.70) to determine the function $q(\eta)$; (b) calculate K_{IN} as a function of R; (c) calculate the crack tip opening displacement w_T as a function of R; and (d) compare the results of parts (b) and (c) with those of parts (a) and (b) in the previous exercise.

7.24 For a Dugdale model, show that the crack opening profile in the cohesive zone for a semi-infinite crack in an infinite body is given by

$$w(\xi) = \frac{8Rf_t'}{\pi E'}\int_\xi^1 \eta^{-1/2}(\eta-\xi)^{1/2}d\eta = \frac{8Rf_t'}{\pi E'}\left[\sqrt{1-\xi} - \xi \ln\frac{1+\sqrt{1-\xi}}{\sqrt{\xi}}\right] =$$

$$= \frac{8Rf_t'}{\pi E'}\left[\sqrt{1-\xi} - \frac{\xi}{2}\ln\frac{1+\sqrt{1-\xi}}{1-\sqrt{1-\xi}}\right], \quad \text{with} \quad \xi = \frac{x}{R} \tag{7.5.74}$$

7.25 Show that for the Dugdale model, $\Delta a_\infty = R/3$.

7.26 For a rectangular softening, determine the asymptotic values R_c and $\Delta a_{\infty c}$ at peak load as a function of ℓ_{ch}.

8

Crack Band Models and Smeared Cracking

Modeling of fracture by discrete line cracks, which has been discussed in the preceding chapters, is not the only viable approach. Another approach, which has gained wide popularity in finite element analysis of concrete structures (Meyer and Okamura, Eds., 1986) and is used almost exclusively in design practice, is to represent fracture in a smeared manner. In this approach, introduced by Rashid (1968), infinitely many parallel cracks of infinitely small opening are imagined to be continuously distributed (smeared) over the finite element. This can be conveniently modeled by reducing the material stiffness and strength in the direction normal to the cracks after the peak strength of the material has been reached. Such changes of the stiffness matrix are relatively easy to implement in a finite element code, and, hence, the appeal of smeared cracking. The evolution of the cracking process down to full fracture implies *strain softening*, a term which describes the postpeak gradual decline of stress at increasing strain.

The term evolved from the terminology of plasticity where work hardening describes the gradual increase of yield stress resulting in a rising stress-strain diagram of a slope that is positive but smaller than the elastic slope. After it was realized that the hardening is not merely a function of the plastic work, a scalar, but depends on all the components of the strain tensor, the term strain hardening has been adopted. From the viewpoint of plasticity, the postpeak decline of stress may be regarded as a gradual decrease of the yield limit, i.e., softening. This phenomenon again is not just a function of work (in which case we could speak of work softening) but of all the strain components; hence, strain softening.

The smeared cracking (with strain softening), however, leads to certain theoretical difficulties which were initially unknown or unappreciated. They consist of the so-called localization instabilities and spurious mesh sensitivity of finite element calculations. After years of controversies and polemics, it has now been generally accepted that these difficulties can be adequately tackled by supplementing the material model with some mathematical condition that prevents localization of smeared cracking into arbitrarily small regions. The simplest way to attain this goal is the crack band model, which is the object of this chapter.

Since it is essential to understand why fracture cannot be consistently and objectively described just by postulating a stress-strain curve with softening and nothing else, we first analyze in this chapter the strain localization in systems displaying softening. We start with the series coupling of discrete elements (Section 8.1), which serves as the starting point for the analysis of the localization of strain in a softening bar (Section 8.2). From this, it follows that some kind of localization limiter must be associated with the softening stress-strain curve to get meaningful results. Next, we analyze the basic issues in the crack band model, in the simplest uniaxial approximation (Section 8.3). Then we deal with the underlying stress-strain relations with softening, first in the simple uniaxial version (Section 8.4) and then in full three-dimensional analysis (Section 8.5). After this, we discuss the triaxial features of the crack band models and smeared cracking, with emphasis placed on the numerical issues (Section 8.6). A comparison of the crack band and cohesive crack approaches closes the chapter (Section 8.7).

8.1 Strain Localization in the Series Coupling Model

Whenever a structure contains elements that may soften, localization of the strain can take place. This section analyzes this phenomenon for the simple, yet important, quasi-static uniaxial case. The case of two nominally identical elements coupled in series is first presented and studied from the point of view of the imperfection approach to bifurcation (no two elements can be exactly identical), and then from the

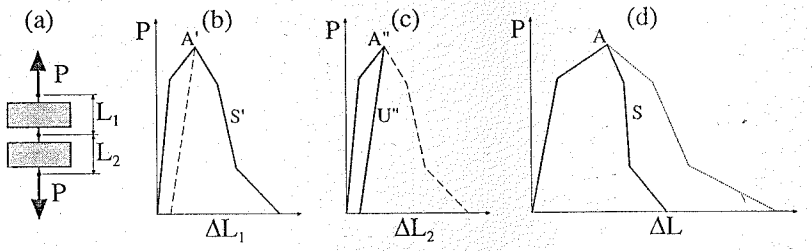

Figure 8.1.1 (a) Series coupling of two softening elements. (b) Load-displacement curve of one element. (c) Resulting load-displacement curve (full line).

point of view of the more general thermodynamic analysis of bifurcations. Next, as a simple extension, a chain of many softening elements is analyzed to show that, after reaching the peak load, only one element will be stretched further, while all the remaining elements unload. This is the starting point for the analysis of a softening continuous homogeneous bar, considered in the next section.

8.1.1 Series Coupling of Two Equal Strain Softening Elements: Imperfection Approach

Consider two nominally identical elements **1** and **2** coupled in series as shown in Fig. 8.1.1a. Assume that each element has a load-elongation (P-ΔL) curve displaying softening as sketched in Fig. 8.1.1b for element **1**. In this plot, the full line is for monotonic extension, and the dashed line corresponds to unloading (shortening) right at the peak. The question is: What is the load-elongation response of the series coupling of the two elements?

A quick answer, extrapolated from the more usual cases of hardening structures would be: Just multiply the elongation by a factor of two. Wrong! Softening breaks down the usual rules. To clarify this, we take first the imperfection approach to bifurcation. In this approach, one realizes that no two elements can be really identical. One of them must have a strength (peak load) slightly smaller than the other one. Assume that such is the case for element **1**. So the element **2**, whose curve is depicted in Fig. 8.1.1c, has a strength only slightly larger than element **1**. The difference is so slight that it cannot be discerned at the scale of the drawing.

As the series coupling is extended, both elements **1** and **2** load up until the peak A' of element **1** is reached. Upon further extension, element **1** must begin to soften, following path A'-S' with decreasing load. Since the load on both elements is identical, the load on element **2** must decrease, too. But since element **2** has not yet reached the peak, it is not going to soften. It is going to *unload* following the path A"-U".

Therefore, as soon as one element reaches the peak, further straining leads to softening of this element and to unloading of the other. We say that strain *localizes* into one element due to softening. Fig. 8.1.1d shows the resulting P-ΔL curve as a full line. The dotted line represents the (wrong) result obtained by assuming that both elements go into the softening regime (we call it homogeneous deformation, same extension in each element). Note that the rising portion of the curve (the hardening part) displays a displacement that is twice the displacement for a single element, the classical result. The difference lies only in the softening portion of the curve.

The foregoing result (see also Bažant and Cedolin 1991, Sec. 13.2) is based on the idea that the strength of the two elements cannot be identical. Note that the amount by which they differ is immaterial. The same will happen if the difference were only one part in 10^{12}, which is much less than what can be experimentally detected.

We have assumed that element **1** was the weaker element. In practice, we cannot know *a priori* which of the two elements is going to break. We can only state that, if the loading system is perfectly symmetric, the probabilities of failure through one or other element must be equal, so that 50% of tests will show failure of element **1** and 50% failure of element **2**.

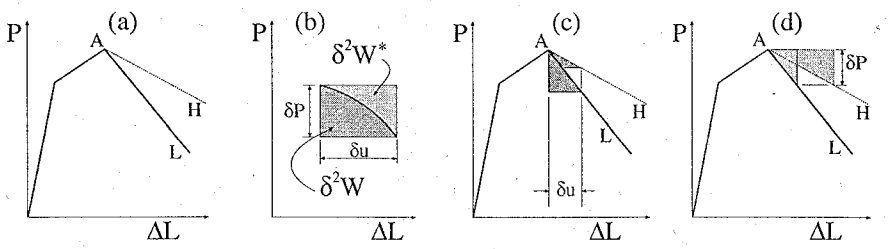

Figure 8.1.2 Series coupling of two strictly identical softening elements: (a) the two possible paths, (b) graphical representation of second-order work and second-order complementary work, (c) postpeak, second-order work, (d) postpeak, second-order complementary work.

8.1.2 Series Coupling of Two Equal Strain Softening Elements: Thermodynamic Approach

The foregoing discussion makes use of inhomogeneities or imperfections to get a general conclusion. However, this result may be also obtained on the basis of thermodynamics. To do so, we consider a series coupling of two identical elements, and consider the possibility of bifurcation at the peak load. The two possible resulting paths are depicted in Fig. 8.1.2a. Path A-H (dotted line) corresponds to a homogeneous deformation, while path A-L (full line) corresponds to softening that localizes into one of the elements, while the other unloads. Which is the preferred path? Following Bažant and Cedolin (1991, Sec. 10.2), for the correct path, the second-order work $\delta^2\mathcal{W} = \frac{1}{2}\delta P\,\delta u$ for imposed displacement increment δu must be minimum, or, alternatively, the second-order complementary work $\delta^2\mathcal{W}^* = \delta P\,\delta u - \delta^2\mathcal{W}$ for imposed load increment δP must be maximum.

Fig. 8.1.2b shows the graphical representation of the second-order work and second-order complementary work for a softening incremental process. Note that the values of the second-order areas are negative because $\delta P < 0$. Therefore, the foregoing principles may be restated by expressing that the second-order area below the P-u curve must be maximum at fixed δu, and that the second-order area over the P-u curve must be minimum at fixed δP.

Figs. 8.1.2c-d show the application of the foregoing principles to our case. It is obvious that the correct path is that for which the localization occurs (see also Bažant and Cedolin 1991, Sec 13.2).

8.1.3 Mean Stress and Mean Strain

Whatever the nature of the foregoing elements, we can define the mean uniaxial stress as the load per unit representative area of the cross section, and the mean strain of each element and the mean strain of the whole coupling as the elongation per unit initial length, i.e., we set, in general,

$$\sigma = \frac{P}{A}, \qquad \varepsilon = \frac{\Delta L}{L} \tag{8.1.1}$$

where A is the representative area.

The advantage of this representation is that the hardening portions of the (mean) stress-strain curves are identical for each of the elements and for the series coupling. This is not so, however, for the softening part of the curves. Let ε_{h1} be the mean strain on the hardening branch of the curve for any one of the two elements. Further, let ε_{u1} be the strain at the same stress level on the unloading branch emanating from the peak, and let ε_{s1} be the strain at the same stress level on the softening part of the curve, as indicated in Fig. 8.1.3c–d. The curves in this figure are the same as those in Fig. 8.1.1, with a change of scale. The resulting (mean) stress-strain curve is shown in Fig. 8.1.3d, in which the mean strain at the given stress level is given by

$$\varepsilon = \begin{cases} (L_1\varepsilon_{h1} + L_2\varepsilon_{h2})/(L_1 + L_2) = \varepsilon_{h1} & \text{for hardening} \\ (L_1\varepsilon_{s1} + L_2\varepsilon_{u2})/(L_1 + L_2) = \varepsilon_{u1} + \frac{1}{2}(\varepsilon_{s1} - \varepsilon_{u1}) & \text{for softening} \end{cases} \tag{8.1.2}$$

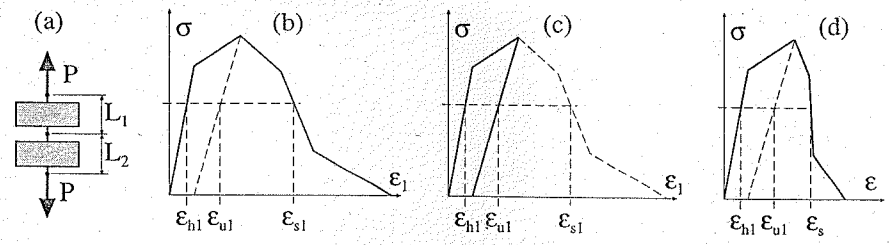

Figure 8.1.3 Series coupling of two softening elements: load-average strain curves.

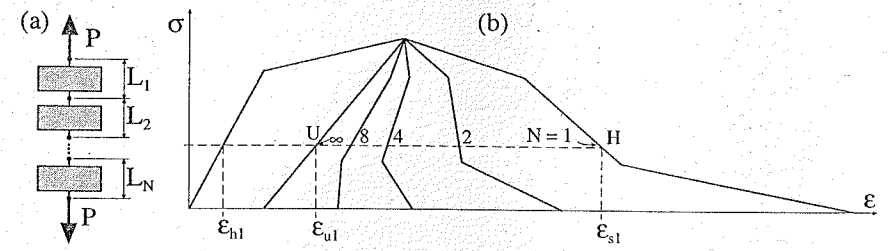

Figure 8.1.4 (a) Series coupling of N equal softening elements. (b) Stress vs. average-strain curves for various values of N.

8.1.4 Series Coupling of N Equal Strain Softening Elements

Consider now a chain of N nominally identical softening elements (Fig. 8.1.4a). Following the same reasoning as in the previous analysis, it is immediately obvious that after reaching the peak, only one of the elements, say element **1**, will soften, while the remaining $N-1$ will unload. Keeping this in mind, we consider how the mean strain will evolve as a function of N.

The mean strain of the whole chain is

$$\varepsilon = \frac{\sum_{i=1}^{N} L_i \varepsilon_i}{\sum_{i=1}^{N} L_i} = \frac{1}{N} \sum_{i=1}^{N} \varepsilon_i \tag{8.1.3}$$

where i indicates the element number, and ε_i the strain of that element. Expressing the fact that on the hardening branch all the strains are identical and equal to ε_{h1} and that on the softening branch the strain of the first element is ε_{s1} while the strain of the remaining $N-1$ elements is ε_{u1}, we get the following result for the mean stress-strain curve:

$$\varepsilon = \begin{cases} \varepsilon_{h1} & \text{for hardening} \\ \varepsilon_{u1} + \frac{1}{N}(\varepsilon_{s1} - \varepsilon_{u1}) & \text{for softening} \end{cases} \tag{8.1.4}$$

Fig. 8.1.4b plots the foregoing analytical results for N=1, 2, 4, 8, and ∞ based on the curve of Fig. 8.1.3b (note that the horizontal scale has been expanded). The construction of the softening branch is very easy to perform graphically: at each stress level, take the segment UH where U and H are the points, respectively, on the unloading and softening branches for a single element. Then, take a segment N times smaller with origin at U. The other end of the segment determines the point of the softening branch of the series coupling of N elements.

One essential result of this analysis is that, while the peak load does not change with the number of elements, the brittleness does so in the sense that the larger the number of elements, the steeper the softening branch gets. In the limit of an infinite number of elements, the behavior is perfectly brittle.

Exercises

8.1 Analyze the response of a series coupling of two equal elements whose load-displacement curve shows a perfect plateau at peak load. For simplicity, assume that the load-elongation curve has the shape of a trapezium, rising linearly from $(0,0)$ to (P_u, u_0), then extending horizontally to (P_u, u_1), and finally descending linearly to $(0, u_2)$, where $u_0 < u_1 < u2$.

8.2 Consider the series coupling of elements that have a triangular load-displacement curve and are identical except for small imperfections. Assume that for one element the peak occurs at 1.2 kN for an elongation of 5 μm, and that a zero load is reached for an elongation of 200 μm. Determine and make a sketch of the load-displacement curve for (a) 2 elements, (b) 10 elements, (c) 100 elements, and (d) determine the number of elements for which the load drops vertically just after the peak.

8.3 Consider the series coupling of elements with exponential softening. The load-displacement curve for one single element is given by the equations

$$\Delta L = \begin{cases} C_0 P & \text{for} \quad \Delta L \le C_0 P_u \\ C_0 P + u_0 \ln(P_u/P) & \text{for} \quad \Delta L \ge C_0 P_u \end{cases} \tag{8.1.5}$$

in which $C_0 = 1.1$ μm/kN, $P_u = 3.1$ kN, $u_0 = 68.2$ μm. Determine: (a) the energy required to break one element, (b) the load-elongation curve for a coupling of 10 elements, (c) same for 100 elements (draw the curve). (d) Determine also the lowest number of elements for which the resulting softening branch displays a vertical tangent.

8.2 Localization of Strain in a Softening Bar

In the preceding section we obtained some general results concerning a series coupling of discrete elements, for which the reasoning is somewhat easier than for a continuous bar. Now let us discuss the behavior of a uniaxially stressed bar of a homogeneous material.

It may appear that using a classical stress-strain formulation including softening is a natural way to introduce fracture (loss of strength down to zero). However, this is not straightforward. If no other precaution is taken, the resulting model is both physically incorrect and numerically ill-posed. Let us see why.

8.2.1 Localization and Mesh Objectivity

Consider a homogeneous bar of initial length L (Fig. 8.2.1a) made of a material whose stress-strain curve (uniaxial) is assumed to exhibit softening, as sketched in Fig. 8.2.1b. Because of the hypothesis of homogeneity, we can imagine the bar to be subdivided in N identical shorter bars (N being arbitrary) which then act as N equal elements coupled in series, as sketched in Fig. 8.2.1c. We have seen in the previous section that when N elements are coupled in series, the strain localizes after the peak in only one of them, so that the resulting σ-ε curves look similar to that in Fig. 8.1.4b.

Therefore, the postpeak softening of the bar depends totally on the assumed subdivision, as indicated in Fig. 8.2.1d. This has two direct consequences: on purely mechanical grounds, the result is absurd because the physical result cannot depend on the *imagined* subdivision; on numerical grounds, it implies that the result one would obtain by using finite elements would completely depend on the number of elements or element size. This is a subjective choice of the analyst, and, thus, is not an objective property, as pointed out by Bažant (1976). This last property is referred to as lack of *mesh objectivity,* or as *spurious mesh sensitivity.*

Keeping the numerical point of view, we must realize that the response of the foregoing model is reached upon infinite mesh refinement, i.e., for $N \to \infty$. This means that strain localization is predicted to occur only within one infinitely thin element, i.e., an element of infinitely small length and volume. Now, is that consistent with the principles of thermodynamics? Yes, it is. We stated in the previous section that among many possible equilibrium paths, the actual one is that in which the second-order complementary work $\delta^2 \mathcal{W}^*$ at constant δP is maximum. Since, in the softening branch, δP is negative, the maximum $\delta^2 \mathcal{W}^*$ occurs for the path with the largest (positive) inverse slope. As shown in the figure, this slope does indeed correspond to considering infinitely many elements (Fig. 8.2.1d).

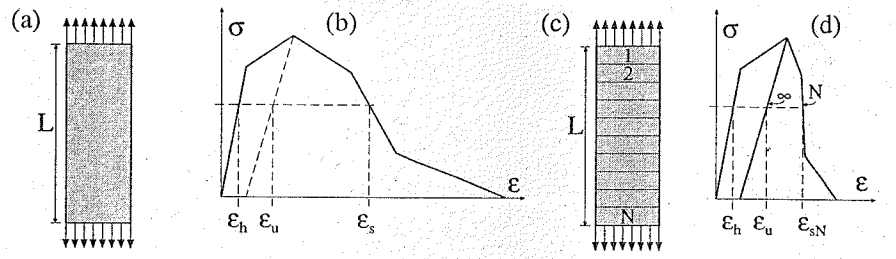

Figure 8.2.1 (a) Homogeneous bar. (b) Stress-strain curve of the material. (c) Subdivision of the bar into N equal elements. (d) Resulting stress-strain curve.

A further implication is that any variable that is ultimately bounded by the length or the volume will vanish. (We say that a variable ϕ is ultimately bounded by volume V if $|\phi| < MV$, for some finite $M > 0$.) This is so for the inelastic displacement and the energy dissipation after the peak. We say that the corresponding physical quantities have *measure zero*. Let us take a closer look at this problem for one special, yet important case.

8.2.2 Localization in an Elastic-Softening Bar

Consider a homogeneous bar of length L (Fig. 8.2.2a) that has a stress-strain curve of the elastic-softening type, as depicted in Fig. 8.2.2b, and is characterized by a linear elastic behavior up to the peak, followed by strain-softening. We can then write the strain on the softening branch as

$$\varepsilon_s = \frac{\sigma}{E} + \varepsilon^f \tag{8.2.1}$$

where E is the elastic modulus and ε^f is the inelastic *fracturing* strain, graphically defined as shown in Fig. 8.2.2b. Unloading from the peak is assumed to be fully elastic. We further assume that the softening branch is unique, i.e., that a unique relationship exists between σ and ε^f as long as ε^f increases monotonically:

$$\sigma = \phi(\varepsilon^f) \tag{8.2.2}$$

This function can be extracted from the σ-ε curve and plotted independently as shown Fig. 8.2.2c. We can also compute the work γ_F required to fully break a unit volume of material (the fracture energy density): it is the area under the σ-ε curve, and so the area under the σ-ε^f curve:

$$\gamma_F = \int_0^\infty \sigma \, d\varepsilon^f = \int_0^\infty \phi(\varepsilon^f) \, d\varepsilon^f \tag{8.2.3}$$

Note that Figs. 8.2.2 and 7.1.3 and the foregoing integral are similar to the definition of G_F in (7.1.8). It might seem that the correspondence is immediate and logical. It is not.

Consider a quasi-static process in which the bar is monotonically stretched. Up to the peak, the strain is uniform, equal to the elastic strain. At peak, just as seen before, a bifurcation can occur so that a portion of the bar, of length $h \leq L$, continues stretching, while the rest of the bar unloads elastically (Fig. 8.2.2d). The total elongation of the bar in the softening branch is thus:

$$\Delta L = \frac{\sigma}{E}(L-h) + \left[\frac{\sigma}{E} + \varepsilon^f\right] h = \frac{\sigma}{E} L + \varepsilon^f h \tag{8.2.4}$$

where we see that the first term in the last inequality is the elastic elongation. Therefore, we can define the fracturing elongation as

$$\Delta L^f = \varepsilon^f h \tag{8.2.5}$$

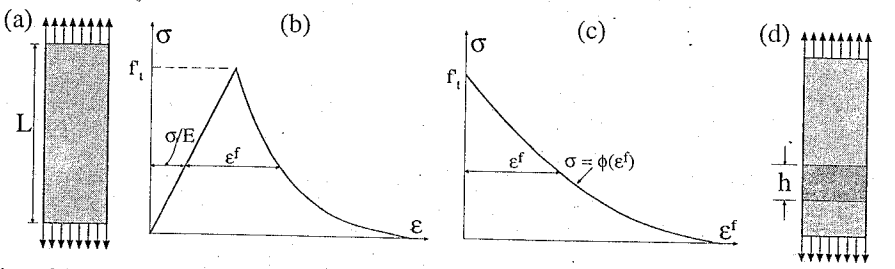

Figure 8.2.2 (a) Homogeneous bar. (b) Elastic-softening stress strain curve. (c) Stress-fracturing strain curve. (d) Bar with a softening band of length h.

On the other hand, the total work supply required to break the whole specimen is just the work required to break the softening portion (the remainder is always elastic) so that

$$\mathcal{W}_F = A \int_0^\infty \sigma \, d(h\varepsilon^f) = Ah \int_0^\infty \sigma \, d\varepsilon^f = Ah\gamma_F \tag{8.2.6}$$

where A is the area of the cross section of the bar.

Up to now h has been arbitrary, but what is its preferred value? To find it, we apply again the maximum second-order work condition ($\delta^2 W^* = \max$) and find immediately that the thermomechanical solution is $h = 0$, in complete concordance with the previous result $N = \infty$ for equally sized elements. It follows from this essential result and from (8.2.5) and (8.2.6) that, according to this model, both the inelastic displacement and the fracture work are zero. This is physically unacceptable and contrary to experiment.

8.2.3 Summary: Necessity of Localization Limiters

The foregoing simple analysis corresponds to static loading and shows that the simple stress-strain model with strain softening leads to unacceptable behavior both physically and computationally: (**1**) the softening zone has a zero width and volume; (**2**) the inelastic strain and fracture work are zero; and (**3**) the computational results are mesh-unobjective.

Further analyses indicate that similar conclusions apply to dynamic situations. For example, Bažant and Belytschko (1985) analyzed the problem of two converging elastic waves propagating from the ends of a bar towards its center, where they add up to exceed the tensile strength. The results show that failure is instantaneous and occurs again over a zone of zero width, and with zero energy dissipation. Belytschko, Bažant et al. (1986) reached similar conclusions for converging elastic waves in a sphere or a cylinder; although the fracture pattern was chaotic, with fracture occurring at many locations, the results still had zero measure and were mesh unobjective (see also Bažant and Cedolin 1991, Sec. 13.1).

The conclusion is that these models are not suitable at all because they allow localization in a region of zero volume. Therefore, if a continuum formulation based on stress-strain curves with strain softening is to be used, it is necessary to complement it with some conditions that prevent the strain from localizing into a region of measure zero. Such conditions are generically called *localization limiters* (Bažant and Belytschko 1985).

The model with the simplest localization limiter is the crack band model that we introduce next. Models with more general limiters are the nonlocal models that are presented in Chapter 13.

Exercises

8.4 Consider a bar with a triangular stress-strain curve defined as $E\varepsilon = \sigma$ for $E\varepsilon \leq f'_t$, and $E\varepsilon = (1+m)f'_t - m\sigma <$ for $f'_t \leq E\varepsilon \leq (1+m)f'_t$, where $E = 30$ GPa, $f'_t = 3$ MPa, $E = 30$ GPa, and $m = 21$; the stress is zero for $E\varepsilon > (1+m)f'_t$. Determine the load-elongation curve and the energy supplied to break the bar if its length is 0.5 m and the softening localizes in a zone of width (a) $h = 25$ cm, (b) $h = 10$ cm, (c) $h = 3$ cm, (d) $h = 1$ cm.

8.5 In the previous exercise, determine the width of the softening zone for which the stress drops vertically to zero right after the peak.

8.6 Consider a bar that has an exponential stress-strain curve defined as

$$E\varepsilon = \begin{cases} \sigma & \text{for} \quad E\varepsilon \le f_t' \\ \sigma + m f_t' \ln(f_t'/\sigma) & \text{for} \quad E\varepsilon \le f_t' \end{cases} \tag{8.2.7}$$

in which $E = 27$ GPa, $f_t' = 3.1$ MPa, $m = 12$. Determine the load-elongation curve and the energy supplied to break the bar if its length is 0.5 m and the softening localizes in a zone of width (a) $h = 25$ cm, (b) $h = 10$ cm, (c) $h = 3$ cm, (d) $h = 1$ cm.

8.7 In the previous exercise, determine the width of the softening zone for which the tangent to the stress-elongation curve right after the peak becomes vertical.

8.3 Basic Concepts in Crack Band Models

From the preceding analysis it is clear that, in order to make strain softening an acceptable constitutive relation, localization of strain softening into arbitrarily small regions must be prevented. This is, in general, achieved by some mathematical concept, called the localization limiter. There are various such concepts of varying degrees of generality and complexity. The most general concept is the nonlocal continuum concept, which will be discussed in Chapter 13. Now we describe a rather simple albeit less general concept, known as the crack band model, which was proposed in general terms in Bažant (1976), and was developed in full detail for sudden cracking in Bažant and Cedolin (1979, 1980, 1983) and Cedolin and Bažant (1980), and for gradual strain softening in Bažant (1982) and Bažant and Oh (1983a). The basic attribute of the crack band model is that the given constitutive relation with strain softening must be associated with a certain width h_c of the crack band, which represents a reference width and is treated as a material property. Here we discuss the most basic aspects only, with the help of simple uniaxial models. The three-dimensional analysis is deferred until Section 8.6.

8.3.1 Elastic-Softening Crack Band Models

As for cohesive cracks, the prepeak stress-strain relation can be nonlinear, but for many purposes it is enough to assume a linear behavior up to the peak followed by softening (Section 8.2.2). Then, the stress-elongation curve is given by (8.2.4), for arbitrary h. In Bažant's approach, the width of the band cannot be less than a certain characteristic value h_c. Thus, substituting $h = h_c$ in (8.2.4), we get an expression that is formally identical to the corresponding expression for the cohesive crack if we identify $h_c\varepsilon^f$ with the cohesive crack opening displacement w:

$$h_c\varepsilon^f = w \tag{8.3.1}$$

Thus, the stress-elongation curve for the band model and for the cohesive model will coincide if we relate the softening curve of stress vs. fracturing strain $\phi(\varepsilon^f)$ to the softening curve of stress vs. crack opening of the cohesive crack, i.e.,

$$\phi(\varepsilon^f) = f(w) = f(h_c\varepsilon^f) \qquad \text{or} \qquad f(w) = \phi(w/h_c) \tag{8.3.2}$$

where $f(w)$ is the equation of the softening curve for the cohesive crack model. Therefore, there is a unique relationship between the crack band model and the cohesive crack model, at least for the simple elastic-softening case that we are analyzing. The correspondence is illustrated in Fig. 8.3.1 which shows the softening curve for the cohesive crack (Fig. 8.3.1a) and the corresponding stress-strain curve for the crack band (Fig. 8.3.1b). Also shown is the correspondence for the initial linear approximation to the curve, the horizontal intercept of which satisfies $\varepsilon_1 = w_1/h_c$. It follows that a linear approximation for the softening of crack bands will be a good approximation in the same circumstances as it was for the cohesive crack model, principally for peak loads of not too large specimens, if notched, but any size specimens, if unnotched). This explains why the use of linear softening was very successful in the work of Bažant and Oh (1983a).

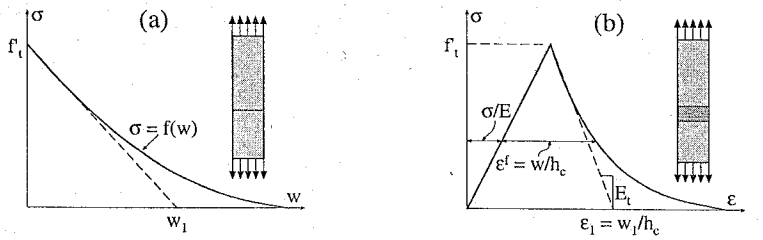

Figure 8.3.1 Correspondence between the softening curve of the cohesive crack model (a), and the stress-strain curve of the crack band model (b).

The correspondence is obviously maintained for the specific fracture energy G_F. Indeed, from (8.2.6) it follows that the energy required to form a complete crack (or a fully softened band) is

$$G_F = \frac{\mathcal{W}_F}{A} = h_c\gamma_F \tag{8.3.3}$$

From this, the characteristic size ℓ_{ch} can be easily obtained in terms of the properties of the crack band model as

$$\ell_{ch} = \frac{EG_F}{f_t'^2} = h_c\frac{E\gamma_F}{f_t'^2} \tag{8.3.4}$$

The characteristic size, ℓ_1, based on the initial linear softening is then

$$\ell_1 = \frac{Ew_1}{2f_t'} = h_c\frac{E\varepsilon_1}{2f_t'} \tag{8.3.5}$$

where ε_1 is the horizontal intercept of the initial tangent (Fig. 8.3.1b).

A parameter of interest in numerical calculations using the crack band model is the softening modulus E_t for the linear approximation (Fig. 8.3.1b). It is a simple matter to show that

$$2\ell_1 = h_c\left(1 - \frac{E}{E_t}\right) \tag{8.3.6}$$

The correspondence between the two models can further be systematized by defining a characteristic strain ε_{ch} and a reduced fracturing strain $\hat{\varepsilon}^f$ as

$$\varepsilon_{ch} = \frac{h_c f_t'}{G_F} = \frac{f_t'}{\gamma_F} \qquad \text{and} \qquad \hat{\varepsilon}^f = \frac{\varepsilon^f}{\varepsilon_{ch}} \tag{8.3.7}$$

With this, the nondimensional expression for the softening function is identical to that for the cohesive model, with the obvious change $\hat{\varepsilon}^f \leftrightarrow \hat{w}$., i.e.:

$$\hat{\sigma} = \hat{f}(\hat{\varepsilon}^f) \tag{8.3.8}$$

Therefore, all the softening curves discussed in the previous chapter can be directly implemented in the crack band model. The only difference between the results for one and other model is in the strain and displacement distribution. Figs. 8.3.2a and b show the comparison of the axial displacement distribution in a bar for a cohesive crack and a crack band model. Figs. 8.3.2c and d show the corresponding strain distributions. Obviously, the difference is nil for engineering purposes if $h_c \ll L$. This is almost invariably true in practical situations because, as we will see later in more detail, h_c is of the order of a few maximum aggregate sizes (Bažant and Oh 1983a).

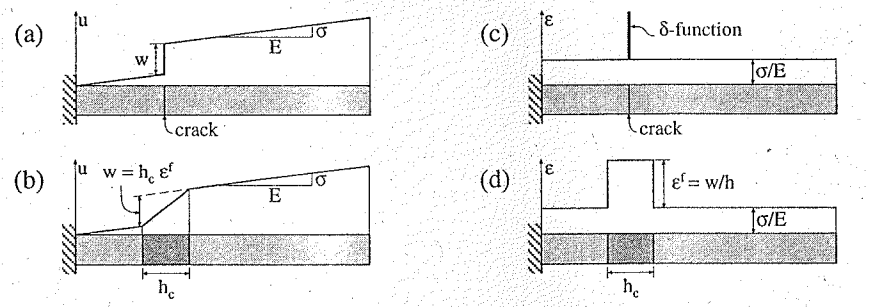

Figure 8.3.2 Comparison of the distributions of axial displacement and of strain in a bar for the cohesive crack model (a, c) and the crack band model (b, d).

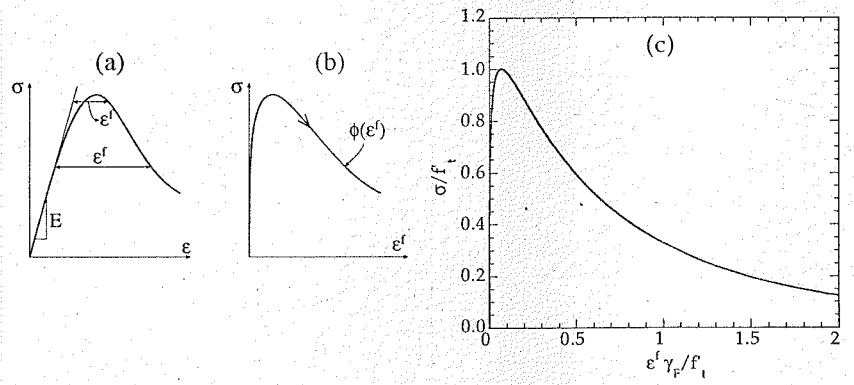

Figure 8.3.3 (a) Curvilinear stress-strain curve. (b) Curvilinear stress-fracturing strain curve. (c) Plot of the curve defined in Eq. (8.3.9).

8.3.2 Band Models with Bulk Dissipation

The cracking in reality does not begin upon reaching the tensile strength, but earlier, and so the diagram of stress vs. strain should have the form shown in Fig. 8.3.3a. As discussed in Section 7.1.6 for cohesive crack models, such behavior can be incorporated into the computational models with relative conceptual simplicity, but it considerably complicates the numerical treatment and experimental interpretation. Moreover, at least for concrete, neglecting the prepeak nonlinearity is generally acceptable for practical engineering use, and so the elastic-softening models we previously discussed are those most used. This seems to be clearly established (Planas, Elices and Guinea 1992) when there is one main crack, i.e., sharp localization occurs, because then the large postpeak strains dominate over the prepeak deformation. However, for situations where the localization is not sharp, the prepeak nonlinearity may play a dominant role, and its inclusion might be necessary. This may be the case in the prelocalization stages when there is reinforcement or when the stress field has a high gradient (as in the case for shrinkage stresses).

In our discussion of cohesive crack models, the inclusion of bulk dissipation (prepeak inelasticity) required defining an inelastic constitutive equation for the bulk in addition to the softening curve for the cohesive crack. One of the appealing features of the crack band model is that such a dichotomy is not necessary. Indeed, it is enough to define a single curvilinear stress-strain curve such as that shown in Fig. 8.3.3a. Then we can split the strain into the elastic and inelastic or fracturing part and use the curve of stress vs. inelastic strain as shown in Fig. 8.3.3b. For example, Bažant and Chern (1985a) proposed

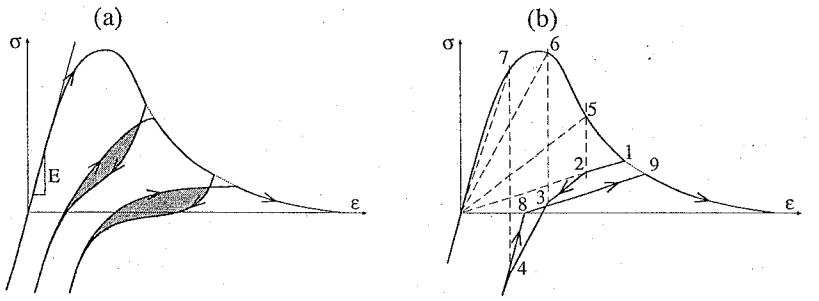

Figure 8.3.4 (a) General trend for the unloading-reloading branches found in experiments. (b) Construction of the unloading branch according to the secant-tangent rule (Bažant and Chern 1985a,b).

the following power-exponential curve:

$$\sigma = \phi(\varepsilon^f) = C_1 \varepsilon^{fp} e^{-b\varepsilon^{fq}} \tag{8.3.9}$$

where C_1, p, b, and q are constants. Fig. 8.3.3c shows the appearance of this curve for $p = 1/3, q = 0.55$ as derived by Bažant and Chern (1985a) by fitting of various experimental data. Note that the curve has been nondimensionalized so that its peak and area are equal to one.

Alternatively, the complete stress-strain curve can be given in the form $\sigma = \psi(\varepsilon)$. This is equivalent to giving the $\sigma(\varepsilon^f)$ curve in parametric form as:

$$\begin{aligned} \sigma &= \psi(\varepsilon) \\ \varepsilon^f &= \varepsilon - \tfrac{1}{E}\psi(\varepsilon) \end{aligned} \tag{8.3.10}$$

Among the formulas of this kind we have the power-exponential form (Bažant 1985a):

$$\sigma = E\varepsilon\, e^{-b\varepsilon^q} \tag{8.3.11}$$

where E is the elastic modulus and b, and q are constants. Another expression is

$$\sigma = \frac{E\varepsilon}{1 + a\varepsilon + b\varepsilon^q} \tag{8.3.12}$$

which was introduced by Saenz (1964) for compression strain softening, and in which a, b and q are constants.

8.3.3 Unloading and Reloading

For general applications in finite element programs, one must also specify what happens when, after partial or full cracking, the material is unloaded or reloaded. Experimentally observed behavior at unloading and reloading is rather complicated and looks approximately as sketched in Fig. 8.3.4a which is characterized by hysteretic loops of considerable area (Reinhardt and Cornelissen 1984; Hordijk 1991). In most finite element programs, however, it is assumed that unloading and reloading are linear. In the next section, devoted to the uniaxial softening models, we show how these linear unloading-reloading curves are generated within theoretical frameworks that can be easily generalized to the general three-dimensional models.

If the detailed uniaxial unloading-reloading curves need to be reproduced, the expressions developed to generate realistic unloading-reloading curves in cohesive crack models (Section 11.7.4) are easily incorporated into the crack band model through the basic relationship (8.3.1).

A simpler rule, called the secant-tangent rule, was proposed in the frame of crack band models by Bažant and Chern (1985a,b), as illustrated in Fig. 8.3.4b. Given the stress-strain diagram for monotonic

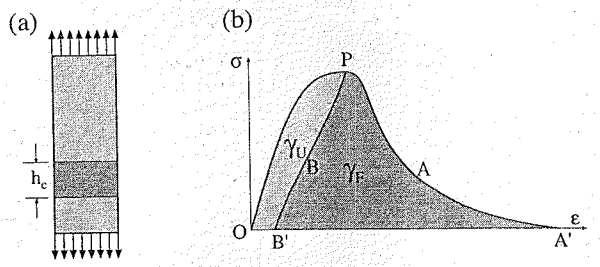

Figure 8.3.5 Energy dissipation in a crack band model with prepeak inelasticity.

stretching, $\sigma = \psi(\varepsilon)$, the secant-tangent rule assumes that the unloading has always the same slope as the secant-modulus for virgin loading at the same strain value, i.e.,

$$d\sigma = \frac{\psi(\varepsilon)}{\varepsilon} d\varepsilon \qquad \text{if } d\varepsilon < 0 \tag{8.3.13}$$

Graphically, this means (Fig. 8.3.4b) that segment $\overline{23}$ is parallel to the secant $\overline{05}$, segment $\overline{34}$ is parallel to the secant $\overline{06}$, etc., where points 5, 6, 7 are obtained from points 2, 3, 4 by vertical projections onto the virgin stress-strain curve.

For reloading one may assume either the same path as for unloading, or, better, a straight line reloading up to point 8 on the strain axis and then either a straight line back to point 1 where unloading started or a straight line $\overline{89}$ parallel to the secant $\overline{01}$. The tangent-secant rule underestimates the area of the hysteresis loops, but it has the advantage that it yields, without any additional material parameters, an approximately correct location of point 4 at which the initial elastic slope is resumed. Furthermore, using the rule shown by curve $\overline{489}$, point 9 at which the virgin curve is reached again is approximately correct. The tangent-secant rule was applied in a finite element program for combined smeared cracking, creep, and shrinkage of concrete (Bažant and Chern 1985a,b).

8.3.4 Fracture Energy for Crack Bands With Prepeak Energy Dissipation

For stress-strain curves with prepeak inelasticity, the energy dissipation consists of two terms. One corresponds to the energy dissipated in the prepeak range, which is proportional to the volume, and the second corresponds to the energy dissipated after peak which, in the cases of localization in a single band, is proportional to the volume of the band $h_c A$, where A is the area of the main surface of the crack band. Therefore, the problem is identical to that for the cohesive crack with bulk dissipation (Section 7.1.6).

An analysis analogous to that for the cohesive cracks was performed by Elices and Planas (1989): for a uniform bar in tension (Fig. 8.3.5a), with the stress-strain curve shown in Fig. 8.3.5b, the material follows initially the path OP up to the peak. Then the bifurcation occurs and the material outside the crack band follows the unloading path PBB' while the material in the crack band follows the path PAA'. Therefore, the total work of fracture is

$$\mathcal{W}_F = A(L - h_c)\ \text{area}(OPBB'O) + Ah_c\ \text{area}(OPAA'O) = AL\ \text{area}(OPBB'O) + Ah_c\ \text{area}(BB'AA'B) \tag{8.3.14}$$

The area $OPBB'O$ (lightly shaded in the figure) is the energy supplied to a unit volume when it is loaded up to the peak and then unloaded; we represent it by γ_U. The area $BB'AA'B$ (darker shading in the figure) represents the *extra* energy supply required to break a unit volume of material in the crack band. Therefore, we may write the foregoing equation as

$$\mathcal{W}_F = AL\gamma_U + Ah_c\gamma_F \tag{8.3.15}$$

Now, identifying the second term as the surface energy dissipation, we can apply (8.3.3) and get an

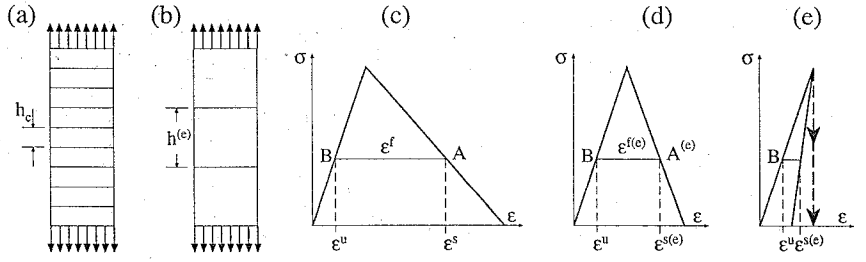

Figure 8.3.6 (a) Bar discretized in finite elements of size h_c. (b) Bar discretized in finite elements of arbitrary size $h^{(e)}$. (c) Triangular stress-strain curve for a physical band of width h_c. (d) Corresponding stress-strain curve for an element of size $h^{(e)}$, in which $\overline{BA}^{(e)} = \overline{BA}\, h^{(e)}/h_c$. (e) Same for too large an element, leading to snapback; the arrows indicate sudden failure at peak load.

expression identical to (7.1.19). From this point on, the analysis is identical to that for the cohesive cracks with bulk dissipation, which leads to a dependence of the mean fracture energy given by (7.1.22). This can obviously be recast in terms of the properties of the stress-strain curve using (8.3.3):

$$G_{Fm} = h_c\gamma_F \left[1 + \alpha_U \eta\left(\frac{D}{\ell_{ch}}\right)\right], \qquad \alpha_U = \frac{\gamma_U E}{f_t'^2}, \qquad \ell_{ch} = \frac{E h_c \gamma_F}{f_t'^2} \tag{8.3.16}$$

8.3.5 Simple Numerical Issues

Strict application of the crack band model, as formulated by Bažant, with h_c equal to a material constant, would require a finite element mesh in which the cracking band has exactly a width h_c. Thus, if the crack-band location is not known in advance, all the finite elements would have to be of width h_c as depicted in Fig. 8.3.6a for the uniaxial case. This is unpractical and, fortunately, unnecessary. The fundamental reason is that h_c does not enter explicitly the essential macroscopic parameters, of which the most important is $G_F = h_c\gamma_F$. Therefore, if finite elements larger than h_c need to be used, it is possible to keep the essential response if we preserve the fracture energy. To do so, an adequate approximation is to distribute uniformly the fracturing strain over the element and rescale the softening part of the stress-strain curve to keep G_F constant. The resulting stress-strain curve will depend on the element size, and must be scaled so that

$$h^{(e)}\gamma_F^{(e)} = h_c\gamma_F \qquad \Rightarrow \qquad \gamma_F^{(e)} = \frac{h_c}{h^{(e)}}\gamma_F \tag{8.3.17}$$

where $h^{(e)}$ is the size of the element and $\gamma_F^{(e)}$ the density of fracture energy to be used for this element.

For models of the elastic-softening type with stress-strain curves such as the one shown in Fig. 8.3.1b, the scaling is easy: just multiply ε^f by the factor in the preceding formula, i.e.,

$$\varepsilon^{f(e)} = \frac{h_c}{h^{(e)}}\varepsilon^f \tag{8.3.18}$$

Note that only the fracturing part of the strain must be scaled. The result of the scaling is shown in Figs. 8.3.6c-e for the simple linear softening. Note also that if the size of the element is too large, as deliberately shown in Fig. 8.3.6e, the resulting softening branch for the stress-strain curve of the element will show a snapback. In these cases, the finite element will become unstable at the snapback point, and the stress will drop suddenly to zero. Then the energy dissipated cannot be made equal to G_F, since all the elastic energy in the element is released. Therefore, either the element must be kept small so that no snapback would occur, or the curve must be modified to preserve the energy dissipation. This problem will be addressed in Section 8.6 in a wider three-dimensional framework.

The matters are a bit more complicated if the stress-strain curve has a prepeak nonlinearity as in Fig. 8.3.7a. In that case, the strain in the hardening and unloading branches must not be scaled; only the

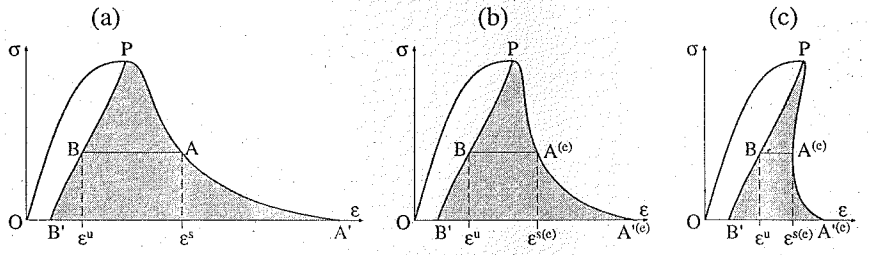

Figure 8.3.7 (a) Definition of the unloading and softening branches, for a physical band, of width h_c; (b) unloading and softening branches to be used in a finite element of a larger width $h^{(e)}$, for which $\overline{BA^{(e)}} = \overline{BA}\, h^{(e)}/h_c$; (c) same, but for an element so large that it leads to snapback.

strain contribution to the surface component of energy must. Therefore, the strain on the softening branch has to be scaled so that

$$\varepsilon^{s(e)} - \varepsilon^u = \frac{h_c}{h^{(e)}}(\varepsilon^s - \varepsilon^u) \tag{8.3.19}$$

where ε^s and ε^u are the strains on the softening branch and on the unloading branch, respectively, for the same level of stress (Fig. 8.3.5a–c). This can be rewritten as

$$\varepsilon^{s(e)} = \frac{h_c}{h^{(e)}}\varepsilon^s - \left(\frac{h_c}{h^{(e)}} - 1\right)\varepsilon^u \tag{8.3.20}$$

Thus, as shown in Fig. 8.3.7b–c, only the part of the softening curve on the right of the unloading branch is to be scaled. This may substantially complicate the use of otherwise simple stress-strain curves (i.e., with simple, beautiful expressions). Note, again, that snapback may occur in this case, too, if the element is too large, as shown in Fig. 8.3.7c.

In the foregoing it is implicitly assumed that the fracture will localize in a single element, since we showed that this is *the* solution in the preceding two sections. However, if a homogeneous case, such as the tensioned bar (or, in three dimensions, a pure bend beam), is numerically analyzed, and if the elements are given exactly the same properties, a normal finite element code will not catch the bifurcation. The reason is that the program will search for a solution by extrapolating from the previous step, and thus all elements will go through the peak into the softening branch simultaneously. And they will stay there! To avoid sophisticated bifurcation analysis (which is more elegant and more robust, but much more complicated), a simple expedient may be used: put imperfections into the material. Then either one element selected at random is taken to be a few percent weaker than the rest, or the strength of each element is assigned at random using a narrow strength distribution function. This is necessary only for structures with a nominally homogeneous distribution of elastic stresses and strains (laboratory specimens, typically). In most structures the elastic fields have stress concentrations which trigger localization without the need for introducing imperfections. (However, in some situations, the danger remains that the loading step is too large for the imperfections assumed to trigger localization. Theoretically, without bifurcation analysis, one is not sure, in general, that a localization has not been missed.)

We have addressed here two basic aspects of the numerical computation: the stress-strain curves to use, and the way to trigger the localization. This, of course, does not exhaust the discussion on the numerical models, but the other important aspects are fundamentally three-dimensional and are discussed later in Section 8.6, after presenting the three-dimensional softening models.

8.3.6 Crack Band Width

From the foregoing analysis it transpires that, in a finite element formulation with a free element size, the strain-softening curve must be adjusted according to the element size so that the calculations would yield macroscopically consistent results whatever the element size. This is close to saying that the crack band width h_c is arbitrary since it is replaced by $h^{(e)}$ without a noticeable effect (as long as the element size

is kept small). This means that h_c cannot be determined from fracture tests in which a single crack (or crack band) is formed.

The value of h_c, however, does have an effect in those situations where cracking does not localize but remains distributed over large zones. This may happen as a consequence of a dense reinforcement grid or in problems such as shrinkage, where the mass of concrete in front of the drying zone restrains the cracking zone and may (but need not) force the cracking to remain distributed. Thus, the value of h_c can be identified only by comparing the results of fracture tests with the results of tests in which the cracking is forced to be distributed. The problem is the same as that in determining the characteristic length for nonlocal models, and we will discuss it in more detail in Chapter 13.

In a crude manner, the value of h_c can be approximately identified from fracture tests for specimens of various geometries, in which the cracking is localized to a different extent. This has been done in Bažant and Oh (1983a), with the conclusion that the crack band width $h_c = 3d_a$ where d_a = maximum aggregate size, is approximately optimal. However, the optimum was weak, and crack band width anywhere between $2d_a$ and $5d_a$ would have given almost equally good results.

A better test for determining h_c was conceived by Bažant and Pijaudier-Cabot (1989). Localization was prevented by gluing parallel thin rods on the surface of a uniaxially tensioned prism. However, a uniform field of strain-softening was still not achieved. For details, see Section 13.2.4.

Exercises

8.8 Give a detailed proof of Eq. (8.3.6).

8.9 Determine the uniaxial stress-strain curves for a concrete which, according to experimental measurements, has an elastic modulus of 25 GPa, a tensile strength of 2.8 MPa, and a fracture energy of 95 N/m, and is assumed to display an elastic-softening behavior with triangular softening and a crack band width of 50 mm (approximately equal to $3d_a$ with $d_a = 16$ mm).

8.10 Determine the uniaxial stress-strain curves to be used for the same material as defined in the previous exercise if the numerical analysis is to be performed using finite elements 20 cm in size.

8.11 Determine the maximum size of the finite elements to be used in a numerical analysis with the same material in order for the stress-strain curve to be stable.

8.12 Determine the uniaxial stress-strain curves for a concrete which, according to experimental measurements, has an elastic modulus of 25 GPa, a tensile strength of 2.8 MPa, and a fracture energy of 95 N/m, and is assumed to display an elastic-softening behavior with exponential softening and a crack band width of 50 mm (approximately equal to $3d_a$ with $d_a = 16$ mm).

8.13 Determine the uniaxial stress-strain curves to be used for the material defined in the previous exercise if the numerical analysis is to be performed using finite elements 20 cm in size.

8.14 Determine the maximum size of the finite elements to be used in a numerical analysis with the foregoing exponential material in order for the stress-strain curve to be stable (not to exhibit snapback).

8.15 For the material defined by Eq. (8.3.9), determine the fracturing strain ε_u^f and stress f_t' at which the peak occurs as a function of the constants C_1, p, b, and q. Show that the equation can be rearranged to read $\sigma = f_t'\xi^p \exp[-p(\xi^q - 1)/q]$, in which $\xi = \varepsilon^f/\varepsilon_u^f$.

8.16 For the material defined by Eq. (8.3.9), show that the fracture energy density γ_F can be written as

$$\gamma_F = \frac{C_1}{qb^{(p+1)/q}}\Gamma\left(\frac{p+1}{q}\right)$$

where $\Gamma(n)$ is the Eulerian Gamma function defined as $\Gamma(n) = \int_0^\infty x^{n-1}e^{-x}dx$.

8.17 Consider a material with a stress-strain curve given by $\sigma = E\varepsilon e^{-b\varepsilon}$. Show that E is indeed the elastic modulus. Determine b in terms of E and f_t'. Determine, as a function of E and f_t', (a) the total energy density absorbed by a material element that follows the softening branch; (b) the energy density absorbed by a material element loaded up to the peak and then unloaded, if it is assumed that the unloading is linear with the same elastic modulus as for the initial loading; (c) the density of fracture energy γ_F; and (d) show that for this model the ratio h_c/ℓ_{ch} is constant and determine its value. [Answers: (a) $7.39f_t'^2/E$, (b) $1.45f_t'^2/E$, (c) $5.94f_t'^2/E$, (d) $h_c/\ell_{ch} \approx 0.17$.]

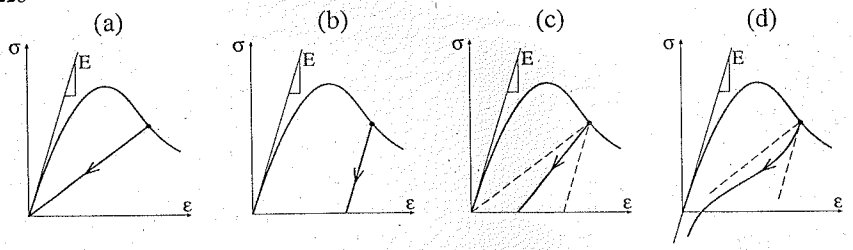

Figure 8.4.1 Types of stress-strain curves: (a) stiffness degradation; (b) yield limit degradation; (c) mixed behavior; (d) more realistic behavior with nonlinear unloading.

8.4 Uniaxial Softening Models

After explaining the basic concepts in crack band models, we can now discuss in detail the uniaxial version of various simple constitutive models for strain softening. Depending on the behavior at unloading, one may distinguish three basic types of models :

1. Continuum damage mechanics, in which strain-softening is due solely to degradation of elastic moduli and no other inelastic behavior takes place. The basic characteristic of such theory is that the material unloads along a straight line pointed toward the origin (Fig. 8.4.1a).
2. Plasticity with yield limit degradation, in which the constitutive relation is the same as in plasticity except that the yield limit is decreasing, rather than increasing. The elastic moduli remain constant (Fig. 8.4.1b). The basic characteristic is that the unloading slope is constant, equal to the elastic modulus E.
3. A mixed theory, in which both the elastic moduli and the yield limit suffer degradation. This behavior, for which the unloading slope is intermediate (as shown Fig. 8.4.1c), is normally a better description of experimental reality.

The foregoing classification neglects the fact that the unloading-reloading response is actually nonlinear, as discussed in Section 8.3.3 and depicted in Fig. 8.4.1d. Models including such behavior can be generated, but they are considerably more complex, and are a subject for specialized studies that will not be treated here. As an exception, the microplane model, which implements this kind of behavior naturally, will be discussed at length in Chapter 14.

8.4.1 Elastic-Softening Model with Stiffness Degradation

As a simple continuum model of a material fracturing in tension, we can adopt the elastic-softening model whose behavior for monotonic stretching was described in Fig. 8.2.2. To give a physical content to the model, we can assume that this behavior corresponds to an elastic matrix with an array of densely distributed cracks normal to the load direction (Fig. 8.4.2a). Thus, we assume that the total strain is the sum of the elastic strain of the elastic matrix, ε^{el}, and the strain contributed by the crack opening, ε^f:

$$\varepsilon = \varepsilon^{el} + \varepsilon^f = \frac{\sigma}{E} + \varepsilon^f \tag{8.4.1}$$

where E is the elastic modulus of the matrix (i.e., of the virgin material between the cracks). For monotonic straining the assumed behavior is that shown in Fig. 8.2.2. Consider now the unloading behavior after the specimen has been loaded until a certain maximum inelastic strain $\tilde{\varepsilon}^f$ (Figs. 8.4.2b–d). Let us further assume that unloading is straight to the origin. This means that during unloading, the cracks close so that they are completely closed at zero stress. As depicted in (Fig. 8.4.2b), $\tilde{\varepsilon}^f$ represents the maximum cracking strain reached before unloading, and ε^f the actual cracking strain. Obviously, for such unloading

$$\varepsilon^f = \frac{\tilde{\varepsilon}^f}{\phi(\tilde{\varepsilon}^f)}\sigma \tag{8.4.2}$$

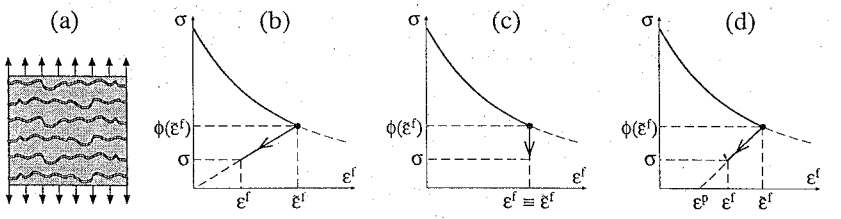

Figure 8.4.2 (a) Densely cracked elastic material. (b) Model with cracks completely closed after full unloading. (c) Model with totally prevented crack closure. (d) Mixed type model with partial crack closure upon unloading.

But this equation also holds if the loading is monotonic (i.e., if fracture is taking place) because then $\varepsilon^f = \tilde{\varepsilon}^f$ and $\sigma = \phi(\tilde{\varepsilon}^f)$. However, we must impose the condition that the line that corresponds to monotonic loading can never be crossed. This can be expressed in various ways, but two are most useful: one in terms of σ and $\tilde{\varepsilon}^f$, and the other in terms of ε^f and $\tilde{\varepsilon}^f$:

$$\sigma - \phi(\tilde{\varepsilon}^f) \le 0 \qquad \text{or} \qquad \varepsilon^f - \tilde{\varepsilon}^f \le 0 \tag{8.4.3}$$

Note that while ε^f can decrease, $\tilde{\varepsilon}^f$ is a nondecreasing variable.

Now, the foregoing results can be reformulated so as to look as a genuine continuum damage model. To this end, one may *define* a derived variable ω, the *damage*, as

$$\frac{\omega}{1-\omega} = E\frac{\tilde{\varepsilon}^f}{\phi(\tilde{\varepsilon}^f)} \qquad \text{or} \qquad \omega = \frac{E\tilde{\varepsilon}^f}{E\tilde{\varepsilon}^f + \phi(\tilde{\varepsilon}^f)} \tag{8.4.4}$$

Then we just insert this definition into (8.4.2) and the result into (8.4.1), which yields the classical form of continuum damage mechanics for an elastic matrix:

$$\varepsilon = \frac{\sigma}{E(1-\omega)} \tag{8.4.5}$$

We will introduce this expression in a more standard way after we analyze the strength degradation model and the mixed model for this elastic softening model.

8.4.2 Elastic-Softening Model with Strength Degradation

Consider now the same basic parallel crack model of Fig. 8.4.2a, but assume that upon unloading the cracks cannot close, as depicted in Fig. 8.4.2c. This is, of course, a tremendous simplification, but frictional grain interlock, as well as debris and surface mismatch, can prevent cracks to a large extent from closing in materials such as concrete. Obviously, the resulting model is of a plastic type with softening such that $\varepsilon^f \equiv \varepsilon^p$ where ε^p is the plastic strain.

Now we need only to specify that, since we do not consider compression, $\varepsilon^f = \tilde{\varepsilon}^f$ at all times and that the monotonic curve cannot be exceeded. As before, we thus have

$$\sigma - \phi(\tilde{\varepsilon}^f) \le 0 \tag{8.4.6}$$

as the plastic criterion. Note that in this case we cannot use the criterion in terms of ε^f. Note also that it may seem that making a distinction between ε^f and $\tilde{\varepsilon}^f$ is superfluous. However, for the three-dimensional case the distinction will be essential because ε^f is a second-order tensor, while $\tilde{\varepsilon}^f$ will remain a scalar (known as the equivalent uniaxial inelastic strain).

8.4.3 Elastic-Softening Model with Stiffness and Strength Degradation

We consider the same model as before, but consider now that, upon unloading, some permanent strain ε^p remains at zero stress, as depicted in Fig. 8.4.2d. We can simply write that, on the unloading-reloading

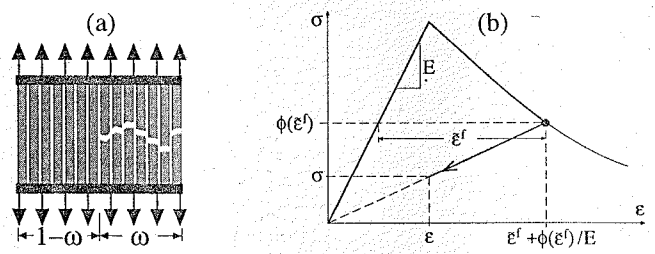

Figure 8.4.3 (a) Parallel micro-rod coupling (Dougill 1976). (b) Determination of the damage parameter in terms of the maximum inelastic strain.

branch,

$$\varepsilon^f = \varepsilon^p + \frac{\tilde{\varepsilon}^f - \varepsilon^p}{\phi(\tilde{\varepsilon}^f)}\sigma \tag{8.4.7}$$

The only extra information required is the evolution of ε^p. The simplest assumption is that it is a unique function of $\tilde{\varepsilon}^f$. For example, Ortiz (1985) assumed (in a much more complex framework) that the permanent strain is a fixed fraction of the (maximum) inelastic strain, i.e.,

$$\varepsilon^p = \alpha\tilde{\varepsilon}^f \tag{8.4.8}$$

where α is a constant between 0 (for pure damage) and 1 (for pure plasticity).

8.4.4 A Simple Continuum Damage Model

Let us now briefly review a very simple damage model. We base it on Dougill's approach in which a material element is considered to be formed, ideally, by many infinitesimal rods connected in parallel (Fig. 8.4.3a). We assume that the rods are identical in all but strength, which is randomly distributed. Upon stretching, the weaker rods fail first. At a given strain level ε, a fraction ω of the rods have failed. Then, the resulting stress is given by

$$\sigma = E(1-\omega)\varepsilon \tag{8.4.9}$$

Note that this is the average stress. The stress in the surviving rods is that for the virgin, undamaged material. Therefore, the relationship between the macrostress σ and the microstress τ (also called the true-stress) is

$$\tau = \frac{\sigma}{1-\omega} \tag{8.4.10}$$

This is the basic relation in continuum damage mechanics, initiated by Kachanov (see, e.g., Lemaitre and Chaboche 1985). This relation applies not only to brittle materials in which the relationship between the true stress and the strain is linear, as we have here, but to any other (true) stress-strain relationship.

The model must specify the evolution of damage. This is done on the basis of the uniaxial stress-strain curve as shown in Fig. 8.4.3b. Assuming that the data are in the form of the $\sigma(\tilde{\varepsilon}^f)$ curve, we get the damage at each point by writing

$$1-\omega = \frac{\sigma}{E\varepsilon} = \frac{\phi(\tilde{\varepsilon}^f)}{\phi(\tilde{\varepsilon}^f) + E\tilde{\varepsilon}^f} \tag{8.4.11}$$

from which (8.4.11) follows. So, the two formulations are fully equivalent, even though the underlying micromodels seem to be completely different.

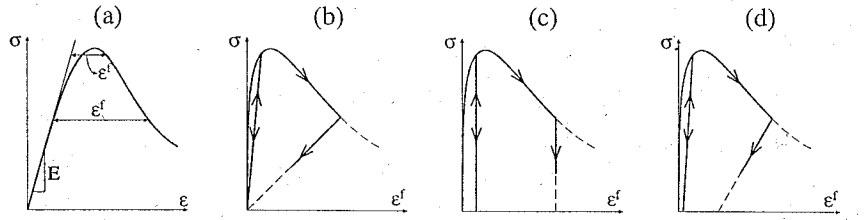

Figure 8.4.4 Models with prepeak inelasticity: (a) stress-strain curve for monotonic loading; (b) stiffness degradation; (c) strength degradation; (d) mixed behavior.

8.4.5 Introducing Inelasticity Prior to the Peak

Although, for concrete in tension, the inelastic strain prior to the peak is relatively small, for some reinforced materials the prepeak nonlinearity can be important and must be taken into account. This can be done exactly as before, with the only assumption that the cracking strain (or damage) starts before the peak is reached. This is illustrated in Fig. 8.4.4a, which shows the full $\sigma(\varepsilon)$ curve, and Figs. 8.4.4b-d, which show the three possibilities of unloading behavior.

Therefore, to get a model incorporating the prepeak nonlinearity, it suffices to use the adequate expression for the function $\phi(\tilde{\varepsilon}^f)$. Some candidates for such a model were given in Section 8.3.2.

We recall here that, when used in finite element formulations in which the element width h is greater than the characteristic crack band width h_c, the softening part of the curve must be scaled as indicated in Section 8.3.5.

8.4.6 Crack Closure in Reverse Loading and Compression

For concrete as well as for other quasibrittle materials, the basic inelastic deformation mechanism in tension is cracking. If the material is subjected to tensile stress producing a crack, then is unloaded and the stress reversed into compression, the crack closes and the stiffness in compression is recovered to a large extent. As already pointed out, a nonlinear unloading behavior such as that sketched in Fig. 8.4.1d is observed (except at strong lateral confinement). However, the simpler models based on damage mechanics may be more convenient for computational purposes, and then some mechanism must be devised to ensure that the compliance reduction due to damage, as shown in Fig. 8.4.5a, would not appear on the compression side. Then, the split form (8.4.1) together with (8.4.2) is most efficient in handling the problem. It suffices to write that, for $\sigma < 0$, the crack opening must be zero; this may be compactly written as

$$\varepsilon = \frac{\sigma}{E} + \frac{\tilde{\varepsilon}^f}{\phi(\tilde{\varepsilon}^f)}\langle\sigma\rangle^+ \tag{8.4.12}$$

where $\langle\sigma\rangle^+$ is the positive part of σ, defined as σ for positive values and zero for negative values, or, in algebraic terms:

$$\langle\sigma\rangle^+ = \frac{\sigma + |\sigma|}{2} \tag{8.4.13}$$

The behavior becomes elastic, characterized by the initial elastic modulus, as soon as the stress becomes negative (Fig. 8.4.5b).

For the case of pure strength degradation, no special precaution needs to be taken since, by definition, the crack opening is fully irrecoverable. For the case of mixed unloading behavior (Fig. 8.4.4d), the positive part must include the entire expression (8.4.7), and so the total strain may be written as:

$$\varepsilon = \frac{\sigma}{E} + \left\langle \varepsilon^p + \frac{\tilde{\varepsilon}^f - \varepsilon^p}{\phi(\tilde{\varepsilon}^f)}\sigma \right\rangle^+ \tag{8.4.14}$$

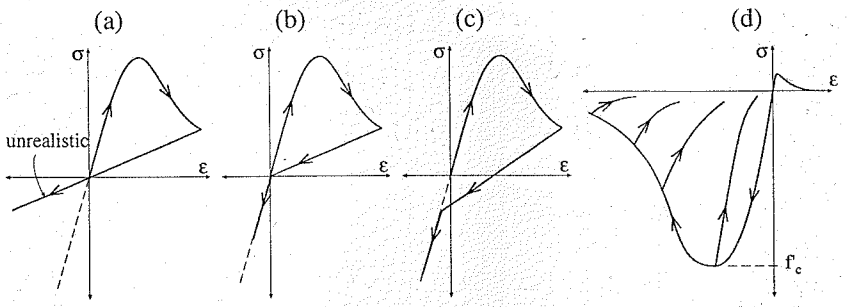

Figure 8.4.5 Reversing the stress sign: (a) invalid result with stiffness degradation also in compression; (b) model with crack closure; (c) stress-strain curve showing softening in compression as well as in tension.

In this way, the material recovers the undamaged behavior in compression as soon as the unloading branch reaches the initial elastic line, as shown in Fig. 8.4.5c.

Certainly, inelastic strain and cracking occur in compression, too. In practical analysis of concrete structures, especially in the analysis of beams and plates based on a uniaxial or biaxial stress-strain diagram, it is normally assumed that the stress-strain diagram of concrete in uniaxial compression also exhibits a peak followed by strain softening (Fig. 8.4.5d). As a consequence of this hypothesis, all localization phenomena described for tension occur for compression as well.

This means that one needs to also use fracture mechanics for compression behavior. Similar to tension, one needs to introduce either a softening band in compression (Bažant 1976) or one might postulate a compressive fictitious crack, as suggested by Hillerborg (1989). If, however, triaxial stress-strain relations are considered, such assumptions do not reflect realistically the actual mechanism of compression failure. Compression strain softening is not due to large strain in the direction of compression, unlike tensile strain softening, but is due to volume expansion of the material which causes large strains in the directions *transverse* to the direction of compression. So, compression softening is a strictly triaxial phenomenon, while tensile strain softening can, to a large extent, be treated as a uniaxial phenomenon. If volume expansion (transfer of strains) is prevented, e.g., by strong enough confining reinforcement or encasement of concrete in a strong enough pipe, then there is no compression softening and the stress-strain relation has no peak in compression.

A realistic triaxial stress-strain relation for compression strain softening must reflect these features. But many existing triaxial constitutive models do not, and the biaxial ones, in fact, cannot because they do not involve volume expansion as a variable. In any case, whether compression softening is modeled directly as a function of the compression strain or as a triaxial phenomenon associated with volume expansion, the fracture mechanics aspects associated with localization of compression softening need to be taken into account. Much research remains to be done in this direction.

8.4.7 Introducing Other Inelastic Effects

In the foregoing we have adopted the simplest approach and assumed that the inelastic behavior is completely due to cracking. This allows building models with a minimum of information. Indeed, for the pure damage or pure strength-degradation models all that is needed is the function $\phi(\varepsilon^f)$ deduced from a tensile test. For the mixed model, a further function relating ε^p to ε^f is required.

However, this simple approach neglects other sources of inelastic behavior that may take place in the bulk material between the cracks, such as plastic-type strains, creep (viscoelasticity or viscoplasticity), or shrinkage. A simple, yet effective way of modeling more complex behaviors is to relax the assumption of elastic material between cracks implicit in (8.4.1) and allow the bulk to suffer inelastic strains, too. This can be conveniently sketched as a series coupling of the cracking strain, that we represent by a fracturing element in Fig. 8.4.6, with a bulk element that can be purely elastic as in Fig. 8.4.6a, or include inelastic strains as in 8.4.6b, which are represented by a black-box where we can introduce the desired inelastic

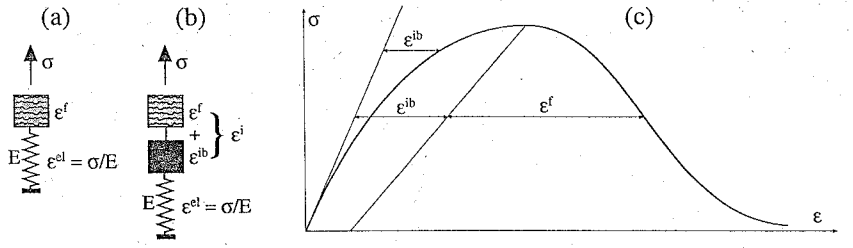

Figure 8.4.6 (a) Elastic-fracturing series coupling. (b) Elastic-bulk-inelastic-fracturing model. (c) Stress-strain curve split in which all the prepeak inelasticity is confined to the bulk and all the postpeak softening is confined into the fracturing element.

behavior. For example, Bažant and Chern (1985a) used a fracturing element coupled with a viscoelastic element and a shrinkage element. This means that the inelastic strain is now split into an inelastic strain associated with bulk behavior ε^{ib} and an inelastic strain associated to fracturing ε^f, that is,

$$\varepsilon = \frac{\sigma}{E} + \varepsilon^{ib} + \varepsilon^f \tag{8.4.15}$$

Focusing on time-independent models, the bulk inelasticity and the fracturing strain can each be modeled as done in the foregoing analysis in which a single inelasticity mechanism was assumed. Of course, more information is required to model the behavior. In particular, one function $\phi_b(\tilde{\varepsilon}^{ib})$ is required to describe the growth of the inelastic bulk strain, in addition to the function $\phi_f(\tilde{\varepsilon}^f)$ that describes the evolution of the fracturing strain.

Obviously, the experimental determination of the two functions is very difficult. One particular simplifying hypothesis may help to get an easy-to-handle model. It consists in assuming that all the prepeak inelasticity in tension is due to the bulk inelasticity. Then the stress-strain curve in the softening branch may be split as shown in Fig. 8.4.6c, so that the fracturing part would be the only part that has to be scaled according to the size of the element. So, Eq. (8.3.20) is reduced to the simple form

$$\varepsilon^{f(e)} = \frac{h_c}{h^{(e)}}\varepsilon^f \tag{8.4.16}$$

However, this is a split for mathematical convenience only, since most material scientists will agree that cracking (fracturing) starts before the peak. Nevertheless, since the amount of cracking prior to the peak is only a small fraction of the total, the *ad hoc* split can be justified on practical grounds.

Due to the enormous variety of combinations that arise as soon as one combines the two inelastic strain mechanisms, the following analysis will be restricted only to the fracturing mechanism. The other mechanism can be added as convenient based on classical inelasticity models *without* softening.

Exercises

8.18 Consider the uniaxial constitutive equation $\sigma = E\varepsilon e^{-b\varepsilon}$ and assume that it unloads to the origin. Determine the evolution law for the damage parameter ω. [Answer: $\omega = 1 - e^{-b\tilde{\varepsilon}}$.]

8.19 Consider the uniaxial elastic-softening model defined by an exponential softening curve $\sigma = f'_t e^{-(\varepsilon^f/\varepsilon_0)}$ for monotonic straining, and assume that the unloading is to the origin. (a) Show that the full stress-strain curve can be written as $\varepsilon = (1/E + C^f)\sigma$ in which C^f is a function of $\tilde{\varepsilon}^f = \max(\varepsilon^f)$, and determine this function. (b) Determine the fracturing work supply per unit volume of material γ^f, defined as the external work supply density when the fracturing strain increases up to $\tilde{\varepsilon}^f$ and then the stress is fully released. [Answer: $\gamma^f = f'_t\varepsilon_0[1 - (1 + \tilde{\varepsilon}^f/2\varepsilon_0)\exp(-\varepsilon/\varepsilon_0)$.] (c) Determine γ_F, the fracture work per unit volume for complete rupture.

8.20 For the model in the previous exercise, (a) determine the rate of the fracturing work density; (b) show that $\dot{\gamma}^f = \sigma^2\dot{C}^f/2$; (c) generalize the result to *any* model that unloads to the origin.

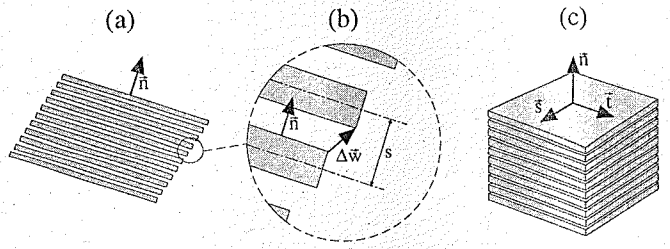

Figure 8.5.1 (a) Idealized crack band. (b) Detail of crack displacements. (c) Base vectors.

8.21 Write the rate of fracturing work (as defined in the previous two exercises) for a model with stiffness degradation as a function of the damage parameter ω.

8.5 Simple Triaxial Strain-Softening Models for Smeared Cracking

The smeared cracking models have the advantage that they can capture the influences of all the triaxial stress and strain components on the fracture process provided that the triaxial stress-strain relation is known. Unfortunately, formulation of this relation, which is needed for finite element programs, is a difficult problem of constitutive modeling. There is in the literature a huge number of models trying to adequately model fracture of concrete and similar materials in general triaxial situations. A whole book would be required to describe all of them and their modifications and possible extensions. In this section, we just touch the simplest models for smeared cracking, focusing on tensile stress states. Although they do not suffice to describe the complete behavior of concrete at complex triaxial stress states and histories, such as those with high compression stresses parallel to the crack planes, they are adequate for many practical instances of tensile cracking.

8.5.1 Cracking of Single Fixed Orientation: Basic Concepts

For many purposes one can assume that the cracks in concrete are parallel and have a fixed direction, which does not change during the loading process. This is a reasonable approximation for those loading processes in which the axes of principal stress and strain directions do not change drastically since first cracking. We can then consider, as in Section 8.4.1, that a cracked zone has formed consisting of an elastic material intersected by an array of densely distributed parallel cracks. Our task is to describe how the equations must be arranged to incorporate the response of this array of cracks to triaxial loading.

We consider that in an initially isotropic elastic material the maximum principal stress reached the tensile strength, and so a zone of cracked material formed. After that, the cracking process can be idealized as shown in Fig. 8.5.1a, which shows a crack band, formed by layers of elastic material separated by parallel cracks whose normal is defined by the unit vector $\vec{n}$. This normal vector is fixed and coincides with the maximum principal stress direction at the onset of cracking. Let s be the mean spacing of the cracks and $\Delta\vec{w}$ the mean displacement between the faces of the cracks (Fig. 8.5.1b). We can define the mean cracking strain *vector* $\vec{\varepsilon}^f$ as the crack opening per unit crack band width, i.e.,

$$\vec{\varepsilon}^f = \frac{\Delta\vec{w}}{s} \tag{8.5.1}$$

Now, take point O in the cracked zone as a reference (Fig. 8.5.1a). Let $\mathbf{x}_0$ be its position vector, and let A be any other point within the cracked zone, with position vector $\mathbf{x}$. The distance between O and A measured normal to the cracks is (Fig. 8.5.1a) $OA' = (\mathbf{x} - \mathbf{x}_0) \cdot \vec{n}$, where the dot indicates the scalar (internal) product. Hence, the number of cracks between the two points is $(\mathbf{x} - \mathbf{x}_0) \cdot \vec{n}/s$ and,

correspondingly, the displacement generated by the cracks is

$$\mathbf{u}^f = \frac{(\mathbf{x} - \mathbf{x}_0) \cdot \vec{n}}{s} \Delta\vec{w} = [(\mathbf{x} - \mathbf{x}_0) \cdot \vec{n}] \Delta\vec{w} \tag{8.5.2}$$

Taking the gradient of the displacement function, and then its symmetric part, we get the macroscopic small strain tensor that corresponds to the cracking:

$$\boldsymbol{\varepsilon}^f = \frac{1}{2} \left(\vec{n} \otimes \vec{\varepsilon}^f + \vec{\varepsilon}^f \otimes \vec{n} \right) = \left(\vec{\varepsilon}^f \otimes \vec{n} \right)^S \tag{8.5.3}$$

where from now on we use $\mathbf{T}^S$ to indicate the symmetric part of an arbitrary second-order tensor $\mathbf{T}$. The foregoing result indicates that the cracking strain is not a general symmetric tensor, since it has three of the six possible components identically zero. Indeed, taking an orthonormal base $\{\vec{n}, \vec{s}, \vec{t}\}$ so that the unit vectors $\vec{s}$ and $\vec{t}$ are parallel to the cracks (Fig. 8.5.1c), we easily find that

$$\varepsilon^f_{tt} = \varepsilon^f_{ss} = \varepsilon^f_{ts} = 0 \tag{8.5.4}$$

The fracturing strain tensor thus has only three degrees of freedom, corresponding to the three components of the vector $\vec{\varepsilon}^f$.

The foregoing equations define the kinematics of the problem. Before getting any further, we must emphasize that a consistent set of rules must be used to properly define the foregoing vectors. It is implied in our sketch in Fig. 8.5.1b that one of the two faces of the crack is taken as reference; then $\vec{n}$ is taken as the unit normal to that face external to the uncracked material, and $\delta\vec{w}$ is the displacement of the other face of the crack relative to the first. The reader can easily verify that, upon changing the reference to the other face of the crack, $\vec{n}$ and $\vec{\varepsilon}^f$ change sign but $\boldsymbol{\varepsilon}^f$ remains unchanged.

The total strain tensor is obtained by adding up the elastic strain to the fracturing strain:

$$\boldsymbol{\varepsilon} = \frac{1+\nu}{E}\boldsymbol{\sigma} - \frac{\nu}{E}\mathrm{tr}\,\boldsymbol{\sigma}\,\mathbf{1} + \left(\vec{\varepsilon}^f \otimes \vec{n} \right)^S \tag{8.5.5}$$

where E and ν are, respectively, the elastic modulus and Poisson's ratio of the bulk (uncracked) material. This is one of the basic equations of the fixed crack models. Note that it provides six equations, while we need nine equations. Given the strain tensor, we need to compute the stress tensor and the fracturing strain *vector*, nine components in all. The remaining three equations must relate the crack opening to the stress.

Since the basic internal variable is the vector $\vec{\varepsilon}^f$, rather than the fracturing strain tensor $\boldsymbol{\varepsilon}^f$, it is natural to look for a relationship between $\vec{\varepsilon}^f$ and the traction vector $\vec{\sigma}$ on the crack faces, rather than trying to directly connect $\boldsymbol{\varepsilon}^f$ to the stress tensor $\boldsymbol{\sigma}$. Therefore, we assume that the cracking behavior of the material is defined by a vectorial relationship of the form:

$$\vec{\sigma} = \boldsymbol{\sigma}\vec{n} = \vec{\Phi}(\vec{\varepsilon}^f, \vec{n}, \cdots) \tag{8.5.6}$$

where $\vec{\Phi}$ must be understood as a functional which, given crack orientation, evolution of $\vec{\varepsilon}^f$ and, possibly, some other variables acting as parameters, yields the traction vector on the crack faces. Various definitions of this functional have been proposed and more could be invented. We discuss next some of the possibilities.

8.5.2 Secant Approach to Cracking of Fixed Orientation

For application to problems with monotonic crack opening close to mode I, Bažant and Oh (1983a) proposed a crack band model in which the stress-strain relations have a secant form, with varying secant compliances. Here we give an enhanced version that explicitly considers the crack sliding (crack shearing) and that naturally leads to a damage formulation of the cracking problem.

Consider first proportional paths in which the microcrack opening and shearing increase monotonically. For these very particular paths we can assume the traction vector to be a function of the fracturing strain vector, i.e.,

$$\vec{\sigma} = \vec{F}(\vec{\varepsilon}^f, \vec{n}) \tag{8.5.7}$$

where $\vec{F}(\cdot)$ is a vector-valued function of two vector arguments. Note that $\vec{\sigma}$ is made to depend on the orientation of the crack; this is essential to disclose the structure of $\vec{F}(\cdot)$. The material containing the crack band is assumed isotropic. Therefore, we require that, if we rotate simultaneously the crack and the crack strain vector, we must obtain a traction vector rotated by the same angle. This means that the function $\vec{F}(\vec{\varepsilon}^f, \vec{n})$ must be isotropic, i.e., that

$$\vec{F}(\mathbf{Q}\vec{\varepsilon}^f, \mathbf{Q}\vec{n}) = \mathbf{Q}\vec{F}(\vec{\varepsilon}^f, \vec{n}) \tag{8.5.8}$$

for any orthogonal second-order tensor $\mathbf{Q}$. A classical representation theorem (Spencer 1971) then requires the traction vector to have the form

$$\vec{\sigma} = S_N(\varepsilon_N^f, \varepsilon_T^f)\varepsilon_N^f \vec{n} + S_T(\varepsilon_N^f, \varepsilon_T^f)\vec{\varepsilon}_T^f \tag{8.5.9}$$

where $S_N(\varepsilon_N^f, \varepsilon_T^f)$ and $S_T(\varepsilon_N^f, \varepsilon_T^f)$ are scalar functions that have the meaning of normal and tangent secant stiffnesses; ε_N^f is the normal component of $\vec{\varepsilon}^f$, $\vec{\varepsilon}_T^f$ is the vectorial component of $\vec{\varepsilon}^f$ in the plane of the cracks, and ε_T^f is the magnitude of that component. Algebraically,

$$\varepsilon_N^f = \vec{\varepsilon}^f \cdot \vec{n}\,, \qquad \vec{\varepsilon}_T^f = \vec{\varepsilon}^f - \varepsilon_N^f \vec{n}\,, \qquad \varepsilon_T^f = |\vec{\varepsilon}_T^f| = \sqrt{\vec{\varepsilon}_T^f \cdot \vec{\varepsilon}_T^f} \tag{8.5.10}$$

If we similarly define the normal and shear components of the traction vector, i.e.,

$$\sigma_N = \vec{\sigma} \cdot \vec{n}\,, \qquad \vec{\sigma}_T = \vec{\sigma} - \sigma_N \vec{n}\,, \qquad \sigma_T = |\vec{\sigma}_T| = \sqrt{\vec{\sigma}_T \cdot \vec{\sigma}_T} \tag{8.5.11}$$

the foregoing equations reduce to

$$\sigma_N = S_N(\varepsilon_N^f, \varepsilon_T^f)\varepsilon_N^f \qquad \text{and} \qquad \vec{\sigma}_T = S_T(\varepsilon_N^f, \varepsilon_T^f)\vec{\varepsilon}_T^f \tag{8.5.12}$$

which has a beautiful uncoupled form, with $\vec{\sigma}_T$ parallel to $\vec{\varepsilon}_T^f$. Certainly we could have assumed this from the onset. But we now have proved that this is the *most general* possibility consistent with the initial assumption (8.5.7) and the condition of isotropy. This means that we need to specify two functions of two variables to determine the material behavior for proportional monotonic loading.

No doubt, many simplifications will be required to characterize limited experimental evidence. However, before attempting such simplifications, let us find the general structure of the stress-strain relations. First we solve for the components $\vec{\varepsilon}^f$ from (8.5.12) and substitute them into (8.5.3) to get the expression of the fracturing strain tensor:

$$\boldsymbol{\varepsilon}^f = C_N \sigma_N \, \vec{n} \otimes \vec{n} + C_T (\vec{\sigma}_T \otimes \vec{n})^S \tag{8.5.13}$$

C_N and C_T are the normal and shear compliances, defined as

$$C_N = \frac{1}{S_N(\varepsilon_N^f, \varepsilon_T^f)}\,, \qquad C_T = \frac{1}{S_T(\varepsilon_N^f, \varepsilon_T^f)} \tag{8.5.14}$$

where a dependence on ε_N^f and ε_T^f is implied (although hidden from now on). This expression is now substituted into (8.5.5) to get the total strain tensor as

$$\boldsymbol{\varepsilon} = \frac{1+\nu}{E}\boldsymbol{\sigma} - \frac{\nu}{E}\mathrm{tr}\,\boldsymbol{\sigma}\,\mathbf{1} + C_N \sigma_N \, \vec{n} \otimes \vec{n} + C_T (\vec{\sigma}_T \otimes \vec{n})^S \tag{8.5.15}$$

For computational purposes this relation is best expressed in a component form relative to the base $\{\vec{n}, \vec{s}, \vec{t}\}$ in Fig. 8.5.1c, arranging the stresses in the six-dimensional column matrix $(\sigma_{nn}, \sigma_{ss}, \sigma_{tt}, \sigma_{ns}, \sigma_{st}, \sigma_{tn})^T$ and the strains in the corresponding column matrix $(\varepsilon_{nn}, \varepsilon_{ss}, \varepsilon_{tt}, \gamma_{ns}, \gamma_{st}, \gamma_{tn})^T$ where $\gamma_{\mu\nu} = 2\varepsilon_{\mu\nu}$. It turns out that the equations for the normal and shear components are mutually uncoupled and can be written as

$$\begin{Bmatrix} \varepsilon_{nn} \\ \varepsilon_{ss} \\ \varepsilon_{tt} \end{Bmatrix} = \frac{1}{E}\begin{bmatrix} 1+EC_N & -\nu & -\nu \\ -\nu & 1 & -\nu \\ -\nu & -\nu & 1 \end{bmatrix} \begin{Bmatrix} \sigma_{nn} \\ \sigma_{ss} \\ \sigma_{tt} \end{Bmatrix} \tag{8.5.16}$$

and

$$\begin{Bmatrix} \gamma_{ns} \\ \gamma_{st} \\ \gamma_{tn} \end{Bmatrix} = \frac{1}{G}\begin{bmatrix} 1 & 0 & 0 \\ 0 & 1+GC_T & 0 \\ 0 & 0 & 1+GC_T \end{bmatrix} \begin{Bmatrix} \sigma_{ns} \\ \sigma_{st} \\ \sigma_{tn} \end{Bmatrix} \tag{8.5.17}$$

where $G = E/2(1+\nu)$ is the shear modulus.

The foregoing secant equations are particularly simple: they depend only on the two functions C_N and C_T that appear in only three diagonal elements. Now we must specify how these functions evolve. In the early times of the smeared crack applications (see Rots 1988, for the basic references), before fracture mechanics concepts became widely accepted, the structural finite element codes used to set both the normal and tangential stiffnesses to zero just after cracking starts. This is equivalent to setting $C_N = C_T = \infty$ in the foregoing equations. This turned out to lead to numerical problems because of the sudden energy release implied by such approximation, and a certain amount of shear stiffness was retained, such that $\gamma_{sn} = \sigma_{sn}/(\beta_s G)$, where β_s was called the shear retention factor (Suidan and Schnobrich 1973; Yuzugullu and Schnobrich 1973), whose value was of a few tenths, typically 0.2. This is equivalent to setting the shear compliance C_T equal to a constant of value

$$C_T = \frac{1-\beta_s}{\beta_s G} \tag{8.5.18}$$

The introduction of the shear retention factor, however, is not satisfactory for four reasons: (1) it has no physical interpretation, (2) it is difficult to measure experimentally (if possible at all), (3) it leads to a behavior in which the material always has a stiffness in shear even if the crack is widely open, which is completely unrealistic, and (4) it seems a variable made to play with in numerical simulations. At any rate, for cases in which the cracking occurs close to mode I, the importance of the shear retention factor is not great. However, the results by Rots (1988) indicate that very low values of β_s —even zero— give better results in most cases.

For the normal compliance, Bažant and Oh (1983a) introduced a progressively degrading compliance as dictated by the uniaxial tension data. This is the equivalent to postulating that shearing the crack does not contribute to degradation in the normal direction. This is certainly a simplification, but can be realistic if the magnitude of shear is limited. This hypothesis allows a complete determination of the normal compliance C_N from the uniaxial stress-strain curve. Then, for monotonic straining normal to the crack, we have

$$C_N = \frac{\varepsilon_N^f}{\phi(\varepsilon_N^f)} \tag{8.5.19}$$

where $\phi(\varepsilon_N^f)$ is the function $\sigma = \phi(\varepsilon^f)$ which is deduced from uniaxial tests and has been repeatedly analyzed in the two previous sections (only the name of the argument changes, since for uniaxial loading $\varepsilon^f \equiv \varepsilon_N^f$).

The foregoing hypothesis implies that the cracking process is controlled by ε_N^f. For very small ε_N^f very little damage exists and the shear compliance should be small; for very large ε_N^f the damage is large and the shear compliance should be correspondingly large. Thus it seems logical, as done by Rots (1988) in a slightly different formulation to be defined later, to take C_T as an increasing function of C_N. The simplest of all is to assume C_T as proportional to C_N, i.e.,

$$C_T = c_T C_N(\varepsilon_N^f) \tag{8.5.20}$$

where c_T is a constant that should be determined by experiment.

This is a very simplified model, devised for monotonic crack opening, that can be easily brought to a more general formulation involving unloading to the origin, i.e., to a damage model as described next.

8.5.3 Scalar Damage Model for Cracking of Fixed Orientation

To convert the foregoing model into a damage model with unloading to the origin, it suffices to postulate that C_N and C_T are functions, not of the instantaneous value of ε_N^f, but of its maximum past value, defined as $\bar{\varepsilon}_N^f$. Thus, C_N and C_T get "frozen" as soon as ε_N^f starts to decrease.

Although not strictly necessary, we may define a normal damage function similar to (8.4.4):

$$\omega_N = \frac{EC_N}{1+EC_N} \quad \text{and} \quad \omega_T = \frac{GC_T}{1+GC_T} \tag{8.5.21}$$

from which (8.5.16) and (8.5.17) reduce to

$$\begin{Bmatrix} \varepsilon_{nn} \\ \varepsilon_{ss} \\ \varepsilon_{tt} \end{Bmatrix} = \frac{1}{E} \begin{bmatrix} 1/(1-\omega_N) & -\nu & -\nu \\ -\nu & 1 & -\nu \\ -\nu & -\nu & 1 \end{bmatrix} \begin{Bmatrix} \sigma_{nn} \\ \sigma_{ss} \\ \sigma_{tt} \end{Bmatrix} \tag{8.5.22}$$

and

$$\begin{Bmatrix} \gamma_{ns} \\ \gamma_{st} \\ \gamma_{tn} \end{Bmatrix} = \frac{1}{G} \begin{bmatrix} 1 & 0 & 0 \\ 0 & 1/(1-\omega_T) & 0 \\ 0 & 0 & 1/(1-\omega_T) \end{bmatrix} \begin{Bmatrix} \sigma_{ns} \\ \sigma_{st} \\ \sigma_{tn} \end{Bmatrix} \tag{8.5.23}$$

If we adopt the simple form (8.5.20) and select $C_T = 2(1+\nu)C_N$, the model further simplifies, because then

$$\omega_N = \omega_T = \omega = \frac{E\bar{\varepsilon}^f_N}{E\bar{\varepsilon}^f_N + \phi(\bar{\varepsilon}^f_N)} \tag{8.5.24}$$

where we noted that the expression is identical to that for the uniaxial case (8.4.4). This is the simplest possible model with unloading to the origin that is based only on the information from the uniaxial test.

8.5.4 Incremental Approach to Cracking of Fixed Orientation

The foregoing formulation can obviously be rewritten in incremental form, which is obtained by differentiating the equations. However, it is possible to directly formulate an incremental formulation that, in general, is not equivalent to a secant formulation because it does not satisfy the integrability conditions. This happens with the incremental approach proposed by Rots (1988) which is briefly outlined now.

The incremental form is obtained by establishing relationships between the rates of the variables. Eqs. (8.5.5) and (8.5.6) are replaced by

$$\dot{\boldsymbol{\varepsilon}} = \frac{1+\nu}{E}\dot{\boldsymbol{\sigma}} - \frac{\nu}{E}\mathrm{tr}\,\dot{\boldsymbol{\sigma}}\,\mathbf{1} + \left(\dot{\bar{\varepsilon}}^f \otimes \vec{n}\right)^S \tag{8.5.25}$$

$$\dot{\vec{\sigma}} = \dot{\boldsymbol{\sigma}}\vec{n} = \mathbf{S}^t\dot{\bar{\varepsilon}}^f \tag{8.5.26}$$

where the superimposed dot indicates the time rate, and $\mathbf{S}^t$ is a second-order tensor defining the tangent stiffnesses for the cracks. The structure of this tensor depends on the details of the model. The tensor need not be symmetric. It may have up to nine independent components, which are reduced to five if one assumes that the tensor depends only on the crack orientation $\vec{n}$ and the instantaneous cracking strain vector $\vec{\varepsilon}^f$. At any rate, much more information is required than is currently available from the experimental knowledge, and strong simplifications are introduced. Rots (1988) assumed that the normal and tangent components of stress and strain were mutually proportional, with no mixed stiffness terms. With this assumption, the equations are similar to those for the secant formulation. In particular, (8.5.12) is replaced by

$$\dot{\sigma}_N = S^t_N(\varepsilon^f_N)\dot{\varepsilon}^f_N \quad \text{and} \quad \dot{\vec{\sigma}}_T = S^t_T(\varepsilon^f_N)\dot{\bar{\varepsilon}}^f_T \tag{8.5.27}$$

where S^t_N and S^t_T are incremental (tangent) stiffnesses. Rots (1988) further assumed that both S^t_N and S^t_T depended only on the normal cracking strain ε^f_N, but introduced independent functions to describe them. S^t_N is derived from the uniaxial tensile test and is related to the secant stiffness and the softening function $\phi(\varepsilon^f_N)$ by

$$S^t_N = \frac{\partial(S_N\,\varepsilon^f_N)}{\partial\varepsilon^f_N} = \frac{\partial\phi(\varepsilon^f_N)}{\partial\varepsilon^f_N} \tag{8.5.28}$$

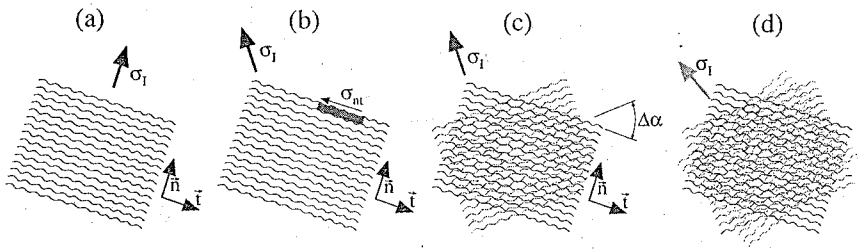

Figure 8.5.2 Multiple cracking: (a) primary cracks; (b) shear stress built up due to principal stress rotation; (c) secondary cracking formed; (d) tertiary cracking.

For the incremental shear stiffness S^t_T, Rots introduced a decreasing function that was infinite for zero crack opening and decreased progressively to vanish for the normal cracking strain at which the normal stress drops to zero. He showed that this is equivalent to using an incremental shear retention factor varying from 1 just after crack creation, down to 0 for a fully broken material.

At first glance, it may appear that this formulation is equivalent to the secant formulation. It is not; indeed, if we differentiate (8.5.12) to get the rate equations for the secant model (with the assumption that the stiffnesses depend only on the normal cracking strain), we find that the equation for the normal component is equivalent, but the equation for the shear component is

$$\dot{\vec{\sigma}}_T = S_T(\varepsilon^f_N)\dot{\bar{\varepsilon}}^f_T + \frac{\partial S_T(\varepsilon^f_N)}{\partial\varepsilon^f_N}\bar{\varepsilon}^f_T\,\dot{\varepsilon}^f_N \tag{8.5.29}$$

This is certainly not equivalent to (8.5.27) except for proportional straining (see exercises), and gives a lower tangential stiffness than (8.5.27) because S_T is decreasing. No comparative analysis of the two approaches has been performed to date. The difference is analogous to that between the incremental and the total-strain theories of plasticity. The latter is known to give better (softer) stiffness predictions for the first deviation from a proportional loading (predicting the so-called vertex effect), and the same probably applies here.

8.5.5 Multi-Directional Fixed Cracking

A difficult question with the foregoing formulation is the orientation of cracking. The practice which has been and is still typical of most large finite element codes is to set the crack direction to be normal to the maximum principal stress at the moment the tensile strength (or the tensile yield surface) is reached (Fig. 8.5.2a). During the subsequent loading process, the direction of the maximum principal stress can rotate. At the moment the cracks begin to form, there is, by definition, no shear stress on the cracking planes. However, due to keeping the cracking orientation fixed and assuming shear interlocking of the opposite crack faces, shear stresses can arise later if the principal stress direction rotates (Fig. 8.5.2b). It was for this reason that the diagonal compliances or stiffnesses for shear had to be included in Eqs. (8.5.17) and (8.5.23).

When the principal stress direction rotates, it is possible that the tensile strength f'_t is reached again in another direction that is inclined with regard to the normal of the originally formed cracks. In that case, it is assumed that a second system of smeared cracks forms in the direction normal to the current principal stress (Fig. 8.5.2c). This system is inclined at some general angle $\Delta\alpha$ with regard to the orientation of the primary cracks. The cracking strain due to the formation of secondary cracks is then superposed on the original cracking strain, which means that another fracturing strain tensor $(\bar{\varepsilon}^f_2 \otimes \vec{n})^S$ is added to the right-hand side of Eq. (8.5.5). The orientation of the secondary cracks is also kept fixed even when the principal stress directions subsequently rotate during the loading process. Thus, it may happen that the tensile strength is again reached in a third direction (Fig. 8.5.2d), in which case tertiary smeared cracks begin to form and the corresponding cracking strain needs to be again superimposed in Eq. (8.5.5).

The laws governing the secondary and tertiary cracking strains may be assumed to be the same as

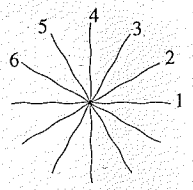

Figure 8.5.3 Multi-crack system with fixed angular separation.

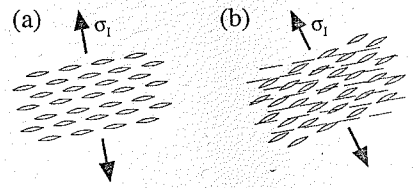

Figure 8.5.4 Rotating crack process: (a) Primary cracks form; (b) secondary cracks form and become dominant.

for the primary cracking, although some formulations allow for interaction between the various crack systems. The formulation of multiple cracking with fixed directions, which has been worked out in the greatest generality perhaps by de Borst (1986), can obviously get quite complicated when some crack systems open and cause others to close. Special computational strategies must then be devised to follow the possible bifurcation paths.

In the method just described, the secondary (and tertiary) cracks can have arbitrary orientations with regard to the primary ones. In this manner, cracks of many directions can form. In that case, it may be more convenient to assume that the cracks may form only in certain specified spatial orientations which are uniformly distributed among all spatial directions (Fig. 8.5.3). Such an assumption is also more realistic because it prevents the angle between intersecting cracks from being too small (say 10°, which is unlikely to occur). This approach, in which, again, the cracking strains from all the assumed discrete crack orientations are superimposed, makes it possible to describe the fact that a principal stress of a certain direction may cause microcracking with various intensities at various orientations (this is captured more systematically by the context of the microplane approach to be discussed in Chapter 14; see Carol and Prat 1990, and Carol and Bažant 1997).

8.5.6 Rotating Crack Model

When the smeared cracks of the primary direction start forming, which is the start of strain softening, there is actually only a system of discontinuous microcracks. If the maximum principal stress direction rotates, these microcracks partially close and microcracks of a new orientation begin to form (Fig. 8.5.4a). Eventually the secondary microcracks may become the major ones and the primary ones may get nearly closed. Although a precise description would be rather difficult (and would perhaps be best done in terms of the microplane model, Chapter 14), the fact that the previously formed microcracks may to a large extent close and microcracks of a new orientation may become dominant can be better described by assuming that the direction of smeared cracking rotates (Fig. 8.5.4b) and remains always normal to the maximum principal stress. In reality, of course, a crack, once formed, cannot actually rotate.

The notion of a rotating crack (also called swinging crack), originally proposed by Cope et al. (1980) and reformulated by Gupta and Akhbar (1984), and Crisfield and Wills (1987), is just a computational convenience. The reality is more complicated than the preceding discussion suggests. Even for a constant principal stress direction, the microcracks during the process of crack formation do not have the same orientation; due to heterogeneity of the microstructure, microcracks arise in all directions, and one can

only say that the microcracks that are normal to the maximum principal stress direction are the statistically dominant ones.

The rotating crack model can be formulated in a way very similar to the fixed crack model, although the resulting equations are simpler. Consider first a single crack system. By the very definition of the model, the normal to the cracks $\vec{n}$ is now coincident with $\mathbf{p}_\mathrm{I}$, the unit vector in the direction of the maximum principal strain, which coincides with the principal stress direction. Then, the crack displacements are in pure opening and we can write, referring to Fig. 8.5.1b

$$\Delta\vec{w} = \Delta w\,\mathbf{p}_\mathrm{I} \qquad \Rightarrow \qquad \vec{\varepsilon}^f = \varepsilon^f\,\mathbf{p}_\mathrm{I} \tag{8.5.30}$$

Proceeding again as in Eqs. (8.5.3)–(8.5.5) with $\vec{n}$ replaced by $\mathbf{p}_\mathrm{I}$, we get the total strain tensor as

$$\boldsymbol{\varepsilon} = \frac{1+\nu}{E}\boldsymbol{\sigma} - \frac{\nu}{E}\mathrm{tr}\,\boldsymbol{\sigma}\,\mathbf{1} + \varepsilon^f\,\mathbf{p}_\mathrm{I}\otimes\mathbf{p}_\mathrm{I} \tag{8.5.31}$$

in which the fracturing strain tensor now depends on only one scalar variable, ε^f.

As for the equation governing microcracking, Eq. (8.5.6) now becomes a scalar equation since, by definition $\boldsymbol{\sigma}\mathbf{p}_\mathrm{I} = \sigma_\mathrm{I}\mathbf{p}_\mathrm{I}$, where σ_I is the principal stress with principal direction $\mathbf{p}_\mathrm{I}$. Thus, we need only a relationship between ε^f and σ_I. This coincides with the uniaxial stress-fracturing strain relation (for the monotonic loading case), i.e.,

$$\sigma_\mathrm{I} = \phi(\varepsilon^f) = S_N(\varepsilon^f)\varepsilon^f \tag{8.5.32}$$

in which we keep the nomenclature in the previous sections to keep the meaning clear. From the foregoing equation, we can solve for ε^f (at constant secant stiffness) and get the secant formulation:

$$\boldsymbol{\varepsilon} = \frac{1+\nu}{E}\boldsymbol{\sigma} - \frac{\nu}{E}\mathrm{tr}\,\boldsymbol{\sigma}\,\mathbf{1} + C_N\sigma_\mathrm{I}\,\mathbf{p}_\mathrm{I}\otimes\mathbf{p}_\mathrm{I} \tag{8.5.33}$$

The component expression for this equation is particularly simple if the axes are taken along the principal stress and strain directions:

$$\begin{Bmatrix}\varepsilon_\mathrm{I}\\ \varepsilon_\mathrm{II}\\ \varepsilon_\mathrm{III}\end{Bmatrix} = \frac{1}{E}\begin{bmatrix}1+EC_N & -\nu & -\nu\\ -\nu & 1 & -\nu\\ -\nu & -\nu & 1\end{bmatrix}\begin{Bmatrix}\sigma_\mathrm{I}\\ \sigma_\mathrm{II}\\ \sigma_\mathrm{III}\end{Bmatrix} \tag{8.5.34}$$

in which the similarity with (8.5.16) is blatant.

In the foregoing, Eq. (8.5.32) is valid for virgin loading. Unloading and reloading require further rules. The simplest is a damage model in which C_N is taken to be a function of $\tilde{\varepsilon}^f$, the maximum fracturing strain ever reached. Then, if $\varepsilon^f < \tilde{\varepsilon}^f$, the unloading-reloading proceeds at constant C_N and, for virgin loading, $\varepsilon^f = \tilde{\varepsilon}^f$ and C_N increases.

The model can further be extended by considering three mutually orthogonal jointly rotating systems of cracks, normal to the three principal stress and strain directions. Each system is allowed to follow an independent cracking process, same as described before, characterized by fracturing strains ε^f_ν, with ν = I, II, or III. The resulting equation, which incorporates the three fracturing strains, can be written as

$$\boldsymbol{\varepsilon} = \frac{1+\nu}{E}\boldsymbol{\sigma} - \frac{\nu}{E}\mathrm{tr}\,\boldsymbol{\sigma}\,\mathbf{1} + \sum_{\nu=\mathrm{I}}^{\mathrm{III}} C_N(\tilde{\varepsilon}^f_\nu)\,\sigma_\nu\,\mathbf{p}_\mathrm{I}\otimes\mathbf{p}_\nu \tag{8.5.35}$$

whose component form is

$$\begin{Bmatrix}\varepsilon_\mathrm{I}\\ \varepsilon_\mathrm{II}\\ \varepsilon_\mathrm{III}\end{Bmatrix} = \frac{1}{E}\begin{bmatrix}1+EC_N(\tilde{\varepsilon}^f_\mathrm{I}) & -\nu & -\nu\\ -\nu & 1+EC_N(\tilde{\varepsilon}^f_\mathrm{II}) & -\nu\\ -\nu & -\nu & 1+EC_N(\tilde{\varepsilon}^f_\mathrm{III})\end{bmatrix}\begin{Bmatrix}\sigma_\mathrm{I}\\ \sigma_\mathrm{II}\\ \sigma_\mathrm{III}\end{Bmatrix} \tag{8.5.36}$$

Note that although there are three different damage components, the behavior of the material is described with only one material function which can, in principle, be determined from the uniaxial test.

8.5.7 Generalized Constitutive Equations with Softening

It is possible to put the constitutive equations with softening into a very general framework that embraces most known models. The most general thermomechanical approach is outside the scope of this book, and the reader may refer to the book by Lemaitre and Chaboche (1985).

A general constitutive equation may be based on three fundamental concepts:

1. A set of independent internal variables, p_k, which together with the infinitesimal strain tensor ε (or the stress tensor σ) are assumed to characterize uniquely the instantaneous state of the body at a given point. The internal variables may represent a physical magnitude or be abstract in nature. They can be related to kinematic events or to structural features. For example, the vector $\vec{\varepsilon}^f$ in the smeared crack models is intended to represent the internal kinematics of cracks and $\vec{n}$, the crack orientation, is a structural internal variable. It must be noted that, when a set of internal variables is chosen, any other set, uniquely related to the first, is strictly equivalent and, consequently, can be used instead of the first. This makes the physical interpretation of a given set of internal variables somewhat ambiguous.
2. A system of equations relating the stress to the strain and to the internal variables:

$$\varepsilon = \mathbf{E}(\sigma, p_k) \tag{8.5.37}$$

where $\mathbf{E}(\cdot)$ is a symmetric tensor-valued function. In modern thermodynamic formulations $\mathbf{E}(\cdot)$ is derived from a free energy function, which is a scalar function to be specified instead of $\mathbf{E}(\cdot)$. Usually, $\mathbf{E}(\cdot)$ is assumed to be linear in the infinitesimal strain tensor, that is,

$$\varepsilon = \boldsymbol{C}(p_k)\sigma + \varepsilon^p(p_k) \tag{8.5.38}$$

where $\boldsymbol{C}(p_k)$ is the secant fourth-order compliance tensor, depending only on the internal variables; $\varepsilon^p(p_k)$ is the irrecoverable or plastic strain tensor, which again depends only on the internal variables. When $\varepsilon^p(p_k) \equiv \mathbf{0}$ and $\boldsymbol{C}(p_k) \equiv \boldsymbol{C}^{el} = \text{constant}$, the elastic behavior is obtained. When $\varepsilon^p(p_k)$ varies, and $\boldsymbol{C}(p_k) \equiv \boldsymbol{C}^{el} = \text{constant}$, a model displaying strength degradation is obtained. When $\varepsilon^p(p_k) \equiv \mathbf{0}$ and $\boldsymbol{C}(p_k)$ is variable, one obtains a model displaying stiffness degradation, which always unloads to the origin ($\sigma = \mathbf{0}$ for $\varepsilon = \mathbf{0}$, and vice versa). When both $\boldsymbol{C}(p_k)$ and $\varepsilon^p(p_k)$ are variable, a general damage model with mixed behavior is obtained.
3. A set of *flow rules,* which specify the way in which the internal variables increase during loading. This is a delicate yet essential point, since assigning different flow rules to models having the same set of internal variables and the same structure for the stress-strain relation will lead to different behaviors. Moreover, the flow rules must be consistent with the irreversibility condition posed by the second law of thermodynamics. A detailed discussion of this important aspect is outside the scope of this book, so only general aspects will be mentioned. (By analogy with plasticity, the term "flow rule" is used even though "cracking rule" would be more logical in models in which cracking dominates.)

The flow rules may be specified at many different levels of generality. One relatively simple way is to use one or more loading functions obtained by direct generalization of the theory of classical plasticity. For the simplest case of a single yield surface, a loading function $F(p_k, \sigma, \mu)$ is specified, in which μ is one further internal variable that governs hardening and softening (it can be singled out from the beginning). The loading function defines the region in which the behavior is elastic (i.e., in which $d\mu = 0$ and $dp_k = 0$ for any k) which can be written as

$$F(p_k, \sigma, \mu) \leq 0 \tag{8.5.39}$$

The associated flow rules are:

$$\dot{p}_k = H_k(p_k, \sigma, \mu)\dot{\mu} \qquad \text{with} \qquad \dot{\mu} \geq 0 \tag{8.5.40}$$

where μ is the hardening-softening variable which takes the place of the plastic multiplier and $H_k(p_k, \sigma, \mu)$ are the hardening-softening functions. The flow rule for μ itself is deduced from the consistency condition requiring that $F(p_k, \sigma, \mu)$ remain equal to 0 if $\dot{\mu} > 0$.

Although this is a rather general formulation, it is not the only one possible. Formulations of the endochronic type and multi-yield surface type are also possible.

In the literature, one can find many models meant to describe more or less general softening behaviors, from the simplest, with a single scalar internal variable (plus the hardening-softening variable), to very sophisticated models in which the internal variables are tensors of second or fourth order (even eighth-order tensors have been proposed as internal variables). For example, a very interesting model was proposed by Ortiz (1985) in which the full fourth-order compliance tensor is one internal variable (equivalent to a set of 21 internal variables, the independent components of the compliance tensor), and the second-order tensor of plastic strain a further internal variable (equivalent to a set of six scalar variables). However, this model is too complex to be described here in detail. Only two very simple models will be briefly discussed: Mazars' scalar (isotropic) damage model and Rankine's associated plastic model with strain softening.

8.5.8 Mazars' Scalar Damage Model

Mazars (1981, 1984, 1986) developed a series of damage models, which aim at damage in tension and compression. When specialized for tension, the only primary internal variable is the scalar damage ω, varying form $\omega = 0$ (for no damage), to $\omega = 1$ (for complete failure). The hardening-softening variable is $\mu \equiv \tilde{\varepsilon}$ where $\tilde{\varepsilon}$ has the meaning of an equivalent uniaxial strain. The equations for this model are

$$\varepsilon = \frac{1}{1-\omega}\left(\frac{1+\nu}{E}\sigma - \frac{\nu}{E}\text{tr}\,\sigma\,\mathbf{1}\right) \tag{8.5.41}$$

$$\omega = Q(\tilde{\varepsilon}) \tag{8.5.42}$$

$$\tilde{\varepsilon} = \max\left(\varepsilon^+\right) \qquad \text{with} \qquad \varepsilon^+ = \sqrt{\langle\varepsilon\rangle^+ \cdot \langle\varepsilon\rangle^+} \tag{8.5.43}$$

$Q(\tilde{\varepsilon})$ is a scalar function characterizing the material and $\langle\varepsilon\rangle^+$ is the positive (or tensile) part of the strain tensor, defined as the tensor possessing the same principal directions as ε and having principal values that coincide with those of ε when positive and are set to zero when negative. This model is restricted to tensile damage since, by its very definition, no damage is introduced if the principal strains are negative. Note also that, due to its simplicity, brought about by the scalar nature of the internal variable, the flow rule takes an integrated form.

The function $Q(\tilde{\varepsilon})$ is uniquely determined from the uniaxial stress-strain curve. Indeed, taking the axis x_1 to lie along the specimen axis and the axes x_2 and x_3 to be normal to it, it turns out that in uniaxial tension $\langle\varepsilon\rangle^+{}_{ij} = \varepsilon_{11}\delta_{1i}\delta_{1j}$, so that for monotonic straining $\tilde{\varepsilon} = \varepsilon^+ = \varepsilon_{11} = \varepsilon$ (where ε denotes the axial strain). Then, if the stress strain curve is given by $\sigma = \psi(\varepsilon)$, we substitute this into (8.5.41), solve for ω, and equate the result to (8.5.42) to get

$$\omega = Q(\tilde{\varepsilon}) = 1 - \frac{\psi(\tilde{\varepsilon})}{E\tilde{\varepsilon}} \tag{8.5.44}$$

The main problem with this model is that the prediction for the transverse strain is unrealistic. Indeed, it is easily verified that, for uniaxial tension in the direction of x_1, we have $\varepsilon_{22} = \varepsilon_{33} = -\nu\varepsilon_{11}$ at all times. This means that, for full fracture, when $\varepsilon_{11} \to \infty$, we get $\varepsilon_{22} = \varepsilon_{33} \to -\infty$, which is unrealistic. Therefore, a directional scalar damage model such as that given by (8.5.33) in which C_N is the scalar damage variable and $\tilde{\varepsilon}^f$ the hardening-softening variable, may often be more suitable to describe the fracture behavior.

8.5.9 Rankine Plastic Model with Softening

This is a very simple model with strength degradation, which exhibits a certain analogy with the rotating crack model. In the rotating crack model the inelastic strain has the same principal directions as the stress tensor, while in Rankine plasticity this holds for the inelastic strain *increments.*

The formulation is classical. The compliance tensor is fixed, and so we write

$$\varepsilon = \varepsilon^{el} + \varepsilon^p \tag{8.5.45}$$

where the only primary internal variable is taken to be ε^p. The loading function is taken to be the Rankine yield criterion,

$$\sigma_1 - \phi(\bar{\varepsilon}^p) \leq 0 \tag{8.5.46}$$

where σ_1 is the largest principal strain, $\bar{\varepsilon}^p$ the equivalent plastic uniaxial strain, and ϕ is a function defining the evolution of the strength. This means that the inelastic strain occurs when the major principal stress attains the instantaneous strength. The flow rule simply states that the inelastic strain takes place in the direction of the maximum principal strain, i.e.:

$$\dot{\varepsilon}^p = \mathbf{p}_1 \otimes \mathbf{p}_1 \dot{\bar{\varepsilon}}^p \tag{8.5.47}$$

where $\mathbf{p}_1$ is a unit eigenvector corresponding to the principal stress σ_1.

The reader can easily check that for uniaxial tension under monotonic straining, $\bar{\varepsilon}^p = \varepsilon^p$ and $\sigma_I = \sigma$. So, the function $\phi(\bar{\varepsilon}^p)$ is nothing more than the curve of stress vs. inelastic strain for uniaxial tension.

8.5.10 A Simple Model with Stiffness and Strength Degradation

It is relatively simple to build a model with mixed properties, by combining the simple rotating crack model given by Eq. (8.5.33) and the foregoing plastic Rankine model. We assume the total strain to be split into the elastic and fracturing parts,

$$\varepsilon = \varepsilon^{el} + \varepsilon^f \tag{8.5.48}$$

and assume further that the fracturing strain ε^f can be split into a term linear in the stress and a permanent (irreversible) strain tensor ε^p:

$$\varepsilon^f = C^f \sigma_1 \mathbf{p}_1 \otimes \mathbf{p}_1 + \varepsilon^p \tag{8.5.49}$$

in which C^f is the inelastic unloading-reloading compliance (which replaces the secant compliance C_N). The evolution of C^f is given in integrated form as a function of the hardening variable $\bar{\varepsilon}^f$, while the evolution of ε^p is given in incremental form as before:

$$C^f = \eta(\bar{\varepsilon}^f) \tag{8.5.50}$$

$$\dot{\varepsilon}^p = \mathbf{p}_1 \otimes \mathbf{p}_1 \frac{dH(\bar{\varepsilon}^f)}{d\bar{\varepsilon}^f} \dot{\bar{\varepsilon}}^f \tag{8.5.51}$$

where $\eta(\bar{\varepsilon}^f)$ and $H(\bar{\varepsilon}^f)$ are material functions which will be related in the sequel to the uniaxial stress-strain curve. The evolution of the hardening-softening parameter $\bar{\varepsilon}^f$ is deduced from the loading function and the consistency condition which is taken according to the Rankine criterion:

$$\sigma_1 - \phi(\bar{\varepsilon}^f) \leq 0 \tag{8.5.52}$$

Considering the uniaxial tensile test with monotonic stretching, let us call σ, ε^f and ε^p the axial components of the stress, and fracturing and permanent strain tensors, respectively, we obviously have $\sigma_1 = \sigma$ and, by definition, $\varepsilon^f = \bar{\varepsilon}^f$, and so $\phi(\bar{\varepsilon}^f)$ is again the softening function. On the other hand, $\mathbf{p}_1$ is a vector coinciding with the axis of the uniaxial tension. And according to (8.5.51), the permanent strain is readily integrated; it has only a nonzero component, namely the axial one,

$$\varepsilon^p = H(\bar{\varepsilon}^f) \tag{8.5.53}$$

Substituting this into (8.5.48) and identifying the axial components (the remaining ones are all zero), we get

$$\bar{\varepsilon}^f = \eta(\bar{\varepsilon}^f)\phi(\bar{\varepsilon}^f) + H(\bar{\varepsilon}^f) \tag{8.5.54}$$

from which we can solve for $\eta(\bar{\varepsilon}^f)$:

$$\eta(\bar{\varepsilon}^f) = \frac{\bar{\varepsilon}^f - H(\bar{\varepsilon}^f)}{\phi(\bar{\varepsilon}^f)} \tag{8.5.55}$$

Therefore, given $\phi(\bar{\varepsilon}^f)$ and $H(\bar{\varepsilon}^f)$, the properties of the material are completely determined. Note that, according to (8.5.53) $H(\bar{\varepsilon}^f)$ is nothing else than the permanent strain which is obtained when the specimen in a uniaxial test is stretched up to $\bar{\varepsilon}^f$ and then unloaded. If no further information is available, it may be assumed that this is a fixed proportion α of the maximum inelastic strain, i.e., $H(\bar{\varepsilon}^f) = \alpha\bar{\varepsilon}^f$ (in which $\alpha \leq 1$). With this, the flow rules can be rewritten as

$$C^f = (1-\alpha)\frac{\bar{\varepsilon}^f}{\phi(\bar{\varepsilon}^f)} \tag{8.5.56}$$

$$\dot{\varepsilon}^p = \alpha\, \mathbf{p}_1 \otimes \mathbf{p}_1 \dot{\bar{\varepsilon}}^f \tag{8.5.57}$$

This constitutes the simplest triaxial generalization of the uniaxial model described in Section 8.4.3, and may also be viewed as a strongly simplified version of Ortiz's model (1985). However, one useful feature of Ortiz's model is that it describes softening in compression as well as tension, which is obviously not the case with this simplified version.

Exercises

8.22 Show that ε^f in (8.5.13) can be written in a general tensorial form as

$$\varepsilon^f = (C_N \boldsymbol{A} + C_T \boldsymbol{B})\boldsymbol{\sigma} \tag{8.5.58}$$

where $\boldsymbol{A}$ and $\boldsymbol{B}$ are (for constant $\vec{n}$) constant fourth-order tensors which are given in cartesian components by

$$A_{ijkl} = n_i n_j n_k n_l\,, \qquad B_{ijkl} = \frac{1}{2}\delta_{ik}n_l n_j + \frac{1}{2}\delta_{jk}n_l n_i - n_i n_j n_k n_l \tag{8.5.59}$$

8.23 Consider a fixed-direction crack model with elastic-softening behavior defined by exponential softening in uniaxial tension, $\sigma = f'_t e^{-\varepsilon^f/\varepsilon_0}$. Determine the evolution of the axial and transverse stress components in uniaxial extension, in which $\varepsilon_{11} = \varepsilon$ increases monotonically and all the remaining components of the strain tensor are zero.

8.24 Show that the response for the uniaxial extension in the preceding exercise is identical for fixed and rotating crack models as long as the strain-softening curve is the same.

8.25 Consider a fixed-direction crack model with elastic-softening behavior defined by exponential softening in uniaxial tension, $\sigma = f'_t e^{-\varepsilon^f/\varepsilon_0}$. Determine the evolution of the axial and transverse strains in a plane stress tension test, in which $\varepsilon_{11} = \varepsilon$ increases monotonically and $\varepsilon_{33} = \sigma_{22} = 0$, the shear components being zero.

8.26 Consider a fixed-direction crack model that exhibits elastic-softening behavior defined by exponential softening in uniaxial tension, $\sigma = f'_t e^{-\varepsilon^f/\varepsilon_0}$, and is amenable to the scalar damage model described in Section 8.5.3. Referring to cartesian axes $\{x_1, x_2, x_3\}$, consider a process in which the stress components $\sigma_{22} = \sigma_{33} = \sigma_{23} = \sigma_{13} = 0$, while the fracturing strain tensor evolves such that $\varepsilon^f_{11} = \varepsilon_0\lambda$, $\varepsilon^f_{12} = \varepsilon_0\lambda^2$ in which λ increases monotonically starting at $\lambda = 0$. All the remaining components are zero. Assuming that $\nu = 0.2$, determine: (a) the evolution of the stress components; (b) the evolution of the maximum principal stress; and (c) whether a secondary crack forms. [Hint: Note that for $\lambda \to 0$, the shear component is negligible, and thus the crack band forms normal to x_1.]

8.27 Same as the preceding exercise except that $\varepsilon^f_{12} = \varepsilon_0\lambda\mu$ in which λ increases monotonically starting at $\lambda = 0$ and μ varies in a way to be determined. Determine the upper bound for μ as a function of λ so that secondary cracking would not occur. Determine the evolution of the stress for the limiting case. [Answer: $|\mu| < 2(1-\nu)e^{2\lambda}\sqrt{1-e^{-\lambda}}$.]

8.28 Generalize the foregoing result to any softening function $\phi(\bar{\varepsilon}^f)$.

8.29 Show that the tangent approach with S_N and S_T depending only on ε^f_N cannot be distinguished from Rots' incremental approach for proportional microcracking, i.e., for loadings such that $\vec{\varepsilon}^f_T = \varepsilon^f_N \vec{m}$, where $\vec{m}$ is an arbitrary vector in the crack plane. Find S^t_T in terms of S_T for this particular case.

8.30 Consider a material conforming to Mazars' isotropic damage model with elastic-softening behavior defined by exponential softening in uniaxial tension, $\sigma = f'_t e^{-\varepsilon^f/\varepsilon_0}$. Determine the evolution of the axial

and transverse stress components in uniaxial extension, in which $\varepsilon_{11} = \varepsilon$ increases monotonically and all the remaining components of the strain tensor are zero.

8.31 Consider a thin layer of a material conforming to Mazars' isotropic damage model with elastic-softening behavior defined by exponential softening in uniaxial tension, $\sigma = f_t' e^{-\varepsilon^f/\varepsilon_0}$. This layer is sandwiched between two thick plates of an elastic material with the same elastic moduli as the adjacent material, and the sandwich is subjected to uniaxial tension normal to the layer. Neglecting end effects, determine the evolution of the stress tensor in the layer as a function of the strain of the layer in the normal direction (assume that the transverse strain in the layer is dictated by the transverse strain in the elastic plates, which is, in turn, dictated by the elastic Poisson effect).

8.32 Carry out the algebra leading to (8.5.56) and (8.5.57).

8.33 Determine the strain evolution in a material element following the general model in Section 8.5.10 if the response is elastic-softening with an exponential softening curve $\sigma = f_t' e^{-\varepsilon^f/\varepsilon_0}$. Consider that the element is subjected to proportional loading with $\sigma_{11} = 2\sigma_{22}$ and all the remaining stress components are equal to zero, while $\varepsilon_{11} \equiv \varepsilon$ increases monotonically up to $1.4\varepsilon_0$ and then the element is unloaded. Take $\varepsilon_0 = 10 f_t'/E$ and $\nu = 0.2$.

8.6 Crack Band Models and Smeared Cracking

In Section 8.3.5, we discussed a simple way to determine the stress-strain curve for a finite element of any size based on the stress-strain curve for the band. However, this applied only for the uniaxial case, which is extremely simple. In this section, we will address the complexities raised by the triaxial nature of most practical problems, although we consider principally two-dimensional problems. We start by seeking the triaxial strain-softening equations for a finite element of any size.

8.6.1 Stress-Strain Relations for Elements of Arbitrary Size

To be precise, we limit the analysis to elastic-softening materials and consider a fracturing model with one definite cracking orientation (fixed or rotating). Consider first a case in which the crack band evolves with the cracks oriented parallel to one of the directions of the finite element mesh, as depicted in Fig. 8.6.1a–c. It is intuitively clear that the stress-strain relations for the direction normal to the band must be very close to the uniaxial formulation deduced in Section 8.3.5. However, in that uniaxial formulation, the transversal strains were ignored, while in the actual three- or two-dimensional elements, a mismatch of strains parallel to the cracks can occur between the crack band that softens and the remainder of the element that unloads. In view of the other simplifications involved, this might not cause a serious error, but it is not difficult to enforce the proper interface continuity requirements at this interface. In fact, the formulation in Section 8.4.2 ensures compatibility automatically.

Consider the simple case in Fig. 8.6.1d. After the stress peak, the material inside the crack band softens, while the rest of the element unloads (for the elastic-softening case considered here, unloading means elastic behavior). We want to enforce that the strain components in the plane of the cracks be the same for the unloading and softening regions, which, with reference to the base vectors in Fig. 8.5.1c, is written as

$$\varepsilon^u_{tt} = \varepsilon^s_{tt}\,, \qquad \varepsilon^u_{ss} = \varepsilon^s_{ss} \qquad \text{and} \qquad \varepsilon^u_{ts} = \varepsilon^s_{ts} \tag{8.6.1}$$

where superscripts u and s refer to the unloading region and to the softening band. Now, according to the hypothesis of elastic-softening behavior, the strain tensor in the unloading region is related to the stress tensor by the elastic relations, while the strain tensor in the softening band is given by (8.5.5), and so we have:

$$\boldsymbol{\varepsilon}^u = \frac{1+\nu}{E}\boldsymbol{\sigma}^u - \frac{\nu}{E}\text{tr}\,\boldsymbol{\sigma}^u\,\mathbf{1} \tag{8.6.2}$$

$$\boldsymbol{\varepsilon}^s = \frac{1+\nu}{E}\boldsymbol{\sigma}^s - \frac{\nu}{E}\text{tr}\,\boldsymbol{\sigma}^s\,\mathbf{1} + \left(\vec{\varepsilon}^f \otimes \vec{n}\right)^S \tag{8.6.3}$$

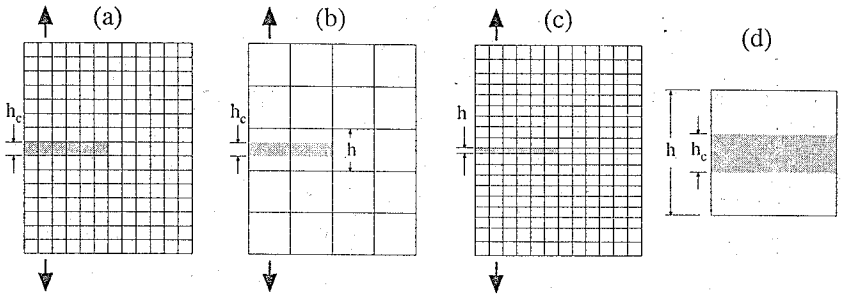

Figure 8.6.1 Rectangular panel with various mesh sizes, identical (a), larger (b), or smaller (c) than the crack band width h_c. (d) Detail of an element with an embedded crack band.

Therefore, writing the components appearing in (8.6.1), and taking into account (8.5.4), we can reduce the strain conditions to identical conditions in stresses, i.e.,

$$\sigma^u_{tt} = \sigma^s_{tt}\,, \qquad \sigma^u_{ss} = \sigma^s_{ss} \qquad \text{and} \qquad \sigma^u_{ts} = \sigma^s_{ts} \tag{8.6.4}$$

If we now take into account that the traction vectors on the interface of the softening and unloading parts must be equal, i.e.,

$$\boldsymbol{\sigma}^u\vec{n} = \boldsymbol{\sigma}^s\vec{n} \tag{8.6.5}$$

it turns out that the remaining three components of the stress tensors in the two regions must also be mutually equal. Therefore, the compatibility and continuity equations are satisfied if the stress tensors in the softening band and in the unloading region are identical, so that we can write

$$\boldsymbol{\sigma}^u = \boldsymbol{\sigma}^s = \boldsymbol{\sigma} \tag{8.6.6}$$

Since the stress tensors are the same, the two regions are fully coupled in series. The average strain in the element can be obtained by stipulating that the virtual work of the mean fields is equal to the sum of the virtual works in the unloading and softening portions, that is

$$\boldsymbol{\sigma}\cdot\delta\boldsymbol{\varepsilon}^{(e)}V^{(e)} = \boldsymbol{\sigma}^u\cdot\delta\boldsymbol{\varepsilon}^u V^u + \boldsymbol{\sigma}^s\cdot\delta\boldsymbol{\varepsilon}^s V^s \tag{8.6.7}$$

where $V^{(e)}, V^u$, and V^s are, respectively, the volumes of the element, the unloading region and the softening region. By virtue of (8.6.6), this condition is identically satisfied for all the stress states and virtual strain increments if

$$\boldsymbol{\varepsilon}^{(e)} = (1-f)\boldsymbol{\varepsilon}^u + f\boldsymbol{\varepsilon}^s \tag{8.6.8}$$

where f is the volume fraction of the crack band. Substituting (8.6.6) into (8.6.2) and (8.6.3) and the results in (8.6.8) we get the final expression

$$\boldsymbol{\varepsilon}^{(e)} = \frac{1+\nu}{E}\boldsymbol{\sigma} - \frac{\nu}{E}\text{tr}\,\boldsymbol{\sigma}\,\mathbf{1} + f\left(\vec{\varepsilon}^f \otimes \vec{n}\right)^S \tag{8.6.9}$$

which shows that the equation for the element has a structure identical to the original stress-strain model, except that the fracturing strain is affected by the factor f. This factor is trivially equal to h_c/h for the simple cases shown in Fig. 8.6.1 in which the elements are rectangular and the crack band is perpendicular to one pair of sides.

This case occurs frequently in the analysis of test results for mode I crack growth, and its use was pioneered by Bažant and Oh (1983a), who analyzed with success a tremendous amount of experimental data. Bažant and Oh used a crack band model with a finite strain slope in a finite element analysis with square meshes. In computations, small increments of the load-point displacement were prescribed, and the reaction, representing the load P, was calculated in each loading step. The same stress-strain relation was assumed to hold for all the finite elements, although only some of them entered nonlinear behavior.

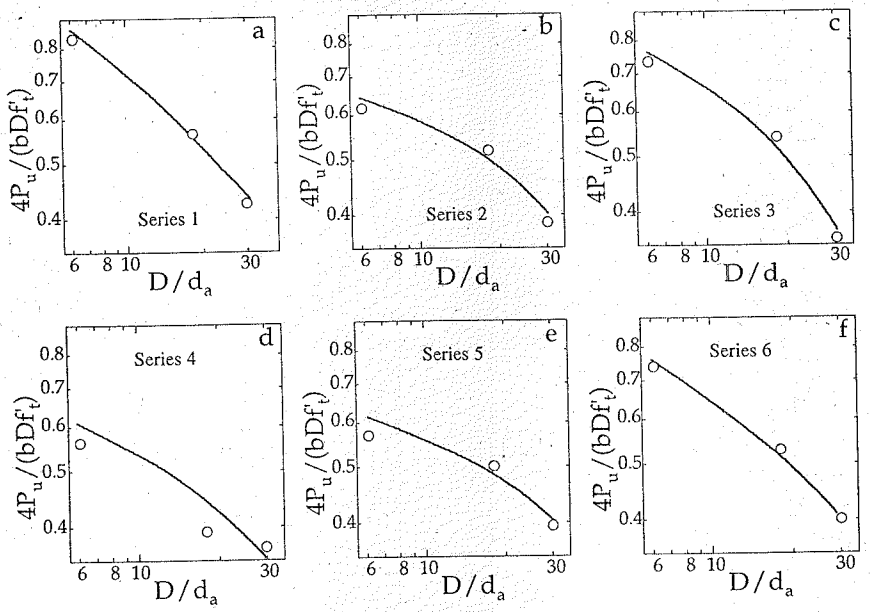

Figure 8.6.2 Comparison of the peak load predictions of the crack band model of Bažant and Oh (1983a) with the experimental data of Walsh (1972).

A plane stress state was assumed for all the calculations. Although the width of the crack band (size of the square elements) was found to have very little effect, its optimum was approximately $w_c = 3d_a$ (d_a = maximum aggregate size), and this value was used throughout the computations.

The crack band theory was able to reproduce with accuracy the experimental results of Naus (1971), Walsh (1972), Kaplan (1961), Mindess, Lawrence and Kesler (1977), Huang (1981), Carpinteri (1980), Shah and McGarry (1971), Gjørv, Sorensen and Arnesen (1971), Hillerborg, Modéer and Petersson (1976), Sok, Baron and François (1979), Wecharatana and Shah (1980), Brown (1972), and Entov and Yagust (1975). As an example, we plot in Fig. 8.6.2a–f the results for the six Walsh's series (1972) described in Section 1.5 (see Tables 1.5.1 and 1.5.1, Series A1-A6, and Figs. 1.5.1 and 1.5.2).

8.6.2 Skew Meshes: Effective Width

The foregoing considerations are, of course, applicable even when a crack band of width h_c is embedded in a finite element of size h and is inclined with respect to the size of the element (Fig. 8.6.3a), an issue that has been used repeatedly in various fields. The idea of embedding a band of strain softening in a finite element was first developed for plastic shear bands (Pietruszczak and Mróz 1981), and the subsequent development of a finite element with an embedded crack band (Willam, Bićanić and Sture 1986; Willam, Pramono and Sture 1989) was mathematically analogous. Recently, a general and fully consistent three-dimensional formulation for an embedded strain-softening band in general finite elements was presented by Dvorkin, Cuitiño and Gioia (1990).

In the present formulation, the only modification that is necessary is to substitute a proper value for the volume fraction of the crack band within the element f. For square meshes, Bažant and Oh (1983a) proposed to use an effective bandwidth for the element h_b such that

$$f = \frac{h_c}{h_b} \qquad \text{with} \qquad h_b = \frac{h}{\cos\theta} \tag{8.6.10}$$

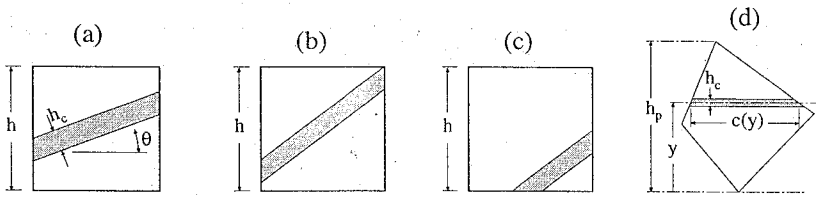

Figure 8.6.3 (a) Element skew to the crack band. (b) Centered band, with large volume fraction. (c) Lateral band, with small volume fraction. (d) Sketch to define the average volume fraction.

where θ is the angle between the band and the base of the element. An approximate generalization of this rule to irregular elements was proposed in Bažant (1985a). In general, however, such extrapolations to irregular elements can hardly be satisfactory, and a more general approach is needed.

The problem, however, is not trivial. The reason is that the volume fraction, when the crack band is inclined with respect to the element side, or the element is irregular, is not well defined: it depends on the precise position of the crack band with respect to the element. This is illustrated in Figs. 8.6.3b and c, for which the volume fractions are in the proportion 2:1, approximately. Therefore, either information on the position of the band within the element must be given —which is not possible if ordinary elements are used— or else, the bandwidth must be defined in an average sense. The average can be obtained in the following manner. Consider a bidimensional element of thickness b, arbitrary size and shape, and arbitrarily oriented with respect to the band, which is drawn horizontal (Fig. 8.6.3d). Let y be the axis normal to the band, with its origin at the lowest point of the element. If the band is located at distance y, as shown in the figure, the volume of the band is approximately given by $V(y) = h_c b c(y)$ where $c(y)$ is the length of the intercept of the center of the band with the element. Let $\varphi(y)dy$ be the probability that the band lies at a distance between y and $y + dy$. Then the average volume of the band is given by

$$V_b = h_c b \int_0^{h_p} \varphi(y) c(y)\, dy \tag{8.6.11}$$

where h_p is the maximum ordinate of the element, which coincides with the *projected element size*. If the probability density is uniform, then $\varphi = 1/h_p$ and we get

$$V_b = \frac{h_c}{h_p} b \int_0^{h_p} c(y)\, dy \tag{8.6.12}$$

but $b\int_0^{h_p} c(y)\, dy$ is the volume of the element, and therefore,

$$f = \frac{h_c}{h_p} \tag{8.6.13}$$

This indicates that for equally probable distributions, the element bandwidth coincides with the projected size of the element (projected on the normal of the crack band). This coincides with the formula proposed by Bažant (1985a) for rectangular meshes, and has been implemented in commercial finite element codes (e.g., SBETA; Červenka and Pukl 1994). However, it must be clearly understood that it is an average value, which may differ appreciably from the actual value for a particular element in a particular mesh.

The foregoing calculation is based on the assumption that the strain is uniform within the element, which is generally not the case because quadratic or higher order elements are used with various possible integration schemes (i.e., distribution of integration points). In such cases, the analysis would have to be redone starting from the virtual work equation (8.6.7), a task that is not straightforward. Rots (1988) used a trial-and-error method to determine the effective bandwidths of the elements for a particular problem, and Oliver (1989) proposed an objective formulation of an integral to define h_b. Červenka et al. (1995) empirically found that using the projected element size gave a still larger dissipation for inclined bands, and proposed a correction factor γ so that

$$h_b = \gamma h_p \tag{8.6.14}$$

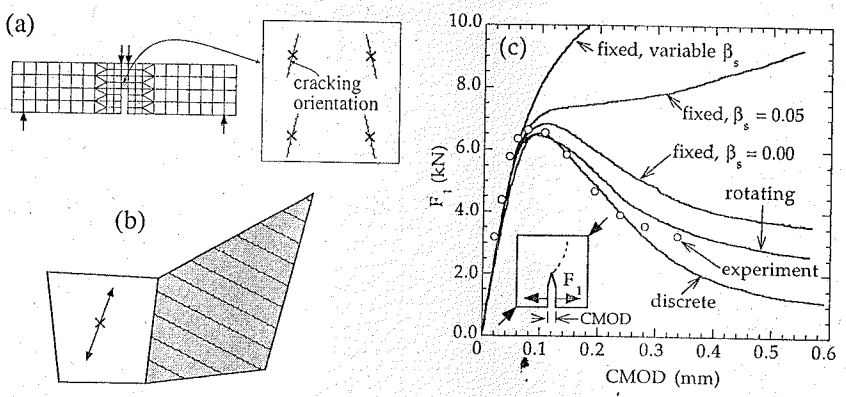

Figure 8.6.4 (a) Skew cracking orientation at the integration points. (b) Inclined cracking in the shaded element induces stress in the uncracked element (from Rots 1989). (c) Load-CMOD curves for a compact specimen under mixed mode loading (from Rots 1989).

Here γ varies linearly from 1 for element sides perpendicular to the band to $\gamma = 1.5$ for sides at 45°; in the case of irregular elements, an average side angle needs to be used. With this correction, they obtained results approximately independent of the orientation of the mesh, for mode I cases (bending and tension).

It seems that using conventional finite elements with plain smearing, as used in most finite element codes, implies a variable degree of uncertainty in the definition of the element bandwidth for meshes skew to the band. There are two alternatives to circumvent this problem: (1) use remeshing techniques to achieve a mesh in which the band runs parallel and perpendicular to the sides of the elements it crosses (see Fig. 8.7.3b), or (2) use enriched elements with embedded strain discontinuities similar to those described in Section 7.2.3. In fact, the displacement discontinuity in Oliver's element depicted in Fig. 7.2.10 is numerically implemented as a thin band with large, but finite, constant strain, very similar to an embedded crack band.

8.6.3 Stress Lock-In

As pointed out before, the crack band analysis for mode I and elements aligned with the crack path gives, in general, good results. Various details of numerical modeling, however, deserve attention. Leibengood, Darwin and Dodds (1986) modeled the crack band by square elements with four integration points straddling the line of symmetry. They showed that the results for the crack band and the discrete crack closely match each other if the cracking directions at the integration points within the finite elements are forced to be parallel to each other and to the symmetry line of the crack band. But if this parallelism is not enforced, the cracks form at different orientations at each integration point of the same element, as shown in Fig. 8.6.4a. Then the response predicted by the crack band model is somewhat stiffer than that predicted by the discrete crack model, even if the element sides are parallel to the true crack.

The reason for this behavior is that the integration points lying out of the symmetry plane sense the shear components, and so the cracks form at an angle. This results in spurious fracturing strain components parallel to the crack path, which cause large strains in the neighboring elements parallel to the main crack path, which results in overall stiffening. Although the crack growth is actually in mode I, the problem is aggravated because, at the integration points, the loading is interpreted as mixed mode. This is manifested by a spurious sensitivity of the solution to the shear retention factor β_s, which, for mode I, should be nil. A solution to this problem is to determine the crack normal and the cracking strain on the average or at a single integration point at the center of the element. This is actually the only way consistent with the hypothesis that the cracking strain is uniformly distributed over the element.

The foregoing problem is related to the phenomenon known as *stress lock-in*, that appears in mixed mode problems, when the crack grows skew to the mesh (Rots 1988, 1989). The stress lock-in consists

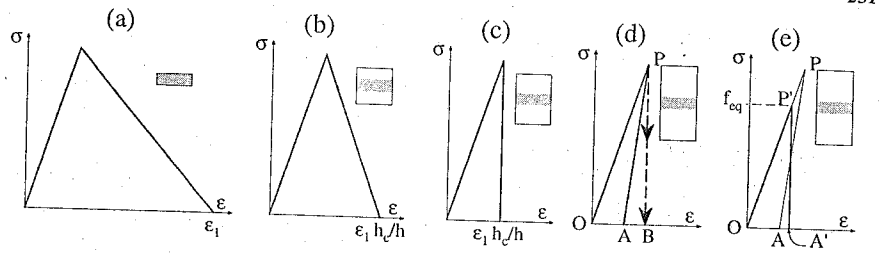

Figure 8.6.5 Linear softening and tensile stress modification.

in the effect that the elements near the crack band remain stressed after a nearly complete failure of the elements in the crack band, because the inelastic strain in the band induces stresses in the neighbors, as sketched in Fig. 8.6.4b. Rots' (1988, 1989) results indicate that the degree of stress lock-in is very sensitive to the shear retention factor, as illustrated by the results in Fig. 8.6.4c, corresponding to a double cantilever beam tested by Kobayashi et al. (1985). The fixed crack must be used with a zero shear retention factor to get a better approximation. In the example shown, the smeared crack model with the best behavior is the rotating crack model, but in other cases (single-notch sheared beams, for example), the fixed crack with a zero shear retention factor may be better (Rots 1988, 1989).

The only effective solution to this problem (keeping classical finite elements) is to first run the calculations with a standard mesh to get the approximate crack path, and then remesh to get mesh lines aligned with the crack path and run the calculation again (see also Section 8.7.4).

8.6.4 Use of Elements of Large Size

In all the foregoing analyses, it is assumed that the finite element is small enough for the resulting stress-strain curve to be stable. If the element is too large, then the resulting stress-strain curve has a snapback, as shown in Fig. 8.3.6d. If this occurs, the finite element analysis will be very difficult to stabilize and will dissipate more energy than it actually should. It may be argued that the problem should be solved by using smaller elements, but this may be computationally too expensive and it may be worth using larger elements if the accuracy is not greatly sacrificed.

To simplify the problem, let us consider the simple linear softening depicted in Fig. 8.6.5a for the actual crack band thickness h_c. If the element size is $h > h_c$, the stress-strain curve for the element is as shown in Fig. 8.6.5b. The softening branch becomes vertical when $\varepsilon_1 h_c/h = f_t'/E$ (see Fig. 8.6.5c), i.e., for $h = h_c \varepsilon_c E/f_t'$. Since in this linear case $G_F = h_c f_t' \varepsilon_1/2$, eliminating h_c leads to the simple condition

$$h = 2\ell_{ch} \tag{8.6.15}$$

Thus, for $h > 2\ell_{ch}$, a snapback occurs as shown in Fig. 8.6.5d. Because in the finite element computation the nodal displacements are controlled, the stress will drop to zero as soon as the peak is reached and the dissipated energy will appear to be the area OPB instead of the area OPA which is the correct value. This means that using larger elements will make the material appear tougher than it actually is.

A solution to this problem (Bažant 1985b,c) is to replace the actual stress-strain curve with snapback by a stress-strain diagram of the same area having a vertical stress drop (Fig. 8.6.5e). To keep the same area, one must reduce the tensile strength from f_t' to f_{eq} so that

$$h\frac{f_{eq}^{\,2}}{2E} = G_F \qquad \Rightarrow \qquad f_{eq} = f_t'\sqrt{\frac{2\ell_{ch}}{h}} \tag{8.6.16}$$

Thus, the strength must be reduced in inverse proportion to the square root of the element size. For the case of vertical stress drop, the fracture process zone has the smallest length permitted by the finite element subdivision. Therefore, this represents the closest possible approximation to LEFM. Since the element size is normally taken proportional to the structure size, this means that the crack band model with a vertical drop yields an approximate equivalent LEFM behavior for structures of large sizes. However,

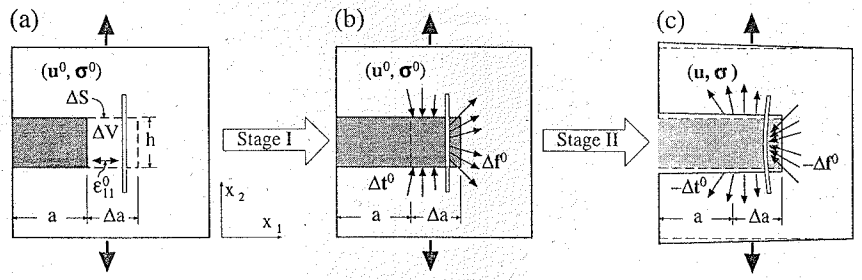

Figure 8.6.6 Sketch of the computational procedure of Bažant and Cedolin (1979, 1980): (a) initial state; (b) intermediate state; (c) final state.

this is not the only way to handle the problem of brittle behavior with large elements. In the following, an energy-based analysis is presented as a possible alternative.

8.6.5 Energy Criterion for Crack Bands with Sudden Cracking

As just described, if the cracks are assumed to form suddenly, i.e., the stress to drop suddenly to zero, a spurious mesh sensitivity and lack of objectivity appears because of the dependence of the apparent energy dissipation on the element size. This effect is eliminated by the previous equivalent strength method, but can also be eliminated by directly applying an energy criterion analogous to linear elastic fracture mechanics. The proper form of the energy criterion, which was obtained by Bažant and Cedolin (1979, 1980) by generalization of Rice's (1968b) energy analysis of the extension of a notch, can be formulated as follows. The crack band extension by length Δa into volume ΔV (of the next finite element, Fig. 8.6.6) may be decomposed for calculation purposes into two stages.

Stage I. Smeared cracks are created in concrete inside volume ΔV of the element ahead of the crack in the direction of tensile principal stress (Fig. 8.6.6b), while at the same time, the deformations and stresses in the rest of the body are imagined to remain fixed (frozen). This means that one must introduce surface tractions $\Delta \mathbf{t}^0$ applied on the boundary ΔS of volume ΔV, and distributed forces $\Delta \mathbf{f}^0$ applied at the concrete-steel interface, such that they replace the action of concrete that has cracked upon the remaining volume $V - \Delta V$ and upon the reinforcement within ΔV.

Stage II. Next, forces $\Delta \mathbf{t}^0$ and $\Delta \mathbf{f}^0$ (Fig. 8.6.6c) are released (unfrozen) by gradually applying the opposite forces $-\Delta \mathbf{t}^0$ and $-\Delta \mathbf{f}^0$, reaching in this way the final state.

Let $\mathbf{u}^0$ and $\boldsymbol{\varepsilon}^0$ be the displacement vector and strain tensor before the crack band advance, and let $\mathbf{u}$ and $\boldsymbol{\varepsilon}$ be the same quantities after the crack band advance. For the purpose of analysis, the reinforcement may be imagined to be smeared in a separate layer coupled in parallel and undergoing the same strains as concrete in the crack band. The interface forces between steel and concrete, $\Delta \mathbf{f}^0$, then appear as volume forces applied on the concrete layer.

Upon passing from the initial to the intermediate state (Stage I), the strains are kept unchanged while cracking goes on. Thus, the corresponding stress changes within concrete in ΔV are given by $\Delta\sigma_{11} = \sigma_{11}^0 - E'\varepsilon_{11}^0 = (\varepsilon_{11}^0 + \nu'\varepsilon_{22}^0)E'/(1-\nu'^2) - E'\varepsilon_{11}^0; \Delta\sigma_{22} = \sigma_{22}^0; \Delta\sigma_{12}^c = 0$ (cracks are assumed to propagate in the principal stress direction). Here, σ_{ij}^0 denote the components of stress carried before cracking by the concrete alone (they are defined as the forces in concrete per unit area of the steel-concrete composite); and E and ν are the Young's modulus and Poisson's ratio of concrete. The values $E' = E$ and $\nu' = \nu$ apply to plane stress and $E' = E/(1-\nu^2)$ and $\nu' = \nu/(1-\nu)$ to plane strain. The change in strain energy of the system during Stage I in Fig. 8.6.6b is given by the elastic energy initially stored in ΔV and released by cracking, i.e.,

$$\Delta U_1 = -\int_{\Delta V} \frac{1}{2}(\boldsymbol{\sigma}^0 \cdot \boldsymbol{\varepsilon}^0 - E'\varepsilon_{11}^{0\,2})dV. \tag{8.6.17}$$

The change in strain energy during Stage II is given by the work done by the forces $\Delta \mathbf{t}^0$ and $\Delta \mathbf{f}^0$ while

they are being released, i.e.,

$$\Delta U_2 = \int_{\Delta S} \frac{1}{2}\Delta \mathbf{t}^0 \cdot (\mathbf{u} - \mathbf{u}^0)dS + \int^{\Delta V} \frac{1}{2}\Delta \mathbf{f}^0 \cdot (\mathbf{u} - \mathbf{u}^0)dV. \tag{8.6.18}$$

Coefficients $1/2$ must be used because forces $\mathbf{t}$ and $\mathbf{f}$ at the end of Stage II are reduced to zero.

If the concrete is reinforced, part of the energy is consumed by the bond slip of reinforcing bars during cracking within volume ΔV. This part may be expressed as $\Delta W_b = \int_s F_b \delta_b ds$, in which δ_b represents the relative slip between the bars and the concrete which is required to accommodate fracture advance; F_b is the average bond force during displacement δ_b per unit length of the reinforcing bar (force during the slip); and s is the length of the bar segment within the actual fracture process zone of width h_c (and not within volume ΔV, since the energy consumed by bond slip would then depend on the element size).

The energy criterion for the crack band extension may now be expressed as follows:

$$\begin{aligned} \Delta U = U'\Delta a = G_f \Delta a - \Delta U_1 - \Delta U_2 - \Delta W_b > 0 \quad &\text{stable, no propagation} \\ = 0 \quad &\text{equilibrium propagation} \\ < 0 \quad &\text{unstable} \end{aligned} \tag{8.6.19}$$

Here ΔU is the energy that must be externally supplied to the structure to extend the crack band of width h by length Δa. (ΔU = total energy in the case of rapid, or adiabatic fracture, and Helmholtz free energy in the case of slow, isothermal fracture.) If $\Delta U > 0$, then no crack extension can occur without supplying energy to the structure, and so the crack band is stable and cannot propagate. If $\Delta U < 0$, crack band extension causes a spontaneous energy release by the structure, which is an unstable situation, and so the crack extension must happen dynamically, the excess energy $-\Delta U$ being transformed into kinetic energy. If $\Delta U = 0$, no energy needs to be supplied and none is released, and so the crack band can extend in a static manner.

For practical calculations, the volume integral in Eq. (8.6.17) needs to be expressed in terms of nodal displacements using the distribution functions of the finite element. The boundary integral in Eq. (8.6.18) is evaluated from the change of nodal forces acting on volume ΔV from the outside. The energy ΔU_2 released from the surrounding body into ΔV may also be alternatively calculated as the difference between the total strain energy contained in all the finite elements of the structure before and after the crack band advance. According to the principle of virtual work, the result is exactly the same as that from Eq. (8.6.18). This calculation, however, is possible only if the structure is perfectly elastic whereas Eq. (8.6.18) is correct even for inelastic behavior outside the process zone, providing Δa is so small that $\mathbf{t}$ and $\mathbf{f}$ vary almost linearly during Stage I.

It may also be noted that Pan, Marchertas and Kennedy (1983) calculated ΔU_2 in their crack band finite element program by means of the J-integral, keeping the integration contour the same for various crack lengths. This calculation must yield the same ΔU_2 if the integration contour passes through only the elastic part of the structure, except for crossing the crack band behind the fracture process zone where the stresses are already reduced to zero.

Under general loading, the crack band may propagate through a mesh of finite elements in an inclined direction, in which case the band has a zig-zag shape. This means that the crack length increment during the breakage of the next element is not well defined, and an effective crack extension Δa_e must then be used for the element. This crack extension is easily determined based on the effective bandwidth of the element, by writing that (for two dimensions) the area of the element ΔA_e must be identical to the effective bandwidth h_e times the effective crack extension Δa_e, and thus

$$\Delta a_e = \frac{\Delta A_e}{h_e} \tag{8.6.20}$$

where, if no further analysis is available, it may be assumed that the effective bandwidth is the projected element size h_p. For rectangular meshes this reduces to the formula proposed by Bažant (1985a).

The ability of the energy balance and equivalent strength methods to describe the fracture processes in large structures was demonstrated in a series of papers by Bažant and Cedolin (1979, 1980, 1983) and by Bažant and Oh (1983a). As an example of their results, we consider here the problem of a plain concrete panel with a center crack, as depicted in Fig. 8.6.7a. Bažant and Cedolin (1980) analyzed the results for

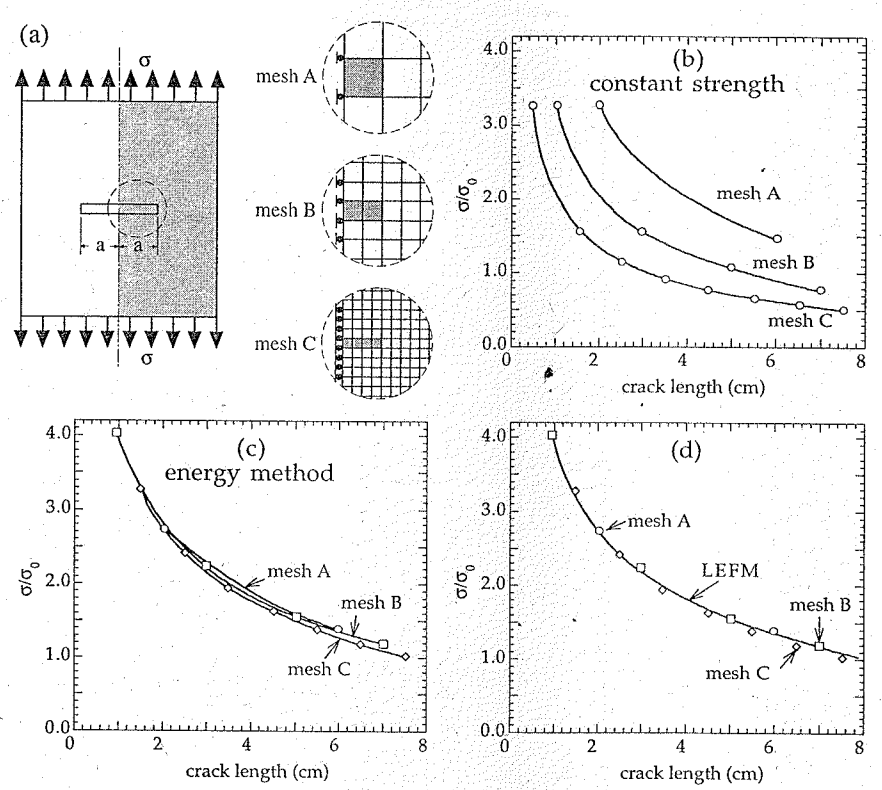

Figure 8.6.7 (a) Center-cracked panel analyzed by Bažant and Cedolin (1980). (b) Mesh-dependent results derived from constant-strength formulations. (c) Mesh independent results based on the energy formulation. (d) Comparison of the finite element results with the exact LEFM predictions.

three finite element meshes with element sizes in the relation 1:2:4, as sketched in Fig. 8.6.7a. If the classical tensile strength criterion (i.e., constant tensile strength) with sudden drop is used, the results shown in Fig. 8.6.7b are found, where it appears that the effect of the element size is tremendous. The strength for each crack length is seen to be smaller, the smaller the element size. This result may be expected because the results must converge to LEFM with an apparent fracture energy equal to the elastic energy density at fracture $f_t'/2E$ times the element width h. This means that $G_{F\text{apparent}} \propto h \to 0$ for $h \to 0$, and the strength tends to zero for infinite mesh refinement, which is obviously wrong.

On the contrary, Fig. 8.6.7c shows the result obtained following the energy balance method, which shows very little influence of the mesh size. The curves for the equivalent strength method closely follow the results of the energy method (Bažant and Cedolin 1980). To check that the results of the crack band analysis are not only mesh independent, but also accurate, it suffices to compare them with the prediction deduced from LEFM analysis, which can be obtained in closed form for this case (using the solutions for the center cracked panel and $K_{Ic} = \sqrt{EG_F}$). The comparison in Fig. 8.6.7d shows that the correspondence is excellent.

From the foregoing, we can conclude that if the mesh refinement is feasible so that $h < 2\ell_{ch}$, and if each element displays progressive softening, the classical finite element analysis suffices to get consistent results. For larger elements, either the equivalent strength approximation in Section 8.6.4 or the energy balance method just described, will give mesh-independent and accurate results.

Exercises

8.34 Consider a rectangular uniform mesh, with elements of dimensions h_x and h_y in the horizontal and vertical directions, respectively, and a crack band extending at an angle θ from the horizontal. Show that the mean or effective width for these elements is $h_b = h_x \sin\theta + h_y \cos\theta$. Show that for square meshes of size h, this reduces to $h\sqrt{2}\cos(45° - \theta)$ (Bažant 1985a).

8.35 Consider a rectangular uniform mesh, with elements of dimensions h_x and h_y in the horizontal and vertical directions, respectively, and a crack band extending at an angle θ from the horizontal. Show that the effective crack extension Δa_{eff} when a crack band extends by one element is given by $\Delta a_{\text{eff}} = h_x h_y/(h_x \sin\theta + h_y \cos\theta)$. Show that for square meshes of size h, this reduces to $h/[\sqrt{2}\cos(45° - \theta)]$ (Bažant 1985a).

8.36 To make a simple and fast analysis of a concrete gravity dam, a bidimensional model is generated, having approximately square elements with 3 m sides. The elastic modulus, strength, and fracture energy are estimated to be $E = 19$ GPa, $f_t' = 21$ MPa and $G_F = 92$ N/m. Determine the stress-strain curve with sudden strength drop that should be used.

8.7 Comparison of Crack Band and Cohesive Crack Approaches

During the 1980s, there was a lively debate on the relative merits and deficiencies of the crack band and cohesive crack representations of concrete fracture. There are four aspects of comparison to consider: (**1**) the ability to describe fracture that has localized in a single crack; (**2**) the ability to describe distributed fracture; (**3**) the ability to describe the micromechanical level; and (**4**) the possibility to predict fracture of arbitrary direction.

8.7.1 Localized fracture: Moot Point Computationally

First, we should recall that the cohesive crack model (i.e., the fictitious crack model of Hillerborg) and the crack band model yield about the same results (with differences of only about 1%, for $h = h_c$) if the stress-displacement relation in the fictitious crack model and the stress-strain relation in the crack band model are calibrated through Eq. (8.3.1), that is, if the crack opening displacement w is taken as the fracturing strain ε^f that is accumulated over the width h_c of the crack band. This equivalence, for example, follows from the fact that in the crack band model the results are almost insensitive to the choice of h_c, as well as h, and in the limit for $h \to 0$ the crack band model becomes identical to the fictitious crack model (provided that the fracture energy equivalence is preserved, of course).

Thus, the question "Discrete crack or crack band?" is moot from the viewpoint of computational modeling. The only point worthy of debate is computational effectiveness and convenience. In the cases where boundary integral methods can be applied, the use of the cohesive crack model can be computationally more efficient. When the general finite element method is used, these two models appear to be about equal when the fracture propagates along the mesh lines. However, the programming of the crack band model is generally easier, and that is why it has been preferred in the industry. For other fracture paths, there are various differences but special methods must be used for both models.

8.7.2 Nonlocalized Fracture: Third Parameter

As we recall from Section 7.1.3, if the shape of the tensile softening curve is fixed, then the cohesive crack (fictitious crack) model is defined by two material parameters, G_F and f_t'. The crack band model, on the other hand, is defined by three material parameters, G_F, f_t', and h_c. For the fictitious crack model, too, a third material parameter with dimensions of length, namely ℓ_{ch}, has been defined (see Section 7.1.3); however, this is a derived parameter, not an independent one, while h_c is an independent material parameter. Why does the crack band model, in its simplest form, have one more material parameter?

In answer to this question, we must first recall from Section 8.3.6 that, for localized fracture, the effect of the value of h_c on the results is almost negligible, provided, of course, that the softening part of the stress-strain diagram is adjusted so as to always yield the same fracture energy G_F for any value of

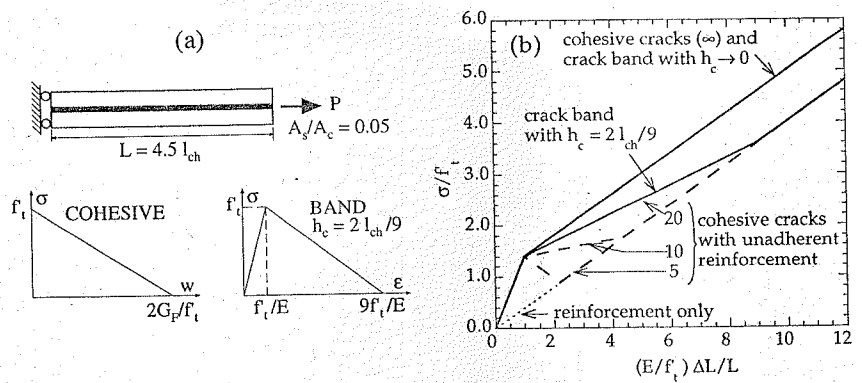

Figure 8.7.1 (a) Reinforced concrete bar and definition of linear cohesive crack model and the corresponding band model. (b) Resulting stress–mean strain curves for several possibilities (full lines are for adherent bar, dashed lines for unbonded bar).

h_c. Therefore, in the case of isolated fracture, the crack band model has, in effect, only two material parameters, G_F and f_t', just like the fictitious crack model.

The value of crack band width, h_c, however, does make a difference in the case of nonlocalized fracture, that is, when densely spaced parallel cracks can form. Such situations, in which the strain softening state is stable against localization (in the macroscopic sense), can arise in various situations; for example, when there is sufficient reinforcement that can stabilize distributed cracking against localization (this occurs when the reinforcement is so strong that the tangential stiffness matrix of the composite of steel and cracked concrete is positive definite even though that of cracked concrete alone is not). Another possibility is the parallel cracks caused by drying shrinkage, which may be stabilized (against localization into isolated fractures) by the intact concrete in front of the cracks, due to shear stiffness of the material. The same situation can arise in bending, if the beam is sufficiently reinforced.

From these examples it transpires that the physical significance of h_c is not really the width of the actual cracking zone at the fracture front but the minimum possible spacing of parallel cohesive cracks, each of which is equivalent to one crack band. Since adjacent crack bands cannot overlap (the material cannot be cracked twice), the distance between the symmetry lines of the adjacent crack bands is at least h_c.

Now, is it necessary that the minimum possible spacing of parallel cracks be a material fracture parameter? In the early analysis of the problem it seemed, based on some examples, that it was so. For example, Bažant (1985b, 1986a) discussed the problem of a reinforced concrete bar loaded in centric tension, see Fig. 8.7.1, where the reinforcing bar represents five percent of the cross section area. In that case, smeared cracking is stable against localization. Bažant's (1985b, 1986a) interpretation was that the cohesive cracks could form at any spacing, s, and as far as the fictitious crack model is concerned, these cracks could be arbitrarily close. He concluded that the number of cracks per unit length can approach infinity while each crack can have a finite opening width w. But this would mean that, according to the fictitious crack model, the energy dissipated by the cracking of concrete in the bar could approach infinity – a paradoxical result. On the other hand, if there is such a condition as the minimum spacing s, then, of course, the energy dissipated by the cracking in the bar is bounded, even according to the computations based on the fictitious crack model.

However, Bažant's theoretical example can be reinterpreted in different terms, as done by Planas and Elices (1993b). For these authors, the cracks can be infinitely close while having a vanishingly small crack opening. This implies that no appreciable softening takes place, and thus the concrete deforms at $\sigma = f_t'$. Therefore, the heavily reinforced concrete behaves in an elastic-perfectly plastic fashion. Moreover, this solution, with infinitely many cracks, is consistent with Bažant's simplified analysis, which assumed that the cross-sections of the bar remained plane during the stretching process and that full bond existed between the bar and the concrete. However, it is easily shown that if two cracks form at any finite spacing

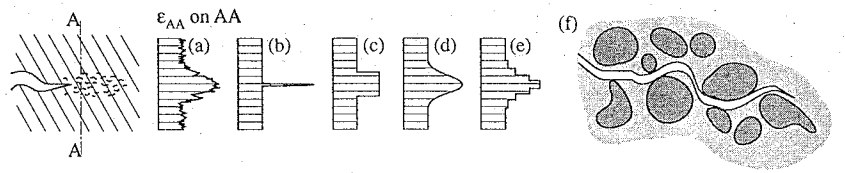

Figure 8.7.2 Strain distribution across the fracture process zone: (a) actual distribution; (b) cohesive crack approximation; (c) crack band model approximation; (d) nonlocal approximation; (e) finite element approximation (adapted from report of ACI Committee 446 1992). (f) Tortuous crack path.

s, the subsequent infinitesimal loading step causes the tensile strength to be exceeded at the middle point between them. Therefore, a third crack must form and we have cracks spaced at $s/2$. Repeating the reasoning *ad infinitum* it turns out that if the bar is bonded *and* if we assume plane cross sections to remain plane, then the only solution consistent with the cohesive crack model is that cohesive cracks form infinitely close to each other. However, we know by experiment that, at the end, a collection of discrete cracks appear, even for strongly reinforced bars. The key point in the explanation of this effect is that, upon localization, the sections cease to be plane, an effect that cannot be caught by the simple classical analysis.

It is worth to note that the solution based on the assumption of Planas and Elices does converge to the crack band solution for $h_c \to 0$, as shown in Fig. 8.7.1 by the full lines. The dashed lines correspond to localized crack solutions valid only if bond is neglected, in which case the reinforcement is not interacting with concrete except at the ends of the bar, and then the bifurcation analysis given in the first section indicates that both the cohesive crack model and the crack band model predict that a single crack will occur.

Therefore, the simplified analysis of this problem seems to show that, in accordance with Planas and Elices (1993b) hypothesis, it is still possible to use the cohesive crack model for fully distributed cracking in conjunction with an associated elastic-perfectly plastic Rankine model. The problem still remains, however, of determining when the fracture will localize. In their work on shrinkage, Planas and Elices made some special assumptions for the localization point, but pointed out that the actual localization must be determined by bifurcation analysis, which could be based on the principle of minimum second-order work (as done in the simple case of the series coupling model in Section 8.1.2 and justified thermodynamically in Bažant and Cedolin 1991, Sec. 10.1).

8.7.3 Relation to Micromechanics of Fracture

The normal microstrains across the fracture process zone may be distributed roughly as shown in Fig. 8.7.2a. The discrete fictitious crack model simplifies this random strain distribution as a Dirac delta function, Fig. 8.7.2b. The crack band model simplifies it as a rectangular strain distribution, Fig. 8.7.2c. The nonlocal continuum model, which we will discuss in Chapter 13, describes this strain distribution as a smooth bell-shaped profile across the crack band, as shown in Fig. 8.7.2d (cf. Bažant and Pijaudier-Cabot 1988). The finite element approximation to the nonlocal continuum simplifies the strain distribution in the form of several steps as in Fig. 8.7.2e. Now, which representation is more correct?

Among the simple distributions, i.e., those for the fictitious cohesive crack and the crack band (Figs. 8.7.2b-c) neither one is better or worse, as an approximation to the true distribution in Fig. 8.7.2a. Efforts have been made to physically observe the microcracks and strains throughout the fracture process zone. In optical microscopic observations, distributed cracking has not been seen in concrete (although it has been clearly observed in ceramics). The explanation might be that it is difficult to distinguish new very fine microcracks from the pre-existing ones, or that the microcracks on the fringes of the fracture process zone have extremely small openings while being extremely numerous and thus still contributing significantly to the overall relative displacement across the width of the fracture process zone.

With regard to the optical observations, it must be noted that fracture in concrete is normally highly tortuous, meandering to each side of the fracture axis by a distance approximately equal to the maximum aggregate size (Fig. 8.7.2f). Now, even if all the microcracking is concentrated on a line, but this line is

highly tortuous, the fracture is represented by a straight line crack no better than by a crack band of width of about two aggregate sizes. So, even if cohesive cracks are a reality for concrete, one still cannot claim that a *straight* fictitious crack is a more realistic model than a crack band.

It is also pertinent to mention that measurements of the localizations of the acoustic emission during the fracture process in concrete (Labuz, Shah and Dowding 1985; Maji and Shah 1988) indicate, despite considerable scatter, that the locations of the emission sources are spread over a relatively wide band in the frontal region of fracture. This tends to support the crack band model. On the other hand, various measurements of strains on the surface, for example by interferometry (Cedolin, DeiPoli and Iori 1983, 1987) or by laser holography (Miller, Shah and Bjelkhagen 1988), indicate that very high strains are concentrated within a very narrow zone at the front of fracture. This might be better modeled by a cohesive crack than a crack band. It should be noted, though, that the fracture strains might be localized at the surface of concrete specimens to a greater extent than in the invisible interior, due to the wall effect as well as other effects.

In view of the foregoing three arguments, there seems to be no compelling reason for rejecting either the crack band model or the cohesive (fictitious) crack model. The choice seems to be a matter of convenience of analysis. When the fracture shape is known in advance, both formulations appear to be about equally convenient. However, if the shape of the fracture is unknown in advance, the crack band model might be more convenient.

8.7.4 Fracture of Arbitrary Direction

Finite element modeling of fracture is easy and accurate only if the fracture runs along the mesh lines. If the fracture path is known in advance, either from experience or some preliminary calculations, then it is possible to design the mesh to accommodate the fracture path as a smooth path along the mesh lines. In general practical problems, however, the fracture path is not known. It is one of the unknowns to be found by analysis. In such general situations, which need to be tackled in general purpose finite element programs, there are basically two possibilities to proceed: either to modify the finite element mesh each time the fracture advances, or to keep a fixed mesh and allow the fracture to have a rugged boundary and zig-zag shape (Fig. 8.7.3c). The second possibility is not possible with the fictitious crack model, since it would cause serious problems with interlocking in the case of shear. On the other hand, the first possibility, that is, remeshing, exists both for the discrete fictitious crack and for the crack band, although in practice it has so far been used apparently only for the cohesive crack approach. The automatic remeshing (Fig. 8.7.3a,b) at crack advance is not simple to program; however, various research groups have nevertheless succeeded in developing finite element programs which do just that (see Section 7.2.3). So far, however, the remeshing approach has not gained a wide popularity, due to the complexity of remeshing.

Although remeshing has not yet been used in conjunction with the crack band modeling of fracture, one must realize that this is a possibility which would be no more complex than remeshing for the cohesive crack. The algorithm for remeshing as developed by Ingraffea and co-workers (Section 7.2.3) could, no doubt, be easily adapted for remeshing in the case of crack bands (Fig. 8.7.3b).

As normally perceived, however, one of the advantages of the crack band approach is that fracture of arbitrary direction can be represented without any remeshing. The next element that undergoes cracking is decided on the basis of either the strength criterion (for the tensile sudden stress drop) or the stress-strain relation with strain softening. The zig-zag band is normally found to propagate roughly in the direction of previous cracking, however, it is possible under certain situations (for example a strip of concentrated shear stress) to obtain propagation of the band of cracked elements in a direction that is inclined to the direction of cracking in the elements. This represents shear fracture or mixed mode fracture (e.g., Bažant and Pfeiffer 1986).

However, as discussed in Section 8.6.2 and Section 8.6.3, there are certain errors associated with a zig-zag crack band. Due to the inevitable development of shear stresses on the planes parallel to the overall direction of the zig-zag band, there is some degree of interlocking, i.e., an increased resistance to shear, larger than that obtained with a smooth crack (cohesive crack) or a smooth band with remeshing (Fig. 8.7.3a,b). Although, to a large extent, the errors are tolerable compared to other errors involved in the analysis of fracture, remedies are needed to obtain accurate results.

The problem can be partially alleviated by using a square mesh in which each square is subdivided

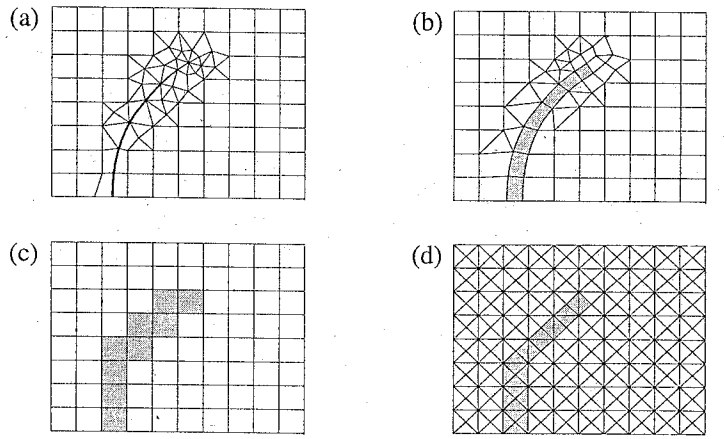

Figure 8.7.3 Description of fracture path inclined with respect to initial mesh lines: (a) cohesive crack with remeshing; (b) crack band with remeshing; (c) zig-zag crack band in a square mesh; (d) mesh allowing better representation of inclined fracture.

into four triangular elements. In this case, there are not only horizontal and vertical mesh lines, but also mesh lines at 45° inclinations (Fig. 8.7.3d). This kind of mesh, which allows approximating an arbitrary fracture propagation direction more closely, should always be used with the crack band model when the propagation direction is unknown.

A better remedy is to employ a nonlocal approach, to be discussed in the next chapter. This, however, brings the penalty that there must be several finite elements across the width of the crack band, which in turn necessitates either a more refined mesh in the fracture zone or an artificial increase of the width of the crack band (with the corresponding modification of the postpeak stress-strain relation). Probably the simplest solution is to use a standard mesh (of the type shown in Fig. 8.7.3d) to get the approximate crack path, and then remesh to fit the mesh lines to the crack path, as indicated in Fig. 8.7.3b, and recalculate.

10

Brittleness and Size Effect in Structural Design

Except for a terse review in the introduction to the book, we have so far focused on fracture specimens and have not given adequate attention to real structures, reinforced as well as unreinforced. We will focus attention on them in this chapter, however, with a deeper focus on some structures than others. After dealing in the first section with the general aspects of brittleness and size effect and the general procedures to introduce them in practical formulations, we will devote three sections to a relatively thorough analysis of two important types of structural failure: the diagonal shear of longitudinally reinforced beams (Section 10.2 and Section 10.3), and the reinforced beams in bending —with particular emphasis on lightly reinforced beams (Section 10.4). The last section of the chapter will concisely review some of the main issues for other structural elements, from torsion of beams to reinforced columns.

10.1 General Aspects of Size Effect and Brittleness in Concrete Structures

In the preceding chapter, it became obvious that the strength of geometrically similar specimens of a quasibrittle material —particularly concrete— can be written in the general form

$$\sigma_{Nu} = f_t' \phi\left(\frac{D}{\ell}, \text{geometry}\right) \tag{10.1.1}$$

where f_t' is the tensile strength, D a characteristic structural dimension, and ℓ a characteristic material size; we explicitly indicate that the function depends on geometry, which is equivalent to say that the dependence on D/ℓ is different for different structural types and loading.

The material characteristic size ℓ (as well as the function ϕ itself) is different for the various existing models. However, as shown in the previous chapter, all the models can be set to give very similar size effect predictions over the practical experimental range; thus, there is a strong correlation between the fracture parameters of the various models for a given material.

In principle, the foregoing equation can be computed for every geometry and material model. In practice, computations can be very complex except for some simple cases. Thus, simplified expressions are convenient to extrapolate the experimental results. The simplest of these expressions is Bažant's size effect law expounded in Chapters 1 and 6 —Eqs. (1.4.10) or (6.1.5). As discussed in the previous chapter, this law can be generalized to give more precise descriptions over a broader range of sizes and a broader range of geometries. However, the extended size effect laws, including those derived from cohesive models, require information that is usually lacking for the classical tests on which the formulas for the codes were based. Therefore, in this chapter, we mostly use the simplest (Bažant's) law in comparing the experimental trends and the theoretical size effect. The correlations in the previous chapter can then be used to shift to other models.

In this section, we first discuss the conditions under which Bažant's size effect law is expected to give a good description of the size effect; we then analyze the existing proposals to characterize the structural brittleness through a brittleness number. We conclude the section by examining the general methodology proposed by Bažant to generate size effect corrections to ultimate loads in codes, including the effect of reinforcement.

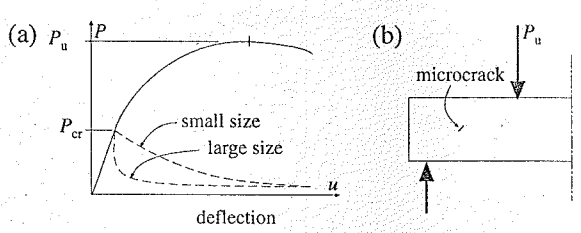

Figure 10.1.1 (a) Load-deflection curves for a relatively ductile structure (full line), and for a brittle structure that fails at first cracking (dashed line). (b) A brittle structure failing at crack initiation, the crack at maximum load still being microscopic.

10.1.1 Conditions for Extending Bažant's Size Effect Law to Structures

As briefly mentioned in Section 1.4.3, extension of the size effect law to real structures that have no notches is valid only if the following two additional hypotheses are fulfilled:

1. The structure must not fail at macrocrack initiation.
2. The shapes and lengths of the main fracture at the maximum loads of similar structures of different sizes must also be geometrically similar.

According to the available experimental evidence as well as finite element simulations, the foregoing assumptions appear to be satisfied for many types of failure of reinforced concrete structures within the size range that has been investigated so far. Let us examine the reasons for this, and the exceptions, more closely.

In a structure failing at crack initiation, the maximum load P_u is equal to the initial cracking load P_{cr} as indicated by the dashed load-deflection curve in Fig. 10.1.1a; in such a failure, the crack at maximum load is still microscopic, as shown in Fig. 10.1.1b. The case $P_u \approx P_{cr}$ can occur for metallic structures with initial flaws. But since the main purpose of reinforcing concrete is to prevent failure at crack initiation, good practice requires designing concrete structures in such a manner that $P_u \gg P_{cr}$ as illustrated by the solid load-deflection curve in Fig. 10.1.1a. For some types of failure this is explicitly required by the design codes (for example the ACI code requires that, for the bending failure, the maximum load, after applying the capacity reduction factor, be at least $1.25P_{cr}$, and for a good design it is normally much larger); furthermore, this is indirectly enforced by many other design code provisions on reinforcement layout. Then, the major cracks at P_u necessarily intersect a major portion of the cross section (say 30% – 90%).

There are, of course, cases in which the first condition is not met. This is the case for unnotched unreinforced structures such as the beams for rupture modulus tests (see Section 9.3), and some cases of footings, retaining walls, and pavement slabs. Except for these, and some cases of more theoretical than practical interest involving large under-reinforced structures, there is hardly any case of a structure failing at crack initiation, and so it is of little interest to develop the size effect formulation for failures at small cohesive cracks for other structure types.

The second hypothesis is illustrated in Fig. 10.1.2. This hypothesis means that the main fracture at the maximum load has the shape AB and $A'B'$. Point B' is located at same relative distance to the boundaries as point B. If the fracture front at the maximum load of the larger structure were at point C' rather than B', the size effect law could not apply. Likewise, it could not apply if the main fracture at maximum load were $A'B'$ or $A'E'$ for the larger structure in Fig. 10.1.2.

It appears that a deviation from this similarity of the main fractures at the maximum load is the main reason for the deviations from the size effect law which are observed in the Brazilian split-compression failure of cylinders of very large sizes (see Section 9.4).

The large major crack in a typical concrete structures at maximum load has the same effect as the notches in fracture specimens. In effect, well-designed structures develop, in a stable manner, large cracks which behave the same as notches. However, there is a small difference. In fracture specimens, the notches are cut precisely. In real structures, the growth of large major cracks is influenced by the

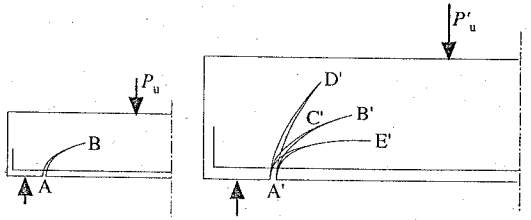

Figure 10.1.2 Illustration of the condition of crack similarity at peak load. Crack $A'B'$ in the large structure is similar to crack AB in the small structure. Cracks $A'C'$, $A'D'$, and $A'E'$ are not.

randomness of material properties, originating from material heterogeneity. Thus, the major fractures in similar structures of various sizes can be geometrically similar only on the average, in the statistical sense. In individual cases, there are deviations. For example, point B' can have a slightly smaller relative distance to the top boundary than point B. The consequence of this randomness is that in real structures in which there are no notches the measured maximum load values are more scattered than in fracture specimens. Further randomness is, of course, caused by environmental effects and their random fluctuations, by inferior quality control, etc. For this reason, the question of the precise shape of the size effect curve [for example, the question whether exponent r in Eq. (9.1.34) should be different from 1] is not practically very important.

It may be useful to also recall some other previously introduced assumptions. If the size effect should not be mixed with other influences, we must consider structures made of the same material, which means the same mix proportions and the same aggregate size distribution. If the maximum aggregate size d_a were increased in proportion to the structure size, the material in structures of different sizes would be different. This is not only because of the increased d_a, but also because a change in d_a requires a change in the mix proportions, particularly in the specific cement content.

10.1.2 Brittleness Number

The concept of brittleness of structural failure, which is the opposite of ductility, is an old one, but for a long time, the definition of brittleness has been fuzzy and has not stabilized. One of the fundamental reasons is that the apparent brittleness depends simultaneously on the material, the geometry of the structure and loading, and the size of the structure. Therefore, it is not easy to find a single figure properly incorporating all these influences.

The first idea in quantifying the brittleness is to look for a quantity that is vanishingly small for the perfect plasticity limit and infinitely large for the elastic-brittle limit. A number with these properties is the ratio D/ℓ appearing in the general size effect law (10.1.1). Therefore, any variable proportional to it is a good candidate to be a brittleness number:

$$\beta_n \propto \frac{D}{\ell} \tag{10.1.2}$$

Over the years, there have been various proposals for brittleness numbers of these forms. Well known in the metals community is the brittleness characterization based on Irwin's estimate of the nonlinear zone (see Section 5.2.2) which is at the basis of the ASTM E 399 condition for validity of the fracture toughness test. This brittleness number, say β_K, can be written as

$$\beta_K = \frac{D f_t'^2}{K_{Ic}^2} \tag{10.1.3}$$

With this definition, the condition for valid fracture toughness measurements reduces to $\beta_K \geq 2.5$.

In the field of concrete, probably the first ratio used as a brittleness number was put forward by Hillerborg

and co-workers. It was defined as

$$\beta_H = \frac{D}{\ell_{ch}}, \qquad \ell_{ch} = \frac{EG_F}{f_t'^2} \tag{10.1.4}$$

in which G_F refers to the fracture energy of the underlying cohesive crack model. Note that the foregoing two equations are essentially identical, because of Irwin's relationship $K_{Ic} = \sqrt{EG_F}$.

The foregoing brittleness numbers are useful to compare various materials and sizes for a given structural shape and loading, but they cannot be used directly to compare the brittleness of different structural geometries, because the dependence of brittleness on geometry is not included in their definition.

Pertaining to this category, but with a slightly different definition, is Carpinteri's brittleness number s_C (Carpinteri 1982):

$$s_C = \frac{G_F}{Df_t'} \tag{10.1.5}$$

We notice that it is the inverse of a brittleness (the more brittle, the smaller s_C), and should better be called a ductility number. Note also that it is related to the Hillerborg brittleness by

$$s_C = \frac{f_t'}{E}\,\frac{1}{\beta_H} \tag{10.1.6}$$

This means that Carpinteri's brittleness number can be used to compare brittleness of various materials only as long as they have the same f_t'/E ratio. It has the same limitations as β_H in not giving comparable results for different geometries.

To get a brittleness number that embodies the influences of material, geometry, and shape, we may recall the concept of intrinsic size defined in Section 5.3.3 and use the brittleness number defined as

$$\beta_n \propto \frac{\overline{D}}{\ell} \tag{10.1.7}$$

in which $\overline{D}$ is given by (5.3.11) and (5.3.12). The first brittleness number of this category was introduced by Bažant (1987a; also Bažant and Pfeiffer 1987), although the concept of intrinsic size was still to come. Bažant's brittleness number was defined as

$$\beta = \frac{\overline{D}}{c_f} = \frac{D}{D_0} \tag{10.1.8}$$

where the second expression is the original definition, which is equivalent to the first because of (6.2.2).

Brittleness numbers similar in concept, but based on the cohesive crack model have also been extensively used. Planas and Elices (1989a, 1991a) introduced the obvious extension of Hillerborg's brittleness number as

$$\beta_P = \frac{\overline{D}}{\ell_{ch}} \tag{10.1.9}$$

which gives a unified representation of the size effect and brittleness properties in the medium and large range of sizes ($\beta_P > 0.04$) for most laboratory geometries (Llorca, Planas and Elices 1989; Guinea, Planas and Elices 1994a).

The foregoing definition of β_P is, however, sensitive to the shape of the softening curve. Although (as discussed in Chapters 7 and 9) there is not much variability of shapes for ordinary concrete, it turned out to be better to use a brittleness number that refers the intrinsic size to the properties of the initial portion of the softening curve, characterized by the tensile strength and the horizontal intercept w_1 (Fig. 7.1.8); its definition is

$$\beta_1 = \frac{\overline{D}}{\ell_1}, \qquad \ell_1 = \frac{Ew_1}{2f_t'} \tag{10.1.10}$$

This brittleness number adequately captures the fracture properties for small and medium sizes, including most practical situations ($0.1 < \beta_1 < 1$). Moreover, from the Planas-Elices correlation (7.2.14), we get

$$\beta \approx 5.3\beta_1 \tag{10.1.11}$$

and it turns out that the two brittlenesses can be interchangeably used since the factor 5.3 is independent of the shape and size of the structure as well as of the material, as long as the material softening curve can be approximated by a straight line in its first part. This is usually the case for concrete. For granite, there is also evidence of this fact (Rocco et al. 1995). In the remainder of this chapter we will mainly use Bažant's brittleness number β.

10.1.3 Brittleness of High Strength Concrete

High strength concrete (HSC) is known to be more brittle than normal strength concrete (NC). This is so because c_f is smaller for HSC and then, for a given geometry $D_0^{HSC} < D_0^{NC}$. Therefore, considerable care must be exerted in extrapolating the results obtained for NC to HSC.

There are few data to establish general correlations. Gettu, Bažant and Karr (1990), based on size effect tests on notched beams, proposed the following approximate formula for HSC:

$$\frac{c_f^{HSC}}{c_f^{NC}} = \frac{D_0^{HSC}}{D_0^{NC}} \approx \left(\frac{f_c'^{NC}}{f_c'^{HSC}}\right)^{1/3} \tag{10.1.12}$$

where it is understood that the aggregate size is identical for both NC and HSC. However, this equation is a rough approximation. The aggregate shape, strength, and stiffness, or whether a crushed aggregate or river aggregate is used, etc. may have significant influence, too. Further studies are needed, but it is clear that the transitional size is substantially less for HSC and so the behavior is more brittle for HSC than for NC.

10.1.4 Size Effect Correction to Ultimate Load Formulas in Codes

In principle, plastic limit analysis is a wrong theory for the majority of the design code provisions which deal with brittle failures, such as diagonal shear, torsion, punching, pullout, etc. So, in fact, is LEFM. The theoretically best approach would be to base the design on nonlinear fracture mechanics taking into account the large size of the fracture process zone. However, as pointed out in the previous section, this would be quite complicated for the basic design problems covered by the code, and not really necessary because a highly accurate fracture analysis is not necessary for most situations. A simple way to obtain the load capacities corresponding to nonlinear fracture mechanics is to exploit the size effect law (1.4.10). Two kinds of formulas are possible:

1. One can start from the formula based on plastic limit analysis which now exists in the code, and introduce in it a correction due to the size effect law.
2. Alternatively, one can set up the ultimate load formula based on LEFM, and again introduce into it a correction according to the size effect law.

The first kind is no doubt preferable to the concrete engineering societies, because it makes it possible to retain the formulas that now exist in the codes, and introduce in them only a relatively minor correction (of course, the formula needs to be slightly scaled up because, for normal sizes, it must give about the same load capacity as before, even after the reduction for the typical structure size according to the size effect law has been introduced). Obviously, the accuracy of this type of correction would decrease with increasing size, as the behavior is getting more brittle and more remote from the size to which plastic limit analysis approximately applies. Some structures of normal sizes exhibit failures that are closer to limit analysis than to LEFM. For such structures, the accuracy by the first type of correction is adequate.

However, for very large structures or for certain types of failure (anchor pullout, diagonal shear), the failure is known to be very brittle, actually closer to LEFM than to plastic limit analysis. In that case, the second kind of formula, based on LEFM, must be expected to give a more realistic result. The error of this correction increases with a decreasing structure size and is the smallest for large sizes close to the LEFM asymptote.

In the remainder of this section, we discuss how to introduce the size effect correction into the formulas existing in the codes. We consider first the ideal case of plain concrete structures (or structures for which the steel does not contribute appreciably to strength, such as anchor pullout). Then we analyze how these formulas must be modified to include the contribution of the reinforcement.

10.1.5 Size Effect Correction to Strength-Based Formulas

For reinforced structures in which the steel does not contribute appreciably to the overall strength, one can expect a structural size effect approximately given by (1.4.10). This equation contains two parameters, Bf_t' and D_0, which would need to be specified for the new design formulas in the codes. Now, for very small sizes we must have $\sigma_{Nu} = \sigma_{Nu}^p$ in which σ_{Nu}^p is the plastic limit (i.e., the strength computed from plasticity or limit analysis). Therefore, in (1.4.10) we must have $Bf_t' = \sigma_{Nu}^p =$ and we can rewrite that equation as

$$\sigma_{Nu} = \frac{\sigma_{Nu}^p}{\sqrt{1+\beta}}, \qquad \beta = \frac{D}{D_0} \tag{10.1.13}$$

Since the design formulae in the code have been based both on limit analysis and experiments, one can assume that the code formula provides a prediction of the ultimate strength σ_{Nu}^C which coincides with the foregoing formula for the size used in the experiments that served to validate the code formula. We thus must have

$$\sigma_{Nu}^C = \frac{\sigma_{Nu}^p}{\sqrt{1+\beta_r}}, \qquad \beta = \frac{D_r}{D_0} \tag{10.1.14}$$

where D_r is the size of specimens used in the calibration tests (on average).

Solving for σ_{Nu}^p from (10.1.14) and substituting in (10.1.13) we get the size effect correction to the formulas in the code as

$$\sigma_{Nu} = \sigma_{Nu}^C \sqrt{\frac{1+\beta_r}{1+\beta}}, \qquad \beta = \frac{D}{D_0}. \tag{10.1.15}$$

where σ_{Nu}^C is the value obtained from the current formula in the code.

Assuming that D_r can be estimated from the data on the test series in the literature, the only parameter that needs to be estimated is D_0. Its theoretical calculation is more difficult because it depends both on the geometry of the structure and on the fracture properties of the material. Indeed, from (6.1.4) we have

$$D_0 = \frac{2k_0'}{k_0} c_f \tag{10.1.16}$$

which shows that D_0 consists of two factors. The first factor, $2k_0'/k_0$, is purely geometrical and can be easily determined by elastic calculations for notched specimens of positive geometry in which the relative crack length is well determined. For unnotched specimens, the problem is not well posed because the substitution of $\alpha_0 = 0$ leads to $D_0 = \infty$. Thus, slow crack growth must take place, as described in the previous section, and then α_0 is an unknown. Therefore, for these geometries the geometric factor must be determined either experimentally or by numerical simulation using a nonlinear fracture model.

The second factor is a material property which should, in principle, be experimentally determined for each concrete, but this would be impractical. The optimum approach would be to get a sound correlation between c_f and the basic characteristics of concrete, particularly f_c' and the aggregate size d_a. Unfortunately, such correlation is still unavailable.

Certain approximations, however, exist for some particular cases. For example, although the theoretical and experimental support is limited, Bažant and co-workers suggested that approximately $c_f \propto d_a$, where d_a is the maximum aggregate size. Thus, according to (10.1.16), for a fixed structural geometry also $D_0 \propto d_a$. The proportionality factor can be obtained by analysis of the existing experimental data. For example, from the tests of diagonal shear failure of beams, one can recommend the value $D_0 = 25d_a$. These values are only estimates based on seven classical data series studied by Bažant and Kim (1984) and Bažant and Sun (1987); see Section 10.2.2. However, the size of the beam was not the only parameter varied and the size range was not broad enough; because of other influences, such as differences in the shear span and the overall span to length ratio, as well as the use of different concretes, the scatter of these data was very large. Nevertheless, the size effect trend is clearly evident and makes it possible to obtain the aforementioned value of D_0, valid, of course, only for diagonal shear (see Section 10.2).

10.1.6 Effect of Reinforcement

To counteract brittle failure, one may use densely distributed reinforcement such as shear (or torsional) stirrups in beams. Together with the longitudinal reinforcement of beams, the shear reinforcement alone, at its yield limit, can resist a certain load, characterized by a nominal stress σ_{Nu}^s. When the structure is sufficiently large, there may be enough strain energy stored in the structure to drive a crack through the entire cross section at a load that only slightly exceeds the load carried by plastic reinforcement. However, there can be no size effect if that load is not exceeded. So, the size effect law must be applied only to the portion of the load capacity or nominal stress that is in excess of σ_{Nu}^s, that is

$$\sigma_{Nu} = \sigma_{Nu}^s + \sigma_{Nu}^c, \qquad \sigma_{Nu}^c = \frac{\sigma_{Nu}^{cp}}{\sqrt{1+\beta(\rho)}}, \qquad \beta(\rho) = \frac{D}{D_0(\rho)} \tag{10.1.17}$$

where σ_{Nu}^{cp} is a possible contribution of concrete to the overall strength at the plastic limit, $D_0(\rho)$ is a function with the dimension of length, and ρ is the steel reinforcement ratio. Note the explicit dependence of the brittleness number on the steel ratio.

The procedure to determine σ_{Nu}^{cp} is analogous to that sketched in the previous section, and requires no more than using the classical formulas of the code in (10.1.15). The determination of $D_0(\rho)$ is more difficult. For plain concrete, Eq. (10.1.16) shows that D_0 is a constant that is determined by the material fracture property c_f and the structure geometry. Now, the structure geometry is altered by the presence of the reinforcement. Therefore, the geometrical factor must depend on the steel ratio as well as on other dimensionless ratios defining the layout of the reinforcement.

Let us now sketch a possible unified framework for the influence of the steel ratio on the value of D_0. We write β in the form (10.1.8) and substitute the general form (5.3.11) for $\overline{D}$:

$$\beta = \frac{\overline{D}}{c_f} = \frac{K_I}{c_f 2\partial_a K_I} \tag{10.1.18}$$

where ∂_a denotes partial differentiation with respect to a. Next, we use the superposition principle and write the condition that the stress intensity factor is the sum of the stress intensity without reinforcement, minus the stress intensity factor caused by the steel-concrete interaction. The negative sign is due to the fact that the steel forces tend to close the crack. The resulting equation for K_I can always be written in the form

$$K_I = \sigma_N \sqrt{D} k(\alpha) - \rho \sigma_s \sqrt{D} k_s(\alpha) \tag{10.1.19}$$

where σ_s is the stress in the steel bar and $k_s(\alpha)$ a shape factor taking into account the steel distribution.

The simplest behavior one can encounter is that in which the effect of the reinforcement is exactly equivalent to decreasing the externally applied load (a pure parallel coupling). For such cases, $k_s(\alpha) \propto k(\alpha)$ and

$$\beta(\rho) = \beta(0) = \beta\,, \qquad D_0(\rho) = D_0(0) = D_0 \tag{10.1.20}$$

Pure cases of this kind are difficult to find in practice, but the results of Bažant and Kim (1984) seem to indicate that this is approximately valid for longitudinal reinforcement in diagonal shear.

For a densely distributed reinforcement, the behavior is quite different and one cannot assume that $k_s \propto k$. The result for $D_0(\rho)$ is then obtained as

$$D_0(\rho) = \frac{1 - m_1\rho}{1 - m_0\rho} D_0\,, \qquad m_1 = \frac{\sigma_s k_s(\alpha_0)}{\sigma_N k(\alpha_0)}\,, \qquad m_0 = \frac{\sigma_s k_s'(\alpha_0)}{\sigma_N k'(\alpha_0)} \tag{10.1.21}$$

For small values of ρ, we can take a MacLaurin expansion and write

$$D_0(\rho) \approx (1 + m\,\rho)\, D_0\,, \qquad m = m_0 - m_1 \tag{10.1.22}$$

This is the form postulated by Bažant and Sun (1987) for the influence of the stirrups on the size effect in diagonal shear. As it transpires from the foregoing derivation, m is a geometrical factor that can be, in principle, determined either from experiment or from numerical simulation. As an example, for

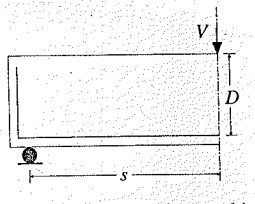

Figure 10.1.3 Longitudinally reinforced beam subjected to constant shear.

the diagonal shear of beams, Bažant and Sun (1987) proposed the following formula, determined by optimization of data fits and the condition that $m \to 0$ for short spans and $m \to$ constant for large spans:

$$m = 400\left[1 + \tanh\left(2\frac{s}{D} - 5.6\right)\right] \tag{10.1.23}$$

where s is the shear span and D the effective depth of the reinforcement (see Fig. 10.1.3).

10.2 Diagonal Shear Failure of Beams

10.2.1 Introduction

In the current ACI Standard 318 (Sec. 11.3), the nominal shear strength is not based on the ultimate load data but on data on the load that causes the formation of the first large cracks. The current ACI formula can be written:

$$\sigma_{Nu} \equiv v_c = \sigma_1\left(1.9\sqrt{\frac{f'_c}{\sigma_1}} + 2500\rho_w\frac{D}{s'}\right) \le 3.5\sigma_1\sqrt{\frac{f'_c}{\sigma_1}}, \qquad \sigma_1 = 1 \text{ psi} = 6.895 \text{ kPa} \tag{10.2.1}$$

where $v_c = V_c/(b_w D)$ nominal shear strength provided by concrete, D = effective depth of the longitudinal steel, b_w = width of the beam web, f'_c = compressive strength of concrete, ρ_w = longitudinal steel reinforcement ratio, and

$$s' = \frac{M_u}{V_u} \tag{10.2.2}$$

in which V_u = factored shear force at ultimate, M_u = factored moment at ultimate. For the case of constant shear of Fig. 10.1.3 $s' = s$.

If the first diagonal shear crack were considered to be very small compared to beam depth D, no size effect would occur, as implied by Eq. (10.2.1). However, it seems that most data refer to the formation of relatively large cracks, in which the size effect ought to occur even though it is ignored in Eq. (10.2.1).

The fact that the strength-based failure criterion used in contemporary design codes is not very realistic is, for example, confirmed by the extremely large scatter of the vast amount of test data available in the literature (Park and Paulay 1975; Bažant and Kim 1984; Bažant and Sun 1987). Moreover, in the commentary to the ACI Code (Sec. R11.3.2.1) it is acknowledged that the diagonal shear failure experiments of Kani (1966, 1967) reveal a decrease of the shear strength with the depths of the beam. These results are not considered in the code ACI 318-89, which is justified by assuming the code to be based on the load at initiation of very small cracks rather than formation of first large cracks or the ultimate load. For deep beams such that $L/D < 5$ (L = clear span of the beam), the nominal shear strength is obtained by multiplying Eq. (10.2.1) with the factor $(3.5 - 2.5s'/D)$, which is intended to introduce the increase of the shear strength from the first cracking load to the ultimate load in deep beams. (This is explained by assuming that the mode of shear resistance changes from flexure to arch action or the action of diagonal compression struts.)

Some revisions to the code that partially addressed some concerns stemming from fracture mechanics were proposed by ACI–ASCE Committee 426 (1973, 1974, 1977) and by MacGregor and Gergely (1977),

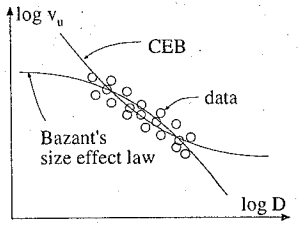

Figure 10.2.1 Experimental data are available only for a range over which both the CEB formula and Bažant's equation describe the results adequately, given the large experimental scatter.

but have not been incorporated into the ACI Code (they were proposed on the basis of an exhaustive study of experimental data obtained prior to 1974). Reinhardt (1981a) analyzed some suitably chosen test data and in 1981 found that there was a size effect and that it agreed quite well with LEFM. Later, however, the LEFM size effect was found to be too strong by Bažant and Kim (1984).

These authors, and also Bažant and Sun (1987), concluded from a statistical analysis of over 400 test series that the code approach to design, which is not based on the maximum load, does not provide a uniform margin of safety against failure of beam of various sizes because it ignores size effect. They noted that introduction of the size effect law leads to a better agreement with the ultimate load test data compared to the current ACI Code formulas which lack the size effect (as well as an LEFM-type formula proposed by Reinhardt, in which the nominal strength decreases inversely to the $\sqrt{D}$, which is too strong).

An empirical formula for the size effect in diagonal shear has been introduced in the CEB Model Code design recommendations (CEB 1991). It has the form $v_u = v_0(1 + \sqrt{D_0/D})$, where v_0 and D_0 are constants. This formula, however, has the opposite asymptotic behavior than the size effect law. For large sizes, it approaches a horizontal asymptote, and for small sizes it approaches an inclined asymptote of slope -1/2, which cannot be logically justified. The reason that this formula compared acceptably with the test data is that the data used pertained only to the middle of the size range. Due to scatter, distinguishing various laws without any theory is impossible for such limited data, as illustrated in Fig. 10.2.1.

The diagonal shear strength was also investigated using the cohesive crack model by Gustafsson (1985) and Gustafsson and Hillerborg (1988), but not with the aim to produce code formulas. Rather, their objective was to show that a size effect was theoretically predicted and to investigate how the shear strength is influenced by the fracture properties, particularly the fracture energy.

Other models have also been used to analyze the diagonal shear of beams. Jenq and Shah (1989) extended their two parameter model to describe crack growth in mixed mode and applied it to diagonal shear. A nonlocal microplane has also been used to analyze the size effect in diagonal shear of beams (Bažant, Ožbolt and Eligehausen 1994; Ožbolt and Eligehausen 1995)

In this section, some of the most important results of the aforementioned works are summarized. In the next section, a recent modification of the classical truss model (or strut-and-tie model) is described which approximately captures the effect of energy release and explains the physical mechanism of size effect in a simple, easily understandable way.

10.2.2 Bažant-Kim-Sun Formulas

Bažant and Kim (1984) and Bažant and Sun (1987) developed a set of phenomenological equations to describe the dependence of the diagonal shear strength on the size, shape, and steel ratios of beams failing in diagonal shear. The work of Bažant and Kim has three essential ingredients. The first one is the general structure of the formula which is based on the approach described in Section 10.1.5, and thus takes the form (10.1.13). The second is the development of a rather general expression for σ^p_{Nu} derived by analyzing the arch action and the composite beam action and summing their contributions. The combination of these

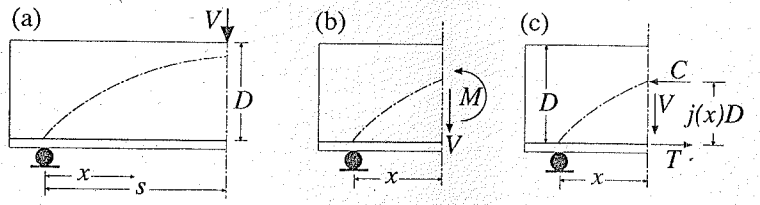

Figure 10.2.2 Diagonal shear strength analysis of Bažant and Kim (1984): (a) geometry; (b) actions at intermediate cross section; (c) decomposition of normal forces.

two ingredients lead the authors to the general formula for the shear strength effect:

$$\sigma_{Nu} \equiv v_u = \frac{v_u^p}{\sqrt{1 + D/D_0}} \tag{10.2.3}$$

$$v_u^p = \sigma_1 k_1 \rho^p \left[\left(\frac{f_c'}{\sigma_1} \right)^q + k_2 \sqrt{\rho} \left(\frac{D}{s} \right)^r \right] , \qquad \sigma_1 = 1 \text{ psi} = 6.895 \text{ kPa} \tag{10.2.4}$$

in which we recognize the numerator v_u^p as equivalent to σ_{Nu}^p, and where p, q, r, k_1, and k_2 are dimensionless constants.

The expression for v_u^p is similar to that used in the ACI Code (10.2.1), but it is to a greater extent based on mechanics analysis and contains more empirical parameters, namely k_1, k_2, p, q, and r. As pointed out in Section 10.1.5, the parameter D_0, characterizing the size effect, must also be empirically determined.

Bažant and Kim's derivation of the general expression for v_u^p follows the classical trends in simplified structural analysis. Consider the end portion of the beam as depicted in Fig. 10.2.2a. The overall actions V and M at a cross-section at x are as shown in Fig. 10.2.2b. The normal forces at the cross-section can be decomposed into the steel force $T(x)$ and the compressive resultant on the concrete, $C(x)$, located at distance $j(x)D$ above the reinforcement (Fig. 10.2.2c). Then, from the horizontal equilibrium condition, we have $C(x) = T(x)$, and from the condition of equilibrium of moments,

$$M(x) = T(x) j(x) D \tag{10.2.5}$$

The overall equilibrium equation for the beam requires that $V = \partial M(x)/\partial x$ and thus

$$V = V_1 + V_2 , \qquad V_1 = \frac{dT(x)}{dx} j(x) D , \qquad V_2 = \frac{dj(x)}{dx} T(x) D \tag{10.2.6}$$

where V_1 and V_2 are known as the composite beam action and arch action, respectively. Bažant and Kim empirically approximated $j(x)$ by a power law function:

$$j(x) = k \rho^{-m} \left(\frac{x}{s} \right)^r \frac{dj(x)}{dx} T(x) D \tag{10.2.7}$$

The value of dT/dx is obtained from the equilibrium condition along the reinforcement which requires $dT/dx = n_b \pi D_b \tau_b$, where n_b is the number of bars, πD_b their perimeter, and τ_b the shear bond stress. Since the perimeter of the bars is proportional to the square root of their area —hence, proportional to $\sqrt{\rho}$— and the ultimate bond strength is roughly proportional to $f_c'^q$ with $q = 1/2$, Bažant and Kim were able to write V_1 at the critical section $x = s$ as

$$V_1 = k_0 \rho^{1/2 - m} f_c'^q b D \tag{10.2.8}$$

where k_0 is a constant. Next, using (10.2.7) and assuming that the critical cross section for arch action is at $x = D$, and that, at failure, the steel stress is a constant, they found

$$V_2 = c_0 \rho^{1-m} \left(\frac{x}{s} \right)^r b D \tag{10.2.9}$$

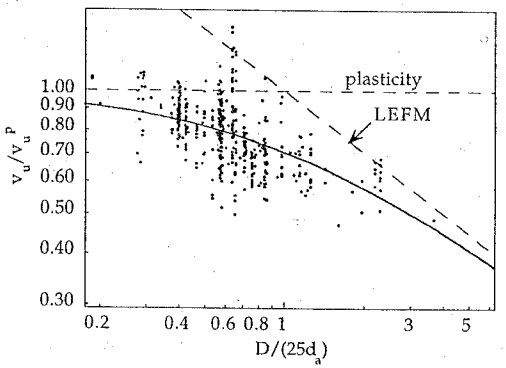

Figure 10.2.3 Size-effect plot for Bažant-Kim-Sun formula, compared to 461 available data points for beams without stirrups (data from Bažant and Sun 1987).

Substituting the last two expressions into the first of (10.2.6) and rearranging leads to Eq. (10.2.4) for v_u^p (where the dummy stress σ_1 has been introduced for dimensional compatibility).

Bažant and Kim compared this formula to a large number of tests from the literature in order to get average values for the foregoing empirical parameters. It was shown that Bažant's size effect law was able to describe the size dependence of the classical data by Kani (1966, 1967) and Walraven (1978). As shown in Section 1.5, this finding was further supported by the tests by Bažant and Kazemi (1991); Fig. 1.5.7, series K1 and K2.

Comparison of equation (10.2.3) to the results from seven classical data series was used by Bažant and Kim to optimize the parameters in that equation. The values of the parameters so determined were as follows :

$$p = \frac{1}{3} , \quad q = \frac{1}{2} , \quad r = \frac{5}{2} , \quad k_1 = 10, \quad k_2 = 3000, \quad D_0 = 25 d_a \tag{10.2.10}$$

With this formula, Bažant and Kim were able to fit 296 experimental data points with a coefficient of variation of 30%, much better than the ACI formula.

Later, Bažant and Sun (1987) further improved Eq. (10.2.4) by introducing the effect of maximum aggregate size d_a. This led to the replacement of the value 10 for the factor k_1 in (10.2.10) with the expression

$$k_1 = 6.5 \left(1 + \sqrt{c_0/d_a} \right) , \qquad c_0 = 0.2 \text{ in} = 5.1 \text{ mm} \tag{10.2.11}$$

Bažant and Sun also collected and tabulated a still larger set of data than Bažant and Kim (1984), involving 461 test data, and showed that the improved formula gives still better results, reducing the coefficient of variation to 25%. Fig. 10.2.3 shows the size effect plot for the 461 data points.

Bažant and Sun further introduced in the formula the influence of the stirrups that the ACI code neglects. Although in the original work the approach was completely empirical, a theoretical background is now provided by the analysis in Section 10.1.6. The equations (10.1.22) and (10.1.23) introduce the modification of the size effect due to the stirrups. Thus, the final formula taking all factors into account is

$$v_u = v_u^s + v_u^{pc} \left[1 + \frac{D}{D_0} \right]^{-1/2} \tag{10.2.12}$$

in which v_u^s, v_u^{pc} and D_0 are given by

$$v_u^s = \rho_v f_{yv} (\sin\alpha + \cos\alpha) \tag{10.2.13}$$

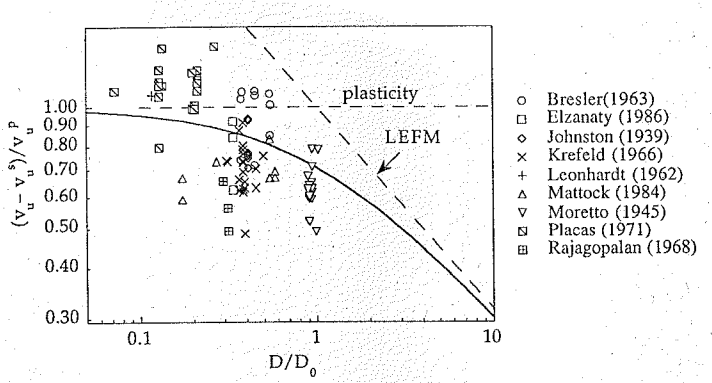

Figure 10.2.4 Size-effect plot for Bažant-Kim-Sun formula, compared to 87 available data points for beams of rectangular cross section with stirrups (data from Bažant and Sun 1987).

$$v_u^{pc} = \sigma_1 c_1 \sqrt[3]{\rho}\left[\sqrt{\frac{f_c'}{\sigma_1}} + 3000\sqrt{\frac{\rho}{(s/D)^5}}\right], \qquad \sigma_1 = 1 \text{ psi} = 6.895 \text{ kPa} \tag{10.2.14}$$

$$D_0 = 25 d_a (1 + m\rho_v) \tag{10.2.15}$$

in which ρ_v is the steel ratio of stirrups ,f_{yv} the yield strength of the stirrups, $c_1 = 6.5$, and m is given by (10.1.23). The foregoing value of c_1 is adequate to obtain the best fit on average. For design, c_1 is reduced to $c_1 = 4.5$.

Fig. 10.2.4 shows the size effect plot for Bažant-Kim-Sun formula and 87 available data points for beams of a rectangular cross section with stirrups from the test data listed by Bažant and Sun (1987). Although the scatter is large, the experimental results lie relatively close to the Bažant-Kim-Sun formula, closer than to other expressions including the ACI formulas.

10.2.3 Gustafsson-Hillerborg Analysis

Gustafsson (1985) and Gustafsson and Hillerborg (1988) performed approximate analysis of diagonal shear failure of reinforced beams of various depths. In their analysis, they assumed that a single polygonal cohesive crack with linear softening was formed as depicted in Fig. 10.2.5a, while the bulk of the concrete remained linear elastic. The interaction between steel and concrete was represented by the curve of shear stress vs. bond slip displacement, which was assumed to be of the elastic-perfectly plastic type (Fig. 10.2.5b). The behavior of the reinforcing steel was assumed to be linear elastic all the time. To determine the strength of the beam, 5 possible crack paths, as shown in Fig. 10.2.5c, were analyzed using finite elements. A typical, albeit idealized, load-displacement curve is shown in Fig. 10.2.5d. There is a maximum M caused by the failure of the concrete in tension followed, eventually, by a snapback. However, since in the computation the material surrounding the crack is assumed to be linear elastic, the load starts to increase again due to progressive stressing of the reinforcement. If the material behavior were really elastic, the load would increase forever along the dashed curve, approaching an asymptote (dash-dot line) corresponding to a fully cracked concrete sewed up by the reinforcement.

Of course, this is not actually possible, and failure does occur either by yielding of reinforcement or by crushing of concrete in the compressed ligament. In the analysis of Gustafsson and Hillerborg, only the crushing of concrete is considered. To this end, at each crack growth step Gustafsson and Hillerborg make a check of the integrity of the ligament based on the criterion described below. The computation ends at a certain point C in Fig. 10.2.5d when the crushing criterion is satisfied. Gustafsson and Hillerborg found that point C lies above point M for the cracks closer to the loading cross-section (path 1) and goes down as the path deviates more and more from the vertical. Fig. 10.2.5e sketches the values of the load

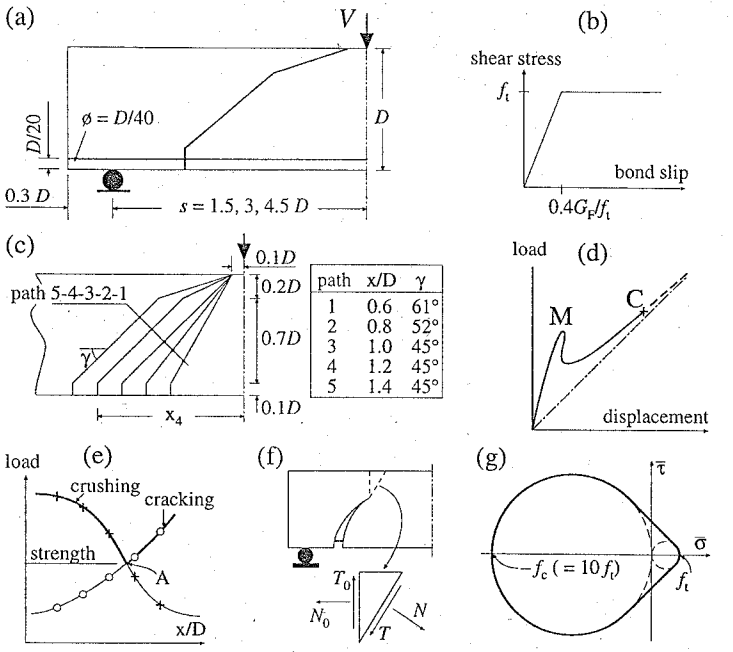

Figure 10.2.5 Gustafsson-Hillerborg model. (a) Geometry of the problem with polygonal cohesive crack path. (b) Bond stress-slip relationship. (c) Crack paths considered in the calculation. (d) Idealized load-displacement curve. (e) Cracking and crushing load vs. crack path mouth position and definition of beam strength. (f) Normal and shear forces across the ligament. (g) Crushing criterion. (Adapted from Gustafsson 1985.)

corresponding to points M (circles) and C (crosses) vs. the relative position of the crack mouth x/D (see Fig. 10.2.5a). Since the strength for a given path is given by the upper branch (heavy line), Gustafsson and Hillerborg assumed that the actual strength of the beam corresponds to the path with less strength, given by point A in the figure. For this path, the loads for point M and C are identical (identical cracking and crushing strength).

A few words regarding the crushing failure criterion. At each step in the calculation, the resultant normal and shear forces(N_0, T_0) across the uncracked ligament were computed (Fig. 10.2.5f). From them and the equilibrium condition, the normal and shear forces (N, T) across any plane at an arbitrary angle could be computed, as well as the corresponding average stresses $(\overline{\sigma}, \overline{\tau})$. Gustafsson and Petersson postulated that crushing failure occurred as soon as, for some orientation, a criterion defined by a condition $F(\overline{\sigma}, \overline{\tau}) = 0$ was met, where the criterion was graphically defined as depicted in Fig. 10.2.5g.

Using the foregoing approach, Gustafsson and Hillerborg analyzed the influence of the size (beam depth), the steel ratio ρ, and the shear span ratio s/D. Fig. 10.2.6 summarizes the results of their computations. Although Gustafsson and Hillerborg proposed a size effect in which $v_u \propto D^{-1/4}$ for $0.4 \leq D/\ell_{ch} \leq 5$, as suggested by other researchers, it appears that an exponent of -0.3 instead of -0.25 fits the results better (dashed lines in Fig. 10.2.6).

10.2.4 LEFM Analyses of Jenq and Shah and of Karihaloo

Jenq and Shah (1989) analyzed diagonal shear fracture using LEFM. They considered the idealized diagonal crack shown in Fig. 10.2.7a and approximated the solution as the superposition of the cases

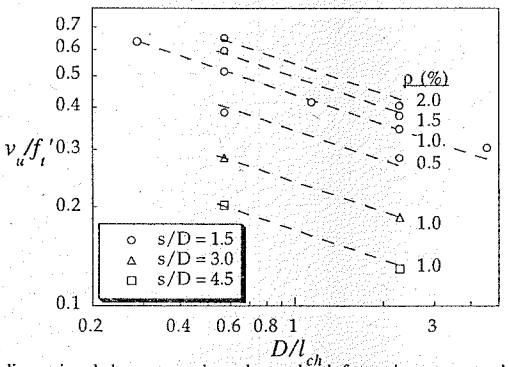

Figure 10.2.6 Nondimensional shear strength vs. beam depth for various span-to-depth ratios and steel ratios according to Gustafsson and Hillerborg model (data from Gustafsson 1985). The dashed lines correspond to power law expressions of the form $v_u \propto D^{-0.3}$.

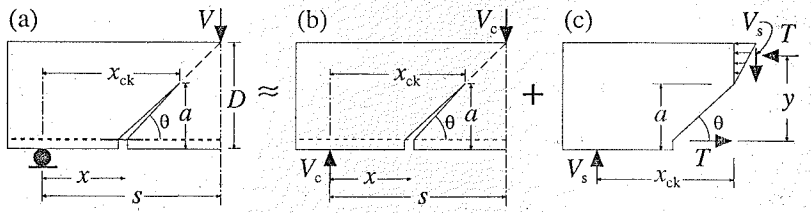

Figure 10.2.7 Jenq and Shah's (1989) analysis of diagonal shear.

shown in Figs. 10.2.7b-c. The first case corresponds to the concrete taking a load V_c such that the stress intensity factor at the crack tip is K_{Ic}. The second case corresponds to concrete plus reinforcement taking a load V_s computed from classical no-tension strength of material analysis (no crack singularity, neutral axis at the crack tip, linear stress distribution along the ligament). Note that in this model only the situation at ultimate load is considered, and the equations that follow cannot be used to analyze the crack growth. This means, in particular, that a_c is the critical crack length (actually its vertical projection), understood as the crack length at peak load.

Because there is no closed-form expression for the precise geometry in Fig. 10.2.7b, Jenq and Shah (1989) assumed that the stress intensity factor can be approximated by the stress intensity factor of a pure bend beam with a symmetric edge notch of depth a subjected to the bending moment corresponding to the cross section at the mouth of the crack (i.e.: $M = V_c x$; note that it is not clear why the moment should not be taken at the cross section at the tip of the crack, $M^* = V_c x_{ck}$). According to this, the crack growth condition is

$$K_{Ic} = \frac{6V_c x}{bD^2}\sqrt{D}k(\alpha)\,, \qquad \alpha_c = \frac{a_c}{D} \tag{10.2.16}$$

where in the first fraction we recognize the expression for the nominal stress in bending ($6M/bD^2$) and $k(\alpha)$ is given, for example, by Srawley's expression (5.4.8). From this we get

$$V_c = \frac{K_{Ic}bD^{3/2}}{6xk(\alpha_c)}\,, \qquad \alpha_c = \frac{a_c}{D} \tag{10.2.17}$$

On the other hand, the equilibrium of moments for the case in Fig. 10.2.7c requires

$$V_s = T(x)\frac{y}{x_{ck}}\,, \qquad y = D - c - \frac{1}{3}(D - a_c) = \frac{2D}{3} + \frac{a}{3} - c \tag{10.2.18}$$

Given x and a_c (together with the initial geometry of the beam), the foregoing equations determine V if the distribution of the steel force $T(x)$ is known. Jenq and Shah (1989) assume as a simplification that this distribution can be approximated by a power law:

$$T(x) = T_{\max}\left(\frac{x}{s}\right)^N \tag{10.2.19}$$

where $T_{\max}$ is the value of the steel force below the concentrated load. Based on test data by Ferguson and Thompson (1962, 1965), Jenq and Shah (1989) proposed a formula for $T_{\max}$. They made an intensive numerical analysis of the influence of the exponent N, from which they recommended the value $N = 2.5$. The recommended expression for $T_{\max}$ is:

$$T_{\max} = 2.509 s f_t' \sqrt{\frac{\rho}{D}} \tag{10.2.20}$$

where the result is in kN if s and D are in mm and f_t' in MPa. This result is strictly valid only for beam thicknesses of 10 in (254 mm) and for a single steel bar. To obtain a dimensionally correct equation, it is better to express the force carried out by the steel at the central section as the length of the steel bars s, times their perimeter $n_b \pi D_b$, times the average bond shear stress (Karihaloo 1992) $\overline{\tau_b}$:

$$T_{\max} = s n_b \pi D_b \overline{\tau_b} \tag{10.2.21}$$

Setting now $n_b \pi D_b^2/4 = \rho b D$ and $\overline{\tau_b} \propto f_t'/D$, as deduced by Jenq and Shah from the Ferguson and Thompson data (1962, 1965), we get the result

$$T_{\max} = L_b s \sqrt{\frac{n_b \rho b}{D}} f_t'\,, \qquad L_b = 2.509 \text{ m} \tag{10.2.22}$$

The value of L_b is determined so that this formula coincides with (10.2.20) for $n_b = 1$ and $b = 254$ mm.

Given x (or θ) and a_c, the shear strength is determined from the foregoing equations setting $v_u = (V_c + V_s)/bD$; the result is

$$v_u = \frac{K_{Ic}\sqrt{D}}{6xk(\alpha_c)} + L_b \frac{s}{D}\sqrt{\frac{n_b \rho}{bD}} f_t' \left(\frac{x}{s}\right)^N \frac{y}{x_{ck}} \tag{10.2.23}$$

Karihaloo analyzed this model and improved it in a series of papers (Karihaloo 1992, 1995; So and Karihaloo 1993). First he modified the way the model is applied and used it as a forensic engineering tool by using the values of x and a_c as measured (optically) in a test. Using this method on two beam tests, he concluded that the Jenq-Shah model predicted shear strengths that were too low (see exercise 10.3). So and Karihaloo (1993) extended the range of applicability of (10.2.20) to include other parameters. They reevaluated the results of Ferguson and Thompson (1962, 1965) and proposed a new formula that takes into account the bar diameter and the number of bars; for an embedment length L_e, the formula reads

$$T_{\max} = F_1 L_e \sqrt{4 n_b \pi \rho b D}\, \overline{\tau_b} \tag{10.2.24}$$

where F_1 is a reduction factor for $n_b = 2$ (the formula is strictly applicable only for one or two bars):

$$F_1 = \frac{93 + 135A_2 - 7A_2^2}{93 + 135A_1 - 7A_1^2}\,, \qquad A_1 = \frac{b}{D_b} - 1\,, \qquad A_2 = \frac{b}{2D_b} - 1 \tag{10.2.25}$$

The average ultimate bond shear strength $\overline{\tau_b}$ is given by

$$\overline{\tau_b} = F_2 \left[0.4684\sqrt{f_c'}\left(\frac{\rho L_e}{D_b}\right)^n + \langle 0.0271(c - 1.5D_b)\rangle\right]\,, \qquad n = -0.8205 D_b^{-0.2933} \tag{10.2.26}$$

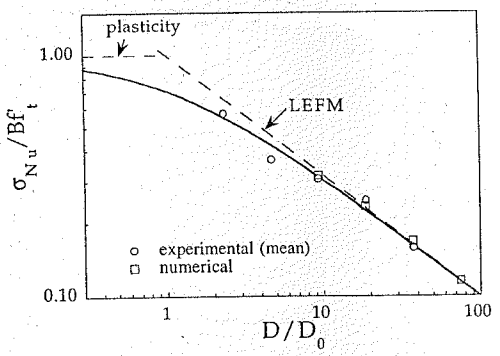

Figure 10.2.8 Comparison of experimental results for diagonal shear with computed values obtained using a nonlocal microplane model (data from Bažant, Ožbolt and Eligehausen 1994). The fit by Bažant's size effect law is also shown.

where all the dimensions must be in millimeters and f'_c in MPa. The factor F_2 is given by

$$F_2 = \begin{cases} 0.3889 + 0.1184\dfrac{s}{D} - 0.0068\left(\dfrac{s}{D}\right)^2, & \dfrac{s}{D} \le 17.5 \\ 0.9, & \dfrac{s}{D} > 17.5 \end{cases} \tag{10.2.27}$$

Although this equation substantially improves the Jenq-Shah expression for $T_{\max}$, the problem of the shape of the distribution (particularly the value of exponent N in (10.2.19)), still remains. Karihaloo (1995) further improved the treatment of the LEFM crack growth condition by explicitly considering the mixed mode condition at the crack tip. But even with this enhancement, the strength predictions of the model were too low, even for exponents N as low as 1.25.

10.2.5 Finite Element Solutions with Nonlocal Microplane Model

Additional insight and even partial validation of the design formulas for brittle failures of concrete structures, including diagonal shear, can be gained from careful finite element analysis based on a realistic material model verified over a broad range of experimentally observed behavior. One such model appears to be the nonlocal finite element model combined, on the material level, with the microplane model for the stress-strain relation (Bažant, Ožbolt and Eligehausen 1994). These models, which will be discussed in detail in Chapters 13 and 14, provided, for the diagonal shear tests of Bažant and Kazemi, the results shown by the triangular data points in Fig. 10.2.8. The figure also shows the test data and the best fit by the size effect law. It is seen that the agreement is quite close.

10.2.6 Influence of Prestressing on Diagonal Shear Strength

The effect of longitudinal prestressing on the diagonal shear of longitudinally reinforce beams was addressed by Bažant and Cao (1986) and also by Gustafsson (1985). Similar to the procedure of Bažant, Kim and Sun, Bažant and Cao first used simple equilibrium considerations to get an approximate expression for v_u^p and then applied the size effect correction (10.1.13). Their result is:

$$v_u = v_u^p\left(1 + \frac{D}{D_0}\right)^{-1/2}, \qquad v_u^p = \frac{D}{s}\left(c_1\sigma_1\sqrt{\frac{f'_c}{\sigma_1}} + c_2\sigma_{cc}\right) \tag{10.2.28}$$

where D_0, c_1, and c_2 are empirical constants, s is the shear span, and σ_{cc} the uniaxial stress due to prestressing; $\sigma_1 = 1$ psi $= 6.895$ MPa is introduced for dimensional compatibility. From the analysis of

235 test results from the literature, Bažant and Cao proposed the following values of the constants:

$$D_0 = 25d_a\,, \qquad c_1 = 4.9\,, \qquad c_2 = 0.54 \tag{10.2.29}$$

These values yield the average shear strength; for design, they proposed the values $c_1 = 4$, $c_2 = 0.4$.

It must be realized that although the analysis of data showed a clear size effect, the scatter was so large that the values of the parameters are merely roughly indicative. Nevertheless, the study of Bažant and Cao also shows that the proposed formula provides a better agreement with test results than other formulas found in the literature such as the ACI formula or the formula proposed by Sozen, Zwoyer and Siess (1958).

In contrast to nonprestressed beams, the arch action was not considered in the derivation of the foregoing formula. However, in prestressed beams it is difficult to distinguish the arch action from the effect of prestress. To some extent, the separate consideration of shear force $c_2\sigma_{cc}D/s$ associated with prestress substitutes for the consideration of arch action. However, improvements might be in order.

The foregoing formula did not anchor the size effect into a complete plasticity solution, which should be applicable for an infinitely small size. However, according to the size effect data, the plasticity solution would be applicable, in theory, for beam depths smaller than the aggregate size, and thus it is not clear whether the application of plasticity is permitted. It calls for further research to determine whether this might be so and, if it would, then one could draw on various elegant plasticity solutions for diagonal shear (for example, the recent developments in truss analogy, see Section 10.3).

Exercises

10.1 Karihaloo (1992) reported tests on two reinforced concrete beams tested in three-point bending. The dimensions of the beams were as follows (refer to Fig 10.2.7 for notation): $s = 800$ mm, $D = 150$ mm, $b = 100$ mm, $c = 25$ mm. Beam number 1 was reinforced with one ribbed bar 12 mm in diameter and beam number 2 with two ribbed bars of the same characteristics, giving steel ratios of 0.0075 and 0.015, respectively. The steel had a yield strength $f_y = 463$ MPa. The concrete mix had the following characteristics: $d_a = 20$ mm, $f'_c = 38$ MPa, $E = 30$ GPa, $f_t = 3.4$ MPa. The fracture toughness was estimated (from tests on similar mixes) as $K_{Ic} = 1.27\,\text{MPa}\sqrt{\text{m}}$. Beam number 1 failed in bending with a main crack close to the central cross-section, while beam number 2 failed in diagonal shear. The failure loads were approximately equal to 24 kN and 33 kN, respectively (note that this is the total load $P = 2V$). (a) Determine the expected strength of the beams according to the Bažant, Kim and Sun's formula whenever applicable. (b) Determine the design strength according to the Bažant, Kim and Sun's model, and determine the actual safety factor for the beam that failed in diagonal shear.

10.2 Consider the beams in the previous example. (a) Make an estimate of the values of G_F and ℓ_{ch} to be used in the Gustafsson-Hillerborg model. (b) Plot the experimental results on a copy of Fig. 10.2.6. (c) Give at least two reasons for each beam (not necessarily the same) why the results of Hillerborg and Petersson cannot be applied directly.

10.3 Consider again the beams in the previous examples. (a) Determine the shear strength of beam number 2 using the Jenq-Shah model with $N = 2.5$, with the following assumptions (based on the observed failure, taken from Karihaloo 1992): $x \approx 250$ mm, $a_c \approx 125$ mm, $\theta \approx 45°$. Compare the result to the experimental value. (b) Determine the value of exponent N that should be used to make the model deliver the observed strength.

10.3 Fracturing Truss Model for Shear Failure of Beams

The truss model of Ritter (1899) and Mörsch (1903), also called the strut-and-tie model, has been widely used in successively refined versions to analyze the failure of beams in diagonal shear (Nielsen and Braestrup 1975; Thürlimann 1976; Collins 1978; Collins and Mitchell 1980; Marti 1980, 1985; Schlaich, Schafer and Jannewein 1987; Hsu 1988, 1993; Collins, Mitchell et al. 1996). A fracture model retaining the basic hypotheses of the truss model has recently been proposed. It explains the size effect observed in this type of structures based on the concepts previously analyzed in Section 9.5, particularly the generation and growth of a band of axial splitting cracks parallel to the compressive principal stress (Bažant 1996b), or alternatively a shear compression crack propagating across the strut. In this section we present the

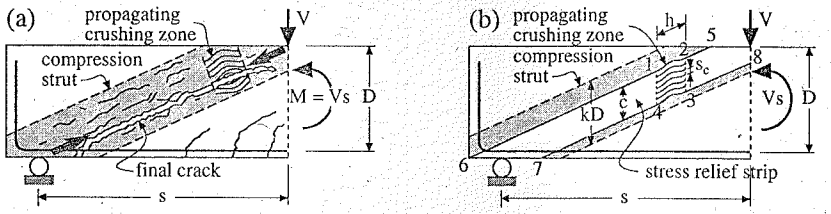

Figure 10.3.1 (a) Compression strut in a beam without stirrups and crushing zone propagating across the compression strut during failure, (b) stress relief zones caused by crushing band propagating across compression strut in beams of different sizes.

basic hypotheses underlying the model and two alternative theoretical analyses, one based on the stress relief zone and strain energy release, and the other based on the stress redistribution and complementary energy. The section closes by discussing the size effect on the cracking load, which is sometimes claimed to be free from size effect.

10.3.1 Basic Hypotheses of Fracturing Truss Model

Consider the sheared beam in Fig. 10.1.3 (which shows only the left-end portion of the beam). For the sake of simplicity, the beam is considered to have a rectangular cross section (a generalization to flanged cross sections, however, would not be difficult). The analysis of the size effect performed by Bažant (1996b) rests on the two following hypotheses:

Hypothesis I: *The failure modes at maximum load of beams of different sizes are geometrically similar.*

This means that, for example, the shear span s and the length c of the material failure zone at maximum load are geometrically similar (Fig. 10.3.1). In other words, the ratios s/D and c/D are assumed to be constant. The hypothesis is applicable only within a certain range of sizes. However, experience from testing as well as finite element analysis indicates that this range covers the size range of practical interest.

Hypothesis II: *The maximum load is determined by the compression failure in the inclined compression struts.*

The compression failure must be interpreted as a temporary incremental strain-softening in compression (or progressive crushing) of concrete in the strut, characterized by a negative slope of the stress-strain diagram. Hypothesis II means that the concrete in the compression strut is suffering splitting cracks in the direction of compression only during a certain, possibly short, portion of the loading history during which the applied load is reaching its maximum. It does not mean that the concrete will get crushed completely once the load will be reduced to zero (such complete crushing is seen only in T-beams; Leonhardt 1977). During the postpeak softening, the splitting cracks may interconnect to produce what looks like compression shear cracks in the horizontal or vertical direction (Fig. 10.3.2) (however, if the failure were assumed to be caused by propagation of a horizontal or vertical shear crack across the strut, the calculation results would be the same). Thus, after the failure is completed, the failure might not look as crushed concrete but as a diagonal crack and a shear crack. The lack of complete crushing may be caused by the failure process taking place under a decreasing load, after the maximum load. The concrete in the strut may have been partially damaged by compression splitting but need not have disintegrated.

Denying the existence of progressive failure of the compression strut at maximum load would be tantamount to denying the validity of the truss model (strut-and-tie model). If this model is valid, then (**1**) diagonal tensile cracks must form before the maximum load, (**2**) the tensile and shear stresses (crack-bridging or cohesive stresses) transmitted across these cracks must be negligible compared to compression stresses in the struts, and (**3**) the compression struts between these cracks must be aligned in the direction of the compressive principal stress in concrete. Only under these conditions, the concrete, stirrups, and

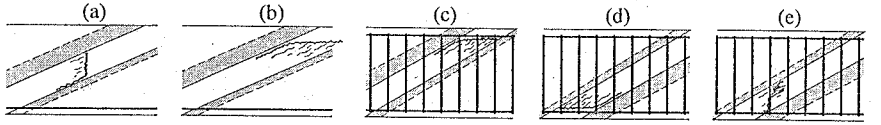

Figure 10.3.2 Splitting crack interconnection to form horizontal or vertical compression-shear cracks: (a,b) beams without stirrups; (c–e) beams with stirrups.

longitudinal bars may be treated as a truss. Assuming that the stirrups and longitudinal bars are designed strong enough, the truss can fail only in concrete. Because the concrete is in uniaxial compression, the failure must be compression failure.

The stresses transmitted across the diagonal cracks are, of course, nonzero, because the cracks are not open widely enough at maximum load. But the important point, which justifies the truss model, is that these stresses are much smaller in magnitude than the compression stresses in the struts.

The energy release due to fracture propagation can be calculated in two ways: (**1**) from the change of the strain energy of the structure-load system at constant displacement, or (**2**) from the change of the complementary energy of the structure at constant load (see Chapter 3). We will examine both approaches in a simplified manner and show that they give approximately the same results.

10.3.2 Analysis Based on Stress Relief Zone and Strain Energy for Longitudinally Reinforced Concrete Beams Without Stirrups

The typical pattern of cracks forming during the failure of a simply supported beam is seen in Fig. 10.3.1a. Although after the failure only one final crack emerges, cracks of various orientations form during the loading process. The first cracks caused by shear loading are tensile cracks of inclination approximately 45°. On approach to the maximum load, these cracks interconnect and form a larger crack running approximately along the line connecting the application point of the load V to the support in Fig. 10.3.1a. This major crack is free of shear stresses and has approximately the direction of the maximum principal compression stress, σ_{II}.

According to the truss model (or strut-and-tie model), we may imagine that most of the load is transferred through the shaded zone called the compression strut (in the case of distributed load, it would be a compressed arch). The normal stress in the direction orthogonal to the strut is essentially zero and the material can expand freely in that direction.

The failure behavior is approximately idealized as shown in Fig. 10.3.1b for two geometrically similar beams of different size. Although for calculation purposes the compression strut is assumed to represent a one-dimensional bar connecting the point of application of V and the support, it has a finite effective width, denoted as kD (Fig. 10.3.1b) where D is the depth to the reinforcement and k is approximately a constant, independent of the beam size.

According to experimental evidence, supported by finite element results, a beam (with a positive bending moment) fails at maximum load due to compression failure of the concrete, usually near the upper end of the compression strut, provided that the longitudinal bar is anchored sufficiently so that it cannot slip against concrete near the support. Aside from the fact that the compression failure (axial splitting or compression shear crack) occurs only within a portion of the length of the strut, the basic premise of the present analysis is that the width h of the cracking zone in the direction of the strut is for a given concrete approximately a constant (which is probably approximately proportional to the maximum aggregate size and also depends on Irwin's characteristic length and on other material characteristics).

The fact that h, in contrast to the length and width of the stress-relieved strip in the strut (the white strip 56785 in Fig. 10.3.1b), is not proportional to the beam size is the cause of the size effect. If the width h of the crushing zone were proportional to the beam size, there would be no size effect. For calculation purposes, we will assume that the compression failure of the material consists of a band 12341 of splitting cracks (Fig. 10.3.1b) growing vertically across the strut upward or downward, or both (which of these is immaterial for the present analysis). These cracks may interconnect after the peak load to produce what looks as a shear crack.

Microscopically, the compression failure may be regarded as internal buckling of an orthotropically damaged material (Bažant and Xiang 1994, 1997; see Section 9.5). The failure begins by formation of dense axial splitting microcracks in the direction of maximum compression, which greatly reduces the transverse stiffness of the material, thus causing the microslabs of the material between the microcracks to buckle laterally. The details of the process are, however, not needed for the present analysis. Neither is it important that the crushing band is pictured to propagate vertically. If it propagated across the strut in an inclined or horizontal direction, the calculation results would be about the same.

The growth of the splitting crack band, which causes the load-deflection curve to reach a maximum load and subsequently decline, relieves the compression stress from the strip 56785 shown in Fig. 10.3.1b. The reason that the boundaries of the stress relief zone, that is, the lines 16, 25, 38, and 47, are parallel to the direction of the strut is that the material is heavily weakened by cracks parallel to the strut. Otherwise, a more realistic assumption would be a triangular shape of the stress relief zone, as considered in the case of tensile failures (Section 1.4; see also the remark at the end of Section 9.5).

Now, how to make the size effect intuitively clear with minimum calculations? To this end, note that the area of the stress relief zone 56785 in Fig. 10.3.1b is proportional to ca, where c is the length of the crack band at failure. Since $ca = (c/D)(a/D)D^2$, and c/D and a/D are constants, independent of D, the area of the stress relief zone is proportional to D^2. Because the average strain energy density in the strut is proportional to the nominal shear stress at ultimate load, v_u^2, the total energy release from the stress-relieved strip 56785 of the strut is proportional to $v_u^2 D^2$. However, assuming the energy dissipation per unit volume of the crack band to be constant, the energy dissipation in the entire cracking band is proportional to D, because the area of the crushing band is proportional to $ch = (c/D)hD$. Therefore, varying the beam size D, $v_u^2 D^2$ must be proportional to D, which means that v_u must be proportional to $1/\sqrt{D}$. This represents a very strong size effect corresponding to LEFM.

In summary, the cause of the size effect is simply the fact that the energy release from the structure is approximately proportional to $v_u^2 D^2$ whereas the energy consumed by fracture is approximately proportional to D.

Let us now do the calculations in detail, following the stress relief zone approximation illustrated in Section 3.2.2. The condition that the entire shear force V must be transmitted by the compression strut yields, for the axial compression stress in the strut, the following expression:

$$\sigma_c = \frac{1}{bkD}\frac{V}{\sin\theta\cos\theta} = \frac{v_u}{k}\left(\frac{s}{D}+\frac{D}{s}\right) \tag{10.3.1}$$

in which θ is the inclination angle of the compression strut from the horizontal (note that $\tan\theta = D/s$). The strain energy density in the strut is $\sigma_c^2/2E_c$, where E_c is the elastic modulus of concrete. The volume of the strut is sbc (where b = beam width). Therefore, the loss of strain energy from the beam caused by stress relief during the formation of the crack band at constant load-point displacement is, approximately:

$$\Delta\mathcal{U}_c = -\frac{\sigma_c^2}{2E_c}sbc = -\frac{v_u^2}{2E_c k^2}\left(\frac{s}{D}+\frac{D}{s}\right)^2 sbc \tag{10.3.2}$$

The minus sign expresses the fact that this is an energy loss rather than gain. The energy release rate due to the growth of the cracking band is obtained from (2.1.15) as

$$\mathcal{G} = -\frac{1}{b}\left[\frac{\partial\mathcal{U}_c}{\partial c}\right]_u = -\frac{1}{b}\left[\frac{\partial\Delta\mathcal{U}_c}{\partial c}\right]_u = -\frac{v_u^2 s}{2E_c k^2}\left(\frac{s}{D}+\frac{D}{s}\right)^2 \tag{10.3.3}$$

The energy dissipated by the cracking zone may be expressed on the basis of the fracture energy G_f characterizing the axial splitting microcracks in the crack band. The length of these cracks is h (width of the band), and their average spacing is denoted as s_c. The number of axial splitting cracks in the band is c/s_c. Thus, the total energy dissipated by the crack band is $W_f = (c/s_c)bhG_f$. Differentiating with respect to c, we find that the energy dissipation in the crack band per unit length of the band and unit width of the beam (which we call $\mathcal{R}$ because it has the meaning of a crack growth resistance) is:

$$\mathcal{R} = \frac{h}{s_c}G_f \tag{10.3.4}$$

In this equation, however, it would be too simplistic to consider h to be a constant through the entire evolution of the crack band. Naturally, the crack band must initiate from a small zone of axial splitting cracks. The length of these cracks first extends in the direction of the strut until they reach a certain characteristic length h_0. After that the crack band grows across the strut at roughly constant width $h = h_0$ (see the intuitive picture of the subsequent contours of the crack zone in Fig. 10.3.1a). Such behavior may be simply described by the equation

$$h = \frac{c}{w_0 + c}h_0 \tag{10.3.5}$$

in which h_0, w_0 = positive constants; h_0 represents the final width of the crack band. Thus, strictly speaking, our hypothesis of a constant width of the cracking zone means that the final width rather than h is a constant.

The increase of $\mathcal{R}$ with c, as described by (10.3.4) with (10.3.5), represents an R-curve behavior (because $\mathcal{R}$ represents the resistance to fracture). The R-curve behavior in tensile fracture is also caused by the growth of the fracture process zone size. Here, however, this growth is expressed indirectly in terms of the length of the axial splitting cracks in the cracking band.

It is also conceivable that, instead of a band of parallel splitting cracks, a shear crack would propagate in a direction inclined to the compression strut (Fig. 10.3.2). In that case

$$\mathcal{R} = G_{fs}\frac{c}{h_0 + c} \tag{10.3.6}$$

where G_{fs} = fracture energy of the shear crack and h_0 now characterizes the R-curve behavior of the shear crack. This is mathematically identical to (10.3.4) if one sets $G_f = G_{fs}s_c/h_0$, and so we will not pursue it further.

The balance of energy during equilibrium propagation of the crushing band requires that $\mathcal{G} = \mathcal{R}$. Substituting here the expressions in (10.3.3)–(10.3.5), one obtains the result:

$$v_u = v_p\left(1 + \frac{D}{D_0}\right)^{-1/2} \tag{10.3.7}$$

in which the following notations have been made

$$D_0 = w_0\frac{D}{c} \tag{10.3.8}$$

$$v_p = c_p K_c\left(\frac{s}{D}+\frac{D}{s}\right)^{-1} \tag{10.3.9}$$

$$K_c = \sqrt{E_c G_f}, \qquad c_p = k\sqrt{\frac{2h_0}{w_0 s_c}\frac{c/D}{s/D}} \tag{10.3.10}$$

Here the expression for K_c is that for the fracture toughness (the critical stress intensity factor) of the axial splitting microcracks. An important point is that, because of our assumptions (constant c/D and s/D), the values of D_0, v_p, and c_p are constant, independent of size D. The value v_p is the limiting (asymptotic) value of the nominal shear strength for a very small size D.

Eq. (10.3.7) represents the size effect law discussed in Chapters 1 and 6. This law was introduced into the analysis of diagonal shear failure by Bažant and Kim (1984), however, on the basis of a more general and less transparent argument (see Section 10.2.2).

By the same calculation procedure, it can also be easily shown that if and only if, contrary to our hypothesis, the width h of the crushing band were proportional to D instead of obeying (10.3.5), there would be no size effect. If constant w_0 were taken as 0, one would have $v_u \propto D^{-1/2}$, which is the size effect of linear elastic fracture mechanics (LEFM), representing the strongest size effect possible. However, the experimental data exhibit a weaker size effect, which implies that the constant w_0 should be considered finite.

As seen in Chapters 1 and 6, the size effect curve given by (10.3.7) represents a smooth transition from a horizontal asymptote corresponding to the strength theory or plastic limit analysis to an inclined

asymptote of slope $-1/2$, corresponding to LEFM. The approach to the horizontal asymptote means that the plasticity approach, that is, the truss model (or strut-and-tie model), can be used only for sufficiently small beam sizes D.

For very small beam sizes D, we may substitute in (10.3.1) $\sigma_c = f_c^b$ = compression strength of the strut, and replace v_u by plastic nominal strength v_p. From this we can solve:

$$v_p = k f_c^b \left(\frac{s}{D} + \frac{D}{s}\right)^{-1} \tag{10.3.11}$$

which is an alternative to (10.3.9). Thus, the size effect law in (10.3.7) can be alternatively written as

$$v_u = k f_c^b \left(\frac{s}{D} + \frac{D}{s}\right)^{-1} \left(1 + \frac{D}{D_0}\right)^{-1/2} \tag{10.3.12}$$

which also shows the effect of the relative shear span s/D on the nominal shear strength. Note that f_c^b cannot be expected to represent the uniaxial compression strength f_c' of concrete because the progressively fracturing concrete in the strut is under high transverse tensile strain in the other diagonal direction and has been orthotropically damaged by cracking parallel to the strut due to previous high transverse tensile stress (Hsu 1988, 1993). So f_c^b is a certain biaxial strength of concrete, depending both on the uniaxial compression strength f_c' and the direct tensile strength f_t'. This dependence needs to be calibrated by shear tests of beams.

It is interesting to determine the ratio to the nominal strength for bending failure, σ_{Nu}^b. The ultimate bending moment in the cross section under the load V is $M_u = V_u s = \sigma_N^b bsD$. From the moment equilibrium condition of the cross section under the load V, we also have $M_u = (f_y \rho bD) k_b D$, in which f_y is the yield strength of the longitudinal reinforcing bars, ρ is the reinforcement ratio (which means that ρbD is the cross section area of the longitudinal reinforcing bars), and $k_b D$ represents the arm of the internal force couple at the ultimate load. As is well known, k_b is approximately constant. Equating the expressions for M_u, we obtain $\sigma_N^b = \rho f_y k_b D/s$. Considering now (10.3.12), we conclude that:

$$\frac{\sigma_N^b}{v_u} = \frac{\rho f_y k_b}{k f_c^b} \left(\frac{s}{D} + \frac{D}{s}\right) \sqrt{1 + \frac{D}{D_0}} \tag{10.3.13}$$

This equation shows that the ratio of the nominal bending strength to the nominal shear strength of the beam decreases when the relative shear span s/D increases, which confirms a well-known fact. It means that slender beams, for which s/D is large, fail by bending, while deep beams, for which s/D is small, fail by shear. However, as is clear from (10.3.13), the relative shear span $(s/D)_{tr}$ at the transition between the shear and bending failures is not constant but is larger for a larger beam size D. To express it precisely, one sets $\sigma_N^b = v_u$ in (10.3.13), and needs to solve (10.3.13) for s/D, which is a cubic equation. The transitional shear span obviously exhibits a size effect.

The foregoing analysis assumes the reduction of the compressive stress σ_c all the way to zero. Similar to the analysis of compression fracture in Section 9.5, it could be that the compression stress σ_c is reduced to some small but finite residual strength σ_r. However, the residual stress is anyway likely to be smaller than for uniaxial compression, due to the existence of large tensile strain. A finite σ_r seems more realistic when we consider beams with stirrups, which provide some degree of confinement. If σ_r were nonzero for the present case, it would have the effect of adding a constant term to the right hand side of (10.3.7).

The tensile strength of concrete, f_t', has played no direct role in the foregoing analysis. The tensile strength is not a material parameter in LEFM, nor in the R-curve model of nonlinear fracture. It does appear in the cohesive (fictitious) crack model or the crack band model. However, those models are too complicated for achieving a simple analytical solution. The tensile strength, of course, controls the initiation of the inclined shear cracks, however, their growth is governed by fracture energy. In the present analysis we take the view that the inclined cracks due to shear loading have already formed before the maximum load.

Does shear stress transmission across cracks due to friction and aggregate interlock play any role? It could, although according to the present analysis, it cannot be significant. As shown in Fig. 10.3.1a, only cracks rather curved within the area of the compression strut can be subjected to shear and normal loading. Their capability of shear stress transmission decreases with the crack width, and the crack width

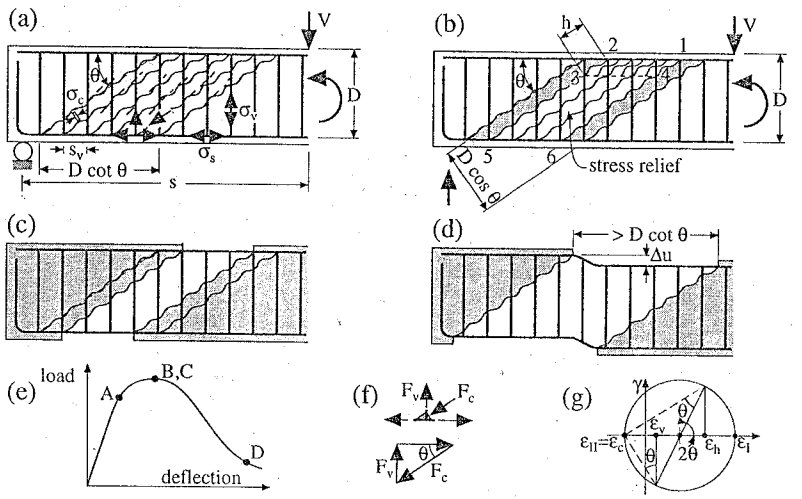

Figure 10.3.3 Evolution of diagonal cracks in beam with stirrups under shear loading: (a) diagonal crack formation before maximum load, (b) growth of crushing band across compression strut during failure at maximum load, (c) beam at maximum load with the crushed and stress-relieved parts of the compression strut removed, (d) state of beam without crushed and stress-relieved concrete after collapse (i.e., when the load has been reduced to a small value), (e) location of the states represented in Figs. a–d on the load deflection curve, (f) equilibrium of forces in stirrups and struts, and (g) Mohr circle of strains.

may be assumed to increase with an increasing beam size, which obviously would also introduce a size effect (this idea was proposed by Reineck 1991). The cracks are most inclined to the compression strut direction and are opened the most widely at the bottom of the beam. However, the maximum load appears to be controlled by progressive compression crushing near the major crack at the top of the beam. For this reason, the effect of crack opening on the shear stress transmission across cracks can hardly play a major role in the size effect on the maximum load.

10.3.3 Analysis Based on Stress Relief Zone and Strain Energy for Longitudinally Reinforced Concrete Beams With Stirrups

Consider now a beam with stirrups (Fig. 10.3.3a). The stirrups cause the diagonal cracks due to shear to be more densely distributed. The first hairline cracks, shown by the dashed lines in Fig. 10.3.3a, form near the neutral axis, with inclination about 45° before the maximum load. These cracks later interconnect and form continuous major cracks at inclination angle θ with the horizontal (Fig. 10.3.3a). These cracks run in the direction of the maximum principal compressive stress σ_{II}, transmitting no shear stresses. They are, of course, cohesive cracks transmitting tensile bridging stresses. These stresses will probably be less than one half of the tensile strength, f_t', while the compression stresses in the truss will be equal or nearly equal to the compressive strength of concrete, f_c'. So, it is safe to assume that the tensile principal stress is negligible ($sigma_1 \approx 0$) compared to the compressive principal stress, which justifies treating the beam approximately as a truss. This makes the truss statically determinate. It is this circumstance that makes the well-known simple analysis of the truss model (or strut-and-tie model) possible. If σ_I were not negligible, the truss model would be invalid.

The failure at maximum load is assumed to be caused by the progressive crushing of concrete in the compression struts between the major inclined cracks. Similar to beams without stirrups, a crack band which consists of dense axial splitting microcracks first widens to its full width h and then propagates sideways as shown in Fig. 10.3.3b. For the case of a positive bending moment, this crack band probably forms near the top of the beam and may be assumed to propagate horizontally, to the left or to the right,

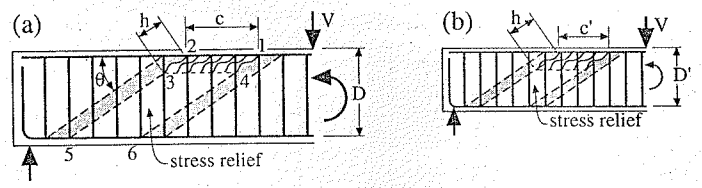

Figure 10.3.4 Stress relief zones caused by a crack band propagating across the compression strut in beams of different sizes with stirrups. The beam in (b) is similar to the beam in (a) except that the crack band width h is the same.

or both. The location and direction of the propagation of the crack band is actually not important for the present analysis, and the same results would be obtained if the band propagated at other inclinations to the compression strut. An important point, however, is that the final length h_0 of the axial splitting cracks, that is, the final width h_0 of the band, is a material property, independent of the size of the beam. If the width h_0 of the band were proportional to beam depth D, there would be no size effect. Since it is less than proportional to D, there must be size effect.

Thus, the cause of the size effect is the localization of the compression failure of the strut into a crack band of a fixed width, and the growth of this band across the strut.

An important point is that the stirrups as well as the longitudinal steel bars are not necessarily yielding during the failure at maximum load. They might not have yielded before the crushing of the strut began, or they may have yielded and unloaded. There is no reason why the yielding of steel should occur simultaneously with the progressive compression crushing.

The formation of the crack band 12341 (Fig. 10.3.3b) may again be assumed to relieve the compression stress from the entire length of the compression struts in the region 12561 (Fig. 10.3.3b). This causes a release of strain energy from the compression struts, which is then available to drive the propagation of the crack band. This represents the mechanism of failure at maximum load.

With the stress relieved from the compression struts, the beam acts essentially as shown in Fig. 10.3.3c, as if there were a gap in concrete (provided the residual strength of crushed concrete is neglected). However, since the steel is not in general yielding, this does not represent a failure mechanism. A failure mechanism can be created only when a sufficient number of compression struts fail as shown in Fig. 10.3.3d, in which case even nonyielding bars permit free movement because the bending resistance of the bars is negligible. However, this type of collapse mechanism corresponds to a postpeak state at which the load is already reduced to a very small value (such as state D in Fig. 10.3.3e). Thus, the stress relief at maximum load does not imply the structure has become a mechanism.

First, let us explain the size effect mechanism in the simplest possible terms. The area of the compression struts from which the compression stress is relieved, that is, area 12561 in Fig. 10.3.4, is proportional to cD, which is equal to $(c/D)D^2$. But since the failure is assumed to be geometrically similar for beams of different sizes (shown in Fig. 10.3.4), c/D is a constant, and so the area of the stress relief zone is proportional D^2. The strain energy density before the stress relief is proportional to $v_u^2/2E_c$, and so the total energy release is proportional to $v_u^2 D^2$. The area of the crack band is proportional to $ch = (c/D)hD$. Since both h and c/D are constant for beams of different sizes, the area of the crack band is proportional to D, and so is the energy dissipated in the crack band. So, considering the failures of geometrically similar beams of different sizes, $v_u^2 D^2$ must be proportional to D, which means that v_u must be proportional to $1/\sqrt{D}$. Again, same as for the beam without stirrups, we thus obtain a size effect, and it is the strong size effect of LEFM. In practice, the size effect for smaller beam sizes is weaker because of the R-curve behavior of the crack band 12341.

We assume the stirrups to be uniformly distributed (smeared). Equilibrium on a vertical cross section of the beam (Figs. 10.3.4 and 10.3.3f) requires that

$$\sigma_c = -\frac{F_c}{bD\cos\theta} = -\frac{v_u bD}{\sin\theta}\frac{1}{bD\cos\theta} = -\frac{2v_u}{\sin 2\theta} \tag{10.3.14}$$

in which θ is the inclination of the compression struts, F_c = compression force in the strut per length D, and σ_c is the compression stress transmitted by the strut (which, in general, is not equal to the standard

compression strength f_c' of concrete and depends on the size of the beam in a manner to be determined). Equilibrium on an inclined cross section of the beam parallel to the compression struts further requires that

$$\sigma_v = (Vs_v/A_v D)\tan\theta = v_u s_v b\tan\theta/A_v \tag{10.3.15}$$

in which A_v = cross section of the stirrups, s_v = spacing of the stirrups, and σ_v = tensile stress in the stirrups, which, in general, is not equal to the yield stress. The stress in the longitudinal bars is obtained from the moment equilibrium condition in a cross section and is $\sigma_s = M/A_s k_b D$, in which M = bending moment, A_s = cross section area of the longitudinal bars, and $k_b D$ = arm of the internal force couple in the cross section.

We do not attempt to determine the angle θ of the diagonal cracks and the struts by fracture analysis. The diagonal cracks delineating the struts start to form before the maximum load, and not during failure. For the sake of simplicity, we assume the orientation of the major diagonal cracks not to rotate and adopt the method introduced into the truss model by Mitchell and Collins (1974) in their compression field theory, in which they used the compatibility condition for the average strains in the truss in a similar way as Wagner (1929) used the compatibility condition for approximate analysis of the shear buckling of the webs of steel beams. The average strains of the truss are defined as the strains of a homogeneously deforming continuum that is attached to the joints of the truss at the nodes (tops and bottoms of the stirrups). According to the Mohr circle shown in Fig. 10.3.3g (in which ε denotes the strains, and ε_h is the strain in the longitudinal bars), the overall compatibility of the average strains of the struts, the stirrups, and the longitudinal bars requires that

$$\tan^2\theta = \frac{\varepsilon_v - \varepsilon_c}{\varepsilon_h - \varepsilon_c} = \frac{(\sigma_v/E_s) - f(\sigma_c)}{(\sigma_s/E_s) - f(\sigma_c)} \tag{10.3.16}$$

Here the strains have been expressed in terms of the stresses assuming the steel not to be yielding and denoting by $f(\sigma_c)$ the stress-strain diagram of concrete. (For the precise method in which the strains entering (10.3.16) are calculated, see Mitchell and Collins 1974.) The foregoing calculation, of course, requires that the diagonal cracks and the struts be aligned with the direction of the compressive principal strain, which coincides with the direction of the compressive principal stress.

Fracture analysis begins by expressing the strain energy change (Fig. 10.3.4) caused by the formation of the crack band of length c at constant load-point displacement:

$$\Delta\mathcal{U}_c = -\frac{(\sigma_c - \sigma_r)^2}{2E_c} cD \tag{10.3.17}$$

The minus sign reflects the fact that this is an energy loss rather than gain.

The stress σ_r in the foregoing equation represents the residual compression strength of the crack band of concrete. In this study, the residual compression strength σ_r is considered to be an empirical property. However, it can be mathematically expressed on the basis of the concept of internal buckling of a material heavily damaged by axial splitting microcracks, as proposed in Bažant (1994a) and Bažant and Xiang (1997); see Section 9.5.

The energy release rate may be calculated as:

$$\mathcal{G} = -\frac{1}{b}\left[\frac{\partial\Delta\mathcal{U}_c}{\partial c}\right]_u = \frac{(\sigma_c - \sigma_r)^2}{2E_c} D \tag{10.3.18}$$

The energy dissipation rate (fracture resistance) of the crack band is again given by (10.3.4), i.e., $\mathcal{R} = G_f h/s_c$, in which the width of the crack band may be assumed to evolve again according to (10.3.6), i.e., $h = h_0 c/(w_0 + c)$.

Substituting now (10.3.14) and (10.3.15) into (10.3.18), and using the fracture propagation criterion $\mathcal{G} = \mathcal{R}$, we obtain an equation which can be easily solved for v_u. This provides the result:

$$v_u = v_p\left(1 + \frac{D}{D_0}\right)^{-1/2} + v_r \tag{10.3.19}$$

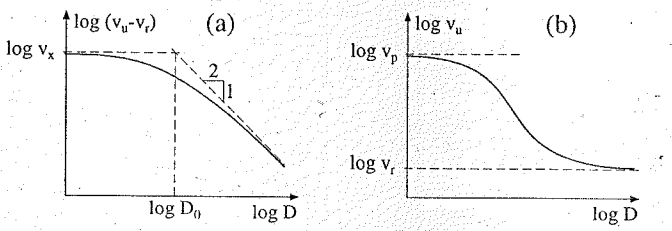

Figure 10.3.5 Size effect in shear failure of concrete beam in terms of the logarithm of either v_u or $v_u - v_r$.

in which we introduced the notations:

$$D_0 = w_0 \frac{D}{c} \tag{10.3.20}$$

$$v_r = \frac{\sin 2\theta}{2}\sigma_r, \qquad v_p = K_c \sqrt{\frac{h_0}{2 s_c w_0}} \sqrt{\frac{c}{D}} \sin 2\theta \tag{10.3.21}$$

The size effect described by (10.3.19) is plotted in Fig. 10.3.5 in two ways, in terms of $\log(v_u - v_r)$ and in terms of $\log v_u$. By virtue of the residual compression strength, the nominal shear strength of the beam tends at infinite size to a finite value. An equation of the form of (10.3.19) was proposed on the basis of general considerations in Bažant (1987a).

The question whether the confinement of concrete by stirrups suffices to cause the residual compression strength σ_r, and thus the residual nominal strength v_r, to be nonzero needs to be studied further. It is on the safe side to take $v_r = 0$, in which case, the effect of stirrups on the residual nominal strength provided by concrete is neglected.

10.3.4 Analysis Based on Stress Redistribution and Complementary Energy

The truss model also allows an easy alternative calculation of the energy release on the basis of complementary energy $\mathcal{U}_c^*$. For the sake of simplicity, we now consider the residual strength $v_r = 0$, although a generalization to finite v_r would be feasible.

In the truss model, we isolate the representative cell limited by the shaded zone in Fig. 10.3.4. This cell must alone be capable to resist the applied shear force V. The compression failure of concrete in the band 12341 (Fig. 10.3.4) is considered to completely relieve the stress from the inclined strip 12561. If the applied shear force V is kept constant, the stress in the cell must redistribute such that all of the compression force in the inclined strut is carried by the remaining strips, shaded in Fig. 10.3.4. After that, all of the complementary energy in concrete in the cell is contained in the shaded strips. According to Bažant (1996b), the energy density is given by the shaded area in Fig. 10.3.6, and so the complementary energy density may be expressed as $\mathcal{U}_c^* = \left(\bar{\sigma}_c^2/2E_c\right)\mathcal{V}$ in which $\mathcal{V} = b(D\cos\theta - c\sin\theta)D/\sin\theta =$ volume of the shaded strips (Fig. 10.3.4), $\bar{\sigma}_c = F_c/b(D\cos\theta - c\sin\theta) =$ average normal stress in the direction of the strut, and $F_c = V/\sin\theta = v_u bD/\sin\theta =$ compression force transmitted by the strut. This yields for the complementary energy, after the stress redistribution at constant shear force V, the expression:

$$\mathcal{U}_c^* = \left(\frac{v_u D}{\sin\theta}\right)^2 \frac{bD}{2E_c(D\cos\theta - c\sin\theta)\sin\theta} \tag{10.3.22}$$

According to (2.1.21), the energy release rate is obtained by differentiation of the complementary energy at constant load (or constant shear force V):

$$\mathcal{G} = \frac{1}{b}\left[\frac{\partial \mathcal{U}_c^*}{\partial c}\right]_V = \frac{v_u^2 bD^3}{2E_c \sin^2\theta (D\cos\theta - c\sin\theta)^2} \tag{10.3.23}$$

This must be equal to the energy dissipation rate, which is given by the following equations, same as

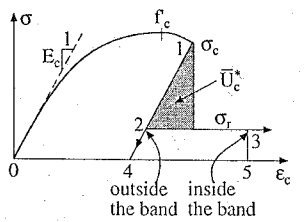

Figure 10.3.6 Compression stress-strain diagram of concrete with unloading after peak stress and area representing the strain energy release.

before:

$$\mathcal{R} = \frac{h}{s_c} G_f, \quad h = \frac{h_0 c}{w_0 + c} \tag{10.3.24}$$

There is now one difference from the previous approach. In (10.3.18), the energy release rate was constant, while in (10.3.23) it increases with c. This difference should not surprise since both solutions are approximate. In the case of variable $\mathcal{G}$, which is a typical case in fracture mechanics, the crack length at maximum load, that is, at a loss of stability, need not be considered as empirical, as done in our previous calculation based on the strain energy change, but can be calculated from the stability criterion. It is well known that, at the limit of stability, the curve of energy release rate at constant load must be tangent to the R-curve (see Section 5.6.3):

$$\frac{\partial \mathcal{G}}{\partial c} = \frac{d\mathcal{R}}{dc} \tag{10.3.25}$$

(This stability criterion could not be applied to the previous case with (10.3.18), because in that case, due to the approximations made, we had $\partial\mathcal{G}/\partial c = 0$ and thus c was indeterminate.) Because $\mathcal{G} = \mathcal{R}$, an equivalent condition is

$$\frac{1}{\mathcal{G}}\frac{\partial \mathcal{G}}{\partial c} = \frac{1}{\mathcal{R}}\frac{d\mathcal{R}}{dc} \tag{10.3.26}$$

which is more convenient. We may now substitute here the expressions in (10.3.23) and (10.3.24), and carry out the differentiations. This leads to a quadratic equation for c/D, whose only real solution is

$$\frac{c}{d} = \frac{3w_0}{4d}\left(-1 + \sqrt{1 + \frac{8d}{9w_0}\cot\theta}\right) \tag{10.3.27}$$

This represents a theoretical expression for the length of the crack band at maximum load (i.e., at stability loss).

It may now be observed that c/D tends to zero as the size $D \to \infty$. In that limiting case, the stress relief region would become an infinitely narrow strip, which would not be a realistic model. Therefore, (10.3.27) is meaningful only for sufficiently small sizes. For this reason, and for the sake of simplicity, we consider the second term under the square root in (10.3.27) to be small compared to 1. Because $\sqrt{1+2x} \approx 1 + x$ when $x \ll 1$, (10.3.27) for small D yields the approximation:

$$\frac{c}{D} = \frac{\cot\theta}{3} \tag{10.3.28}$$

Substituting this into the fracture propagation criterion $\mathcal{G} = \mathcal{R}$, along with (10.3.23) and (10.3.24), we obtain an equation whose solution furnishes the simple result:

$$v_u = v_p\left(1 + \frac{D}{D_0}\right)^{-1/2} \tag{10.3.29}$$

in which we have introduced the notations:

$$D_0 = 3w_0 \tan\theta \tag{10.3.30}$$

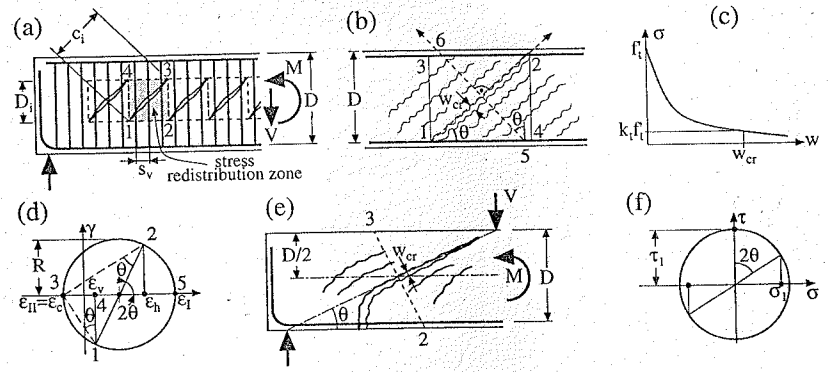

Figure 10.3.7 (a) Stress redistribution zones for initial diagonal shear cracks. (b) Localization of the openings of diagonal cracks into one major diagonal crack in a beam with stirrups. (c) Tensile stress-displacement diagram for the opening of a cohesive crack. (d) Mohr circle of strains. (e) Localization of openings of diagonal cracks into one major crack in a beam without stirrups. (f) Mohr circle of stresses.

$$v_p = K_c\sqrt{\frac{2h_0}{27s_c w_0}}\sin 2\theta\sqrt{\cot\theta} \tag{10.3.31}$$

The result we have obtained has the same form as (10.3.19), although the expressions for the size effect constants D_0 and v_p are partly different. The differences reveal the degrees of uncertainty caused by the simplifications of analysis we made. The comparison of (10.3.19) and (10.3.29) indicates that the general form of the size effect we obtained ought to be realistic although the coefficients D_0 and v_p cannot be fully predicted by the present theory but must be corroborated on the basis of experiments.

10.3.5 Size Effect on Nominal Stress at Cracking Load

It has been suggested that the size effect might not be of concern because the current ACI Code (ACI Committee 318, 1992) and other codes are intended to provide safety against the cracking load at which large diagonal cracks form, rather than against the collapse load, which is considerably higher. However, the nominal stress corresponding to the cracking load also exhibits size effect. There are two possibilities to define the cracking load.

Load Causing Cracks of Given Relative Depth

One possibility is to define the cracking load as the load that produces initial diagonal shear cracks of a depth D_i representing a given percentage of beam depth D, i.e., such that the ratio D_i/D is a given constant (Fig. 10.3.7a), say 0.5. We imagine an array of the initial cracks, as shown in Fig. 10.3.7a. The formation of each initial crack causes stress redistribution in triangular zones 1321 and 1341, shaded in Fig. 10.3.7a. (In contrast to Fig. 10.3.4, the stress relief zones are not strips, nor elongated triangles, because the material is not orthotropically damaged before the initial cracks form.) For the sake of simplicity, these zones may be assumed to consist of triangles with angles roughly $\theta = 45°$, each two triangles making a square. The shape of these zones and the length of the initial cracks obviously determines their spacing.

Before the initial diagonal cracks form, the vertical stress in the beam is 0, and so the stirrups have no stress, while shear force V is resisted by shear stresses in concrete taken approximately as $v = V/bd$. The complementary energy initially contained in the shaded square cell in Fig. 10.3.7a is $\mathcal{U}_0^* = (v^2/2G_c)b(c_i\cos\theta)(c_i\sin\theta) = v^2(1+\nu)bc_i^2\sin\theta\cos\theta/E_c$, where $G_c = E_c/2(1+\nu)$ = elastic shear modulus of concrete, ν = Poisson ratio ($\nu \approx 0.18$), and c_i is defined in Fig. 10.3.7a. After the initial cracks form, the diagonal tensile stress in the shaded square zone is reduced to 0 and the applied shear stress v is

then carried by truss action in the cell, i.e., by tensile stress σ_v in the vertical stirrups, given by (10.3.15), and by diagonal compressive stress σ_c, given by (10.3.14). So the complementary energy contained in the cell after the initial cracks form is approximately calculated as $\mathcal{U}_1^* = (\sigma_c^2/2E_c)b(c_i\sin\theta)(c_i\cos\theta) + (\sigma_v^2/2E_s)A_v(c_i^2/s)\sin\theta\cos\theta$, where $\sigma_v = vbs\tan\theta/A_v, \sigma_c = -v/\sin\theta\cos\theta$. For the sake of simplicity, we assume $\theta = 45°$. The complementary energy change per crack at constant V is $\Delta\mathcal{U}^* = \mathcal{U}_1^* - \mathcal{U}_0^*$, which yields

$$\Delta\mathcal{U}^* = \frac{bc_i^2v^2}{E_c}\left(\frac{1-\nu}{2} + \frac{bs}{4nA_v}\right), \qquad n = \frac{E_s}{E_c} \tag{10.3.32}$$

Consider now the final infinitesimal crack length increment δc_i by which the crack size c_i is reached (the shaded square zone in Fig. 10.3.7a grows with c_i, and at the end of this increment, it touches the square zone corresponding to the adjacent crack). During this increment, the change of complementary energy is $[\partial(\Delta\mathcal{U}^*)/\partial c_i]\delta c_i$. This must be equal to the energy consumed and dissipated by the crack, which is $b\mathcal{R}\delta c_i$; $\mathcal{R}$ is the crack resistance, which represents the critical energy release rate required for crack growth. In general, $\mathcal{R}$ depends on c_i, representing an R-curve behavior. This dependence may be approximately described as

$$\mathcal{R} = G_f\frac{c_i}{c_0 + c_i} \tag{10.3.33}$$

where c_0 is a positive constant. For large enough c_i, $\mathcal{R} = G_f$ = fracture energy of the material. The balance of energy during the crack length increment requires that

$$\frac{\partial(\Delta\mathcal{U}^*)}{\partial c_i}\delta c_i = b\mathcal{R}\delta c_i \tag{10.3.34}$$

Substituting (10.3.32) here, we obtain an equation whose solution yields, for the size effect on the applied nominal shear stress v_{cr} at initial cracking, the following equation:

$$v_{cr} = v_{cr0}\left(1 + \frac{D}{D_{cr0}}\right)^{-1/2} \tag{10.3.35}$$

in which the following constants have been introduced:

$$D_{cr0} = c_0\frac{D}{c_i}, \qquad v_{cr0} = \left[\frac{E_cG_f}{c_0}\left(2 + \frac{bs}{2nA_v} - \frac{1+\nu}{2}\right)^{-1}\right]^{1/2} \tag{10.3.36}$$

Note that the ratio D/c_i is assumed to be a given constant by which the cracking load is defined. Equation (10.3.35) shows that the applied nominal shear stress at cracking follows again Bažant's size effect law. As a special case, this equation applies to a beam without stirrups ($A_v = 0$).

Load Causing Cracks of Given Opening Width

Another possibility is to define the cracking load as the load that produces cracks of a given critical width w_{cr}. Consider first the beams with stirrups. Under a certain load, a number of parallel diagonal cracks may initiate. The cracks are cohesive. This means that crack-bridging stresses are transmitted across the cracks (due to aggregate pullout and other phenomena). Reduction of the crack-bridging stress to zero requires a considerable opening displacement of the crack, as is clear from the typical stress-displacement diagram used in the cohesive (fictitious) crack model; see Chapter 7. Furthermore, it is known that when many parallel cracks form, only one of them may open widely, while the others unload and close. In fact, such a localization of crack openings into one among many parallel cracks is a necessity unless there is enough reinforcement to ensure a stiffening rather than softening behavior (see Chapter 8; also Chapter 12 in Bažant and Cedolin 1991). Thus, unless the stirrups are extremely strong, the situation as shown in Fig. 10.3.7b must be expected.

Since the reduction of the crack-bridging stress to zero requires a very large opening, we consider that the stress is reduced only to a certain small but finite fraction k_t of the tensile strength f_t' of concrete.

Consider now the relative displacement between points 5 and 6 at the bottom and top of the beam, lying on a line normal to the cracks after one large crack forms. This displacement may be approximately expressed as $\Delta u_I = (D/\cos\theta)(k_t f_t'/E_c) + w_{cr}$, in which $D/cos\theta$ is the length of the line segment 56, and w_{cr} is a critical crack opening displacement at which the crack bridging stress is reduced from f_t' to $k_t f_t'$ (Fig. 10.3.7c). Dividing this by the length of segment 56, we obtain the average normal strain in the direction orthogonal to the diagonal cracks:

$$\bar{\varepsilon}_{I_{cr}} = \frac{\Delta u_I}{D/\cos\theta} = \frac{k_t f_t'}{E_c} + \frac{w_{cr}\cos\theta}{D} \tag{10.3.37}$$

Displacement Δu_1 or strain $\bar{\varepsilon}_{Icr}$ must be compatible with the overall deformation of the truss. Imagining the nodes of the truss to be attached to a homogeneously deforming continuum, this condition means that strain $\bar{\varepsilon}_{Icr}$ must be tensorially compatible with the normal strains ε_c in the inclined struts and ε_v in the vertical stirrups, as well as with the principal direction angle θ. This strain compatibility condition may be easily deduced from the Mohr circle in Fig. 10.3.7d. Noting that $14 = (\varepsilon_v - \varepsilon_c)\cot\theta$, $R = 05 = 01 = 14/\sin 2\theta = (\varepsilon_v - \varepsilon_c)\cot\theta/\sin 2\theta$, $\bar{\varepsilon}_I = \varepsilon_c + 2R$, we obtain the following expression for the average strain in the direction orthogonal to the diagonal cracks:

$$\bar{\varepsilon}_I = \varepsilon_c + \frac{\varepsilon_v - \varepsilon_c}{\sin^2\theta} = \frac{\varepsilon_v}{\sin^2\theta} - \varepsilon_c\cot^2\theta \tag{10.3.38}$$

In terms of the stresses, $\varepsilon_v = \sigma_v/E_s$, $\varepsilon_c = \sigma_c/E_c$, in which E_s = elastic modulus of steel and E_c = secant modulus for the compression strut at the moment the diagonal cracks form, which is less than the initial elastic modulus but larger than the secant modulus for the peak stress point of the compression stress-strain diagram. Here the stresses may be expressed from the equilibrium conditions of the truss: $\sigma_v = v_{cr}s_v b\tan\theta/A_v$, $\sigma_c = -2v_{cr}/\sin 2\theta$, where A_v = cross section area of one stirrup, and $v_{cr} = V_{cr}/bD$ = nominal stress corresponding to the shear force at the moment of formation of large diagonal cracks. Substituting these expressions into (10.3.38), we obtain:

$$\bar{\varepsilon}_I = \frac{2}{\sin 2\theta}\left(\frac{s_v b}{A_v E_s} + \frac{\cot^2\theta}{E_c^{\text{sec}}}\right) v_{cr} \tag{10.3.39}$$

Setting this expression equal to (10.3.37), we obtain an equation for v_{cr}, the solution of which furnishes the result:

$$v_{cr} = v_\infty + v_0\frac{w_{cr}}{D} \tag{10.3.40}$$

Here we introduced the notations:

$$v_0 = \sin\theta\cos^2\theta\left(\frac{s_v b}{A_v E_s} + \frac{\cot^2\theta}{E_c^{\text{sec}}}\right)^{-1}, \qquad v_\infty = \frac{k_t f_t' v_{cr}^0}{E_c\cos\theta} \tag{10.3.41}$$

Equation (10.3.40) describes a size effect which is an alternative to (10.3.35). The asymptotic constant value v_∞ exists because we assume that the critical crack opening w_{cr} corresponds to nonzero crack bridging stress $k_t f_t'$; if this stress were neglected, we would obtain $v_\infty = 0$.

Consider now a beam without stirrups. This problem is more complicated because there is no truss model that could give the value of the average strain along the line 23 in Fig. 10.3.7c. Other simplifications are, therefore, needed to obtain a simple result. We will assume that the normal strains along the line segment 23 in Fig. 10.3.7e may be approximated according to the beam theory. The shear stress in the vertical plane is distributed parabolically, and so, at point 1 at mid depth of the beam (neutral axis), it has the value $\tau_1 = 1.5v_{cr}$. From the Mohr circle in Fig. 10.3.7f, we then obtain the normal stress σ_1 in the direction 23 at point 1 and the corresponding strain: $\bar{\varepsilon}_1 = 1.5v_{cr}\sin 2\theta/E_c$. The normal strain in the direction 23 may also be assumed distributed parabolically, in which case the average normal strain along this line is $\bar{\varepsilon}_1 = v_{cr}\sin 2\theta/E_c$. Multiplying this by the length of segment 23, we obtain the relative displacement between points 2 and 3 in the direction 23:

$$\Delta u_{23} = \bar{\varepsilon}_1\frac{D}{\cos\theta} = \frac{v_{cr}}{E_c}\sin 2\theta\frac{D}{\cos\theta} \tag{10.3.42}$$

At the same time, in analogy to (10.3.37):

$$\Delta u_{23} = \frac{D}{\cos\theta}\frac{k_t f_t'}{E_c} + w_{cr} \tag{10.3.43}$$

Equating the last two expressions, we obtain the same equation as (10.3.41), that is, $v_{cr} = v_\infty + v_0(w_c/D)$, in which we now make the notations:

$$v_\infty = \frac{2k_t f_t'}{3\sin 2\theta}, \quad v_0 = \frac{E_c w_{cr}}{3\sin\theta} \tag{10.3.44}$$

10.3.6 Conclusions

1. The fracture modification (Bažant 1996b) of the classical widely used truss model (or the strut-and-tie model) for the shear failure of reinforced concrete beams describes the energy release and localization of damage into a band of compression splitting cracks (or a compression-shear crack) within a portion of the compressed concrete strut.
2. If the analysis of the maximum load based on the truss model is valid (and if the stirrups are designed sufficiently strong), the concrete strut must undergo compression softening (with progressive fracture) during the portion of loading history in which the maximum load is reached.
3. Analysis of the energy release into the crack band shows that a size effect on the nominal strength at shear failure of a reinforced concrete beam must occur and that it should approximately follow Bažant's size effect law. Conversely, the fracture behavior of the truss model (strut-and-tie model), particularly the damage localization with energy release, provides an explanation of the size effect widely observed in many tests as shown in the previous section.
4. The applied nominal shear stress that causes the initial large diagonal cracks also exhibits a size effect. The law of this size effect depends on how the large diagonal cracks are defined.
5. The foregoing size effect formulae have not yet been calibrated and verified by the available test results for beams. The expressions for the coefficients in these formulas need to be studied further in order to develop a design procedure incorporating the size effect.

10.4 Reinforced Beams in Flexure and Minimum Reinforcement

In this section, we examine with some detail the existing approaches to the failure of beams in bending. In general, it is accepted that strongly reinforced beams that fail by steel yielding are mostly fracture-insensitive. So, structures of this type have not been much investigated from the viewpoint of fracture mechanics. However, there are situations in which fracture plays a role; two extreme cases have been investigated by various authors: (1) failure of concrete in compression for normally reinforced concrete, and (2) failure of lightly reinforced beams.

The first type of failure, which was investigated by Hillerborg (1990), will be discussed in Section 10.5.12, mainly to show that even if normally reinforced beams are not sensitive to fracture in tension, they do show size effect due to fracture in compression. Investigations on the second case tremendously expanded in recent years. They will be discussed now.

10.4.1 Lightly Reinforced Beams: Overview

The question of minimum reinforcement calls for answering two problems: (1) stability of a system of interacting cracks, which ensures that the cracks will remain densely spaced, and (2) avoidance of snapback in bending at a cross section with only one crack. The first problem controls the spacing of bending cracks in beams which in turn controls their width. A certain minimum reinforcement is required to prevent a large crack spacing, causing a large crack opening. This problem is important for serviceability under normal loads and small overloads. The second problem, which is important for preventing sudden catastrophic failure without warning, will be discussed now.

In recent years, the analysis of lightly reinforced beams and of minimum reinforcement received considerable attention. This is probably due to the widespread feeling that this is a problem that can be handled with relative ease using fracture mechanics. In particular, lightly reinforced beams in three-point bending fail by a single crack across the central cross section, as opposed to normally reinforced beams in which multiple or distributed cracking occurs prior to collapse.

Before reviewing the various theoretical approaches to this problem, let us describe the main empirical facts. Figs. 10.4.1a–c show load-displacement curves measured for various reinforcement ratios. Fig. 10.4.1a shows the results by Bosco, Carpinteri and Debernardi (1990b), for concrete reinforced with standard ribbed steel. Fig. 10.4.1b shows some results reported by Hededal and Kroon (1991) on a similar material; note that in these tests, the beams had a short notch —5% of beam depth— on the tension side of the beam, which explains the sharper peak. Fig. 10.4.1c shows very recent results of Planas, Ruiz and Elices (1995) for lightly reinforced beams made of microconcrete. Although the materials and the test arrangements were quite different, the results are clearly similar.

From their tests and the theoretical analysis to be described later (Section 10.4.4), Ruiz, Planas and Elices (1993, 1996) suggested that for steel with low strain hardening, the load-deflection curve can generally be sketched as shown in Fig. 10.4.1d. A linear portion OL is followed by a nonlinear zone up to the peak LM after which a U-shaped portion MNP follows, ending at point P at which the reinforcement yields (if the reinforcement is elastic-perfectly plastic). This is followed by a relatively long tail PT with mild softening which theoretically has no end (for ideal steel) but in practice ends by steel necking and fracture. Since the steel never follows exactly an ideal plastic behavior with a sharp transition from elastic to plastic, the actual curve may look closer to the dashed curve $NP'T$ which rounds the corner at P due to strain-hardening.

In an ideal situation (no internal stresses due to shrinkage, no thermal gradients, nor chemical reactions) the linear limit depends only on the tensile strength of concrete, with $\sigma_N^L \approx f_t'$ (we do not care here about the 5% difference due to the concentrated load that was discussed in Section 9.3 with reference to the rupture modulus). After that limit, a fracture zone starts to grow towards the reinforcement across the cover, and the load-displacement curve for similar unreinforced beams is approximately followed (dashed line). When the fracture zone approaches or reaches the steel, two phenomena occur simultaneously: (**1**) the fracture zone is *sewed up* by the reinforcement, which is still elastic thus requiring an extra load to continue cracking; and (**2**) steel pullout and slip takes place. Therefore, the peak and near postpeak in the load-displacement curve and its neighborhood is controlled by three factors: (**a**) The steel ratio; (**b**) the bond-slip properties; and (**c**) the steel cover.

The influence of the steel ratio on the peak load was already illustrated in Figs. 10.4.1a–c. The influence of the bond is illustrated in Fig. 10.4.1e which shows the results of Planas, Ruiz and Elices (1995) for a fixed steel ratio and for two different types of reinforcement: ribbed bars with strong bond, and smooth bars with weak bond. It is clear that the bond strength modifies substantially the response. Finally, the influence of the cover is not so evident and little experimental support is available. However, that the cover must play a role can be inferred by the following reasoning. If the cover is large enough, the specimen load will exhibit a peak before the fracture zone reaches the reinforcement; then, after some load decrease, the growing fracture zone will reach the reinforcement and will be arrested, thus engendering hardening followed by a second peak and further softening. Therefore, the cover must influence the response. Indeed, Ruiz and Planas (1995) have detected, both experimentally and theoretically, the existence of the double peak, as shown in Fig. 10.4.1f. Certainly there also must be an indirect effect of the cover thickness and bar spacing because these variables are known to modify the bond strength, but this is a secondary influence in the usual analysis.

Several models have been proposed to describe the foregoing results; they can be classified as pertaining to three wide groups: (**1**) models that make use of LEFM as the basic tool; (**2**) models that use a simplified smeared cohesive cracks; and (**3**) models that use cohesive cracks. In the following, we describe the mean features of these three groups of models.

10.4.2 Models Based on LEFM

All the LEFM models are rooted in the model first proposed by Carpinteri (1981, 1984; also 1986, Sec. 6.2). Figs. 10.4.2a–c show the basic superposition in Carpinteri's approach: the reinforced beam with a crack of length a subjected to bending (Fig. 10.4.2a) is approximated by a beam subjected to the bending

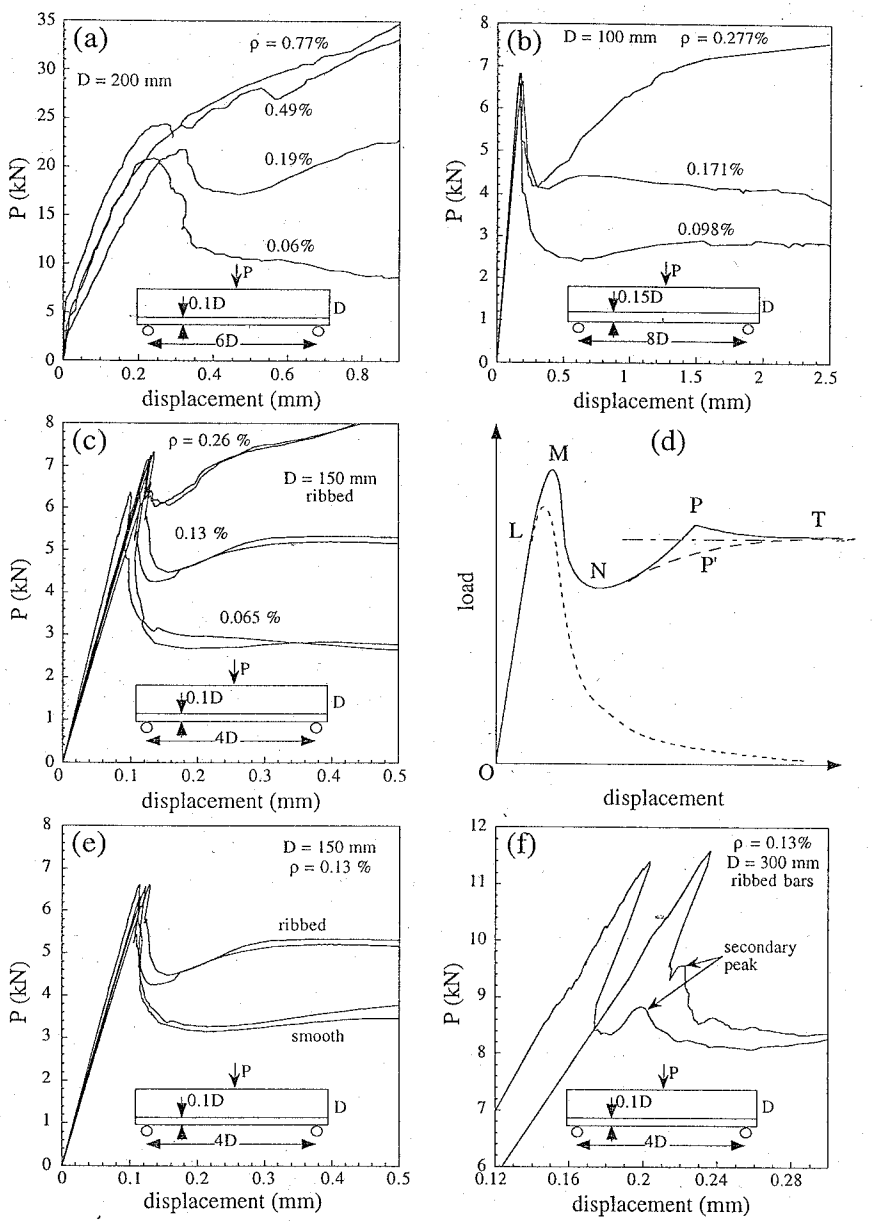

Figure 10.4.1 Influence of steel ratio on the load-displacement curves: (a) data from Bosco, Carpinteri and Debernardi (1990b); (b) data from Hededal and Kroon (1991); (c) data from Planas, Ruiz and Elices (1995) for microconcrete. (d) General trend of the load-displacement curve according to Ruiz, Planas and Elices (see the text for details). (e) Influence of bond on the response (after Planas, Ruiz and Elices 1995). (d) Experimental double peaks for a relatively thick cover (data from Ruiz and Planas 1995).

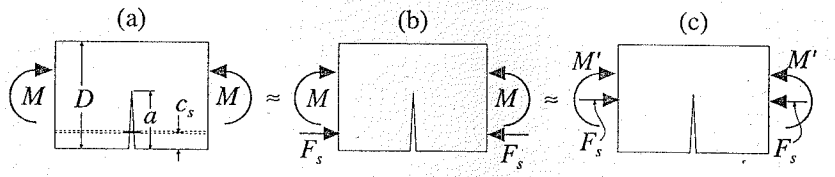

Figure 10.4.2 Carpinteri's LEFM approximation.

moment and to the steel force applied *remotely* from the crack plane (Fig. 10.4.2b). Next, the steel action is decomposed in a standard way into a bending moment and a centric force (Fig. 10.4.2c).

With this decomposition, we can easily write the stress intensity factor as:

$$K_I = \frac{6M'}{bD^2}\sqrt{D}k_M(\alpha) - \frac{F_s}{bD}\sqrt{D}k_\sigma(\alpha)\,, \qquad \alpha = \frac{a}{D}\,, \qquad M' = M - F_s\left(\frac{D}{2} - c_s\right) \tag{10.4.1}$$

where $k_M(\alpha)$ and $k_\sigma(\alpha)$ are the shape function for pure bending and for a uniform remote tension, respectively, and c_s is the steel cover (see Fig. 10.4.2). An approximate, but accurate, expression for $k_M(\alpha)$ is given, for example, by (3.1.1) for $S/D = \infty$; an expression for $k_\sigma(\alpha)$ can be found in most stress intensity factor manuals (e.g., Tada, Paris and Irwin 1985).

Carpinteri also calculated the additional rotation caused by to the crack θ_c according to the method described in Section 5.5.2 with $P_1 \equiv M$, $\theta_c \equiv u_1$, and $P_2 \equiv F$, with the result

$$\theta_c = \frac{6M'}{E'bD^2}v_{MM}(\alpha) - \frac{F_s}{E'bD}v_{M\sigma}(\alpha)\,, \qquad M' = M - F_sD\left(\frac{1}{2} - \gamma\right) \tag{10.4.2}$$

where $\gamma = c_s/D$ is the relative cover thickness and

$$v_{MM}(\alpha) = 12\int_0^\alpha k_M^2(\alpha')d\alpha'\,, \qquad v_{M\sigma}(\alpha) = 12\int_0^\alpha k_M(\alpha')k_\sigma(\alpha')d\alpha' \tag{10.4.3}$$

Carpinteri assumed that the steel behavior was elastic-perfectly plastic, and that the crack was closed ($\theta_c = 0$) while the steel remained elastic. Therefore, the crack growth takes place only when the steel yields and, simultaneously, $K_I = K_{Ic}$. With these conditions, it is easy to obtain the parametric equations of the moment-rotation curves (with parameter α). Indeed, setting $F_s = \rho bDf_y$ (where ρ is the steel ratio and f_y the steel yield stress) and $K_I = K_{Ic}$ in the foregoing equations, the solutions can be written as

$$\frac{\sigma_N\sqrt{D}}{K_{Ic}} = \frac{1}{k_M} + \left(3 - 6\gamma + \frac{k_\sigma}{k_M}\right)N_p \tag{10.4.4}$$

$$\frac{\theta_c E'\sqrt{D}}{K_{Ic}} = \frac{v_{MM}}{k_M} + \frac{k_\sigma v_{MM} - k_M v_{M\sigma}}{k_M}N_p \tag{10.4.5}$$

where, as always, $\sigma_N = 6M/bD^2$, and N_p is Carpinteri's brittleness number for reinforced beams in bending defined as

$$N_p = \rho\sqrt{\frac{D}{\ell_p}}\,, \qquad \ell_p = \left(\frac{K_{Ic}}{f_y}\right)^2 \tag{10.4.6}$$

Here we have introduced the length ℓ_p to emphasize the similitude of this brittleness number to those based on Irwin's or Hillerborg's characteristic size: the only change is to replace the tensile strength of concrete by the tensile strength of the reinforcement f_y.

One of the limitations of this model is that, due to the simplifications involved in its derivation, the crack cannot grow while the steel remains elastic and does not slip (in reality, it must slip). This limitation was removed, using very different methods, by Baluch, Azad and Ashmawi (1992) and by Bosco and Carpinteri (1992).

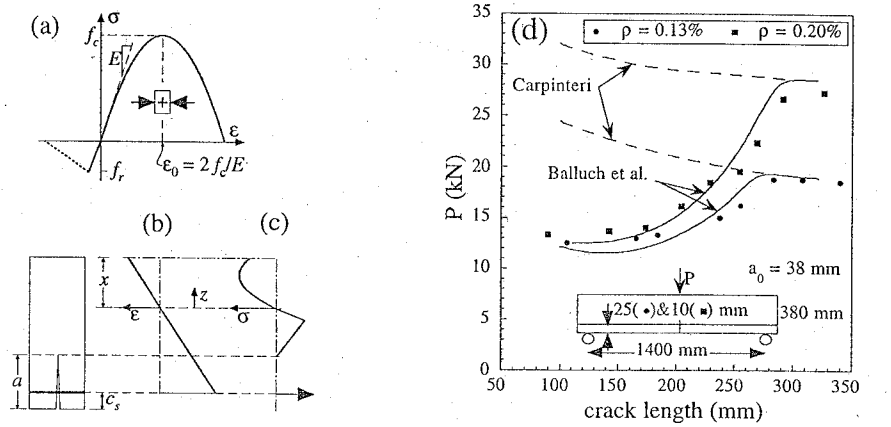

Figure 10.4.3 Model of Baluch, Azad and Ashmawi (1992): (a) stress-strain curve for concrete; (b) strain distribution; (c) stress distribution; (d) comparison of experimental and theoretical curves of load vs. crack length for lightly reinforced beams with a notch.

The model of Baluch, Azad and Ashmawi keeps Carpinteri's solution after steel yielding, but relaxes the assumption that the crack remains closed while the steel is elastic. In the elastic regime for steel, the model retains the stress intensity equation (10.4.1) and the condition $K_I = K_{Ic}$, which can be rewritten as

$$K_{Ic} = \frac{6M}{bD^2}\sqrt{D}\,k_M(\alpha) - \frac{F_s}{bD}\sqrt{D}\left[\left(3 - 6\frac{c}{D}\right)k_M(\alpha) + k_\sigma(\alpha)\right] \tag{10.4.7}$$

which provides one equation with two unknowns, namely, M and F_s (α is given in this context). To determine F_s, Baluch et al. introduced a classical analysis based on a stress-strain formulation with the following assumptions: (**1**) the stress-strain curve is as depicted in Fig. 10.4.3a, parabolic in compression and linear in tension down to the failure stress f_r which is taken to coincide with the modulus of rupture rather than with the tensile strength; (**2**) the softening in tension is linear, as depicted by the dotted line in Fig. 10.4.3a, but the softening slope depends on the geometry as indicated later; (**3**) the strain distribution is linear (Fig. 10.4.3b); (**4**) the fracture process zone is represented by a linear distribution of stress which is zero at the crack tip as shown in Fig. 10.4.3c. Note that the essential difference with respect to other formulations is that here the softening curve for concrete in tension is *not* related to the strain in a predefined way; rather, the form of the spatial distribution of stress is postulated. With these hypotheses, and given the stress-strain curve of the steel, it is possible to determine a relationship between F_s and M. For elastic behavior of the steel, the strain distribution is obtained from Fig. 10.4.3b:

$$\varepsilon = \frac{F_s}{A_sE_s}\,\frac{z}{D - c_s - x} \tag{10.4.8}$$

where A_s is the steel cross section and E_s its elastic modulus; x is the depth of the neutral axis. From this, the stress distribution can be determined as sketched in Fig. 10.4.3c. Then, the equilibrium of forces provides an equation with the two unknowns F_s and x, and the equilibrium of moments a further equation with the three unknowns F_s, x, and M. Complementing these two equations with (10.4.7), we get a system that determines the three aforementioned unknowns. This system must be solved numerically. Baluch, Azad and Ashmawi (1992) use two iteration loops: given a, they assume a value for F_s and solve iteratively for x from the condition of equilibrium of forces (inner iteration loop); then they compute M from the equilibrium of moments and from (10.4.7); if the two values coincide, this is the solution for the given crack depth; if not, they start over with a new value of F_s (outer iteration loop).

Baluch, Azad and Ashmawi (1992) checked their model by comparing the load-crack length curves for two lightly reinforced notched beams tested in three-point bending (the determination of load-displacement

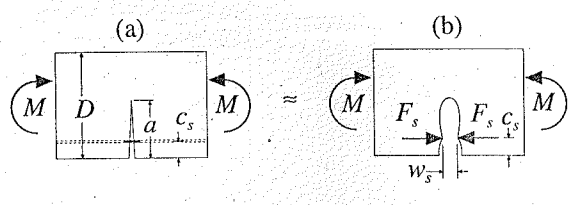

Figure 10.4.4 LEFM approximation of Bosco and Carpinteri (1992).

or moment-rotation curves were not included as part of the formulation). Fig. 10.4.3d shows the experimental results and the theoretical predictions (the dashed curves correspond to Carpinteri's model; note that the prediction of both models coincide after the yielding of steel). Note also that, much like what we indicated for the load-displacement curves in Fig 10.4.1c, the theory predicts a sharp change of slope upon steel yielding, while the experiments show a rounded transition.

Bosco and Carpinteri (1992) adopted an approach radically different from the one just discussed. They modified the initial Carpinteri's model by letting the force of the reinforcement act on the crack faces rater than remotely from the crack plane, as shown in Figs. 10.4.4a–b. However, the slip of reinforcement which must occur near the crack faces was neglected (even though elasticity indicates infinite stress at the point of intersection of the steel bar with the crack face). With this, the expression for the stress intensity factor reads

$$K_I = \frac{6M}{bD^2}\sqrt{D}\,k_M(\alpha) - \frac{F_s}{bD}\sqrt{D}\,k_F(\alpha,\gamma)\,, \qquad \alpha = \frac{a}{D}\,, \qquad \gamma = \frac{c_s}{D} \tag{10.4.9}$$

where $k_M(\alpha)$ is the same as in Eq. (10.4.1), and $k_F(\alpha,\gamma)$ is the shape factor for a pair of forces acting on the faces of the crack; a closed form expression for this shape factor can be found in Tada, Paris and Irwin (1985).

Now it is no longer necessary to assume that the crack is closed everywhere while the steel is elastic; it is enough to assume that the crack is closed at the point where the reinforcement crosses it. Allowance for bond slip could also be made; however, Bosco and Carpinteri did not consider this possibility. The method in Section 5.5.2 is used to determine expressions for the rotation and the crack opening at the reinforcement level with $P_1 \equiv M, u_1 \equiv \theta_c$ and $P_2 \equiv -F_s, u_2 \equiv w_s$, where w_s is the crack opening at the reinforcement level. The resulting expressions are as follows:

$$\theta_c = \frac{6M}{E'bD^2}v_{MM}(\alpha) - \frac{F_s}{E'bD}v_{MF}(\alpha,\gamma) \tag{10.4.10}$$

$$w_s = \frac{M}{E'bD}v_{MF}(\alpha,\gamma) - \frac{F_s}{E'b}v_{FF}(\alpha,\gamma) \tag{10.4.11}$$

where $v_{MM}(\alpha)$ is given by the first of (10.4.3), while $v_{MF}(\alpha,\gamma)$ and $v_{FF}(\alpha,\gamma)$ are given by

$$v_{MF}(\alpha,\gamma) = 12\int_\gamma^\alpha k_M(\alpha',\gamma)k_F(\alpha',\gamma)\,d\alpha'\,, \qquad v_{FF}(\alpha,\gamma) = 2\int_\gamma^\alpha k_F^2(\alpha',\gamma)\,d\alpha' \tag{10.4.12}$$

The integration is carried out over the crack portion in excess of cover thickness. This is so because for shorter cracks the stress intensity factor caused by the point loads is zero, i.e., $k_F(\alpha,\gamma) = 0$ for $\alpha < \gamma$.

Assuming that the functions v_{MM}, v_{MF} and v_{FF} have been determined, Eqs. (10.4.9)–(10.4.11) completely solve the problem of crack propagation. Two cases can arise:

Case 1: The steel is still in elastic state. In this situation, we set $w_s = 0$ in (10.4.11), solve for F_s from the resulting equation and substitute it in (10.4.9), simultaneously setting $K_I = K_{Ic}$; then we solve

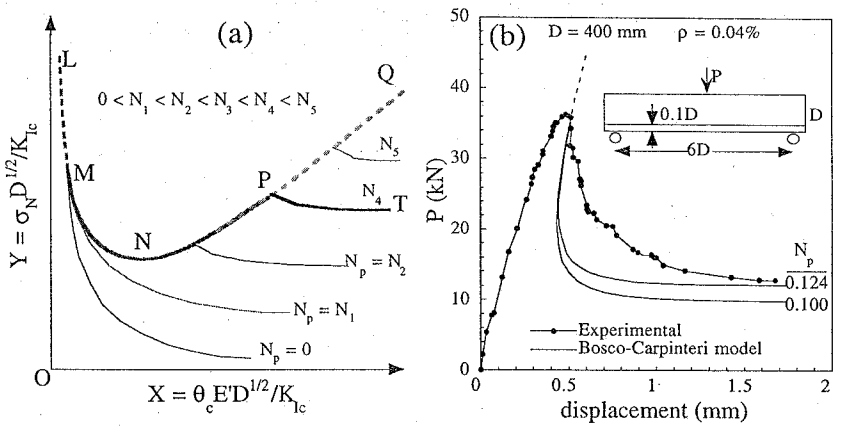

Figure 10.4.5 Bosco-Carpinteri model: (a) dimensionless load-curvature plot; (b) Massabò's (1994) fit to experimental curves by Bosco, Carpinteri and Debernardi (1990b)

the resulting equation for M. Finally, the rotation follows from (10.4.9). The final results are:

$$\left.\begin{aligned} \frac{\sigma_N\sqrt{D}}{K_{Ic}} &= \frac{v_{FF}}{k_M v_{FF} - 6k_F v_{MF}} \\ \frac{\rho\sigma_s\sqrt{D}}{K_{Ic}} &= \frac{v_{MF}}{k_M v_{FF} - 6k_F v_{MF}} \\ \frac{\theta_c E'\sqrt{D}}{K_{Ic}} &= \frac{1}{6}\,\frac{6v_{FF}v_{MM} - v_{MF}^2}{k_M v_{FF} - 6k_F v_{MF}} \end{aligned}\right\} \quad \text{for} \quad \sigma_s < f_y \tag{10.4.13}$$

where the arguments of the shape functions have been dropped for brevity, and σ_s is the stress in the steel. Note that the right hand sides of these equations are independent of the brittleness number N_p defined in (10.4.6). If the value of σ_s resulting from the foregoing equations exceeds the steel yield stress f_y, then we move to the next case.

Case 2: The steel yields. In this case, we set $F_s = bDf_y$ in (10.4.9)–(10.4.11) and solve for M (or σ_N) and θ_c (it might be useful to also check that $w_s > 0$; otherwise, we are in case 1). The resulting equations then are

$$\left.\begin{aligned} \frac{\sigma_N\sqrt{D}}{K_{Ic}} &= \frac{1}{k_M} + \frac{k_F}{k_M}N_p \\ \frac{\theta_c E'\sqrt{D}}{K_{Ic}} &= \frac{v_{MM}}{k_M} - \frac{k_F v_{MM} + v_{MF}k_M}{k_M}N_p \\ \frac{6w_s E'}{K_{Ic}\sqrt{D}} &= \frac{1}{k_M} - \frac{k_F v_{MF} + 6v_{FF}k_M}{k_M}N_p \end{aligned}\right\} \quad \text{for} \quad w_s > 0 \tag{10.4.14}$$

The plot of the $\sigma_N(\theta_c)$ curves in terms of the nondimensional variables $X = \theta_c E'\sqrt{D}/K_{Ic}$ and $Y = \sigma_N\sqrt{D}/K_{Ic}$ consists of two parts as sketched in Fig. 10.4.5a. The arc MNP is a part of the fixed curve $LMNPQ$ which is given by (10.4.13); this curve depends only on the relative steel cover γ, but is independent of the beam size, of the amount and quality of steel, and of the properties of concrete; it is a pure geometrical property. The arc PT corresponds to the solution for yielded steel and its shape is concave with a horizontal asymptote which corresponds to fully broken concrete. This branch PT depends only on the brittleness number N_p as sketched in the figure (and also on the relative cover thickness which is constant for geometrically similar beams).

In the foregoing equations, the rotation includes only the additional rotation caused by the crack at

remote cross sections. When dealing with the load-displacement curves, one can either subtract the elastic displacement from the total displacement to isolate the rotation due to the crack, or conversely, one can add the elastic displacement (analytically computed) to the concentrated rotation determined by the foregoing theory. This last approach was used in a recent work by Massabò (1994) to analyze the experimental results of Bosco, Carpinteri and Debernardi (1990a,b).

Massabò (1994) determined the values of v_{MM}, v_{MF}, and v_{FF} for each α and γ by numerically performing the integrations in (10.4.3) and (10.4.12). The integration for v_{FF} deserves further comments because as written in (10.4.12), its value is infinite. This is so because, for simplicity, the load was assumed to be applied at a single point, which always gives a logarithmic singularity at the load-point. In reality, the action of the reinforcement is distributed over a certain area which is of the order of the diameter of the bars. This problem can be easily handled by assuming, for example, that the force is uniformly distributed and using the general formulas to determine the crack opening profile as given in Section 5.2. But this requires a double integration which greatly complicates the solution of the problem. Therefore, Massabò (1994) proposed to take this effect into account by performing the integral over an interval that does not include the load-point, as follows:

$$v_{FF}(\alpha,\gamma) = 2\int_{\gamma+\epsilon}^{\alpha} k_F^2(\alpha',\gamma)\, d\alpha' \qquad (10.4.15)$$

Here, for a single layer of steel bars, ϵ is a small value proportional (but not identical) to the ratio D_b/D, with D_b = diameter of the bars.

Fig. 10.4.5b shows the kind of agreement with the experiments attained with the model of Bosco and Carpinteri. Note that the postpeak behavior is reasonably well predicted, but the model predicts a very large initial strength (for short cracks). This is a general limitation for the LEFM-based models because the stress intensity factor is always zero for uncracked specimens, implying that, in strict LEFM, a crack can never initiate in an unnotched specimen. Therefore, all these models must be interpreted as approximately describing the evolution of the fracture after the crack has formed; the crack initiation itself can be described only by recourse to nonlinear fracture mechanics, as in the models to be described next.

10.4.3 Simplified Cohesive Crack Models

In the literature, there are two slightly different approaches that use the cohesive crack model in a simplified form that avoids finite element computations. One model was put forward by the research group at Aalborg University (Ulfkjær, Brincker and Krenk 1990; Ulfkjær et al. 1994) and the other by the group at the University of New Mexico (Gerstle et al. 1992).

The basic idea is to describe the fictitious crack as a smeared crack of width h as shown in Fig. 10.4.6a. It is further assumed, based on the hypothesis of plane cross sections remaining plane, that the strain distribution along the beam depth is linear (Fig. 10.4.6b). Then, assuming a linear softening curve, the stress distribution can be computed as sketched in Fig. 10.4.6c. The stress-strain curve in tension is completely determined by the tensile strength f_t' and the critical crack opening w_c, as shown in Fig. 10.4.6d. The stress-strain curve in compression is assumed to be linear all the way to complete fracture. The essential difference between the two approaches is that Ulfkjær et al. consider a smeared band width proportional to the size, $h = \eta D$, while Gerstle et al. consider a width twice the instantaneous cohesive crack length ($h = 2y$, see Fig. 10.4.6).

Although the analytical approaches vary, the essential steps are the same: (1)write the strain distribution as a function of the curvature κ and the position of the neutral axis x; (2) use the stress-strain curves for concrete and steel to express the stress distribution and the steel force as a function of κ and x (this includes the determination of y); (3) write the equation of equilibrium of forces and solve for x as a function of κ; (4) write the equation of equilibrium of moments; (5) finally, from the three equations deduced in (2)-(4), solve for y, x, and M for any given κ. Obviously, the system of equations depends on the load level because of the discontinuity in the derivatives of the stress-strain curves for concrete and steel.

As pointed out before, the smearing band width assumed in these models is different. Ulfkjær et al. assume $h = \eta D$, with $\eta = 0.5$. This value of η was based on comparisons of the load-displacement (moment-curvature) diagrams for unreinforced beams predicted by the approximate model and by accurate finite element computations. Gerstle et al. assume *a priori* that $h = 2y$ and verify that, for an unreinforced

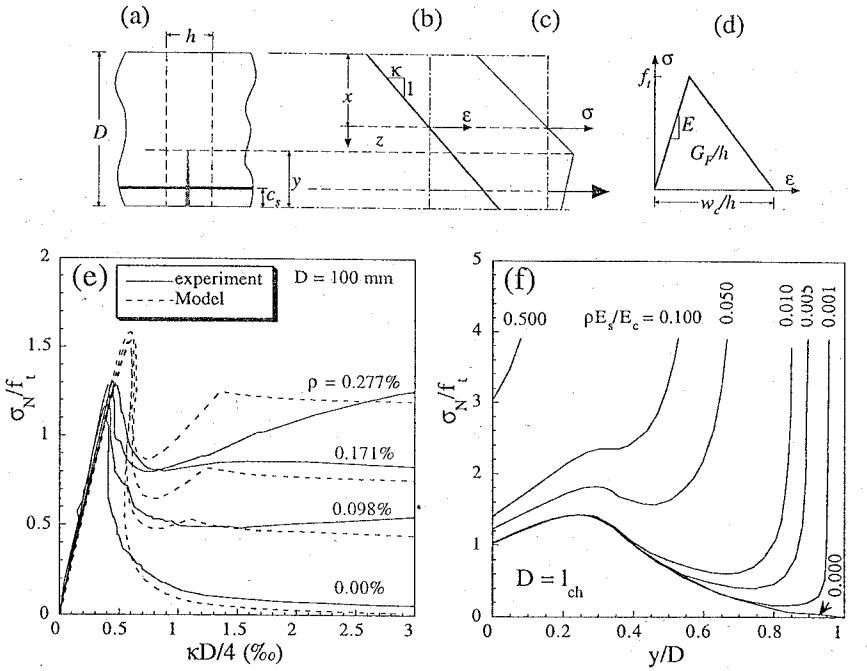

Figure 10.4.6 Simplified cohesive crack models. (a) Smearing band. (b) Strain distribution. (c) Stress distribution. (d) Approximate stress-strain curve. (e) Experimental and theoretical nominal stress-rotation curves computed by Ulfkjær et al. (1994). (f) Theoretical nominal stress-cohesive crack length curves computed according to the model by Gerstle et al. (1992).

beam, the moment vs. cohesive crack length curve predicted by their model is reasonably close to the curve obtained by finite elements. However, this verification has been done only for the ascending part of the curve and only for one size. Further validation is necessary.

Secondary differences between these models are that, in the formulation of Ulfkjær et al., the steel cover is arbitrary and the steel is allowed to yield in a perfectly plastic manner, while Gerstle et al. consider only a vanishing cover thickness to obtain simpler expressions and assume the steel to be always elastic, as is manifested by the increasing load value at the tail of the curves in Fig 10.4.6f.

10.4.4 Models Based on Cohesive Cracks

The cohesive crack model has been used by several investigators to analyze lightly reinforced beams in three-point bending. All the analyses up to now simplify the problem by assuming that a single cohesive crack forms at the central cross section while the concrete in the bulk behaves elastically and the steel is elastic-perfectly plastic. The various analyses differ in the computational method and in the way they incorporate the effect of the reinforcement.

Hawkins and Hjorsetet (1992) use a commercial finite element code to simulate the experiment of Bosco, Carpinteri and Debernardi (1990b). They use the method described in Section 7.2.3 in which the cohesive zone is modeled by an array of elastic-softening springs. Although they do not explicitly consider bond slip, they made two kinds of analysis: one standard (called P-MAX) in which perfect adherence was assumed, and another (called P-MIN) in which the cross sections were forced to remain plane. In the first case, a large strain is generated in the reinforcement as soon as the crack tip reaches it, which causes the steel to yield. In the second case, the strain is smeared over the element width, which is similar (although

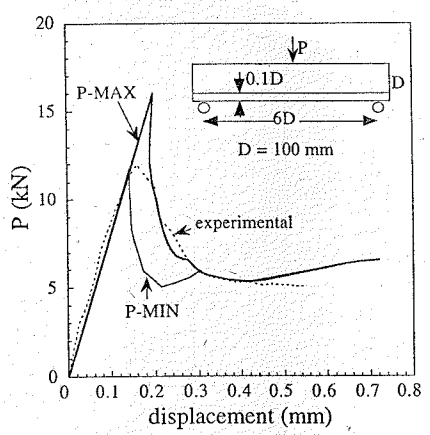

Figure 10.4.7 Numerical load-displacement curves computed by Hawkins and Hjorsetet (1992) using a cohesive crack model; P-MAX curve corresponds to perfect bond; P-MIN to plane cross sections.

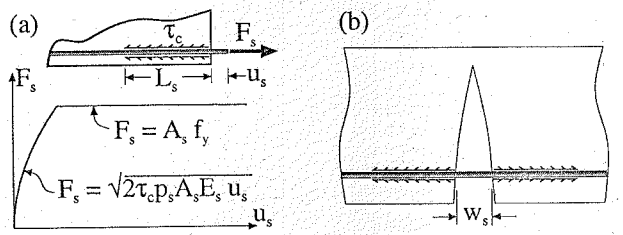

Figure 10.4.8 Simple pullout model (a) and application to the reinforced beam (b) (from Ruiz 1996).

not identical) to having a slip length equal to the element width. Fig. 10.4.7 shows the results of the computations together with the experimental results of Bosco, Carpinteri and Debernardi (1990b). Note that the P-MAX and P-MIN predictions differ appreciably, especially as far as the peak load is concerned; this indicates that the bond must play an important role in defining the minimum reinforcement.

Hededal and Kroon (1991) and Ruiz et al. (Ruiz, Planas and Elices 1993, 1996; Ruiz and Planas 1994, 1995; Planas, Ruiz and Elices 1995; Ruiz 1996) use very similar computational procedures, traceable to Petersson's influence matrix method (see Section 7.4). The two groups consider bond slip in a very similar fashion, but use a different way to implement it numerically. They both consider the same classical load-displacement curve which is obtained for pullout from a rigid half-space, depicted in Fig. 10.4.8a. They also assume that, in the actual test, the steel displacement u_s is given by half the crack opening at the reinforcement, w_s (Fig. 10.4.8b); therefore, the force-crack opening displacement is given by

$$F_s = \begin{cases} \sqrt{\tau_c p_s A_s E_s w_s} & \text{for } w_s < w_y = \dfrac{A_s f_y^2}{p_s E_s \tau_c} \\ A_s f_y & \text{for } w_s < w_y \end{cases} \qquad (10.4.16)$$

where F_s is the resultant tensile force in the steel at the central cross section, τ_c is the bond shear strength (rigid-plastic behavior assumed), p_s and A_s are the perimeter and the area of the reinforcement, and E_s, and f_y are the elastic modulus and the yield limit of steel (elastic-perfectly plastic behavior is assumed).

Hededal and Kroon (1991) introduce the action of the steel on the concrete as the force F_s concentrated at the surface of the cohesive crack and treat it as a cohesive force with a load-crack opening curve as deduced from (10.4.16). Their theoretical predictions compare quite realistically with their experimental

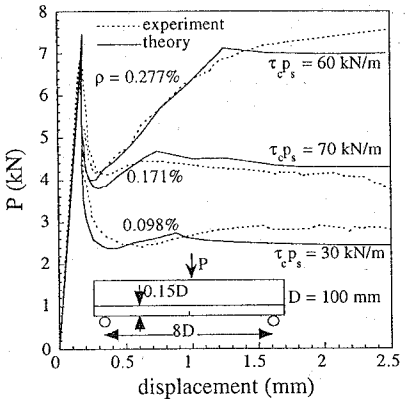

Figure 10.4.9 Comparison of the numerical and experimental results of Hededal and Kroon (1991).

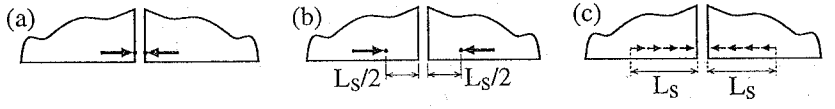

Figure 10.4.10 Approximations analyzed by Planas, Ruiz and Elices (1995): (a) concentrated forces on the crack faces; (b) concentrated forces at the center of gravity of the bond stresses; (c) distributed bond stresses. (From Planas, Ruiz and Elices 1995.)

results as shown in Fig. 10.4.9. In making the predictions, Hededal and Kroon use material parameters determined from independent experiments, except for the bond strength which they select in each case to give a good fit of the postpeak values. The softening curve for concrete is assumed to be bilinear and is determined from tests on notched plain concrete specimens. The steel bars are threaded bars rather than conventional reinforcing steel bars. The ultimate load and the apparent elastic modulus are determined from tensile tests. Note that Hededal and Kroon use the product $\tau_c p_s$ instead of τ_c to characterize the bond strength; $\tau_c p_s$ is the shear force per unit length of reinforcement.

Ruiz and Planas (1994) and Ruiz, Planas and Elices (1993) use a different numerical approach which incorporates the effect of the reinforcement by means of internal stresses. This allows considering the steel-concrete interaction to be located within the concrete rather than at the surface. They analyze the three options depicted in Fig. 10.4.10a–c. In their first approach, they analyze the case of perfect bond with the steel-concrete interaction represented by two forces acting on the crack faces (Fig. 10.4.10a; Ruiz, Planas and Elices 1993; Ruiz 1996).

This analysis reveals that the cohesive crack growth process follows the stages shown in Fig. 10.4.11a-e: in stage (a), the cohesive zone extends through the cover and may go through the first peak if the cover is thick; then the cohesive crack is pinned by the steel and hardening occurs until, as shown in (b), the tensile strength is reached at points ahead of the reinforcement; from then on, two separate cracks exist at both sides of the reinforcement until the yield strength is reached in the steel as shown in (c); then a softening phase begins, with an open crack extending across the reinforcement as shown in (d).

The analysis confirms Hawkins and Hjorsetet's (1992) conclusion that perfect adherence implies a very sharp and high peak. However, it also turns out that this peak depends strongly on the width (diameter) of the reinforcement or, if the steel force is concentrated at a node, on the width of the elements used in the computations. The reason is that, in this approach, the steel force is modeled as a nodal force, which causes that the computational procedure smears this force roughly over an element width, and thus one never deals with a concentrated force but with a distributed force; if the force were really concentrated at a

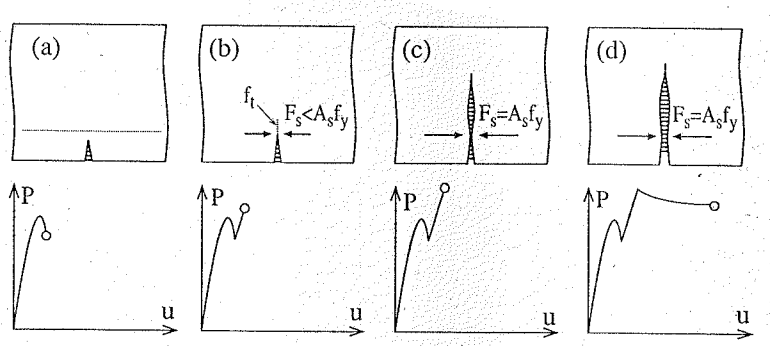

Figure 10.4.11 Crack growth process for full bond of reinforcement: (a) The cover cracks; (b) new crack forms ahead of the reinforcement; (c) steel yields; (d) full crack formed. (Adapted from Ruiz 1996.)

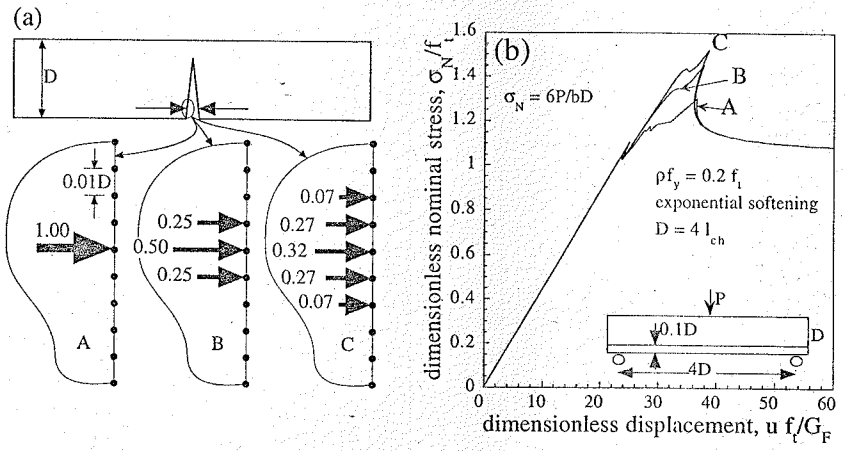

Figure 10.4.12 Influence of distributing the steel force on the crack faces: (a) three possible distributions; (b) corresponding load-displacement curves. (After Ruiz 1996.)

point, the compliance would be infinite and the peak would decrease. This effect is shown in Fig. 10.4.12, where the effect of smearing the force over 1, 3, or 5 nodes is shown for equal elements 1/100 of the beam depth in size (Ruiz 1996). It is clear that the wider the reinforcement, the stiffer the response.

The foregoing problem —the effect of the element size or reinforcement width— appears whenever the steel force is concentrated at the crack faces, even if the bond slip is taken into account. To avoid introducing the width of the reinforcement as a further variable, Planas, Ruiz and Elices (1995) and Ruiz (1996) let the steel-concrete interaction occur inside the concrete as shown in Fig. 10.4.10b–c. The simplest approach uses a concentrated force acting at the center of gravity of the shear stress distribution, much like in the approach by Bažant and Cedolin (1980), called the effective slip-length model. The location of the concentrated forces varies with the crack opening at the level of steel as follows:

$$L_e = \frac{L_s}{2} = \sqrt{\frac{A_s E_s}{4\tau_c p_s} w_s} \qquad (10.4.17)$$

where L_s is the slip length, which is readily obtained from the simple pullout model.

To solve the numerical problem in a computationally inexpensive way, Ruiz et al. first write the actual

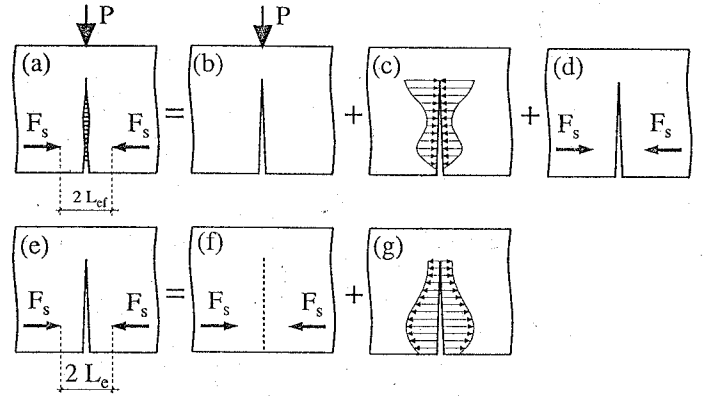

Figure 10.4.13 Successive decomposition of the problem as a sum of elastic problems (from Ruiz 1996).

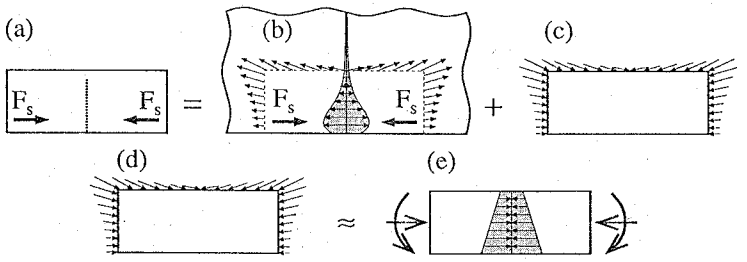

Figure 10.4.14 Approximate closed form solution for the internal pair of forces (from Ruiz 1996).

problem (Fig. 10.4.13a) as the superposition of the three elastic cases shown in Figs. 10.4.13b-d. The first two cases are the classical cases appearing in plain concrete. The third case —introducing crack openings, but no stresses— is handled as shown in Figs. 10.4.13e-g which involve the determination of the stresses engendered on the central cross section in an uncracked beam: this is an internal stress field which is then handled in a way similar to thermal or shrinkage stresses (Petersson 1981; Planas and Elices 1992b, 1993b). The only problem is the determination of the stresses in the auxiliary problem in Fig 10.4.13f. This is approximately solved in closed form as follows (Ruiz and Planas 1994; Ruiz 1996).

The actual problem —Fig. 10.4.14a— is considered as the elastic solution for two concentrated loads parallel to the surface of an elastic half-space (Fig. 10.4.14b) plus the elastic solution for the beam subjected to surface tractions canceling those in the previous solution (Fig. 10.4.14c). The last problem is approximately solved by replacing it with a mechanically equivalent linear stress distribution at the cross-section, as sketched in Fig. 10.4.14d-e. The complete stress distribution can thus be obtained in a closed form from Melan's (1932) elastic solution for a point load parallel to the surface of the half-space. The integration of the surface tractions and their moments, required to find the solution in Fig. 10.4.14e, can be performed analytically (a symbolic mathematical package was used by Ruiz to get the closed form quadratures; see Ruiz 1996 for details).

The model was further refined by Ruiz (1996) to allow distributed bond stresses to be directly used as shown in Fig. 10.4.13a. The stress distribution caused by the reinforcement can be obtained in a closed form by integrating the solution for the concentrated load. This is cumbersome but feasible if one of the modern symbolic mathematical packages is used. However, detailed comparisons showed that the differences with respect to the effective slip-length approach are negligible for most practical cases (Ruiz 1996).

This model was successfully used to describe the tests on microconcrete performed by Ruiz et al. as

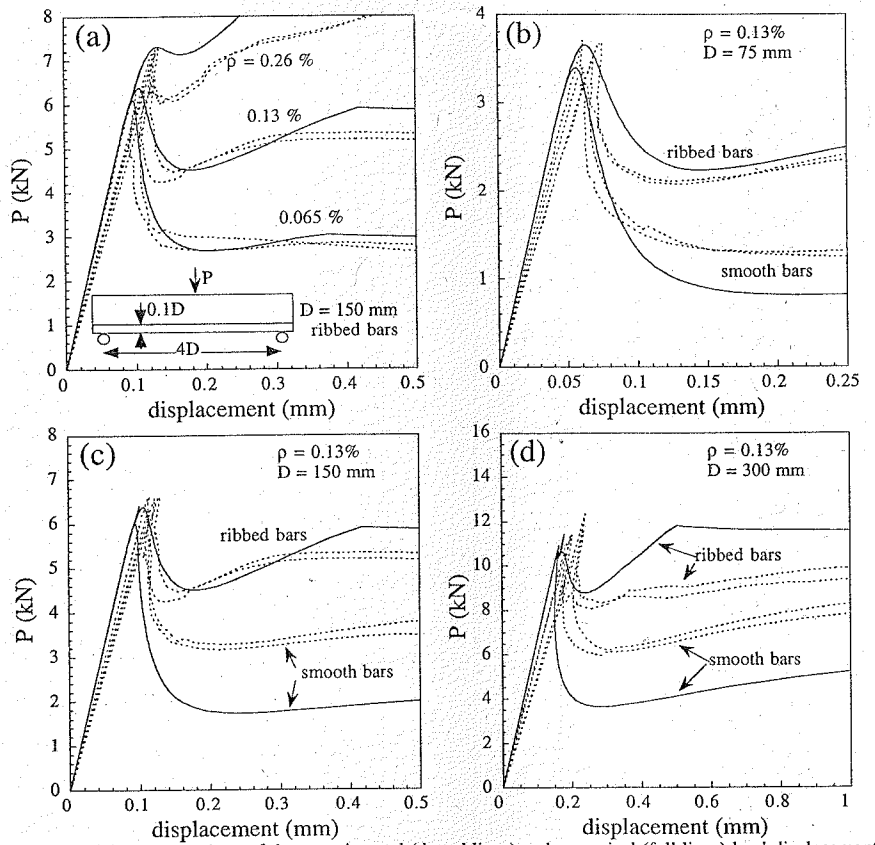

Figure 10.4.15 Comparison of the experimental (dotted lines) and numerical (full lines) load-displacement curves (from Planas, Ruiz and Elices 1995): (a) influence of the reinforcement ratio; (b–d) influence of the bond strength on beams with the same reinforcing ratio but different depth. Note that the bond was determined from independent pullout tests: no parameter fitting has been done.

illustrated in Fig 10.4.15a (Ruiz and Planas 1995; Planas, Ruiz and Elices 1995; Ruiz 1996). The important point in this comparison is that all the parameters required to make the predictions were determined by independent tests. In particular, the bond strength τ_c was determined form pullout tests; much better fits can be achieved if the value of τ_c is adequately selected for each test. Moreover, the model, conceptually simple as it is, shows that the problem is governed by four dimensionless parameters. These parameters are the following:

$$D^* = \frac{D}{\ell_1}, \qquad \rho = \frac{A_s}{A_c}, \qquad f_y^* = \frac{f_y}{f_t'}, \qquad \mu = \sqrt{\frac{n\tau_c p_s \ell_1}{f_t' A_s}} \tag{10.4.18}$$

where ℓ_1 is the characteristic size based on the initial linear softening defined in (10.1.10), ρ is the steel ratio, f_y^* is the relative yield strength of steel, μ is a dimensionless parameter which characterizes the bond, and $n = E_s/E_c$ is the ratio of the elastic moduli of steel and concrete.

The foregoing model was used to investigate the influence of various parameters on the behavior of lightly reinforced beams. The most important result is that a closed-form expression has been found for

the first peak of the load-displacement curve. Since this first peak occurs at the initial stages of cracking, before much softening take place, the peak load is controlled by the characteristics of the initial straight portion of the softening curve. Consequently, as discussed in Section 7.2.4, the size effect is controlled by ℓ_1, rather than by $\ell_c h$; see (7.1.17). Moreover, since the steel remains elastic at this stage, the yield strength of steel cannot influence the value of this first peak. This means that the nominal stress at the first peak σ_{Nc} can be written as

$$\sigma_{Nc} = f_t' \phi \left(\frac{D}{\ell_1}, \frac{c_s}{\ell_1}, \rho, \mu \right) \tag{10.4.19}$$

where ϕ is a dimensionless function and c_s is the steel cover. Numerical simulations showed that this function may be, in a crude approximation, expressed as

$$\sigma_{Nc} = f_r + \rho f_t' \mu \, 6 \left(1 - \frac{c_s}{D} \right) \psi \tag{10.4.20}$$

where f_r is the rupture modulus and ψ a factor depending on the beam depth and cover thickness, approximately given by

$$\psi = \left(\frac{D}{\ell_1} \right)^{1/4} - 3.61 \frac{c_s}{\ell_1} \geq 0 \tag{10.4.21}$$

where the last inequality defines the range of application of the formula.

Note that the modulus of rupture in the foregoing formulas is itself size-dependent and can be approximated by the formula (9.3.12) due to Planas, Guinea and Elices (1995).

10.4.5 Formulas for Minimum Reinforcement Based on Fracture Mechanics

In most cases, the minimum reinforcement must ensure that the ultimate (collapse) load (point T in Fig. 10.4.1d) be equal to the first peak load (point M in Fig. 10.4.1d). Based on purely experimental grounds, Bosco and Carpinteri (1992) proposed a formula which correlates the brittleness number $N_{p_{\min}}$ at which the minimum reinforcement condition is met, to the compressive strength of the concrete, f_c:

$$N_{p_{\min}} = 0.1 + 0.23 \frac{f_c}{\sigma_1}, \qquad \sigma_1 = 100 \text{ MPa} \tag{10.4.22}$$

From this and the definition (10.4.6), we can solve for $\rho_{\min}$ and get

$$\rho_{\min} = \frac{K_{Ic}}{f_y \sqrt{D}} \left(0.1 + 0.23 \frac{f_c}{\sigma_1} \right), \qquad \sigma_1 = 100 \text{ MPa} \tag{10.4.23}$$

Note that this formula is purely empirical since the first peak of the load cannot be adequately predicted with the model of Bosco and Carpinteri (1992).

Baluch, Azad and Ashmawi (1992) proposed the following formula for minimum reinforcement based on the model described in Section 10.4.2:

$$\rho_{\min} = \frac{1.9134 K_{Ic}^{0.82}}{f_y^{0.9922} (1.7 - 2.6 c_s/D)} \tag{10.4.24}$$

where K_{Ic} and f_y must be expressed, respectively, in MPa$\sqrt{\text{m}}$ and MPa. Note that the lack of dimensional consistency indicates that there is a certain degree of empiricism in this equation. (In the original paper, there is a misprint in the formula using units of N and mm —the factor in the numerator should appear in the denominator; here the standard IS units are used, and the formula has been checked against the tabulated values in that paper.)

Gerstle et al. (1992) pushed the definition of $\rho_{\min}$ further by requiring that the load increase monotonically all the time during the test (e.g., curve for $\rho E_s/E_c = 0.10$ in Fig. 10.4.6f). The formula they proposed is

$$\rho_{\min} = \frac{E_c}{E_s} \left(\sqrt{0.0081 + 0.0148 \frac{f_t' D}{E_c w_c}} - 0.0900 \right)^{1/2} \tag{10.4.25}$$

Note that this formula, due to the particular definition of the authors, does not depend on the strength of the reinforcement, but only on its elastic properties. We will see that this formula gives values far larger than the other models and larger than the currently accepted values in the codes.

Hawkins and Hjorsetet (1992) also proposed a formula for minimum reinforcement based on the cohesive crack model as well as some concepts derived from Carpinteri's approach. Their final formula reads

$$\rho_{\min} = 0.175 \frac{f_r D}{f_y (D - c_s)} \tag{10.4.26}$$

where f_r is the rupture modulus for an unreinforced beam of the same dimensions as the actual reinforced beam. According to these authors the modulus of rupture can be computed using a cohesive crack model with the appropriate softening curve. Therefore, it is possible to use the equation (9.3.12) to get a closed-form expression as

$$\rho_{\min} = 0.175\zeta \left(1 + \frac{1}{0.85 + 2.3D/\ell_1}\right) \frac{f_t' D}{f_y (D - c_s)}, \quad \ell_1 = \frac{E_c w_1}{2 f_t'} \tag{10.4.27}$$

where $\zeta = 1.046$ for three-point bending and 1 for four-point bending.

None of the preceding formulas take into account the bond strength. Ruiz, Planas and Elices (1996) and Ruiz (1996) have proposed a formula taking this effect into account. The formula is based on the cohesive crack model, more specifically on the expression (10.4.20) giving the first peak load. The final plastic collapse load is obtained from elementary considerations of equilibrium of moments as

$$\sigma_{Np} = \rho f_y \, 6 \left(1 - \frac{c_s}{D}\right) \tag{10.4.28}$$

Then, setting $\sigma_{Nc} = \sigma_{Np}$, solving for $\rho = \rho_{\min}$, and inserting (9.3.12), one gets

$$\rho_{\min} = \frac{\zeta}{6(1 - c_s/D)} \frac{1 + (0.85 + 2.3D/\ell_1)^{-1}}{f_y/f_t' - \mu \left[(D/\ell_1)^{1/4} - 3.61 c_s/\ell_1\right]} \tag{10.4.29}$$

Comparing the aforementioned models is not straightforward because they are based on different assumptions and depend on different parameters. This means that the predictions can be similar for certain conditions and differ for other conditions; no exhaustive comparison has been done to date. Fig. 10.4.16 shows the dependence on size of the minimum reinforcement for the various models in a particular case defined as follows:

1. The concrete is assumed to be characterized by $f_t' = 4$ MPa, $f_c = 40$ MPa, $E_c = 30$ GPa, $G_F = 160$ N/m (total fracture energy, as determined from the work-of-fracture test). For Carpinteri's and Baluch's model, it is assumed that Irwin's relation holds: $K_{Ic} = \sqrt{E_c G_F} = 2.19$ MPa$\sqrt{\text{m}}$. For Gerstle's formula, linear softening is assumed with $w_c = w_1 = 2G_F/f_t' = 80$ μm. For Hawkins' formula, Petersson's bilinear softening is assumed with $w_1 = G_F/f_t' = 48$ μm. For Ruiz's models, bilinear softening is assumed with $w_1 = G_F/f_t' = 40$ μm.
2. The steel is assumed to have $E_s = 210$ GPa, $f_y = 480$ MPa.
3. The cover of concrete reinforcement is assumed to be of constant thickness $c_s = 24$ mm.
4. For Ruiz's model, the bond parameter μ is taken to be constant. This is achieved by using bars of the same diameter for all beam sizes. Two values are considered: $\mu = 10$ (weak bond,16 mm diameter bars with $\tau_c \approx 0.4 f_t'$) and $\mu = 40$ (strong bond, 8 mm diameter bars with $\tau_c \approx 3 f_t$).

Fig. 10.4.16a shows the entire set of curves with a vertical logarithmic scale making it clear that the formulas of Baluch, Azad and Ashmawi (1992) and of Gerstle et al. (1992) give too large values. Fig. 10.4.16b shows an enlarged plot (with a linear scale) in which some code specifications have been included for comparison. From the plots it is evident that, for small beam depths, the models of Bosco and Carpinteri, Hawkins and Hjorsetet, and Ruiz, Planas and Elices give very similar results, slightly higher than those specified by ACI 318(92), and higher that the specifications of the Model Code and Eurocode 2. For medium and large sizes, the model of Bosco and Carpinteri gives values sharply below those of ACI and the other models, while the formula of Hawkins and Hjorsetet gives values very close to those given

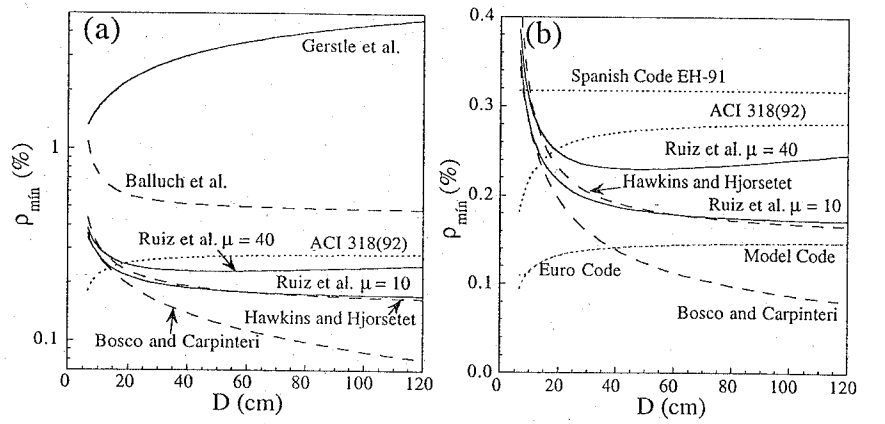

Figure 10.4.16 Comparison of minimum reinforcement formulas for various models (data from Ruiz 1996).

by the formula of Ruiz et al. in the case of weak bond, both giving values between those in the Model Code and the ACI Code. For a strong bond, the model of Ruiz et al. predicts a minimum reinforcement that first decreases with the size and then increases, with values between those recommended by the ACI code and the Spanish Code.

Exercises

10.4 Show that in the plot of Fig. 10.4.5a the position of the asymptotes on the right is given by $Y = 6(1 - \gamma)N_p$, where $1 - \gamma = 1 - c_s/D$ is the relative depth of the reinforcement.

10.5 Derive Eq. (10.4.28) in detail.

10.5 Other Structures

In this section, we give a brief account of some of the existing results for structures or structural elements not included in the preceding analysis: torsion of beams, punching of slabs, anchor pullout, bond-slip of reinforcing bars, beam and ring failure of pipes, concrete dams, footings, pavements, keyed joints, failure of joints, break-out of boreholes, and compression failure of concrete beams.

10.5.1 Torsional Failure of Beams

Torsion leads to another type of brittle failure of reinforced concrete beams. The classical test data existing in the literature, which were analyzed by Bažant and Şener (1987), and particularly the data by Humphrey (1957), Hsu (1968), and McMullen and Daniel (1975), reveal that a size effect exists, but cannot indicate which equation should describe it because the data were too scattered, the size range was too narrow, and geometrical similarity was not maintained.

Geometrically similar tests of size range 1:4 were conducted on microconcrete beams with reduced maximum aggregate size by Bažant, Şener and Prat (1988). The tests were made both on unreinforced beams and beams reinforced longitudinally. These tests clearly revealed a strong size effect and were shown to agree well with the size effect law. The results were briefly described in Section 1.5, Fig. 1.5.7 (series J1 and J2). From these tests it appears that the size effect in torsion is very strong, and the behavior is quite close to the LEFM asymptote. However, the scatter of the limited experimental data is quite large, and more extensive tests are needed. The scatter is larger for longitudinally reinforced beams, which

may be attributed to the fact that bond failure must accompany a torsional crack, and bond failure is a phenomenon of high random scatter.

The code formulas for torsion of beams with rectangular cross section are based on the plastic limit analysis solution, which indicates that the nominal shear strength in torsion (Park and Paulay 1975) is $v_u = T/(\alpha_p b^2 D)$, $\alpha_p = [1 - (b/3D)]/2$, where T = torque, b = length of the shorter side of the rectangular cross section, D = length of the longer side (depth). Since the small size limit of the size effect law should coincide with the plastic solution, Bažant, Şener and Prat (1988) proposed the correction indicated, in general, by Eq. (10.1.13) and showed that it agrees well with the data. Calculations with the microplane model by Bažant, Ožbolt and Eligehausen (1994) also agree quite well with the experimental points and the size effect correction.

No test data seem to exist on the size effect in torsional failure of reinforced concrete beams with stirrups. However, it may be expected that the stirrup effect would be similar to that discussed for diagonal shear, and that the size effect would disappear beyond a certain critical reinforcement ratio of the stirrups.

Torsion in beams is normally combined with bending, and so the interaction diagram between the maximum torque and the maximum bending moment is of considerable interest for design. Hawkins (1985) examined the test results of Wiss (1971) on diagonal tension cracking combined with torsion and bending. Using an energy based fracture criterion for failure under combined loading, he calculated the interaction diagram and showed it to be circular (when the maximum shear force and the maximum torque are normalized with respect to their values for pure torsion or pure shear). He suggested this was an argument for applicability of fracture mechanics, pointing out that the strength-based criteria yield a straight-line interaction diagram. However, this is not sufficient proof of fracture mechanics applicability because the lower-bound plastic limit analysis also gives a circular interaction diagram (e.g., Hodge 1959).

10.5.2 Punching Shear Failure of Slabs

Quasibrittle behavior accompanied by a transitional size effect is also characteristic of the punching shear failure of reinforced concrete slabs. For the nominal shear strength in to punching shear, ACI currently uses the formula

$$v_u^p = k_1\sigma_1[1 + (k_2 D/b)]\sqrt{\frac{f_c'}{\sigma_1}}, \qquad \sigma_1 = 1 \text{ psi } = 6.895 \text{ kPa} \tag{10.5.1}$$

in which k_1, k_2 = empirical constants, D = thickness of the slabs, and b = punch diameter (ACI Committee 318, 1989). This equation was derived by strength analysis based on a modified Coulomb yield criterion, which exhibits no size effect. Based on a series of displacement-controlled punching shear tests on geometrically similar two-way reinforced circular slabs of three different sizes (1:2:4), made of concrete of reduced aggregate size, Bažant and Cao (1987) proposed a size-dependent generalization of this formula based on (10.1.13):

$$\sigma_{Nu} = \sigma_{Nu}^p\left(1 + \frac{D}{D_0}\right)^{-1/2} \qquad \text{with } \sigma_{Nu}^p = c_1 f_t'\left(1 + c_2\frac{D}{b}\right) \tag{10.5.2}$$

where $c_1 f_t'$, c_2, and D_0 are empirical constants. The test results by which this formula was calibrated are shown in Section 1.5, Fig. 1.5.7, along with the optimum fit by the size effect law (series L1). The size effect was considerably milder than in the diagonal shear tests, which might be due to the fact that the largest slab was not sufficiently large. Fig. 1.5.8 shows the load-deflection diagrams measured on the small, medium, and thick plates. This figure illustrates how the postpeak softening is getting steeper with an increasing size and thus confirms a transition from relatively ductile behavior (the small slab with mild postpeak slope) to very brittle behavior (the largest slab, with a very steep postpeak drop).

The fact that the size effect should be considered in calculating the punching shear strength of slabs was also confirmed by the study of Broms (1990), which was focused on punching shear under high biaxial (radial) compressive stresses and suggested a formula of the type $v_c = v_c^0(k/D)^{1/3}$. The exponent $1/3$, according to the present theory, cannot be right for extrapolations to very large sizes; however, in the middle of the size effect transition, it works well. From the test data alone, it is not possible to say what should be the exact form of the size effect formula. Nevertheless, the presence of the size effect, and thus inapplicability of plastic limit analysis, is clearly verified by the test results.

Cryptodome failure of nuclear reactor vessel slab. The failure of thick prestressed concrete nuclear reactor vessels (primary vessels for gas-cooled reactors which were intensely researched between 1960–1980) is known to occur through a conical surface similar to the punch failure (called cryptodome), rather than by bending. The design of these nuclear reactor vessels has been done according to strength criteria, however, it now appears that, because of the similarity to the punching shear failure, a fracture behavior exhibiting a size effect should be expected (Bažant 1989b). If nuclear power is revived, this question should be researched further.

10.5.3 Anchor Pullout

The current ACI Code provisions for the pullout failures of bars and anchors are based on plastic limit analysis (ACI Committee 408, 1979; ACI Committee 349, 1989). However, the size effect is very strong in this kind of failure, and considerable work has been done in the last decade to increase the understanding of anchor pullout in terms of fracture mechanics, a topic of considerable interest because it is at the base of the design of anchors and of the recently introduced nondestructive test method for concrete strength based on pullout of a headed stud (the Swedish "lok" test).

The ACI Code provision (Sec. 15.8.3) requires that the "anchor bolts and mechanical connections shall be designed to reach their design strength prior to anchorage failure or failure of surrounding concrete". This means the anchor bar must yield before fracture occurs, but this can be ensured only if the load causing the fracture is correctly predicted. ACI Committee 349 (1989) recommends that "the design pullout strength of concrete, P_d, for any anchorage shall be based on a uniform tensile stress of $4\sqrt{f_c'}$ acting on an effective stress area which is defined by the projected area of stress cones radiating toward the attachment from the bearing edge of the anchors". This gives the pullout force P_u and nominal strength

$$P_u = k_1\sigma_1\sqrt{\frac{f_c'}{\sigma_1}}\pi D^2, \qquad \sigma_{Nu} \equiv \frac{P_u}{\pi D^2} = k_1\sigma_1\sqrt{\frac{f_c'}{\sigma_1}}, \qquad \sigma_1 = 1 \text{ psi} = 6.895\text{kPa} \tag{10.5.3}$$

in which k_1 = empirical constant, f_c' = standard compression strength of concrete, and D = the embedment depth of the anchor bolt. This expression obviously corresponds to plastic limit analysis, the size effect being ignored.

A clear confirmation of a strong size effect in the pullout failure of reinforced concrete bars without anchors was provided by the tests of Bažant and Şener (1988); see Fig. 1.5.6 (series I1). They tested microconcrete cubes of size ratio 1:2:4. The bar diameter and the embedment length were scaled so as to maintain geometric similarity. As is seen from Fig. 1.5.6, in the logarithmic size effect plot, the test results lie very close to the LEFM asymptote. This reveals an extremely high brittleness number for this type of failure. Eligehausen and Ožbolt (1990) and Bažant, Ožbolt and Eligehausen (1994) further showed that these test results agreed closely with nonlocal finite element solutions using a realistic material model for concrete (the microplane model).

Eligehausen and Sawade (1989) proposed a LEFM-based formula for pullout strength. This formula was written as

$$P_u = 2.1\sqrt{EG_F}D^{3/2} \quad \text{or } \sigma_{Nu} = 0.67 f_t'\sqrt{\frac{\ell_{ch}}{D}} \tag{10.5.4}$$

in which the fracture parameters appear explicitly. To avoid the explicit use of fracture parameters — which have not been measured in most of the available test series in the literature, Eligehausen et al. (1991) proposed the following formula based only on the cube compression strength:

$$P_u = a_1\sqrt{f_{cc}}\,D^{3/2} \tag{10.5.5}$$

They evaluated the results of 209 pullout tests of headed anchors carried out at different laboratories. In all tests, the failure occurred by a conical crack surface. The tests were done on concretes of various strengths, and, therefore, the measured maximum loads were normalized to the cube compression strength $f_{cc} = 25$ MPa, by multiplying them with the factor $\sqrt{25/f_{cc}}$. The normalized failure loads are plotted in Fig. 10.5.1 as a function of the effective embedment depth D, together with the fit of Eq. (10.5.5). From this fit it turns out that $a_1 \approx 15.5$ for P_u in N, f_{cc} in MPa, and D in mm. The formula is seen to closely describe the experimental results, which means that the nominal strength almost follows LEFM. This was confirmed numerically by Eligehausen and Ožbolt (1990) using a microplane nonlocal model: the LEFM formula and Bažant's size effect law differed less than 6% up to embedment length of 400 mm.

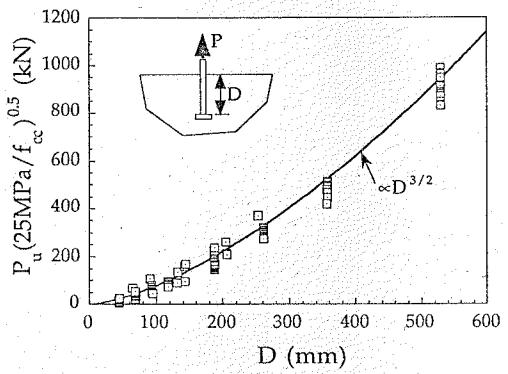

Figure 10.5.1 Size effect in the pullout of headed studs (data from Eligehausen et al. 1991).

Apart from the nonlocal microplane model just mentioned, many different approaches have been used in the last decade to analyze this interesting problem. A two-dimensional LEFM analysis with a mixed-mode crack was used by Ballarini, Shah and Keer (1985) to study the pullout of rigid anchor bolts. They used the Green's function for a concentrated force in an elastic half space, represented the crack opening by means of dislocations and thus reduced the problem to a system of singular integral equations, whose numerical solution yielded the mixed-mode stress intensity factor. The calculations provided the crack profiles and crack growth. Stability checks were made and the results were compared with anchor pullout experiments. An interesting point was that if the support reactions are sufficiently removed from the axis of the anchor, crack propagation becomes unstable and the load capacity is reduced (this is obviously due to the higher stored energy when the support reactions act farther away). On the other hand, for support reactions close to the anchor axis, as well as for sufficiently deep embedments, the crack propagation was found to be stable.

The pullout of circular disc-shaped anchors was studied by Elfgren, Ohlsson, and Gylltoft (1989). They used the finite element discrete crack approach, in which the tensile and shear softening were taken into account according to the formulation of Gylltoft (1984). They studied straight cracks inclined by 45° and 67° from the pullout axis as well as a crack starting at angles 73° and curving according to the principal tensile stress direction. They found the lowest pullout strength to occur for the 45° straight crack. They did not study the size effect, nor the effect of geometry.

The plane stress and axisymmetric problems of anchor pullout were analyzed by numerous researchers in a recent round-robin contest (Elfgren 1990) using various numerical procedures based on various fracture mechanics models, from LEFM to lattice models. Elfgren and Swartz (1992) published summaries of the contributions and a state-of-the-art report is in preparation by Elfgren, Eligehausen, and Rots.

Some of the results can be found in the proceedings of a special seminar on anchorage engineering held at Vienna Technical University in 1992 (Rossmanith, ed., 1993).

10.5.4 Bond and Slip of Reinforcing Bars

The bond and slip of reinforcing bars embedded in concrete is an important and certainly difficult phenomenon. In the previous sections, the bond strength was considered a secondary "internal" problem which was treated by means of very simple models of perfectly plastic shear-slip behavior. The ACI Code, too, gives simple provisions for the so-called development length of reinforcing bars, representing the length of embedment in concrete required for ensuring that the bar can develop its full yield capacity. These formulas are also based on plasticity. The development length is obtained by balancing the steel force at yield $F_s = f_y A_s$, against the bond strength $\tau_c p_s L_s$, where p_s is the perimeter of the reinforcement and L_s the slip (development) length. Taking then $\tau_c \propto f_t' \propto \sqrt{f_c'}$ leads to ACI empirical formulas in which the development length is $C_1 A_s f_y / \sqrt{f_c'}$ or $C_2 f_y / \sqrt{f_c'}$, where C_1 and C_2 are empirical constants

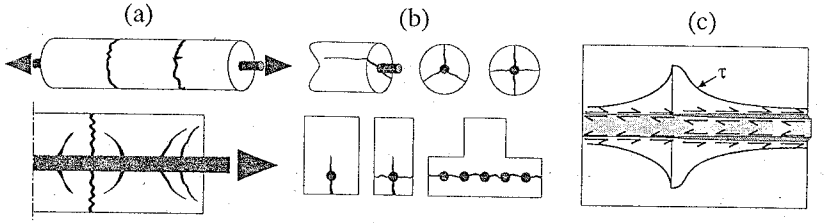

Figure 10.5.2 Cracking in bar pullout: (a) Transverse cracks; (b) longitudinal (splitting cracks); (c) shear-slip interfacial crack.

defined in the code. The code also gives various modifications of these formulas to take into consideration the clear spacing of parallel bars, thickness of concrete cover, and corrections for the case of lightweight aggregate concretes and for epoxy coated reinforcement. The formulas, however, do not consider any size effect associated with the brittleness of concrete.

In reality, the problem of bond and slip is a fracture problem; even more, it is a multiple fracture problem, and a three-dimensional one. Fig. 10.5.2 sketches the three kinds of cracks or crack systems involved in the pullout of a bar from a concrete cylinder or prism. The first system of cracks is transverse to the prism, as shown in Fig. 10.5.2a; the cracks are conical in shape (secondary cracks) or plane (principal cracks). The second system of cracks is longitudinal to the prism; the cracks are generated by hoop stresses and vary in number depending of the morphology of the cross-section (Fig. 10.5.2b). The third system of cracks consists of the shear cracks generated at the interface of steel and concrete; the jump in displacements at the interface is the crack sliding (Fig. 10.5.2c).

The role of transverse fracture of concrete in the bond between concrete and deformed reinforcing bars was first studied by Gylltoft (1984) and by Ingraffea et al. (1984). Gylltoft examined the role of fracture in axisymmetric pullout of bars from concrete blocks. He considered both monotonic and cyclic loading, carried out experiments, and was able to successfully predict the load-slip diagrams observed in the pullout tests. Special crack elements that involve linear strain softening of concrete in tension and a linear strain hardening in shear were used to model the interface. Ingraffea et al. (1984) used a discrete mixed-mode nonlinear fracture model in axisymmetric finite element analysis. They applied the cohesive crack model to characterize the tensile softening at each bond crack, and adopted the aggregate interlock model of Fenwick and Paulay (1968) to characterize the shear softening. The study of Ingraffea et al. (1984) indicated that secondary cracking around the primary cracks contributed to bond slip. Placing special interface elements at the primary crack locations, and comparing numerical results to test results for a center-cracked reinforced concrete plate under uniform tension, Ingraffea et al. (1984) calculated the degradation of stiffness and the crack opening profiles. Ingraffea et al. used in their finite element program (FRANC) a sophisticated technique for remeshing around the crack tip as the crack tip advances. Rots (1988, 1992) analyzed the problem of transverse cracking concomitant with longitudinal cracking. He used a smeared crack approach for the secondary cracks, and a discrete crack approach modeled by interface elements for the primary cracks.

A problem in the foregoing analysis is to correctly handle longitudinal cracking that occurs simultaneously with transverse cracking. In reality, a three-dimensional formulation ought to be used to analyze the problem in detail; however, this would require an enormous computational effort. Axisymmetric formulations have been used, with the expedient of using a circumferential stress-strain relationship that is a smeared version of a cohesive crack. This is done as in Chapter 8 for the uniaxial case, except that now the stress is the circumferential stress σ_θ and the cracking strain is ε_θ^c. These are related to each other and to the crack opening by

$$\varepsilon_\theta^c = n^c \frac{w(r)}{2\pi r} \Rightarrow \sigma_\theta = f[w(r)] = f\left(\frac{2\pi r}{n^c}\varepsilon_\theta^c\right) \tag{10.5.6}$$

where $w(r)$ is the opening of each crack at a distance r from the rotational axis, n^c the number of cracks, and $f(w)$ the softening function (for a single crack). Note that the number of cracks n^c must be assumed

before the calculation and cannot be inferred from the analysis. It is usually selected between 2 and 4, based on experience.

An entire family of simplified analyses of longitudinal splitting cracks taking into account the fracture behavior of concrete was developed based on modifications of the initial approach by Tepfers (1973, 1979). Tepfers assumes that the rise of interfacial shear stresses τ is accompanied by a rise of a contact normal stress σ. He further postulates that at splitting failure, σ and τ are related by a Coulomb-type law that he writes as

$$\sigma = \tau \tan\phi \tag{10.5.7}$$

where ϕ is a constant complementary friction angle. Tepfers then reduces the analysis to an axisymmetric problem of a thick-walled concrete tube subjected to inner pressure σ. Tepfers considers only elastic-brittle behavior and elastic-perfectly plastic behavior. Keeping this approach, several researchers extended Tepfers' analysis to include softening and fracture. All these analyses use further simplifications, such as neglecting Poisson's effect, and use the circumferential smeared cracking as given by (10.5.6). The main difference is in the kind of softening curve used by the various authors: van der Veen (1991) uses a power-law softening (Reinhardt 1984); Reinhardt and Van der Veen (1992) and Reinhardt (1992) use the CHR softening curve (Cornelissen, Hordijk and Reinhardt 1986b; see Section 7.2.1); Rosati and Schumm (1992) use a hyperbolic law; and Noghabai (1995a,b) uses a linear softening. As a further difference, Rosati and Schumm (1992) consider, instead of the Coulomb criterion (10.5.7), a Mohr-Coulomb condition given by $\sigma = (\tau - \tau_0) \tan\phi$, in which τ_0 is a constant "cohesion".

The problem of discrete longitudinal splitting cracks was directly addressed by Choi, Darwin and McCabe (1990). They used a three-dimensional finite element method to analyze test results and design code provisions on the bond failure of epoxy-coated or uncoated steel bars as a function of the bar size, variations in interface characteristics, and specimen geometry. Splitting fractures observed in the tests were well reproduced by the computational model —based on a cohesive crack model— and the results provided support to some empirical code provisions. The computational results described well the increase of pullout strength with the cover thickness.

Recently, Noghabai (1995a,b) considered the numerical analysis of longitudinal splitting cracks based on the boundary conditions in Tepfers' approach (concrete thick-walled tube with internal stress σ) and analyzed localized cracking using three numerical approaches with the same underlying material model (a cohesive crack with linear or nonlinear softening). The first numerical procedure —the so-called discrete crack approach— was carried out by placing 28 radial layers of interface elements incorporating the stress-crack opening relationship. The strength of the layers was randomly assigned to promote localization into a small number of cracks. The second numerical procedure was the classical smeared crack approach, with the crack opening distributed within the elements. The third procedure used enriched shape functions to describe the displacement jump within each element —the so-called inner softening band finite elements (Klisinski, Runesson and Sture 1991; Klisinski, Olofsson and Tano 1995). The three procedures gave similar results for the curves of pressure vs. radial deformation, although none were able to continue into the structural softening branch. The inner softening band method seems very promising for capturing the cracking pattern. Still, the weakest link in the model is the relationship between the normal and shear stresses. A realistic relationship between the normal and shear stresses at the interface must somehow be related to the slip between steel and concrete.

The third type of crack involved in the pullout process is the shear-slip (mode II) crack occurring at the steel-concrete interface (see Fig. 10.5.2c, where the separation between the bar and the concrete is grossly exaggerated). A straightforward approach is to treat this shear-slip crack as a cohesive crack, i.e., to postulate that a certain relationship exists between the transferred shear stress τ and the relative slip s:

$$\tau = t(s) \tag{10.5.8}$$

where $t(s)$ is the softening function for shear-slip. Introduced by Bažant and Desmorat (1994), this is a very simplified model which does not take into account friction and dilatancy occurring at the interface. More sophisticated models involving the crack opening due to dilatancy and the influence of the normal stress may be formulated, but will not be further described (for an overview of models and a thorough discussion of the coupling between normal and shear stresses and displacements, see Cox 1994). The simple model defined by (10.5.8) can, however, suffice to get a rough picture of the influence of the bond degradation on the overall response in bar pullout.

A simple and crude mathematical model which, nevertheless, realistically captures some aspects of fracture and the size effect was used by Bažant and Desmorat (1994), who considered a uniaxially stressed bar (or fiber) embedded in a concrete bar also behaving in an uniaxial manner, each with the cross section remaining plane and orthogonal to the bar axis. The interface between the bar and the concrete tube is characterized by the $\tau - s$ relation (10.5.8). For the sake of simplicity, this relation was assumed linear (triangular stress-displacement diagram). The solution can then be obtained analytically, by integration of the differential equation of equilibrium in the axial coordinate x. The solution yields simple formulas. It is found that, during failure, zones of slip initiate at the beginning of embedment of the bar or at the bar end, or both, and spread along the bar as the end displacement of the bar is increased, as sketched (for a more general case) in Fig. 10.5.2c. For geometrically similar situations, a strong size effect is observed. The size effect is caused by the fact that the ratio of the length of the slipped zone to the bar diameter decreases with increasing diameter, i.e., the slip zone localizes. For a sufficiently small size, the slip zone at the maximum load extends over the entire length of the bar embedment, and for a size approaching infinity, the relative length of the slipped zone tends to zero. The calculated size effect curve turned out to be very close to the generalized size effect law proposed by Bažant [Eq. (9.1.34)], with the exponent $r = 1.25$ for a concave nonlinear softening law. The one-dimensional solution may, of course, be expected to be good only when the slip zone is very long or very short compared to the bar diameter and the concrete cover around the bar is not too thick. In general, three-dimensional fracture analysis is, of course, required. Nevertheless, despite the one-dimensional simplification, it seems that the generalized size effect law indicated by this analysis may be applied as a simple approach to practical problems.

Further tests of bar pullout from normal and high strength concrete cubes were conducted by Bažant, Li and Thoma (1995). In these tests, it was tried to separate the effect of radial fractures emanating from the bar and the bond crack along the bar. The tests were designed so that no radial fractures would form and the bar would fail only due to bond fracture and slip. This was achieved by using a relatively short embedment of the bar in the concrete cube. The results again revealed a strong size effect. Because of the absence of radial cracks, it was admissible to compare the results to the aforementioned one-dimensional solution of Bažant and Desmorat (1994). The comparison was satisfactory although large scatter prevents considering this as a validation of the Bažant and Desmorat's equation.

A similar degree of brittleness as in pullout occur in the failure of splices of reinforcing bars in which the lapped bars are not connected and the tensile force in the bars is transmitted through the concrete in which the bars are embedded. The codes provide empirieal provisions for the length of overlap and for the so-called development length over which the yield force of the bar can be transmitted from concrete to the bar. These formulas are of the strength theory type which exhibit no size effect. Şener (1992) reports experiments which confirm that splices indeed exhibit a strong size effect which may be well described by Bažant's size effect law and is rather close to LEFM (in more detail, Şener, Bažant and Becq-Giraudon 1997). The aforementioned type of correction of the existing formula —Eq. (10.1.13)— is also needed in this case.

10.5.5 Beam and Ring Failures of Pipes

In the failure of pipes, it has for a long time been recognized that the apparent strength is different for the transverse bending that leads to ring-type failure (Fig. 10.5.3a) and for longitudinal bending of the whole pipe that leads to beam-type failure (Fig. 10.5.3b). Gustafsson and Hillerborg (1985) analyzed such failures using the fictitious (cohesive) crack model. A plot of the size effect that they obtained is shown in Fig. 10.5.3c. In this plot, σ_N is defined as the maximum elastic stress according to mechanics of materials theory. Thus, for the ring failure, we have

$$\sigma_{Nu} = \frac{3F_u D}{\pi t^2}, \qquad D = \frac{D_i + D_o}{2} \tag{10.5.9}$$

where F_u is the maximum force per unit length of pipe, D_i and D_o the inner and outer diameters, respectively, and t the pipe thickness. The nominal stress for the beam failure is

$$\sigma_{Nu} = \frac{M_u D_0}{2I}, \qquad I = \frac{\pi}{64}(D_0^4 - D_i^4) \tag{10.5.10}$$

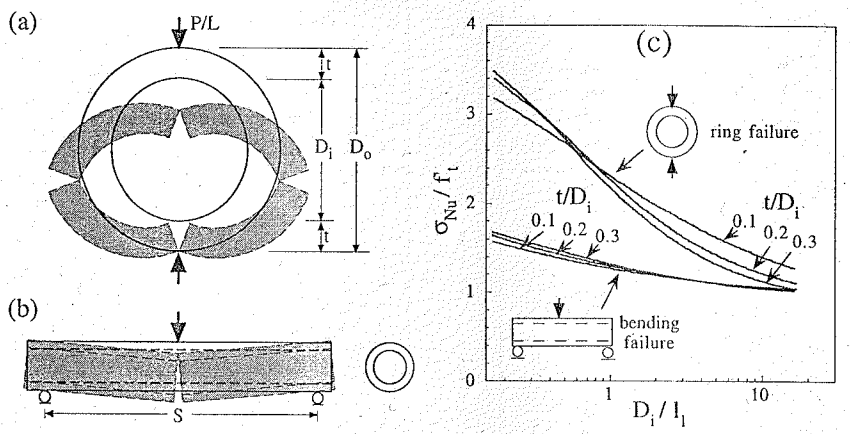

Figure 10.5.3 Size effect in unreinforced concrete pipes according to the computations of Gustafsson and Hillerborg (1985): (a) scheme of ring (crushing) failure; (b) scheme of bending (beam) failure; (c) strength vs. size for the two types of failure. (σ_{Nu} = is the maximum elastically-computed stress at peak load, see the text.)

in which M_u is the ultimate bending moment (at the failure cross section), and I is the centroidal moment of inertia of the ring cross section. It is apparent that the size effect displays the same general trends as the size effect for the modulus of rupture (Section 9.3), and, thus, is expected to have similar properties. Indeed, the plot in Fig. 10.5.3c is a modification of Gustafsson and Hillerborg's results which uses the property that, for unnotched specimens, the size effect curve is independent of the softening when plotted as a function of D/ℓ_1 where ℓ_1 is the characteristic size associated to the initial linear softening. Gustafsson and Hillerborg performed the computations using Petersson's bilinear softening curve (Section 7.2.1), and produced plots of σ_{Nu}/f_t vs. D/ℓ_{ch}; the plot in Fig. 10.5.3c has been rescaled by taking into account that for such softening $\ell_1 = 0.6\ell_{ch}$ and in the given form can be applied to any softening curve with initially linear softening.

From the foregoing results, it follows that smaller pipes are seen to be stronger and more ductile in their postpeak response than larger pipes (D_i in the figure is the inner pipe diameter). It follows from this analysis that a size independent "modulus of rupture" currently used in design (ACI Committee 318, 1989) is unconservative for large pipes. Gustafsson and Hillerborg also observed that the ring-type failure is more size sensitive than the beam-type failure (Fig. 10.5.3c).

The failure of pipes was also studied by Bažant and Cao (1986), who considered the test results from Gustafsson (1985) and Brennan (1978). They compared the available test results to Bažant's size effect law and concluded that the size effect is strong and that Bažant's size effect law could be used. However, it must also be cautioned that the size effect law should not be fully applicable in this case, because the pipes reach their maximum load after only a small crack growth (that is, a large crack does not develop before failure). Thus, the size effect is primarily due to the formation of the fracture process zone, as characterized, for example, by the cohesive crack model or crack band model. Therefore, Bažant's size effect law might not work well if the range of sizes is increased or the scatter of measurements reduced.

10.5.6 Concrete Dams

Concrete dams typically fail by fracture. However, even though they are unreinforced, they do not fail at crack initiation. Rather, very large cracks, typically longer than one-half of the cross section, grow in a stable manner before the maximum load is reached. Therefore, if geometrically similar dams of different sizes with geometrically similar cracks are considered, a strong size effect, essentially following Bažant's size effect law [Eq. (1.4.10)], must be expected.

Even though the large aggregate size used in dams (up to 250 mm in older dams and about 75 mm in recent dams) forces the fracture process zone to be considerably larger than in normal structural concretes

(with aggregates up to 30 mm in size), most dams are so large that their global failure may be, in most situations, analyzed by LEFM (Ingraffea, Linsbauer and Rossmanith 1989; Linsbauer et al. 1988a,b; Saouma, Ayari and Boggs 1989). Large cracks are often produced in dams as a result of thermal and shrinkage stresses or differential movements in the foundations and abutments, and, in an earthquake, as a result of large inertial forces and dynamic reactions from the reservoir. Cracking is often promoted by weak construction joints. Currently, the design, its computer evaluation, and analysis of seismic response, are being done on the basis of the strength theory; however, fracture mechanics should, in principle, be introduced. This is particularly needed for evaluating the performance of dams that have already developed large cracks, which is known to occur frequently. Evaluation of the effectiveness of repair methods also calls for fracture mechanics.

LEFM analysis with mixed-mode cracks was applied by Linsbauer et al. (1988a,b) to determine the profile and growth of a crack from the upstream and downstream faces of a doubly curved arched dam. On the basis of their anisotropic mixed-mode fracture analysis, Saouma, Ayari and Boggs (1989) found that the classical method of analysis is normally much more conservative than fracture analysis. This conclusion suggests that fracture analysis might not be needed to obtain safe designs, but there is an opportunity to optimize the design. The U.S. Army Corps of Engineers (1991) have issued guidelines that require applying fracture mechanics for the safety and serviceability analysis of existing cracked dams (Saouma, Broz et al. 1990). The existing computational studies considered only two dimensional cracks (Ingraffea, Linsbauer and Rossmanith 1989; Linsbauer et al. 1988a,b; Saouma, Ayari and Boggs 1989). Three-dimensional cracks (Martha et al. 1991) still need to be studied, and so does the propagation of cracks along interfaces between concrete and rock or along construction joints.

For analyzing dam fracture, the proper value of fracture energy (or fracture toughness), and of the effective length of the fracture process zone c_f, needs to be known for concretes with very large aggregates. This question was experimentally studied by Brühwiler and Wittmann (1990), Saouma, Broz et al. (1991), Bažant, He et al. (1991), and He et al. (1992). The last mentioned study utilized geometrically similar wedge-splitting fracture specimens with maximum cross section dimension 6 ft., and exploited the size effect method for determining the fracture energy of the material. The effect of moisture content and water pressure in the crack on the fracture energy was found by Saouma, Broz et al. (1991) to be important. Zhang and Karihaloo (1992) studied the stability of a large vertical crack extending from the upstream phase of a buttress-type dam. They treated concrete as a viscoelastic material, took into account tensile strain softening, and demonstrated feasibility of the fracture analysis.

Since large fractures often grow in dams slowly, over a period of many years, the effects of loading rate and duration need to be understood. These effects were studied by Bažant, He et al. (1991). Testing dam concrete as well as normal concretes, Bažant (1991a) and Bažant and Gettu (1990) observed that the slower the loading, the more brittle the response (in the sense that in the logarithmic size effect plot, the response points move to the right, i.e., closer to the LEFM asymptote, as the load duration is increased or the loading rate is decreased; see Chapter 11 for details and mathematical modeling.

One interesting question, which was provoked by Bažant (1990b) is the question of safety or the so-called "no-tension" design. It has been a widespread opinion that fracture analysis of dams can be avoided by using the so-called "no-tension" design, which is based on an elasto-plastic analysis with a yield criterion in which the tensile yield limit is zero or nearly zero (Rankine criterion or a special case of Mohr-Coulomb criterion).

However, it was demonstrated (Bažant 1991a) that such a design is not guaranteed to be safe. The stress intensity factor at the tip of a large crack that satisfies the no-tension criterion according to the elasto-plastic analysis can be, and often is, non-zero and positive. For the latter, Bažant's size effect law ought to apply, and thus it follows that, for a given crack and dam geometry and a fixed nominal stress characterizing the loading, there always exists a certain critical dam size such that for larger sizes the critical value of the stress intensity (fracture toughness) is exceeded. Examples of this have been given by Gioia, Bažant and Pohl (1992) and Bažant (1996a). The detailed study by Bažant (1996a) led to the following conclusions:

I. For a brittle (or quasi-brittle) elastic structure, the elastic-perfectly plastic analysis with a zero value of the tensile yield strength of the material is not guaranteed to be safe because it can happen that: (a) the calculated length of cracks or cracking zones corresponds to an unstable crack propagation, (b) the uncracked ligament of the cross section, available for resisting horizontal sliding due to shear loads, is predicted much too large, compared to the fracture mechanics prediction, (c) the

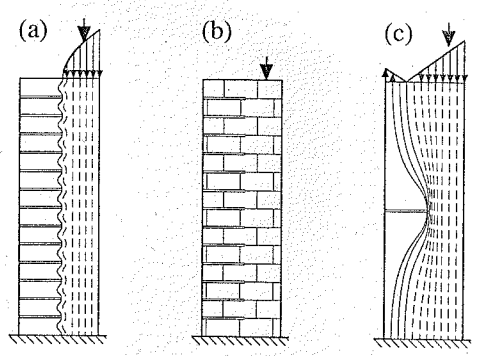

Figure 10.5.4 Crack patterns and lines of principal stress. (a) Closely spaced cracks and trajectories of minimum principal stress for no-toughness design; (b) closely spaced cracks for dry masonry; (c) approximate trajectories of minimum principal stress for $K_{Ic} > 0$. (Adapted from Bažant 1996a.)

calculated load-deflection diagram lies lower than that predicted by fracture mechanics, or (d) the load capacity for a combination of crack face pressure and loads remote from the crack front is predicted much too large, compared to the fracture mechanics prediction.

2. Due to the size effect, the preceding conclusions are true, not only for zero fracture toughness (no-toughness design), but also for finite fracture toughness, provided the structure is large enough.
3. The no-tension limit design cannot always guarantee the safety factor of the structure to have the specified minimum value. Fracture mechanics is required for that.
4. Increasing the tensile strength of the material can cause the load capacity of a brittle (or quasi-brittle) structure to decrease or even drop to zero.
5. The no-tension limit design would be correct if the tensile strength of the material were actually zero throughout the whole structure. This is true for dry masonry with sufficiently densely distributed joints, but not for concrete (or for jointed rock masses).

One simple explanation of the foregoing conclusions is that the finiteness of the tensile strength of the material at points farther away from the cracks or rock joints (or construction joints) of negligible tensile strength causes the structure to store more strain energy. Thus, energy can be released at a higher rate during crack propagation.

The reason that an increase of strength of the material from zero to a finite value causes a crack to propagate is illustrated in Fig. 10.5.4. For zero tensile strength (which is the case of dense cracking, Fig. 10.5.4a, or dry masonry, Fig. 10.5.4b), there are many cracks and the tensile principal stress trajectories are essentially straight. But for finite strength, these trajectories get compressed at the crack tip as shown in Fig. 10.5.4c, which causes stress concentration and crack propagation.

The results of the finite element study by Gioia, Bažant and Pohl (1992) are summarized in Fig. 10.5.5. The geometry of the cross section of the Koyna dam, which was stricken by an earthquake in 1967, was considered. Fig. 10.5.5a shows the finite element mesh and the shape of the critical crack for the loading considered. Finite element solutions were compared according to no-tension plasticity and according to fracture mechanics. The yield surface of no-tension plasticity was a particular case of Otossen's (1977) yield surface (described also in Chen 1982, Sec. 5.7.1) for the tensile strength approaching zero. Because the origin of the stress space must lie inside the yield surface, the calculations have actually been run for a very small but nonzero value of the tensile yield strength of concrete, approximately 10 times smaller than the realistic value. Similarly, the no-toughness design was approximated in the finite element calculations by taking the K_{Ic}-value to be approximately 10 times smaller than the realistic value. The crack length obtained by fracture mechanics is very insensitive to the K_{Ic} value because K_I represents a small difference of two large values: K_I due to water pressure minus K_I due to gravity load.

In the calculations, some of whose results are plotted in Fig. 10.5.5b-c, the height of the water overflow

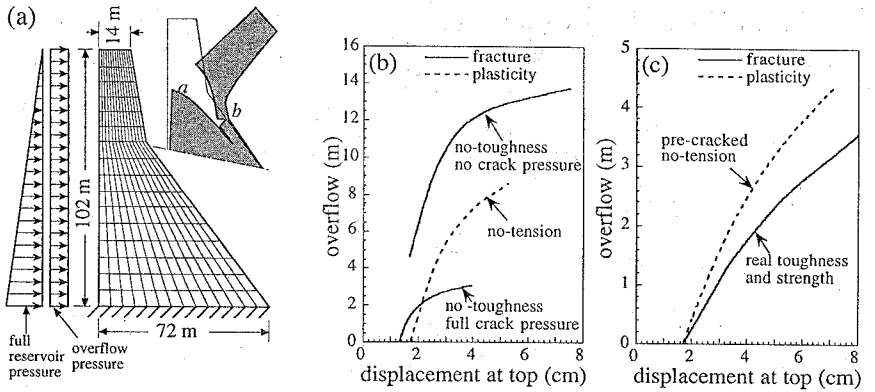

Figure 10.5.5 Koyna dam analyzed by Gioia, Bažant and Pohl (1992): (a) finite element mesh and failure mode; (b) comparison of curves of overflow height vs. deflection for no-tension plasticity analysis and no-toughness fracture analysis; (c) curves for no-tension limit analysis and fracture analysis with realistic values of strength and toughness. (Adapted from Bažant 1996a; the peak and postpeak branches obtained by Jirásek for the branched crack b are not shown.)

above the crest of the dam was considered as the load parameter. A downward curving crack, which was indicated by calculations to be the most dangerous crack, was considered (Fig. 10.5.5a).

The differences between the no-tension limit design and fracture mechanics have been found to be the most pronounced for the case when water penetrates into the crack and applies pressure on the crack faces, as shown in Fig. 10.5.5b. Because plastic analysis cannot describe crack growth, the dam has been assumed to be precracked and loaded by water pressure along the entire crack length.

From the results in Fig. 10.5.5c, it is seen that the diagram of the load parameter vs. the horizontal displacement at the top of the dam lies lower for fracture mechanics than it does for no-tension plasticity. In other words, the resistance offered by the dam to the loading by water is lower according to the fracture mechanics solution, with a realistic value of K_{Ic}, than it is according to no-tension plasticity. It should be added that, for these finite element calculations, the maximum of the load-deflection diagram could not be reached for realistic heights of overtopping of the dam. The reason has been found by Jirásek and Zimmermann (1997). A descent of the load is caused by crack branching due to the formation of a secondary crack (crack b in Fig. 10.5.5), the possibility of which was not checked by Gioia, Bažant and Pohl (1992). If this is considered, a maximum load point occurs on curves in Figs. 10.5.5b–c, and another curve descends from that point.

10.5.7 Footings

One well-documented case of fracture in a footing comes from the collapse of the New York State Thruway Bridge over the Schoharie Creek in 1987, which caused the death of 10 people. A flood produced scouring under the foundation plinth supporting a pier, which caused fracture of the plinth which was very weakly reinforced. Although crack stability and propagation were not analyzed (Wiss, Janney, Eltsner Associates, Inc., and Mueser Rutledge Consulting Engineers 1987), finite element analysis based on nonlinear fracture mechanics of discrete cracks was used by Swenson and Ingraffea (1991) who concluded that although the bridge failed primarily because of scouring beneath the foundation plinths (pier footing), a necessary complementary cause was unstable fracture in the pier. It was recommended that foundation plinth bridges of this type should be designed with consideration of crack propagation stability and crack arrest. In the disaster, the crack must have become unstable before it ceased to be small compared to the cross section size, and, therefore, the behavior described by the size effect law due to Bažant probably did not play a significant role. Rather, a boundary layer type size effect due to formation on the fracture process zone of a cohesive crack, same as in the case of the modulus of rupture, must have played a significant role.

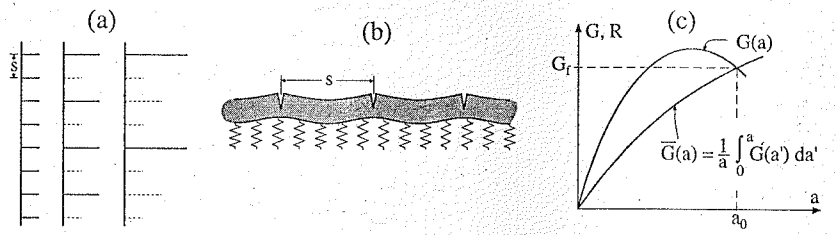

Figure 10.5.6 (a) Crack distribution at the surface of a half space. (b) Crack distribution in a pavement. (c) Determination of the initial crack jump by intersection of instantaneous and average energy release curves.

10.5.8 Crack Spacing and Width, with Application to Highway Pavements

The prediction of the spacing and opening of cracks in asphalt or concrete pavements of roads and runways is important for their durability assessment. This problem is similar to the ice plate—a plate resting on Winkler elastic foundation—but the foundation is much stiffer. Similar to the problem of sea ice penetration (Section 9.6), the crack spacing also is important for the size effect.

One basic problem is the spacing s of parallel planar cracks initiating from a half space surface (Fig. 10.5.6a), which was solved approximately by Bažant and Ohtsubo (1977) and Bažant, Ohtsubo and Aoh (1979), and rigorously by Li, Hong and Bažant (1995) (see also Bažant and Cedolin 1991, Ch. 13). The crack opening at the crack mouth is approximately $w = -s\varepsilon^0$, where ε^0 is the free shrinkage strain or thermal (cooling) strain ($\varepsilon^0 < 0$).

The problem of crack spacing in pavements has been solved according to the theory of plate (beam) on Winkler elastic foundation (Fig. 10.5.6b) by Hong, Li and Bažant (1997). The calculated values of crack spacing were in relatively good agreement with the previously reported observations on asphalt concrete pavements.

The theory of initiation of parallel equidistant cracks from a smooth surface, developed in Li and Bažant (1994b) as an extension of the approximate crack spacing criterion proposed by Bažant and Ohtsubo (1977) and Bažant, Ohtsubo and Aoh (1979) (see also Bažant and Cedolin 1991, Ch. 13), was applied in the aforementioned study. Although the strength concept must be applied for the crack initiation stage, the cracks are considered simply as LEFM cracks afterward. The theory, which was studied rigorously in Li, Hong and Bažant (1995), rests on the following three conditions:

1. Just before crack initiation from a smooth surface, the stress at the surface reaches the material strength limit, f'_t.
2. After initial cracks of a certain initial length a_0 form (by a dynamic jump), the energy release rate must be equal to the fracture energy of the material or the R-curve value.
3. The total energy release due to the initial crack jump must be equal to the energy needed to produce the initial cracks, according to the fracture energy G_f or the R-curve (an equivalent statement is that the average of energy release rate during the initial crack formation must be equal to the value of the fracture energy G_f or the average value of the R-curve, as illustrated in Fig. 10.5.6c).

The problem can be solved if the stress intensity factor (or energy release rate) as a function of the crack length, the crack spacing and the load parameter (e.g., the penetration depth of the cooling or drying front) is known. For the elastic halfspace, the stress intensity factor has been solved from a Cauchy integral equation (Li, Hong and Bažant 1995). The solution of conditions 2 and 3 graphically represents the intersection of the curves giving the energy release rate and the average energy release rate (the intersection always exists if the fracture geometry is, or becomes, positive); see Fig. 10.5.6c. All three conditions together allow solving three unknowns: the initial crack spacings, the initial crack length, and the load level (load parameter) at which the cracks initiate. Generalization to the full cohesive crack model is possible.

A different basic problem is how a system of parallel cracks evolves after it has initiated. Often it happens that every other crack stops growing and closes when a certain critical length a_{cr} is reached

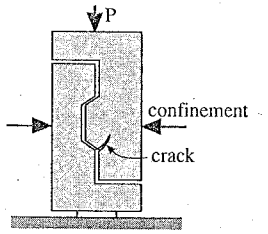

Figure 10.5.7 Specimen used in studying cracking in keyed joints in segmental box girder sections (after Buyukozturk, Bakhoum and Beattie 1990).

(Fig. 10.5.6a). The value of a_{cr} is decided by stability and bifurcation analysis of the interacting crack system (Bažant and Ohtsubo 1977; Bažant, Ohtsubo and Aoh 1979; Bažant and Cedolin 1991, Ch. 13; Bažant and Wahab 1979, 1980). The increase of spacing of the opened crack causes their opening width (due to shrinkage or strain) to increase. Although this problem has been analyzed only two-dimensionally so far, the crack pattern viewed orthogonally to the surface of halfspace is often hexagonal or random, calling for three-dimensional analysis.

10.5.9 Keyed Joints

Rectangular sheared keys are used to improve the resistance against shear slip of joints between the segments of prestressed box-girder bridges. Buyukozturk and Lee (1992a) showed that this is a very brittle type of failure, exhibiting a strong size effect close to LEFM. They used LEFM mixed-mode fracture analysis (Swartz and Taha 1990, 1991) to study the failure of typical shear keys used in bridge construction (Fig. 10.5.7). In contrast to the diagonal shear cracks in beams, which can be counteracted by shear reinforcement (stirrups), a diagonal crack which is initiated at the shear key may also propagate parallel to the joint. Such a path is not crossed by any shear reinforcement (Buyukozturk, Bakhoum and Beattie 1990).

The design provisions of the Post-Tensioning Institute (1988) for the segments of prestressed box-girder bridges are at present empirical and follow the strength theory, exhibiting no size effect. They are based on the shear capacities determined by tests of prestressed beams failing by flexure-shear cracks or web-shear cracks. An enhanced formula was proposed by Buyukozturk, Bakhoum and Beattie (1990), but this was still free from size effect.

Based on their mixed-mode LEFM analysis, Buyukozturk and Lee calculated design charts corresponding to the failure criterion

$$C_k^2 K_I^2 + K_{II}^2 = K_{Ic}^2 \tag{10.5.11}$$

where K_I, K_{II} = stress intensity factors in Mode I and Mode II, K_{Ic} = Mode I fracture toughness of concrete, and C_k = empirical constant (which obviously represents the ratio of Mode II fracture toughness to K_{Ic}). The high brittleness of failure is further compounded by the use of high strength concrete in these bridges. Another aggravating factor for brittleness is the presence of large uniaxial compressive stresses normal to the joint, which are beneficial by increasing friction but detrimental increasing the brittleness. Thus, even though this relatively small size of the shear keys would indicate the use of nonlinear fracture mechanics with a transitional size effect (following the size effect law), it appears that LEFM is applicable.

10.5.10 Fracture in Joints

Cracks in joints differ from cracks in bulk material in three respects. (**1**) Cracks in concrete usually (albeit probably not always) propagate in the direction normal to the maximum principal stress as in Mode I, but a crack in a joint is subjected to normal as well as shear loading and is of a mixed-mode. (**2**) The roughness of a crack in a smooth joint can be much smaller than the roughness of a crack in the bulk of concrete. Thus, aggregate interlock plays a lesser role and friction dominates as a means of transferring

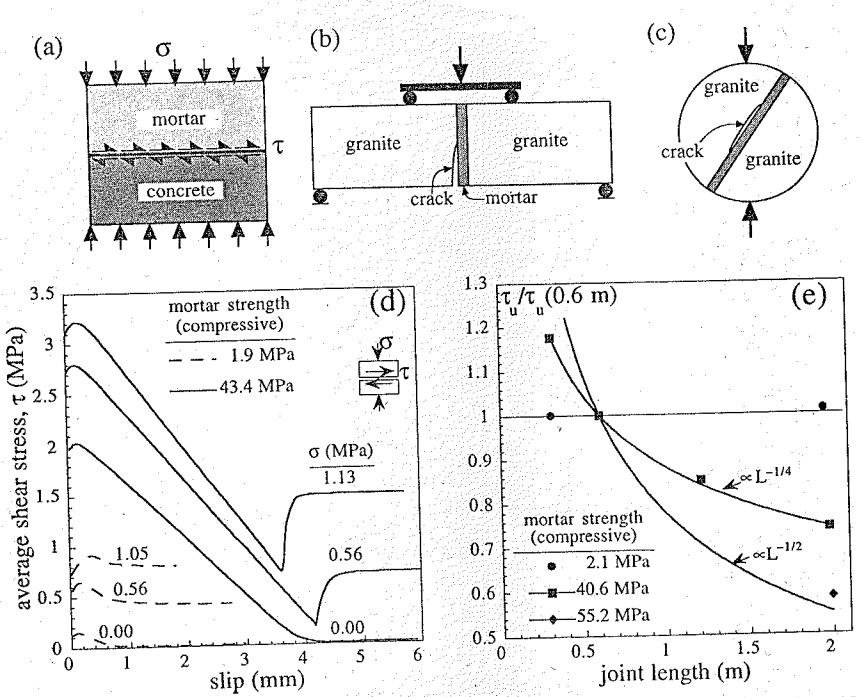

Figure 10.5.8 Fracture of joints: (a) sketch of tests by Reinhardt (1982); (b–c) tests by Buyukozturk and Lee (1992b); (d) average shear stress-slip curves for Reinhardt's tests; (e) size effect in Reinhardt's tests.

shear stresses across a joint. (3) A crack in concrete exhibits considerable dilatancy associated with shear slip, but in a smooth joint, the dilatancy may be quite small.

The behavior of joints of dissimilar materials was investigated experimentally by Reinhardt (1982) and by Buyukozturk and Lee (1992b). Reinhardt tested joints of strong concrete and mortar of variable strength subjected to various compressive normal stresses (Fig. 10.5.8a). Buyukozturk and Lee tested sandwich specimens of granite and mortar with an interfacial crack (Fig. 10.5.8a) as a means of characterizing the aggregate-mortar interface, although their results could be useful for macroscopic structures as well.

Fig. 10.5.8d shows shear stress-slip curves for the same joint length, two different mortar strengths and, in each case, three different compressive normal stresses across the joint. It is seen that the stress first rises abruptly with very little slip up to a certain maximum and then, for the joints made in high strength mortar, a steep drop of stress follows, while for the joints made in low strength mortar only a mild drop is seen. After the development of a full crack, a frictional plateau gets established with the residual shear capacity determined by the compressive stress across the joint. This capacity does not depend on the slip magnitude, nor on the mortar strength. (It might be noted, though, that the response shown could have been influenced by the stiffness of the loading frame as well as the response frequency of the servo-controller.)

A plot of the normalized shear strength of the three different joints vs. the length of the joint is shown in Fig. 10.5.8e. The joint made with low strength mortar was found to exhibit no dependence of the shear strength on the joint length, i.e., no size effect. On the other hand, the joint made with a mortar of high strength exhibited a strong size effect close to LEFM (in this case, the joint strength decreased as $L^{-1/2}$, with l = joint length). The joint made with a mortar of medium strength was found to exhibit an intermediate size effect.

The interfacial crack propagation was interpreted by Reinhardt (1982) on the basis of the LEFM

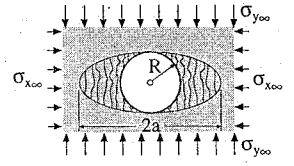

Figure 10.5.9 Break-out of boreholes; $|\sigma_{y\infty}| \gg |\sigma_{x\infty}|$.

solutions of Sih (1973), Rice and Sih (1965), and Erdogan (1963) for particular geometries of cracks at the interface of two dissimilar halfspaces. Buyukozturk and Lee (1992b) also interpreted their tests in terms of LEFM, based on solutions by Suo and Hutchinson (1989). The LEFM treatment of interfacial crack theory is outside the scope of this book; it is a conceptually involved topic, because the power series expansion that is relatively simple to handle for the single material problem (Section 4.3) has complex exponents for the bimaterial case. The dominant solution of the displacement field still decays as $r^{1/2}$ near the tip, but displays an oscillating behavior near the origin. For example, it can be shown that the dominant term for the crack opening at a distance r from the crack tip takes the form

$$w(r) \propto \sqrt{r}\ \cos(\phi + \omega \ln r) \tag{10.5.12}$$

where ϕ and ω depend on the loading, geometry, and elastic properties of the two materials; $\omega = 0$ if the two bodies have identical elastic constants. Note that when r approaches zero (the crack tip), the factor $\cos(\phi + \omega \ln r)$ oscillates between -1 and 1 with frequency tending to infinity (because $\lim_{r\to 0}(\ln r) = -\infty$). This means that the solution always includes negative crack openings, which are not physically admissible (there would be interpenetration of the opposite faces of the crack). This is but one of the difficulties involved in the interfacial crack problem. The interested reader is referred to the original papers and to recent papers by Rice (1988), Hutchinson (1990), and He and Hutchinson (1989).

10.5.11 Break-Out of Boreholes

When the mass of rock (or concrete) in which a borehole has been drilled is subjected to large compressive stresses, it may suddenly collapse in a brittle manner. This type of failure is called the break-out. The classical approach to the break-out has been by plasticity. However, because the failure occurs by cracking, fracture mechanics appears to be more appropriate. Its use, of course, inevitably leads to size effect, which is known to occur in the break-out of boreholes in rock, as experimentally demonstrated by Nesetova and Lajtai (1973), Carter (1992), Carter, Lajtai and Yuan (1992), Yuan, Lajtai and Ayari (1993), and Haimson and Herrick (1989).

An approximate energy-based analytical solution of the break-out has been obtained (Bažant, Lin and Lippmann 1993) under the simplifying assumption that the splitting cracks occupy a growing elliptical zone as sketched in Fig. 10.5.9 (although in reality this zone is narrower and closer to a triangle). The assumption of an elliptical boundary permits the energy release from the surrounding infinite solid to be easily calculated (Bažant, Lin and Lippmann 1993) according to Eshelby's (1956) theorem for uniform eigenstrains in ellipsoidal inclusions in infinite medium. According to the theorem (see, e.g., Mura 1987), the following approximate expression for the energy release from the infinite rock mass has been derived:

$$\Delta\mathcal{U} = -\frac{\pi(1-\nu^2)}{2E}[(a+2R)R\sigma_{x\infty}^2 + (2a+R)a\sigma_{y\infty}^2 - 2aR\sigma_{x\infty}\sigma_{y\infty} - 2a^2\sigma_{cr}^2] \tag{10.5.13}$$

in which R = borehole radius, a = principal axis of the ellipse (Fig. 10.5.9), $\sigma_{x\infty}$ and $\sigma_{y\infty}$ = remote principal stresses, E = Young's modulus of the rock, and ν = Poisson ratio. A similar analysis as that for the propagating band of axial splitting cracks, already explained in Section 9.5, has provided a break-out stress formula of the type

$$\sigma_{Nu} \approx C_0 D^{-2/5} + C_1 \tag{10.5.14}$$

where C_0 and C_1 are constants.

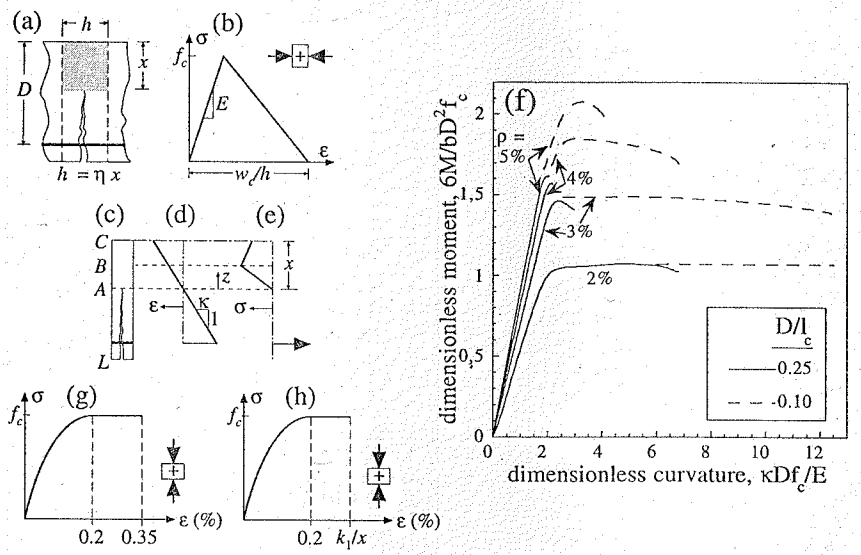

Figure 10.5.10 Hillerborg's (1990) analysis of bending of reinforced concrete beam: (a) sketch of the failure cross section; (b) stress-strain curve in compression; (c) no-tension zone (L–A), elastic zone (A–B), and softening zone (B–C); (d) strain profile; (e) stress profile; (f) moment-curvature diagrams for various sizes; (g) stress-strain curve in compression according to the CEB-FIP Model Code; (h) stress-strain curve with size-dependent cut-off proposed by Hillerborg (1990).

10.5.12 Hillerborg's Model for Compressive Failure in Concrete Beams

Hillerborg's (1990) model for compressive failure in concrete beams follows, in the formal aspects, the classical bending theory for concrete: a uniaxial stress-strain relation with plane cross sections remaining plane and no-tension for concrete. The essential difference is that he introduces softening and strain localization in compression to explain the size effect on ductility.

Fig. 10.5.10a shows the central section of the beam where the inelastic behavior is represented by a no-tension crack and a compressed zone (shaded in the figure) of width h into which the strain will localize. Hillerborg assumes that

$$h = \eta x \tag{10.5.15}$$

as indicated in the figure, where x is the depth of the compressed zone, and η is a constant (approximately equal to 0.8). Hillerborg further assumes linear softening expressed by a stress-displacement $\sigma(w)$ curve, where w here has the meaning of an inelastic displacement in compression, equivalent to the crack opening in tension. Fig. 10.5.10b shows the corresponding stress-strain curve. Note that the slope depends on the depth of the compression zone x, hence also on the size of the beam. w_c is assumed to be a material property, and so is the compressive strength f_c and the elastic modulus E.

According to these hypotheses, the beam depth (Fig 10.5.10c) is divided into three parts: over part LA no stress is transferred (except across the reinforcement), over part AB the concrete is compressed and elastic, and over BC the concrete undergoes crushing and strain localization. The strain is assumed to vary linearly as shown in Fig. 10.5.10d, so that

$$\varepsilon = \kappa z \tag{10.5.16}$$

where κ is the curvature. From this, together with the stress-strain curves of the steel and of the concrete already defined, the stress profile can be computed as a function of the position of the neutral line x and

the curvature κ, as sketched in Fig. 10.5.10e. Then x is computed from any given κ from the equilibrium of forces, and next the bending moment is computed from the equilibrium of moments. In this way, the full moment-curvature diagram is obtained.

The essential feature is that, since the stress-strain curve of concrete is made to depend on the depth of the compression zone, the resulting moment-curvature diagrams are size-dependent. More specifically, they depend on the dimensionless size D^* defined as

$$D^* = \frac{D}{\ell_c}, \qquad \ell_c = \frac{w_c E}{2 f_c} \tag{10.5.17}$$

ℓ_c represents the characteristic material length for fracture in compression. Fig. 10.5.10f illustrates Hillerborg's results, which clearly display an increase of brittleness with the size and with an increasing steel ratio.

Certainly this model is crude, but offers one simple way of taking into account the softening behavior in compression to predict a size-dependent response of concrete in bending. This is not actually included in the codes, which take size-independent stress-strain curves for concrete in compression, such as the parabola-rectangle diagram of the CEB-FIP Model Code shown in Fig. 10.5.10g. Hillerborg suggests a simple way of using this kind of diagrams to include the size effect: the strain cut-off ε_u is made to depend on the depth of the compression zone as

$$\varepsilon_u = \frac{k_1}{x} \tag{10.5.18}$$

where k_1 is a parameter, with dimensions of length, which includes the fracture properties in compression —roughly proportional to ℓ_c in (10.5.17)— and which might, eventually, depend on the geometrical details of the beam. However, further research is required, both on the experimental and theoretical sides, to settle on the best model that should go into the code provisions.

13

Nonlocal Continuum Modeling of Damage Localization

In concrete and other quasibrittle materials, fracture develops as a result of localization of distributed damage due to microcracking. In discrete fracture models which have been discussed in previous chapters, the damage due to distributed cracking is lumped into a line, but this is not sufficiently realistic for all applications. The width and microcracking density distribution at the fracture front may vary depending on structure size, shape, and type of loading.

Such behavior can be captured only by continuum damage models. However, such models cannot be implemented in the sense of the classical, local continuum, i.e., a continuum in which the stress at a point depends only on the strain at the same point. Rather, one must adopt the more general concept of a nonlocal continuum, defined as a continuum in which the stress at a point depends also on the strains in the neighborhood of that point or some type of average strain of the neighborhood. The reasons for introducing the nonlocal concept are both mathematical and physical:

1. The mathematical reason is that, as we discussed in Chapter 8 (Bažant 1986c), a local strain softening continuum exhibits spurious damage localization instabilities, in which all damage is localized into a zone of measure zero. This leads to spurious mesh sensitivity. The energy that is consumed by cracking damage during structural failure depends on the mesh size and tends to zero as the mesh size is refined to zero. The reason is that the energy dissipation, as described by the local stress–strain relation per unit volume, and thus also the total dissipation, converges to zero if all damage is localized into a band of single element width as the element size tends to zero. Such spurious localization on a set of measure zero is prevented by the nonlocal concept.
2. The physical reason is that microcracks interact (Bažant 1994b; Bažant and Jirásek 1994a,b)). The formation or growth of one microcrack either promotes or inhibits the formation or growth of adjacent microcracks. Continuum smearing of such interactions inevitably leads to some kind of a nonlocal continuum. The interaction of microcracks is the physical reason why a continuum model for distributed strain softening damage ought to be nonlocal. A secondary physical reason is that a crack has a macroscopically nonnegligible dimension, causing the crack growth to depend on the macroscopic stress field in a zone larger than the crack (Bažant 1987c, 1991b).

Spatial averaging integrals and interaction integrals are not the only way to describe a nonlocal continuum. If the strain field in the neighborhood of a point is expanded into a Taylor series, the strains in the neighboring points are approximately characterized by the spatial partial derivatives (gradients) of the strain tensor at the given point. Thus, the nonlocal continuum may alternatively be defined as a continuum in which the stress at a point depends not only on the strain at that point but also on the successive gradients of the strain tensor at that point (Bažant 1984b, Triantafyllidis and Aifantis 1986). This approach may be regarded as a generalization of Cosserat's couple stress continuum or Eringen's micropolar elasticity. Cosserat's continuum was considered as an alternative approach to achieve regularization of the strain-localization problem in softening materials, but they have been superseded by fully nonlocal or high-gradient models, and will not be presented here. The interested reader may refer, among others, to the works by de Borst, R. (1990) Vardoulakis (1989), de Borst (1991), de Borst and Sluys (1991), and Dietsche and Willam (1992).

In Chapter 8 we have already seen the crudest but simplest type of nonlocal approach—the crack band model, in which the dependence of stress on the average deformation of a certain representative volume

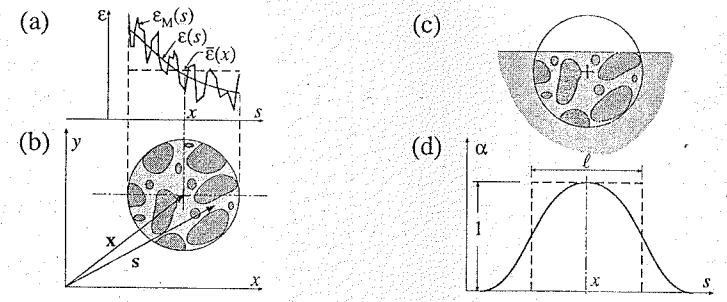

Figure 13.1.1 Spatial averaging. (a) Profiles of micro strain and average strain along a segment centered at point x in the center of a representative volume. (b) Sketch of the representative volume centered at x. (c) Representative volume near the surface of the body. (d) Uniform vs. smoothly decaying averaging functions. (Adapted from Bažant 1990c.)

of the material is enforced by prescribing the minimum crack band width, coinciding with a minimum element size (the reason is that, in a constant strain finite element, the strain approximates the average strain of the material within the element area). The first part of this chapter will describe the nonlocal models based on the idea of averaging, approached in a phenomenological manner. The second part of this chapter will present a recent development in which the nonlocal concept is derived from micromechanical analysis of crack interactions. The mathematical aspects of localization instabilities and bifurcations will not be discussed in detail and the reader is referred to the book by Bažant and Cedolin (1991, Ch. 13).

13.1 Basic Concepts in Nonlocal Approaches

13.1.1 The Early Approaches

The concept of nonlocal continuum for materials with a randomly heterogeneous microstructure was originally conceived and extensively studied for elastic materials (Eringen 1965, 1966; Kröner 1967; Levin 1971; Kunin 1968; Eringen and Edelen (1972); Eringen and Ari 1983). For such materials, the constitutive relation is considered as a relation between the average continuum stress tensor $\bar{\boldsymbol{\sigma}}(\mathbf{x})$ and strain tensor $\bar{\boldsymbol{\varepsilon}}(\mathbf{x})$, which are defined as the statistical averages of the randomly scattered microstresses over a suitable representative volume of the material centered at point x (Fig. 13.1.1a–b).

Intuitively, the justification for nonlocal averaging may be explained by Fig. 13.1.1b, showing a representative volume of the material with an aggregate microstructure. (The representative volume is, in the statistical theory, defined as the smallest volume for which the statistics of the microstructure are not changed by shifting the volume.) The formation of a crack in the center of this element obviously does not depend only on the continuum strain at the center of the crack, but on the overall deformation of this representative volume, which determines the strain energy content and thus the energy release from this volume.

The simplest way to introduce a nonlocal strain measure is to define the average strain tensor as

$$\bar{\boldsymbol{\varepsilon}}(\mathbf{x}) = \frac{1}{V_r(\mathbf{x})}\int_V \alpha(|\mathbf{x}-\mathbf{s}|)\boldsymbol{\varepsilon}(\mathbf{s})dV(\mathbf{s}) = \int_V \hat{\alpha}(\mathbf{x},\mathbf{s})\boldsymbol{\varepsilon}(\mathbf{s})dV(\mathbf{s}) \tag{13.1.1}$$

in which $\boldsymbol{\varepsilon}(\mathbf{x})$ is the usual (local) strain tensor at point x, V the volume of the structure, and $\alpha(r)$ is a scalar function of the distance $r = |\mathbf{x}-\mathbf{s}|$ between the point at which the average is taken and the point contributing to that average; V_r is a normalizing factor introduced so that, for uniform strain, the average is also uniform and coincides with the local value. It is a simple matter to find the required relationships

between V_r, α, and $\hat{\alpha}$

$$V_r(\mathbf{x}) = \int_V \alpha(|\mathbf{x}-\mathbf{s}|)dV(\mathbf{s}) \quad \text{and} \quad \hat{\alpha}(\mathbf{x},\mathbf{s}) = \frac{\alpha(|\mathbf{x}-\mathbf{s}|)}{V_r(\mathbf{x})} \tag{13.1.2}$$

The function $\alpha(r)$ decays with the distance from point x and is zero or nearly zero at points sufficiently remote from x. The simplest is the uniform averaging function, for which $\alpha = 1$ in a sphere of diameter ℓ and 0 outside. For points in the interior of the body whose distance to any boundary is larger than $\ell/2$, V_r is the volume of the averaging sphere $V_r = \pi\ell^3/6$. However, for points closer to the surface, the part of the sphere that protrudes outside the body does not contribute to the integral in (13.1.2) and V_r must be considered a variable (Fig. 13.1.1c).

We may note that according to (13.1.1) and (13.1.2), α may be multiplied by an arbitrary factor without introducing any change in the nonlocal variable, because V_r also gets multiplied by the same factor. This means that we can rescale α at will. In the following, we scale α so that the value of α at the origin is 1, i.e.,

$$\alpha(0) = 1 \tag{13.1.3}$$

as depicted in Fig. 13.1.1d.

The convergence of numerical solutions is slightly better if α is a smooth bell-shaped function (Fig. 13.1.1d, full line) rather than rectangular (Fig. 13.1.1d, dashed line). According to Bažant (1990c), an effective choice is the function

$$\alpha = \left[1-(r/\rho_0\ell)^2\right]^2 \quad \text{if} \quad |r| < \rho_0\ell, \qquad \alpha = 0 \quad \text{if} \quad |r| \geq \rho_0\ell \tag{13.1.4}$$

where $r = |\mathbf{x}-\mathbf{s}|$ is the distance from point x, ℓ is the characteristic length (a material property, Fig. 13.1.1), and ρ_0 is a coefficient chosen in such a manner that the volume under function α given by Eq. (13.1.4) is equal to the volume of the uniform distribution in Fig. 13.1.1d. From this requirement, one may calculate that $\rho_0 = \sqrt[3]{35}/4 = 0.8178$. In the earlier works, the normal (Gaussian) distribution function has also been used instead of Eq. (13.1.4) and was found to work well, although its values are nowhere exactly zero. Note that the limit of nonlocal continuum for $\ell \to 0$ is the local continuum (because $\bar{\varepsilon} \to \varepsilon$).

The foregoing approximation deals with three-dimensional averaging. In many cases, however, two- or one-dimensional approximations are required. In those cases, similar definitions can be written for the averaging operator. For the two-dimensional case V_r must be replaced by A_r, a representative area, and the integrals become surface integrals. For the uniaxial case the integrals reduce to simple integrals and V_r is replaced by a reference length L_r. It is an easy matter to see that if the size of the representative zone is ℓ in either dimension, and the averaging is uniform, then, for interior points $A_r = \pi\ell^2/4$ and $L_r = \ell$. For the bell-shaped function (13.1.4), the values of ρ_0 to be used for two and one dimensions are adjusted so that they give the same values for A_r and L_r as the uniform distribution (see the exercises at the end of this section).

Now that we have introduced the concept of nonlocal averaging, formulating the equations of a nonlocal continuum seems to be a simple matter: Just replace some or all of the classical local variables by their nonlocal averages. However, this is not easy because, in general, some physically problematic features appear and the model does not work at all. In the remainder of this section we focus on uniaxial models to illustrate some of the problems that may arise and the approaches devised to overcome them, leading to various useful models.

13.1.2 Models with Nonlocal Strain

The simplest model imaginable is the nonlocal version of the classical linear elastic model. Its uniaxial version simply reads

$$\sigma(x) = E\bar{\varepsilon}\,, \qquad \bar{\varepsilon} = \frac{1}{L_r}\int_L \alpha(|s-x|)\,\varepsilon(s)\,ds \tag{13.1.5}$$

where σ and ε are the uniaxial stress and strain. Consider, for the sake of simplicity, an infinitely long bar subjected to uniaxial stress σ, and assume that the averaging rule is rectangular, such that $\alpha(r) = 1$

for $|r| < \ell/2$ and zero otherwise. The equilibrium of the bar requires σ to be constant, and so we need to solve the equation

$$\frac{E}{\ell}\int_{x-\ell/2}^{x+\ell/2} \varepsilon(s)\, ds = \sigma \qquad (= \text{const.}) \tag{13.1.6}$$

This is an integral equation that accepts as a trivial solution $\varepsilon = \sigma/E$. However, the solution is not unique. Indeed, we can write the general solution as $\varepsilon = \sigma/E + \varepsilon^*$ and substitute into the foregoing equation to find that the condition to be satisfied by the unknown function ε^* is

$$\int_{x-\ell/2}^{x+\ell/2} \varepsilon^*(s)\, ds = 0 \tag{13.1.7}$$

This equation simply states that the mean of the function over any segment of length ℓ is zero. There are infinitely many solutions of this equation since any harmonic function whose wavelength is a submultiple of ℓ satisfies this condition, i.e., any function of the type

$$\varepsilon^*(s) = A\cos\frac{2\pi n\, s}{\ell} + B\cos\frac{2\pi n\, s}{\ell} \tag{13.1.8}$$

is a solution whatever the constants A and B and the nonzero integer n.

It may be shown that many bell-shaped curves also lead to multiple solutions. To avoid this problem, the averaging function α must have the property that its Fourier transform is positive for any wave number (see Bažant and Cedolin 1991, Sec. 13.10). One particular possibility is to take a weight function with a Dirac δ-spike at its center. Then the nonlocal elastic equation (13.1.5) can be rewritten as

$$\sigma = \gamma E\varepsilon + (1-\gamma)E\bar{\varepsilon}\,, \qquad \bar{\varepsilon} = \frac{1}{L_r}\int_L \alpha_s(|s-x|)\,\varepsilon(s)\, ds \tag{13.1.9}$$

in which the first term comes from the spike, and $0 < \gamma < 1$; γ is a constant that measures the relative weight of the spike, and α_s is the smooth part of the weight function. It is obvious that for $\gamma = 1$ the response is purely local (in which case the elastic solution is unique), while for $\gamma = 0$ the response is purely nonlocal and displays the aforementioned multiple solutions. If γ is selected large enough, then the multiple solutions can be avoided.

This kind of approach, with intermediate values of γ, can be interpreted as a parallel coupling of a local elastic model with a nonlocal model, in which γ has the meaning of the volume fraction of local medium. Such a model may also be regarded as a nonlocal continuum model overlaid by a local elastic continuum. The overlay by an ordinary elastic continuum (called the imbricate continuum) was introduced to stabilize the solutions for softening nonlocal continua (Bažant, Belytschko and Chang 1984; Bažant 1986c). However, such an overlay prevents strain-softening from reducing the stress to zero. Other later formulations were proposed, such that this artificial expedient could be avoided.

Before proceeding to other models, we may note that in the foregoing simple analysis the multiplicity of solutions arises because the strain can accept *alternating* solutions. This is so because the strain can, in principle, take any value, positive or negative. However, if nonlinear ever-increasing variables (such as cumulated plastic work or damage) were to appear in nonlocal equations similar to (13.1.7), then no arbitrary solution could exist, because the average of a nonnegative variable cannot be zero unless the variable vanishes everywhere. This is at the root of the most recent nonlocal models in which the stress and strain are considered to be local, while some nondecreasing internal variable is taken as nonlocal. We will examine a number of models of this kind in the sequel. But before doing so, it is useful to generalize the nonlocal idea of averaging to other kinds of operators, in particular, differential operators which lead to the so called *gradient models*.

13.1.3 Gradient Models

Consider an uniaxial model in which a certain scalar variable —for example, the uniaxial strain— is assumed to be nonlocal, as given by the second of (13.1.5), and assume further that the function α is a rectangular or bell-shaped function as sketched in Fig. 13.1.1d. If we further assume that the bar is

very long compared to ℓ, so that the averaging integral would extend from $-\infty$ to $+\infty$, then, setting $u = s - x$, we may rewrite the expression for the nonlocal variable as

$$\bar{\varepsilon} = \frac{1}{\ell}\int_{-\infty}^{+\infty} \alpha(|u|)\,\varepsilon(x+u)\, du \tag{13.1.10}$$

If the local variable ε is assumed to be smooth and varying slowly over a segment centered at x in which α is different from zero, we can approximate $\varepsilon(x+u)$ by a truncated Taylor power series expansion about point x. Thus, we get the following expansion:

$$\bar{\varepsilon}(x) = \varepsilon(x) + \frac{\partial\varepsilon}{\partial x}(x)\ell\mu_1 + \frac{\partial^2\varepsilon}{2\partial x^2}(x)\ell^2\mu_2 + \cdots + \frac{\partial^n\varepsilon}{n!\partial x^n}(x)\ell^n\mu_n \tag{13.1.11}$$

in which μ_i are the dimensionless moments of the weight function, defined as

$$\mu_n = \int_{-\infty}^{+\infty} \alpha(|s|)\frac{s^n\, ds}{\ell^{n+1}} \tag{13.1.12}$$

Since α is even, the odd moments are equal to zero, and only the even moments need to be retained in the foregoing expansion. In cases in which the local variable (ε in this example) varies slowly over the length ℓ (and thus can be approximated by an arc of second-degree parabola), a two-term expansion is a good approximation of the nonlocal variable. Therefore, setting $\mu_2\ell^2/2 = (\lambda/2\pi)^2$, we get

$$\bar{\varepsilon} \approx \varepsilon(x) + \ell^2\mu_2\frac{\partial^2\varepsilon}{2\partial x^2}(x) = \varepsilon(x) + \left(\frac{\lambda}{2\pi}\right)^2\frac{\partial^2\varepsilon}{\partial x^2}(x) \tag{13.1.13}$$

as proposed by Bažant (1984b, Eqs. 44, 55, 64,70 and 73).

We thus see that, under certain smoothness conditions, the nonlocal integral operator can be approximated by a differential operator involving even-order gradients. For the second-order case, the differential operator reduces to the *harmonic* operator in (13.1.13).

The harmonic operator as well as fourth-order differential operators have been proposed to describe materials with softening. They have the advantage of leading to differential equations which are easier to treat analytically and numerically than the integral equations posed by the full nonlocal approach (following Bažant 1984b, such models, called second gradient models, have also been introduced by Mühlhaus and Aifantis 1991, de Borst and Mühlhaus 1992, and others).

It is easy to show that the gradient approaches also display multiple solutions if the nonlocal variable can take arbitrary positive or negative values. We thus turn attention to the nonlocal models (including their gradient approximations) based on assuming that the nonlocal variable is one irreversible (nondecreasing) internal variable.

13.1.4 A Simple Family of Nonlocal Models

A set of nonlocal models with a common underlying local formulation can be formulated with relative ease, as done by Planas, Elices and Guinea (1993, 1994). These models have the advantage of decoupling the material nonlinearity, involved in the softening curve, from the nonlinearity introduced by the localization. To be specific, we select the uniaxial softening model with strength degradation described in Section 8.4.2, for which

$$\varepsilon = \frac{\sigma}{E} + \varepsilon^f \tag{13.1.14}$$

$$\bar{\varepsilon}^f = \max(\varepsilon^f) \tag{13.1.15}$$

$$\sigma \le \phi(\bar{\varepsilon}^f) \tag{13.1.16}$$

where in the last condition the equality holds whenever ε^f and $\bar{\varepsilon}^f$ are both increasing.

We know from the analysis in Section 8.3 that this model leads to strain localization into a zone of measure zero. To avoid this, various nonlocal modifications are possible. The simplest is probably to modify only the last equation (13.1.16) and let it depend on a nonlocal variable Ω. Since the last equation defines the evolution of strength, we can call this type of model a nonlocal strength model.

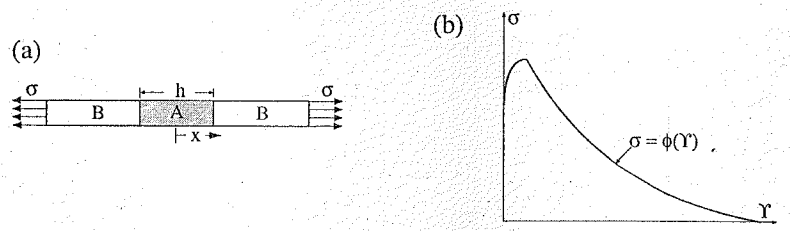

Figure 13.1.2 (a) Bar subjected to tension, with a localized zone A and unloading zones B. (b) Postpeak softening curve of stress vs. nonlocal fracturing strain Υ. (Adapted from Planas, Elices and Guinea 1993.)

There are various ways to include nonlocality in the strength equation. A simple one is to modify (13.1.16) to read

$$\sigma \leq \phi(\Upsilon) \tag{13.1.17}$$

Υ is a nonlocal variable defined from the fracturing strain distribution as

$$\Upsilon(x) = \mathcal{F}\left[\varepsilon^f(s); x\right] \tag{13.1.18}$$

in which $\mathcal{F}\left[\varepsilon^f(s); x\right]$ denotes a spatial operator relating the distribution of inelastic strains to the nonlocal variable. This operator can, in principle, be of the differential or integral type, or of other types.

To see how the general equations are obtained, consider a very long bar (i.e., neglect the end effects) and assume that, upon reaching the peak, strain localization occurs within zone A while over the remainder of the bar unloading takes place (Fig. 13.1.2a). This means that $\varepsilon^f > 0$, and $\sigma = \phi(\Upsilon)$ for $x \in A$, and $\varepsilon^f = 0$ and $\sigma \leq \phi(\Upsilon)$ for $x \in B$. Equilibrium further requires that $\sigma =$ constant along the bar. Therefore, if we assume, as usual, that after peak the function $\phi(\Upsilon)$ is monotonically decreasing as depicted in Fig. 13.1.2b, the foregoing conditions can be rewritten as

$$\varepsilon^f > 0 \text{ and } \Upsilon = \Upsilon_A \quad \text{for } x \in A \tag{13.1.19}$$

$$\varepsilon^f = 0 \text{ and } \Upsilon \leq \Upsilon_A \quad \text{for } x \in B \tag{13.1.20}$$

in which Υ_A is the constant value that the nonlocal variable assumes in the softening zone. Given Υ_A, the stress is obviously obtained as $\sigma = \phi(\Upsilon_A)$.

Substituting now Υ from (13.1.18) in the two last equations, the problem is reduced to the functional equation

$$\mathcal{F}\left[\epsilon^f(s); x\right] = \Upsilon_A \qquad \text{for} \qquad x \text{ and } s \in A \tag{13.1.21}$$

subjected to the restriction

$$\mathcal{F}\left[\epsilon^f(s); x\right] \leq \Upsilon_A \qquad \text{for} \qquad x \in B \text{ and } s \in A \tag{13.1.22}$$

The solution of this equation yields the distribution of ε^f for each Υ_A, which is the basic problem to solve. Note that appropriate jump conditions at the interface between zones A and B may be necessary to complete the solution. They depend on the type of operator envisaged. Note also that the zone A over which localization takes place is not known *a priori*, and so it must ensue as a part of the solution. This means that, even if the nonlocal operator $\mathcal{F}$ is linear, the overall problem is not.

We turn next to the analysis of three types of operators and their properties. They are all linear operators, and so the localization problem in Eqs. (13.1.21)–(13.1.22) is quasi-linear. In this way, the material nonlinearity, included in the softening function, is decoupled from the localization problem, which sheds light on the mathematical aspects of the problem.

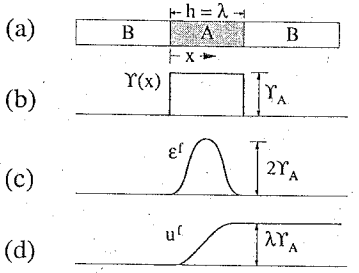

Figure 13.1.3 Nonlocal gradient model with harmonic operator. (a) Bar subjected to tension, with a localized zone A and unloading zones B. Distributions for Υ (b), ε^f (c) and inelastic displacement u^f (d). (Adapted from Planas, Elices and Guinea 1993.)

13.1.5 A Second-Order Differential Model

Consider the differential harmonic operator in Eq. (13.1.13). Then (13.1.21) reduces to the equation

$$\varepsilon^f + \left(\frac{\lambda}{2\pi}\right)^2 \frac{\partial^2 \varepsilon^f}{\partial x^2} = \Upsilon_A \qquad \text{for} \qquad x \in A \tag{13.1.23}$$

whose general solution is

$$\varepsilon^f = \Upsilon_A + C\cos\left(\frac{2\pi x}{\lambda} + \psi\right) \qquad \text{for} \qquad x \in A \tag{13.1.24}$$

where C and ψ are arbitrary constants. To determine these constants and the possible size of the localization zone, the jump conditions between the regions A and B must be determined. These conditions are obtained easily if the solution is analyzed in the sense of the theory of distributions. Then, since $\varepsilon^f = \Upsilon = 0$ at the interior points of B and $\Upsilon = \Upsilon_A$ at the interior points of A, the solution for Υ has C^{-1} continuity, therefore, the solution for for ε^f must have C^{n-1} continuity, where n is the differential order of the operator (a jump in the n-th derivative exists). In our case $n = 2$, and so ε^f must have C^1 continuity, i.e., it must be continuous, with a continuous first derivative.

Taking the x origin to lie at the left interface between parts A and B, as shown in Fig. 13.1.3a, and requiring that at this point both ε^f and its first derivative must vanish, we get $C = -\Upsilon_A$ and $\psi = 0$, from which the possible solution takes the form

$$\varepsilon^f = \Upsilon_A\left(1 - \cos\frac{2\pi x}{\lambda}\right) = 2\Upsilon_A \sin^2\frac{\pi x}{\lambda} \tag{13.1.25}$$

Writing now the continuity conditions at the right interface between A and B, we find that the size h of the localization zone can take only discrete values $h = m\lambda$, with $m = 1, 2, \cdots$. Thus, a periodic solution with an integer number of wavelengths is possible. However, we immediately see that the inelastic displacement and energy requirements are minimum for the smallest possible size, i.e., for a single wavelength. Figs. 13.1.3b–d show the resulting distributions for Υ, ε^f and u^f, where $u^f = \int_{-\infty}^{x} \varepsilon^f \, dx$ is the displacement associated with the fracturing strain.

Note that in solving this problem we assume that there is a region B in which the material unloads, and that the softening region A is continuous. Obviously, there also exist solutions in which (a) the strain is uniform along the bar and $\varepsilon^f = \Upsilon_A$ everywhere, or (b) there exist various nonoverlapping distributions identical in shape to that in Fig. 13.1.3c. However, it is easy to see that the single wavelength solution in this figure is energetically preferred.

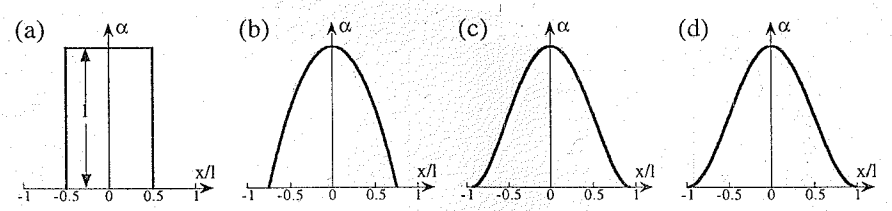

Figure 13.1.4 Examples of weight functions: (a) Rectangular; (b) second-degree parabola, $\alpha(x) = 1 - (x/0.75\ell)^2$; (c) fourth-degree parabola, Eq. (13.1.4) with $\rho_0 = 15/16$; (d) cosine, $\alpha = 1 + \cos(\pi x/\ell)$. (Adapted from Planas, Elices and Guinea 1993.)

13.1.6 An Integral-Type Model of the First Kind

A simple integral functional was investigated by Planas, Elices and Guinea (1993, 1994). It leads to an integral equation of the first kind. Its solution, surprisingly, can be obtained in a closed form, and it turns out to be a cohesive crack.

In this model, the expression for the nonlocal variable is

$$\Upsilon(x) = \mathcal{F}\left[\varepsilon^f(s); x\right] \equiv \frac{1}{L_r}\int_L \alpha(|s-x|)\,\varepsilon^f(s)\,ds \tag{13.1.26}$$

in which the weight function α is assumed to be smooth and to have a maximum only at the center. This function is normalized so that $\alpha(0) = 1$, and L_r is given by the uniaxial version of (13.1.2), which ensues by replacing the volume integral by a simple integral and V_r by L_r. For very long bars (L extending from $-\infty$ to $+\infty$) $L_r = \ell =$ characteristic length. Examples of such weight functions are given in Fig. 13.1.4.

Planas, Elices and Guinea (1993, 1994) showed that when a very long bar is considered and the foregoing expression for the functional is substituted into Eqs. (13.1.21)–(13.1.22), the resulting problem accepts a solution consisting of a Dirac's δ-function:

$$\varepsilon^f = w\delta(x)\,, \qquad \text{with} \qquad w = \Upsilon_A \ell \tag{13.1.27}$$

where we assume the origin of coordinates to coincide with the spike location; w is the displacement jump associated with the δ-function, i.e., the crack opening. Since $\sigma = \phi(\Upsilon_A)$, the foregoing result indicates that the solution of this nonlocal model is physically equivalent to a cohesive crack model with a softening function

$$\sigma = f(w) = \phi\left(\frac{w}{\ell}\right) \tag{13.1.28}$$

Note also the remarkable similitude of the foregoing result and Eq. (8.3.2) for the crack band model.

That the foregoing expression is indeed a solution is easily shown by substituting (13.1.27) into (13.1.26) and performing the integration; the result is

$$\Upsilon(x) = \Upsilon_A\,\alpha(x) \tag{13.1.29}$$

which shows that, since $\alpha(0) = 1$, $\Upsilon = \Upsilon_A$ at the origin where $\varepsilon^f > 0$, and $\Upsilon < \Upsilon_A$ everywhere else, as required. Fig. 13.1.5b shows the distribution for the nonlocal variable Υ; Figs. 13.1.5c–d display the distributions for the fracturing strain and displacement.

Certainly, however, this is not the only solution, at least on pure mathematical grounds. First, the location of the δ-spike is arbitrary. Second, an array of any number of δ-functions is also possible, which is equivalent to having multiple cohesive cracks. However, the principle of minimum second-order work indicates, similar to the localization analysis in Chapter 8, that only one crack will occur in reality. Planas, Elices and Guinea (1994) further showed that if the weight function satisfies very mild conditions, solutions with bounded strains distributed over a finite support are not possible. Therefore, it appears that the single δ-spike is *the* solution of this simple nonlocal model. This provides theoretical support for the cohesive crack models.

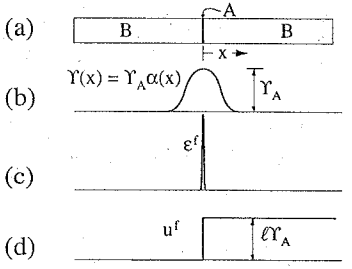

Figure 13.1.5 Nonlocal integral model of the first kind. (a) Bar subjected to tension, with a localized zone reduced to point A and unloading zones B. Distributions for Υ (b), ε^f (c), and inelastic displacement u^f (d). (Adapted from Planas, Elices and Guinea 1993.)

13.1.7 An Integral-Type Model of the Second Kind

Although the foregoing integral model involves a localization limiter in the sense that the solution for the inelastic strain has a finite measure (i.e., the model gives a finite inelastic displacement, w, and a finite energy dissipation), the localization still occurs over a segment of vanishing size. Planas, Guinea and Elices (1996) have extended the analysis to include a linear term along with the integral term in (13.1.26). They take the integral operator as

$$\Upsilon(x) = \mathcal{F}\left[\varepsilon^f(s); x\right] \equiv -\gamma\,\varepsilon^f(x) + \frac{1+\gamma}{L_r}\int_L \alpha(|s-x|)\,\varepsilon^f(s)\,ds \tag{13.1.30}$$

in which γ is constant. Obviously, for $\gamma = 0$ we recover the previous model. Considering again a very long bar in which localization takes place in region A far from both ends as sketched in Fig. 13.1.2a, we have $L_r = \ell$. Taking the x-origin to lie at the center of the localization zone, as depicted in Fig. 13.1.2a, we can reduce Eqs. (13.1.21)–(13.1.22) to the following Fredholm integral equation of the second kind:

$$-\gamma\,\varepsilon^f(x) + \frac{1+\gamma}{\ell}\int_{-h/2}^{h/2} \alpha(|s-x|)\,\varepsilon^f(s)\,ds = \Upsilon_A \qquad \text{for } x \in [-h/2, h/2] \tag{13.1.31}$$

subjected to the restrictions

$$\varepsilon^f(x) \geq 0 \qquad \text{for } x \in [-h/2, h/2] \tag{13.1.32}$$

$$\frac{1+\gamma}{\ell}\int_{-h/2}^{h/2} \alpha(|s-x|)\,\varepsilon^f(s)\,ds \leq \Upsilon_A \qquad \text{for } x \notin [-h/2, h/2] \tag{13.1.33}$$

Here it is understood that $\varepsilon^f(x) = 0$ for $x \notin [-h/2, h/2]$. The integral equation (13.1.31) is a Fredholm equation of the second kind that can be solved for a given h by any of several known methods (see, e.g., Mikhlin 1964; Press et al. 1992). The key point here is that h is not known *a priori*, but that it has to be obtained as part of the solution, because if h is picked at random the solution will fail to satisfy (13.1.32) or (13.1.33), or both.

Planas, Guinea and Elices (1996) investigated the behavior of the problem both theoretically and numerically. On the theoretical side they showed that, for the solutions with a zero-measure to be excluded, γ must be positive. They also showed that the solution for ε^f must be continuous across the interfaces between the softening and unloading regions. On the numerical side, they investigated symmetric modes of localization by discretizing the bar in equal elements of constant ε^f and using point collocation at the center of the elements. The integral was evaluated using a single integration point in the center of each element. A certain value of h was initially assumed and the resulting linear system was solved using standard methods (LU decomposition). It was found that if h was too small, condition (13.1.33) was violated, as shown for one particular case in Fig. 13.1.6a by the full lines, while if h was too large, (13.1.32) could not be fulfilled, as shown in the same figure by the dashed line. The solution was

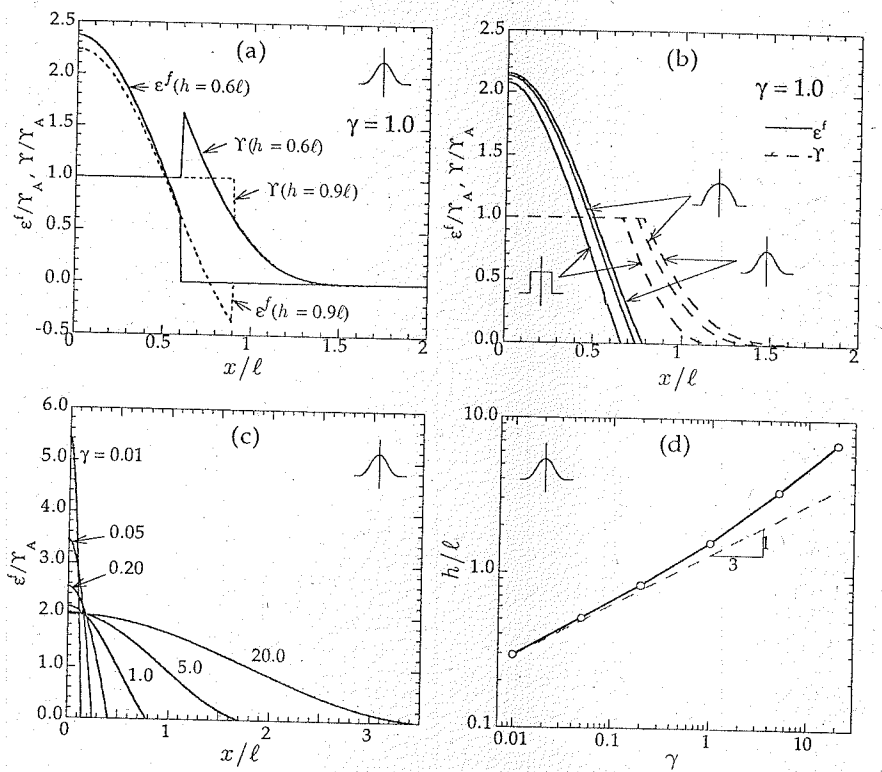

Figure 13.1.6 Uniaxial nonlocal model of the second kind. (a) Solutions of the integral equation (13.1.31) for too small a value of h (full lines) and for too large a value of h (dashed lines). (b) Complete solutions of the problem for various weight functions. (c) Distributions of fracturing strains for various γ. (d) Influence of the factor γ on the width h of the localization zone. (After Planas, Guinea and Elices 1996.)

found iteratively, first with relatively large elements ($\ell/12$ in size) and then for a refined mesh (element size $\ell/100$ to $\ell/1000$ depending on the cases). The results can be summarized as follows:

1. The distribution of ε^f is parabolic in shape and is not very sensitive to the shape of the weight function α, as shown in Fig. 13.1.6b, in which the distributions for the α-functions in Figs. 13.1.4a, b, and d are compared for $\gamma = 1$. We see that h varies only between 1.3ℓ and 1.6ℓ, approximately.
2. The width h of the softening zone is very much influenced by the value of γ, as shown in Fig. 13.1.6c. Indeed, since the exact solution for $\gamma = 0$ is known to be the Dirac δ-function for which $h = 0$, we must have $h \to 0$ for $\gamma \to 0$. For the cases investigated by Planas, Guinea and Elices (1996) the asymptotic relationship is of the power-type: $h \propto \gamma^m \ell$ where m is of the order of 1/3, as shown in Fig. 13.1.6d.

13.1.8 Nonlocal Damage Model

In a series of papers, Bažant and Pijaudier-Cabot developed an isotropic nonlocal damage model, whose uniaxial version was thoroughly investigated (Bažant and Pijaudier-Cabot 1988; Pijaudier-Cabot and Bažant 1987, 1988). The underlying local damage model is similar to the damage models analyzed in

Sections 8.4.1 and 8.4.4, which can be rewritten as

$$\sigma = (1 - \Omega) E \varepsilon \tag{13.1.34}$$

Ω is the damage, a nondecreasing variable that is made nonlocal using adequate flow rules. Bažant and Pijaudier-Cabot used two different sets of flow rules which are equivalent in the local version but lead to slightly different models in the nonlocal version. For the underlying local model they assume, based on energy considerations, that the driving force for the growth of damage is the damage energy release rate Y, defined as

$$Y = -\frac{\partial \overline{\mathcal{U}}}{\partial \Omega} = \frac{1}{2} E \varepsilon^2 \tag{13.1.35}$$

in which $\overline{\mathcal{U}} = (1/2)\sigma\varepsilon = (1/2)(1-\Omega)\varepsilon^2$ is the elastic energy density. Once the driving force is defined, the evolution of Ω is assumed to be described by a unique function of the maximum driving force ever experienced by the material:

$$\Omega = F(\tilde{Y}) \qquad \text{with} \qquad \tilde{Y} = \max(Y) \tag{13.1.36}$$

where $F(\tilde{Y})$ is a monotonically increasing function of $\tilde{Y}$. Because $F(\tilde{Y})$ is monotonic, it turns out that $F[\max(Y)] = \max[F(Y)]$, and thus, on purely nonlocal grounds, the foregoing growth rule is strictly equivalent to writing

$$\Omega = \max(\omega) \qquad \text{with} \qquad \omega = F(Y) \tag{13.1.37}$$

Although these two formulations are equivalent in the local framework, they lead to two different nonlocal models according to whether the nonlocal averaging is applied to Y in (13.1.36) or to ω in (13.1.37). In the first case Pijaudier-Cabot and Bažant (1987) introduced the nonlocal variable $\overline{Y}$ as

$$\overline{Y}(x) = \frac{1}{L_r} \int_L \alpha(|s - x|)\, Y(s)\, ds \tag{13.1.38}$$

and then modified (13.1.36) to read

$$\Omega = F(\tilde{\overline{Y}}) \qquad \text{with} \qquad \tilde{\overline{Y}} = \max(\overline{Y}) \tag{13.1.39}$$

They called this the *energy averaging* approach because of the meaning of Y. In their second formulation (Bažant and Pijaudier-Cabot 1988) they averaged the intermediate variable ω in (13.1.37) (which they called the *damage averaging* approach). The new nonlocal variable $\overline{\omega}$ is defined as

$$\overline{\omega}(x) = \frac{1}{L_r} \int_L \alpha(|s - x|)\, \omega(s)\, ds \qquad \text{with} \qquad \omega = F(Y) \tag{13.1.40}$$

and then the evolution of Ω is defined as

$$\Omega = \tilde{\overline{\omega}} \qquad \text{with} \qquad \tilde{\overline{\omega}} = \max(\overline{\omega}) \tag{13.1.41}$$

Recently, Jirásek (1996) showed that averaging of different variables yields models with very different postpeak responses, and suggested that averaging of the inelastic strain or damage seems to be most realistic.

Pijaudier-Cabot and Bažant (1987, 1988) used the energy average model to investigate dynamic strain localization in a bar subjected to two shock waves traveling from both ends and converging in the center of the bar. The analyses confirmed that the nonlocal formulation does prevent zero measure fracture modes. Furthermore, the computations were shown to be mesh-objective. In a further work, Bažant and Pijaudier-Cabot (1988) analyzed the static localization in a bar subjected to tension. Although the complete analysis is globally nonlinear, it is incrementally linear, and the incremental formulation for the initiation of localization takes a form similar to that described in the preceding paragraph, namely, that of a Fredholm equation of the second kind subjected to certain restrictions. To see this, consider the damage average formulation (13.1.41), and assume that the bar is homogeneously deformed up to a point

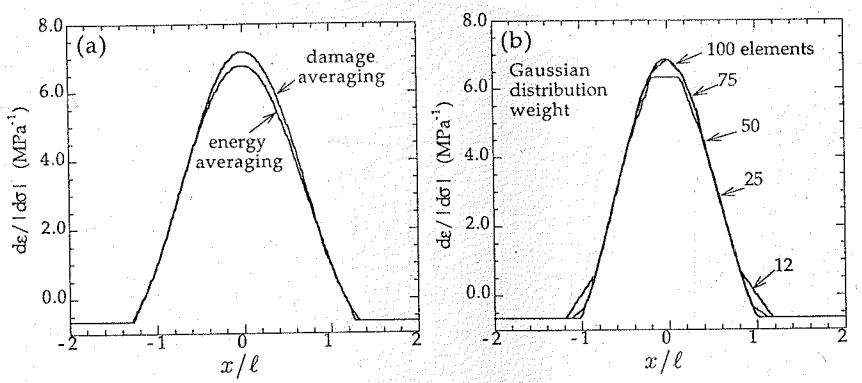

Figure 13.1.7 (a) Incremental strain distribution at the onset of localization in the nonlocal damage model. (b) Convergence to the solution for successive mesh refinement. (After Bažant and Pijaudier-Cabot 1988.)

on the softening branch. We want to analyze the initiation of localization, and so we consider the rate (or incremental) equation derived by differentiating (13.1.34) with respect to time:

$$E(1-\Omega_0)\dot{\varepsilon}_0 - E\varepsilon_0\dot{\Omega} = \dot{\sigma} \qquad (= \text{const.}) \tag{13.1.42}$$

Here we have set $\Omega = \Omega_0$ and $\varepsilon = \varepsilon_0$. These are the values reached prior to localization, which are, by hypothesis, uniform. Note also that equilibrium requires $\dot{\sigma}$ to be uniform. Inserting (13.1.40) into (13.1.41) and differentiating, we get

$$\dot{\Omega} = \left\langle \frac{F'(Y_0)E\varepsilon_0}{L_r}\int_L \alpha(|s-x|)\,\dot{\varepsilon}(s)\,ds \right\rangle = \frac{F'(Y_0)E\varepsilon_0}{L_r}\left\langle \int_L \alpha(|s-x|)\,\dot{\varepsilon}(s)\,ds \right\rangle \tag{13.1.43}$$

in which $F'(Y) = dF(Y)/dY$ and $\langle\cdot\rangle$ are the Macauley brackets, equal to its argument if it is positive, or zero if it is negative; the second equality holds because $F'(Y)$ and ε are positive (remember that $F(Y)$ is monotonically increasing). Therefore, (13.1.42) can be rewritten as follows:

$$E(1-\Omega_0)\dot{\varepsilon}(x) - 2EF'(Y_0)Y_0\left\langle \frac{1}{L_r}\int_L \alpha(|s-x|)\,\dot{\varepsilon}(s)\,ds \right\rangle = \dot{\sigma} \qquad (= \text{const.}) \tag{13.1.44}$$

This is an integral equation of the second kind in $\dot{\varepsilon}$ which, however, is not linear because of the presence of the Macauley brackets. Bažant and Pijaudier-Cabot solved this integral equation numerically for various weight functions and characteristic lengths. They found the typical strain-rate profiles shown in Fig. 13.1.7a. They also found that the size h of the localized zone was proportional to ℓ, and that the convergence with mesh refinement was fully satisfactory, as shown in Fig. 13.1.7b.

The results for the strain-rate profiles are remarkably similar to those found in the previous paragraph for the so-called integral model of the second kind, and Planas, Guinea and Elices (1996) examined whether the two problems were related. It turned out that they were: it suffices to write the problem in terms of an inelastic strain rate $\dot{\varepsilon}^f$ defined as

$$\dot{\varepsilon}^f = \dot{\varepsilon} - \frac{\dot{\sigma}}{E(1-\Omega_0)} \tag{13.1.45}$$

Solving this equation for $\dot{\varepsilon}$ and inserting the result into (13.1.44), the integral equation is transformed into

$$\frac{(1-\Omega_0)}{2F'(Y_0)Y_0}\dot{\varepsilon}^f(x) - \left\langle \frac{\dot{\sigma}}{E(1-\Omega_0)} + \frac{1}{L_r}\int_L \alpha(|s-x|)\,\dot{\varepsilon}^f(s)\,ds \right\rangle = 0 \tag{13.1.46}$$

Now, to analyze this problem we can split the bar, as before, into region A in which localization occurs (and hence the expression into angle brackets is positive) and region B in which unloading occurs and

thus $\dot{\varepsilon}^f = 0$ and the expression in brackets is negative. Taking further into account that the stress evolves along the softening branch for which $\dot{\sigma} = -|\dot{\sigma}| < 0$, the foregoing equation can be split into two:

$$-\frac{(1-\Omega_0)}{2F'(Y_0)Y_0}\dot{\varepsilon}^f(x) + \frac{1}{L_r}\int_L \alpha(|s-x|)\,\dot{\varepsilon}^f(s)\,ds = \frac{|\dot{\sigma}|}{E(1-\Omega_0)} \qquad \text{for } x \in A \tag{13.1.47}$$

$$\frac{1}{L_r}\int_L \alpha(|s-x|)\,\dot{\varepsilon}(s)\,ds \le \frac{|\dot{\sigma}|}{E(1-\Omega_0)} \qquad \text{for } x \in B \tag{13.1.48}$$

For very long bars, this system reduces to (13.1.31)–(13.1.33) if we introduce the following correspondences

$$\dot{\varepsilon}^f \to \varepsilon^f\,, \qquad \frac{|\dot{\sigma}|/E}{2F'(Y_0)Y_0 - (1-\Omega_0)} \to \Upsilon_A\,, \qquad \frac{(1-\Omega_0)}{2F'(Y_0)Y_0 - (1-\Omega_0)} \to \gamma \tag{13.1.49}$$

This result, combined with the analysis in the previous paragraph, shows that the relationship between the characteristic length ℓ and the extent of the localization zone h depends on the characteristics of the softening function at the point where the localization occurs. This was pointed out by Bažant and Pijaudier-Cabot (1988), and can now be quantitatively assessed using the plot in Fig. 13.1.6d and the expression for γ from the preceding formula.

Exercises

13.1 Consider the bell-shaped averaging function defined in (13.1.4), restricted to two dimensions. Determine ρ_0 so that the value of $A_r = \int_A \alpha(|\mathbf{s}-\mathbf{x}|)dA(\mathbf{s})$ coincide with that for a uniform distribution over a circle of diameter ℓ. [Hint: use polar coordinates to carry out the integral and get $\rho_0 = \sqrt{3}/2$.]

13.2 Consider the bell-shaped averaging function defined in (13.1.4), restricted to one dimension. Determine ρ_0 so that the value of $L_r = \int_L \alpha(|s-x|)ds$ coincide with that for a uniform distribution over a segment of length ℓ.

13.3 Consider a nonlocal model with a uniform weight function and its high gradient harmonic approximation. Determine the relationship between ℓ and λ.

13.4 Consider a nonlocal model with the parabolic weight function defined in Fig. 13.1.4b, and its high gradient harmonic approximation. Determine the relationship between ℓ and λ.

13.5 Show that the energy and damage averaging in (13.1.39) and (13.1.41) are exactly equivalent if $F(Y)$ is linear in Y.

13.6 Show that along the softening branch $2F'(Y)Y - (1-\Omega) > 0$ if no localization occurs, and that the denominators in (13.1.49) are always positive.

13.7 Bažant and Pijaudier-Cabot use a (local) damage function given by

$$F(Y) = 1 - \frac{1}{1 + b\langle Y - Y_t\rangle} \tag{13.1.50}$$

where $b = 20.5\ (\text{MPa})^{-1}$ and $Y_t = 8.54$ MPa. With $E = 32$ GPa, they analyzed the initiation of localization at various uniform strains. For the particular strain $\varepsilon_0 = 0.003$, they found that the size of the localization zone was $h \approx 2\ell$ for a bell-shaped weight function. Verify that this is consistent with the results predicted by the nonlocal strength theory of the second kind. To this end, compute first Y_0 and Ω_0; then compute γ from (13.1.49) and use the curve in Fig. 13.1.6d to find h/ℓ.

13.2 Triaxial Nonlocal Models and Applications

In the preceding section we discussed the most basic issues of the nonlocal models based on simple uniaxial cases. Now we address various other possible phenomenological formulations with features that are essentially three-dimensional, and show the general aspects of some practical applications. We also address the most basic problem of making an experimental determination of the characteristic length ℓ.

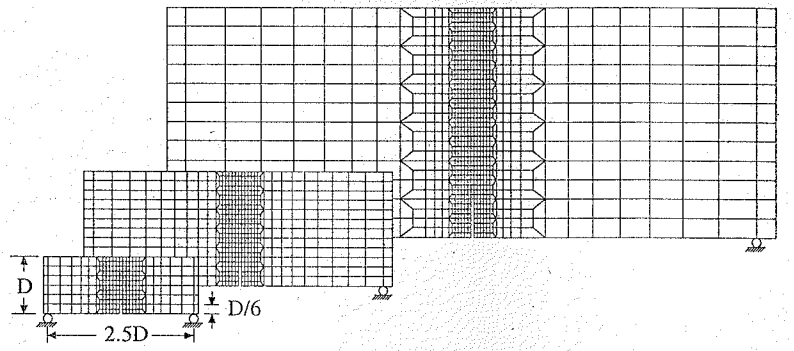

Figure 13.2.1 Finite element meshes used by Bažant and Lin (1988a) to analyze three-point bending of notched specimens of three sizes in the ratios 1:2:4 (from Bažant and Lin 1988a).

13.2.1 Triaxial Nonlocal Smeared Cracking Models

The nonlocal concept can, in principle, be applied to any inelastic constitutive model. It has been applied to the smeared cracking model described in Chapter 8. There are two variants of this model, both of which have been studied. One variant is the cracking of fixed direction (Section 8.5.3) in which the damage ω, which is used to modify the compliance matrix, is considered to be a function of the normal strain ϵ_{nn} in the direction normal to the cracks. The nonlocal generalization is obtained by considering the nonlocal damage $\overline{\omega}$ to be the same function of the averaged strain $\overline{\epsilon}_{nn}$ in the direction normal to the cracks (for details, see Bažant and Lin 1988a).

Another variant is the rotating crack model, for which the local formulation was presented in Section 8.5.6. Again, the nonlocal generalization is obtained by replacing the dependence of the normal compliance C_N on the local principal strain by an identical dependence calculated as a function of the nonlocal principal strain $\overline{\epsilon}_1$. Of course, when the cracks do not rotate, the first and second variant coincide. When they rotate, the second variant seems to be closer to reality.

The model was used by Bažant and Lin (1988a) to simulate three-point-bend fracture specimens, and particularly the size effect. Fig. 13.2.1 shows the finite element meshes for three specimens sizes in the proportions 1:2:4. Fig. 13.2.2 shows a comparison of the nonlocal finite element analysis with test results. The strain-softening law has been considered in two forms: exponential (dashed) and linear (dash-dot). The calculations are compared to the test results of Bažant and Pfeiffer (1987) and to the optimum fit of these results with the size effect law, Eq (1.4.10). The results demonstrate that the nonlocal model eliminates mesh sensitivity (because the ratio of the element size to specimen size is very different for the three specimens). They also demonstrate that the transitional size effect is well described by the nonlocal model. The width of the fracture process zone is, in these calculations, found to be roughly 2.7 ℓ, where ℓ = characteristic length, in agreement with the calculations of Bažant and Pijaudier-Cabot (1988).

Fig. 13.2.3 shows finite element calculations on unnotched beams with deliberately slanted meshes. These calculations show that the nonlocal model in which the characteristic length is sufficiently larger than the element size is free of directional mesh bias. The cracking band can propagate in any direction, without bias, to the mesh lines or the diagonal directions.

13.2.2 Triaxial Nonlocal Models with Yield Limit Degradation

The plasticity models can also be adapted to nonlocal analysis of distributed damage. To this end, plastic hardening is replaced by softening, which means, for example, that the plastic hardening modulus H becomes negative, as illustrated by the negative slope in Fig. 13.2.4 for a Mohr-Coulomb yield surface model. If this is done, of course, Drucker's stability postulate for plasticity ceases to be satisfied, but this is not fundamentally incorrect (see Chapters 10 and 13 in Bažant and Cedolin 1991) because this postulate cannot be expected to apply in the case of damage. The nonlocal concept is introduced into the model

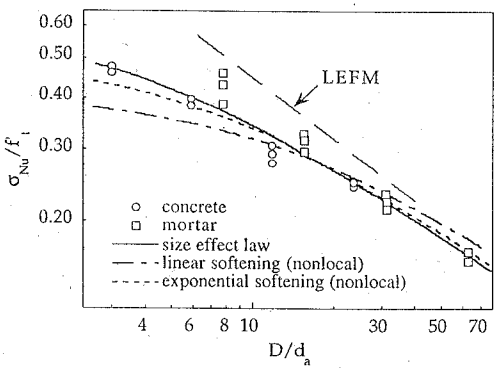

Figure 13.2.2 Size effect plot comparing the test results of Bažant and Pfeiffer (1987) to the size effect law as well as to finite element results of the nonlocal smeared cracking model for linear and exponential softenings (after Bažant and Lin 1988a).

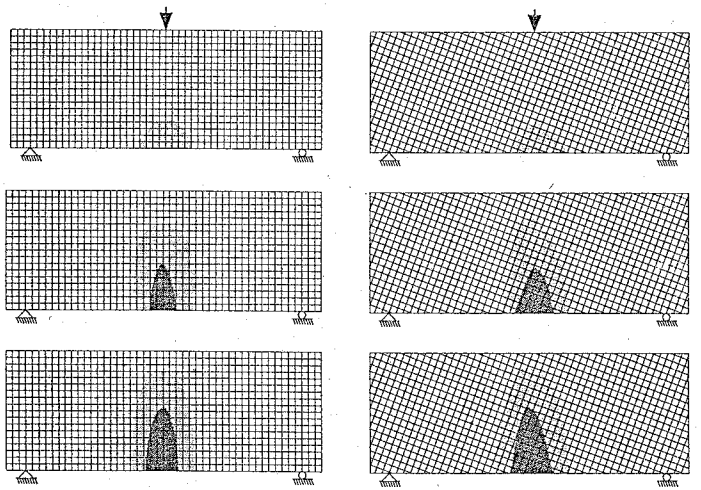

Figure 13.2.3 Strain localization zones at three loading stages for a mesh aligned with the crack path (left) and for a skew mesh (right) (from Bažant and Lin 1988a).

by replacing the plastic strain increment, as soon as it is calculated, by its spatial average and using this average in the constitutive relation.

A debatable feature of this formulation is the fact that Prager's continuity condition of plasticity (consistency condition) is satisfied by the local rather than the nonlocal plastic strain increments, which means that the constitutive law is local and the nonlocality is introduced as separate adaptation. This approach appears to be in line with the conclusions of the analysis of crack interactions (Bažant 1994b) which will be explained later. Some theorists (e.g., de Borst) have insisted that the continuity relation must be satisfied by the nonlocal strains, which, however, would cause a tremendous complication of the model because the continuity condition would become an integral equation over the entire structure. Such a complexity would defeat the advantages of the nonlocal approach. It is true, however, that if Prager's continuity condition is not satisfied by nonlocal strains, there is no precisely defined nonlocal constitutive law. Theoretically, this is a weak point of this type of formulation.

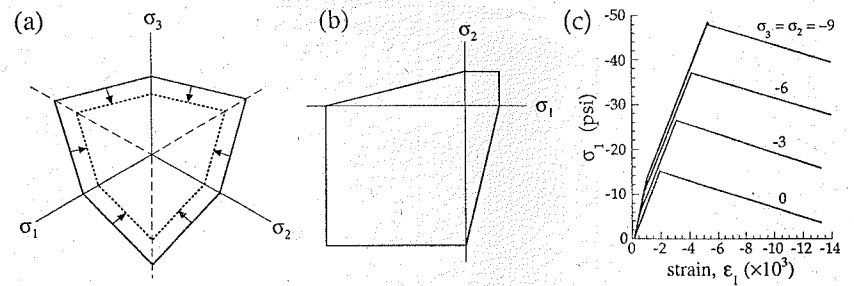

Figure 13.2.4 Mohr-Coulomb yield criterion with strain-softening due to yield limit degradation: (a) yield locus in the deviatoric stress space; (b) yield locus in the principal stress plane; (c) triaxial stress-strain curves with softening for various confining stresses. (Adapted from Bažant and Lin 1988b.)

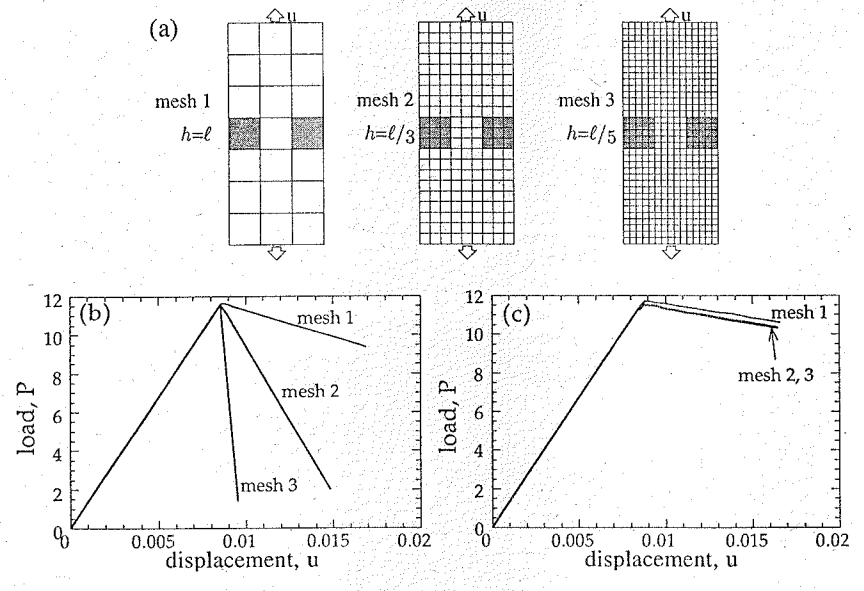

Figure 13.2.5 Analysis of mesh sensitivity. (a) Rectangular panel with various mesh subdivisions; and the corresponding load-displacement curves for (b) local modeling, and (c) nonlocal modeling . (Adapted from Bažant and Lin 1988b.)

Fig. 13.2.5 shows an example (Bažant and Lin 1988b) of a rectangular panel solved by meshes of three different refinements. The local plasticity solution with a degrading yield limit gives the response in Fig. 13.2.5b and the nonlocal model gives the responses shown in Fig. 13.2.5c.

This model has also been applied to the analysis of failure of a tunnel excavation in grouting soil; see Fig. 13.2.6, which shows meshes of four different refinements and the boundaries of the strain softening zones obtained by the four meshes. Note again that the nonlocal approach is basically free of mesh sensitivity.

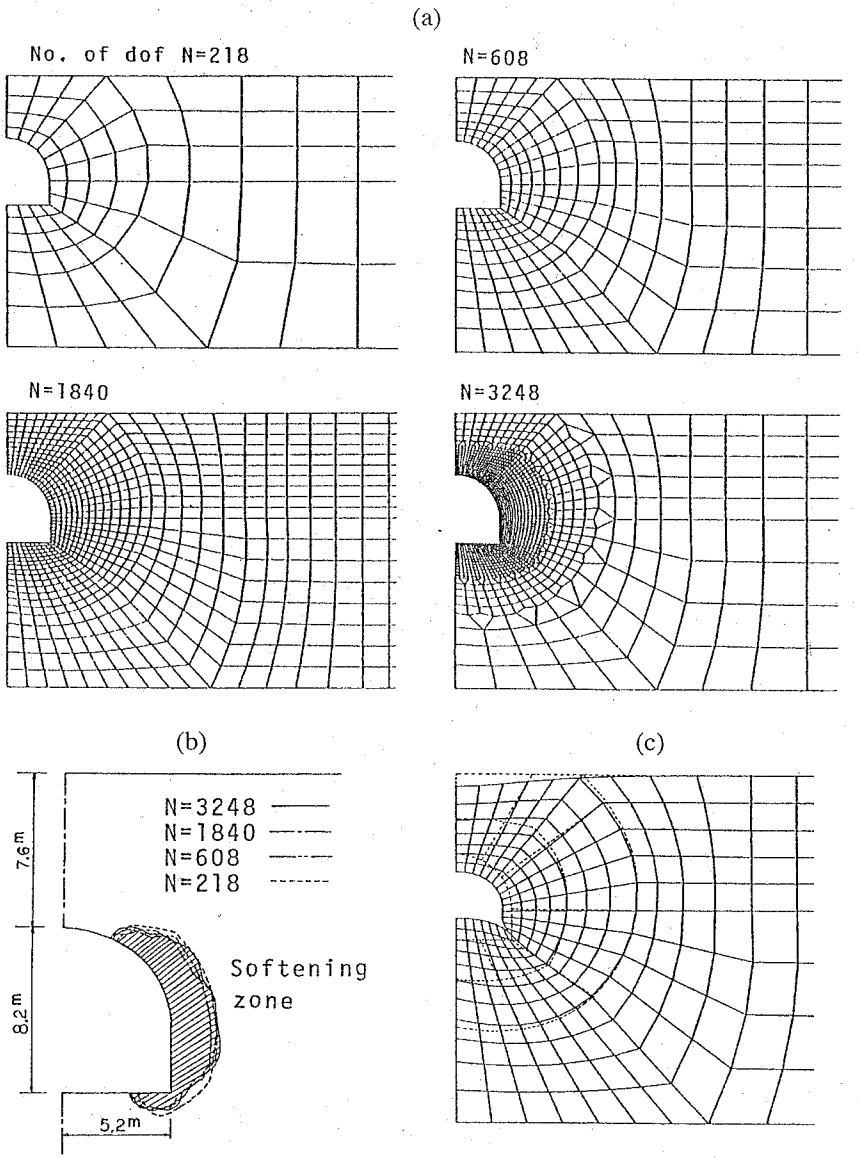

Figure 13.2.6 Bažant and Lin's (1988b) finite element analysis of a tunnel excavation in a grouted soil with a degrading yield limit: (a) finite element meshes; (b) boundaries of the softening zone at full tunnel excavation obtained for the four meshes shown in (a); (c) exaggerated deformation at full excavation. (Adapted from Bažant and Lin 1988b.)

13.2.3 Nonlocal Microplane Model

The most powerful and versatile approach to complex constitutive modeling, including strain softening, appears to be the microplane model which will be explained in the next chapter. Suffice to say at this point that the nonlocal microplane approach has proven very effective and provided, so far, the best finite element results in the modeling of damage and failure of concrete structures, including the size effect.

13.2.4 Determination of Characteristic Length

The characteristic length is a parameter that controls the spread of the nonlocal weight function. It may be defined as the diameter of an averaging region (line segment, circle, or sphere in one-, two-, or three-dimensions) with a uniform weight function that has the same volume as the actual weight function used. The characteristic length ℓ cannot be directly measured but must be inferred indirectly from test of suitable types. There are two types of tests suitable for this purpose: (1) the use of size effect, and (2) the use of elastically restrained tests. Let us examine each of the two possibilities.

(a) Use of size effect. The size effect is the most blatant and most important manifestation of nonlocality. It is necessary to carry out tests of geometrically similar notched specimens of sufficiently different sizes and determine the size effect plot (Chapter 6). Then the characteristic length of the nonlocal model needs to be varied until the finite element calculations match the experimentally determined size effect curve in the optimum way. Generally, it is observed that the transitional size D_0 of the size effect plot (intersection of the horizontal and inclined asymptotes) is approximately (but not exactly) proportional to the value of characteristic length ℓ. Therefore, an effective strategy is to assume characteristic length ℓ', calculate by a nonlocal finite element code the nominal strength of specimens of different sizes, and trace the size effect curve. Optimum fitting of this curve with the size effect law makes it possible to obtain the horizontal and vertical asymptotes and determine their intersection D_0. Then the best estimate of the corrected characteristic length is

$$\ell = \ell' D_0 / D_0' \tag{13.2.1}$$

The process is then repeated and the value of ℓ corrected iteratively. Normally no more than two corrections are required for convergence.

(b) Elastically restrained tensile test. Another approximate way of determining ℓ was proposed by Bažant and Pijaudier-Cabot (1989). A long prismatic specimen of concrete, with a thickness of only a few aggregate sizes, is cast and many longitudinal thin steel rods are glued to its surfaces by epoxy as shown in Fig. 13.2.7. It is assumed that the glued steel bars are sufficient to force the strain in the specimen to be uniformly distributed, and for this reason the specimen must be as thin as possible. If that is the case, the tensile load-deflection diagram directly yields the stress-strain curve for the fracture process zone of concrete. This is illustrated in Fig. 13.2.7c, where the inclined straight line of slope K_s gives the stress carried by steel bars and epoxy alone, and the shaded zone represents the additional contribution due to concrete. If the slope of the load-deflection curve is always positive, localization should not happen according to uniaxial localization analysis. Thus, plotting the results in terms of the average stress and average strain, the shaded area in Fig. 13.2.7c gives the energy W_s dissipated per unit volume of the fracture process zone, on the average. Hence, the average width of the softening zone $\hat{h}$ should approximately be given by

$$\hat{h} = G_f / W_s \tag{13.2.2}$$

which has the dimension of length because $G_f \sim$ J/m^2 and $W_s \sim$ J/m^3. The fracture energy G_f is determined by any of the previously discussed methods. A particular nonlocal model is then needed to correlate $\hat{h}$ and ℓ, although it may be assumed that $h \approx \ell$ (Bažant and Pijaudier-Cabot 1989).

In practice, however, it turned out that this method gives only a crude estimate of the characteristic length because the specimen with tensile restraining elastic bars does not behave uniaxially. The deformation becomes nonuniform transversely and there is some degree, although not a large degree, of localization, as transpired from a thorough investigation by Berthaud, Ringot and Schmitt (1991). Further development would be required before ℓ can be accurately determined by this method.

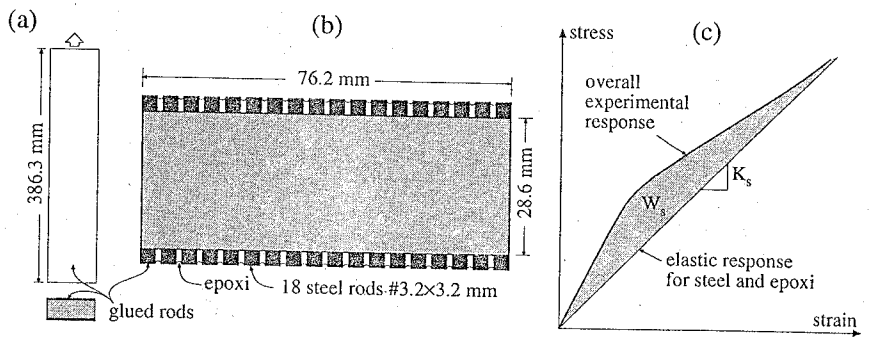

Figure 13.2.7 Bažant and Pijaudier-Cabot's (1989) method to determine the characteristic length for concrete: (a) sketch of restrained specimen; (b) cross-section with the arrangement of the steel bars at the surface of concrete; (c) sketch of the stress-strain curves for the specimen with the glued rods. (Adapted from Bažant and Pijaudier-Cabot 1989.)

13.3 Nonlocal Model Based on Micromechanics of Crack Interactions

13.3.1 Nonlocality Caused by Interaction of Growing Microcracks

The local constitutive law may be written in the incremental form

$$\Delta\boldsymbol{\sigma} = \boldsymbol{E}(\Delta\boldsymbol{\varepsilon} - \Delta\boldsymbol{\varepsilon}'') = \boldsymbol{E}\Delta\boldsymbol{\varepsilon} - \Delta\mathbf{S} \tag{13.3.1}$$

where $\Delta\boldsymbol{\sigma}$ and $\Delta\boldsymbol{\varepsilon}$ are the increments of the stress and strain tensors, $\boldsymbol{E}$ is the fourth-rank tensor of elastic moduli of uncracked material, $\Delta\boldsymbol{\varepsilon}''$ the inelastic strain increment tensor, and $\Delta\mathbf{S}$ the inelastic stress increment tensor.

In a nonlocal continuum formulation, this equation is replaced by

$$\Delta\boldsymbol{\sigma} = \boldsymbol{E}\Delta\boldsymbol{\varepsilon} - \Delta\tilde{\mathbf{S}} \tag{13.3.2}$$

where $\Delta\tilde{\mathbf{S}}$ is the nonlocal inelastic stress increment tensor. In the phenomenological approach discussed in the previous sections, this tensor is directly obtained by a spatial averaging integral

$$\Delta\tilde{\mathbf{S}}(\mathbf{x}) = \Delta\overline{\mathbf{S}} = \int_V \hat{\alpha}(\mathbf{x},\boldsymbol{\xi})\Delta\mathbf{S}(\boldsymbol{\xi})\, dV(\boldsymbol{\xi}) \tag{13.3.3}$$

completely analogous to (13.1.1), in which we remember that the weight function α is to be postulated. Following Bažant (1994b), we now describe how the equation governing the evolution of $\Delta\tilde{\mathbf{S}}$ can be developed from the mechanics of crack interactions.

Consider an elastic solid that contains, at the beginning of the load step, many microcracks numbered as $\mu = 1, \ldots N$ (Fig. 13.3.1). On the macroscale, the microcracks are considered to be smeared, as required by a continuum model. Exploiting the principle of superposition, we may decompose the loading step of prescribed load or displacement increment into two substeps:

I In the first substep, the cracks (already opened) are imagined temporarily "frozen" (or "filled with a glue"), that is, they can neither grow and open wider nor close and shorten. Also, no new cracks can nucleate. The stress increments, caused by strain increments $\Delta\boldsymbol{\varepsilon}$ and transmitted across the temporarily frozen (or glued) cracks (I in Fig. 13.3.1), are then simply given by $\boldsymbol{E}\Delta\boldsymbol{\varepsilon}$. This is represented by the line segment $\overline{13}$ (Fig. 13.3.2) having the slope of the initial elastic modulus E.

II In the second substep, the prescribed boundary displacements and loads are held constant, the cracks are "unfrozen" (or "unglued"), and the stresses transmitted across the cracks are relaxed. This is equivalent to applying pressures (surface tractions) on the crack faces (II in Fig. 13.3.1). In

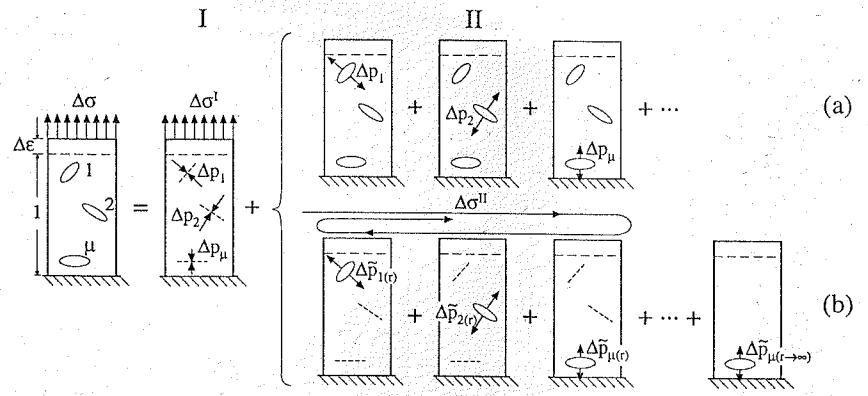

Figure 13.3.1 Superposition method for solid with many cracks. In part I, the cracks are closed and $\Delta\sigma^{\mathrm{I}} = E\Delta\varepsilon$. In part II, the stresses Δp_i on the crack faces generated in part I are released, either simultaneously (alternative **a**) or iteratively keeping all the cracks closed but one (alternative **b**); adapted from Bažant 1994b.

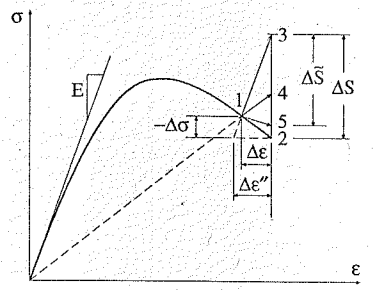

Figure 13.3.2 Local and nonlocal inelastic stress increments during loading step (adapted from Bažant 1994b).

response to these pressures, the cracks are now allowed to open wider and grow (remaining critical according to the crack propagation criterion), or to close and shorten. Also, new cracks are now allowed to nucleate.

If cracks neither grew nor closed (nor new cracks nucleated), the unfreezing (or unglueing) at prescribed increments of loads or boundary displacements that cause macro-strain increment $\Delta\varepsilon$ would engender the stress drop $\overline{34}$ down to point 4 on the secant line $\overline{01}$ (Fig. 13.3.2). The change of state of the solid would then be calculated by applying the opposite of this stress drop onto the crack surfaces. However, when the cracks propagate (and new cracks nucleate), a larger stress drop defined by the local strain-softening constitutive law and represented by the segment $\Delta\mathrm{S} = \overline{32}$ in Fig. 13.3.2 takes place. Thus, the normal surface tractions

$$\Delta p_\mu = \mathbf{n}_\mu \cdot \Delta\mathbf{S}_\mu \mathbf{n}_\mu \tag{13.3.4}$$

representing the normal component of tensor $\Delta\mathbf{S}_\mu$, must be considered in the second substep as loads Δp_μ that are applied onto the crack surfaces (Fig. 13.3.1), the unit normals of which are denoted as $\mathbf{n}_\mu$. (Note that for mode II or III cracks, a similar equation could, in general, be written for the tangential tractions on the crack faces.)

Let us now introduce two simplifying hypotheses:

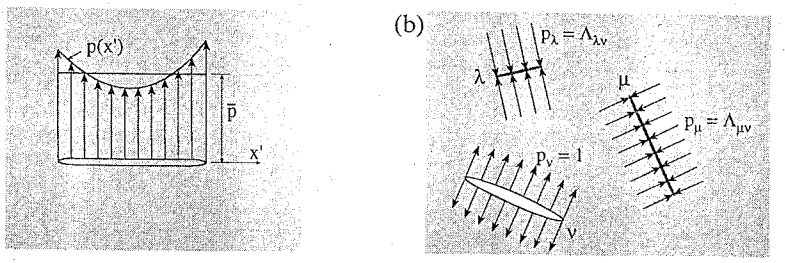

Figure 13.3.3 Details of crack interactions: (a) Actual crack pressure distribution and mean pressure; (b) mean pressure distributions generated at cracks number λ and μ by a unit uniform pressure at crack ν, all other cracks being frozen. (Adapted from Bažant 1994b.)

1. Although the stress transmitted across each temporarily frozen crack varies along the crack, we consider only its average, i.e., Δp_μ is constant along each crack (Fig. 13.3.3a). This approximation, which is crucial for our formulation, was introduced by Kachanov (1985, 1987a). He discovered by numerical calculations that the error is negligible except for the rare case when the distance between two crack tips is at least an order of magnitude less than their size.
2. We consider only mode I crack openings, i.e., neglect the shear modes (modes II and III). This is often justified, for instance in materials such as concrete, by a high surface roughness which prevents any significant relative slip of the microcrack faces (the mode II or III relative displacements that can occur on a macroscopic crack are mainly the result of Mode I openings of microcracks that are inclined with respect to the macrocrack).

A simple-minded kind of superposition method would be to unfreeze all the cracks, load by pressure only one crack at a time, and then superpose all the cases (Fig. 13.3.1a). In this approach, the pressure on each crack, Δp_μ, would be known. But one would still have to solve a body with many cracks.

A better kind of superposition method is that adopted by Kachanov (1985, 1987a, which was also used by Datsyshin and Savruk (1973), Chudnovsky and Kachanov (1983), Chudnovsky, Dolgopolski and Kachanov (1987), and Horii and Nemat-Nasser (1985), and, in a displacement version, was introduced by Collins (1963). In this kind of superposition, all that is needed is the solution of the given body for the case of only *one* crack, with all the other cracks considered frozen (Fig. 13.3.1b). The cost to pay for this advantage is that the pressures to be applied at the cracks are unknown in advance and must be solved. By virtue of Kachanov's approximation, we apply this kind of superposition only to the average crack pressures. The opening and the stress intensity factor of crack μ are approximately characterized by the *uniform* crack pressure $\Delta\tilde{p}_\mu$ that acts on a *single* crack within the given solid that has elastic moduli $\boldsymbol{E}$ and contains no other crack. This pressure is solved from the superposition relation:

$$\Delta\tilde{p}_\mu = \overline{\Delta p_\mu} + \sum_{\nu=1}^{N} \Lambda_{\mu\nu}\Delta\tilde{p}_\nu \qquad \mu = 1, \ldots N \tag{13.3.5}$$

where the superimposed bar indicates averaging over the crack length; $\Lambda_{\mu\nu}$ are the crack influence coefficients representing the average pressure (Fig. 13.3.3b) at the frozen crack μ caused by a unit uniform pressure applied on unfrozen crack ν, with all the other cracks being frozen (Fig. 13.3.1b); and $\Lambda_{\mu\mu} = 0$ because the summation in (13.3.5) must skip $\nu = \mu$. The reason for the notation for $\Delta\tilde{p}_\mu$ with a tilde instead of an overbar is that the unknown crack pressure is uniform by definition and thus its distribution over the crack area never needs to be calculated and no averaging of pressure actually needs to be carried out.

Note that the exact solution requires considering pressures $\Delta p_\mu(x')$ and $\Delta\tilde{p}_\mu(x')$ that vary with coordinate x' along each crack. In numerical analysis, the crack must then be subdivided into many intervals. This could hardly be reflected on the macroscopic continuum level, but is doubtless unimportant at that level.

Substituting (13.3.4) into (13.3.5), we obtain

$$\Delta(\mathbf{n}_\mu \cdot \tilde{\mathbf{S}}_\mu \mathbf{n}_\mu) = \overline{\Delta(\mathbf{n}_\mu \cdot \mathbf{S}_\mu \mathbf{n}_\mu)} + \sum_{\nu=1}^{N} \Lambda_{\mu\nu} \Delta(\mathbf{n}_\nu \cdot \tilde{\mathbf{S}}_\nu \mathbf{n}_\nu) \tag{13.3.6}$$

Now we adopt a third simplifying hypothesis. In each loading step, the influence of the microcracks at macro-continuum point of coordinate vector $\boldsymbol{\xi}$ upon the microcracks at macro-continuum point of coordinate vector $\mathbf{x}$ is determined only by the dominant microcrack orientation. This orientation is normal to the unit vector $\mathbf{n}_\mu$ of the maximum principal inelastic macro-stress tensor $\Delta\tilde{S}^{(1)}$ at the location of the center of microcrack μ. We use the definition:

$$\Delta\tilde{S}_\mu^{(1)} = \Delta(\mathbf{n}_\mu \cdot \tilde{\mathbf{S}}_\mu \mathbf{n}_\mu) = [\mathbf{n}_\mu \cdot \tilde{\mathbf{S}}_\mu \mathbf{n}_\mu]_{\text{new}} - [\mathbf{n}_\mu \cdot \tilde{\mathbf{S}}_\mu \mathbf{n}_\mu]_{\text{old}} \tag{13.3.7}$$

The subscripts 'new' and 'old' denote the values at the beginning and end of the loading step, respectively. According to this hypothesis, the dominant crack orientation generally rotates from one loading step to the next. Eq. (13.3.6) may now be written as:

$$\Delta\tilde{S}_\mu^{(1)} - \sum_{\nu=1}^{N} \Lambda_{\mu\nu} \Delta\tilde{S}_\nu^{(1)} = \overline{\Delta S_\mu^{(1)}} \tag{13.3.8}$$

The values of $\Delta\tilde{\mathbf{S}}_\mu$ are graphically represented in Fig. 13.3.2 by the segment $\Delta\tilde{S} = \overline{35}$. This segment can be smaller or larger than segment $\overline{32}$.

Alternatively, one might assume $\mathbf{n}_\mu$ to approximately coincide with the direction of the maximum principal strain. Such an approximation is simpler to use in finite element programs, and it might be realistic enough, especially when the elastic strains are relatively small.

When the principal directions of the inelastic stress tensor $\mathbf{S}$ do not rotate, the increment operators Δ can of course be moved inside each product in (13.3.6), i.e., $\Delta(\mathbf{n}_\mu \cdot \tilde{\mathbf{S}}_\mu \mathbf{n}_\mu) = \mathbf{n}_\mu \cdot \Delta\tilde{\mathbf{S}}_\mu \mathbf{n}_\mu$, etc. One might wonder whether this should not be done even when these directions rotate (i.e., when $\mathbf{n}_\mu$ varies), which would correspond to crack orientations being fixed when the cracks begin to form. But according to the experience with the so-called rotating crack model, empirically verified for concrete, it is more realistic to assume that the orientation of the dominant cracks rotates with the principal direction of $\mathbf{S}$.

It might seem in the foregoing equations we should have taken only the positive part of tensor $\Delta\mathbf{S}_\mu$. But this is not necessary since the unloading criterion prevents $\Delta\mathbf{S}_\mu$ from being negative.

13.3.2 Field Equation for Nonlocal Continuum

Now comes the most difficult step. We need to determine the nonlocal macroscopic field equation which represents the continuum counterpart of (13.3.8). The homogenization theories as known are inapplicable, because they apply only to macroscopically uniform fields while the nonuniformity of the macroscopic field is the most important aspect for handling localization problems. The following simple concept has been proposed (Bažant 1994b):

The continuum field equation we seek is the equation whose discrete approximation can be written in the form of the matrix crack interaction relation (13.3.8).

This concept leads to the following field equation for the continuum approximation of microcrack interactions (Bažant 1994b):

$$\Delta\tilde{S}^{(1)}(\mathbf{x}) - \int_V \Lambda(\mathbf{x}, \boldsymbol{\xi}) \Delta\tilde{S}^{(1)}(\boldsymbol{\xi}) dV(\boldsymbol{\xi}) = \overline{\Delta S^{(1)}(\mathbf{x})} \tag{13.3.9}$$

Indeed, an approximation of the integral by a sum over the continuum variable values at the crack centers yields (13.3.8). Here we denote $\Lambda(\mathbf{x}_\mu, \boldsymbol{\xi}_\nu) = \mathcal{E}(\Lambda_{\mu\nu})/V_c$ = crack influence function, V_c is a constant that may be interpreted roughly as the material volume per crack, and $\mathcal{E}$ is a statistical averaging operator which yields the average (moving average) over a certain appropriate neighborhood of point $\mathbf{x}$ or $\boldsymbol{\xi}$. Such statistical averaging is implied in the macro-continuum smoothing and is inevitable because, in a random crack array, the characteristics of the individual cracks must be expected to exhibit enormous random scatter.

It must be admitted that the sum in (13.3.8) is an unorthodox approximation of the integral from (13.3.9) because the values of the continuum variable are not sampled at certain predetermined points such as the chosen mesh nodes but are distributed at random, that is, at the microcrack centers. Another point to note is that (13.3.8) is only one of various possible discrete approximations of (13.3.9). Since this approximation is not unique, the uniqueness of (13.3.9) as a continuum approximation is not proven. Therefore, acceptability of (13.3.9) will also depend on computational experience (which has so far been favorable; see Ožbolt and Bažant 1996).

When (13.3.9) is approximated by finite elements, it is again converted to a matrix form similar to (13.3.8). However, the subscripts for the sum then runs over the integration points of the finite elements. This means the crack pressures (or openings) that are translated into the inelastic stress increments are only sampled at these integration points, in the sense of their density, instead of being represented individually as in (13.3.8). Obviously, such a sampling can preserve only the long-range interactions of the cracks and the averaging. The individual short-range crack interactions will be lost, but they are so random and vast in number that aspiring to represent them in any detail would be futile.

For macroscopic continuum smearing, the averaging operator $\overline{\cdots}$ over the crack length now needs reinterpretation. Because of the randomness of the microcrack distribution, the macro-continuum variable at point $\mathbf{x}$ should represent the spatial average of the effects of all the possible microcrack realizations within a neighborhood of point $\mathbf{x}$ whose size is roughly equal to the spacing ℓ of the dominant microcracks (which is, in concrete, approximately determined by the spacing of the largest aggregates, which is in turn proportional to the maximum aggregate size); hence,

$$\overline{\Delta S^{(1)}(\mathbf{x})} = \int_V \Delta S^{(1)}(\boldsymbol{\xi}) \alpha(\mathbf{x}, \boldsymbol{\xi}) dV(\boldsymbol{\xi}) \tag{13.3.10}$$

The weight function $\alpha(\mathbf{x}, \boldsymbol{\xi})$ is analogous to that in Eq. (13.1.1). It should vanish everywhere outside the domain of a diameter roughly equal to ℓ. For computational reasons, it seems preferable that α have a smooth bell shape. Because of randomness of the microcrack distribution, function $\alpha(\mathbf{x}, \boldsymbol{\xi})$ may be considered as rotationally symmetric (i.e., same in all directions, or isotropic).

Strictly speaking, the macroscopic averaging domain could be a line segment in the direction of the dominant microcrack (that is, normal to $\Delta S^{(1)}(\mathbf{x})$), or an elongated, roughly elliptical domain. However, averaging only along a line segment seems insufficient for preventing damage from localizing into a line, in the case of a homogeneous uniaxial tension field, and it would also be at variance with the energy release argument for nonlocality of damage presented in Bažant (1987c, 1991b).

Equation (13.3.9) represents a Fredholm integral equation (i.e., an integral equation of the second kind with a square-integrable kernel) for the unknown $\Delta\tilde{S}^{(1)}(\mathbf{x})$, which corresponds in Fig. 13.3.2 to the segment $\overline{35}$. The inelastic strain increment tensors $\Delta S^{(1)}(\mathbf{x})$ on the right-hand side, which correspond in Fig. 13.3.2 to the segment $\overline{32}$, are calculated from the strain increments using the given local constitutive law (for example, the microplane model, continuum damage theory, plastic-fracturing theory, or plasticity with yield limit degradation).

13.3.3 Some Alternative Forms and Properties of the Nonlocal Model

The solution of (13.3.9) can be written as:

$$\Delta\tilde{S}^{(1)}(\mathbf{x}) = \overline{\Delta S^{(1)}(\mathbf{x})} - \int_V K(\mathbf{x}, \boldsymbol{\xi}) \overline{\Delta S^{(1)}(\boldsymbol{\xi})} dV(\boldsymbol{\xi}) \tag{13.3.11}$$

in which function $K(\mathbf{x}, \boldsymbol{\xi})$ is the resolvent of the kernel $\Lambda(\mathbf{x}, \boldsymbol{\xi})$. (This resolvent could be calculated numerically in advance of the nonlocal finite element analysis, but it would not allow a simple physical interpretation and a closed-form expression.) With the notation

$$\Psi_{\mu\nu} = \delta_{\mu\nu} - \Lambda_{\mu\nu} \tag{13.3.12}$$

where $\delta_{\mu\nu}$ = Kronecker delta, Eq. (13.3.8) can be transformed to

$$\sum_\nu \Psi_{\mu\nu} \Delta\tilde{S}_\nu^{(1)} = \overline{\Delta S_\mu^{(1)}} \tag{13.3.13}$$

The macro-continuum counterpart of this discrete matrix relation is

$$\int_V \Psi(\mathbf{x},\boldsymbol{\xi})\Delta\tilde{S}^{(1)}(\boldsymbol{\xi})dV(\boldsymbol{\xi}) = \overline{\Delta S^{(1)}(\mathbf{x})} = \int_V \Delta S^{(1)}(\boldsymbol{\xi})\alpha(\mathbf{x},\boldsymbol{\xi})dV(\boldsymbol{\xi}) \tag{13.3.14}$$

which represents an integral equation of the first kind for the unknown function $\Delta\tilde{S}^{(1)}(\boldsymbol{\xi})$. Obviously,

$$\Psi(\mathbf{x},\boldsymbol{\xi}) = \delta(\mathbf{x}-\boldsymbol{\xi}) - \Lambda(\mathbf{x},\boldsymbol{\xi}) \tag{13.3.15}$$

where $\delta(\mathbf{x}-\boldsymbol{\xi})$ = Dirac delta function in two or three dimensions; indeed, substitution of this expression into Eq. (13.3.14) yields Eq. (13.3.9).

Defining the inverse square matrix:

$$[B_{\mu\nu}] = [\Psi_{\mu\nu}]^{-1} \tag{13.3.16}$$

we may write the solution of the equation system (13.3.13) as

$$\Delta\tilde{S}^{(1)}_\mu = \sum_\nu B_{\mu\nu}\overline{\Delta S^{(1)}_\nu} = \sum_\lambda C_{\mu\lambda}\Delta S^{(1)}_\lambda, \quad C_{\mu\lambda} = \sum_\nu B_{\mu\nu}\alpha_{\nu\lambda}. \tag{13.3.17}$$

with $\alpha_{\nu\lambda} = \alpha(\mathbf{x}_\nu, \boldsymbol{\xi}_\lambda)$. The macro-continuum counterpart of the last equation is

$$\Delta\tilde{S}^{(1)}(\mathbf{x}) = \int_V B(\mathbf{x},\boldsymbol{\xi})\overline{\Delta S^{(1)}(\boldsymbol{\xi})}dV(\boldsymbol{\xi}) = \int_V C(\mathbf{x},\boldsymbol{\xi})\Delta S^{(1)}(\boldsymbol{\xi})dV(\boldsymbol{\xi}) \tag{13.3.18}$$

where $B(\mathbf{x}_\mu, \boldsymbol{\xi}_\nu) = \mathcal{E}(B_{\mu\nu})/V_c$ and $C(\mathbf{x},\boldsymbol{\xi}) = \int_V B(\mathbf{x},\boldsymbol{\xi})\alpha(\boldsymbol{\xi},\mathbf{x})dV(\boldsymbol{\xi})$. The kernel $B(\mathbf{x},\boldsymbol{\xi})$ represents the resolvent of the kernel $\Psi(\mathbf{x},\boldsymbol{\xi})$ of (13.3.14). Furthermore,

$$B(\mathbf{x},\boldsymbol{\xi}) = \delta(\mathbf{x}-\boldsymbol{\xi}) - K(\mathbf{x},\boldsymbol{\xi}) \tag{13.3.19}$$

because substitution of this equation into Eq. (13.3.18) furnishes Eq. (13.3.11). With (13.3.18) we have reduced the nonlocal formulation to a similar form as (13.3.3) for the previous nonlocal damage formulations (Pijaudier-Cabot and Bažant 1987; Bažant and Pijaudier-Cabot 1989; Bažant and Ožbolt 1990, 1992). However, the presence of the Dirac delta function in the last equation makes Eq. (13.3.18) inconvenient for computations. Aside from that, it seems inconvenient to calculate in finite element codes function $B(\mathbf{x},\boldsymbol{\xi})$. Another difference is that the weight function (i.e., the kernel) is anisotropic (and, in the present simplification, associated solely with the principal inelastic stresses).

Note also that if we set $\Lambda(\mathbf{x},\boldsymbol{\xi}) = 0$, the present model would become identical to the aforementioned previous nonlocal damage model. But this would not be realistic. The directional and tensorial interactions characterized by $\Lambda(\mathbf{x},\boldsymbol{\xi})$ appear to be essential.

Because the nonlocal integral in (13.3.21) is additive to the local stress $\Delta\mathbf{S}$, the present nonlocal model can be imagined as an overlay of two solids that are forced to have equal displacements at all points: (i) the given solid with all the damage due to cracks, but local behavior (no crack interactions); and (ii) an overlaid solid that describes only crack interactions. The nonlocal stress $\Delta\tilde{\mathbf{S}}$ represents the sum of the stresses from both solids. This is the stress that is to be used in formulating the differential equilibrium equations for the solid.

For the sake of simplicity, we have so far assumed that the influence of point $\boldsymbol{\xi}$ on point $\mathbf{x}$ depends only on the orientation of the maximum principal inelastic stress at $\boldsymbol{\xi}$. Since at $\boldsymbol{\xi}$ there might be cracks normal to all the three principal stresses (denoted now by superscripts $i = 1,2,3$ in parentheses), it might be more realistic to consider that each of them separately influences point $\mathbf{x}$. In that case, Eqs. (13.3.8) and (13.3.9) can be generalized as follows:

$$\Delta\tilde{S}^{(i)}_\mu - \sum_{\nu=1}^{N}\sum_{j=1}^{3}\Lambda^{(ij)}_{\mu\nu}\Delta\tilde{S}^{(j)}_\nu = \overline{\Delta S^{(i)}_\mu} \tag{13.3.20}$$

$$\Delta\tilde{S}^{(i)}(\mathbf{x}) - \int_V \sum_{j=1}^{3}\Lambda^{(ij)}(\mathbf{x},\boldsymbol{\xi})\Delta\tilde{S}^{(j)}(\boldsymbol{\xi})dV(\boldsymbol{\xi}) = \overline{\Delta S^{(i)}(\mathbf{x})} \qquad (i = 1,2,3) \tag{13.3.21}$$

Similar generalizations can be made in the subsequent equations, too. Note that when the body is infinite, all the present summations or integrations are assumed to follow a special path labeled by $\odot$, which will be defined in the next section.

The heterogeneity of the material, such as the aggregate in concrete, is not specifically taken into account in our equations. Although the heterogeneity obviously must influence the nonlocal properties (e.g., Pijaudier-Cabot and Bažant 1991), this influence is probably secondary to that of microcracking. The reason is that the prepeak (hardening) inelastic behavior, in which microcracking is much less pronounced than after the peak while the heterogeneity is the same, can be adequately described by a local continuum. The main effect of heterogeneity (such as the aggregates in concrete, or grains in ceramics) is indirect; it determines the spacing, orientations, and configurations of the microcracks.

13.3.4 Admissibility of Uniform Inelastic Stress Fields

In the previous nonlocal formulations, the requirement that a field of uniform inelastic stress and damage must represent at least one possible solution led to the aforementioned normalizing condition for the weight function α. Similarly, we must now require that the homogeneous stress field $\Delta\tilde{S}^{(1)} = \overline{\Delta S^{(1)}}$ satisfy (13.3.8) and (13.3.9) identically. This yields the conditions that the integral of $\Lambda(\mathbf{x},\boldsymbol{\xi})$ or the sum of $\Lambda_{\mu\nu}$ over an infinite body vanish. However, the asymptotic behavior of $\Lambda(\mathbf{x},\boldsymbol{\xi})$ for $r \to \infty$ which will be discussed later causes this integral or sum to be divergent. Therefore, the conditions must be imposed in a special form—the integral in polar coordinates is required to vanish only for a special path, labeled by $\odot$, in which the angular integration is completed before the limit $r \to \infty$ is calculated, that is,

$$\int_V^{\odot}\Lambda(\mathbf{x},\boldsymbol{\xi})dV(\boldsymbol{\xi}) = \lim_{R\to\infty}\int_0^R\left(\int_0^{2\pi}\Lambda(\mathbf{x},\boldsymbol{\xi})r\,d\phi\right)dr = 0 \text{ (for 2D)}$$

$$\int_V^{\odot}\Lambda(\mathbf{x},\boldsymbol{\xi})dV(\boldsymbol{\xi}) = \lim_{R\to\infty}\int_0^R\left(\int_0^{2\pi}\int_0^{\pi}\Lambda(\mathbf{x},\boldsymbol{\xi})r^2\sin\theta\,d\theta\,d\phi\right)dr = 0 \text{ (for 3D)} \tag{13.3.22}$$

r, ϕ are polar coordinates; r, θ, ϕ are spherical coordinates. Furthermore, again labeling by $\odot$ a similar summation path (or sequence) over all the cracks ν in an infinite body, the following discrete condition needs to also be imposed:

$$\sum_\nu^{\odot}\Lambda_{\mu\nu} = 0 \tag{13.3.23}$$

This condition applies only to an array of infinitely many microcracks that are, on the macroscale, perfectly random and distributed statistically uniformly over an infinite body (or are periodic). By the same reasoning, for an infinite body we must also have

$$\int_V^{\odot}K(\mathbf{x},\boldsymbol{\xi})dV(\boldsymbol{\xi}) = 0 \tag{13.3.24}$$

$$\int_V^{\odot}\Psi(\mathbf{x},\boldsymbol{\xi})dV(\boldsymbol{\xi}) = \int_V^{\odot}B(\mathbf{x},\boldsymbol{\xi})dV(\boldsymbol{\xi}) = \int_V^{\odot}C(\mathbf{x},\boldsymbol{\xi})dV(\boldsymbol{\xi}) = 1; \tag{13.3.25}$$

and in the discrete form

$$\sum_\nu^{\odot}\Psi_{\mu\nu} = \sum_\nu^{\odot}\alpha_{\mu\nu} = \sum_\nu^{\odot}B_{\mu\nu} = \sum_\nu^{\odot}C_{\mu\nu} = 1 \tag{13.3.26}$$

For integration paths in which the radial integration up to $r \to \infty$ is carried out before the angular integration, the foregoing integrals and sums are divergent.

13.3.5 Gauss-Seidel Iteration Applied to Nonlocal Averaging

For the purpose of finite element analysis, we will now assume that subscripts μ and ν label the numerical integration points of finite elements, rather than the individual microcracks. This means that the microcracks are represented by their mean statistical characteristics sampled only at the numerical integration points.

In finite element programs, nonlinearity is typically handled by iterations of the loading steps. Let us, therefore, examine the iterative solution of (13.3.8) or (13.3.13), which represents a system of N linear algebraic equations for N unknowns $\Delta\tilde{S}_\mu^{(1)}$ if $\Delta S_\mu^{(1)}$ are given. The matrix of $\Psi_{\mu\nu}$ is, in general, nonsymmetric (because the influence of a large crack on a small crack is not the same as the influence of a small crack on a large crack). This nonsymmetry seems disturbing until one realizes that this is so only because of our choice of variables $\Delta\tilde{S}_\nu^{(1)}$ and $\overline{\Delta S_\mu^{(1)}}$, which do not represent thermodynamically conjugate pairs of generalized forces and generalized displacements. If $\overline{\Delta S_\mu^{(1)}}$ were expressed in terms of the crack opening volumes, then the matrix of the equation system resulting from (13.3.8) or (13.3.13) would have to be symmetric (because of Betti's theorem) and also positive definite (if the body is stable). These are the attributes mathematically required for convergence of the iterative solution by Gauss-Seidel method (e.g., Rektorys 1969; Collatz 1960; Korn and Korn 1968; Varga 1962; Fox 1965; Strang 1980). Aside from that, convergence of the iterative solution of (13.3.8) or (13.3.13) must also be expected on physical grounds (because it is mechanically equivalent to the relaxation method, which always converges for stable elastic systems).

In the r-th iteration, the new, improved values of the unknowns, labeled by superscripts $[r+1]$, are calculated from the previous values, labeled by superscript $[r]$, either according to the recursive relations:

$$\Delta\tilde{p}_\mu^{[r+1]} = \overline{\Delta p_\mu} + \sum_{\nu=1}^{N} \Lambda_{\mu\nu}\Delta\tilde{p}_\nu^{[r]} \tag{13.3.27}$$

$$\Delta\tilde{S}_\mu^{(1)[r+1]} = \overline{\Delta S_\mu^{(1)}} + \sum_{\nu=1}^{N} \Lambda_{\mu\nu}\Delta\tilde{S}_\nu^{(1)[r]} \qquad (\mu = 1, ..., N) \tag{13.3.28}$$

or according to the recursive relations:

$$\Delta\tilde{p}_\mu^{[r+1]} = \overline{\Delta p_\mu} + \sum_{\nu=1}^{\mu-1} \Lambda_{\mu\nu}\Delta\tilde{p}_\nu^{[r+1]} + \sum_{\nu=\mu+1}^{N} \Lambda_{\mu\nu}\Delta\tilde{p}_\nu^{[r]} \qquad (\mu = 1, ..., N) \tag{13.3.29}$$

$$\Delta\tilde{S}_\mu^{(1)[r+1]} = \overline{\Delta S_\mu^{(1)}} + \sum_{\nu=1}^{\mu-1} \Lambda_{\mu\nu}\Delta\tilde{S}_\nu^{(1)[r+1]} + \sum_{\nu=\mu+1}^{N} \Lambda_{\mu\nu}\Delta\tilde{S}_\nu^{(1)[r]} \quad (\mu = 1, ..., N) \tag{13.3.30}$$

Equation (13.3.28), also known as the Gauss method or Jacobi method, is less, but normally only slightly less efficient than (13.3.30), in which the latest approximations are always used. The values of $\Delta S_\mu^{(1)}$ may be used as the initial values of $\Delta\tilde{S}_\mu^{(1)[r]}$ in the first iteration.

It is possible to derive Eqs. (13.3.27) and (13.3.28) more directly, rather than from (13.3.5). To this end, we note that the sequence of iterations is identical to a solution by the relaxation method in which one crack after another is relaxed (i.e., its pressure reduced to zero) while all the other cracks are frozen (so in each relaxation step, one has a problem with one crack only), as illustrated in Fig. 13.3.1b. Each relaxation produces pressure on the previously relaxed cracks. After relaxing all the cracks one by one, the cycle through all the cracks is repeated again and again. This kind of relaxation is known in mechanics to converge in general (this was numerically demonstrated for a system of cracks and inclusions by Pijaudier-Cabot and Bažant 1991). The solution to which the relaxation process converges is obviously that defined by Eq. (13.3.8). (Note also that this relaxation argument in fact represents a simple way to prove the superposition equation (13.3.5).)

For structural engineers, it is interesting to note the similarity with the Cross method (moment distribution method) for elastic frames. Relaxing the pressure at one crack while all the other microcracks are frozen (glued) is analogous to relaxing one joint in a frame while all the other joints are held fixed.

Repeating this for each joint, and then repeating the cycles of such relaxations of all the joints, eventually converges to the exact solution of the frame.

The macro-continuum counterpart of the Gauss-Seidel iterative method, which converges to the solution of the Fredholm integral equation (13.3.9), is analogous to (13.3.28) and is given by the following relation for successive approximations (iterations):

$$\Delta\tilde{S}^{(1)[r+1]}(\mathbf{x}) = \overline{\Delta S^{(1)}(\mathbf{x})} + \int_V \Lambda(\mathbf{x}, \boldsymbol{\xi})\Delta\tilde{S}^{(1)[r]}(\boldsymbol{\xi})\, dV(\boldsymbol{\xi}) \tag{13.3.31}$$

The discrete approximation of the last relation is the equation that ought to be used in finite element programs with iterations in each step. We see that the form of averaging is different from that assumed in the phenomenological models we described. There are now two additive spatial integrals: one for close-range averaging of the inelastic stresses from the local constitutive relation, and one for long-range crack interactions based on the latest iterates of the inelastic stresses.

In programming, the old iterates need not be stored in the computer memory. So the superscripts $[r]$ and $[r+1]$ may be dropped and equations (13.3.9) and (13.3.31) may be replaced by the following assignment statements:

$$\Delta\tilde{S}_\mu^{(1)} \leftarrow \overline{\Delta S_\mu^{(1)}} + \sum_{\nu=1}^{N} \Lambda_{\mu\nu}\Delta\tilde{S}_\nu^{(1)} \qquad (\mu = 1, 2, ...N) \tag{13.3.32}$$

$$\Delta\tilde{S}^{(1)}(\mathbf{x}) \leftarrow \overline{\Delta S^{(1)}(\mathbf{x})} + \int_V \Lambda(\mathbf{x}, \boldsymbol{\xi})\Delta\tilde{S}^{(1)}(\boldsymbol{\xi})\, dV(\boldsymbol{\xi}) \tag{13.3.33}$$

A strict implementation of Gauss-Seidel iterations suggests programming each iteration loop for Eq. (13.3.32) to be contained within another loop for the iterations of the loading step in which the displacement and strain increments in the structure are solved. However, it is computationally more efficient to use one common iteration loop serving both purposes. Then, of course, the iteration solution is not exactly the Gauss-Seidel method because the strains are also being updated during each iteration. There is already some computational experience (Ožbolt and Bažant 1996) showing that convergence is still achieved.

The common iteration loop has the advantage that it permits using the explicit load-step algorithm for structural analysis. In each loading step of this algorithm, one evaluates in each iteration at each integration point the elastic stress increments $\boldsymbol{E}\Delta\boldsymbol{\varepsilon}$ and the local inelastic stress increments $\Delta\mathbf{S}$ from fixed strains $\Delta\boldsymbol{\varepsilon}$; then one uses (13.3.32) to calculate from $\Delta\mathbf{S}$ the nonlocal inelastic stress increments $\Delta\tilde{\mathbf{S}}$ for all the integration points, solves new nodal displacements by elastic structural analysis, and, finally, updates the strains.

13.3.6 Statistical Determination of Crack Influence Function

The basic characteristic of the new formulation is the crack influence function Λ, whose rate of decay is determined by a certain characteristic length ℓ. This function represents the stress field due to pressurizing a single crack in the given elastic structure, all other cracks being absent. In practice, the structure is always finite, and thus the values of $\Lambda_{\mu\nu}$ should, in principle, be calculated taking into account the geometry of the structure. However, the crack is often very small compared to the dimensions of the structure. Then the present formulation has the advantage that one can use, as a very good approximation, the stress field for a single crack in an infinite body, which is well known and calculated easily. This is, of course, not possible for cracks very near the boundary of the structure.

The cracks in structures are distributed randomly and their number is vast. Thus, on the macro-continuum level, function $\Lambda_{\mu\nu}$ cannot characterize the stress fields of the individual cracks. Rather, it should characterize the stress field of a representative crack obtained by a suitable statistical averaging of the random situation on the microstructure level.

A method of rigorous mathematical formulation of the macroscopic continuum crack influence function Λ was briefly proposed in the addendum to Bažant (1994b) and was developed in detail in Bažant and Jirásek (1994a). This method will now be described.

The crack that is pressurized by unit pressure, as specified in the definition of Λ, will be called the source crack, and the frozen crack in the structure on which the influence is to be found will be called

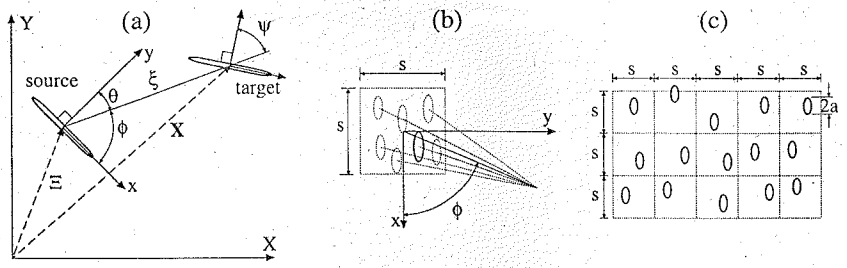

Figure 13.3.4 Definition of relative crack locations: (a) general position of the source crack and target crack; (b) various possible random locations of the source crack influencing a target crack; (c) dominant cracks appearing in regions of size s that determine their typical spacing. (Adapted from Bažant and Jirásek 1994a.)

the target crack (Fig. 13.3.4a). For the purpose of calculations, the target crack is, of course, closed and glued, as if it did not exist, and the stresses transmitted across the target crack are calculated assuming the body to be continuous. In the following, the global axes will be denoted with capital letters and the position vectors of the target and source cracks by $\mathbf{X}$ and Ξ (Fig. 13.3.4a). We take axes (x, y) to be, respectively, parallel and perpendicular to the source crack with origin at its center, and call $\boldsymbol{\xi}$ the vector from the source to the target crack (Fig. 13.3.4a). Then function $\Lambda(\mathbf{0}, \boldsymbol{\xi})$ represents the influence of a source crack centered at $\mathbf{x} = \mathbf{0}$ on a target crack centered at $\boldsymbol{\xi}$ (Fig. 13.3.4a).

At the given macro-continuum point, there may or may not be a crack in the microstructure. Function Λ corresponding to that point must reflect the smeared statistical properties of all the possible microcracks occurring near that point. To do this, we must idealize the random crack arrangements in some suitable manner.

We will suppose that the center of the source crack can occur randomly anywhere within a square of size s centered at point $\mathbf{x} = \mathbf{0}$; see Fig. 13.3.4b,c, where various possible cracks are shown by the dashed curves, but only one of these, the crack showed by the solid lines, is actually realized. The value of s is imagined to represent the typical spacing of the dominant cracks. In a material such as concrete, approximately $s \approx m d_a$ where d_a = spacing of the largest aggregate pieces and m = coefficient larger than 1 but close to 1 (m would equal d_a if the aggregates were arranged at the densest ideal packing and if there were no mortar layers within the contact zones).

To simplify the statistical structure of the system of dominant cracks, one may imagine the material to be subdivided by a square mesh of size s as shown in Fig. 13.3.4c, with one and only one crack center occurring within each square of the mesh. This is, of course, a simplification of reality because the underlying square mesh introduces a certain directional bias (as is well known from finite element analysis of fracture). It would be more realistic to assume that the possible zone of occurrence of the center of each crack is not a square but has a random shape and area about $s \times s$, and that all these areas are randomly arranged. But this would be too difficult for statistical purposes, and probably unimportant with respect to the other simplifications of the model.

Let us now center coordinates x and y in the center of the square $s \times s$, as shown in Fig. 13.3.4b, and consider the influence of a source crack within this square on a target crack at coordinates $\boldsymbol{\xi} \equiv (\xi, \eta)$. The macroscopic crack influence function should describe the influence of any possible source crack within the given square in the average, smeared macroscopic sense. Therefore, $\Lambda(\mathbf{0}, \boldsymbol{\xi})$ is defined as the mathematical expectation $\mathcal{E}$ with regard to all the possible random realizations of the source crack center within the given square $s \times s$, that is

$$\Lambda(0, \boldsymbol{\xi}) = \mathcal{E}\left[\sigma^{(1)}(\xi - x, \eta - y)\right] \tag{13.3.34}$$

The vector $(\xi - x, \eta - y) = \mathbf{r}$ = vector from the center $\mathbf{x} \equiv (x, y)$ of a source crack to the center

$\boldsymbol{\xi} \equiv (\xi, \eta)$ of the target crack. In detail,

$$\Lambda(0, \boldsymbol{\xi}) = \frac{1}{s^2} \int_{-s/2}^{s/2} \int_{-s/2}^{s/2} w(x, y) \sigma^{(1)}(\xi - x, \eta - y)\, dx dy \tag{13.3.35}$$

Here $\sigma^{(1)}$ is the field of the maximum principal stresses caused by applying a unit pressure on the faces of the source crack, and the integrals represent the statistical averaging over the square $s \times s$ (Fig. 13.3.4b). Certain specified weights $w(x, y)$ have been introduced for this averaging. At first, one might think that uniform weights w might be appropriate, but that would not be realistic near the boundaries of the square because a crack cannot intersect a crack centered in the adjacent square, and, in practice, cannot even lie too close. Rigorously, one would have to consider the joint probability of the occurrences of the crack center locations in the adjacent squares, but this would be too complicated. We prefer to simply reduce the probability of occurrence of the source crack as the boundary of the square is approached. For numerical computations we choose a bell-shaped function in both the x and y directions, given as

$$w(x, y) = w_0 \left[1 - \left(\frac{2x}{s}\right)^2\right]^2 \left[1 - \left(\frac{2y}{s}\right)^2\right]^2, \qquad w_0 = \frac{225}{64} \tag{13.3.36}$$

for $x \le s/2, y \le s/2$, and $w(x, y) = 0$ otherwise; constant w_0 is selected so the integral of $w(x, y)$ over the square $s \times s$ be equal to 1. It may be added that there is also a practical reason for introducing this weight function. If the weights were uniform over the square, function Λ would not have a smooth shape, which would be inconvenient and probably also unrealistic for a continuum model.

The stress field $\sigma^{(1)}$ to be substituted into (13.3.36) is given for two dimensions by the well-known Westergaard's solution (see Chapter 4). However, the integral in Eq. (13.3.35) is difficult to evaluate analytically, and it is better to use numerical integration to obtain Λ.

The asymptotic properties of function Λ for large r can nevertheless be determined easily (Bažant 1992b, 1994b) by considering the lines of influence from various possible source cracks to the given target crack as shown in Fig. 13.3.4b. If the target crack is very far from the square in which the source crack is centered, all the possible rays of influence are nearly equally long and come from nearly the same direction. Therefore, the integral in Eq. (13.3.35) should exactly preserve the long range asymptotic field $\sigma^{(1)}$.

13.3.7 Crack Influence Function in Two Dimensions

Consider now a crack in an infinite solid, subjected to uniform pressure σ (Fig. 13.3.3b). According to Westergaard's solution (Chapter 4) the stress distribution can be written as

$$\sigma_{xx} = \mathrm{Re} Z - y\, \mathrm{Im}\, Z' - \sigma, \qquad \sigma_{yy} = \mathrm{Re} Z + y\, \mathrm{Im}\, Z' - \sigma, \qquad \tau_{xy} = -y\, \mathrm{Re}\, Z' \tag{13.3.37}$$

in which σ_{xx} and σ_{yy} are the normal stresses, τ_{xy} is the shear stress, and

$$Z = \sigma z \left(z^2 - a^2\right)^{-1/2}; \qquad z = r\, \mathrm{e}^{\mathrm{i}\phi} \tag{13.3.38}$$

Here $2a$ = crack length, $\mathrm{i}^2 = -1$, $Z' = dZ/dz$, and r, ϕ = polar coordinates with origin at the crack center and angle ϕ measured from the crack direction x. For $r \gg a$ we have the approximation:

$$Z = \sigma \left(1 - \frac{a^2}{r^2\, \mathrm{e}^{2\mathrm{i}\phi}}\right)^{-1/2} = \sigma \left(1 + \frac{a^2}{2r^2}\, \mathrm{e}^{-2\mathrm{i}\phi} + \ldots\right) = \sigma \left(1 + \frac{a^2}{2z^2} + \ldots\right) \tag{13.3.39}$$

From this, we calculate

$$\mathrm{Re}\, Z = \sigma \left(1 + \frac{a^2}{2r^2} \cos 2\phi + \ldots\right), \qquad Z' = \sigma(-a^2 z^{-3} + \ldots)$$

$$y\, \mathrm{Im}\, Z' = \sigma a^2 r \sin\phi\ \mathrm{Im}\left(-r^{-3} \mathrm{e}^{-3\mathrm{i}\phi}\right) = -\sigma a^2 r^{-2} \sin\phi\,(-\sin 3\phi) \tag{13.3.40}$$

Substituting this into (13.3.37) and using the formulas for products of trigonometric functions, we get the following simple result for the long-range ($r \gg a$) asymptotic field (Bažant 1992b, 1994b):

$$\sigma_{xx} = \sigma k(r)\,\frac{\cos 4\phi}{2}, \qquad \sigma_{yy} = \sigma k(r)\left(\cos 2\phi - \frac{\cos 4\phi}{2}\right)$$
$$\tau_{xy} = \sigma k(r)\,\frac{\sin 4\phi - \sin 2\phi}{2} \tag{13.3.41}$$

where $k(r) = a^2/r^2$. Subscripts x, y refer to cartesian coordinates with origin at point ξ coinciding with the crack center and axis y normal to the crack; σ_{xx} and σ_{yy} are the normal stresses, τ_{xy} is the shear stress; and ϕ are polar coordinates with origin at the crack center, with the polar angle ϕ measured from axis x. The principal stresses $\sigma^{(1)}$ and $\sigma^{(2)}$ and the first principal stress direction $\phi^{(1)}$ are given by:

$$\sigma^{(1)} = \sigma k(r)\left(\frac{\cos 2\phi}{2} + \sin\phi\right), \qquad \sigma^{(2)} = \sigma k(r)\left(\frac{\cos 2\phi}{2} - \sin\phi\right) \tag{13.3.42}$$
$$\tan 2\phi^{(1)} = -\cot 3\phi$$

The foregoing expressions describe the long-range form of function $\Lambda(\mathbf{x}, \xi)$. It does not matter that they have a r^{-2} singularity at the crack center, because they are invalid for not too large r. Note that the average of each expression over the circle r = constant is zero, which is, in fact, a necessary property.

By virtue of considering only principal stress directions, $\Lambda(\mathbf{x}, \xi)$ is a scalar. All the information on the relative crack orientations is embedded in the values of this function. The principal stress direction at point ξ, which can be regarded as the dominant crack direction at that location (Fig. 13.3.4a), is all the directional information needed to calculate the stress components at point x; see (40), in which $r = \|\mathbf{x} - \xi\|$ = distance between points x and ξ. The value of $\Lambda(\mathbf{x}, \xi)$, needed for (13.3.31) or (9), may be determined as the projection of the stress tensor at point x onto the principal inelastic stress direction at that point. According to Mohr circle: $2\Lambda(\mathbf{x}, \xi) = (\sigma_{xx} + \sigma_{yy}) + (\sigma_{xx} - \sigma_{yy})\cos 2(\psi - \theta) - 2\tau_{xy}\sin 2(\psi - \theta)$ in which θ, ψ = angles of the principal inelastic stress directions at points ξ, x, respectively, with the line connecting these two points (i.e., with the vector $\mathbf{x} - \xi$). Substituting here for σ_{xx}, etc., the expressions from (13.3.41), one obtains a trigonometric expression which can be brought by trigonometric transformations (Planas 1992) to the form:

$$\Lambda(\mathbf{x}, \xi) = -\frac{k(r)}{2\ell^2}\left[\cos 2\theta + \cos 2\psi + \cos 2(\theta + \psi)\right] \tag{13.3.43}$$

where $\theta = 90° - \phi$. Note that the function $\Lambda(\mathbf{x}, \xi)$ is symmetric. This is, of course, a necessary consequence of the fact that the body is elastic.

Two properties contrasting with the classical nonlocal formulations explained before should be noted: (1) the crack influence function is not isotropic but depends on the polar angle (i.e., is anisotropic), and (2) it exhibits a shielding sector and an amplification sector. We may define the amplification sector as the sector in which σ_{yy} (the stress component normal to the crack plane) is positive, and the shielding sector as the sector in which σ_{yy} is negative. The amplification sector $\sigma_{yy} \geq 0$, according to (13.3.41), is the sector $\phi \leq \phi_b$ where

$$\phi_b = 55.740° \tag{13.3.44}$$

The sector in which the volumetric stress $\sigma_{xx} + \sigma_{yy}$ (first stress invariant) is positive is $\phi \leq 45°$. The sector in which $\sigma_{xx} \geq 0$ is $\phi \leq 22.5°$ and $\phi \geq 67.5°$. The sector in which $2\,\tau_{\max} = \sigma_{xx} - \sigma_{yy} \geq 0$ is $\phi \leq 45°$. The maximum principal stress $\sigma^{(1)}$ is positive for all angles ϕ, and the minimum principal stress $\sigma^{(2)}$ is positive for $\phi < 21.471°$.

The consequence of the anisotropic nature of the crack influence function is that interactions between adjacent cracks depend on the direction of damage propagation with respect to the orientation of the maximum principal inelastic stress. In a cracking band that is macroscopically of mode I (Fig. 13.3.5a), propagating in the dominant direction of the microcracks, the microcracks assist each other in growing because they lie in each other's amplification sectors. In a cracking band that is macroscopically of mode II (Fig. 13.3.5b), the microcracks are mutually in the transition between their amplification and shielding sectors, and thus interact little. Under compression, a band of axial splitting cracks may propagate

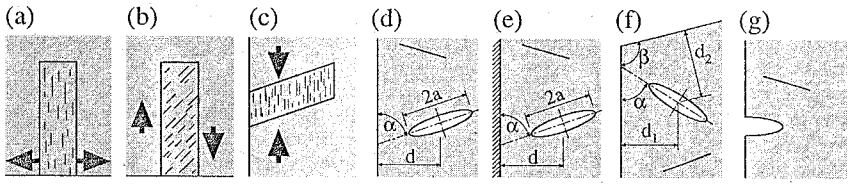

Figure 13.3.5 Crack bands and cracks near boundary (from Bažant 1994b).

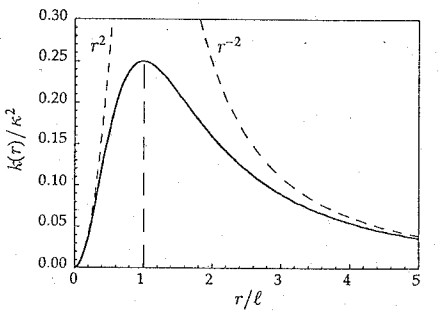

Figure 13.3.6 Radial dependence of Λ.

sideways (Fig. 13.3.5c), and in that case, the microcracks inhibit each other's growth because they lie in each other's shielding sectors. Differences in the kind of interaction may explain why good fitting of test data with the previous nonlocal microplane model required using a different material characteristic length for different types of problems (e.g., mode I fracture specimens vs. diagonal shear failure of reinforced beam).

For small r, function $\Lambda(\mathbf{x}, \xi)$ is a result of interactions in all directions. As the first approximation, these interactions may be assumed to cancel each other. Accordingly, we replace function $k(r) = a^2/r^2$ by a simple function of the same asymptotic properties for $r \to \infty$ which does not have a singularity at $r = 0$ and for $r \to 0$ approaches 0 with a horizontal tangent:

$$k(r) = \left(\frac{\kappa\ell r}{r^2 + \ell^2}\right)^2 \tag{13.3.45}$$

Here κ is an empirical constant such that $\kappa\ell$ roughly represents the average or effective crack size a for the macro-continuum; ℓ is a certain constant representing what may be called the characteristic distance of crack interactions (it represents the radial distance to the peak in Fig. 13.3.6). This length may be identified with what has been called the characteristic length of the nonlocal continuum. It reflects the dominant spacing of the microcracks, which in turn is determined by the size and spacing of the dominant inhomogeneities such as aggregates in concrete.

The foregoing expressions give the crack influence function Λ_∞ which is exact asymptotically for $r \to \infty$ but is only a crude approximation for small r. It is now convenient to represent the complete crack influence function Λ in the form:

$$\Lambda(0, \xi) = \Lambda_\infty(\xi, \eta) + \Lambda_1(\xi, \eta) \tag{13.3.46}$$

where Λ_1 represents a difference that is decaying to infinity faster (i.e., as a higher power of r) than Λ_∞ and can, therefore, be neglected for sufficient distances r from the center of the source crack.

The complete function Λ was determined by numerical integration of Eq. (13.3.35) using a dense square mesh; see 13.3.7a (Bažant and Jirásek 1994a). The target crack was considered parallel to the source crack, and $a/s = 0.25$. The asymptotically correct analytical expression for the crack influence

function from Eq. (13.3.45) is plotted in Fig. 13.3.7b. After its subtraction from the Λ_∞ values, one obtains the plot of the difference Λ_1 shown in Fig. 13.3.7c. A table of numerical values of Λ_1 was reported in Bažant and Jirásek (1994a)).

Function $\Lambda_1(x, y)$ obviously depends on the relative crack size a/s. However, it has been found that it depends on a/s only very little when $a/s \geq 0.25$. For smaller a/s, the crack interactions are probably unimportant. So perhaps a single crack influence function expression could be used for all the cases.

A statistical definition of Λ in three dimensions that is analogous to Eq. (13.3.35) can obviously be written, too.

13.3.8 Crack Influence Function in Three Dimensions

The case of three dimensions (3D) is not difficult when the cracks are penny-shaped (i.e., circular) and the boundary is remote. The stresses around such cracks have traditionally been expressed as integrals of Bessel functions (Sneddon and Lowengrub 1969; Kassir and Sih 1975), which are however cumbersome for calculations. Recently, though, Fabrikant (1990) ingeniously derived the following closed-form expressions:

$$\sigma_{xx} = \frac{\sigma_1 + \operatorname{Re}\sigma_2}{2}, \qquad \sigma_{yy} = \frac{\sigma_1 - \operatorname{Re}\sigma_2}{2}, \qquad \tau_{xy} = \frac{\operatorname{Im}\sigma_z}{2}$$
$$\tau_{xz} = \operatorname{Re}\tau_z, \qquad \tau_{yz} = \operatorname{Im}\tau_z \tag{13.3.47}$$

in which

$$\sigma_z = \frac{2\sigma}{\pi}(B - D), \qquad \sigma_1 = \frac{2\sigma}{\pi}[(1 + 2\nu)B + D]$$
$$\sigma_2 = e^{2i\phi}\,\frac{2\sigma}{\pi}\,\frac{a l_1^2 l_3}{l_2^2 l_4^2}\left(1 - 2\nu + \frac{z^2[a^2(6l_2^2 - 2l_1^2 + \rho^2) - 5l_2^4]}{l_4^4 l_3^2}\right)$$
$$\tau_z = -e^{i\phi}\,\frac{2\sigma}{\pi}\,\frac{z l_1[a^2(4l_2^2 - 5\rho^2) + l_1^4]l_3}{l_2 l_4^6} \tag{13.3.48}$$
$$B = \frac{a l_3}{l_4^2} - \arcsin\frac{a}{l_2}, \qquad D = \frac{a z^2[l_1^4 + a^2(2a^2 + 2z^2 - 3\rho^2)]}{l_4^6 l_3}$$
$$l_1 = \frac{L_2 - L_1}{2}, \qquad l_2 = \frac{L_2 + L_1}{2}, \qquad l_3 = \sqrt{l_2^2 - a^2}, \qquad l_4 = \sqrt{l_2^2 - l_1^2}$$
$$L_1 = \sqrt{(a - \rho)^2 + z^2}, \qquad L_2 = \sqrt{(a + \rho)^2 + z^2}$$

in which a = crack radius; r, θ, ϕ are the spherical coordinates (Fig. 13.3.8) attached to cartesian coordinates x, y, z at point $\boldsymbol{\xi}$, with angle θ measured from axis z which is normal to the crack at point $\boldsymbol{\xi}$; r = distance between points $\mathbf{x}$ and $\boldsymbol{\xi}$; ρ, ϕ, z are the cylindrical coordinates with origin at the crack center; and ρ, ϕ are polar coordinates in the crack plane, angle ϕ being measured from axis x.

The long-range asymptotic form of the foregoing stress field has been derived (Bažant 1994b). The derivation is easy if one notes that, for large r, $L_1 \approx r - a\sin\theta, L_2 \approx r + a\sin\theta$ (see the meaning of L_1 and L_2 in Fig. 13.3.8a), $l_1 \approx a\sin\theta, l_2 \approx r$ and, for $r \gg a$, $\arcsin(a/l_2) \approx [1 + (a^2/6l_2^2)]a/l_2$, $\sqrt{l_2^2 - a^2} \approx r[1 - (a^2/2r^2)]$. The result is the following long-range asymptotic field:

$$\sigma_{\rho\rho} = \sigma k(r)\left[(1 + 2\nu)\left(\sin^2\theta - \frac{2}{3}\right) + (1 - 2\nu - 5\cos^2\theta)\sin^2\theta\right]$$
$$\sigma_{\phi\phi} = \sigma k(r)\left[(1 + 2\nu)\left(\sin^2\theta - \frac{2}{3}\right) - (1 - 2\nu - 5\cos^2\theta)\sin^2\theta\right]$$
$$\sigma_{zz} = \sigma k(r)\left(\sin^2\theta - \frac{2}{3}\right) \tag{13.3.49}$$
$$\sigma_{\rho z} = -\sigma k(r)\sin 2\theta\,(4 - 5\sin^2\theta), \qquad \sigma_{\rho\phi} = \sigma_{\phi z} = 0$$

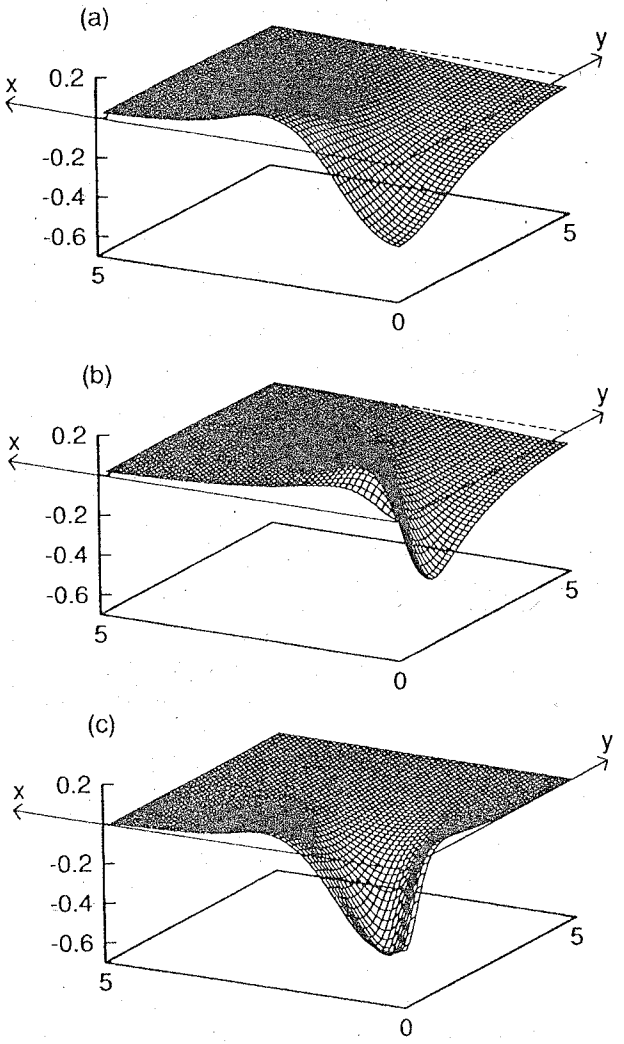

Figure 13.3.7 Crack influence function determined by Bažant and Jirásek (1994a)): (a) total crack influence function for the case of parallel source and target cracks, (b) analytical expression having the correct long-range asymptotic field, and (c) difference of the crack influence functions in (a) and (b). (From Bažant and Jirásek 1994a.)

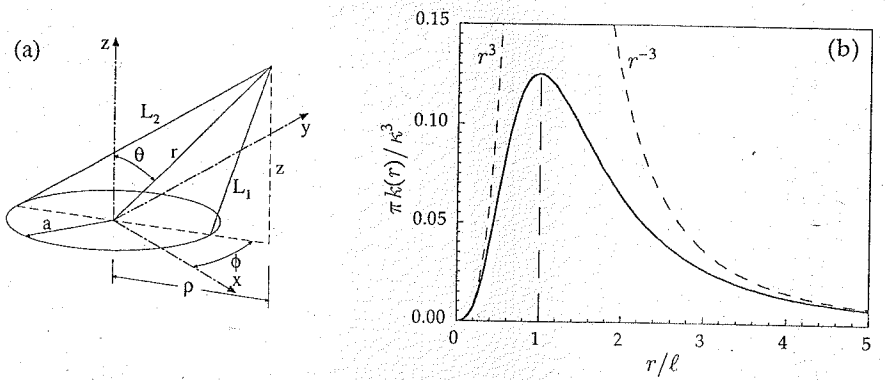

Figure 13.3.8 Crack influence function in three dimensions: (a) definition of coordinates for a penny-shaped crack (adapted from Bažant 1994b); (b) radial dependence of the influence function.

in which, for three dimensions, $k(r) = a^3/(\pi r^3)$. For the same reasons as those that led to Eq. (13.3.45), this expression may be replaced by

$$k(r) = \frac{1}{\pi}\left(\frac{\kappa \ell r}{r^2 + \ell^2}\right)^3 \tag{13.3.50}$$

(Fig. 13.3.8b) which is asymptotically correct for $r \to \infty$ and nonsingular at $r = 0$. The crack influence function based on (13.3.49) satisfies again the condition that its spatial average over every surface $r =$ constant be zero.

For large distances r, the crack influence function in three dimensions asymptotically decays as r^{-3}, whereas in two dimensions, it decays as r^{-2}. Again, in contrast to the phenomenological models we expounded before, the weight function (crack influence function) is not axisymmetric (isotropic) but depends on the polar or spherical angles (i.e., is anisotropic).

Further note that one can again distinguish a shielding sector and an amplification sector. According to the change of sign of σ_{zz} in Eq. (13.3.49), the boundary of these sectors is given by the angle

$$\theta_b = \arcsin\sqrt{2/3} = 54.736^\circ \tag{13.3.51}$$

or $90^\circ - \theta_b = 35.264^\circ$. Thus, the amplification sector $\theta \geq \theta_b$ is significantly narrower in three than in two dimensions.

In the case of a field that is translationally symmetric in z, one might wonder whether integration over z might yield the two-dimensional crack influence function. However, this is not so because the two-dimensional crack influence function represents in three dimensions the effect of an infinite strip (of thickness dx) at coordinate x of pressurized cracks aligned in the z direction on the stresses in a strip of glued cracks at coordinate ξ. This cannot yield the same properties as the field of one penny-shaped crack.

13.3.9 Cracks Near Boundary

When the boundary is near, the crack influence function should be obtained by solving the stress field of a pressurized crack located at a certain distance d from the boundary; Fig. 13.3.5d–g. Obviously, the function will depend on d as a parameter, i.e., $\Lambda(\mathbf{x}, \boldsymbol{\xi}, d)$. Functions Λ will be different for a free boundary, fixed boundary, sliding boundary, and elastically supported boundary or interface with another solid (Fig. 13.3.5d–g). When the crack is near a boundary corner (Fig. 13.3.5f), Λ represents the solution of the stress field of a pressurized crack in the wedge, and will depend on the distances from both boundary planes of the wedge. These solutions will be much more complicated than for a crack in infinite body, and

simplifications will be needed. On the other hand, because of the statistical nature of the crack system, exact solutions of these problems are not needed. Only their essential features are.

A crude but simple approach to the boundary effect is to consider the same weight function as for an infinite solid, protruding outside the given finite body. In the previous nonlocal formulations, based on the idea of spatial averaging, the same weight function as for the infinite solid has been used in the spatial integral and the weight function has simply been scaled up (renormalized), so that the integral of the weight function over the reduced domain would remain 1. In the present formulation, such scaling would have to be applied to all the weight functions whose integral should be 1, i.e., α, ψ, B, C. For those weight functions whose integral should vanish, a different scaling would be needed to take the proximity of the boundary into account; for example, the values at the boundary should be scaled up so that the spatial integral would always vanish, as indicated in (13.3.22). As a reasonable simplification, this might perhaps be done by replacing the $\Lambda_{\mu\nu}$ values for the integration points $\boldsymbol{\xi}_\nu$ of the boundary finite elements by $k_b\Lambda_{\mu\nu}$ where the multiplicative factor k_b is determined from the condition that $\sum_{\nu=1}^{N} \Lambda_{\mu\nu} = 0$ (with the summation carried over all the points in the given finite body);

$$k_b = -\sum_{\text{interior } \nu} \Lambda_{\mu\nu} \Big/ \sum_{\text{boundary } \nu} \Lambda_{\mu\nu} \tag{13.3.52}$$

13.3.10 Long-Range Decay and Integrability

Consider now an infinite two-dimensional elastic solid in which the stress, strain, and cracking are macroscopically uniform. All the microcracks are of the same size a, and the area per crack is s^2. The stress σ applied on each microcrack is the same. From (13.3.41) we calculate the contribution to the nonlocal integral from domain V_1 outside a circle of radius R_1 that is sufficiently large for permitting the approximation $k(r) \approx a^2/r^2$;

$$\int_{V_1}^{\odot} (\sigma_{xx} + \sigma_{yy})dV = \lim_{R\to\infty} \int_{r=R_1}^{R} \int_{\phi=0}^{2\pi} \frac{\sigma a^2 \cos 2\phi}{2r^2} \frac{r\,d\phi\,dr}{s^2} = \frac{\sigma a^2}{2s^2} \int_{r=R_1}^{\infty} \int_{\phi=0}^{2\pi} \frac{\cos 2\phi}{r} d\phi\,dr \tag{13.3.53}$$

Now an important observation, to which we already alluded: the last expression is an improper integral which is divergent (because it is divergent when the integrand is replaced by its absolute value; see e.g., Rektorys 1969). This also means that the value of the integral depends on the integration path. For some path the integral may be convergent, and that path, shown in (13.3.53), has been labeled by $\odot$. So we must conclude that a homogeneous ΔS field, that is, a field with a uniform length increment of all the cracks in an infinite body that is initially in a statistically uniform state, is impossible.

But this is not all that surprising. As known from the analysis of bifurcation and stable equilibrium path, strain-softening damage (which is due to microcrack growth) must localize (e.g., Bažant and Cedolin 1991). So, in practice, the two-dimensional domain of the integrals such as the last one must not be infinite in two directions. It can be infinite in only one direction, as is the case for a localization band. The basic reason for this situation is that the asymptotic decay r^{-2}, which we have obtained, is relatively weak—much weaker than the exponential decay assumed in previous works (for an exponential decay, the integration domain could be infinite in all directions without causing this kind of problem).

A similar analysis of uniform damage can be carried out for an infinite three-dimensional solid, and the conclusion is that the integration domain, that is, the zone of growing microcracks, can be infinite in only two directions (a localization layer), but not in three.

A similar divergence of the integral over infinite space has been known to occur in other problems of physics, for example, in calculation of the stresses from periodically distributed inclusions, or the light received from infinitely many statistically uniformly distributed stars. For a perspicacious mathematical study of this type of problem, see Furuhashi, Kinoshita and Mura (1981).

13.3.11 General Formulation: Tensorial Crack Influence Function

In Eq. 13.3.9, the principal stress orientations at points $\mathbf{x}$ and $\boldsymbol{\xi}$ are reflected in the values of the scalar function $\Lambda(\mathbf{x}, \boldsymbol{\xi})$. For the purpose of general analysis, however, it seems more convenient to use a tensorial crack influence function referred to common structural cartesian coordinates $X \equiv X_1, Y \equiv X_2, Z \equiv X_3$,

and transform all the inelastic stress tensor components to X, Y, Z. The local cartesian coordinates $x \equiv x_1, y \equiv x_2, z \equiv x_3$ at point ξ are chosen so that axis y coincides with the direction of the maximum principal value of the inelastic stress tensor $\overline{\mathbf{S}}(\xi)$, and axes x and z coincide with the other two principal directions.

Equations (13.3.32) and (13.3.33) may be rewritten in common structural coordinates as follows:

$$\Delta\tilde{S}_{\mu_{IJ}} \leftarrow \overline{\Delta S_{\mu_{IJ}}} + \sum_{\nu=1}^{N}\sum_{i=1}^{3} R^{(i)}_{\nu_{IJkl}}\Lambda^{(i)}_{\mu\nu_{kl}}\Delta\tilde{S}^{(i)}_{\nu} \qquad (\mu = 1, 2, \ldots N) \tag{13.3.54}$$

$$\Delta\tilde{S}_{IJ}(\mathbf{x}) \leftarrow \overline{\Delta S_{IJ}(\mathbf{x})} + \int_V \sum_{i=1}^{3} R^{(i)}_{IJkl}(\xi)\Lambda^{(i)}_{kl}(\mathbf{x},\xi)\Delta\tilde{S}^{(i)}(\xi)dV(\xi) \tag{13.3.55}$$

in which, similar to (13.3.21), we included the influence of the dominant cracks normal to the principal stress direction at each point; $R^{(i)}_{IJkl}(\xi)$ or $R^{(i)}_{\nu_{IJkl}} = c_{kI}c_{lJ}$ = fourth-rank coordinate rotation tensor (programmed as a square matrix when the stress tensors are programmed as column matrices) at point ξ or ξ_μ; c_{kI}, c_{lJ} = coefficients of rotation transformation of coordinate axes (direction cosines of new axes) from local coordinates x_i at point ξ (having, in general, a different orientation at each ξ) to common structural coordinates X_I ($c_{kI} = \cos(x_k, X_I), X_I = c_{kI}x_k, \sigma_{IJ} = c_{kI}c_{lJ}\sigma_{kl}$); subscripts I, J, or k, l refer to cartesian components in the common structural coordinates or in the local coordinates at ξ; and $\Lambda^{(i)}_{\mu\nu_{kl}}$ or $\Lambda^{(i)}_{kl}(\mathbf{x},\xi)$ = components of a tensorial discrete or continuous nonlocal weight function (crack influence function, replacing the scalar function Λ), which are equal to ℓ^{-2} times the cartesian stress components σ_{kl} for $\sigma = 1$ as defined by (13.3.41) for two dimensions, or ℓ^{-3} times such cartesian components as defined by (13.3.49) for three dimensions (with $r = \|\mathbf{x} - \xi\|$).

13.3.12 Constitutive Relation and Gradient Approximation

As is clear from the foregoing exposition, the constitutive relation is defined only locally. It yields the inelastic stress increment $\Delta\overline{S^{(1)}(\mathbf{x})}$, illustrated by segment $\overline{32}$ shown in Fig. 13.3.2. In the previous nonlocal formulations, by contrast, the nonlocal inelastic strain, stress, or damage was part of the constitutive relation. This caused conceptual difficulties as well as continuity problems with formulating the unloading criterion. Furthermore, in the case of nonlocal plasticity, this may also cause difficulties with the consistency condition for the subsequent loading surfaces.

Here these difficulties do not arise, because the nonlocal spatial integral is separate from the constitutive relation. Thus the unloading criterion can, and must, be defined strictly locally. If plasticity is used to define the local stress-strain relation, the consistency condition of plasticity is also local.

In principle, the nonlocal model based on crack interaction can be applied to any constitutive model for strain-softening, for example, parallel smeared cracking, isotropic damage theory, plasticity with yield limit degradation, plastic-fracturing theory, and endochronic theory. But to fully realize the potential of this approach, a more realistic model, such as the microplane model, appears more appropriate and has already been applied by Ožbolt and Bažant (1996). This will be discussed and documented in the next chapter.

Recently there has been much interest in limiting localization of cracking by means of the so-called gradient models. These models can be looked at as approximations of the nonlocal integral-type models, and can be obtained by expanding the nonlocal integral in Taylor series (Bažant 1984b); see Section 13.1.3. Unlike the present model, there have been only scant and vague attempts at physical justifications for the gradient models, especially for aggregate-matrix composites such as concrete. It seems that the physical justification for the gradient models of such materials must come indirectly, through the integral-type model. However, if that is the case, the present results signal a problem. If the spatial integral in (13.3.9) were expanded into Taylor series and truncated, the long-range decay of the type r^{-2} or r^{-3} could not be preserved. Yet it seems that this decay is important for microcrack systems. If so, then the gradient approximations are physically unjustified.

13.3.13 Localization of Oriented Cracking into a Band

The nonlocal model based on crack interactions has been applied to the problem of localization of unidirectional cracking into an infinite planar band parallel to the cracks (Bažant and Jirásek 1994b)). The body either is infinite or is an infinite planar layer parallel to the cracks, of thickness L. This represents the most fundamental localization problem, which is one dimensional, with the coordinate x normal to the cracks as the only coordinate. Due to translational symmetry in directions x and z parallel to the layer, the constitutive relation given by Eq. (13.3.9) with (13.3.43) can be integrated in the direction y parallel to the layer (the original problem is considered two-dimensional, although generalization to three dimensions would be possible). For the approximate crack interaction function (Eq. (13.3.43) with (13.3.45)) with $\theta = \psi = 0$), which is asymptotically correct at infinity, the integral can be evaluated analytically. This yields the following one-dimensional field equations for the increments of stresses and strains

$$\Delta\sigma = C(x)\Delta\varepsilon(x) - \Delta\tilde{S}(x) \tag{13.3.56}$$

$$\Delta\tilde{S} = \int_{-\infty}^{\infty}\hat{\Phi}(x,\xi)\Delta S(\xi)d\xi + \int_{-\infty}^{\infty}\hat{\Lambda}(x,\xi)\Delta\tilde{S}(\xi)d\xi \tag{13.3.57}$$

$$\hat{\Phi}(x,\xi) = \int_{-\infty}^{\infty}\Phi(x,0;\xi,\eta)d\eta, \quad \hat{\Lambda}(x,\xi) = \int_{-\infty}^{\infty}\Lambda(x,0;\xi,\eta)d\eta \tag{13.3.58}$$

$$\hat{\Lambda}(x,\xi) = \frac{\pi\kappa^2}{\ell}\left[\frac{16\zeta^6 + 24\zeta^4 + 6\zeta^2 + 1}{4(1+\zeta^2)^{3/2}} - 4|\zeta|^3\right] \tag{13.3.59}$$

$\zeta = (x - \xi)/\ell$; C = elastic material stiffness (modulus); $\hat{\Phi}$ is the one-dimensional weight function for spatial averaging, corresponding to the averaging over crack surface in Kachanov's method; and $\hat{\Lambda}$ is the one-dimensional crack influence function. Note that function $\hat{\Lambda}(x,\xi)$ is always positive, in contrast to the two-dimensional function Λ.

The solutions of Eqs. (13.3.56)–(13.3.59) have been studied numerically, by introducing a discrete subdivision in coordinate x and reducing the equations to a matrix form. As the boundary condition, the layer of thickness L was considered fixed at both surfaces. The localization profiles of strain increment $\Delta\varepsilon$, beginning from a state of uniform strain of various magnitudes, have been calculated and the evolution of the strain profile during loading has been followed. Fig. 13.3.9a shows the evolution of the strain profile across the layer, obtained for a local stress-strain relation that is linear up to the peak and then decays exponentially. Fig. 13.3.9b shows the stress-displacement diagram obtained for various ratios L/ℓ of the thickness of the layer to the nonlocal characteristic length. It is clear that the formulation prevents localization into a layer of zero thickness and enforces a smooth strain profile through the localization band. It is also seen that the size effect on the postpeak softening slope is obtained realistically. An interesting point is that localizations according to this formulation can happen even before attaining the maximum load. For further details, see Bažant and Jirásek (1994b).

13.3.14 Summary

The inelastic stress increments in a microcracking material are equal to the stresses that the load increment would produce on the cracks if they were temporarily "frozen" (or "glued"), i.e., prevented from opening and growing. The nonlocality arises from two sources: (1) *crack interactions*, which means that application of the pressure on the crack surfaces that corresponds to the "unfreezing" (or "ungluing") of one crack produces stresses on all the other frozen cracks; and (2) averaging of the stresses due to unfreezing over the crack surface, which is needed because crack interactions depend primarily on the stress average over the crack surface (or the stress resultant) rather than the macroscopic stress corresponding to the microcrack center. The crack interactions (source 1) can be solved by Kachanov's (1987a) simplified version of the superposition method, in which only the average crack pressures are considered.

The resulting nonlocal continuum model involves two spatial integrals. One integral, which corresponds to source (1) and has been absent from previous nonlocal models, is long-range and has a weight function whose spatial integral is 0; it represents interactions with remote cracks and is based on the long-range

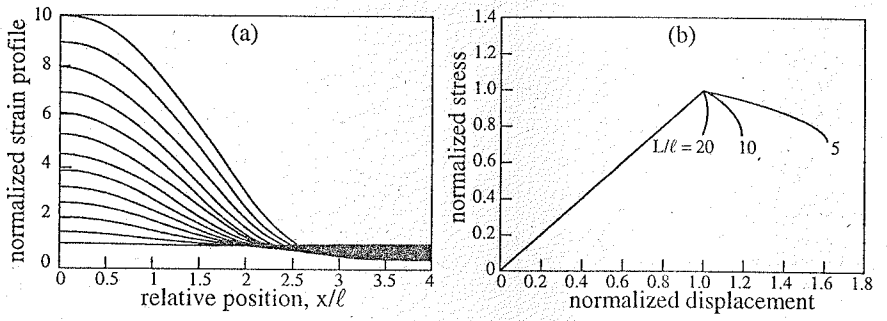

Figure 13.3.9 Localization in a bar predicted by nonlocal model based on crack interactions: (a) normalized strain profiles along a bar; the profiles are symmetric with respect to the origin, and an exponential softening law was used; (b) load-displacement diagrams for various bar lengths L. (From Jirásek and Bažant 1994.)

asymptotic form of the stress field caused by pressurizing one crack while all the other cracks are frozen. Another integral, corresponding to source (2), is short-range, involves a weight function whose spatial integral is 1, and represents spatial averaging of the local inelastic stresses over a domain whose diameter is roughly equal to the spacing of major microcracks (which is roughly equal to the spacing of large aggregates in concrete).

As an approach to continuum smoothing when the macroscopic field is nonuniform, one may seek a continuum field equation whose possible discrete approximation coincides with the matrix equation governing a system of interacting microcracks.

The long-range asymptotic weight function of the nonlocal integral representing crack interactions (source 1) has a separated form which is calculated as the remote stress field of a crack in infinite body. It decays with distance r from the crack as r^{-2} in two dimensions and r^{-3} in three dimensions. This long-range decay is much weaker than assumed in previous nonlocal models. In consequence, the long-range integral diverges when the damage growth in an infinite body is assumed to be uniform. This means that only the localized growth of damage zones can be modeled.

In contrast to the previous nonlocal formulations, the weight function (crack influence function) in the long-range integral is a tensor and is not axisymmetric (isotropic). Rather, it depends on the polar or spherical angle (i.e., is anisotropic), exhibiting sectors of shielding and amplification. The weight function is defined statistically and can be obtained by evaluating a certain averaging integral in which the integrand is the stress field of one pressurized crack in the given structure.

When an iterative solution of crack interactions according to the Gauss-Seidel iterative method is considered, the long-range nonlocal integral based on the crack influence function yields the nonlocal inelastic stress increments explicitly. This explicit form is suitable for iterative solutions of the loading steps in nonlinear finite element programs. The nonlocal inelastic stress increments represent a solution of a tensorial Fredholm integral equation in space, to which the iterations converge.

The constitutive law, in this new formulation, is strictly local. This is a major advantage. It eliminates difficulties with formulating the unloading criterion and the continuity condition, experienced in the previous nonlocal models in which nonlocal inelastic stresses or strains have been part of the constitutive relation.

14

Material Models for Damage and Failure

Computer analysis of concrete structures requires a general and robust material model for distributed cracking and other types of strain-softening damage such as softening plastic-frictional slip. The material model must perform realistically under a wide range of circumstances. The problem can be approached through two types of models: (1) the continuum approach, in which case the structure is usually solved by finite element discretization (although boundary elements and other methods are possible), and (2) the discrete (or lattice) approach, taking the form of discrete element method or its variants—the random particle model or lattice model. In the former approach, the material is characterized by a general nonlinear triaxial stress-strain relation coupled with a nonlocal formulation. In the latter approach, the material is represented by a lattice of particles and connecting bars for which simple rules of deformation and breakage must be devised.

At present, the continuum approach is more general, more widely applicable to structural analysis under general types of loading. The discrete approach provides some valuable insight into the micromechanics of failure and the role of heterogeneity, but only when the failure is due principally to tensile cracking and fracture. The computational demands of the discrete approach are still prohibitive for large structures and three-dimensional analysis, and attempts to develop the discrete approach for compression or compression-shear failures have so far been unsuccessful. In this chapter, we will first discuss the continuum approach and later briefly review the lattice approach.

The preceding chapter, dealing with nonlocal formulations, already presented one of two necessary components of the continuum approach to general analysis of softening damage due to microcracking and frictional-plastic slip. The other necessary component—the general triaxial stress-strain relation—will be described in this chapter. We have already touched this subject in chapter 8 while describing the triaxial stress-strain relation for the crack-band model, such as the fixed-crack and rotating crack models. But these simple models are not sufficiently general to deal with compression splitting and compression shear, cracking combined with plastic-frictional slip and softening slip.

Formulation of a general constitutive relation for such phenomena is a rather difficult problem, to which numerous studies have been devoted during the last two decades. Although many valuable advances have been made, this chapter will present in detail only one approach—the microplane model, which currently appears most realistic, powerful, and versatile. Other approaches, which use classical types of constitutive relations based on the invariants of the stress and strain tensors and include models such as plasticity, continuum damage mechanics, fracturing theory, plastic-fracturing theory, and endochronic theory, will not be treated.

All the constitutive models describing fracture exhibit properties such as post-peak strain softening and deviations from the normality rule (or Drucker's postulate). As discussed in Chapter 8, these properties, which are inevitable if the constitutive relation should describe cracking, friction, and loss of cohesion realistically, cause well-known mathematical difficulties such as ill-posedness of the boundary value problem, spurious localization instabilities, and spurious mesh sensitivity. To avoid these difficulties, the constitutive relations presented in this chapter must be combined with some kind of localization limiter. The nonlocal approach described in the preceding chapter is an effective method of solving these problems.

It is often thought that the continuum approach cannot be applied to the final stages of failure, in which damage localizes into large continuous cracks. However, the continuum approach can provide a relatively good (albeit not perfect) model for the propagation of such cracks. The reasons have already been explained in Chapter 8, in connection with the crack band model, which may be regarded as the simplest version of the nonlocal approach. The width of the localized damage band has, in most cases, negligible influence on the results of structural analysis. A zero width, that is, a distinct crack, and a

finite width (not excessively large, of course) often yields about the same results. Forcing, through the nonlocal concept, the distinct crack to spread over a width of several finite element sizes, or forcing a narrow damage band to be wider than the real width, is usually admissible, provided that the energy dissipation per unit length of advance of the band is adjusted to remain the same. It should be noted that such spreading of damage over a width of several element sizes is also a convenient way to avoid the directional bias of finite element mesh.

14.1 Microplane Model

The microplane model (Bažant 1984c) trades simplicity of concept for increased numerical work left to the computer. This model represents a generalization of the basic idea of G.I. Taylor (1938), who proposed that the constitutive behavior of polycrystalline metals may be characterized by relations between the stress and strain vectors acting on planes of all possible orientations within the material, and that the macroscopic strain or stress tensor may then be obtained as a summation (or resultant) of all these vectors under the assumption of a static or kinematic micro-macro constraint.

Taylor's idea was soon recognized as the most realistic way to describe the plasticity of metals, but the lack of computers prevented practical application in the early times. Batdorf and Budianski (1949) were first to describe hardening plasticity of polycrystalline metals by a model of this type, and many other researchers subsequently refined or modified this approach to metals (Kröner 1961; Budianski and Wu 1962; Lin and Ito 1965, 1966; Hill 1965, 1966; Rice 1970). Taylor's idea was also developed for the hardening inelastic response of soils and rocks (Zienkiewicz and Pande 1977; Pande and Sharma 1981, 1982; Pande and Xiong 1982).

In all the aforementioned approaches, it was assumed that the stress acting on various planes in the material, called the slip planes, was the projection of the macroscopic stress tensor. This is a static constraint. As shown later, the static constraint prevents such models from being generalized to postpeak strain softening behavior or damage. In an effort to model concrete, it was realized that the extension to damage requires replacing the static constraint by a kinematic constraint, in which the strain vector on any inclined plane in the material is the projection of the macroscopic strain tensor (Bažant 1984c). The kinematic constraint makes it possible to avoid spurious localization among orientations in which all the strain softening localizes preferentially into a plane of only one orientation.

In all applications to metals, the formulations based on Taylor's idea were called the slip theory of plasticity, and in applications to rock, the multi-laminate model. These terms, however, became unsuitable for the description of damage in quasibrittle materials. For example, the salient inelastic behavior of concrete does not physically represent plastic slip (except under extremely high confining stresses), but microcracking. For this reason, the neutral term "microplane model", applicable to any physical type of inelastic behavior, was coined (Bažant 1984c) (although a nondescriptive term such as "Taylor-Batdorf-Budianski model", possibly with the names of further key contributors, could also be used). The term "microplane" reflects the basic feature that the material properties are characterized by relations between the stress and strain components independently for planes of various orientation within the microstructure of the material. This term also avoids confusion with the type of micro-macro constraint, which has always been static in the slip theory of plasticity but must be kinematic for strain-softening of concrete. Also, as introduced for the microplane model (Bažant 1984c), the tensorially invariant macroscopic constitutive relations are obtained from the responses on the microplanes of all orientations in a more general manner than in the slip theory of plasticity—by means of a variational principle (or the principle of virtual work).

The microplane model of concrete was developed in detail first for the tensile fracturing (Bažant and Oh 1983b, 1985; Bažant and Gambarova 1984), and later for nonlinear triaxial behavior in compression with shear (Bažant and Prat 1988b). The reason that these new models used the kinematic rather than static constraint for the microplanes was to avoid spurious instability of the constitutive model due to strain softening (which always occurs for the static constraint). Because the tangential material stiffness matrix loses positive definiteness (due to postpeak strain softening as well as lack or normality), the nonlocal approach, which prevents spurious excessive localization of damage in structures and spurious mesh sensitivity, was combined with the microplane model (Bažant and Ožbolt 1990, 1992; Ožbolt and Bažant 1991, 1992). An explicit formulation and an efficient numerical algorithm for the microplane model of

Bažant and Prat (1988b) was recently presented by Carol, Prat and Bažant (1992). It was also shown that the microplane model with a kinematic constraint can be cast in the form of continuum damage mechanics in which the damage, understood as a reduction of the stress-resisting cross section area fraction in the material, represents a fourth-order tensor independent of the microplane material characteristics (Carol, Bažant and Prat 1991; Carol and Bažant 1997).

Although the microplane model of Bažant and Prat (1988b) was initially thought to perform well for postpeak softening damage in both compression and tension, Jirásek (1993) found that, in postpeak uniaxial tension, large positive lateral strains develop at large tensile strains. He showed that this was caused by localization of tensile strain softening into the volumetric strain while the deviatoric strains on the strain softening microplanes exhibited unloading. It was recognized that this localization of tensile softening damage into one of the two normal strain components in tension (that is the volumetric one), was an inevitable consequence of separating the normal strains into the volumetric and deviatoric parts. However, this separation was previously shown necessary (Bažant and Prat 1988b) for correct modeling of triaxial behavior in compression as well as for achieving the correct elastic Poisson ratio. The problem was overcome by introducing a new concept—the stress-strain boundaries (Bažant 1993c; Bažant, Jirásek et al. (1994); Bažant, Xiang and Prat 1996), which will be described in detail. This concept allows an explicit algorithm and is computationally efficient.

The basic philosophy of microplane model blends well with the philosophy of finite elements. Finite elements represent a discretization with respect to space (or distance), while the microplane model represents a discretization with respect to orientations. In both, the principle of virtual works is used, as will be seen, in analogous ways—to establish the equilibrium relations and stiffness for the postulated kinematic constraint, which is given by the shape (or interpolation) functions for finite elements or by the kinematic constraint between orientations. This analogous structure is suitable for explicit programs (Fig. 14.1.1).

In another sense, the microplane model can be regarded as complementary to the nonlocal concept. Whereas the nonlocal concept handles interactions at distance, the microplane model handles interactions between orientations (Fig. 14.1.2). The nonlocality prevents spurious localization in space, whereas the kinematic constraint of the microplane model prevents localizations between orientations, as will be pointed out.

14.1.1 Macro-Micro Relations

In the classical approach, the constitutive relation is defined by algebraic or differential relations between the stress tensor $\boldsymbol{\sigma}$ and the strain tensor $\boldsymbol{\varepsilon}$, based on the theory of tensorial invariants. In the microplane approach, the constitutive relation is defined as a relation between the stress and strain *vectors* acting on a plane of arbitrary orientation in the material. The orientation of this plane, called the microplane, is characterized by the unit normal $\vec{n}$. The basic hypothesis, which makes it possible to describe strain softening (Bažant 1984c), is that the strain vector $\vec{\varepsilon}_N$ on the microplane (Fig. 14.1.3a) is the projection of the macroscopic strain tensor $\boldsymbol{\varepsilon}$, that is,

$$\vec{\varepsilon}_N = \boldsymbol{\varepsilon}\vec{n} \tag{14.1.1}$$

The stress vector $\vec{\sigma}_N$ on the microplane cannot be exactly equal to the projections of the macroscopic stress tensors $\boldsymbol{\sigma}$ if the strains represent the projections of $\boldsymbol{\varepsilon}$. Thus, static equivalence or equilibrium between the macro and micro levels must be enforced only approximately, by other means. The way to enforce it is to use a variational principle, that is, the principle of virtual work. For equilibrium, it suffices that, for any variation $\delta\boldsymbol{\varepsilon}$, the virtual work of the macrostresses within a unit sphere be equal to the virtual work of the microstresses on the surface elements of the sphere (Bažant 1984c). This condition is written as:

$$\frac{2\pi}{3}\boldsymbol{\sigma}\cdot\delta\boldsymbol{\varepsilon} = \int_\Omega \vec{\sigma}_N\cdot\delta\vec{\varepsilon}_N\, d\Omega \tag{14.1.2}$$

where the dot represents scalar product of two vectors or two second-order tensors.

Remark: A more detailed justification of this relation may be given as follows. We consider a small representative volume of the material, given by a small cube of side Δh. A pair of two parallel sides corresponds

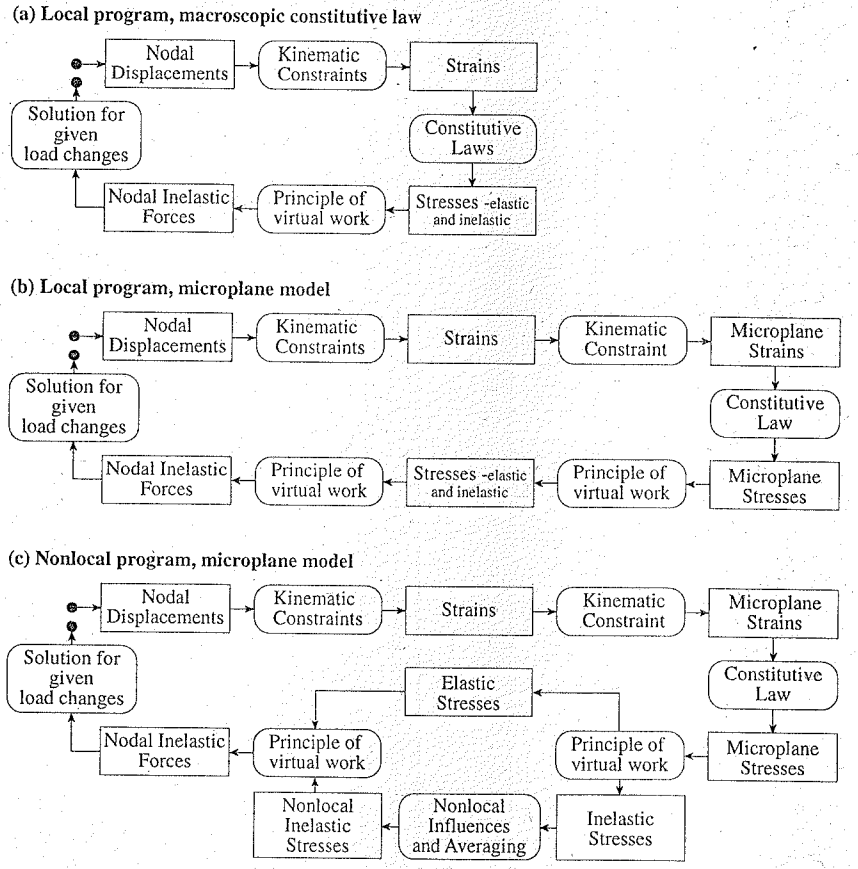

Figure 14.1.1 General flow charts of iteration cycles in load steps of explicit finite element programs (using initial elastic stiffness matrix).

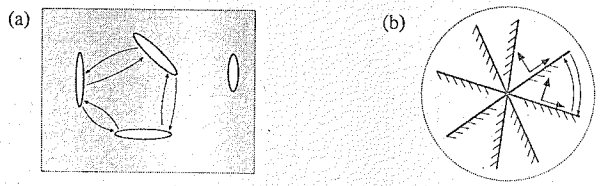

Figure 14.1.2 (a) Interaction at distance (nonlocality) and (b) interaction between orientations (microplane concept).

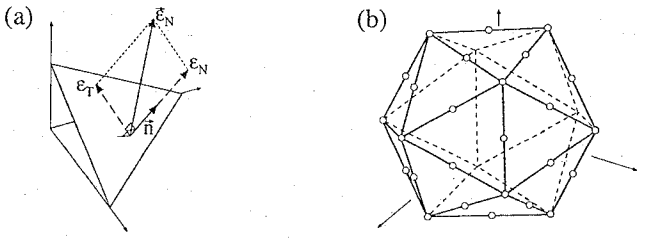

Figure 14.1.3 (a) Microplane normal and microstrain vectors, and normal and shear components of the microstrain vector. (b) Directions of microplane normals (circles) for a system of 21-microplanes per hemisphere (after Bažant and Oh 1986, adapted from Bažant, Xiang and Prat 1996).

to microplane labeled by subscript N, and the other two pairs of sides correspond to orthogonal microplanes labeled by subscripts P, and Q. The strain vectors on these microplanes may be assumed to have the meaning defined by $\Delta\vec{u}_N/\Delta h = \vec{\varepsilon}_N, \quad \Delta\vec{u}_P/\Delta h = \vec{\varepsilon}_P, \quad \Delta\vec{u}_Q/\Delta h = \Delta\vec{\varepsilon}_Q$ in which $\Delta\vec{u}_N, \Delta\vec{u}_P$, and $\Delta\vec{u}_Q$ are the differences in the displacement vector between the opposite sides of the cube in the directions by labeled by N, P, and Q. The equality of the incremental virtual work of stresses within the representative volume on the macrolevel and the work of stresses on the three microplanes representing the sides of the cube implies that $\Delta h^3\boldsymbol{\sigma}\cdot\delta\boldsymbol{\varepsilon} = \Delta h^2(\vec{\sigma}_N\cdot\delta\Delta\vec{u}_N + \vec{\sigma}_P\cdot\delta\Delta\vec{u}_P + \vec{\sigma}_Q\cdot\delta\Delta\vec{u}_Q)$, where δ denotes the variations and Δh^2 = area of the sides of the elementary cube. The strain vectors $\vec{\varepsilon}_N, \vec{\varepsilon}_P$ and $\vec{\varepsilon}_Q$ include the contributions of elastic deformations as well as displacements due to cracking (and possibly also to plastic slip). The cracking or other inelastic deformation happens randomly on planes of various orientations within the material, and the macroscopic continuum must represent these strains statistically, in the average sense. Therefore,

$$\Delta h^3\boldsymbol{\sigma}\cdot\delta\boldsymbol{\varepsilon} = \Delta h^2\frac{1}{\Omega_0}\int_\Omega\left(\vec{\sigma}_N\cdot\delta\Delta\vec{u}_N + \vec{\sigma}_P\cdot\delta\Delta\vec{u}_P + \vec{\sigma}_Q\cdot\delta\Delta\vec{u}_Q\right)d\Omega \tag{14.1.3}$$

in which the integral represents averaging over all spatial orientations; $d\Omega = \sin\theta d\theta d\phi$ where θ, ϕ = spherical angles, Ω = surface of a unit hemisphere, and $\Omega_0 = 2\pi$ = its surface area. Now, obviously, $\int_\Omega \vec{\sigma}_N\cdot\delta\Delta\vec{u}_N d\Omega = \int_\Omega \vec{\sigma}_P\cdot\delta\Delta\vec{u}_P d\Omega = \int_\Omega \vec{\sigma}_Q\cdot\Delta\vec{u}_Q d\Omega$. Thus the variational equation (14.1.3) yields (14.1.2). $\triangle$

Substituting (14.1.1) into the integral in (14.1.2) and factorizing $\delta\boldsymbol{\varepsilon}$, we obtain

$$\left[\frac{2\pi}{3}\boldsymbol{\sigma} - \int_\Omega(\vec{\sigma}_N\otimes\vec{n})^S d\Omega\right]\cdot\delta\boldsymbol{\varepsilon} = 0 \tag{14.1.4}$$

where $\otimes$ indicates tensorial product and superscript S for a tensor denotes the symmetric part of such tensor, i.e., $\mathbf{T}^S = (\mathbf{T}+\mathbf{T}^T)/2$, in which $\mathbf{T}$ is an arbitrary second-order tensor and $\mathbf{T}^T$ its transpose. Since the variational equation (14.1.4) must be satisfied for any variation $\delta\boldsymbol{\varepsilon}$, it is not only sufficient but also necessary that the expression in parentheses vanish. This yields the following fundamental relation from which the macroscopic stress tensor is calculated:

$$\boldsymbol{\sigma} = \frac{3}{2\pi}\int_\Omega(\vec{\sigma}_N\otimes\vec{n})^S d\Omega \tag{14.1.5}$$

To compute the integral over the unit sphere, Gaussian integration can be used, and so the cartesian stress components σ_{ij} are computed as

$$\sigma_{ij} = \frac{3}{2\pi}\int_\Omega s_{ij}d\Omega \approx \sum_{\mu=1}^{N_m} w_\mu s_{ij}^\mu\,, \tag{14.1.6}$$

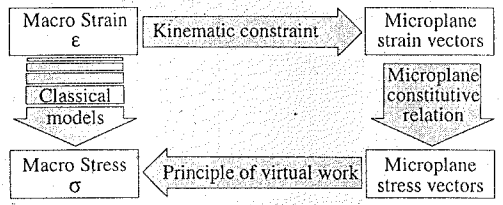

Figure 14.1.4 Flow of calculation between micro- and macro-levels (adapted from Bažant, Xiang and Prat 1996).

in which

$$s_{ij} = \left[(\vec{\sigma}_N \otimes \vec{n})^S\right]_{ij} = \frac{1}{2}(\sigma_{Ni} n_j + \sigma_{Nj} n_i) \tag{14.1.7}$$

and the last expression represents an approximate numerical evaluation of the integral over the hemisphere; subscripts μ represent a chosen set of integration points representing orientations of discrete microplanes defined by unit vectors n_i^μ (shown by the circled points in Fig. 14.1.3b); w_μ are the integration weights associated with these microplanes, normalized so that $\sum_\mu w_\mu = 1$; and superscript μ labels the values corresponding to these directions. While the integral over Ω represents integration over infinitely many microplanes, the numerical approximation represents summation over a finite number of suitably chosen discrete microplanes. The flow of calculation between the macro- and micro-levels is explained by Fig. 14.1.4

Formulation of an optimal numerical integration formula over the surface of a hemisphere is not a trivial matter. The problem has been studied extensively by mathematicians, and Gaussian integration formulas of various degrees of approximation have been developed. The simplest integration formulas, for which all the weights are equal, are obtained by taking the discrete microplanes identical to the faces of a regular polyhedron (Platonic solid). But the regular polyhedron of the largest number of sides is the icosahedron, with 20 faces, which yields 10 microplanes per hemisphere. It has been shown that the accuracy of the corresponding integration formula is insufficient for representing the postpeak stress-strain curve of concrete (this was demonstrated by the fact that rigid-body rotations of the set of discrete microplanes can yield unacceptably large differences in stresses); see Bažant and Oh (1985, 1986). Thus, formulas based on a regular polyhedron cannot be used, which means that the discrete microplanes cannot have equal weights. Determination of the optimum weights is not a trivial matter. The weights must be determined so that the formula would exactly integrate polynomials up to the highest possible degree and that the integration error due to the next higher-degree term of the polynomial be minimized (Bažant and Oh 1986).

One sufficiently accurate formula, which consists of 28 microplanes (i.e., 28 integration points) over a hemisphere, is given by Stroud (1971). A more efficient and only slightly less accurate formula, involving 21 microplanes, was derived by Bažant and Oh (1986) (and was used in the nonlocal finite element microplane program by Ožbolt, and in the program EPIC by Adley at WES). This 21-point formula exactly integrates polynomials up to the 9th degree. The normals to the microplanes of this formula represent the radial directions to the vertices and to the centers of the edges of a regular icosahedron (as shown in Fig. 14.1.3b). Fewer than 21 microplanes cannot give sufficient accuracy (Bažant and Oh 1985).

14.1.2 Volumetric-Deviatoric Split of the Microstrain and Microstress Vectors

It is well known in continuum mechanics that for many purposes it is useful to decompose the strain tensor into its hydrostatic and deviatoric parts, by writing $\boldsymbol{\varepsilon} = (1/3)\text{tr}\,\boldsymbol{\varepsilon}\,\mathbf{1} + \boldsymbol{\varepsilon}'$, where $\mathbf{1}$ is the unit tensor and $\boldsymbol{\varepsilon}'$ the deviatoric strain tensor. When applied to (14.1.1), the following decomposition of the microstrain vector follows

$$\vec{\varepsilon}_N = \varepsilon_V\, \vec{n} + \vec{\varepsilon}_D \tag{14.1.8}$$

in which ε_V is called the volumetric strain and $\vec{\varepsilon}_D$ the deviatoric strain vector acting on the microplane; they are defined as

$$\varepsilon_V = \frac{1}{3}\text{tr}\,\boldsymbol{\varepsilon} \qquad \text{and} \qquad \vec{\varepsilon}_D = \boldsymbol{\varepsilon}'\vec{n} \tag{14.1.9}$$

The deviatoric strain vector is further decomposed into its normal component ε_D that we call deviatoric strain for short, and its component tangential to the microplane that we call the shear strain vector $\vec{\varepsilon}_T$:

$$\varepsilon_D = \vec{\varepsilon}_D \cdot \vec{n} = \boldsymbol{\varepsilon}'\vec{n} \cdot \vec{n} \qquad \text{and} \qquad \vec{\varepsilon}_T = \vec{\varepsilon}_D - \varepsilon_D\, \vec{n} \tag{14.1.10}$$

The microplane strain vector can, thus, be written as

$$\vec{\varepsilon}_N = \varepsilon_V \vec{n} + \varepsilon_D \vec{n} + \vec{\varepsilon}_T \tag{14.1.11}$$

Analogous components σ_V, σ_D, and $\vec{\sigma}_T$ are defined for the microstress vector, and so we write

$$\vec{\sigma}_N = \sigma_V \vec{n} + \sigma_D \vec{n} + \vec{\sigma}_T \tag{14.1.12}$$

Note that both the volumetric and deviatoric components contribute to the normal component at the microplane. We can thus define the total normal microstrain and microstress ε_N and σ_N as

$$\varepsilon_N = \varepsilon_V + \varepsilon_D\,, \qquad \sigma_N = \sigma_V + \sigma_D \tag{14.1.13}$$

Based on the foregoing definitions, a particular microplane constitutive law consists in a set of rules specifying how the microstress components σ_V, σ_D, and $\vec{\sigma}_T$ change as $\varepsilon_V, \varepsilon_D$, and $\vec{\varepsilon}_T$ evolve. The simplest case to be solved is the linear elastic case that we analyze next.

14.1.3 Elastic Response

In the elastic regime we must have a linear relationship between $\vec{\sigma}_N$ and $\boldsymbol{\varepsilon}$ for every $\vec{n}$; therefore, we must seek a relationship of the form

$$\vec{\sigma}_N = \vec{L}(\boldsymbol{\varepsilon}, \vec{n}) \tag{14.1.14}$$

where the function $\vec{L}(\boldsymbol{\varepsilon}, \vec{n})$ is linear in $\boldsymbol{\varepsilon}$. Moreover, isotropy requires that if the microplane (and its normal vector) and the macrostrain tensor are both rotated through any orthogonal tensor $\mathbf{Q}$, the resulting microstress must be correspondingly rotated, i.e.,

$$\vec{L}(\mathbf{Q}\boldsymbol{\varepsilon}\mathbf{Q}^T, \mathbf{Q}\vec{n}) = \mathbf{Q}\vec{\sigma}_N = \mathbf{Q}\vec{L}(\boldsymbol{\varepsilon}, \vec{n}) \tag{14.1.15}$$

which indicates that the function $\vec{L}(\vec{\varepsilon}_N, \vec{n})$ is an isotropic vector-valued function of a second-order tensor and a vector. The most general function of this type that is linear in $\boldsymbol{\varepsilon}$ can be written as

$$\vec{L}(\vec{\varepsilon}_N, \vec{n}) = a_1 \text{tr}\,\boldsymbol{\varepsilon}\, \vec{n} + b_1(\boldsymbol{\varepsilon}\vec{n} \cdot \vec{n})\vec{n} + c_1 \boldsymbol{\varepsilon}\vec{n} \tag{14.1.16}$$

where a_1, b_1, and c_1 are scalar constants. This can readily be rewritten in terms of the volumetric, deviatoric, and shear components of the microstrain:

$$\vec{\sigma}_N = E_V \varepsilon_V\, \vec{n} + E_D \varepsilon_D\, \vec{n} + E_T \vec{\varepsilon}_T \tag{14.1.17}$$

where E_V, E_D, and E_T are microplane elastic moduli corresponding to volumetric, deviatoric, and shear straining. In view of (14.1.12), the foregoing expression can be split into the following three relations:

$$\sigma_V = E_V \varepsilon_V\,, \qquad \sigma_D = E_D \varepsilon_D \qquad \text{and} \qquad \vec{\sigma}_T = E_T \vec{\varepsilon}_T \tag{14.1.18}$$

The microplane elastic moduli can be determined in terms of the macroscopic elastic moduli by identifying the macroscopic stress-strain response predicted by the microplane model with the classical Hooke equations. The macroscopic response is obtained by substituting $\vec{\sigma}_N$ from (14.1.17) into (14.1.5) and

then into the expressions for the microplane strain components in terms of the macrostrain tensor. The resulting macroscopic relationship is

$$\sigma = \frac{E_V}{3}\text{tr}\,\varepsilon\,\mathbf{A} + \frac{E_T}{2}\left(\mathbf{A}\varepsilon' + \varepsilon'\mathbf{A}\right) + (E_D - E_T)B\varepsilon' \tag{14.1.19}$$

where $\mathbf{A}$ and $\boldsymbol{B}$ are, respectively, the following second- and fourth-order tensors:

$$\mathbf{A} = \frac{3}{2\pi}\int_\Omega \vec{n}\otimes\vec{n}\,d\Omega \qquad \text{and} \qquad B = \frac{3}{2\pi}\int_\Omega \vec{n}\otimes\vec{n}\otimes\vec{n}\otimes\vec{n}\,d\Omega \tag{14.1.20}$$

These two tensors can be computed with relative ease using various methods (see the exercises at the end of this section). The result is simple:

$$\mathbf{A} = \mathbf{1} \qquad \text{and} \qquad 5B_{ijkl} = \delta_{ij}\delta_{kl} + \delta_{ik}\delta_{jl} + \delta_{il}\delta_{jk} \tag{14.1.21}$$

where B_{ijkl} are the rectangular cartesian components of $\boldsymbol{B}$. Substituting these expressions into (14.1.19) we get the final expression for the macrostress tensor as:

$$\sigma = \frac{E_V}{3}\text{tr}\,\varepsilon\,\mathbf{1} + \frac{2E_D + 3E_T}{5}\varepsilon' \tag{14.1.22}$$

Comparing now this expression with the classical expression of isotropic elasticity

$$\sigma = \frac{E}{3(1-2\nu)}\text{tr}\,\varepsilon\,\mathbf{1} + \frac{E}{1+\nu}\varepsilon \tag{14.1.23}$$

where E is the elastic modulus and ν the Poisson ratio, we easily find that

$$E_V = \frac{E}{1-2\nu}, \qquad E_D = \frac{5E}{(2+3\mu)(1+\nu)}, \qquad E_T = \mu E_D \tag{14.1.24}$$

where $\mu = E_T/E_D$ is a free parameter which may be chosen.

Parameter μ can be optimized so as to best match the given test data. Bažant and Prat (1988b), who gave relations equivalent to (14.1.24) but in terms of parameter $\eta = E_D/E_V$ instead of μ, found the range of η-values giving the optimum fits of test data for concrete. This range corresponds to μ-values close to 1. Therefore, the value μ= 1 has subsequently been used in all the data fitting that we cite later in this section. Note also that the inverse of (14.1.24) yields E and ν in terms of E_V, E_D, and μ.

As revealed by the study of Carol, Bažant and Prat (1991), the value $\mu = 1$ is also conceptually advantageous because it makes it possible to characterize damage, in the sense of continuum damage mechanics, by a fourth-rank tensor that is independent of the material stiffness properties. This will be discussed in more depth later.

It is interesting to note that for the choice $\mu = (1-4\nu)/(1+\nu)$, one has $E_V = E_D$. Then one can set $\sigma_N = E_N\varepsilon_N$, where $E_N = E_V = E_D$. So, in that case there is no volumetric-deviatoric split. But that would not be realistic for concrete.

One reason that the normal strain on the microplane must be split into the volumetric and deviatoric normal components is that a general model ought to be capable of giving (for any μ) any thermodynamically admissible value of Poisson's ratio, that is, $-1 < \nu < 0.5$. That this is indeed so can be checked by eliminating μ from (14.1.24) and solving for ν, which yields $\nu = (5E_V - 2E_D - 3E_T)/(10E_V + 2E_D + 3E_T)$. This relation also shows that, for the case of no split (which corresponds to the case $E_V = E_D = E_N$), one would have $\nu = (E_N - E_T)/(4E_N + E_T)$, and so the Poisson ratio would be restricted to the range $-1 < \nu < 0.25$. Although this range would suffice for concrete, the microplane model, in principle, could not be fully realistic if it were restricted to Poisson's ratios less than 0.25.

It may also be noted that if the shear stiffness were neglected ($E_T = 0$ or $\mu = 0$), then any Poisson ratio between -1 and 0.5 could still be obtained, provided that the volumetric and deviatoric normal microplane strains would be split. However, if they were not (i.e., $\sigma_N = E_N\varepsilon_N$), which was implied in the initial model of Bažant and Oh (1983b, 1985) for tensile fracturing only, then Poisson's ratio would be restricted to the value $\nu = 0.25$. Such a restriction is not realistic, and besides, the shear stiffness on the microplane level appears to be important for correct modeling of the effect of confining pressure on compression failure.

The main reason for the volumetric-deviatoric split with independent moduli E_V and E_D (Bažant and Prat 1988b) is the absence of a peak and of postpeak strain softening for hydrostatic compression test and uniaxial strain compression test (see the tests of Bažant, Bishop and Chang 1986), while at the same time the loading by uniaxial compressive stress or other compressive loadings with uninhibited volume expansion exhibits stress peak followed by postpeak strain softening. Without the aforementioned split, compressive loading with restricted volume expansion (hydrostatic compression and uniaxial strain) would also, incorrectly, exhibit a peak stress and postpeak strain softening.

In the initial proposal of microplane model with strain softening (Bažant 1984c), the stress-strain relation for the normal and shear components of stresses and strains of the microplanes had the form of incremental plasticity, based on subsequent yield surfaces and loading potentials for the microplane. However, subsequent studies have shown that this was unnecessarily complicated. As it turned out (Bažant and Oh 1985; Bažant and Prat 1988b), one can assume a total algebraic stress-strain relation for these components for the case of virgin loading, that is, σ_V, σ_D, and $\vec{\sigma}_T$ can be assumed to be functions of $\varepsilon_V, \varepsilon_D$, and $\vec{\varepsilon}_T$. Further it turned out that each stress component can be considered to depend only on the associated strain component, with the exception of shear stress $\vec{\sigma}_T$, which is considered to depend on σ_N to express internal friction (and, at high pressures, plasticity). Without the frictional aspect, it is not possible to model standard triaxial tests at high confining pressures.

14.1.4 Nonlinear Microplane Behavior and the Concept of Stress-Strain Boundaries

In the original microplane model for compressive failure (Bažant and Prat 1988b), the stress-strain relations for the microplanes were smooth curves. However, difficulties arose in the handling of the transition from reloading to virgin inelastic loading in the quadrants of negative stress-strain ratio, and complicated rules had to be devised (Hasegawa and Bažant 1993; and Ožbolt and Bažant 1992). Also, the modeling of cyclic loading was difficult. These difficulties can be circumvented with the concept of stress-strain boundaries. However, the main reason for introducing this concept is the modeling of triaxial behavior in tension.

The condition that the response must not exceed a specified boundary curve $\sigma_X = F_X(\varepsilon_X)$—where X indicates the appropriate microplane component— makes it easy to ensure continuity at the transition from elastic behavior, which is defined separately for volumetric and deviatoric components, to the strain-softening damage behavior in tension, which is defined without the volumetric-deviatoric split (Bažant 1993c). It seems next to impossible to devise explicit algebraic stress-strain relations that would describe such transitions without any discontinuity.

The stress-strain boundaries, shown in Fig. 14.1.5, are defined as (Bažant, Xiang and Prat 1996):

$$\sigma_N = F_N(\varepsilon_N), \sigma_V = -F_V(-\varepsilon_V), \sigma_D = -F_D(-\varepsilon_D), \sigma_D = F_D^+(\varepsilon_D), \sigma_T = F_T(\sigma_N) \tag{14.1.25}$$

in which σ_T stand for either σ_M or σ_L (the components of shear stress vector on two arbitrarily assigned orthogonal axes M and L within the microplane). It might seem that, from the viewpoint of rotational invariance in the microplane, the shear stress vector $\vec{\sigma}_T = (\sigma_M, \sigma_L)$ should be considered parallel to $\vec{\varepsilon}_T$, i.e., $\vec{\sigma}_T/|\vec{\sigma}_T| = \vec{\varepsilon}_T/|\vec{\varepsilon}_T|$. Such a formulation (Bažant and Prat 1988b), however, did not perform very well for complex loading paths. It appeared preferable and simpler to consider that σ_T in (14.1.25) stands either for σ_M or σ_L, i.e., $\sigma_M = F_T(\sigma_N)$ and $\sigma_L = F_T(\sigma_N)$, thus allowing $\vec{\sigma}_T$ and $\vec{\sigma}_T$ to be, in general, nonparallel. Of course, this implies a directional bias for the chosen orientations of axes M and L on each microplane. However, due to averaging on the macroscale, such a bias becomes negligible on the macroscale if the orientations of M and L on various microplanes are chosen with nearly equal probability (or frequency) for various possible orientations, and if there are many integration points of finite elements within the representative volume of material.

Function F_T defines only the boundary for positive stresses. The other, for negative stresses, is symmetric. The reason for writing the minus signs in (14.1.25) is that functions F_N, F_V, F_D are defined as positive-valued functions of positive arguments. Function F_T defines only the boundary for the magnitudes of the shear stresses (Fig. 14.1.5d). The dependence of σ_T on σ_N characterizes friction on the microplane, as well as the fact that a widely opened rough crack offers less resistance to shear than a narrow rough crack.

The response anywhere within the boundaries may be simply assumed to be elastic, as given in the rate

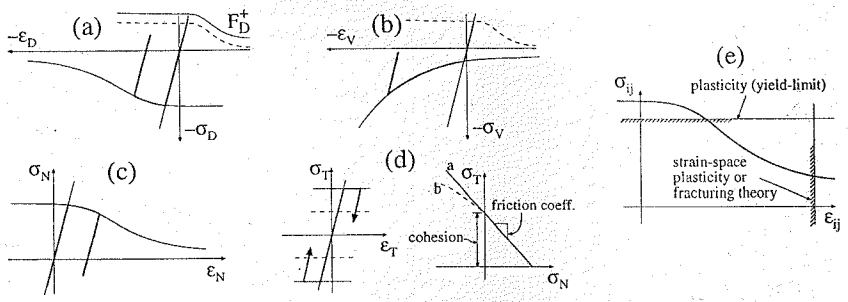

Figure 14.1.5 Stress-strain boundaries. General form for the deviatoric (a), volumetric (b), normal (c), and shear (d) components. For a classical macroscopic formulation, the boundary would be an arbitrary surface in the 12-dimensional σ_{ij}–ε_{ij} as indicated by the thick curve in (e). (Adapted from Bažant, Xiang and Prat 1996.)

form by equations similar to (14.1.18):

$$\dot{\sigma}_V = E_V \dot{\varepsilon}_V \,, \qquad \dot{\sigma}_D = E_D \dot{\varepsilon}_D \,, \qquad \text{and} \qquad \dot{\vec{\sigma}}_T = E_T \dot{\vec{\varepsilon}}_T \tag{14.1.26}$$

This simple assumption, of course, implies the stress-strain path for the microplane to exhibit a sudden change of slope when the elastic response arrives to the boundary curve. However, such changes of slope on the macroscale are not so abrupt because different microplanes reach the boundary at different times. Nevertheless, the response can be made smoother by the formulation in the following remark.

Remark: The response on the microscale can be made smooth by introducing a transition curve between the elastic straight line and the boundary curve. The transition curve, however, cannot be defined as a simple function of strains because the elastic lines and boundary curves are functions of different components. A helpful idea is to define the transition implicitly, in terms of (i) the elastic stress value σ^e and (ii) the boundary curve value σ^b, both of them corresponding to the same strain ε. When $\sigma^b \gg \sigma^e > 0$, the transition curve must nearly coincide with σ^e, and when $\sigma^e = \sigma^b$, it must lie farthest below both curves. These required properties can be achieved by the following formula for the transition curve (Bažant, Xiang and Prat 1996):

$$T(\sigma^e, \sigma^b) = \frac{\sigma^b + \sigma^e + \delta_1}{2} - \delta_0 \ln\left(2\cosh\frac{\sigma^b - \sigma^e - \delta_1}{2\delta_0}\right) \tag{14.1.27}$$

where $\sigma^e = \sigma_D^e, \sigma_N^e$, or σ_T^e; $\sigma^b = \sigma_D^b, \sigma_N^b$, or σ_T^b; and δ_1, δ_0 are constants, which have been chosen as $\delta_1 = 0.10\, f_0\, \text{sign}(\sigma^b)$ and $\delta_0 = 0.24\, f_0\, \text{sign}(\sigma^b)$ with $f_0 = f_D^0, f_N^0$, or f_T^0. For the volumetric boundary, no transition curve is introduced because the slope change is mild.

For $\delta_1 = 0$ the transition curve would approach the elastic curve and the boundary curve asymptotically at $\pm\infty$ (this may be easily checked by noting that, for large $|x|$, $2\cosh x = \exp|x|$). But the response near the origin of stress-strain space must be exactly elastic. Therefore, the left-side asymptote of the transition curve is shifted up by distance δ_1. This causes the transition to intersect the elastic curve. By choosing a small enough δ_1, the slope change at the intersection is small and acceptable.

The transition curve (14.1.27) with $\delta_1 = 0$ approaches the elastic line and the boundary curve exponentially, i.e., very rapidly. Another formula of similar properties was also explored: $T(\sigma^e, \sigma^b) = \{\sigma^b + \sigma^e + \delta_1 - [(\sigma^b - \sigma^e - \delta_1)^2 + \delta_0^2]^{1/2}\}/2$. This formula would be faster to execute computationally (which matters somewhat because it is evaluated a great many times). However, for $\delta_1 = 0$, it approaches the elastic and boundary curves too slowly, much slower than (14.1.27), which is therefore preferable. △

The stress-strain boundary may be regarded as a strain-dependent yield limit. Such an idea could hardly be introduced in the classical macroscopic invariant approach to plasticity, because the boundary would be a surface in a 12-dimensional space of all σ_{ij} and ε_{ij} components. The microplane concept makes the idea of strain-dependent yield limit feasible, in fact simple, because there are only a few components on the microplane level. The strain-dependent yield limit may be illustrated by the curve in Fig. 14.1.5e. The classical (stress space) plasticity is in this figure represented by the horizontal line for the yield limit. Now

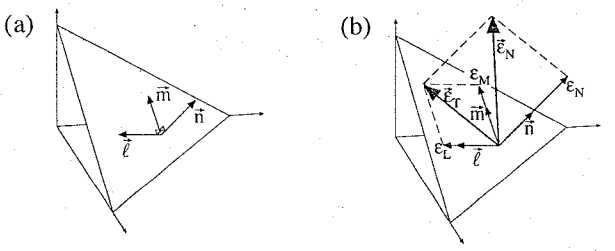

Figure 14.1.6 (a) Orthonormal base associated to a microplane. (b) Microstrain components.

note that plastic metals and fracturing materials (Dougill 1976) have also been satisfactorily described by strain-space plasticity, which corresponds to the vertical line in this figure. Obviously, a general curve should allow a better description because it is a combination of stress-space and strain-space plasticity theories.

14.1.5 Numerical Aspects

In finite element programs, a system of at least 21 microplanes must be associated with each integration point of each finite element (Bažant and Oh 1985, 1986; used in Bažant and Ožbolt 1990). Their number, however, can be reduced for the symmetries of plane stress, plane strain, axisymmetric behavior, and uniaxial stress.

For a given microplane, the normal and shear components of the microstrain vector are conveniently handled by defining an orthonormal base $\{\vec{n}, \vec{m}, \vec{\ell}\}$ (Fig. 14.1.6). Since the selection of $\vec{m}$ and $\vec{\ell}$ is arbitrary, we may, for example, choose vector m_i to be normal to the global axis x_3, in which case the cartesian components of $\vec{m}$ in the global coordinate system are $m_1 = n_2(n_1^2 + n_2^2)^{-1/2}, m_2 = -n_1(n_1^2 + n_2^2)^{-1/2}, m_3 = 0$ but $m_1 = 1$ and $m_2 = m_3 = 0$ if $n_1 = n_2 = 0$. To get a vector m_i normal to axis x_1 or axis x_2, we carry out permutations $123 \to 231 \to 312$ of the indices in the preceding equations. (To minimize directional bias, the procedure of generating vectors m_i should be such that if for one microplane m_i is normal to x_1, for the next numbered microplane it is normal to x_2, for the next to x_3, for the next again to x_1, etc.) The other coordinate vector ℓ_i within the microplane is obtained as vector product, $\vec{\ell} = \vec{m} \times \vec{n}$.

Once the components of the base vectors for the microplane are obtained, the determination of the components of the microstrain vector given the macrostrain tensor immediately follow as:

$$\varepsilon_N = N_{ij}\varepsilon_{ij} \,, \qquad \varepsilon_M = M_{ij}\varepsilon_{ij} \,, \qquad \varepsilon_L = L_{ij}\varepsilon_{ij} \tag{14.1.28}$$

where ε_M and ε_L are the components of the shear microstrain vector (i.e., $\vec{\varepsilon}_T = \varepsilon_M \vec{m} + \varepsilon_L \vec{\ell}$), and the projection tensors $\mathbf{N}$, $\mathbf{M}$, and $\mathbf{L}$ are given in component form by

$$N_{ij} = n_i n_j \,, \qquad M_{ij} = \frac{1}{2}(m_i n_j + m_j n_i) \,, \qquad L_{ij} = \frac{1}{2}(\ell_i n_j + \ell_j n_i) \tag{14.1.29}$$

To write an efficient finite element program, the values of $N_{ij}^\mu, M_{ij}^\mu, L_{ij}^\mu$ should be calculated, for all the discrete microplanes (labeled here by superscript μ), in advance of finite element analysis and stored in memory. The values of n_i^μ and of the weights w_μ in the integration formula (14.1.6) must also be stored in advance.

In each loading step, an explicit computational algorithm can be formulated as follows. First, the new values of macro-strains ε_{ij} are calculated at each integration point from the new (incremented) values of nodal displacements. Then, for each integration point, the new values of $\varepsilon_N, \varepsilon_M$, and ε_L are calculated for all the microplanes from (14.1.28) and the volumetric and deviatoric components ε_V and ε_D are determined from the first of (14.1.9) and (14.1.13). Using these values, the following new stress values

are calculated for each microplane:

$$\sigma_V^e = \sigma_V^i + E_V(\varepsilon_V - \varepsilon_V^i)\,,\ \sigma_D^e = \sigma_D^i + E_D(\varepsilon_D - \varepsilon_D^i)\,,\ \sigma_N^e = \sigma_V^e + \sigma_D^e \tag{14.1.30}$$

$$\sigma_M^e = \sigma_M^i + E_T(\varepsilon_M - \varepsilon_M^i)\,,\ \sigma_L^e = \sigma_L^i + E_T(\varepsilon_L - \varepsilon_L^i)\,,\ \sigma_V' = \mathrm{Max}[\sigma_V^e, -F_V(\varepsilon_V)] \tag{14.1.31}$$

$$\sigma_N' = \sigma_V' + \mathrm{Min}\{\mathrm{Max}[\sigma_D^e, -F_D(\langle -\varepsilon_D\rangle)], F_D^+(\langle\varepsilon_D\rangle)\} \tag{14.1.32}$$

$$\sigma_N = \mathrm{Min}[\sigma_N', F_N(\langle\varepsilon_N\rangle, \hat{\sigma}_V), \hat{\sigma}_V] \tag{14.1.33}$$

Superscripts i denote the previously calculated initial values at the beginning of the loading step, and superscripts e denote the new stress values based on elastically calculated increments; $\langle x\rangle = \mathrm{Max}(x, 0) =$ positive part of x (this symbol, called the Macauley bracket, is used so that functions $F_N, \ldots F_T$ could be defined for only the positive values of strain arguments), and $\hat{\sigma}_V = \sigma_V^i$, but if the load step is iterated, it helps accuracy to take $\hat{\sigma}_V$ as the value of σ_V obtained in the previous iteration. After sweeping through all the microplanes $\mu = 1, \ldots N_m$, one must calculate

$$\overline{\sigma}_V = \sum_{\mu=1}^{N_m} w_\mu \sigma_N^\mu \tag{14.1.34}$$

Then, for each microplane one can calculate

$$\sigma_V = \mathrm{Min}(\sigma_V', \overline{\sigma}_V) \tag{14.1.35}$$

for $\varepsilon_V - \varepsilon_V^i > 0$:

$$\sigma_T' = \mathrm{Min}\{\sigma_T^e, T[\sigma_T^e, F_T(\langle\varepsilon_T\rangle, \sigma_V)]\},\quad \sigma_T = \mathrm{Max}[\sigma_T', -F_T(\langle -\varepsilon_T\rangle, \sigma_V)] \tag{14.1.36}$$

for $\varepsilon_V - \varepsilon_V^i \le 0$:

$$\sigma_T' = \mathrm{Max}\{\sigma_T^e, T[\sigma_T^e, -F_T(\langle -\varepsilon_T\rangle, \sigma_V)]\},\quad \sigma_T = \mathrm{Min}[\sigma_T', F_T(\langle\varepsilon_T\rangle, \sigma_V)] \tag{14.1.37}$$

After sweeping again through all the microplanes, all the new values of the microplane stresses at the end of the loading step are known, and the macrostresses can then be calculated from (14.1.6) where the expression for the components of s_{ij} in terms of the components of the microstress vector is easily seen to be:

$$s_{ij} = \sigma_N N_{ij} + \sigma_M M_{ij} + \sigma_L L_{ij} \tag{14.1.38}$$

The inelastic parts of the new macrostresses must subsequently be modified according to a suitable nonlocal formulation. This subject is discussed later in Section 14.3.

Note that the foregoing algorithm gives the new stresses as explicit functions of the new strains. No equations need to be solved. This is important for computational efficiency.

14.1.6 Constitutive Characterization of Material on Microplane Level

By fitting of various types of test data for concrete, the following functions, characterizing the constitutive properties of the material, have been identified (Bažant, Xiang and Prat 1996):

$$F_V(-\varepsilon_V) = f_V^0 \exp\left(-\frac{\varepsilon_V}{k_1 k_5}\right),\quad f_V^0 = Ek_1k_4,\ \ (\text{any } \varepsilon_V) \tag{14.1.39}$$

$$F_D(-\varepsilon_D) = f_D^0\left(1 - \frac{\varepsilon_D}{k_1 c_2}\right)^{-1},\quad f_D^0 = Ek_1c_4,\ \ (\varepsilon_D \le 0) \tag{14.1.40}$$

$$F_D^+(\varepsilon_D) = c_5 f_D^0\left(1 + \frac{\varepsilon_D}{k_1 c_2 c_5}\right)^{-1},\quad (\varepsilon_D \ge 0) \tag{14.1.41}$$

$$F_N(\varepsilon_N, \sigma_V) = f_N^0\left[1 + \left(\frac{\varepsilon_N}{c}\right)^2\right]^{-1},\ c = c_1k_1 + \left\langle\frac{-c_3\hat{\sigma}_V}{\varepsilon_V}\right\rangle,\ f_N^0 = Ek_1,\ (\varepsilon_N \ge 0) \tag{14.1.42}$$

$$F_T(\sigma_N) = \langle Ek_1k_2 - k3\sigma_N\rangle \tag{14.1.43}$$

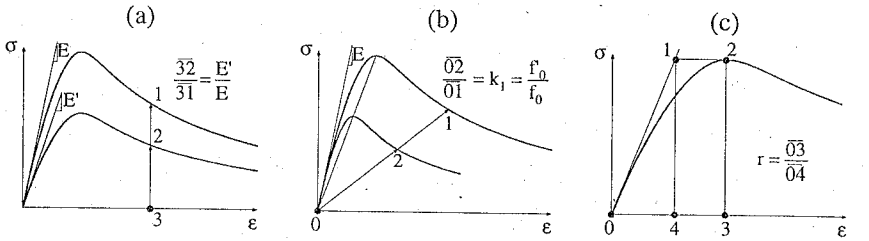

Figure 14.1.7 (a-b) Vertical and radial scaling (affinity transformations) of the stress-strain curves, and (c) concept of ductility as a ratio $\overline{03}/\overline{04}$ (from Bažant, Xiang and Prat 1996).

in which $k_1, \ldots, k_5$ are adjustable empirical constants, which take different values for different types of concretes, while $c_1, \ldots, c_5$ are fixed empirical constants that can be kept the same for all normal concretes. They have the values $c_1 = 5, c_2 = 6, c_3 = 50, c_4 = 130$, and $c_5 = 6$ (parameter c_5 affects almost only the standard triaxial tests at very high pressures). It has been recommended that, in absence of sufficient test data, the adjustable parameters may be taken with the following reference values $k_1 = 72 \times 10^{-6}, k_2 = 0.1, k_3 = 0.05, k_4 = 15$, and $k_5 = 150$. The value of Poisson's ratio may be considered as $\nu = 0.18$. Except for E, all the parameters are dimensionless.

The macroscopic Young's modulus is a parameter whose change causes a vertical scaling transformation (affinity transformation) of all the response stress-strain curves. If this parameter is changed from E to some other value E', all the stresses are multiplied by the ratio E'/E at no change of strains (Fig. 14.1.7a). Parameter k_1 describes radial scaling (affinity transformation) with respect to the origin. If this parameter is changed from k_1 to some other value k_1', all the stresses and all the strains are multiplied by the ratio k_1'/k_1 (Fig. 14.1.7b).

The aforementioned reference values of material parameters along with E =58000 MPa yield the uniaxial compression strength f_c' =42.4 MPa, as calculated by simulating the uniaxial compression test by incremental loading. The strain corresponding to the stress peak has been found to be $\varepsilon_p = 0.0022$. Now, if the user needs a microplane model that yields the uniaxial compressive strength f_c^* and the corresponding strain at peak ε_p^*, one needs to modify the reference values of only two parameters as follows:

$$k_1^* = k_1\frac{\varepsilon_p^*}{\varepsilon_p},\qquad E^* = E\frac{f_c^*}{f_c'}\frac{\varepsilon_p}{\varepsilon_p^*} \tag{14.1.44}$$

Table 14.1.1 shows the values of f_c', f_t' for some typical values of material parameters ("R" in Table 14.1.1 refers to the reference values stated above). It also gives the corresponding ductility $r = \varepsilon_p E/f'$, representing the ratio $\overline{03}/\overline{04}$ in Fig. 14.1.7c. The smaller r, the steeper the postpeak softening. The transformations according to (14.1.44) do not change the ratio r.

The aforementioned reference values of material parameters have been selected so that the ratio of tensile to compressive uniaxial strengths be approximately $f_t'/f_c' = 0.082$; the ratio of equitriaxal to uniaxial compression strength $f_{bc}'/f_c' = 1.17$; the ratio of the strength in pure shear to the uniaxial compressive strength approximately $f_c^s/f_c' = 0.069$; the ratio of residual stress for very large uniaxial compressive strain to the uniaxial compression strength approximately $\sigma_r/f_c' = 0.07$; and the ratio of residual stress for very large shear strain to the shear strength approximately $\tau_r/f_c^s = 0.3$. The transformations according to (14.1.44) do not change these ratios. These ratios can be changed only by adjusting material parameters other than E and k_1.

Parameters k_4 and k_5 can be determined exclusively from the data on hydrostatic compression tests. Taking the logarithm of (14.1.43), the equation can be reduced to a linear regression plot, and thus parameters k_4 and k_5 can be obtained by fitting the data on the hydrostatic compression test, separate from all other parameters (because the value of ε_V for hydrostatic compression is the same for all microplanes and $\varepsilon_D = \varepsilon_M = \varepsilon_L = 0$ for all microplanes). The softening tail in uniaxial compression can be lengthened by increasing c_2 while reducing k_1 a little, and for tension by reducing k_3 while reducing k_1

Table 14.1.1 Strength, ductility, and typical material parameters

Tests	E	k_1	k_2	k_3	k_4	bf k_5	$k_6(10^{-6})$	f'_c	r_c	f'_t	r_t
Hognestad	3900	120	R	R	R	R	R	5.18	1.96	0.46	1.78
van Mier	29000	R	R	R	R	R	R	40.0	1.98	3.75	1.80
Petersson	26000	R	R	R	0.4	R	R	32.1	2.43	3.62	1.65
Bažant	6000	112	R	R	R	12	175	7.55	1.91	0.69	1.73
Green	5100	R	R	R	R	R	125	7.39	1.93	0.66	1.78
Balmer	3500	90	20	R	0.5	18	R	3.05	2.29	0.33	1.71
Bresler	5100	R	R	0.2	R	R	R	6.49	2.36	0.40	2.44
Kupfer	5100	R	40	0.3	.06	R	R	4.86	4.41	0.62	2.22
Launay	5100	R	R	R	0.3	R	R	4.87	2.93	0.77	1.73
Sinha	3200	113	R	R	R	R	R	4.00	2.07	0.36	1.79

"R" means reference values; $r_c = \varepsilon_c^p E/f'_c$, $r_t = \varepsilon_t^p E/f'_t$

a little. The ratio of the tensile-to-compressive strength can be increased by reducing c_4 or k_3. The ratio of the strength in pure shear to the uniaxial compressive strength can be increased by increasing k_2 while reducing c_4 or k_3 a little.

14.1.7 Microplane Model for Finite Strain

In some applications of the microplane model, for example, the impact of missiles into hardened concrete structures or nuclear reactor containments, or the analysis of energy absorption of a highly confined column in an earthquake, very large strains, ranging from 10% to 200%, and shear angles up to 40°, have been encountered in calculations. For such situations, the microplane model must be generalized to finite strain. However, a thorough exposition of the finite strain generalization would require introducing advanced mathematical apparatus that has not yet appeared in this book. Therefore, only a summary of the main results will be given here. The interested reader can find the details in Bažant, Xiang and Prat (1996) and Bažant, Xiang et al. (1996) for the case of moderately large strains (up to about 10%), and in Bažant (1997b) for the case of very large strains (100% or more, with shear angles up to 40°).

The simplest finite strain tensor to use is Green's Lagrangian strain tensor $\mathbf{E} = (\mathbf{F}^T\mathbf{F} - \mathbf{1})/2$ where $\mathbf{F}$ is the deformation gradient and $\mathbf{1}$ the unit tensor (see, e.g., Bažant and Cedolin 1991, Chapter 11). Its conjugate stress tensor, that is the tensor for which Green's Lagrangian strain tensor gives a correct work expression $dW = \mathbf{T} \cdot d\mathbf{E}$, is a tensor called the second Piola-Kirchhoff stress tensor, $\mathbf{T} = \mathbf{F}^{-1}J\mathbf{S}\mathbf{F}^{-T}$ where $J = \det \mathbf{F}$ is the Jacobian of the transformation (giving the relative volume change); $\mathbf{F}^{-T} = (\mathbf{F}^{-1})^T = (\mathbf{F}^T)^{-1}$.

Difficult problems arise in the modeling of very large strains. In finite-strain generalization of the microplane model, a definite physical meaning needs to be attached to the normal and shear strain components on the microplanes. In this regard, the following two conditions must be met:

Condition I. The normal and shear components of the stress tensor used in the constitutive relation must uniquely characterize the normal and shear components of the tensor of true stress $\mathbf{S}$ in the deformed material, called the Cauchy stress tensor.

Condition II. The normal strain component e_N, characterizing the stretch λ_N of a material line segment in the direction $\vec{n}$ initially normal to the microplane, must be independent of the stretches of material line segments in other initial directions. Furthermore, the shear strain component e_{NM} (or e_{NL}), characterizing the change of angle θ_{NM} or θ_{NL} between two initially orthogonal material line segments with initial unit vectors $\vec{n}$ and $\vec{m}$ (or $\vec{n}$ and $\vec{\ell}$), must be independent of the stretches and angle changes in planes other than $(\vec{n}, \vec{m})$ or $(\vec{n}, \vec{\ell})$.

Consider first only condition I. It turns out that, in this regard, the use of the second Piola-Kirchhoff stress tensor is possible only if the largest magnitude of the principal strains is less than about 7% to 10%, i.e., if the strain is only moderately large. It has been shown by numerical examples (Bažant 1997b) that, for large isochoric deformations, the shear components of the second Piola-Kirchhoff stress tensor $\mathbf{T}$ strongly depend on the volumetric component of the Cauchy (true) stress tensor $\mathbf{S}$ (i.e., the true hydrostatic pressure), and the volumetric component of the second Piola-Kirchhoff stress tensor strongly

depends on the shear components of the Cauchy stress tensor. This indicates that the projections of the second Piola-Kirchhoff stress tensor on the microplanes have no physical meaning. They cannot be used to characterize the strength, yield limit and damage on the microplane, nor the phenomenon of friction.

The stress tensor must be referred to the initial configuration of the material (as required for the modeling of a solid remembering the initial state). The only such tensor whose microplane components have a physical meaning is the rotated Kirchhoff stress tensor $\boldsymbol{\tau} = \mathbf{R}^T J\mathbf{S}\mathbf{R}$, where $J\mathbf{S}$ represents the Kirchhoff stress tensor, and $\mathbf{R}$ is the material rotation tensor defined in the polar decomposition of the deformation gradient $\mathbf{F} = \mathbf{R}\mathbf{U} = \mathbf{V}\mathbf{R}$. Here, $\mathbf{U}$ and $\mathbf{V}$ are the right and left stretch tensors. When the principal stress axes do not rotate against the material, the rotated Kirchhoff stress tensor is equal to the Cauchy (true) stress tensor scaled by a scalar factor, J. Only this tensor is free of the aforementioned problems revealed by numerical examples.

A variational procedure can be used to obtain an expression for the finite strain tensor $\boldsymbol{\gamma}$ that is conjugated by work with the rotated Kirchhoff stress tensor $\boldsymbol{\tau}$. If the principal strain axes do not rotate against the material, this tensor is found to be identical to Hencky's (logarithmic) strain tensor. However, when the principal strain axes rotate, one obtains an incremental expression for $d\boldsymbol{\gamma}$ that cannot be integrated. This means that the strain tensor conjugate to the rotated Kirchhoff stress tensor is nonunique, path-dependent (nonholomonic).

The aforementioned path-dependence is strong and unacceptable, except for moderately large strains less than about 7% to 10%. For such strains, and for larger strains for which the rotations of principal strain axes is small, the use of Hencky's strain tensor is advantageous. However, there is also the problem of the efficient calculation of the Hencky tensor. This tensor is defined by the spectral representation, which is computationally demanding for large finite element programs in which this tensor may have to be calculated up to a billion times. Nevertheless, an easy-to-compute very close approximation of the Hencky strain tensor has recently been found (Bažant 1997c).

Consider now condition II. The relative length change of a segment normal to the microplane from length dS (in the initial configuration) to length ds (in the deformed configuration) is characterized, e.g., by $e_N = (ds - dS)/dS$ (called Biot strain or engineering strain). The change of angle between the microplane normal vector $\vec{n}$ and vector $\vec{m}$ in the microplane represents the shear angle θ_{NM}. When Green's Lagrangian strain tensor $\mathbf{E}$ is used, e_N can be expressed (exactly) in terms of the normal component E_N, and θ_{NM} can be expressed (exactly) in terms of the shear component E_{NM} and the normal components E_N, E_M (see, e.g., Malvern 1969, pp.165–166). In other words, the exact change of length in normal direction and of shear angle for a microplane can be expressed solely in terms of the strain tensor components on the same microplane. This is not true, however, for all the other strain tensors, including Hencky's (logarithmic) strain tensor and Biot's strain tensor. For them, the exact e_N and θ_{NM} depend also on the ratio of the principal strains (which seems an inconvenient feature for the programming of microplane model and would increase demands on computer time). This dependence can be neglected only when the maximum principal strain is less than about 25% (Bažant 1997d).

It thus appears that, for large strains (i.e., when the maximum principal strain exceeds 7% to 10%) the only suitable strain and stress tensors are Green's Lagrangian strain tensor and the rotated Kirchhoff stress tensor. These two tensors are not conjugate.

It has normally been considered a taboo to use nonconjugate stresses and strains. However, due to the special character of the present microplane model, the use of nonconjugate stresses and strains in formulating a constitutive relation is admissible if certain precautions are taken (see Bažant 1995d and Bažant, Adley and Xiang 1996). One point to note in this regard is that the constitutive relation in terms of the aforementioned nonconjugate stress and strain tensors is a transformation of the constitutive relation in terms of conjugate stress and strain tensors such that the transformation depends only Green's Lagrangian strain tensor (or the stretch tensor) but, importantly, is independent of the material rotation tensor. Such a transformation is perfectly admissible. The second point to note is that nonnegativeness of energy dissipation is ensured for two reasons: (1) The elastic parts of strains are always small (which ensures that the elastic part of the nonconjugate stress-strain relation preserves energy), and (2) the drop of stress to the boundary surface is carried out in each load step at constant strain and cannot cause negative energy dissipation.

A further precaution that must be taken is that the work done by the stresses (or by the nodal forces on displacements) cannot be directly calculated from the stresses and strains used in the constitutive law, because the areas under the stress-strain curves for the nonconjugate constitutive law do not correctly

characterize energy dissipation. If the work needs to be calculated, one can easily obtain the second Piola-Kirchhoff stress tensor from the rotated Kirchhoff stress tensor and evaluate the work that way. Also, elastic response cannot be described as a functional relation between nonconjugate stresses and strains.

For moderately large strains, of course, the conjugate pair or Green's Lagrangian strain tensor and second Piola-Kirchhoff strain tensor can be used, and has been used by Bažant, Xiang and Prat (1996) in a finite strain generalization of the microplane model. There is, however, a gap in the experimental data for very large strains of concrete. To fill this gap, one must get reconciled with the fact that it is next to impossible to keep the specimen deformation uniform when triaxial deformations become large. Triaxial test data on concrete at strains up to shear angle of 35° at very high hydrostatic pressures (several times the uniaxial compression strength) have recently been obtained by Bažant and Kim (1996b) using a novel type of test, called the 'tube-squash' test. In this test, a thick-walled tube of very ductile steel is filled with concrete, and after curing, it is compressed axially to about half the initial length. The concrete undergoes shear angles over 30°. Due to high confining pressure (which exceeds 1000 MPa), the concrete in the tube retains integrity and small cores can be drilled out from the concrete. These cores show uniaxial compression strength between 20% and 50% of the virgin concrete, both for normal and high strength concretes. In the evaluation of the 'tube-squash test' one must fit the measured load-displacement curves with a finite element program incorporating finite strain constitutive models for both the concrete and the steel.

Finite strain tests need to be also carried out at small hydrostatic (confining) pressures, at which concrete turns into rubble when large deformations occur. A constitutive relation for such rubbelized concrete at finite strain needs to be developed.

Another problem that needs to be resolved for the microplane model is the split of total normal strain into deviatoric and volumetric components. The decomposition of large deformations into their volumetric and deviatoric (strictly speaking, isochoric) parts is, in general, multiplicative. Specifically, it has the form $\mathbf{U} = \mathbf{F}_D\mathbf{U}_V$ (Flory 1961; Sidoroff 1974; Simo 1988; Simo and Ortiz 1985; Lubliner 1986; Bell 1985) where $\mathbf{U}$ is the right stretch tensor, $\mathbf{U}_V$ the volumetric right-stretch tensor, and $\mathbf{F}_D =$ the deviatoric transformation tensor. An additive volumetric-deviatoric decomposition exists only for the Hencky (logarithmic) strain tensor $\mathbf{H}$.

For any type of finite strain tensor, however, an approximate additive decomposition in terms of volumetric strain tensor $\mathbf{E}_V = \varepsilon_V\,\mathbf{1}$ and deviatoric strain tensor $\mathbf{E}_D$ is possible for materials that can exhibit only large deviatoric strains but not large volumetric strains (Bažant 1996c), as is the case for concrete. Unlike $\mathbf{F}_D$, the components of $\mathbf{E}_D$ depend on J, i.e., the relative volume change (unless the Hencky strain tensor is used). However, their dependence on J is, in the case of Green's Lagrangian strain tensor, negligible if the volume change is less than about 3% in magnitude (Bažant, Xiang and Prat 1996; Bažant, Xiang et al. 1996). For Biot strain tensor $\mathbf{E}^b = \mathbf{U} - \mathbf{1}$ (Biot 1965; Ogden 1984; Bažant and Cedolin 1991), the limit is about 8% (for concrete, the volume change is -3% at highest pressure tested so far, which is 300000 psi or 2069 MPa; Bažant, Bishop and Chang 1986). Thus, the classical multiplicative decomposition, which is not as convenient for calculations as the additive decomposition, seems to be inevitable only for materials exhibiting very large volume changes, such as stiff foams. An additive decomposition of the aforementioned kind, developed in Bažant (1996c), was used by Bažant, Xiang and Prat (1996) in the generalization of the microplane model for moderately large finite strains of concrete.

The multiplicative decomposition could nevertheless be implemented in the microplane model by decomposing each loading step into two substeps, pure volumetric deformation followed by pure isochoric deformation, but that would greatly complicate the analysis, especially if the solution is not explicit.

14.1.8 Summary of Main Points

This section has explained the basic concept and the latest formulation of the general microplane model for concrete—a constitutive model in which the nonlinear triaxial behavior is characterized by relations between the stress and strain components on a microplane of any orientation under the constraint that the strains on the microplane are the projections of the macroscopic stress tensor. The microplane model simplifies constitutive modeling because the stress-strain relation on the microplane level involves only a few stress and strain components that have a clear physical meaning. The passage from elastic response to softening damage defined in terms of different variables is effectively handled by the concept of boundaries in the stress-strain space. The advantage of this recently proposed concept is that various boundaries and the elastic behavior can be defined as a function of different variables (strain components). While the stress-strain boundaries for compression are defined separately for volumetric and deviatoric components, the boundary for tension is defined in terms of the total normal strains. This is necessary to achieve a realistic triaxial response at large tensile strains. A smooth transition from the elastic behavior to the boundary curve has also been formulated. The formulation is fully explicit, that is, the stress can be explicitly calculated from given strains.

Exercises

14.1 Based on symmetry properties, show that the rectangular cartesian components of the tensor $\mathbf{A}$ in (14.1.20) satisfy the following properties: (a) the off-diagonal components are zero; (b) the diagonal elements are equal. (c) Demonstrate that $\mathbf{A} = A\mathbf{1}$, where A is a scalar, and (d) compute A. (Hint: compute tr $\mathbf{A} = 3A = (3/2\pi)\int d\Omega$ —Why?)

14.2 Show that $\mathbf{A}$ in (14.1.20) can be written as $\mathbf{A} = (3/4\pi)\int_\Omega \vec{r}\otimes\vec{n}\,d\Omega$ where the integral is now extended to the surface of the whole unit sphere and $\vec{r}$ is the position vector relative to the center of this sphere. Apply the divergence theorem to this surface integral and show that $\mathbf{A} = (3/4\pi)\int_V \text{grad}\,\vec{r}\,dV$ where V is the region defined by the unit sphere. Use this expression to determine $\mathbf{A}$.

14.3 Let B_{ijkl} be the rectangular cartesian components of the fourth-order tensor $\boldsymbol{B}$ in (14.1.20). Show that they satisfy the relations (a) $B_{ijkl}\delta_{kl} = A_{ij}$ and $B_{ijkl}\delta_{jk} = A_{il}$. A basic property of linear elasticity is that the most general cartesian form of an isotropic fourth-order tensor of elastic moduli, say $\boldsymbol{B}$, such that $\boldsymbol{\sigma} = \boldsymbol{B\varepsilon}$ is isotropic, is $B_{ijkl} = B_0\delta_{ij}\delta_{kl} + B_1\delta_{ik}\delta_{jl}$, where B_0 and B_1 are constants. (b) Use the results in (a) to show that for $\boldsymbol{B}$ in (14.1.20) $B_0 = 0$ and $3B_1 =$ tr $\mathbf{A}$. (c) Use the result of the previous exercise to determine B_1.

14.4 Show that $\boldsymbol{B}$ in (14.1.20) can be written as $\boldsymbol{B} = (3/4\pi)\int_\Omega \vec{r}\otimes\vec{r}\otimes\vec{r}\otimes\vec{n}\,d\Omega$ where now the integral is extended to the surface of the whole unit sphere and $\vec{r}$ is the position vector relative to the center of this sphere. Apply the divergence theorem to this surface integral and show that $\boldsymbol{B} = (3/4\pi)\int_V \text{grad}\,(\vec{r}\otimes\vec{r}\otimes\vec{r})\,dV$ where V is the region defined by the unit sphere. Show that the component form of this integral can be reduced to $B_{ijkl} = \delta_{il}J_{jk} + \delta_{jl}J_{ik} + \delta_{kl}J_{ij}$ where $\mathbf{J}$ is the Euler tensor of inertia products for a sphere of unit radius and unit density with respect to its center:

$$\mathbf{J} = \int_V \vec{r}\otimes\vec{r}\,dV \qquad \text{or} \qquad J_{ij} = \int_V x_i x_j\,dV \tag{14.1.45}$$

Use the well-known result that the inertia moment of a homogeneous sphere relative to any diameter is $2mR^2/5$, with $m =$ mass and $R =$ radius of the sphere, to prove that $\mathbf{J} = (1/5)\mathbf{1}$. Finally, determine the general expression for the components B_{ijkl}.

14.2 Calibration by Test Data, Verification and Properties of Microplane Model

Following the general theoretical formulation in the preceding section, we will now demonstrate calibration and verification of the microplane model by fitting of the relevant test data from the literature. We will also show how the data afflicted by localization of damage within the gage length can be decontaminated.

14.2.1 Procedure for Delocalization of Test Data and Material Identification

Until very recently it has been general practice to identify the postpeak stress-strain relation from test data ignoring the fact that the deformation of the specimen within the gage length often becomes nonuniform, due to localization of cracking damage. The fact that damage must localize, except in the smallest possible specimens, was shown in detail in Chapter 8. The correct analysis of localization in strain softening materials led first to the development of the crack band model (Chapter 8), and later to the more sophisticated models described in the preceding chapter. The localization phenomena were already documented in the early eighties. However, because the general problem of identification of material parameters in presence of strain-softening localization (Ortiz 1987) is tremendously complex, the contamination of test

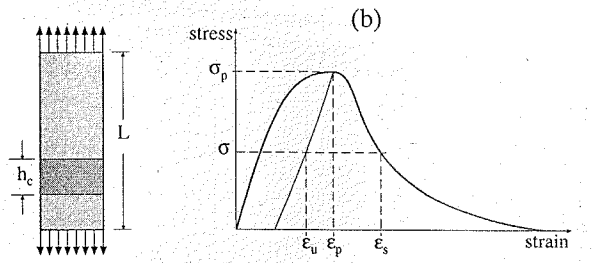

Figure 14.2.1 Underlying crack-band model (series coupling model) for filtering of strain softening localization from laboratory test data.

data by localization has typically been ignored. At the present state of knowledge, however, this is no longer acceptable. The data must be decontaminated, delocalized. An approximate procedure to do that, applicable to any type of constitutive model, was recently proposed by Bažant, Xiang et al. (1996).

The delocalization cannot, and need not, be done with a high degree of accuracy and sophistication. In the identification of the microplane model by Bažant, Xiang et al. (1996), the test data from laboratory specimens have been analyzed taking into account the strain localization in an approximate manner. The idea is to exploit two simple approximate concepts: (1) localization in the series coupling model described in Sections 8.1–8.3, and (2) the effect that energy release due to localization within the cross section of specimen has on the maximum load, as described by Bažant's size effect law (Section 1.4 and Chapter 6).

The strain as commonly observed is the average strain ε_m on a gage length L. According to the series coupling model and the crack band model (Sections 8.1–8.3), the strain may be assumed to localize after the peak into a band of width h_c, as depicted in Fig. 14.2.1a, while the remainder of the gauge length unloads. In this way, the strain of the material inside the localized zone is ε_s —corresponding to the softening branch— while in the remaining part the strain is ε_u, as given by the unloading curve from the peak (Fig. 14.2.1b).

The strain that the constitutive model for damage should predict is the strain ε_s in the localization zone. But this strain is difficult to measure, for three reasons: (1) the size of the localization zone is small, which reduces the accuracy of strain measurements; (2) the location of the localization zone is uncertain, and so one does not know where to place the gage; and (3) the deformation of the localization zone is quite random while the constitutive model predicts the statistical mean of many random realizations (determining this mean requires taking measurements on many specimens). Therefore, a simplified method is desirable based on measuring only the average strain ε_m.

To find the simplified formula, we note that the total increment of the gauge length ΔL (equal to $L\varepsilon_m$ by definition) is obtained by adding the contributions of the softening and unloading regions, i.e.,

$$L\varepsilon_m = h_c\varepsilon_s + (L - h_c)\varepsilon_u \tag{14.2.1}$$

If we further assume that the unloading proceeds parallel to the initial elastic loading (i.e., stiffness degradation up to the peak is negligible), then the unloading strain is $\varepsilon_u = \varepsilon_p - (\sigma_p - \sigma)/E$, where E is the elastic modulus and ε_p and σ_p are the strain and stress at the peak of the stress-strain curve for the given type of loading (Fig. 14.2.1b). So we finally get

$$\text{for } \varepsilon_m > \varepsilon_p: \qquad \varepsilon_s = \frac{L}{h_c}\varepsilon_m - \frac{L - h_c}{h_c}\left(\varepsilon_p - \frac{\sigma_p - \sigma}{E}\right) \tag{14.2.2}$$

To correct the given test data according to (14.2.2), one must obviously know the value of the localization length h_c. It is impossible to determine this length from the reports on the uniaxial, biaxial, and triaxial tests of concrete found in the literature. However, a reasonable estimate can be made by experience from other studies; $\ell \approx 3d_a$ where d_a = maximum size of the aggregate in concrete (for high-strength concretes, ℓ is likely smaller, perhaps as small as $\ell = d_a$).

Bažant, Xiang et al. 1996 further proposed an approximate procedure to filter out of the given tensile test data the size effect on the maximum tensile stress. This procedure was based on the size effect law. According to the size effect on maximum load, they scaled the measured response curve by affinity transformation with respect to the strain axis and in the direction parallel to the elastic slope. Thus, they obtained the response curve with the peak tensile stress corresponding to specimen of size h_c.

14.2.2 Calibration of Microplane Model and Comparison with Test Data

The microplane model we described has been calibrated and compared to the typical test data available in the literature (Bažant, Xiang et al. 1996). They included: (**1**) uniaxial compression tests by van Mier (1984, 1986; Fig. 14.2.2a), for different specimen lengths and with lateral strains and volume changes measured, and by Hognestad, Hanson and McHenry (1955; Fig. 14.2.2b); (**2**) uniaxial direct tension tests by Petersson (1981; Fig. 14.2.2c); (**3**) uniaxial strain compression tests of Bažant, Bishop and Chang (1986; Fig. 14.2.2d); (**4**) hydrostatic compression tests by Green and Swanson (1973; Fig. 14.2.2e); (**5**) standard triaxial compression tests (hydrostatic loading followed by increase of one principal stress) by Balmer (1949; Fig. 14.2.2f); (**6**) uniaxial cyclic compression tests of Sinha, Gerstle and Tulin (1964; Fig. 14.2.2g). (**7**) tests of shear-compression failure envelopes under torsion by Bresler and Pister (1958) and Goode and Helmy (1967; Fig. 14.2.3a); (**8**) tests of biaxial failure envelope by Kupfer, Hilsdorf and Rüsch (1969; Fig. 14.2.3b); and (**9**) failure envelopes from triaxial tests in octahedral plane (π-projection) by Launay and Gachon (1971; Fig. 14.2.3c).

As seen from the figures, good fits of test data can be achieved with the microplane model. In Fig. 14.2.2a it should be noted that the uniaxial compression stress-strain diagrams are well represented for three specimens lengths, $\ell = 5$, 10, and 20 cm (it was already shown that the series coupling describes well the length effect in these tests; see Bažant and Cedolin 1991, Sec. 13.2). Fig. 14.2.2d serves as the basis for calibrating the volumetric stress-strain boundary, and a good fit is seen to be achieved for these enormous compressive stresses (up to 300 ksi or 2 GPa). Fig. 14.2.2f shows that the large effect of the confining pressure in standard triaxial tests can also be captured.

In Fig. 14.2.2g, note that the subsequent stress peaks in cycles reaching into the softening range are modeled quite correctly, and so are the initial unloading slopes. Significant differences, however, appear at the bottom of the cyclic loops, which is due to the fact that the unloading modulus is, in the present model, kept constant (a refinement would be possible by changing the constant unloading slope on the microplane level to a gradually decreasing slope, of course, with some loss of simplicity). It should also be noted that the loading in these tests was quite slow and much of the curvature may have been due to relaxation caused by creep.

In Fig. 14.2.3c note that the model predicts well the shape of the failure envelopes, which is noncircular and nonhexagonal, corresponding to rounded irregular hexagons squashed from three sides. Fig. 14.2.3b shows that the ratio of uniaxial and biaxial compression strengths found in these tests can be modeled.

It must be emphasized that all the solid curves plotted in the figures are the curves that are predicted by the microplane model. The dotted curves in Fig. 14.2.2 are those after correction according to the series coupling model. The dashed curves in Fig. 14.2.2c are those after correction according to the size effect law, and the dotted curves are those after a further correction according to the series coupling model.

Note that only six parameters need to be adjusted if a complete set of uniaxial, biaxial, and triaxial test data is available, and two of them can be determined separately in advance from the volumetric compression curve. If the data are limited, fewer parameters need to be adjusted. The parameters are formulated in such a manner that two of them represent scaling by affinity transformation. Normally only these two parameters need to be adjusted, which can be done by simple closed-form formulas. Thus, we can conclude that the model may be efficiently used to describe concrete behavior in uniaxial, biaxial, and triaxial situations.

14.2.3 Vertex Effects

There is another important property that is exhibited by the microplane model, and not, for example, by macroscopic plasticity models. For a nonproportional path with an abrupt change of direction such that the load increment in the σ_{ij} space is directed parallel to the yield surface, the response of a plasticity model is perfectly elastic, unless this change of direction happens at a corner of the yield surface. But

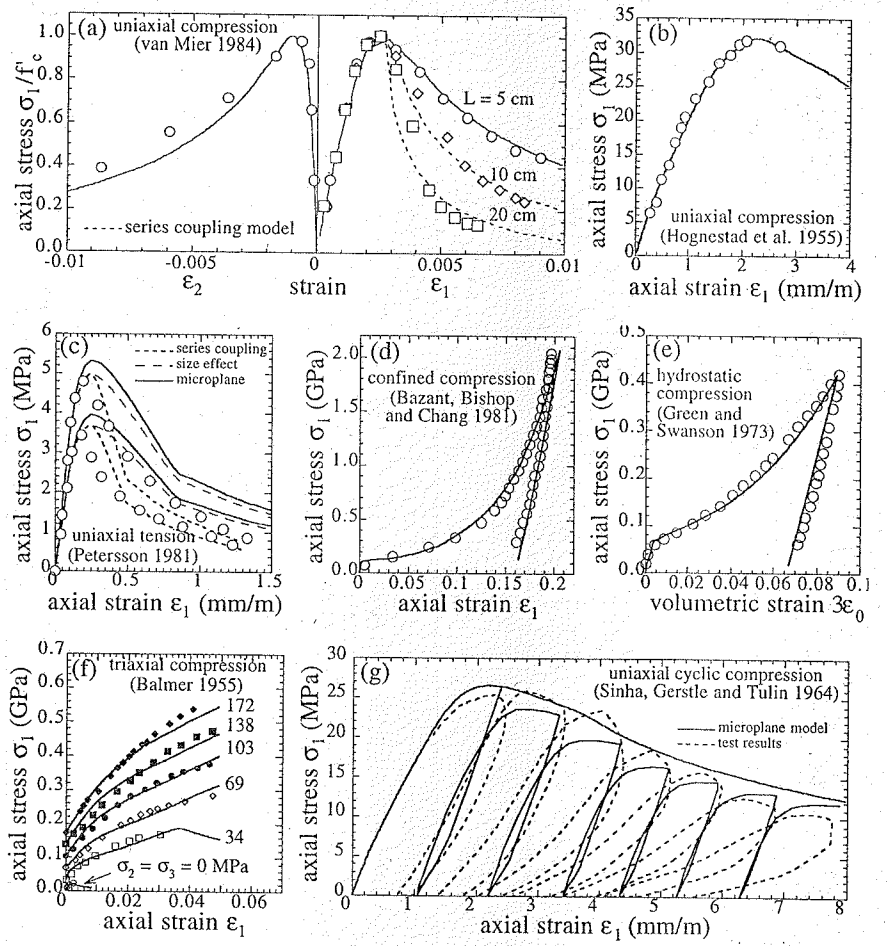

Figure 14.2.2 Experimental results from various sources and best fits with the microplane model (after Bažant, Xiang et al. 1996): (a) uniaxial compression tests by van Mier (1984); (b) uniaxial compression tests by Hognestad, Hanson and McHenry (1955; (c) uniaxial tension tests by Petersson (1981); (d) confined compression test (uniaxial strain) of Bažant, Bishop and Chang (1986); (e) hydrostatic compression test by Green and Swanson (1973); (f) triaxial test data (increasing axial compression at constant lateral confining pressure) by Balmer (1949); (g) uniaxial cyclic compression tests of Sinha, Gerstle and Tulin (1964). (Adapted from Bažant, Xiang et al. 1996.)

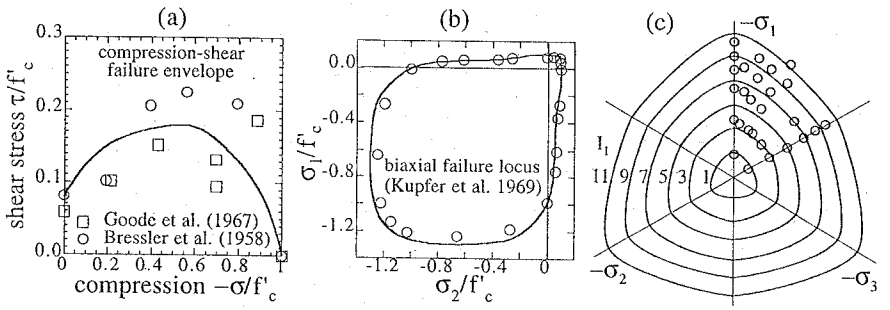

Figure 14.2.3 Fitting of (a) shear compression failure envelope (in torsion) measured by Bresler and Pister (1958), (b) biaxial failure envelope measured by Kupfer, Hilsdorf and Rüsch (1969), and (c) failure envelopes in hydrostatic planes at various pressures measured by Launay and Gachon (1971). (Adapted from Bažant, Xiang et al. 1996.)

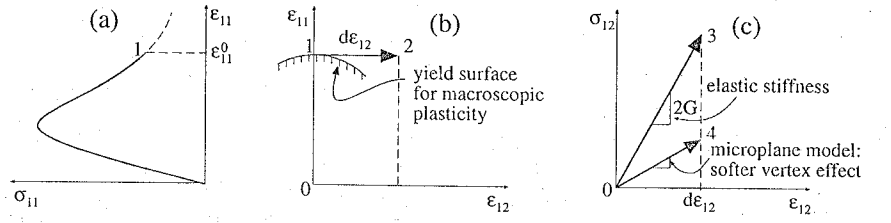

Figure 14.2.4 Vertex effect: (a) preloading in the σ_{11}-ε_{11} space at increasing ε_{11} and zero shear strain; (b) in the ε_{11}-ε_{12} space preloading corresponds to segment $\overline{01}$ and further tangent loading to segment $\overline{12}$; (c) the further tangent loading in the σ_{12}-ε_{12} diagram corresponds to segments $\overline{03}$ in classical plasticity models (fully elastic loading) and to segment $\overline{04}$ when vertex effect is present (after Bažant, Xiang et al. 1996).

in reality, for all materials, this response is softer, in fact much softer, than elastic. It is as if a corner or vertex of the yield surface traveled with the state point along the path.

This effect, called the vertex effect (see Sec. 10.7 in Bažant and Cedolin 1991), is automatically described by the microplane model, but is very hard to model with the usual plastic or plastic-fracturing models. It can be described only by models with many simultaneous yield surfaces, which are prohibitively difficult in the σ_{ij} space. The microplane model is, in effect, equivalent to a set of many simultaneous yield surfaces, one for each microplane component (although these surfaces are described in the space of microplane stress components rather than in the σ_{ij} space).

This is one important advantage of the microplane approach. It is, for example, important for obtaining the correct incremental stiffness for the case when a $d\varepsilon_{12}$-increment (segment $\overline{12}$ in Fig. 14.2.4b) is superimposed on a large strain ε^0_{11} (segment $\overline{01}$) in the inelastic range. Segment $\overline{03}$ in Fig. 14.2.4c is the predicted response according to all classical macroscopic models with yield surfaces, which is elastic, and segment $\overline{04}$ is the prediction of microplane model, which is much softer than elastic (i.e., $d\sigma_{12}/d\varepsilon_{12} < 2G$ where G = elastic shear modulus). Fig. 14.2.4c shows the incremental stiffness $\overline{04}$ calculated for the case of the present reference parameters and $\varepsilon^0_{11} = 0.005$. Indeed, the slope $\overline{04}$ is almost $1/5$ of the slope $\overline{03}$ which would be predicted by plasticity with a simple yield surface.

14.2.4 Other Aspects

To check for the limit of stability and for bifurcations of the response path, the tangential stiffness matrix is needed. The microplane model does not provide it directly, but it can always be computed by incrementing

the strain components (or the displacements) one by one and solving for the corresponding stress changes with the microplane model.

A greater insight into the microplane model, which may be useful for data fitting, can be achieved by separating the geometric aspect of damage (i.e., the effect of reduction of the stress-resisting cross section of the material) from other inelastic phenomena. This separation has been achieved in Carol, Bažant and Prat (1991). Correlation to plasticity models and continuum damage mechanics has been elucidated in Carol and Bažant (1997).

14.3 Nonlocal Adaptation of Microplane Model or Other Constitutive Models

In unconfined straining, the microplane model displays softening. Therefore, localization limiters of some kind must be used to avoid spurious localization and mesh sensitivity, as for all other models with strain softening. This can be easily implemented using a nonlocal adaptation of the microplane model in which the inelastic stress increment is made nonlocal following the theory of microcrack interactions presented in the previous chapter (Bažant 1994b; see §13.3). This approach affects the flow of calculation only partially and a general finite element scheme can be used. Fig. 14.1.1c shows the basic calculation flowchart for this approach in which the nonlocal adaptation is implemented just after the microplane stresses get computed; the flow bifurcates and the inelastic incremental stress is computed following the nonlocal theory with microcrack interactions.

The microplane model as presented, or for that matter any constitutive model for damage, gives a prescription to calculate the stress tensor σ as some tensor-valued function $\mathbf{R}$ of the strain tensor ϵ (and of some further parameters depending on the loading history, e.g., on whether there is loading or unloading). So, $\sigma = \mathbf{R}(\epsilon)$. The most robust (although not always the most accurate) method of structural analysis is to base the solution of a loading step or time step on the incremental elastic stress-strain relation with inelastic strain involving the initial elastic moduli tensor $\boldsymbol{E}$, as explained in Section 13.3.1. Then, for a local formulation, the inelastic stress increment tensor $\Delta\mathbf{S}$ defined in (13.3.1) can be computed as

$$\Delta\mathbf{S} = \boldsymbol{E}(\epsilon_{\text{new}} - \epsilon_{\text{old}}) - \mathbf{R}(\epsilon_{\text{new}}) + \mathbf{R}(\epsilon_{\text{old}}) \tag{14.3.1}$$

in which subscripts old and new label the old and new value of the variables at the beginning and end of the loading step (or time step); and $\mathbf{S}$ is the inelastic stress tensor due to nonlinear behavior. This stress-strain relation is used for both dynamic explicit analysis and static implicit analysis (as the iterative initial stiffness method).

A possible simple approach to introduce nonlocal effects is similar to the isotropic scalar nonlocal approach (Pijaudier-Cabot and Bažant 1987), which was applied to the microplane model by Bažant and Ožbolt (1990, 1992) and Ožbolt and Bažant (1992). In this approach, the elastic parts of stress increments are calculated locally. The inelastic parts of the increments of $\mathbf{S}$ must be calculated nonlocally. This is accomplished by first determining, at each integration point of each finite element, the average (or nonlocal) strains $\bar{\epsilon}$, and then calculating nonlocal $\overline{\Delta\mathbf{S}}$ from these, i.e.,

$$\Delta\sigma = \boldsymbol{E}\Delta\epsilon - \overline{\Delta\mathbf{S}}; \qquad \overline{\Delta\mathbf{S}} = \boldsymbol{E}(\bar{\epsilon}_{\text{old}} - \bar{\epsilon}_{\text{new}}) - \mathbf{R}(\bar{\epsilon}_{\text{new}}) + \mathbf{R}(\bar{\epsilon}_{\text{old}}) \tag{14.3.2}$$

The only modification required in a local finite element program is to insert the spatial averaging subroutine just before the calculation of $\overline{\Delta\mathbf{S}}$.

A better approach is to introduce the crack interaction concept explained in Section 13.3 and write the incremental elastic stress-strain relation as

$$\Delta\sigma = \boldsymbol{E}\Delta\epsilon - \Delta\tilde{\mathbf{S}} \tag{14.3.3}$$

in which $\Delta\tilde{\mathbf{S}}$ is given by Eq. (13.3.9). The spatially averaged strains are not calculated in this approach. The nonlocal part of the analysis proceeds in the following steps:

1. First, $\Delta\mathbf{S}$ is calculated (in the local form) from (14.3.1) according to the microplane model. Then one calculates at each integration point of each finite element the maximum principal direction vectors $\mathbf{n}^{(i)}$ $(i = 1, 2, 3)$ of strain tensor ϵ, for which the value of ϵ_{old} may be used as an approximation.

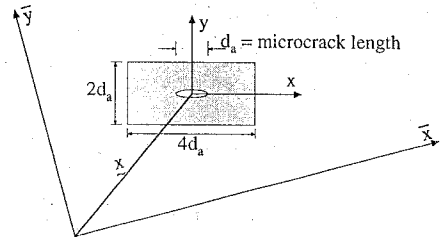

Figure 14.3.1 Local representative volume: orientation and size (adapted from Ožbolt and Bažant 1996).

2. Then one starts a loop on principal strain directions $\mathbf{n}^i$ $(i = 1, 2, 3)$ of tensor ϵ and evaluates the inelastic stress changes in the directions $\mathbf{n}^{(i)}$, that is, $\Delta S^{(i)} = \mathbf{n}^{(i)} \cdot \Delta\mathbf{S}\mathbf{n}^{(i)}$ or $\Delta S^{(i)} = n_i^{(i)} \Delta S_{ij} n_j^{(i)}$. For those principal directions $\mathbf{n}^{(i)}$ for which $\Delta S^{(i)} \leq 0$, the nonlocal calculations are skipped because the inelastic strain is not due to cracking, i.e., one jumps directly to the end of this loop; here we make the assumption that, on the microscale (but not on the macroscale), there is no softening in compression, which is true for the microplane model.
3. The values of $\Delta S^{(i)}$ for the integration points of finite elements are then spatially averaged:

$$\overline{\Delta S}_\mu^{(i)} = \frac{1}{V_\mu} \sum_{\nu=1}^{n} \Delta S_\nu^{(i)} \alpha_{\mu\nu} \Delta V_\nu \tag{14.3.4}$$

where $V_\mu = \sum_{\nu=1}^{n} \alpha_{\mu\nu} \Delta V_\nu$ = normalizing factor, n = number of all the integration points inside the averaging volume, and $\alpha_{\mu\nu}$ = given weight coefficients, whose distribution is suitably chosen with a bell shape in both x and y directions, described by a polynomial of the fourth degree. The bell shape, which is similar to that in the nonlocal damage approach (Chapter 13, Eq. (13.1.5)) is reasonable in that it gives larger contributions to the sum from points that lie closer. Because the spacing of major cracks in concrete is approximately the same as the spacing of the largest aggregate pieces, the size of the averaging volume may be assumed to be approximately proportional to the maximum aggregate size, d_a. For two-dimensional analysis, the region of averaging should probably be taken as a rectangle with its longer side in the direction normal to $\mathbf{n}^{(1)}$ (Fig. 14.3.1)
4. The values of the nonlocal principal inelastic stress increments $\Delta\tilde{S}^{(i)}$ must then be solved from the system of linear equations (13.3.31) based on the crack influence function $\Lambda_{\mu\nu}$. However, as discussed before, exact solution is normally not needed. Depending on the type of program, one of two approximate methods can be used:

   (a) In programs in which the loading step is iterated, these equations may be solved iteratively within the same iteration loop as that used to solve the nonlinear constitutive relation, using the following equation:

$$\Delta\tilde{S}_\mu^{(i)\text{new}} = \overline{\Delta S}_\mu^{(i)} + \frac{1}{V_\mu} \sum_{\nu=1}^{N} \Delta V_\nu \Lambda'_{\mu\nu} \Delta\tilde{S}_\nu^{(i)\text{old}} \qquad (\mu = 1, 2, \ldots N) \tag{14.3.5}$$

   in which $\Lambda'_{\mu\nu}$ = crack influence matrix defined in Eq. (13.3.43), which must, however, be adjusted with factor k_b for finite elements close to the boundary of concrete (Section 13.3.9).

   (b) In explicit finite element programs without iteration, one may calculate from (14.3.5) only the first iterate ($r = 1$), which represents one explicit calculation, requiring only the values of $\Delta S_\mu^{(i)}$ and $\langle \Delta S_\mu^{(i)} \rangle$. The premise of this approximation is that the repetitions of similar calculations (for $r = 1$) in the next loading step (or time step) effectively serve as the subsequent iterations (for $r = 2, 3, 4, \ldots$) because the loading steps in the explicit programs are very small. This of course means that the correct value of $\overline{\Delta S}_\mu^{(i)}$ gets established with a

delay of several steps or time intervals (in other words, the computer program is using nonlocal inelastic stress increments that are several steps old; the nonlocal interactions expressed by the crack influence function are delayed by several steps).

We recall from Section 13.3.9 that the adjustment by factor k_b must ensure that, even if part of the influencing volume protrudes beyond the boundary, the condition $\sum_{\nu=1}^{N} \Lambda'_{\mu\nu} = 0$ be met. Because this condition may be written as $\sum_{\text{interior}} \Lambda_{\mu\nu} + k_b \sum_{\text{boundary}} \Lambda_{\mu\nu} = 0$, the following adjustment is needed for the integration points of the elements adjoining the boundary:

$$\Lambda'_{\mu\nu} = k_b \Lambda_{\mu\nu}; \qquad k_b = -\sum_{\text{interior } \nu} \Lambda_{\mu\nu} \Big/ \sum_{\text{boundary } \nu} \Lambda_{\mu\nu} \tag{14.3.6}$$

For the remaining integration points in the interior, no adjustment is done, i.e., $\Lambda'^{\mu\nu} = \Lambda^{\mu\nu}$.

5. At each integration point of each finite element, the nonlocal inelastic stress increment tensor is then constituted from its principal values according to the following equation:

$$\Delta \tilde{S}_{kl} = \sum_{i=1}^{3} \Delta \tilde{S}^{(i)} n_k^{(i)} n_l^{(i)} \qquad \text{or} \qquad \Delta \tilde{\mathbf{S}} = \sum_{i=1}^{3} \tilde{S}^{(i)} \mathbf{n}^{(i)} \otimes \mathbf{n}^{(i)} \tag{14.3.7}$$

based on the spectral decomposition theorem of a tensor.

Note that if, at some integration point, all the principal values of tensor $\Delta \mathbf{S}$ are nonpositive, then the foregoing nonlocal procedure may be skipped for that point.

14.4 Particle and Lattice Models

A large amount of research, propitiated by the advent of powerful computers, has been devoted to the simulation of material behavior based directly on a realistic but simplified modeling of the microstructure —its particles, phases, and the bonds between them. A spectrum of diverse approaches can be found in the literature spanning an almost continuous transition from the finite element simulations, with the classical hypothesis of continuum mechanics, to discrete particle models and lattice models in which the continuum is approximated *a priori* by a system of discrete elements: particles, trusses, or frames.

An extreme example of the continuum approach —in view of the fineness of material subdivision— is the *numerical concrete* of Roelfstra, Sadouki and Wittmann (1985), Wittmann, Roelfstra and Kamp (1988) and Roelfstra (1988), in which the mortar, the aggregates, and their interfaces are independently modeled by finite elements. This requires generation of the geometry of the material (random placement of aggregates within the mortar) and the detailed discretization of the elements to adequately reproduce the geometry of the interfaces. With a completely different purpose, but with the same kind of analysis, Rossi and Richer (1987) and Rossi and Wu (1992) developed a random finite element model in which the microstructure is not directly modeled, but is taken into account by assigning random properties to the element interfaces. The common feature of these approaches is that, before cracking starts, the displacement field is approximated by a continuous function.

The particle and lattice models do not model the material continuously, but substitute the continuum by an array of discrete elements in the form of particles in contact, trusses, or frames, in such a manner that the displacements are defined only at the centers of the particles, or at the nodes of the truss or frame.

The origin of the particle approach can generally be traced to the development of the so-called distinct element method by Cundall (1971, 1978), Serrano and Rodriguez-Ortiz (1973), Rodriguez-Ortiz (1974), Kawai (1980), and Cundall and Strack (1979) in which the behavior of particulate materials (originally just cohesionless soils and rock blocks) was analyzed simulating the interactions of the particles in contact. This kind of analysis, which deals with a genuine problem of discrete particle systems, used highly simplified contact interaction laws permitted by the fact that the overall response is controlled mainly by kinematic restrictions (grain interlock) rather than by the details of the force-deformation relation at the contacts. However, although the kinematics of the simulations appeared very realistic, the quantitative stress-strain (averaged) response was not quite close to the actual behavior. This shortcoming, which still

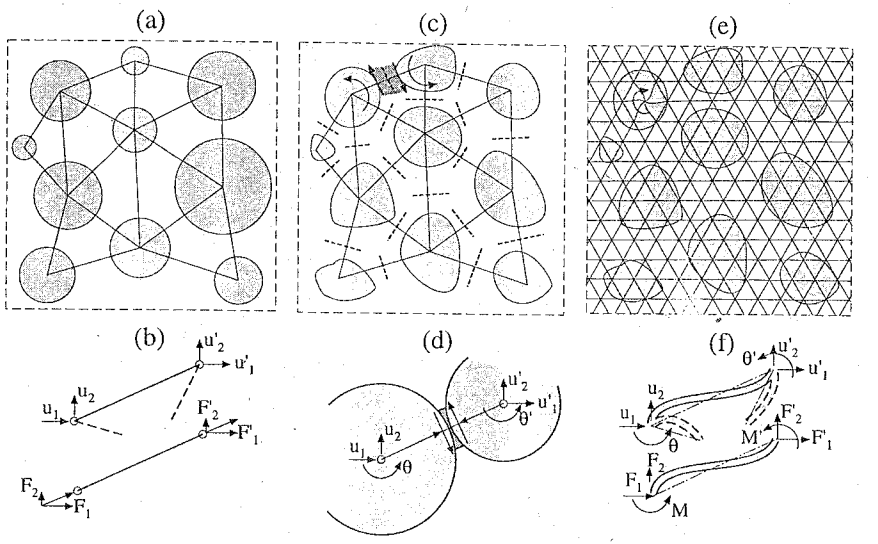

Figure 14.4.1 Various types of lattice models. (a) Pin-joined truss with (b) corresponding displacements and forces at the nodes. (c) Rigid particles in a deformable matrix with (d) the displacements and rotations are transmitted through a deformable layer by normal and shear forces. (e) Triangular regular lattice (originally used by van Mier and Schlangen) formed by (f) beams that stretch and bend.

persists in many modern particle and lattice models, is largely caused by the fact that the simulations are usually two-dimensional while a realistic simulation ought to be three-dimensional.

The basic idea of the particle model can be extended to simulate the particular structure of composite materials, for example, the configuration of the large aggregate pieces of concrete, as done by Zubelewicz (1980, 1983), Zubelewicz and Mróz (1983), and Zubelewicz and Bažant (1987), or the grains in a rock (Plesha and Aifantis 1983). In these cases the model requires defining the force interaction between particles (aggregates or grains) which are caused mainly by the relative displacements and rotations of neighboring particles. Although, for computational purposes, the problem is reduced to a truss (Fig. 14.4.1a–b) or to a frame (Fig. 14.4.1c–d), the basic ingredient of such models is that the geometry (size) of the truss or frame elements and their properties (stiffness, strength, etc.) are dictated by the geometry of the physical structure of the material (stiffness, size, shape, and relative position of aggregates or grains).

In contrast to this, the pure lattice models replace the actual material by a truss or frame whose geometry and element sizes are not related to the actual internal geometry of the material, but are selected freely by the analyst. The truss approach to elasticity, elementary atomistic representations of the physics of elasticity (i.e., arrays of atoms linked by springs shown in textbooks of solid state physics), was already proposed as early as 1941 by Hrennikoff. The lattice models have been championed by theoretical physicists for the simulation of fracturing in disordered materials (Herrmann, Hansen and Roux 1989; Charmet, Roux and Guyon 1990; Herrmann and Roux 1990; Herrmann 1991) and have been developed to analyze concrete fracture by Schlangen and van Mier at Delft University of Technology (Schlangen and van Mier 1992; Schlangen 1993, 1995; van Mier, Vervuurt and Schlangen 1994). In their approach, a regular triangular frame of side length less than the dimensions of the smallest aggregates, is laid over the actual material structure (Fig. 14.4.1e–f) and the properties of each beam are assigned according to the material the beam lies over: mortar, aggregate or interface. However, to eliminate directional bias of fracture, the lattice must be random (see Section 14.4.2).

This section presents a brief overview of the main concepts and results of the particle and lattice models as far as concrete fracture is concerned.

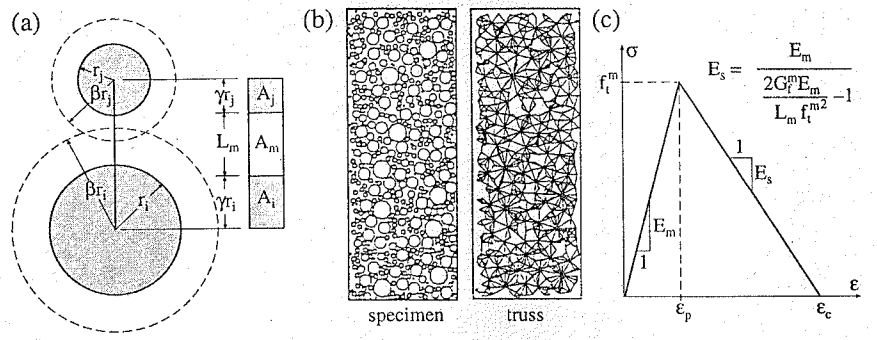

Figure 14.4.2 Random particle model of Bažant, Jirásek et al. (1994): (a) two adjacent circular particles with radii r_i and r_j and corresponding truss member ij; (b) typical randomly generated specimen and its corresponding mesh of truss elements; (c) constitutive law for matrix. (Adapted from Bažant, Tabbara et al. 1990.)

14.4.1 Truss, Frame, and Lattice Models

The simplest model is a pin-jointed truss, in which only the center-to-center forces between the particles are considered (Fig. 14.4.1a–b, Bažant, Tabbara et al. 1990). A more refined model is that of Zubelewicz and Bažant (1987), which imagines rigid particles separated by deformable thin contact layers of matrix that respond primarily by thickness extension-contraction and shear (Fig. 14.4.1c–d). Since the internodal links also transmit shear, moment equilibrium of the nodes needs to be considered, while for the pin-jointed truss it need not. Therefore, this model has three degrees-of-freedom per node (two displacements and one rotation, with corresponding two force components and one moment) for planar lattices, while the pin-jointed model has only two degrees-of-freedom per node. In the spatial case, the model of Zubelewicz and Bažant requires six degrees-of-freedom per node, i.e., three displacements and three rotations, while the pin-jointed The simplest model truss requires only three degrees-of-freedom per node. There is an additional important advantage of shear transmissionThe simplest model —it makes it possible to obtain with the lattice any Poisson ratio, while a random or regular pin-jointed lattice (truss) has Poisson ratio always 1/3 in two dimensions and 1/4 in three dimensions.

The simplest model In the model of Bažant, Tabbara et al. (1990) and Zubelewicz and Bažant (1987), the major particles in the material (large aggregate pieces) are imagined as circular and interacting through links as shown in Fig. 14.4.2. In the initial work of Zubelewicz and Bažant, the link between particles was assumed to transmit both axial forces and shear forces, the latter based on the rotations of particles. In the subsequent model by Bažant, Tabbara et al. (1990), the particle rotations and transmission of shear were neglected and only axial forces were assumed to be transmitted through the links. In such a case, the system of particle links is equivalent to a truss. As pointed out before, the penalty to pay for this simplification is that the Poisson ratio of a random planar truss is always 1/3 (and for a spatial truss 1/4). Another consequence of ignoring particle rotations and interparticle shears is that the fracture process zone obtained becomes narrower. But this can be counteracted by assuming a smaller postpeak softening slope for the interparticle stress displacement law, and also by introducing a greater random scatter in the link properties, both of which tend to widen the fracture process zone.

A random particle configuration must be statistically homogeneous and isotropic on the macroscale. In the simulation of concrete, the configuration must meet the required granulometric distribution of the particles of various sizes, as prescribed for the mix of concrete. The problem of generation of random configurations of particles in contact under such constrains involves some difficult and sophisticated aspects (see, e.g., Plesha and Aifantis 1983).

However, the problem becomes much simpler when the particles do not have to be in contact, as is the case for aggregate pieces in concrete. In that case, a rather simple procedure (Bažant, Tabbara et al. 1990) can proceed as follows: (**1**) using a random number generator, coordinate pairs of particle centers (nodes)

are generated one after another, assuming a uniform probability distribution of the coordinates within the area of the specimens; (**2**) for each generated pair a check for possible overlaps of the particles is made, and if the generated particle overlaps with some previously generated one, it is rejected; (**3**) the random generation of coordinate pairs proceeds until the last particle of the largest size has been placed within the specimen, (**4**) then the entire random placement process is repeated for the particles of the next smallest size, and then again for the next smallest size, etc. (The number of particles of each size is determined in advance according to the prescribed mix ratio and granulometry.)

To determine which particles interact, a circle of radius βr_i is drawn around each particle i (with $\beta \approx 5/3$) as shown by the dashed lines in Fig. 14.4.2a: Two particles interact if their dashed circles intersect each other. See Bažant, Tabbara et al. (1990) for the details of the assignment of the dimensions of the truss element, particularly the cross-section A_m and length L_m of the deformable portion (labeled with subscript m for matrix). In a later study by Jirásek and Bažant (1995a), a uniform stiffness of all the links was assumed.

Fig. 14.4.2b shows a typical computer-generated random particle arrangement resembling concrete, and the corresponding truss (random lattice). Fig. 14.4.2c shows the stress-strain relation for the interparticle links, characterized by the elastic modulus E_m, tensile strength limit f_t^m, and the postpeak softening slope E_s (or alternatively by strain ε_f at complete failure, or by G_f^m, each of which is related to the foregoing three parameters). The microscopic fracture energy of the material, G_f^m, is represented by the area under the stress-strain curve in Fig. 14.4.2c, multiplied by the length of the link. The ratio of ε_f to the strain ε_p at the peak stress may be regarded as the microductility of the material.

The lattices in Fig. 14.4.1a–d attempt to directly simulate the major inhomogeneities in the microstructure of concrete. By contrast, the model introduced by Schlangen and van Mier (1992) takes a lattice (in the early versions regular, but later randomized) that is much finer than the major inhomogeneities. Its nodal locations and links are not really reflections of the actual microstructure (Fig. 14.4.1e–f). Rather, the microstructure is simulated by giving various links different properties, which is done according to the match of the lattice to a picture of a typical aggregate arrangement.

Van Mier and Schlangen take advantage of the available simple computer programs for frames and assume the lattice to consist of beams which resist not only axial forces but also bending. Due to bending, the internodal links (beams), of course, also transmit shear, same as in the model of Zubelewicz and Bažant (Figs. 14.4.1c–d and e–f). This feature is useful, because shears are indeed transmitted between adjacent aggregate pieces and across weak interfaces in concrete, and because arbitrary control of the Poisson ratio is possible. However, the idea of bending of beams is a far-fetched idealization that has nothing to do with reality. No clear instances of bending in the microstructures of concrete can be identified.

The idealization of the links as beams subject to bending implies that a bending moment applied at one node is transmitted to the adjacent node with the carry-over factor 0.5, as is well known from the theory of frames. This value of the carry-over factor is arbitrary and cannot not have anything in common with real behavior. In the model of Zubelewicz and Bažant (Fig. 14.4.1c-d), the shear resistance also causes a transmission of moments from node to node, however, the carry-over factor is not 0.5 and can have different values. The transmission of moments is, in that model, due to shear in contact layers between particles, which is a clearly identifiable mechanism. In consequence of this analysis, it would seem better to consider the carry-over factor in the lattices of van Mier and Schlangen to be an arbitrary number, determined either empirically or by some microstructural analysis. This means that the 6×6 stiffness matrix for the element of the lattice, relating the 6 generalized displacement and force components of a beam sketched in Fig. 14.4.1f, should be considered to have general values in its off diagonal members, not based on the bending solutions for a beam but on other considerations. In fact, the use of such a stiffness matrix would require only an elementary change in the computer program for a frame (or lattice with bending). Of course, if the need for such a modification is recognized, the model and van Mier and Schlangen becomes essentially equivalent to that of Zubelewicz and Bažant, except that the nodes do not represent actual particles and the lattice is much finer than the particles.

The beams in the lattice model of Schlangen and van Mier are assumed to be elastic-brittle, and so, when the failure criterion is met at one of the beams, the link may be removed. This means that at each step the computation is purely elastic. This is computationally efficient, but makes the model predict a far too brittle behavior, even for three-dimensional lattices (van Mier, Vervuurt and Schlangen 1994).

Another important aspect in lattice models is the size of the links. Unlike the lattice of Zubelewicz and Bažant, which directly reflects the particle configurations and thus cannot (and should not) be refined, the

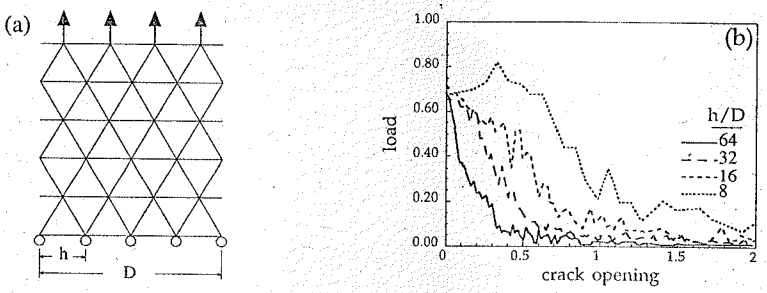

Figure 14.4.3 Dependence of the load-displacement curve on the size of the lattice links: (a) basic element geometry, (b) load-displacement curves for various lattice spacings (adapted from Schlangen 1995).

lattice of van Mier and Schlangen has an undetermined nodal spacing, which raises additional questions. First, as is well known, frames or lattices with bending are on a large scale asymptotically equivalent to the so-called micro-polar (or Cosserat) continuum (e.g., Bažant and Cedolin 1991, Sec. 2.10-2.11). Pin-jointed trusses, on the other hand, asymptotically approach a regular continuum on a large scale. The micropolar continuum is a continuum with nonsymmetric shear stresses and with couple stresses. It possesses a characteristic length, which is essentially proportional to the typical nodal spacing of the lattice approximated by the micro-polar continuum. While, in principle, the presence of a characteristic length is a correct property for a model of concrete, the characteristic length should not be arbitrary but should be of the order of the spacing of the major aggregate pieces. In this regard, the lattice of van Mier and Schlangen appears to be too refined. Moreover, as transpired from recent researches and the previous chapter on nonlocal concepts, the micro-polar character or the presence of characteristic length should refer only to the fracturing behavior and not to the elastic part of its bonds. The model of Schlangen and van Mier goes against this conclusion, since even the elastic response of the lattice is asymptotically approximated by a micro-polar rather than regular continuum.

Furthermore, a question arises about the dependence of the response on the lattice spacing. A recent study of Schlangen (1995) shows that the crack pattern is not strongly affected by the size of the beams, but the load-displacement is affected in much the same way as mesh refinement in local strain-softening models: the finer the lattice, the less the inelastic displacement and the dissipated energy, as illustrated in the load-crack opening curves in Fig. 14.4.3 for a square specimen subjected to pure tension. Indeed, it is easy to imagine that upon infinite refinement the stresses in a beam close to a crack tip must tend to infinity and thus a precracked specimen must fail for a vanishingly small load (roughly proportional to the square root of the beam size). Also, the shorter the beams, the smaller the dissipated energy, because the volume of material affected by the crack is smaller the smaller the elements. Note that the lattice analyzed by Schlangen in Fig. 14.4.3 has random strength in all the cases with identical probabilistic distribution. Therefore, randomness does not relieve mesh sensitivity as sometimes claimed.

The mesh-sensitivity of Schlangen and van Mier's model can probably be artificially alleviated or eliminated by taking a beam strength inversely proportional to the square root of the beam size, similar to the equivalent strength method described in Section 8.6.4 for crack band analysis. However, this is purely speculative and a more sound basis should be built for the lattice models before they can be confidently used as predictive (rather than just descriptive) models. A nonlocal fracture criterion may serve as an alternative solution to the problem, but this would break the computational efficiency of the elastic-brittle beam lattice model. Note that nonlocality (i.e., interaction at finite distance) is automatically implemented in the particle models because the particle distances are finite and fixed, so the lattice size should also be fixed as dictated by the microstructure.

14.4.2 Directional Bias

An important aspect of the model is the generation of the lattice configuration. In many works regular lattices have been used. However, recently Jirásek and Bažant (1995a), and also Schlangen (1995)

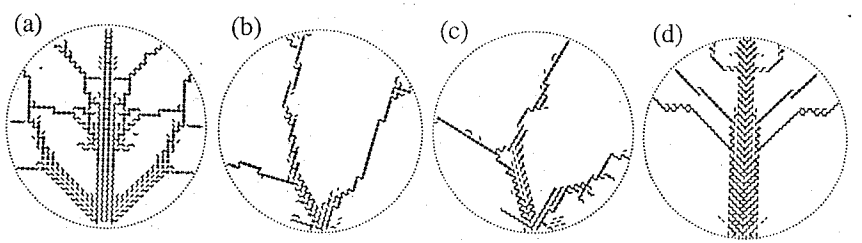

Figure 14.4.4 Failure patterns for various values of α: (a) 0°, (b) 15°, (c) 30°, (d) 45° using a regular lattice with deterministic properties of the links (from Jirásek and Bažant 1995a).

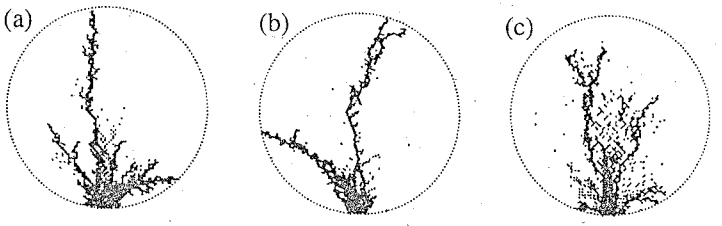

Figure 14.4.5 Failure patterns for various values of α: (a) 0°, (b) 22.5°, (c) 45° using a regular lattice with random strength, elastic stiffness and microfracture energy of the links (from Jirásek and Bažant 1995a).

demonstrated that a regular lattice always impresses a strong bias on the direction of fracture propagation.

For the square lattices with diagonals analyzed by Jirásek and Bažant, it is, of course, possible to choose the elastic stiffnesses of the links in the main directions of the square mesh and the diagonal directions, the corresponding strength limits of the links and the corresponding microfracture energies in such ratios that the lattice is isotropic in terms of elastic properties, strength along straight line cuts, and fracture energies dissipated on such cuts for any orientation of the cut. However, even in that case, the fracture tends to run preferentially among the mesh lines. This has been blatantly demonstrated by simulations of fracture of a circular specimen on which a regular square mesh with diagonals was overlaid; see Fig. 14.4.4. In this particle simulation the fracture was caused by an impact at the bottom of the circle in upward direction. In Fig. 14.4.4a the impact was in the direction of the square mesh lines, in Fig. 14.4.4d in the direction of the diagonals, and in Fig. 14.4.4b and 14.4.4c in two intermediate directions. Note the enormous differences in fracture patterns, which were also manifested by great differences in peak loads and energies dissipated. When all the properties of the links of a regular lattice were randomized, strong directional bias of fracture still remained; see Fig. 14.4.5.

Only when a geometrically random lattice was used in Jirásek and Bažant's (1995a) study, the directional bias was eliminated, except for small random differences between meshes. Similar results were found by Schlangen (1995) for a double-edge notched specimen subjected to shear. These results indicate that random (unstructured) lattices must be used to avoid directional bias.

14.4.3 Examples of Results of Particle and Lattice Models

Bažant, Tabbara et al. (1990) used the random particle system described before (Figs. 14.4.1a–b and 14.4.2) to simulate tensile tests and bending tests on notched specimens. A similar model was used by Jirásek and Bažant (1995a,b) to relate the microscopic features of the model (such as the softening curve and the statistics of strength distribution) to the macroscopic properties, particularly size effect and fracture energy.

Fig. 14.4.6 shows direct tension specimens of various sizes studied computationally by Bažant, Tabbara et al. (1990), with the results displayed in Fig. 14.4.7 as the calculated curves of load (axial force resultant)

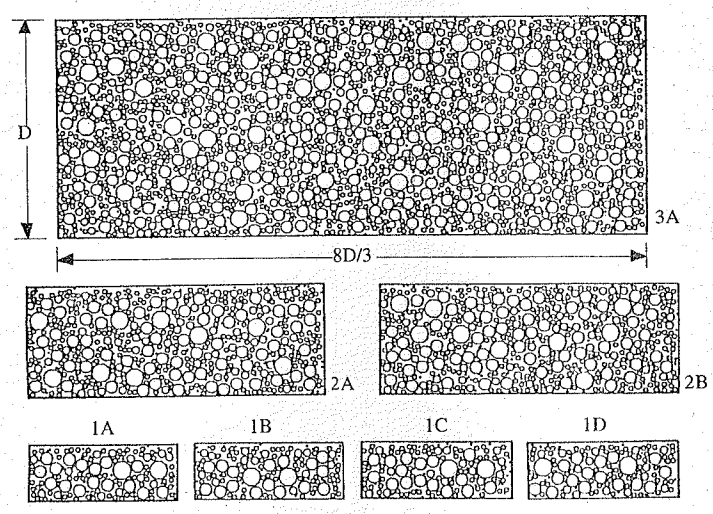

Figure 14.4.6 Geometrically similar specimens of various sizes with randomly generated particles (adapted from Bažant, Tabbara et al. 1990).

vs. relative displacement between the ends.

Fig. 14.4.7b gives the curves for several specimens of the smallest size from Fig. 14.4.6. Fig. 14.4.7c shows the curves for the medium size specimens and Fig. 14.4.7d the curve for one large size specimen. Fig. 14.4.7e shows, in relative coordinates, the average response curves calculated for the small, medium, and large specimens. Note that while the prepeak shape of the load displacement curve is size independent, the postpeak response curve is getting steeper with increasing size.

Fig. 14.4.8 shows the progressive spread of cracking in one of the smallest specimens from Fig. 14.4.6. The cracking patterns are shown for four different points on the load displacement diagram, as seen in Fig. 14.4.8a, the first point corresponding to the peak load. The dashed black lines are the normals to the links that undergo softening and correspond to partially formed cracks. The solid lines are normal to completely broken links and represent fully formed cracks. The gray dashed lines represent normals to the links that partly softened and then unloaded, and correspond to partially formed cracks that are closing. Note from Fig. 14.4.8 that the cracking is at first widely distributed, but then it progressively localizes.

Fig. 14.4.9 shows the calculated peak loads for the specimens from Fig. 14.4.6 in the usual size effect plot of the logarithm of nominal strength vs. logarithm of the size. Bažant, Tabbara et al. (1990) interpreted the results in terms of the classical size effect law Eq. (1.4.10) with relatively good results. The recent results of Bažant explained in Section 9.1, particularly the size effect formula for failures at crack initiation from a smooth surface (Section 9.1.6) suggest that these results must be interpreted using Eq. 9.1.42. Thus the results of Bažant, Tabbara et al. (1990) have been fitted here by the simplest version of this curve (for which $\gamma = 0$). Fig. 14.4.9 shows the resulting fit, which is excellent for the mean values of the data.

Three-point-bend fracture specimens of three sizes in the ratio 1:2:4 were simulated in the manner illustrated in Fig. 14.4.10a. Fig. 14.4.10b shows the size effect plot obtained from the three sizes of the specimens in Fig. 14.4.10a for three different materials. As can be seen, the calculated maximum loads can be well approximated by Bažant's size effect law, Eq. (1.4.10).

By fitting the size effect law to the maximum load obtained by the lattice or particle model for similar specimens of different sizes, one can determine the macroscopic fracture energy G_f of the particle system and the effective length c_f of the fracture process zone (see Chapter 6). It thus appears that fracture simulations with the lattice model or random particle system provide a further verification of the general applicability of the size effect law.

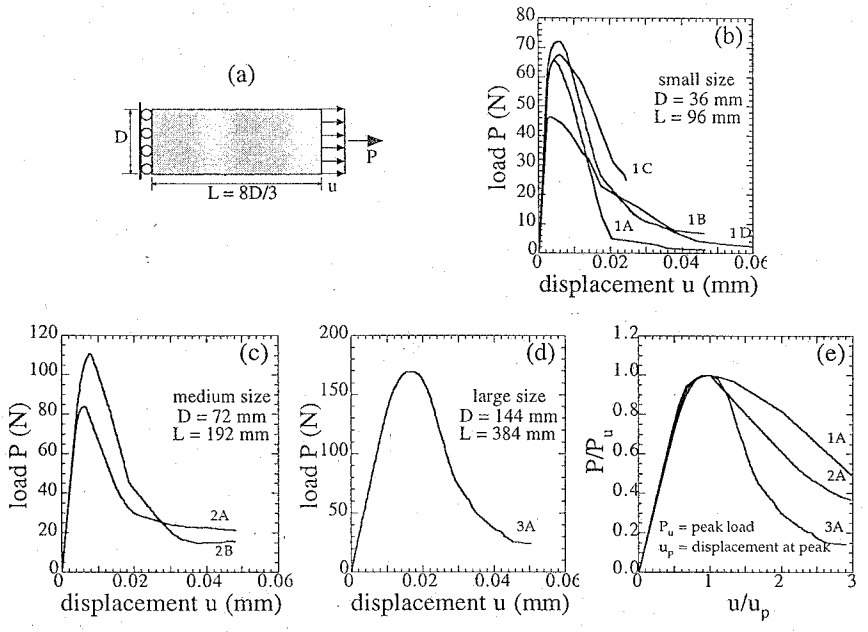

Figure 14.4.7 Results of Bažant, Tabbara et al. (1990) for direct tension of random particle specimens: (a) specimen with $D = 36, 72$, and 144 mm; (b) load-displacement curve for small specimens; (c) load-displacement curve for medium specimens; (d) load-displacement curve for large specimens; (e) normalized load-displacement curves for specimens 1A, 2A, and 3A. (Adapted from Bažant, Tabbara et al. 1990.)

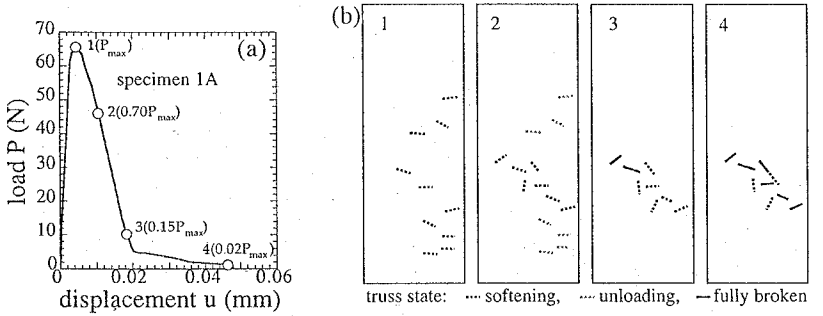

Figure 14.4.8 Results of Bažant, Tabbara et al. (1990) for the evolution of cracking in direct tension of random particle specimens: (a) load-displacement curve for specimen 1A; (b) evolution of cracking with loading and localization. (Adapted from Bažant, Tabbara et al. 1990.)

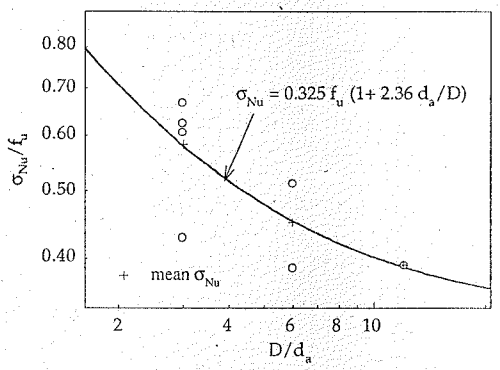

Figure 14.4.9 Size effect plot constructed form maximum load values calculated for direct tension specimens of various sizes by Bažant, Xiang et al. (1996). The solid line is the fit by Eq. (9.1.42) with $\gamma = 0$. f_u is a reference strength taken to be equal to the matrix tensile strength f_t^m (see Fig. 14.4.2c).

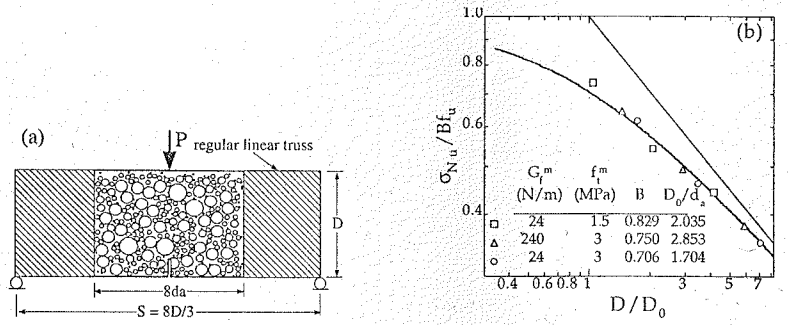

Figure 14.4.10 Simulation of three three-point-bend tests by random particle model. (a) Three-point-bend specimens with $d = 36, 72$, and 144 mm and (b) corresponding size effect plot. (Adapted from Bažant, Tabbara et al. 1990.)

At the same time, the size effect law is seen to be an effective approach for studying the relationship between the microscopic characteristics of the particle system, simulating the microscopic properties of the material, and the macroscopic fracture characteristics.

Such studies have been undertaken by Jirásek and Bažant (1995b). Fig. 14.4.11 show the results of a large number of such simulations, dealing with two dimensional three-point-bend fracture specimens of different sizes. In these specimens, the microductility number, representing the ratio $\varepsilon_c/\varepsilon_p$, was varied (see Fig. 14.4.2b). The coefficient of variation of the microstrength of the particle length, used in random generation of the properties of the links, was also varied (the microstrength was assumed to have a normal distribution).

It was found that both the microductility and the coefficient of the microstrength of the links have a significant effect on the macroscopic fracture energy G_f and on the effective length c_f of the process zone; see Fig. 14.4.11a,c. Randomness of these plots is largely due to the fact that the number of simulations was not very large (the values in the plot are the averages of the values obtained in individual sets of simulations of specimens of different sizes). The plots in Fig. 14.4.11a,c have been smoothed as shown in Fig. 14.4.11b,d by the following bilinear polynomials which provide optimum fits:

$$\bar{G}_f = 2.16 - 1.08\omega_f + 0.48\gamma_f - 0.71\omega_f\gamma_f, \tag{14.4.1}$$

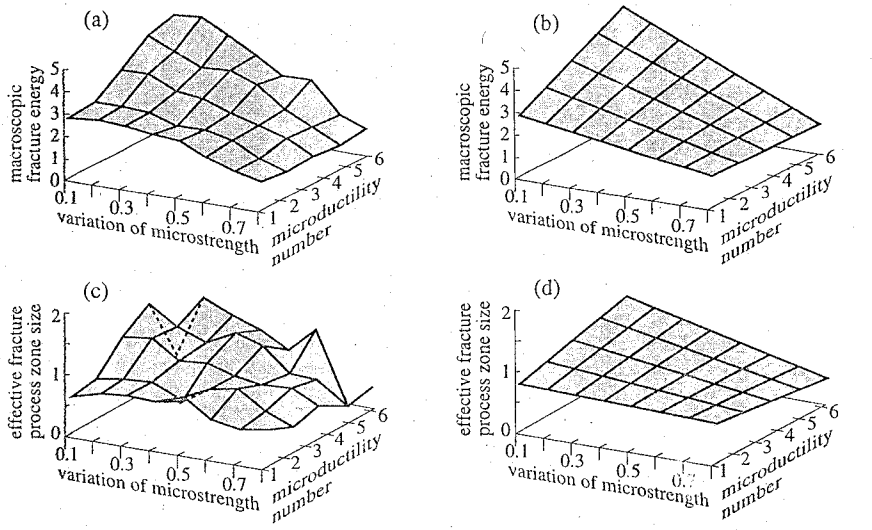

Figure 14.4.11 Normalized fracture energy and normalized effective process zone size as a function of two parameters: (a) and (c) computed, (b) and (d) fitted by bilinear functions (from Jirásek and Bažant 1995b).

$$\bar{c}_f = 0.64 + 0.08\omega_f + 0.09\gamma_f - 0.19\omega_f\gamma_f, \tag{14.4.2}$$

in which the superimposed bars refer to average values, and ω_f and γ_f are the coefficient of variation of microstrength and the microductility number. Obviously, the effect of various other microscopic characteristics of particle systems on their macroscopic fracture properties could also be studied in this manner, exploiting the size effect law.

14.4.4 Summary and Limitations

The lattice models or particle systems are computationally very demanding and a very efficient computational algorithm must be used. A highly efficient algorithm, which was applied to simulation of sea ice fracture, is presented in Jirásek and Bažant (1995a). It is an explicit algorithm for fracture dynamics, but it can also be used for static analysis in the sense of dynamic relaxation method. (Fracturing in particle systems with more than 120,000 degrees-of-freedom was simulated with this algorithm on a desktop 1992 work station.) Computational effectiveness will be particularly important for three-dimensional lattices, the use of which is inevitable for obtaining a fully realistic, predictive model.

As it now stands, the lattice or particle models can provide a realistic picture of tensile cracking in concrete in two-dimensional situations. However, solution of significant three-dimensional problems or nonlinear triaxial behavior as well as simulation of behavior in which compression and shear fracturing is important is still beyond reach. Thus, the lattice or particle models have not attained the degree of generality already available with the finite element approach.

Although computer programs for lattices are attractive by their simplicity, it must nevertheless be recognized that a lattice modeling of a continuum is far less powerful than the finite element method because the stress and strain tensors cannot be simulated by the elements of the lattice and, thus, nonlinear tensorial behavior cannot be directly described. From this viewpoint, the numerical concrete of Roelfstra and Wittmann, seems preferable to the lattice model of van Mier and Schlangen because the particles and mortar are discretized by a much finer mesh of finite elements.

To sum up, lattice models or particle systems have proven to be a useful tool for understanding fracture process and clarifying some relationship between the micro- and macro- characteristics of quasibrittle heterogeneous materials. These models appear to be particularly suited for failures due to tensile fracturing

and capture well the distributed nature of such fracturing and its localization. However, one must keep in mind that these models, in their present form, cannot simulate three-dimensional situations, larger structures (even two-dimensional), compressive and shear fractures, and nonlinear triaxial stress-strain relations. Overall, these models are still far inferior to finite element models and do not really have a predictive capability. No doubt significant improvements may be expected in the near future.

14.5 Tangential Stiffness Tensor Via Solution of a Body with Many Growing Cracks

The power of the microplane model is limited by the assumption of a kinematic (or static) constraint, which is a simplification of reality. To avoid this simplification, one needs to tackle the boundary value problem of the growth of many statistically uniformly distributed cracks in an infinite elastic body. This problem is not as difficult as it seems. It appears possible that an approximate solution of this problem might once supersede the microplane model as the most realistic predictive approach to cracking damage.

The problem of calculating the macroscopic stiffness tensor of elastic materials intersected by various types of random or periodic crack systems has been systematically explored during the last two decades and effective methods such as the self-consistent scheme (Budianski and O'Conell 1976; Hoenig 1978), the differential scheme (Roscoe 1952; Hashin 1988), or the Mori-Tanaka method (Mori and Tanaka 1973) have been developed. A serious limitation of these studies was that they dealt with cracks that neither propagate nor shorten (Fig. 14.5.1a). This means that, in the context of response of a material with growing damage illustrated by the curve in Fig. 14.5.1a, these formulations predict only the secant elastic moduli (such as E_s in Fig. 14.5.1a). Such information does not suffice for calculating the response of a body with progressing damage due to cracking.

To calculate the response of a material with cracks that can grow or shorten, it is also necessary to determine the tangential moduli, exemplified by E_t in Fig. 14.5.1b. Knowledge of such moduli makes it possible, for a given strain increment, to determine the inelastic stress drop $\delta\sigma_{cr}$ (Fig. 14.5.1b). This problem has recently been studied by Bažant and Prat (1995, 1997) and Prat and Bažant (1997). Its solution will now be briefly reviewed.

We consider a representative volume V of an elastic material containing on the microscale many cracks (microcracks). On the macroscale, we imagine the cracks to be smeared and the material to be represented by an approximately equivalent homogeneous continuum whose local deformation within the representative volume can be considered approximately homogeneous over the distance of several average crack sizes. Let $\boldsymbol{\varepsilon}$ and $\boldsymbol{\sigma}$ be the average strain tensor and average stress tensor within this representative volume. To obtain a simple formulation, we consider only circular cracks of effective radius a.

Consider the material to be intersected by N families of random cracks, labeled by subscripts $\mu = 1, 2, \ldots, N$. Each crack family may be characterized by its spatial orientation $\vec{n}_\mu$, its effective crack radius a_μ, and the number n_μ of cracks in family μ per unit volume of the material. The compliance tensor may be considered as the function $\boldsymbol{C} = \boldsymbol{C}(a_1, a_2, \ldots, a_N; n_1, n_2, \ldots, n_N)$. Approximate estimation of this function has been reviewed by Kachanov and co-workers (Kachanov 1992, 1993; Sayers and Kachanov 1991; Kachanov, Tsukrov and Shafiro 1994).

To obtain the tangential compliance tensor of the material on the macroscale, the cracks must be allowed to grow during the prescribed strain increment $\delta\boldsymbol{\varepsilon}$. This means that the energy release rate per unit length

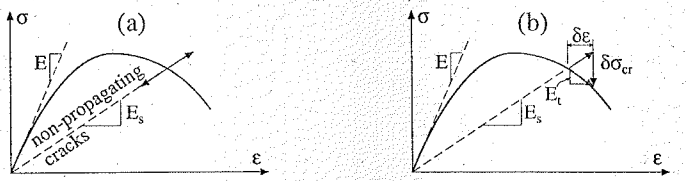

Figure 14.5.1 Stress-strain curves and moduli: (a) effective secant moduli; (b) tangential moduli and inelastic stress decrement due to crack growth.

of the front edge of one crack must be equal to the given critical value $R(a_\mu)$ (or to the fracture energy G_f, in the case of LEFM). For the sake of simplicity, we will enforce the condition of criticality of cracks only in an overall (weak) sense, by assuming that the average overall energy release rate of all the cracks of one family within the representative volume equals their combined energy dissipation rate.

Our analysis will be restricted to the case when the number of cracks in each family is not allowed to change ($\delta n_\mu = 0$), i.e., no new cracks are created and no existing cracks are allowed to close. This does not seem an overly restrictive assumption because a small enough crack has a negligible effect on the response and can always be assumed at the outset. Besides, concrete is full of microscopic cracks (or flaws) to begin with, and no macroscopic crack nucleates from a homogeneous material.

The incremental constitutive relation can be obtained by differentiation of Hooke's law. It reads $\delta\boldsymbol{\varepsilon} = \boldsymbol{C}\delta\boldsymbol{\sigma} + \sum_{\mu=1}^{N}(\partial\boldsymbol{C}/\partial a_\mu)\boldsymbol{\sigma}\,\delta a_\mu$ from which

$$\delta\boldsymbol{\sigma} = \boldsymbol{E}\left(\delta\boldsymbol{\varepsilon} - \sum_{\mu=1}^{N}\frac{\partial\boldsymbol{C}}{\partial a_\mu}\boldsymbol{\sigma}\,\delta a_\mu\right) \tag{14.5.1}$$

where δ denotes infinitesimal variations and $\boldsymbol{C}(a_\mu)$ is the fourth-order macroscopic secant compliance tensor of the material with the cracks, and $\boldsymbol{E}(a_\mu)$ is the fourth-order secant stiffness tensor, whose 6×6 matrix is inverse of the matrix of $\boldsymbol{C}(a_\mu)$.

The surface area of one circular crack of radius a_μ is $A = \pi a_\mu^2$, and the area change when the crack radius increases by δa is $\delta A_\mu = 2\pi a_\mu \delta a_\mu$. We assume we can replace the actual crack radii by their effective radius a_μ.

The crack radius increments δa_μ must be determined in conformity to the laws of fracture mechanics. Let us assume that the cracks (actually microcracks) can be described by equivalent linear elastic fracture mechanics (LEFM) with an R-curve $R(a_\mu)$. This means that the energy release rates must be equal to R_μ (or G_f, in the case of LEFM). For the special case $R(a_\mu) = G_f$ = fracture energy of the matrix of the material, the cracks follow LEFM.

The complementary energy density of the material is $\overline{U}^* = \overline{U}^*(\boldsymbol{\sigma}, a_\mu) = \frac{1}{2}\boldsymbol{\sigma}\cdot\boldsymbol{C}(a_\mu)\boldsymbol{\sigma}$, where the dot indicates scalar product of two second-order tensors. To make the problem tractable, we impose the energy criterion of fracture mechanics (energy balance condition) only in the overall, weak sense. This leads to the following N conditions of crack growth (Bažant and Prat 1995; Prat and Bažant 1997):

$$\left[\frac{\partial\overline{U}^*}{\partial a_\mu}\right]_{\boldsymbol{\sigma}=\text{const.}} = \frac{1}{2}\,\boldsymbol{\sigma}\cdot\frac{\partial\boldsymbol{C}}{\partial a_\mu}\boldsymbol{\sigma} = 2\pi a_\mu n_\mu \kappa_\mu R(a_\mu) \qquad (\mu = 1, 2, \ldots N) \tag{14.5.2}$$

(repetition of subscript μ in this and subsequent equations does not imply summation); κ_μ = crack growth indicator which is equal to 1 if the crack is growing ($\delta a_\mu > 0$) and 0 if it is closing ($\delta a_\mu < 0$), while any value $0 < \kappa_\mu < 1$ can be used if $\delta a_\mu = 0$.

Differentiation of (14.5.2) provides the incremental energy balance conditions:

$$\boldsymbol{\sigma}\cdot\frac{\partial\boldsymbol{C}}{\partial a_\mu}\delta\boldsymbol{\sigma} + \sum_{\nu=1}^{N}\left(\frac{1}{2}\boldsymbol{\sigma}\cdot\frac{\partial^2\boldsymbol{C}}{\partial a_\mu \partial a_\nu}\boldsymbol{\sigma} - 2\pi n_\mu \kappa_\mu G_f \delta_{\mu\nu}\right)\delta a_\nu = 2\pi n_\mu a_\mu G_f \delta\kappa_\mu \qquad (\mu = 1, 2, \ldots N) \tag{14.5.3}$$

where $\delta\kappa_\mu = 0$ except when the crack growth changes to no growth or to closing, or vice versa. The handling of the large jump in κ_μ is exact if $\kappa_\mu = \kappa_\mu^{\text{new}}$ and $a_\mu = a_\mu^{\text{old}}$ because $\delta(\kappa_\mu a_\mu) = (\kappa_\mu a_\mu)^{\text{new}} - (\kappa_\mu a_\mu)^{\text{old}} = \kappa_\mu^{\text{new}}\delta a_\mu + \delta\kappa_\mu a_\mu^{\text{old}}$, exactly.

Substitution of (14.5.1) into (14.5.3) leads to a system of N equations for N unknowns $\delta a_1, \ldots \delta a_N$:

$$\sum_{\nu=1}^{N} A_{\mu\nu}\delta a_\nu = B_\mu \qquad (\mu = 1, \ldots N) \tag{14.5.4}$$

where

$$A_{\mu\nu} = \boldsymbol{\sigma}\cdot\left(\frac{\partial\boldsymbol{C}}{\partial a_\mu}\boldsymbol{E}\frac{\partial\boldsymbol{C}}{\partial a_\nu} - \frac{1}{2}\frac{\partial^2\boldsymbol{C}}{\partial a_\mu \partial a_\nu}\right)\boldsymbol{\sigma} + 2\pi G_f n_\mu \kappa_\mu^{\text{new}}\delta_{\mu\nu} \tag{14.5.5}$$

$$B_\mu = \boldsymbol{\sigma} \cdot \frac{\partial \boldsymbol{C}}{\partial a_\mu} E\delta\varepsilon - 2\pi n_\mu a_\mu^{\text{old}} G_f \delta\kappa_\mu \tag{14.5.6}$$

After solving (14.5.4), evaluating $\delta\boldsymbol{\sigma}$ from (14.5.1) and incrementing $\boldsymbol{\sigma}$, one must check whether the case $\delta\bar{a}_\mu > 0$ and $\sigma_{N\mu} < 0$ (or $\epsilon^{cr}_{N\mu} < 0$) occurs for any μ. If it does, the corresponding equation in the system (14.5.4) must be replaced by the equation $\delta\bar{a}_\mu = 0$. The solution of such a modified equation system must be iterated until the case $\delta\bar{a}_\mu > 0$ and $\sigma_{N\mu} < 0$ (or $\epsilon^{cr}_{N\mu} < 0$) would no longer occur for any μ.

The formulation needs to be further supplemented by a check for compression. The reason is that the energy expression is quadratic, which means that (14.5.2) is invariant when $\boldsymbol{\sigma}$ is replaced by $-\boldsymbol{\sigma}$. Thus, a negative stress intensity factor $K_{I\mu}$ can occur even when (14.5.4) is satisfied, and so the sign of $K_{I\mu}$ must be checked for each crack family μ. The case $K_{I\mu} < 0$ is inadmissible.

Since the present formulation yields only the values of $(K_{I\mu})^2 = E\mathcal{R}(a_\mu)$ but not the values of $K_{I\mu}$, the sign of $K_{I\mu}$ must be inferred approximately. It can be considered the same as the sign of the stress $\sigma_{N\mu} = \vec{n}_\mu \cdot \boldsymbol{\sigma}\vec{n}_\mu$ in the direction normal to the cracks of μ-th family ($\vec{n}_\mu$ = unit vector normal to the cracks). [Alternatively, the sign of $K_{I\mu}$ could be inferred from the sign of the normal component $\epsilon^{cr}_{N\mu} = \vec{n}_\mu \cdot \boldsymbol{\varepsilon}^{cr}_N \vec{n}_\mu$ of the cracking strain tensor $\boldsymbol{\varepsilon}^{cr} = \boldsymbol{C}^{cr}\boldsymbol{\sigma}$.] Approximate though such estimation surely is on the microscale of an individual crack, it nevertheless is fully consistent with the macroscopic approximation of $\boldsymbol{C}$ implied in this model. The reason is that all the composite material models for cracked solids are based on the solution of one crack in an infinite solid, for which the sign of $K_{I\mu}$ coincides with the sign of $\sigma_{N\mu}$ (or $\epsilon^{cr}_{N\mu}$).

Usually the six independent components of $\delta\boldsymbol{\varepsilon}$ are known or assumed, and then (14.5.4) represents a separate system of only N equations for $\delta a_1, \ldots \delta a_N$ (this is a simplification compared to the formulation in the paper, which led to a system of $N + 6$ equations). In each iteration of each loading step, the values of κ_μ are set according to the sign of δa_μ in the preceding step or preceding iteration.

If $\delta a_\mu = 0$, or if (due to numerical error) $|\delta a_\mu|$ is nonzero but less than a certain chosen very small positive number δ, κ_μ is arbitrary and can be anywhere between 0 and 1, which makes equation (14.5.3) superfluous. The condition (14.5.2) of energy balance in the of constant crack length becomes meaningless and must be dropped. It needs to be replaced by an equation giving κ_μ (or $K_{I\mu}$) as a function of $\boldsymbol{\sigma}$), which must be used to check whether κ_μ indeed remains within the interval (0,1). However, it seems that for proportionally increasing loads the case $\delta a_\mu = 0$ is not important and its programming could be skipped, using conveniently the value $\kappa_\mu = 0.5$.

The foregoing solution was outlined in Bažant and Prat (1995) and worked out in detail in Prat and Bažant (1997) (with Addendum in a later issue).

To be able to use (14.5.5), we must have the means to evaluate the effective secant stiffness $\boldsymbol{C}$ as a function of a_μ. Bažant and Prat (1995) and Prat and Bažant (1997) adopted the approximate approach developed by Sayers and Kachanov (1991) using the symmetric second-order crack density tensor

$$\boldsymbol{\alpha} = \sum_{\mu=1}^{N} n_\mu a_\mu^3 \vec{n}_\mu \otimes \vec{n}_\mu \tag{14.5.7}$$

(Vakulenko and Kachanov 1971; Kachanov 1980, 1987b). In this approach, the effective secant compliance $\boldsymbol{C}$ is derived from an elastic potential F which is considered as a function of the crack density tensor $\boldsymbol{\alpha}$ (in addition of the stress tensor $\boldsymbol{\sigma}$):

$$\boldsymbol{\varepsilon} = \frac{\partial F(\boldsymbol{\sigma}, \boldsymbol{\alpha})}{\partial \boldsymbol{\sigma}} = \boldsymbol{C}\boldsymbol{\sigma} \tag{14.5.8}$$

The elastic potential $F(\boldsymbol{\sigma}, \boldsymbol{\alpha})$ can be expanded into a tensorial power series. Sayers and Kachanov (1991) proposed to approximate potential F by a tensor polynomial that is quadratic in $\boldsymbol{\sigma}$ and linear in $\boldsymbol{\alpha}$:

$$F(\boldsymbol{\sigma}, \boldsymbol{\alpha}) = \frac{1}{2}\,\boldsymbol{\sigma} \cdot \boldsymbol{C}^\circ\boldsymbol{\sigma} + \eta_1\,(\boldsymbol{\sigma} \cdot \boldsymbol{\alpha})\text{tr}\,\boldsymbol{\sigma} + \eta_2\,\boldsymbol{\sigma}^2 \cdot \boldsymbol{\alpha} \tag{14.5.9}$$

in which η_1 and η_2 are assumed to depend only on $\alpha = \text{tr}\,\boldsymbol{\alpha} = \sum_\mu n_\mu a_\mu^3$, the first invariant of $\boldsymbol{\alpha}$ (Sayers and Kachanov 1991). The strain tensor follows from (14.5.9):

$$\boldsymbol{\varepsilon} = \boldsymbol{C}^\circ\boldsymbol{\sigma} + \eta_1\,\text{tr}\,\boldsymbol{\sigma}\,\boldsymbol{\alpha} + \eta_1\,\text{tr}\,\boldsymbol{\alpha}\,\boldsymbol{\sigma} + \eta_2\,(\boldsymbol{\alpha}\boldsymbol{\sigma} + \boldsymbol{\sigma}\boldsymbol{\alpha}) \tag{14.5.10}$$

The functions $\eta_1(\alpha)$ and $\eta_2(\alpha)$ can be obtained by taking the particular form of the preceding formulation for the case of random isotropically distributed cracks and equating the results to those obtained using, e.g., the differential scheme (Hashin 1988). To this end, we note that if the orientation, density, and size of cracks is isotropically distributed, then $\boldsymbol{\alpha}$ must be spherical, and since its trace is equal to α, it must be $\boldsymbol{\alpha} = (\alpha/3)\mathbf{1}$. Substituting this into the preceding equation we get for this case:

$$\boldsymbol{\varepsilon} = \boldsymbol{C}^\circ\boldsymbol{\sigma} + \frac{2}{3}\eta_1\,\text{tr}\,\boldsymbol{\sigma}\,\mathbf{1} + \frac{2}{3}\eta_2\,\boldsymbol{\sigma} \tag{14.5.11}$$

Noting now that the resulting behavior in (14.5.11) must be elastic with effective elastic modulus E_{eff} and effective Poisson's ratio ν_{eff}, we get the following relationship between the functions η_i, the effective elastic constants and the α:

$$\eta_1(\alpha) = -\frac{3}{2\alpha}\left(\frac{\nu_{\text{eff}}(\alpha)}{E_{\text{eff}}(\alpha)} - \frac{1+\nu}{E}\right), \qquad \eta_2(\alpha) = \frac{3}{2\alpha}\left[\frac{1+\nu_{\text{eff}}(\alpha)}{E_{\text{eff}}(\alpha)} - \frac{1+\nu}{E}\right] \tag{14.5.12}$$

where E and ν are the elastic constants of the uncracked material (included in $\boldsymbol{C}^\circ$); here we indicate explicitly that the effective elastic constants depend on α. This dependence can be obtained, for example, by using the differential scheme which, for quasibrittle materials, gives better predictions than the self-consistent scheme (Bažant and Prat 1997). The resulting relationships (see e.g., Hashin 1988 for the details of the derivation) are as follows:

$$\alpha = \frac{5}{8}\ln\frac{\nu}{\nu_{\text{eff}}} + \frac{15}{64}\ln\frac{1-\nu_{\text{eff}}}{1-\nu} + \frac{45}{128}\ln\frac{1+\nu_{\text{eff}}}{1+\nu} + \frac{5}{128}\ln\frac{3-\nu_{\text{eff}}}{3-\nu} \tag{14.5.13}$$

$$\frac{E_{\text{eff}}}{E} = \left(\frac{\nu_{\text{eff}}}{\nu}\right)^{10/9}\left(\frac{3-\nu}{3-\nu_{\text{eff}}}\right)^{1/9} \tag{14.5.14}$$

From Eqs. (14.5.7), (14.5.10), and (14.5.12)–(14.5.14) the effective compliance tensor is obtained as a function of a_μ. Then δa_μ is calculated from Eq. 14.5.4 for a given $\delta\boldsymbol{\varepsilon}$ as indicated before.

The crack density may be characterized as a continuous function n_μ of spherical angles ϕ and θ (Prat and Bažant 1997). Function n_μ is then sampled at spherical angles ϕ_μ and θ_μ corresponding to the orientations of the microplanes in the microplane model. For isotropic materials such as concrete, the distribution of n_μ is initially uniform, and a very small but nonzero value must be assigned to every n_μ as the initial condition because no new cracks are allowed to nucleate. For an initially anisotropic material such a rock with joints, function n_μ is assumed to peak at a few specified discrete orientations ϕ_i^*, θ_i^*.

In on-going studies, the R-curves are used by Bažant and co-workers as a means to approximate the effect of plastic strains in the matrix of the material occurring simultaneously with the crack growth. Unlike classical plasticity, the plastic strain cannot be considered here to be smeared in a continuum manner because the cracks cause stress concentrations. Therefore, plasticity of the matrix will get manifested by the formation of a plastic zone at the front edge of each microcrack. As is well known, the effect of such a plastic zone can be approximately described by an R-curve.

References

Achenbach, J. D. and Bažant, Z. P. (1975) "Elastodynamic near-tip stress and displacement fields for rapidly propagating cracks in orthotropic materials." *J. Appl. Mech.-T. ASME,* **42**, 183–189.

Achenbach, J. D., Bažant, Z. P. and Khetan, R. P. (1976a) "Elastodynamic near-tip fields for a rapidly propagating interface crack." *Int. J. Eng. Sci.,* **14**, 797–809.

Achenbach, J. D., Bažant, Z. P. and Khetan, R. P. (1976b) "Elastodynamic near-tip fields for a crack propagating along the interface of two orthotropic solids." *Int. J. Eng. Sci.,* **14**, 811–818.

ACI Committee 318 (1989) *Building Code Requirements for Reinforced Concrete (ACI 318-89) and Commentary (ACI 318R-89).* U.S. Standard, American Concrete Institute, Detroit.

ACI Committee 318 (1992) *Building Code Requirements for Reinforced Concrete (ACI 318-89 Revised 1992).* U.S. Standard, American Concrete Institute, Detroit.

ACI Committee 349 (1989) "Code requirements for nuclear safety structures (ACI 349.1R), Appendix B - Steel embedments." In *Manual of Concrete Practice, Part IV,* American Concrete Institute, Detroit.

ACI Committee 408 (1979) "Suggested development, splice and standard hook provisions for deformed bars in tension." *Concrete Int.,* **1**(7), 44–46. (ACI 408.1R-79.)

ACI Committee 446 (1992) "Fracture mechanics of concrete: Concepts, models and determination of material properties." In *Fracture Mechanics of Concrete Structures,* Z. P. Bažant, ed., Elsevier Applied Science, London, pp. 1–140. (State of Art Report.)

ACI–ASCE Committee 426 (1973) "The shear strength of reinforced concrete members: Chapters 1 to 4." *J. Struct. Div.-ASCE,* **99**, 1091–1187.

ACI–ASCE Committee 426 (1974) "The shear strength of reinforced concrete members: Chapter 5." *J. Struct. Div.-ASCE,* **100**, 1543–1591.

ACI–ASCE Committee 426 (1977) "Suggested revisions to shear provisions for building codes." *ACI J.,* **74**(9), 458–469.

Adamson, R. M., Dempsey, J. P., DeFranco, S. J. and Xie, Y. (1995) "Large-scale *in-situ* ice fracture experiments. Part I: Experimental aspects." In *Ice Mechanics 1995,* J. P. Dempsey and Y. D. S. Rajapakse, eds., The American Society of Mechanical Engineers, New York, pp. 107–128. (AMD-Vol. 207, ASME Summer Meeting, Los Angeles, CA.)

Alexander, M. G. (1987) Test data in Shah and Ouyang (1994).

Alfrey, T. (1944) "Nonhomogeneous stress in viscoelastic media." *Quart. Appl. Math.,* **2**(2), 113–119.

Aliabadi, M. H. and Rooke, D. P. (1991) *Numerical Fracture Mechanics,* Computational Mechanics Publications, Southampton.

Alvaredo, A. M. and Torrent, R. J. (1987) "The effect of the shape of the strain-softening diagram on the bearing capacity of concrete beams." *Mater. Struct.,* **20**, 448–454.

Argon, A. S. (1972) "Fracture of composites." In *Treatise of Materials Science and Technology,* Vol. 1, Academic Press, New York, pp. 79.

Ashby, M. F. and Hallam, S. D. (1986) "The failure of brittle solids containing small cracks under compressive stress states." *Acta Metall.,* **34**(3), 497–510.

ASTM (1983) "Standard test method for plane-strain fracture toughness of metallic materials." In *Annual Book of ASTM Standards,* Vol. 03.01, ASTM, Philadelphia, pp. 519–554. (Standard E399-83.)

ASTM (1991) "Standard test methods for plane-strain fracture toughness and strain energy release rate of plastic materials." In *Annual Book of ASTM Standards,* Vol. 08.03, ASTM, Philadelphia. (Standard D 5045-91.)

Atkins, A.G. and Mai. Y.W. (1985) *Elastic and Plastic Fracture,* Ellis Horwood Ltd., John Wiley & Sons, Chichester, New York.

Ballarini, R., Shah, S. P. and Keer, L. M. (1985) "Crack growth in cement based composites." *Eng. Fract. Mech.,* **20**(3), 433–445.

Balmer, G. G. (1949) *Shearing Strength of Concrete under High Triaxial Stress—Computation of Mohr's Envelope as a Curve.* Report No. SP-23, Struct. Res. Lab., Denver, CO.

Baluch, M. H., Azad, A. K. and Ashmawi, W. (1992) "Fracture mechanics application to reinforced concrete members in flexure." In *Application of Fracture Mechanics to Reinforced Concrete*, A. Carpinteri, ed., Elsevier Applied Science, London, pp. 413–436.

Baluch, M. H, Qureshi, A. B. and Azad, A. K. (1989) "Fatigue crack propagation in plain concrete." In *Fracture of Concrete and Rock*, S.P. Shah and S.E. Swartz, eds., Springer-Verlag, New York, pp. 80–85.

Barenblatt, G. I. (1959) "The formation of equilibrium cracks during brittle fracture, general ideas and hypothesis, axially symmetric cracks." *Prikl. Mat. Mech.*, **23**(3), 434–444.

Barenblatt, G. I. (1962) "The mathematical theory of equilibrium of cracks in brittle fracture." *Adv. Appl. Mech.*, **7**, 55–129.

Barenblatt, G. I. (1979) *Similarity, Self-Similarity and Intermediate Asymptotics*, Plenum Press, New York.

Barsoum, R. S. (1975) "Further application of quadratic isoparametric finite elements to linear fracture mechanics of plate bending and general shells." *Int. J. Fracture*, **11**, 167–169.

Barsoum, R. S. (1976) "On the use of isoparametric finite elements in linear fracture mechanics." *Int. J. Numer. Meth. Eng.*, **10**, 25–37.

Batdorf, S. B. and Budianski, B. (1949) *A Mathematical Theory of Plasticity Based on the Concept of Slip*. Technical Note No. 1871, Nat. Advisory Committee for Aeronautics, Washington, D.C.

Batto, R. A. and Schulson, E. M. (1993) "On the ductile-to-brittle transition in ice under compression." *Acta Metall. Mater.*, **41**(7), 2219–2225.

Bažant, Z. P. (1967) "Stability of continuum and compression strength." *Bulletin RILEM*, **39**, 99–112. (In French.)

Bažant, Z. P. (1968) "Effect of folding of reinforcing fibers on the elastic moduli and strength of composite materials." *Mekhanika Polimerov*, **4**, 314–321. (In Russian.)

Bažant, Z. P. (1972a) "Thermodynamics of hindered adsorption with application to cement paste and concrete." *Cement Concrete Res.*, **2**, 1–16.

Bažant, Z. P. (1972b) "Thermodynamics of interacting continua with surfaces and creep analysis of concrete structures." *Nucl. Eng. Des.*, **20**, 477–505.

Bažant, Z. P. (1974) "Three-dimensional harmonic functions near termination or intersection of singularity lines: A general numerical method." *Int. J. Eng. Sci.*, **12**, 221–243.

Bažant, Z.P. (1975) "Theory of creep and shrinkage in concrete structures: A precis of recent developments." In *Mechanics Today*, Vol. 2, S. Nemat-Nasser, ed., Pergamon Press, Oxford, pp. 1–93.

Bažant, Z. P. (1976) "Instability, ductility and size effect in strain-softening concrete." *J. Eng. Mech. Div.-ASCE*, **102**, 331–344. (Discussion **103**, 357-358, 775-777 and **103**, 501-502.)

Bažant, Z. P. (1982) "Crack band model for fracture of geomaterials." In *Proc. 4th Int. Conf. on Numerical Methods in Geomechanics*, Vol. 3, Z. Eisenstein, ed., pp. 1137–1152.

Bažant, Z. P. (1983) "Fracture in concrete and reinforced concrete." In *Preprints IUTAM Prager Symposium on Mechanics of Geomaterials: Rocks, Concretes, Soils*, Z. P. Bažant, ed., pp. 281–316. (See also Bažant 1985c.)

Bažant, Z. P. (1984a) "Size effect in blunt fracture: Concrete, rock, metal." *J. Eng. Mech.-ASCE*, **110**, 518–535.

Bažant, Z. P. (1984b) "Imbricate continuum and its variational derivation." *J. Eng. Mech.-ASCE*, **110**, 1693–1712.

Bažant, Z. P. (1984c) "Microplane model for strain controlled inelastic behavior." In *Mechanics of Engineering Materials*, C. S. Desai and R. H. Gallagher, eds., J. Wiley, London, pp. 45–59.

Bažant, Z. P. (1985a) "Mechanics of fracture and progressive cracking in concrete structures." In *Fracture Mechanics of Concrete: Structural Application and Numerical Calculation*, G. C. Sih and A. DiTommaso, eds., Martinus Nijhoff, Dordrecht, pp. 1–94.

Bažant, Z. P. (1985b) "Fracture mechanics and strain-softening in concrete." In *Preprints U. S.- Japan Seminar on Finite Element Analysis of Reinforced Concrete Structures*, Vol. 1, pp. 47–69.

Bažant, Z. P. (1985c) "Fracture in concrete and reinforced concrete." In *Mechanics of Geomaterials: Rocks, Concretes, Soils*, Z. P. Bažant, ed., John Wiley & Sons, Chichester, New York, pp. 259–303.

Bažant, Z.P. (1985d) "Comment on Hillerborg's size effect law and fictitious crack model." In *Dei Poli Anniversary Volume*, L. Cedolin et al., eds., Politecnico di Milano, Italy, pp. 335–338.

Bažant, Z. P. (1986a) "Fracture mechanics and strain-softening of concrete." In *Finite Element Analysis of Reinforced Concrete Structures*, C. Meyer and H. Okamura, eds., ASCE, New York, pp. 121–150.

Bažant, Z. P. (1986b) "Distributed cracking and nonlocal continuum." In *Finite Element Methods for Nonlinear Problems*, P. Bergan et al., eds., Springer, Berlin, pp. 77–102.

Bažant, Z. P. (1986c) "Mechanics of distributed cracking." *Appl. Mech. Rev.*, **39**, 675–705.

Bažant, Z. P. (1987a) "Fracture energy of heterogeneous materials and similitude." In *Preprints SEM-RILEM Int. Conf. on Fracture of Concrete and Rock*, S. P. Shah and S. E. Swartz, eds., Society for Experimental Mechanics (SEM), Bethel, pp. 390–402. (See also Bažant 1989a.)

Bažant, Z. P. (1987b) "Snapback instability at crack ligament tearing and its implication for fracture micromechanics." *Cement Concrete Res.*, **17**, 951–967.

Bažant, Z. P. (1987c) "Why continuum damage is nonlocal: Justification by quasi-periodic microcrack array." *Mech. Res. Commun.*, **14**(5/6), 407–419.

Bažant, Z. P., ed. (1988a) *Mathematical Modeling of Creep and Shrinkage of Concrete*, John Wiley & Sons, Chichester, New York.

Bažant, Z. P. (1988b) *Fracture of Concrete*. Lecture Notes for Course 720-D30, Northwestern University, Evanston, Illinois 60208, U.S.A.

Bažant, Z. P. (1989a) "Fracture energy of heterogeneous materials and similitude." In *Fracture of Concrete and Rock*, S. P. Shah and S. E. Swartz, eds., Springer Verlag, New York, pp. 229–241.

Bažant, Z. P. (1989c) "Advances in material modeling of concrete." In *Tenth International Conference on Structural Mechanics in Reactor Technology (SMiRT10)*, Vol. A, A. H. Hadjian, ed., pp. 301–330.

Bažant, Z. P. (1990a) "Justification and improvement of Kienzler and Herrmann's estimate of stress intensity factors of cracked beam." *Eng. Fract. Mech.*, **36**(3), 523–525.

Bažant, Z. P. (1990b) "A critical appraisal of 'no-tension' dam design: A fracture mechanics viewpoint." *Dam Eng.*, **1**(4), 237–247.

Bažant, Z. P. (1990c) "Recent advances in failure localization and nonlocal models." In *Micromechanics of Failure of Quasi-Brittle Materials*, S. P. Shah, S. E. Swartz and M. L. Wang, eds., Elsevier, London, pp. 12–32.

Bažant, Z. P. (1990d) "Smeared-tip superposition method for nonlinear and time-dependent fracture." *Mech. Res. Commun.*, **17**(5), 343–351.

Bažant, Z. P. (1991a) "Rate effect, size effect and nonlocal concepts for fracture of concrete and other quasi-brittle materials." In *Toughening Mechanisms in Quasi-Brittle Materials*, S.P. Shah, ed., Kluwer Academic Publishers, Dordrecht, The Netherlands, pp. 131–154.

Bažant, Z. P. (1991b) "Why continuum damage is nonlocal: micromechanics arguments." *J. Eng. Mech.-ASCE*, **117**(5), 1070–1087.

Bažant, Z. P. (1992a) "Large-scale thermal bending fracture of sea ice plates." *J. Geophys. Res.*, **97**(C11), 17739–17751.

Bažant, Z. P. (1992b) "New concept of nonlocal continuum damage: Crack influence function." In *Macroscopic Behavior of Heterogeneous Materials from Microstructure*, S. Torquato and D. Krajcinovic, eds., The American Society of Mechanical Engineers, New York, pp. 153–160. (AMD–Vol.147, ASME Winter Annual Meeting, Anaheim.)

Bažant, Z. P. (1992c) "Large-scale fracture of sea ice plates." In *Proc., 11th IAHR International Ice Symposium*, Vol. 2, T. M. Hrudey, ed., Univ. of Alberta, Edmonton, Canada, pp. 991–1005.

Bažant, Z. P. (1993a) "Scaling laws in mechanics of failure." *J. Eng. Mech.-ASCE*, **119**(9), 1828–1844.

Bažant, Z. P. (1993b) "Current status and advances in the theory of creep and interaction with fracture." In *Creep and Shrinkage of Concrete*, Z. P. Bažant and I. Carol, eds., E & FN Spon, London, pp. 291–307.

Bažant, Z. P. (1993c) *Concept of Boundaries for Microplane Model*. Internal Research Note, Dept. of Civil Engrg., Northwestern University, Evanston, Illinois 60208, U.S.A.

Bažant, Z. P. (1993d) "Discussion of 'Fracture mechanics and size effect of concrete in tension', by Tang et al. (1992)." *J. Struct. Eng.-ASCE*, **119**(8), 2555–2558.

Bažant, Z. P. (1994a) "Size effect in tensile and compressive quasibrittle failures." In *Size Effect in Concrete Structures*, H. Mihashi, H. Okamura and Z. P. Bažant, eds., E & FN Spon, London, pp. 161–180.

Bažant, Z. P. (1994b) "Nonlocal damage theory based on micromechanics of crack interactions." *J. Eng. Mech.-ASCE*, **120**(3), 593–617. (Addendum and Errata **120**, 1401–1402.)

Bažant, Z. P. (1994c) *Is size effect caused by fractal nature of crack surfaces?*. Report No. 94-10/402i, Department of Civil Engineering, Northwestern University, Evanston, Illinois.

Bažant, Z. P. (1995a) "Scaling theories for quasibrittle fracture: Recent advances and new directions." In *Fracture Mechanics of Concrete Structures*, F. H. Wittmann, ed., Aedificatio Publishers, Freiburg, Germany, pp. 515–534.

Bažant, Z. P. (1995b) *Scaling of Quasibrittle Fracture: I. Asymptotic Analysis Based on Laws of Thermodynamics. II. The Fractal Hypothesis, its Critique and Weibull Connection*. Report No. 95-7/C402s, Dep. of Civil Engineering, Northwestern University, Evanston, Illinois 60208, U.S.A.

Bažant, Z. P. (1995c) "Creep and Damage in Concrete." In *Materials Science of Concrete IV*, J. Skalny and S. Mindess, eds., Am. Cer. Soc., Westerville, Ohio, pp. 355–389.

Bažant, Z. P. (1995d) *Microplane model for concrete. I. Stress-strain boundaries and finite strain.* Internal Report to WES, Vicksburg, Northwestern University.

Bažant, Z. P. (1995e) "Scaling of quasibrittle fracture and the fractal question." *J. Eng. Mater. Technol.-T. ASME,* **117**, 361–367.

Bažant, Z. P. (1995f) "Scaling theories for quasibrittle fracture: Recent advances and new directions." In *Fracture Mechanics of Concrete Structures*, Vol. 1, F.H. Wittmann, ed., Aedificatio Publishers, Freiburg, Germany, pp. 515–534.

Bažant, Z. P. (1996a) "Is no-tension design of concrete or rock structures always safe?—Fracture analysis." *J. Struct. Eng.-ASCE,* **122**(1), 2–10.

Bažant, Z. P. (1996b) *Fracturing Truss Model: Explanation of Size Effect Mechanism in Shear Failure of Reinforced Concrete.* Report No. 96-3/603f, Dept. of Civil Engrg., Northwestern University, Evanston, Illinois; also *J. of Engrg. Mechanics ASCE* 123 (12), in press.

Bažant, Z. P. (1996c) "Finite strain generalization of small-strain constitutive relations for any finite strain tensor and additive volumetric-deviatoric split." *Int. J. Solids Struct.,* **33**(20–22), 2887–2897. (Special issue in memory of Juan Simo.)

Bažant, Z. P. (1996d) "Untitled." Personally communicated research note to J. Planas, November 1996.

Bažant, Z. P. (1996e) "Can scaling of structural failure be explained by fractal nature of cohesive fracture?" In *Size-Scale Effects in the Failure Mechanisms of Materials and Structures*, A. Carpinteri, ed., E & FN Spon, London, pp. 284–289. (Appendix to a paper by Li and Bažant.)

Bažant, Z. P. (1997a) "Scaling of quasibrittle fracture: Asymptotic analysis." *Int. J. Fracture,* **83**(1), 19–40.

Bažant, Z. P. (1997b) "Recent advances in brittle-plastic compression failure: damage localization, scaling and finite strain." In *Computational Plasticity*, D. R. J. Owen, E. Oñate and E. Hinton, eds., Int. Center for Num. Meth. in Eng. (CIMNE), Barcelona, Spain, pp. 3–19.

Bažant, Z. P. (1997c) *Easy-to-compute finite strain tensor with symmetric inverse, approximating Hencky strain tensor.* Report No. 96-9/425e, Northwestern University, Evanston, Illinois. (Submitted to *J. of Engrg. Materials and Technology* ASME.)

Bažant, Z. P. (1997d) "Scaling of quasibrittle fracture: hypotheses of invasive and lacunar fractality, their critique and Weibull connection." *Int. J. Fracture,* **83**(1), 41–65.

Bažant, Z. P. (1997e) "Scaling of structural failure." *Appl. Mech. Rev.,* **50**(10), 593–627.

Bažant, Z. P. and Baweja, S. (1995a) "Justification and refinement of Model B3 for concrete creep and shrinkage. 1. Statistics and sensitivity." *Mater. Struct.,* **28**, 415–430.

Bažant, Z. P. and Baweja, S. (1995b) "Justification and refinement of Model B3 for concrete creep and shrinkage. 2. Updating and theoretical basis." *Mater. Struct.,* **28**, 488–495.

Bažant, Z. P. and Baweja, S. (1995c) "Creep and shrinkage prediction model for analysis and design of concrete structures – model B3." *Mater. Struct.,* **28**, 357–365. (RILEM Recommendation, in collaboration with RILEM Committee TC 107-GCS. Erratum **29**, 126.)

Bažant, Z. P. and Beissel, S. (1994) "Smeared-tip superposition method for cohesive fracture with rate effect and creep." *Int. J. Fracture,* **65**, 277–290.

Bažant, Z. P. and Belytschko, T. B. (1985) "Wave propagation in strain-softening bar: Exact solution." *J. Eng. Mech.-ASCE,* **111**, 381–389.

Bažant, Z. P. and Cao, Z. (1986) "Size effect in brittle failure of unreinforced pipes." *ACI J.,* **83**(3), 369–373.

Bažant, Z. P. and Cao, Z. (1987) "Size effect in punching shear failure of slabs." *ACI Struct. J.,* **84**, 44–53.

Bažant, Z. P. and Cedolin, L. (1979) "Blunt crack band propagation in finite element analysis." *J. Eng. Mech. Div.-ASCE,* **105**, 297–315.

Bažant, Z. P. and Cedolin, L. (1980) "Fracture mechanics of reinforced concrete." *J. Eng. Mech. Div.-ASCE,* **106**, 1257–1306.

Bažant, Z. P. and Cedolin, L. (1983) "Finite element modeling of crack band propagation." *J. Struct Eng.-ASCE,* **109**, 69–92.

Bažant, Z. P. and Cedolin, L. (1991) *Stability of Structures: Elastic, Inelastic, Fracture and Damage Theories*, Oxford University Press, New York.

Bažant, Z. P. and Cedolin, L. (1993) "Why direct tension specimens break flexing to the side." *J. Struct. Eng.-ASCE,* **119**(4), 1101–1113.

Bažant, Z. P. and Chern, J.-C. (1985a) "Strain-softening with creep and exponential algorithm." *J. Eng. Mech.-ASCE,* **111**, 391–415.

Bažant, Z. P. and Chern, J.-C. (1985b) "Concrete creep at variable humidity: Constitutive law and mechanism." *Mater. Struct.,* **18**, 1–20.

Bažant, Z. P. and Desmorat, R. (1994) "Size effect in fiber of bar pullout with interface softening slip." *J. Eng. Mech.-ASCE,* **120**(9), 1945–1962.

Bažant, Z. P. and Estenssoro, L. F. (1979) "Surface singularity and crack propagation." *Int. J. Solids Struct.,* **15**, 405–426. (Addendum **16**, 479–481.)

Bažant, Z. P. and Gambarova, P. (1984) "Crack shear in concrete: Crack band microplane model." *J. Struct. Eng.-ASCE,* **110**, 2015–2035.

Bažant, Z. P. and Gettu, R. (1989) "Determination of nonlinear fracture characteristics and time dependence from size effect." In *Fracture of Concrete and Rock: Recent Developments*, S. P. Shah, S. E. Swartz and B. Barr, eds., Elsevier Applied Science, London, pp. 549–565.

Bažant, Z. P. and Gettu, R. (1990) "Size effect in concrete structures and influence of loading rates." In *Serviceability and Durability of Construction Materials*, B. A. Suprenant, ed., American Society of Civil Engineers (ASCE), New York, pp. 1113–1123.

Bažant, Z. P. and Gettu, R. (1992) "Rate effects and load relaxation: Static fracture of concrete." *ACI Mater. J.,* **89**(5), 456–468.

Bažant, Z. P. and Jirásek, M. (1993) "R-curve modeling of rate and size effects in quasibrittle fracture." *Int. J. Fracture,* **62**, 355–373.

Bažant, Z. P. and Jirásek, M. (1994a) "Damage nonlocality due to microcrack interactions: Statistical determination of crack influence function." In *Fracture and Damage in Quasibrittle Structures: Experiment, Modelling and Computer Analysis*, Z. P. Bažant, Z. Bittnar, M. Jirásek and J. Mazars, eds., E&FN Spon, London, pp. pp.3–17.

Bažant, Z. P. and Jirásek, M. (1994b) "Nonlocal model based on crack interactions: A localization study." *J. Eng. Mater. Technol.-T. ASME,* **116**, 256–259.

Bažant, Z. P. and Kazemi, M. T. (1990a) "Determination of fracture energy, process zone length and brittleness number from size effect, with application to rock and concrete." *Int. J. Fracture,* **44**, 111–131.

Bažant, Z. P. and Kazemi, M. T. (1990b) "Size effect in fracture of ceramics and its use to determine fracture energy and effective process zone length." *J. Am. Ceram. Soc.,* **73**(7), 1841–1853.

Bažant, Z. P. and Kazemi, M. T. (1991) "Size effect on diagonal shear failure of beams without stirrups." *ACI Struct. J.,* **88**(3), 268–276.

Bažant, Z. P. and Keer, L. M. (1974) "Singularity of elastic stresses and of harmonic functions at conical notches or inclusions." *Int. J. Solids Struct.,* **10**, 957–964.

Bažant, Z. P. and Kim, J.-J. (1996a) *Penetration fracture and size effect in sea ice plates with part-through bending cracks.* Report No. 96-10/402p, Dep. of Civil Engineering, Northwestern University, Evanston, Illinois. (Also *J. of Eng. Mech.,* in press.)

Bažant, Z. P. and Kim, J.-J. (1996b) *Tube-squash test and large strains of normal and high-strength concretes with shear angle over 30°.* Report, Northwestern University, Evanston, Illinois. (Submitted to ACI Materials Journal.)

Bažant, Z. P. and Kim, J.-K. (1984) "Size effect in shear failure of longitudinally reinforced beams." *ACI J.,* **81**, 456–468. (Discussion and Closure **82**, 579-583.)

Bažant, Z. P. and Kwon, Y. W. (1994) "Failure of slender and stocky reinforced concrete columns: Tests of size effect." *Mater. Struct.,* **27**, 79–90.

Bažant, Z. P. and Li, Y.-N. (1994a) "Cohesive crack model for geomaterials: Stability analysis and rate effect." *Appl. Mech. Rev.,* **47**(6), S91–S96. (Part of *Mechanics U.S.A. 1994.* ed. by A.S. Kobayashi, Proc. 12th U.S. Nat. Congress of Appl. Mechanics, Seattle, WA, June.)

Bažant Z. P. and Li Y.-N. (1994b) "Penetration fracture of sea ice plate: Simplified analysis and size effect." *J. Eng. Mech.-ASCE,* **120**(6), 1304–1321.

Bažant, Z. P. and Li, Y.-N. (1995a) "Stability of cohesive crack model: Part I—Energy principles." *J. Appl. Mech.-T. ASME,* **62**, 959–964.

Bažant, Z. P. and Li, Y.-N. (1995b) "Stability of cohesive crack model: Part II—Eigenvalue analysis of size effect on strength and ductility of structures." *J. Appl. Mech.-T. ASME,* **62**, 965–969.

Bažant, Z. P. and Li Y.-N. (1995d) "Penetration fracture of sea ice plate." *Int. J. Solids Struct.,* **32**(3/4), 303–313.

Bažant, Z. P. and Li, Y.-N. (1997) "Cohesive crack model with rate-dependent crack opening and viscoelasticity: I. Mathematical model and scaling." *Int. J. Fracture,* in press.

Bažant, Z. P. and Li, Z. (1995c) "Modulus of rupture: Size effect due to fracture initiation in boundary layer." *J. Struct. Eng.-ASCE,* **121**(4), 739–746.

Bažant, Z. P. and Li, Z. (1996) "Zero-brittleness size-effect method for one-size fracture test of concrete." *J. Eng. Mech.-ASCE,* **122**(5), 458–468.

Bažant, Z. P. and Lin, F.-B. (1988a) "Nonlocal smeared cracking model for concrete fracture." *J. Struct. Eng.-ASCE,* **114**(11), 2493–2510.

Bažant, Z. P. and Lin, F.-B. (1988b) "Nonlocal yield limit degradation." *Int. J. Numer. Meth. Eng.,* **26**, 1805–1823.

Bažant, Z. P. and Oh, B. H. (1982) "Strain rate effect in rapid triaxial loading of concrete." *J. Eng. Mech.-ASCE,* **108**(5), 767–782.

Bažant, Z. P. and Oh, B.-H. (1983a) "Crack band theory for fracture of concrete." *Mater. Struct.,* **16**, 155–177.

Bažant, Z. P. and Oh, B.-H. (1983b) "Microplane model for fracture analysis of concrete structures." In *Proc. Symp. on the Interaction of Non-Nuclear Munitions with Structures*, pp. 49–53.

Bažant, Z. P. and Oh, B.-H. (1985) "Microplane model for progressive fracture of concrete and rock." *J. Eng. Mech.-ASCE,* **111**, 559–582.

Bažant, Z. P. and Oh, B.-H. (1986) "Efficient numerical integration on the surface of a sphere." *Z. Angew. Math. Mech.,* **66**(1), 37–49.

Bažant, Z. P. and Ohtsubo, H. (1977) "Stability conditions for propagation of a system of cracks in a brittle solid." *Mech. Res. Commun.,* 4(5), 353–366.

Bažant, Z. P. and Osman, E. (1976) "Double power law for basic creep of concrete." *Mater. Struct.,* **9**, 3–11.

Bažant, Z. P. and Ožbolt, J. (1990) "Nonlocal microplane model for fracture, damage, and size effect in structures." *J. Eng. Mech.-ASCE,* **116**(11), 2484–2504.

Bažant, Z. P. and Ožbolt, J. (1992) "Compression failure of quasi-brittle material: Nonlocal microplane model." *J. Eng. Mech.-ASCE,* **118**(3), 540–556.

Bažant, Z. P. and Panula, L. (1978) "Practical prediction of time-dependent deformations of concrete. Part II – Basic creep." *Mater. Struct.,* **11**, 317–328.

Bažant, Z. P. and Pfeiffer, P. A. (1986) "Shear fracture tests of concrete." *Mater. Struct.,* **19**, 111–121.

Bažant, Z. P. and Pfeiffer, P. A. (1987) "Determination of fracture energy from size effect and brittleness number." *ACI Mater. J.,* **84**(6), 463–480.

Bažant, Z. P. and Pijaudier-Cabot, G. (1988) "Nonlocal continuum damage, localization instability and convergence." *J. Appl. Mech.-T. ASME,* **55**, 287–293.

Bažant, Z. P. and Pijaudier-Cabot, G. (1989) "Measurement of characteristic length of nonlocal continuum." *J. Eng. Mech.-ASCE,* **115**(4), 755–767.

Bažant, Z. P. and Prasannan, S. (1989) "Solidification theory for concrete creep: I. Formulation." *J. Eng. Mech.-ASCE,* **115**(8), 1691–1703.

Bažant, Z. P. and Prat, P. C. (1988a) "Effect of temperature and humidity on fracture energy of concrete." *ACI Mater. J.,* **85**, 262–271.

Bažant, Z. P. and Prat, P. C. (1988b) "Microplane model for brittle plastic material: I. Theory; and II. Verification." *J. Eng. Mech.-ASCE,* **114**, 1672–1702.

Bažant, Z. P. and Prat, P. C. (1995) "Elastic material with systems of growing or closing cracks: Tangential Stiffness." In *Contemporary Research in Engineering Science*, R. Batra, ed., Springer Verlag, New York, pp. 55–65.

Bažant, Z. P. and Prat, P. C. (1997) "Tangential stiffness tensor of material with growing cracks." *Mech. Res. Commun.,* submitted.

Bažant, Z. P. and Schell, W. F. (1993) "Fatigue fracture of high-strength concrete and size effect." *ACI Mater. J.,* **90**(5), 472–478.

Bažant, Z. P. and Şener, S. (1987) "Size effect in torsional failure of longitudinally reinforced concrete beams." *J. Struct Eng.-ASCE,* **113**(10), 2125–2136.

Bažant, Z. P. and Şener, S. (1988) "Size effect in pullout tests." *ACI Mater. J.,* **85**, 347–351.

Bažant, Z. P. and Sun, H.-H. (1987) "Size effect in diagonal shear failure: Influence of aggregate size and stirrups." *ACI Mater. J.,* **84**, 259–272.

Bažant, Z. P. and Wahab, A. B. (1979) "Instability and spacing of cooling or shrinkage cracks." *J. Eng. Mech. Div.-ASCE,* **105**, 873–889.

Bažant, Z. P. and Wahab, A. B. (1980) "Stability of parallel cracks in solids reinforced by bars." *Int. J. Solids Struct.,* **16**, 97–105.

Bažant, Z. P. and Xi, Y. (1991) "Statistical size effect in quasi-brittle structures: II. Nonlocal theory." *J. Eng. Mech.-ASCE,* **117**(11), 2623–2640.

Bažant, Z. P. and Xi, Y. (1994) "Fracture of random quasibrittle materials: Markov process and Weibull-type models." In *Structural Safety and Reliability*, G. I. Schuëller, M. Shinozuka and J. T. P. Yao, eds., A. A. Balkema, Rotterdam–Brookfield, pp. 609–614. (Proc. of ICOSSAR'93—6th Intern. Conf. on Struct. Safety and Reliability, Innsbruck, Austria, Aug. 9–13, 1993.)

Bažant, Z. P. and Xiang, Y. (1994) "Compression failure of quasibrittle materials and size effect." In *Damage Mechanics in Composites*, D. H. Allen and J. W. Ju, eds., The American Society of Mechanical Engineers, New York, pp. 143–148. (AMD–Vol. 185, Winter Annual Meeting, Chicago.)

Bažant, Z. P. and Xiang, Y. (1997) "Size effect in compression fracture: splitting crack band propagation." *J. Eng. Mech.-ASCE,* **123**(2), 162–172.

Bažant, Z. P. and Xu, K. (1991) "Size effect in fatigue fracture of concrete." *ACI Mater. J.,* **88**(4), 390–399.

Bažant, Z. P., Adley, M. D. and Xiang, Y. (1996) "Finite strain analysis of deformations of quasibrittle material during missile impact and penetration." In *Advances in Failure Mechanisms in Brittle Materials*, R. J. Clifton and H. D. Espinosa, eds., The American Society of Mechanical Engineers, New York. (MD–Vol 75, AMD–Vol. 219.)

Bažant, Z. P., Bai, S.-P. and Gettu, R. (1993) "Fracture of rock: Effect of loading rate." *Eng. Fract. Mech.,* **45**(3), 393–398.

Bažant, Z. P., Belytschko, T. B. and Chang, T.-P. (1984) "Continuum model for strain softening." *J. Eng. Mech.-ASCE,* **110**, 1666–1692.

Bažant, Z. P., Bishop, F. C. and Chang, T.-P. (1986) "Confined compression tests of cement paste and concrete up to 300 ksi." *ACI J.,* **83**(4), 553–560.

Bažant, Z. P., Daniel, I. M. and Li, Z. (1996) "Size effect and fracture characteristics of composite laminates." *J. Eng. Mater. Technol.-T. ASME,* **118**, 317–324.

Bažant, Z. P., Gettu, R. and Kazemi, M. T. (1991) "Identification of nonlinear fracture properties from size-effect tests and structural analysis based on geometry-dependent R-curves." *Int. J. Rock Mech. Min. Sci.,* **28**(1), 43–51.

Bažant, Z. P., Glazik, J. L. and Achenbach, J. D. (1976) "Finite element analysis of wave diffraction by a crack." *J. Eng. Mech. Div.-ASCE,* **102**, 479–496. (Discussion **103**, 226–228, 497–499, 1181–1185.)

Bažant, Z. P., Glazik, J. L. and Achenbach, J. D. (1978) "Elastodynamic fields near running cracks by finite elements." *Comput. Struct.,* **26**, 567–574.

Bažant, Z. P., Gu, W.-H. and Faber, K. T. (1995) "Softening reversal and other effects of a change in loading rate on fracture of concrete." *ACI Mater. J.,* **92**, 3–9.

Bažant, Z. P., He, S., Plesha, M. E. and Rowlands, R. E. (1991) "Rate and size effect in concrete fracture: Implications for dams." In *Proc. Int. Conf. on Dam Fracture*, V. Saouma, R. Dungar, and D. Morris, eds., University of Colorado, Boulder, CO, pp. 413–425.

Bažant, Z. P., Jirásek, M., Xiang, Y. and Prat, P. C. (1994) "Microplane model with stress-strain boundaries and its identification from tests with localized damage." In *Computational Modeling of Concrete Structures*, H. Mang et al., eds., Pineridge Press, Swansea, pp. 255–261.

Bažant, Z. P., Kazemi, M. T. and Gettu, R. (1989) "Recent studies of size effect in concrete structures." In *Transactions of the Tenth International Conference on Structural Mechanics in Reactor Technology.*, Vol. H, A. H. Hadjian, ed., pp. 85–93.

Bažant, Z. P., Kazemi, M. T., Hasegawa, T. and Mazars, J. (1991) "Size effect in Brazilian split-cylinder tests: Measurement and fracture analysis." *ACI Mater. J.,* **88**(3), 325–332.

Bažant, Z. P., Kim, J.-J. and Li, Y.-N. (1995) "Part-through bending cracks in sea ice plates: Mathematical modeling." In *Ice Mechanics 1995*, J. P. Dempsey and Y. Rajapakse, eds., The American Society of Mechanical Engineers, New York, pp. 97–105. (AMD-Vol. 207, ASME Summer Meeting, Los Angeles, CA.)

Bažant, Z. P., Kim, J-K. and Pfeiffer, P. A. (1986) "Nonlinear fracture properties from size effect tests." *J. Struct. Eng.-ASCE,* **112**, 289–307.

Bažant, Z. P., Lee, S-G. and Pfeiffer, P. A. (1987) "Size effect tests and fracture characteristics of aluminum." *Eng. Fract. Mech.,* **26**(1), 45–57.

Bažant, Z. P., Li, Z. and Thoma, M. (1995) "Identification of stress-slip law for bar or fiber pullout by size effect tests." *J. Eng. Mech.-ASCE,* **121**(5), 620–625.

Bažant, Z. P., Lin, F.-B. and Lippmann, H. (1993) "Fracture energy release and size effect in borehole breakout." *Int. J. Numer. Anal. Meth. Geomech.,* **17**, 1–14.

Bažant, Z. P., Ohtsubo, R. and Aoh, K. (1979) "Stability and post-critical growth of a system of cooling and shrinkage cracks." *Int. J. Fracture,* **15**, 443–456.

Bažant, Z. P., Ožbolt, J. and Eligehausen, R. (1994) "Fracture size effect: Review of evidence for concrete structures." *J. Struct Eng.-ASCE,* **120**, 2377–2398.

Bažant, Z. P., Şener, S. and Prat, P. C. (1988) "Size effect tests of torsional failure of plain and reinforced concrete beams." *Mater. Struct.,* **21**, 425–430.

Bažant, Z. P., Tabbara, M. R., Kazemi, M. T. and Pijaudier-Cabot, G. (1990) "Random particle model for fracture of aggregate or fiber composites." *J. Eng. Mech.-ASCE,* **116**, 1686–1705.

Bažant, Z. P., Xi, Y. and Baweja, S. (1993) "Improved prediction model for time-dependent deformations of concrete: Part 7 — Short form of BP-KX model, statistics and extrapolation of short-time data." *Mater. Struct.,* **26**, 567–574.

Bažant, Z. P., Xi, Y. and Reid, S. G. (1991) "Statistical size effect in quasi-brittle structures: I. Is Weibull theory applicable?" *J. Eng. Mech.-ASCE,* **117**(11), 2609–2622.

Bažant, Z. P., Xiang, Y., Adley, M. D., Prat, P. C. and Akers, S. A. (1996) "Microplane model for concrete. II. Data delocalization and verification." *J. Eng. Mech.-ASCE,* **122**(3), 255–262.

Bažant, Z. P., Xiang, Y. and Prat, P. C. (1996) "Microplane model for concrete. I. Stress-strain boundaries and finite strain." *J. Eng. Mech.-ASCE,* **122**(3), 245–254. (Erratum in **123**.)

Bell, J. F. (1985) "Contemporary perspectives in finite strain plasticity." *Int. J. Plasticity,* **1**, 3–27.

Belytschko, T. B., Bažant, Z. P., Hyun, Y. W. and Chang, T.-P. (1986) "Strain-softening materials and finite element solutions." *Comput. Struct.,* **23**(2), 163–180.

Belytschko, T., Fish, J. and Englemann, B. E. (1988) "A finite element with embedded localization zones." *Comput. Meth. Appl. Mech. Eng.,* **70**, 59–89.

Bender, M. C. and Orszag, S. A. (1978) *Advanced Mathematical Methods for Scientists and Engineers,* McGraw Hill, New York.

Beremin, F. M. "A local criterion for cleavage fracture of a nuclear pressure vesse steel." *Metall. Trans. A,* **14**, 2277–2287.

Berthaud, Y., Ringot, E. and Schmitt N. (1991) "Experimental measurements of localization for tensile tests on concrete." In *Fracture Processes in Concrete, Rock and Ceramics,* J. G. M. van Mier, J. G. Rots and A. Bakker, eds., E & FN Spon, London, pp. 41–50.

Bieniawski, Z. T. (1974) "Estimating the strength of rock materials." *J. S. Afr. Inst. Min. Metall.,* **74**, 312–320.

Biot, M. A. (1955) "Variational principles of irreversible thermodynamics with application to viscoelasticity." *Phys. Rev.,* **97**, 1163–1169.

Biot, M. A. (1965) *Mechanics of Incremental Deformations,* John Wiley & Sons, New York.

Bittencourt, T. N., Ingraffea, A. R. and Llorca, J. (1992) "Simulation of arbitrary, cohesive crack propagation." In *Fracture Mechanics of Concrete Structures,* Z. P. Bažant, ed., Elsevier Applied Science, London, pp. 339–350.

Blanks, R. F. and McNamara, C. C. (1935) "Mass concrete tests in large cylinders." *ACI J.,* **31**, 280–303.

Bocca, P., Carpinteri, A. and Valente, S. (1990) "Size effects in the mixed crack propagation: Softening and snap-back analysis." *Eng. Fract. Mech.,* **35**, 159–170.

Bocca, P., Carpinteri, A. and Valente, S. (1991) "Mixed mode fracture of concrete." *Int. J. Solids Struct.,* **27**, 1139–1153.

Bocca, P., Carpinteri, A. and Valente, S. (1992) "Fracture mechanics evaluation of anchorage bearing capacity in concrete." In *Application of Fracture Mechanics to Reinforced Concrete,* A. Carpinteri, ed., Elsevier Applied Science, London, pp. 231–265.

Bogdanoff, J. L. and Kozin, F. (1985) *Probabilistic Models of Cumulative Damage,* John Wiley & Sons, New York.

Borodich, F. M. (1992) "Fracture energy in a fractal crack propagating in concrete or rock." *Doklady Akademii Nauk.,* **325**(6), 1138–1141. (In Russian. Transl. in *Trans. Russian Ac. Sci.,* Earth Sci. Sec., **327**(8), 36–40.)

de Borst, R. (1986) *Non-Linear Analysis of Frictional Materials.* Doctoral thesis. Delft University of Technology, Delft, The Netherlands.

de Borst, R. (1990) "Simulation of localization using Cosserat theory." In *Proc., Int. Conf. on Computer-Aided Analysis and Design of Concrete Structures,* N. Bićanić and H.A. Mang, eds., Pineridge Press, Swansea, pp. 931–944.

de Borst, R. (1991) "Simulation of strain localization: A reappraisal of the Cosserat continuum." *Eng. Comput.,* **8**, 317–332.

de Borst, R. and Mühlhaus, H.-B. (1991) "Continuum models for discontinuous media." In *Fracture Processes in Concrete, Rock and Ceramics,* Vol. 2, J. G. M. van Mier, J. G. Rots and A. Bakker, eds., E & FN Spon, London, pp. 601–618.

de Borst, R. and Mühlhaus, H.-B. (1992) "Gradient-dependent plasticity: Formulation and algorithmic aspects." *Int. J. Numer. Meth. Eng.,* **35**, 521–539.

de Borst, R. and Sluys, L. J. (1991) "Localization in a Cosserat continuum under static and dynamic loading conditions." *Comput. Meth. Appl. Mech. Eng.,* **90**, 805–827.

Bosco, C. and Carpinteri, A. (1992) "Fracture mechanics evaluation of minimum reinforcement in concrete structures." In *Applications of Fracture Mechanics to Reinforced Concrete,* A. Carpinteri, ed., Elsevier Applied Science, London, pp. 347–377.

Bosco, C., Carpinteri, A. and DeBernardi, P. G. (1990a) "Fracture of reinforced concrete: Scale effect and snap-back instability." *Eng. Fract. Mech.,* **35**, 665–677.

Bosco, C., Carpinteri, A. and DeBernardi, P. G. (1990b) "Minimum reinforcement in reinforced concrete beams." *J. Struct Eng.-ASCE,* **116**, 427–437.

Brennan, G. (1978) *A Test to Determine the Bending Moment Resistance of Rigid Pipes.* TRRL Supplementary Report No. SR 348, Transport and Road Research Laboratory, Crowthorne, Berkshire.

Bresler, B. and Pister, K. S. (1958) "Strength of concrete under combined stresses." *ACI J.,* **55**(9), 321–345.

Broek, D. (1986) *Elementary Engineering Fracture Mechanics,* 4th edition, Martinus Nijhoff Publishers, Dordrecht.

Broms, C. E. (1990) "Punching of flat plates — A question of concrete properties in biaxial compression and size effect." *ACI Struct. J.,* **87**(3), 292–304.

Brown, J. H. (1972) "Measuring the fracture toughness of cement paste and mortar." *Mag. Concrete Res.,* **24**, 185–196.

Brown, W. F. and Srawley, J. E. (1986) *Plane Strain Crack Toughness Testing of High Strength Metallic Materials,* ASTM Special Technical Publication, No. 410.

Bruckner, A. and Munz, D. (1984) "Scatter of fracture toughness in the brittle-ductile transition region of a ferritic steel." In *Advances in Probabilistic Fracture Mechanics,* C. Sundararajan, ed., The American Society of Mechanical Engineers, New York, pp. 105–111.

Brühwiler, E. (1988) *Fracture Mechanics of Dam Concrete Subjected to Quasi-static and Seismic Loading Conditions.* Doctoral thesis. Laboratory for Building Materials, Swiss Federal Institute of Technology, Lausanne. (Thesis No. 739. In German.)

Brühwiler, E. and Wittmann, F. H. (1990) "The wedge splitting test, a new method of performing stable fracture mechanics tests." *Eng. Fract. Mech.,* **35**, 117–125.

Budianski, B. (1983) "Micromechanics." *Computers and structures,* **16**(1–4), 3–12.

Budianski, B. and Fleck, N. A. (1994) "Compressive kinking of fiber composites: A topical review." *Appl. Mech. Rev.,* **47**(No. 6, Part 2–Supplement, Proc. of 12th U.S. Nat. Congress of Applied Mechanics, Seattle), pp. S246–S255.

Budianski, B. and O'Conell, R. J. (1976) "Elastic moduli of a cracked solid." *Int. J. Solids Struct.,* **12**, 81–97.

Budianski, B. and Wu, T. T. (1962) "Theoretical prediction of plastic strains of polycrystals." In *Proc. Fourth U.S. National Congress of Applied Mechanics,* The American Society of Mechanical Engineers, New York, pp. 1175–1185.

Budianski, B., Fleck, N. A. and Amazigo, J. C. (1997) *On compression kink band propagation.* Report MECH No. 305, Harvard University, Cambrigde, Massachussets. (Submitted to *J. Mech. Phys. Solids.*)

Bueckner, H. F. (1970) "A novel principle for the computation of stress intensity factors." *Z. Angew. Math. Mech.,* **50**, 529–546.

Bui, H. D. (1978) *Mécanique de la Rupture Fragile,* Masson, Paris.

Buyukozturk, O. and Lee, K.M. (1992a) "Implication of mixed-mode fracture concepts." In *Concrete Design Based on Fracture Mechanics,* W. Gerstle and Z. P. Bažant, eds., American Concrete Institute, Detroit, pp. 47–62. (ACI Special Publication SP-134.)

Buyukozturk, O. and Lee, K.M. (1992b) "Interface fracture mechanics of concrete composites." In *Fracture Mechanics of Concrete Structures,* Bažant, Z. P., ed., Elsevier Applied Science, London, pp. 163–168.

Buyukozturk, O., Bakhoum, M. M. and Beattie, S. M. (1990) "Shear behavior of joints in precast concrete segmental bridges." *J. Struct Eng.-ASCE,* **116**(12), 3380–3401.

Carneiro, F. L. L. and Barcellos, A. (1953) "Tensile strength of concrete." *RILEM Bulletin,* **13**, 97–123.

Carol, I. and Bažant, Z. P. (1993) "Solidification theory: A rational and effective framework for constitutive modeling of aging viscoelasticity." In *Creep and Shrinkage of Concrete,* Z. P. Bažant and I. Carol, eds., E & FN Spon, London, pp. 177–188.

Carol, I. and Bažant, Z. P. (1997) "Damage and plasticity in microplane theory." *Int. J. Solids Struct.,* **34**. (In press.)

Carol, I. and Prat, P. C. (1990) "A statically constrained microplane model for the smeared analysis of concrete cracking." In *Computer Aided Analysis and Design of Concrete Structures*, Vol. 2, N. Bićanić and H. Mang, eds., Pineridge Press, Swansea, pp. 919–930.

Carol, I. and Prat, P. C. (1991) "Smeared analysis of concrete fracture using a microplane based multicrack model with static constraint." In *Fracture Processes in Concrete, Rock and Ceramics*, J. G. M. van Mier, J. G. Rots and A. Bakker, eds., E & FN Spon, London, pp. 619–628.

Carol, I., Bažant, Z. P. and Prat, P. C. (1991) "Geometric damage tensor based on microplane model." *J. Eng. Mech.-ASCE,* **117**(10), 2429–2448.

Carol, I., Bažant, Z. P. and Prat, P. C. (1992) "Microplane-type constitutive models for distributed damage and localized cracking in concrete structures." In *Fracture Mechanics of Concrete Structures*, Bažant, Z. P., ed., Elsevier Applied Science, London, pp. 299–304.

Carol, I., Prat, P. C. and Bažant, Z. P. (1992) "New explicit microplane model for concrete: Theoretical aspects and numerical implementation." *Int. J. Solids Struct.,* **29**(9), 1173–1191.

Carpinteri, A. (1980) *Static and Energetic Fracture Parameters for Rocks and Concretes.* Report, Istituto di Scienza delle Costruzioni-Ingegneria, University of Bologna, Italy.

Carpinteri, A. (1981) "A fracture mechanics model for reinforced concrete collapse." In *Proc. IABSE Colloquium on Advanced Mechanics of Reinforced Concrete*, pp. 17–30.

Carpinteri, A. (1982) "Notch sensitivity in fracture testing of aggregative materials." *Eng. Fract. Mech.,* **16**, 467–481.

Carpinteri, A. (1984) "Stability of fracturing process in RC beams." *J. Struct Eng.-ASCE,* **110**, 2073–2084.

Carpinteri, A. (1986) *Mechanical Damage and Crack Growth in Concrete*, Martinus Nijhoff, Dordrecht.

Carpinteri, A. (1989) "Decrease of apparent tensile and bending strength with specimen size: Two different explanations based on fracture mechanics." *Int. J. Solids Struct.,* **25**(4), 407–429.

Carpinteri, A. (1994a) "Fractal nature of material microstructure and size effects on apparent mechanical properties." *Mech. Mater.,* **18**, 89–101.

Carpinteri, A. (1994b) "Scaling laws and renormalization groups for strength and toughness of disordered materials." *Int. J. Solids Struct.,* **31**, 291–302.

Carpinteri, A. (1996) "Strength and toughness in disordered materials: Complete and incomplete similarity." In *Size-Scale Effects in the Failure Mechanisms of Materials and Structures*, A. Carpinteri, ed., E & FN Spon, London, pp. 3–26.

Carpinteri, A. and Chiaia, B. (1995) "Multifractal scaling Law for the fracture energy variation of concrete structures." In *Fracture Mechanics of Concrete Structures*, Vol. 1, F. H. Wittmann, ed., Aedificatio Publishers, Freiburg, Germany, pp. 581–596.

Carpinteri, A. and Chiaia, B. (1996) "A multifractal approach to the strength and toughness scaling of concrete structures." In *Fracture Mechanics of Concrete Structures*, Vol. 3, F. H. Wittmann, ed., Aedificatio Publishers, Freiburg, Germany, pp. 1773–1792.

Carpinteri, A. and Ferro, G. (1993) "Apparent tensile strength and fictitious fracture energy of concrete: A fractal geometry approach to related size effects." In *Fracture and Damage of Concrete and Rock*, H. P. Rossmanith, ed., E & FN Spon, London, pp. 86–94.

Carpinteri, A. and Ferro, G. (1994) "Size effects on tensile fracture properties: A unified explanation based on disorder and fractality of concrete microstructure." *Mater. Struct.,* **27**, 563–571.

Carpinteri, A. and Valente, S. (1989) "Size-scale transition from ductile to brittle failure: A dimensional analysis approach." In *Cracking and Damage, Strain Localization and Size Effect*, J. Mazars and Z. P. Bažant, eds., Elsevier Applied Science, London, pp. 477–490.

Carpinteri, A., Chiaia, B. and Ferro G. (1994) "Multifractal scaling law for the nominal strength variation of concrete structures." In *Size Effect in Concrete Structures*, H. Mihashi, H. Okamura and Z. P. Bažant, eds., E & FN Spon, London, pp. 193–206.

Carpinteri, A., Chiaia, B. and Ferro, G. (1995a) "Multifractal nature of material microstructure and size effects on nominal tensile strength." In *Fracture of Brittle Disordered materials: Concrete, Rock and Ceramics*, G. Baker and B.L. Karihaloo, eds., E & FN Spon, London, pp. 21–50.

Carpinteri, A., Chiaia, B. and Ferro, G. (1995b) "Size effects on nominal tensile strength of concrete structures: Multifractality of material ligaments and dimensional transition from order to disorder." *Mater. Struct.,* **28**, 311–317.

Carpinteri, A., Chiaia, B. and Ferro, G. (1995c) *Multifractal scaling law: An extensive application to nominal strength size effect of concrete structures.* Atti del Dipartimento di Ingegneria Strutturale No. 50, Politecnico di Torino, Italy.

Carter, B. C. (1992) "Size and stress gradient effects on fracture around cavities." *Rock Mech. Rock Eng.,* **25**(3), 167–186.

Carter, B. C., Lajtai, E. Z. and Yuan, Y. (1992) "Tensile fracture from circular cavities loaded in compression." *Int. J. Fracture,* **57**, 221–236.

Castillo, E. (1987) *Extreme Value Theory in Engineering*, Academic Press, Inc., San Diego.

CEB (1991) "CEB-FIP Model Code 1990, final draft." *Bulletin d'Information du Comité Euro-International du Béton.,* **203–205**.

Cedolin, L. and Bažant, Z. P. (1980) "Effect of finite element choice in blunt crack band analysis." *Comput. Meth. Appl. Mech. Eng.,* **24**, 305–316.

Cedolin, L., Dei Poli, S. and Iori, I. (1983) "Experimental determination of the fracture process zone in concrete." *Cement Concrete Res.,* **13**, 557–567.

Cedolin, L., Dei Poli, S. and Iori, I. (1987) "Tensile behavior of concrete." *J. Eng. Mech.-ASCE,* **113**(3), 431–449.

Červenka, J. (1994) *Discrete Crack Modeling in Concrete Structures.* Doctoral thesis. University of Colorado, Boulder, CO.

Červenka, V. and Pukl, R. (1994) "SBETA analysis of size effect in concrete structures." In *Size Effect in Concrete Structures*, H. Mihashi, H. Okamura and Z. P. Bažant, eds., E & FN Spon, London, pp. 323–333.

Červenka, J. and Saouma, V. E. (1995) "Discrete crack modeling in concrete structures." In *Fracture Mechanics of Concrete Structures*, F. H. Wittmann, ed., Aedificatio Publishers, Freiburg, Germany, pp. 1285–1300.

Červenka, V., Pukl, R., Ožbolt, J. and Eligehausen, R. (1995) "Mesh sensitivity in smeared finite element analysis of concrete fracture." In *Fracture Mechanics of Concrete Structures*, F. H. Wittmann, ed., Aedificatio Publishers, Freiburg, Germany, pp. 1387–1396.

Charmet, J. C., Roux, S. and Guyon, E., eds. (1990) *Disorder and Fracture*, Plenum Press, New York.

Chen, W.F. (1982) *Plasticity in Reinforced Concrete*, McGraw-Hill, New York.

Chen, W-F. and Yuan, R. L. (1980) "Tensile strength of concrete: Double-punch test." *J. Struct. Div.-ASCE,* **106**, 1673–1693.

Cho, K. Z., Kobayashi, A. S., Hawkins, N. M., Barker, D. B. and Jeang, F. L. (1984) "Fracture process zone of concrete cracks." *J. Eng. Mech.-ASCE,* **110**(8), 1174–1184.

Choi, O.C., Darwin, D. and McCabe, S.L. (1990) *Bond Strength of Epoxy-Coated Reinforcement to Concrete.* S. M. Report No. 25, University of Kansas Center for Research, Lawrence, KS.

Christensen, R. M. (1971) *Theory of Viscoelasticity*, Academic Press, New York.

Christensen, R. M. and DeTeresa, S. J. (1997) "The kink band mechanism for compressive failure of fiber composite materials." *J. Appl. Mech.-T. ASME,* **64**, 1–6.

Chudnovsky, A. and Kachanov, M. (1983) "Interaction of a crack with a field of microcracks." *Int. J. Eng. Sci.,* **21**(8), 1009–1018.

Chudnovsky, A. and Kunin, B. (1987) "A probabilistic model of crack formation." *J. Appl. Phys.,* **62**(10), 4124–4129.

Chudnovsky, A., Dolgopolsky, A. and Kachanov, M. (1987) "Elastic interaction of a crack with a microcrack array (parts I and II)." *Int. J. Solids Struct.,* **23**, 1–21.

Collatz, L. (1960) *The Numerical Treatment of Differential Equations*, Springer, Berlin.

Collins, M. P. (1978) "Towards a rational theory for RC members in shear." *J. Struct. Div.-ASCE,* **104**, 396–408.

Collins, M. P. and Mitchell, D. (1980) "Shear and torsion design of prestressed and non-prestressed concrete beams." *J. Prestressed Concrete Inst.,* **25**(5), 32–100. (Discussion **26**(6), 96–118.)

Collins, M. P., Mitchell, D., Adebar, P. and Vecchio, F. J. (1996) "General shear design method." *ACI Struct. J.,* **93**(1), 36–45.

Collins, W. D. (1963) "Some coplanar punch and crack problems in three-dimensional elastostatics." *Philos. T. Roy. Soc. A,* **274**(1359), 507–528.

Commission of European Communities (1984) *Eurocode No. 2.* Commission of European Communities.

Cope, R. J., Rao, P. V., Clark, L. A. and Norris, P. (1980) "Modelling of reinforced concrete behaviour for finite element analysis of bridge slabs." In *Numerical Methods for Nonlinear Problems*, Vol. 1, C. Taylor et al., eds., Pineridge Press, Swansea, pp. 457–470.

Cornelissen, H. A. W., Hordijk, D. A. and Reinhardt, H. W. (1986a) "Experimental determination of crack softening characteristics of normal weight and lightweight concrete." *Heron,* **31**(2), 45–56.

Cornelissen, H. A. W., Hordijk, D. A. and Reinhardt, H. W. (1986b) "Experiments and theory for the application of fracture mechanics to normal and lightweight concrete." In *Fracture Mechanics and Fracture Energy of Concrete*, F. H. Wittmann, ed., Elsevier, Amsterdam, pp. 565–575.

Corres, H., Elices, M. and Planas, J. (1986) "Thermal deformation of loaded concrete at low temperatures. 3: Lightweight concrete." *Cement Concrete Res.*, **16**, 845–852.

Costin, D. M. (1991) "Damage mechanics in the post-failure regime." *Mech. Mater.*, **4**, 149–160.

Cotterell, B. (1972) "Brittle fracture in compression." *Int. J. Fract. Mech.*, **8**(2), 195–208.

Cotterell, B. and Rice, J. R. (1980) "Slightly curved or kinked cracks." *Int. J. Fracture*, **16**, 155–169.

Cottrell, A.H. (1961) ISI Special Report No. 69, Iron and Steel Institute.

Cox, J. V. (1994) *Development of a Plasticity Bond Model for Reinforced Concrete — Theory and Validation for Monotonic Applications*. Technical Report No. TR-2036-SHR, Naval Facilities Engineering Service Center, Port Hueneme, CA 93043-4328.

Crisfield, M. A. and Wills, J. (1987) "Numerical comparisons involving different 'concrete-models'." In *IABSE Reports 54, Colloquium on Computational Mechanics of Reinforced Concrete*, Delft University Press, pp. 177–187.

Cundall, P. A. (1971) "A computer model for simulating progressive large scale movements in blocky rock systems." In *Proc. Int. Symp. Rock Fracture.*

Cundall, P. A. (1978) *BALL – A Program to Model Granular Media Using the Distinct Element Method.* Technical Note, Advanced Tech. Group, Dames and Moore, London.

Cundall, P. A. and Strack, O. D. L. (1979) "A discrete numerical model for granular assemblies." *Geotechnique*, **29**, 47–65.

Darwin, D. (1985) "Concrete crack propagation — Study of model parameters." In *Proc. Finite Element Analysis of Reinforced Concrete Structures*, Meyer, C. and Okamura, H., eds., ASCE, New York, pp. 184–203.

Darwin, D. and Attiogbe, E. K. (1986) "Effect of loading rate on cracking of cement paste in compression." In *Proc. Mat. Res. Soc. Symp. No. 64 on Cement Based Composites: Strain Rate Effects on Fracture*, S. Mindess and S. P. Shah, eds., pp. 167–180.

Datsyshin, A. P. and Savruk, M. P. (1973) "A system of of arbitrarily oriented cracks in elastic solids." *J. Appl. Math. and Mech.*, **37**(2), 326–332.

Dauskardt, R. H., Marshall, D. B. and Ritchie, R. O. (1990) "Cyclic fatigue-crack propagation in in magnesia-partially-stabilized zirconia." *J. Am. Ceram. Soc.*, **73**, 893–903

Davies, J. (1992) "Macroscopic study of crack bridging phenomenon in mixed-mode loading." In *Fracture Mechanics of Concrete Structures*, Z. P. Bažant, ed., Elsevier Applied Science, pp. 713–718.

Davies, J. (1995) "Study of shear fracture in mortar specimens." *Cement and Concrete Research*, **25**(5), 1031–1042.

Dietsche, A. and Willam, L. J. (1992) "Localization analysis of elasto-plastic Cosserat continua." In *Damage and Localization*, J. W. Ju and K. C. Valanis, eds., The American Society of Mechanical Engineers, New York, pp. 25–40. (AMD–Vol.142, Winter Annual Meeting, Anaheim.)

Dougill, J. W. (1976) "On stable progressively fracturing solids." *J. Appl. Math. Phys.*, **27**, 423–436.

Droz, P. and Bažant, Z. P. (1989) "Nonlocal analysis of stable states and stable paths of propagation of damage shear bands." In *Cracking and Damage, Strain Localization and Size Effect*, J. Mazars and Z. P. Bažant, eds., Elsevier Applied Science, London, pp. 183–207.

Du, J., Kobayashi, A. S. and Hawkins, N. M. (1989) "FEM dynamic fracture analysis of concrete beams." *J. Eng. Mech.-ASCE*, **115**(10), 2136–2149.

Dugdale, D. S. (1960) "Yielding of steel sheets containing slits." *J. Mech. Phys. Solids*, **8**, 100–108.

Dvorkin, E. N., Cuitiño, A. M. and Gioia, G. (1990) "Finite elements with displacement interpolated embedded localization lines insensitive to mesh size and distortions." *Int. J. Numer. Meth. Eng.*, **30**, 541–564.

Elfgren, L., ed. (1989) *Fracture Mechanics of Concrete Structures*, Chapman and Hall, London.

Elfgren, L. (1990) "Round robin analysis and tests of anchor bolts – Invitation." *Mater. Struct.*, **23**, 78.

Elfgren, L. and Swartz, S.E. (1992) "Fracture mechanics approach to modeling the pull-out of anchor bolts." In *Design Based on Fracture Mechanics*, W. Gerstle and Z. P. Bažant, eds., American Concrete Institute, Detroit, pp. 63–78. (ACI SP-134.)

Elfgren, L., Ohlsson, U. and Gylltoft, K. (1989) "Anchor bolts analyzed with fracture mechanics." In *Fracture of Concrete and Rock*, S.P. Shah and S.E. Swartz, eds., Springer-Verlag, New York, pp. 269–275.

Elices, M. (1987) *Mecánica de la Fractura Aplicada a Sólidos Elásticos Bidimensionales*, Dep. de Publicaciones de Alumnos, ETS de Ingenieros de Caminos, Canales y Puertos, Ciudad Universitaria, 28040, Madrid, Spain. (Fracture Mechanics Applied to Two-Dimensional Elastic Solids.)

Elices, M. and Planas, J. (1989) "Material models." In *Fracture Mechanics of Concrete Structures*, L. Elfgren, ed., Chapman and Hall, London, pp. 16–66.

Elices, M. and Planas, J. (1991) "Size effect and experimental validation of fracture models." In *Analysis of Concrete Structures by Fracture Mechanics*, L. Elfgren, ed., Chapman and Hall, London, pp. 99–127.

Elices, M. and Planas, J. (1992) "Size Effect in Concrete Structures: an R-Curve Approach." In *Application of Fracture Mechanics to Reinforced Concrete*, A. Carpinteri, ed., Elsevier Applied Science, London, pp. 169–200.

Elices, M. and Planas, J. (1993) "The equivalent elastic crack: 1. Load-Y equivalences." *Int. J. Fracture*, **61**, 159–172.

Elices, M. and Planas, J. (1996) "Fracture mechanics parameters of concrete: An overview." *Adv. Cem. Bas. Mat.*, **4**, 116–127.

Elices, M., Guinea, G. V. and Planas, J. (1992) "Measurement of the fracture energy using three-point bend tests: 3. Influence of cutting the P-δ tail." *Mater. Struct.*, **25**, 327–334.

Elices, M., Guinea, G. V. and Planas, J. (1995) "Prediction of size effect based on cohesive crack models." In *Size-Scale Effect in the Failure Mechanisms of Materials and Structures*, A. Carpinteri, ed., E & FN Spon, London, pp. 309–324.

Elices, M., Guinea, G. V. and Planas, J. (1997) "On the measurement of concrete fracture energy using three-point bend tests." *Mater. Struct.*, **30**, 375–376.

Elices, M., Planas, J. and Corres, H. (1986) "Thermal deformation of loaded concrete at low temperatures, 2: Transverse deformation." *Cement Concrete Res.*, **16**, 741–748.

Elices, M., Planas, J. and Guinea, G. V. (1993) "Modeling cracking in rocks and cementitious materials." In *Fracture and Damage of Concrete and Rock*, Rossmanith, H.P, ed., E & FN Spon, London, pp. 3–33.

Eligehausen, R. and Ožbolt, J. (1990) "Size effect in anchorage behavior." In *Fracture Behavior and Design of Materials and Structures*, Vol. 2, D. Firrao, ed., Engineering Materials Advisory Services Ltd. (EMAS), Warley, West Mindlands, U.K., pp. 721–727.

Eligehausen, R. and Sawade, G. (1989) "A fracture mechanics based description of the pull-out behavior of headed studs embedded in concrete." In *Fracture Mechanics of Concrete Structures*, L. Elfgren, ed., Chapman and Hall, London, pp. 281–299.

Eligehausen, R., Fusch, W., Ick, U., Mallée, R., Reuter, M., Schimmelphenning, K. and Schmal, B. (1991) *Tragverhalten von KopfbolzenVerankerung bei Zentrischer Zugbeansprunchung*. Report, Stuttgart University.

England A.H. (1971) *Complex Variable Methods in Elasticity*, Wiley-Interscience.

Entov, V. M. and Yagust, V. I. (1975) "Experimental investigation of laws governing quasi-static development of macrocracks in concrete." *Mech. Solids*, **10**(4), 87–95. (Translation from Russian.)

Eo, S. H., Hawkins, N. M. and Kono S. (1994) "Fracture characteristics and size effect for high-strength concrete beams." In *Size Effect in Concrete Structures*, H. Mihashi, H. Okamura and Z. P. Bažant, eds., E & FN Spon, London, pp. 245–254.

Erdogan, F. (1963) "Stress distribution in a nonhomogeneous elastic plane with cracks." *J. Appl. Mech.-T. ASME*, **30**(2), 232–236.

Erdogan, F. and Sih, G. C. (1963) "On the crack extension in plates under plane loading and transverse shear." *J. Basic Eng.*, **85**, 519–527.

Eringen, A. C. (1965) "Theory of micropolar continuum." In *Proc. Ninth Midwestern Mechanics Conference*, pp. 23–40.

Eringen, A. C. (1966) "A unified theory of thermomechanical materials." *Int. J. Eng. Sci.*, **4**, 179–202.

Eringen, A. C. and Ari, N. (1983) "Nonlocal stress field at Griffith crack." *Cryst. Latt. Def. Amorph. Mat.*, **10**, 33–38.

Eringen, A. C. and Edelen D. G. B. (1972) "On nonlocal elasticity." *Int. J. Eng. Sci.*, **10**, 233–248.

Eshelby, J. D. (1956) "The continuum theory of lattice defects." In *Solid State Physics*, Vol. 3, F. Seitz and D. Turnbull, eds., Academic Press, New York, pp. 79–141.

ESIS Technical Committee 8 (1991) "Recommendation for use of FEM in fracture mechanics." *ESIS Newsletter*, (15), 3–7.

Evans, A. G. and Fu, Y. (1984) "The mechanical behavior of alumina." In *Fracture in Ceramic Materials*, Noyes Publications, Park Ridge, NJ, pp. 56–88.

Evans, R. H. and Marathe M. S. (1968) "Microcracking and stress-strain curves for concrete in tension." *Mater. Struct.*, **1**(1), 61–64.

Fabrikant, V. I. (1990) "Complete solutions to some mixed boundary value problems in elasticity." *Adv. Appl. Mech.*, **27**, 153–223.

Fairhurst, C. and Cornet, F. (1981) "Rock fracture and fragmentation." In *Proc. 22nd U.S. Symp. on Rock Mechanics*, pp. 21–46.

Fathy, A. M. (1992) *Application of Fracture Mechanics to Rocks and Rocky Materials.* Doctoral thesis. Universidad Politécnica de Madrid, Departamento de Ciencia de Materiales, ETS de Ingenieros de Caminos, Ciudad Universitaria, 28040 Madrid, Spain. (In English.)

Feddersen, C. E. (1966) In *Plane Strain Crack Toughness Testing of High Strength Metallic Materials*, W. F. Brown and J. E. Srawley, eds., American Society for Testing and Materials, Philadelphia, pp. 77–79. (Contribution to Discussion, ASTM Special Technical Publication No. 410.)

Fenwick, R. C. and Paulay, T. (1968) "Mechanics of shear resistance of concrete beams." *J. Struct Eng.-ASCE*, **94**, 2235–2350.

Ferguson, P. M. and Thompson, J. N. (1962) "Development length of high strength reinforcing bars in bond." *ACI J.*, **59**, 887–922.

Ferguson, P. M. and Thompson, J. N. (1965) "Development length for large high strength reinforcing bars." *ACI J.*, **62**, 71–93.

Fischer, R. A. and Tippett L. H. C. (1928) "Limiting forms of the frequency distribution of the largest and smallest member of a sample." *Proc., Cambridge Philosophical Society*, **24**, 180–190.

Flory, T. J. (1961) "Thermodynamic relations for high elastic materials." *T. Faraday Soc.*, **57**, 829–838.

Forman, R. G., Kearney, V. E. and Engle, R. M. (1967) "Numerical analysis of crack propagation in cyclic-loaded structures." *J. Basic Eng.*, **89**, 459–464.

Fox, L. (1965) *An Introduction to Numerical Linear Algebra*, Oxford University Press, New York.

Fréchet, M. (1927) "Sur la loi de probabilité de l'écart maximum." *Ann. Soc. Polon. Math*, **6**, 93.

Freudenthal, A. M. (1968) "Statistical approach to brittle fracture." In *Fracture – An Advanced Treatise*, Vol. 2, H. Liebowitz, ed., Academic Press, New York, pp. 591–619.

Freudenthal, A. M. (1981) *Selected Papers by Alfred M. Freudenthal*, Am. Soc. of Civil Engrs., New York.

Freund, L. B. (1990) *Dynamic Fracture Mechanics*, Cambridge University Press, Cambridge and New York.

Furuhashi, R., Kinoshita, N. and Mura, T. (1981) "Periodic distributions of inclusions." *Int. J. Eng. Sci.*, **19**, 231–236.

Galileo Galilei Linceo (1638) *Discorsi i Demostrazioni Matematiche intorno à due Nuove Scienze*, Elsevirii, Leiden. (English transl. by T. Weston, London (1730), pp. 178–181.)

Gálvez, J, Llorca, J. and Elices, M. (1996) "Fracture mechanics analysis of crack stability in concrete gravity dams." *Dam Eng.*, **7**(1), 35–63.

Gdoutos, E. E. (1989) *Problems of Mixed Mode Crack Propagation*, Martinus Nijhoff Publishers, The Hague.

Gerstle, W. H., Partha, P. D., Prasad, N. N. V., Rahulkumar, P. and Ming, X. (1992) "Crack growth in flexural members — A fracture mechanics approach." *ACI Struct. J.*, **89**(6), 617–625.

Gettu, R., Bažant, Z. P. and Karr, M. E. (1990) "Fracture properties and brittleness of high-strength concrete." *ACI Mater. J.*, **87**, 608–618.

Gioia, G, Bažant, Z. P. and Pohl, B. P. (1992) "Is no-tension dam design always safe? – a numerical study." *Dam Eng.*, **3**(1), 23–34.

Gjørv, O. E., Sorensen, S. I. and Arnesen, A. (1977) "Notch sensitivity and fracture toughness of concrete." *Cement Concrete Res.*, **7**, 333–344.

Go, C. G. and Swartz, S. E. (1986) "Energy methods for fracture-toughness determination in concrete." *Exp. Mech.*, **26**(3), 292–296.

Gonnermann, H. F. (1925) "Effect of size and shape of test specimen on compressive strength of concrete." *Proc. ASTM*, **25**, 237–250.

Goode, C. D. and Helmy, M. A. (1967) "The strength of concrete under combined shear and direct stress." *Mag. Concrete Res.*, **19**(59), 105–112.

Gopalaratnam, V. S. and Shah S. P. (1985) "Softening response of plain concrete in direct tension." *ACI J.*, **82**(3), 310–323.

Graham, G. A. C. (1968) "The correspondence principle of linear viscoelasticity theory for mixed boundary value problems involving time-dependent boundary regions." *Q. Appl. Math.*, **26.**, 167–174.

Green, S. J. and Swanson, S. R. (1973) *Static Constitutive Relations for Concrete.* Report No. AFWL-TR-72-2, Air Force Weapons Lab., Kirkland Air Force Base.

Griffith, A. A. (1921) "The phenomena of rupture and flow in solids." *Philos. T. Roy. Soc. A*, **221**, 163–197.

Griffith, A. A. (1924) "The theory of rupture." In *Proceedings of the First International Conference of Applied Mechanics*, pp. 55–63.

Gross, D. (1982) "Spannungsintensitätsfaktoren von rißsystemen." *Ingenieur-Archiv*, **51**, 301–310.

Guinea, G. V. (1990) *Medida de la Energía de Fractura del Hormigón.* Doctoral thesis. Dep. Ciencia de Materiales, Universidad Politecnica de Madrid, ETS de Ingenieros de Caminos, Ciudad Universitaria, 28040 Madrid, Spain. ('Measurement of the Fracture Energy of Concrete', in Spanish.)

Guinea, G. V., Planas, J. and Elices, M. (1990) "On the influence of bulk dissipation on the average specific fracture energy of concrete." In *Fracture Behaviour and Design of Materials and Structures*, Vol. 2, D. Firrao, ed., Engineering Materials Advisory Services Ltd. (EMAS), Warley, West Mindlands, U.K., pp. 715–720.

Guinea, G. V., Planas, J. and Elices, M. (1992) "Measurement of the fracture energy using three-point bend tests: 1. Influence of experimental procedures." *Mater. Struct.*, **25**, 212–218.

Guinea, G. V., Planas, J. and Elices, M. (1994a) "Correlation between the softening and the size effect curves." In *Size Effect in Concrete Structures*, H. Mihashi, H. Okamura and Z. P. Bažant, eds., E & FN Spon, London, pp. 233–244.

Guinea, G. V., Planas, J. and Elices, M. (1994b) "A general bilinear fit for the softening curve of concrete." *Mater. Struct.*, **27**, 99–105.

Guo, Z. and Zhang X. (1987) "Investigation of complete stress-deformation curves for concrete in tension." *ACI Mater. J.*, **84**, 278–285.

Gupta, A. K. and Akbar, H. (1984) "Cracking in reinforced concrete analysis." *J. Struct. Eng.-ASCE*, **110**(8), 1735–1746.

Gustafsson, P. J. (1985) *Fracture Mechanics Studies of Non-Yielding Materials Like Concrete: Modeling of Tensile Fracture and Applied Strength Analyses.* Report No. TVBM-1007, Division of Building Materials, Lund Institute of Technology, Lund, Sweden.

Gustafsson, P. J. and Hillerborg, A. (1985) "Improvements in concrete design achieved through the application of fracture mechanics." In *Application of Fracture Mechanics to Cementitious Composites*, S. P. Shah, ed., Martinus Nijhoff, Dordrecht, pp. 667–680.

Gustafsson, P. J. and Hillerborg, A. (1988) "Sensitivity in the shear strength of longitudinally reinforced beams to fracture energy of concrete." *ACI Struct. J.*, **85**(3), 286–294.

Gylltoft, K. (1983) *Fracture Mechanics Models for Fatigue in Concrete Structures.* Doctoral thesis. Luleå University of Technology, Luleå, Sweden.

Gylltoft, K. (1984) "A fracture mechanics model for fatigue in concrete." *Mater. Struct.*, **17**(97), 55–58.

Haimson, B. C. and Herrick, C. G. (1989) "*In-situ* stress calculation from borehole breakout experimental studies." In *Proc., 26th U.S. Symp. on Rock Mechanics*, pp. 1207–1218.

Hasegawa, T. and Bažant, Z. P. (1993) "Nonlocal microplane concrete model with rate effect and load cycles. I. General formulation. II. Application and verification." *J. Mater. Civil Eng.*, **5**(3), 372–417.

Hasegawa, T., Shioya, T. and Okada, T. (1985) "Size effect on splitting tensile strength of concrete." In *Proc. Japan Concrete Inst. 7th Conf.*, pp. 309–312.

Hashin, Z. (1988) "The differential scheme and its application to cracked materials." *J. Mech. Phys. Solids*, **36**(6), 719–734.

Hassanzadeh, M. (1992) *Behaviour of Fracture Process Zones in Concrete Influenced by Simultaneously Applied Normal and Shear Displacements.* Report No. TVBM-1010, Division of Building Materials, Lund Institute of Technology, Lund, Sweden.

Hawkes, I. and Mellor, M. (1970) "Uniaxial testing in rock mechanics laboratories." *Eng. Geol.*, **4**, 177–285.

Hawkins, N. (1985) "The role for fracture mechanics in conventional reinforced design." In *Application of Fracture Mechanics to Cementitious Composites*, S. P. Shah, ed., Martinus Nijhoff, Dordrecht, pp. 639–666.

Hawkins, N.M. and Hjorteset, K. (1991) "Minimum reinforcement requirements for concrete flexural members." In *Application of Fracture Mechanics to Reinforced Concrete*, A. Carpinteri, ed., Elsevier Applied Science, London, pp. 379–412.

He, M.-Y. and Hutchinson, J. W. (1989) "Crack deflection at an interface between dissimilar elastic materials." *Int. J. Solids Struct.*, **25**, 1053–1067.

He, S., Plesha, M. E., Rowlands, R. E. and Bažant, Z. P. (1992) "Fracture energy tests of dam concrete with rate and size effects." *Dam Eng.*, **3**(2), 139–159.

Hededal, O. and Kroon, I. B. (1991) *Lightly Reinforced High Strength Concrete.* Master thesis. University of Åalborg, Denmark.

Heilmann, H. G., Hilsdorf H. and Finsterwalder, K. (1969) "Festigkeit und Verformung von Beton unter Zugspannungen." *Deustcher Ausshuss fur Stahlbeton,* (Heft 203).

Henshell, R. D. and Shaw, K. G. (1975) "Crack tip finite elements are unnecessary." *Int. J. Numer. Meth. Eng.,* **9**, 495–507.

Herrmann, G. and Sosa, H. (1986) "On bars with cracks." *Eng. Fract. Mech.,* **24**, 889–894.

Herrmann, H. J. (1991) "Patterns and scaling in fracture." In *Fracture Processes in Concrete, Rock and Ceramics*, J. G. M. van Mier, J. G. Rots and A. Bakker, eds., E & FN Spon, London, pp. 195–211.

Herrmann, H. J. and Roux, S., eds. (1990) *Statistical Models for the Fracture of Disordered Media*, North-Holland, New York.

Herrmann, H. J., Hansen, H. and Roux, S. (1989) "Fracture of disordered, elastic lattices in two dimensions." *Phys. Rev. B,* **39**, 637–648.

Hetényi, M. (1946). *Beams on Elastic Foundation*, The University of Michigan Press, Ann Arbor.

Higgins, D. D. and Bailey, J. E. (1976) "Fracture measurements on cement paste." *J. Mater. Sci.,* **11**, 1995–2003.

Hill, R. (1965) "Continuum micromechanics of elastoplastic polycrystals." *J. Mech. Phys. Solids,* **13**, 89–101.

Hill, R. (1966) "Generalized constitutive relations for incremental deformations of metal crystals by multi-slip." *J. Mech. Phys. Solids,* **14**, 95–102.

Hillerborg, A. (1984) *Additional Concrete Fracture Energy Tests Performed by 6 Laboratories According to a Draft RILEM Recommendation.* Report No. TVBM-3017, Division of Building Materials, Lund Institute of Technology, Lund, Sweden.

Hillerborg, A. (1985a) "The theoretical basis of a method to determine the fracture energy G_F of concrete." *Mater. Struct.,* **18**, 291–296.

Hillerborg, A. (1985b) "Numerical methods to simulate softening and fracture of concrete." In *Fracture Mechanics of Concrete: Structural Application and Numerical Calculation*, G. C. Sih and A. DiTomasso, eds., Martinus Nijhoff, Dordrecht, pp. 141–170.

Hillerborg, A. (1989) "Fracture mechanics and the concrete codes." In *Fracture Mechanics: Applications to Concrete*, V. C. Li and Z. P. Bažant, eds., American Concrete Institute, Detroit, pp. 157–169. (ACI Special Publication SP-118.)

Hillerborg, A. (1990) "Fracture mechanics concepts applied to moment capacity and rotational capacity of reinforced concrete beams." *Eng. Fract. Mech.,* **35**, 233–240.

Hillerborg, A. (1991) "Reliance upon concrete tensile strength." In *IABSE Colloquium StuttGart 91: Structural Concrete*, IABSE, Zürich., pp. 589–604.

Hillerborg, A., Modéer, M. and Petersson, P. E. (1976) "Analysis of crack formation and crack growth in concrete by means of fracture mechanics and finite elements." *Cement Concrete Res.,* **6**, 773–782.

Hinch, E. J. (1991) *Perturbation Methods*, Cambridge University Press, Cambridge.

Hodge, P. G. (1959) *Plastic Analysis of Structures*, McGraw Hill, New York.

Hoek, E. and Bieniawski, Z. J. (1965) "Brittle fracture propagation in rock under compression." *Int. J. Fract. Mech.,* **1**, 137–155.

Hoenig, A. (1978) "The behavior of a flat elliptical crack in an anisotropic solid." *Int. J. Solids Struct.,* **14**, 925–934.

Hognestad, E., Hanson, N. W. and McHenry, D. (1955) "Concrete stress distribution in ultimate strength design." *ACI J.,* **52**(4), 455–477.

Hondros, G. (1959) "Evaluation of Poisson ratio and the modulus of materials of low tensile resistance by the Brazilian (indirect tensile) test with particular references to concrete." *Aust. J. Appl. Sci.,* **10**, 243–268.

Hong, A.-P., Li, Y.-N. and Bažant, Z. P. (1997) "Theory of crack spacing in concrete pavements." *J. Eng. Mech.-ASCE,* **123**(3), 267–275.

Hordijk, D. A. (1991) *Local Approach to Fatigue of Concrete.* Doctoral thesis. Delft University of Technology, Delft, The Netherlands.

Hordijk, D. A. and Reinhardt, H. W. (1991) "Growth of discrete cracks in concrete under fatigue loading." In *Toughening Mechanisms in Quasi-Brittle Materials*, S. P. Shah, ed., Kluwer Academic Publishers, Dordrecht, The Netherlands, pp. 541–554.

Hordijk, D. A. and Reinhardt, H. W. (1992) "A fracture mechanics approach to fracture of plain concrete." In *Fracture Mechanics of Concrete Structures*, Z. P. Bažant, ed., Elsevier Applied Science, London, pp. 924–929.

Horii, H. (1989) "Models of fracture process zone and a system of fracture mechanics for concrete and rock." In *Fracture Toughness and Fracture Energy: Test Methods for Concrete and Rock*, H. Mihashi, H. Takahashi and F. H. Wittmann, eds., Balkema, Rotterdam, pp. 409–422.

Horii, H. (1991) "Mechanisms of fracture in brittle disordered materials." In *Fracture Processes in Concrete, Rock and Ceramics*, J. G. M. van Mier, J. G. Rots and A. Bakker, eds., E. & FN Spon, London, pp. 95–110.

Horii, H. and Nemat-Nasser, S. (1982) "Compression-induced non planar crack extension with application to splitting, exfoliation and rockburst." *J. Geophys. Res.,* **87**, 6806–6821.

Horii, H. and Nemat-Nasser, S. (1985) "Elastic fields of interacting inhomogeneities." *Int. J. Solids Struct.,* **21**, 731–745.

Horii, H. and Nemat-Nasser, S. (1986) "Brittle failure in compression, splitting, faulting and brittle-ductile transition." *Philos. T. Roy. Soc.,* **319**(1549), 337–334.

Horii, H., Hasegawa, A. and Nishino, F. (1989) "Fracture process and bridging zone model and influencing factors in fracture of concrete." In *Fracture of Concrete and Rock*, S. P. Shah and S. E. Swartz, eds., Springer-Verlag, New York, pp. 205–214.

Horii, H., Shin, H. C. and Pallewatta, T. M. (1990) "An analytical model of fatigue crack growth in concrete." *Proc. of the Japan Concrete Institute,* **12**, 835–840.

Horii, H., Zihai, S. and Gong, S.-X. (1989) "Models of fracture process zone in concrete, rock, and ceramics." In *Cracking and Damage, Strain Localization and Size Effect*, J. Mazars and Z. P. Bažant, eds., Elsevier Applied Science, London, pp. 104–115.

Hrennikoff, A. (1941) "Solution of problems of elasticity by the framework method." *J. Appl. Mech.-T. ASME,* **12**, 169–175.

Hsu, T. T. C. (1968) "Torsion of structural concrete – Plain concrete rectangular sections." In *Torsion of Structural Concrete*, American Concrete Institute, Detroit, pp. 203–238. (ACI Special Publication SP-18.)

Hsu, T. T. C. (1988) "Softened truss model theory for shear and torsion." *ACI Struct. J.,* **85**(6), 624–635.

Hsu, T. T. C. (1993) *Unified Theory of Reinforced Concrete*, CRC Press, Boca Raton, FL.

Huang, C. M. J. (1981) *Finite Element and Experimental Studies of Stress Intensity Factors for Concrete by Means of Fracture Mechanics and Finite Elements.* Doctoral thesis. Kansas State University, Kansas.

Hughes, B. P. and Chapman, G. P. (1966) "The complete stress-strain for concrete in direct tension." *RILEM Bulletin,* **30**, 95–97.

Humphrey, R. (1957) "Torsional properties of prestressed concrete." *Structural Eng.,* **35**(6), 213–224.

Hutchinson, J. W. (1968) "Singular behaviour at the end of a tensile crack in a hardening material." *J. Mech. Phys. Solids,* **16**, 13–31.

Hutchinson, J. W. (1990) "Mixed mode fracture mechanics of interfaces." In *Metal-Ceramic Interfaces*, M. Ruhle et al., eds., Pergamon Press, New York, pp. 295–306.

Inglis, C. E. (1913) "Stresses in a plate due to the presence of cracks and sharp corners." *T. Inst. Naval Architects,* **55**, 219–241.

Ingraffea, A. R. (1977) *Discrete Fracture Propagation in Rock: Laboratory Tests and Finite Element Analysis.* Doctoral thesis. University of Colorado, Boulder.

Ingraffea, A. R. and Gerstle, W. H. (1985) "Nonlinear fracture models for discrete crack propagation." In *Application of Fracture Mechanics to Cementitious Composites*, S. P. Shah, ed., Martinus Nijhoff, Dordrecht, pp. 247–285.

Ingraffea, A. R. and Heuzé, F. E. (1980) "Finite element models for rock fracture mechanics." *Int. J. Numer. Anal. Meth. Geomech.,* **4**, 25–43.

Ingraffea, A. R. and Saouma, V. (1984) "Numerical modeling of fracture propagation in reinforced and plain concrete." In *Fracture Mechanics of Concrete: Structural Application and Numerical Calculation*, G. Sih and A. DiTommasso, eds., Martinus Nijhoff, Dordrecht, pp. 171–225.

Ingraffea, A. R., Gerstle, W. H., Gergely, P. and Saouma, V. (1984) "Fracture mechanics of bond in reinforced concrete." *J. Struct Eng.-ASCE,* **110**(4), 871–890.

Ingraffea, A. R., Linsbauer, H. and Rossmanith, H. (1989) "Computer simulation of cracking in large arch dam — Downstream side cracking." In *Fracture of Concrete and Rock*, S.P. Shah and S.E. Swartz, eds., Springer-Verlag, New York, pp. 334–342.

Irwin, G. R. (1957) "Analysis of stresses and strains near the end of a crack traversing a plate." *J. Appl. Mech.-T. ASME,* **24**, 361–364.

Irwin, G. R. (1958) "Fracture." In *Handbuch der Physik*, Vol. 6, Flügge, ed., Springer-Verlag, Berlin, pp. 551–590.

Irwin, G. R. (1960) *Structural Mechanics*, Pergamon Press, London.

Irwin, G. R., Kies, J. A. and Smith, H. L. (1958) "Fracture strengths relative to the onset and arrest of crack propagation." *Proc ASTM*, **58**, 640–657.

Isida, M. (1973) "Analysis of stress intensity factors for the tension of a centrally cracked strip with stiffened edges." *Eng. Fract. Mech.*, **5**, 647–655.

Janssen, J. G. (1990) *Mode I Fracture of Plain Concrete under Monotonic and Cyclic Loading: Implementation and Evaluation of a Constitutive Model in DIANA*. Graduate thesis. Delft University of Technology, Delft, The Netherlands.

Jenq, Y. S. and Shah, S. P. (1985a) "A fracture toughness criterion for concrete." *Eng. Fract. Mech.*, **21**(5), 1055–1069.

Jenq, Y. S. and Shah, S. P. (1985b) "Two parameter fracture model for concrete." *J. Eng. Mech.-ASCE*, **111**(10), 1227–1241.

Jenq, Y. S. and Shah, S. P. (1988a) *Geometrical Effects on Mode I Fracture Parameters*. Report to RILEM Committee 89-FMT.

Jenq, Y. S. and Shah, S. P. (1988b) "On the concrete fracture testing methods." In *Fracture Toughness and Fracture Energy: Test Methods for Concrete and Rock*, H. Mihashi, H. Takahashi and F. H. Wittmann, eds., Balkema, Rotterdam, pp. 443–463.

Jenq, Y.S. and Shah, S.P. (1989) "Shear resistance of reinforced concrete beams — A fracture mechanics approach." In *Fracture Mechanics: Applications to Concrete*, V. Li and Z. P. Bažant, eds., American Concrete Institute, Detroit, pp. 237–258. (ACI Special Publication SP-118.)

Jirásek, M. (1993) *Modeling of Fracture and Damage in Quasi-Brittle Materials*. Doctoral thesis. Northwestern University, Evanston, IL.

Jirásek, M. (1996) "Nonlocal models for concrete cracking." Oral presentation at 38th Annual Technical Meeting of Society of Eng. Science in Tempe, Arizona; to appear in *Int. J. Solids Struct.*

Jirásek, M. and Bažant, Z. P. (1994) "Localization analysis of nonlocal model based on crack interactions." *J. Eng. Mech.-ASCE*, **120**(7), 1521–1542.

Jirásek, M. and Bažant, Z. P. (1995a) "Particle model for quasibrittle fracture and application to sea ice." *J. Eng. Mech.-ASCE*, **121**(9), 1016–1025.

Jirásek, M. and Bažant, Z. P. (1995b) "Macroscopic fracture characteristics of random particle systems." *Int. J. Fracture*, **69**(3), 201–228.

Jirásek, M. and Zimmermann, T. (1997) "Nonlocal rotating crack model with transition to scalar damage." In *Computational Plasticity*, Vol. 2, D. R. J. Owen, E. Oñate and E. Hinton, eds., Int. Center for Numer. Meth. in Eng. (CIMNE), pp. 1514–1521.

Jishan, X. and Xixi, H. (1990) "Size effect on the strength of a concrete member." *Eng. Fract. Mech.*, **35**, 687–696.

John, R. and Shah, S. P. (1986) "Fracture of concrete subjected to impact loading." *Cement, Concrete and Aggregates*, **8**(1), 24–32.

John, R. and Shah, S. P., (1990) "Mixed mode fracture of concrete subjected to impact loading." *J. Struct. Eng.-ASCE*, **116**(3), 585–602.

Kachanov, M. (1958) "Time of rupture process under creep conditions." *Izv. Akad. Nauk. SSR, Otd. Tekh. Nauk.*, **No. 8**, 26–31.

Kachanov, M. (1980) "A continuum model of medium with cracks." *J. Eng. Mech.-ASCE*, **106**, 1039–1051.

Kachanov, M. (1982) "A microcrack model of rock inelasticity—Part I. Frictional sliding on microcracks." *Mech. Mater.*, **1**, 19–41.

Kachanov, M. (1985) "A simple technique of stress analysis in elastic solids with many cracks." *Int. J. Fracture*, **28**, R11–R19.

Kachanov, M. (1987a) "Elastic solids with many cracks: A simple method of analysis." *Int. J. Solids Struct.*, **23**, 23–43.

Kachanov, M. (1987b) "On modelling of anisotropic damage in elastic-brittle materials—a brief review." In *Damage Mechanics in Composites*, A. Wang and G. Haritos, eds., The American Society of Mechanical Engineers, New York, pp. 99–105.

Kachanov, M. (1992) "Effective elastic properties of cracked solids: Critical review of some basic concepts." *Appl. Mech. Rev.*, **45**(8), 304–335.

Kachanov, M. (1993) "Elastic solids with many cracks and related problems." In *Advances in Applied Mechanics*, Vol. 30, J. Hutchinson and T. Wu, eds., Academic Press, New York, pp. 259–445.

Kachanov, M. and Laures, J.-P. (1989) "Three-dimensional problems of strongly interacting arbitrarily located penny-shaped cracks." *Int. J. Fracture*, **41**, 289–313.

Kachanov, M., Tsukrov, I., and Shafiro, B. (1994) "Effective moduli of solids with cavities of various shapes." *Appl. Mech. Rev.*, **47**(1), S151–S174.

Kani, G. N. J. (1966) "Basic facts concerning shear failure." *ACI J.*, **63**(6), 675–692.

Kani, G. N. J. (1967) "How safe are our large reinforced concrete beams?." *ACI J.*, **64**(3), 128–141.

Kanninen, M. F. and Popelar, C. H. (1985) *Advanced Fracture Mechanics*, Oxford University Press, New York.

Kaplan, M. F. (1961) "Crack propagation and the fracture of concrete." *ACI J.*, **58**(5), 591–610.

Karihaloo, B. L. (1992) "Failure modes of longitudinally reinforced beams." In *Application of Fracture Mechanics to Reinforced Concrete*, A. Carpinteri, ed., Elsevier Applied Science, London, pp. 523–546.

Karihaloo, B. L. (1995) "Approximate fracture mechanical approach to the prediction of ultimate shear strength of RC beams." In *Fracture Mechanics of Concrete Structures*, F. H. Wittmann, ed., Aedificatio Publishers, Freiburg, Germany, pp. 1111–1123.

Karihaloo, B. L. and Nallathambi, P. (1991) "Notched beam test: Mode I fracture toughness." In *Fracture Mechanics Test Methods for Concrete*, S. P. Shah and A. Carpinteri, eds., Chapman and Hall, London, pp. 1–86.

Karp, S. N. and Karal, F. C. (1962) "The elastic field behavior in the neighbourhood of a crack of arbitrary angle." *Commun. Pur. Appl. Math.*, **15**, 413–421.

Kassir, M. K. and Sih, G. C. (1975) *Three-Dimensional Crack Problems*, Noordhoff International Publishing, Leyden, The Netherlands.

Kawai, T. (1980) "Some considerations on the finite element method." *Int. J. Numer. Meth. Eng.*, **16**, 81–120.

Kemeny, J. M. and Cook, N. G. W. (1987) "Crack models for the failure of rock under compression." In *Proc. 2nd Int. Conf. on Constitutive Laws for Eng. Mat.*, Vol. 2, C. S. Desai et al., eds., Elsevier Science Publisher, New York, pp. 879–887.

Kemeny, J. M. and Cook, N. G. W. (1991) "Micromechanics of deformation in rock." In *Toughening Mechanisms in Quasibrittle Materials*, S. P. Shah, ed., Kluwer, Dordrecht, The Netherlands, pp. 155–188.

Kendall, K. (1978) "Complexities of compression failure." *Philos. T. Roy. Soc. A*, **361**, 254–263.

Kesler, C. E., Naus, D. J. and Lott, J. L. (1972) "Fracture mechanics — Its applicability to concrete." In *Proc. Int. Conf. on the Mechanical Behavior of Materials*, Vol. 4, The Soc. of Mater. Sci., pp. 113–124.

Kienzler, R. and Herrmann G. (1986) "An elementary theory of defective beams." *Acta Mech.*, **62**, 37–46.

Kim, J.-K. and Eo, S.-H. (1990) "Size effect in concrete specimens with dissimilar initial cracks." *Mag. Concrete Res.*, **42**, 233–238.

Kim, J.-K. et al. (1989) *Size Effect on the Splitting Tensile Strength of Concrete and Mortar*. Report No. CM 89-3, Korea Advanced Institute of Science and Technology, Seoul. (Data reported by Kim and Eo 1990.)

Kittl, P. and Díaz, G. (1988) "Weibull's fracture statistics, or probabilistic strength of materials: State of the art." *Res. Mechanica*, **24**, 99–207.

Kittl, P. and Díaz, G. (1989) "Some engineering applications of the probabilistic strength of materials." *Appl. Mech. Rev.*, **42**(11), 108–112.

Kittl, P. and Díaz, G. (1990) "Size effect on fracture strength in the probabilistic strength of materials." *Reliab. Eng. Syst. Safe.*, **28**, 9–21.

Klisinski, M., Olofsson, T. and Tano, R. (1995) "Mixed mode cracking of concrete modelled by inner softening band." In *Computational Plasticity*, D. R. J. Owen et al., eds., Pineridge Press, Swansea, U.K., 1595–1606

Klisinski, M., Runesson, K. and Sture, S. (1991) "Finite element with inner softening band." *J. Eng. Mech.-ASCE*, **117**(3), 575–587.

Knauss, W. G. (1970) "Delayed Failure – The Griffith problem for linearly viscoelastic materials." *Int. J. Fracture*, **6**, 7–20.

Knauss, W. G. (1973) "The mechanics of polymer fracture." *Appl. Mech. Rev.*, **26**, 1–17.

Knauss, W. G. (1974) "On the steady propagation of a crack in a viscoelastic sheet: Experiments and analysis." In *The Mechanics of Fracture*, F. Erdogan, ed., The American Society of Mechanical Engineers, New York, pp. 69–103. (AMD-19.)

Knauss, W. G. (1976) "Fracture of solids possessing deformation rate sensitive material properties." In *Deformation and Fracture of High Polymers*, H. H. Kausch et al., eds., Plenum Press, New York, pp. 501–541.

Knauss, W. G. (1989) "Time dependent fracture of polymers." In *Advances in Fracture Research*, Vol. 4, K. Salama, K. Ravi-Chandar, D. M. R. Taplin and P. Rama Rao, eds., Pergamon Press, Oxford, pp. 2683–2711.

Knein, M. (1927) "Zur theorie des druckversuchs." *Abhandlungen aus dem Aerodynamischen Institut an der Technische Hochschule Aachen*, 7, 43–62.

Knott, J. F. (1973) *Fundamentals of Fracture Mechanics*, Butterworths, London.

Knowles, J. K. and Sternberg, E. (1972) "On a class of conservation laws in linearized and finite elastostatics." *Arch. Ration. Mech. An.*, **44**, 187–211.

Kobayashi, A. S., Hawkins, M. N., Barker, D. B. and Liaw, B. M. (1985) "Fracture process zone of concrete." In *Application of Fracture Mechanics to Cementitious Composites*, S. P. Shah, ed., Martinus Nijhoff, Dordrecht, pp. 25–50.

Korn, G. A. and Korn, T. M. (1968) *Mathematical Handbook for Scientists and Engineers*, 2nd edition, McGraw Hill, New York.

Krafft, J. M., Sullivan, A. M. and Boyle, R.W. (1961) "Effect of dimensions on fast fracture instability of notched sheets." In *Proc. of the Crack-Propagation Symposium*, Vol. 1, pp. 8–28.

Krausz, A. S. and Eyring, H. (1975) *Deformation Kinetics*, Wiley-Interscience.

Krausz, A. S and Krausz, K. (1988) *Fracture Kinetics of Crack Growth*, Kluwer Academic Publishers, Dordrecht.

Kröner, E. (1961) "Zur plastischen verformung des vielkristalls." *Acta Metall.*, **9**, 155–161.

Kröner, E. (1967) "Elasticity theory of materials with long-range cohesive forces." *Int. J. Solids Struct.*, **3**, 731–742.

Kunin, I. A. (1968) "The theory of elastic media with microstructure and the theory of dislocations." In *Mechanics of Generalized Continua*, E. Kröner, ed., Springer Verlag, Berlin, pp. 321–328.

Kupfer, H., Hilsdorf, H. K. and Rüsch, H. (1969) "Behavior of concrete under biaxial stresses." *ACI J.*, **66**, 656–666.

Kyriakides, S., Ascerulatne, R., Perry, E. J. and Liechti, K. M. (1995) "On the compressive failure of fiber reinforced composites." *Int. J. Solids Struct.*, **32**(6–7), 689–738.

Labuz, J. F., Shah, S. P. and Dowding, C. H. (1985) "Experimental analysis of crack propagation in granite." *Int. J. Rock Mech. Min. Sci. & Geomech. Abstr.*, **22**(2), 85–98.

Larsson, R. and Runesson, K. (1995) "Cohesive crack models for semi-brittle materials derived from localization of damage coupled to plasticity." *Int. J. Fracture*, **69**, 101–122.

Larsson, R., Runesson, K. and Åkesson, M. (1995) "Embedded cohesive crack models based on regularized discontinuous displacements." In *Fracture Mechanics of Concrete Structures*, F. H. Wittmann, ed., Aedificatio Publishers, Freiburg, Germany, pp. 899–911.

Launay, P. and Gachon, H. (1971) "Strain and ultimate strength of concrete under triaxial stress." In *Proc. First Int. Conference on Struct. Mechanics in Reactor Technology*, T. Jaeger, ed., paper H1/3, 12 pp.

Lehner, F. and Kachanov, M. (1996) "On modeling of "winged" cracks forming under compression." *Int. J. Fracture*, 77, R65–R75.

Leibengood, L. D., Darwin, D. and Dodds, R. H. (1986) "Parameters affecting FE analysis of concrete structures." *J. Struct. Eng.-ASCE*, **112**(2), 326–341.

Lemaitre, J. and Chaboche, J.-L. (1985) *Mécanique des Matériaux Solides*, Dunod, Paris.

Leonhardt, F. (1977) "Schub bei stahlbeton und spannbeton—Grundlagen der neueren schubbemessung." *Beton und Stahlbetonbau*, **72**(11–12), 270–277 and 295–392.

Levin, V. M. (1971) "The relation between the mathematical expectation of stress and strain tensors in elastic microheterogeneous media." *Prikl. Mat. Mekh.*, **35**, 694–701. (In Russian.)

Li, V. C., Chan, C. M. and Leung, C. K. Y. (1987) "Experimental determination of the tension-softening relations for cementitious composites." *Cement Concrete Res.*, **17**, 441–452.

Li, Y.-N. and Bažant, Z. P. (1994a) "Eigenvalue analysis of size effect for cohesive crack model." *Int. J. Fracture*, **66**, 213–226.

Li Y.-N. and Bažant Z. P. (1994b) "Penetration fracture of sea ice plate: 2D analysis and size effect." *J. Eng. Mech.-ASCE*, **120**(7), 1481–1498.

Li, Y.-N. and Bažant, Z. P. (1996) "Scaling of cohesive fracture (with ramification to fractal cracks)." In *Size-Scale Effects in the Failure Mechanisms of Materials and Structures*, A. Carpinteri, ed., E & FN Spon, London, pp. 274–299.

Li, Y.-N and Bažant, Z. P. (1997) "Cohesive crack model with rate-dependent crack opening and viscoelasticity: Numerical algorithm, behavior and size effect." *Int. J. Fracture*, in press.

Li, Y.-N., Hong, A. N. and Bažant, Z. P. (1995) "Initiation of parallel cracks from surface of elastic half-plane." *Int. J. Fracture*, **69**, 357–369.

Liaw, B. M., Jeang, F. L., Du, J. J., Hawkins, N. M. and Kobayashi, A. S. (1990) "Improved non-linear model for concrete fracture." *J. Eng. Mech.-ASCE*, **1106**(2), 429–445.

Lin, C. S. and Scordelis, A. (1975) "Nonlinear analysis of RC shells of general forms." *J. Struct Eng.-ASCE*, **101**, 523–538.

Lin, T. H. and Ito, M. (1965) "Theoretical plastic distortion of a polycrystalline aggregate under combined and reversed stresses." *J. Mech. Phys. Solids*, **13**, 103–115.

Lin, T. H. and Ito, M. (1966) "Theoretical plastic stress-strain relationship of a polycrystal." *Int. J. Eng. Sci.*, **4**, 543–561.

Lindner, C. P. and Sprague, I. C. (1955) "Effect of depth of beams upon the modulus of rupture of plain concrete." *ASTM Proc.*, **55**, 1062–1083.

Linsbauer, H. and Tschegg, E. K. (1986) "Fracture energy determination of concrete with cube-shaped specimens." *Zement und Beton*, **31**, 38–40. (In German.)

Linsbauer, H., Ingraffea, A. R., Rossmanith, H. and Wawrzynek, P. A. (1988a) "Simulation of cracking in large arch dam: Part I." *J. Struct Eng.-ASCE*, **115**(7), 1599–1615.

Linsbauer, H., Ingraffea, A. R., Rossmanith, H. and Wawrzynek, P. A. (1988b) "Simulation of cracking in large arch dam: Part II." *J. Struct Eng.-ASCE*, **115**(7), 1615–1630.

Llorca, J., Planas, J. and Elices, M. (1989) "On the use of maximum load to validate or disprove models for concrete fracture behaviour." In *Fracture of Concrete and Rock, Recent Developments*, S. P. Shah, S. E. Swartz and B. Barr, eds., Elsevier Applied Science, London, pp. 357–368.

Lofti, H. R. and Shing, P. B. (1994) "Analysis of concrete fracture with an embedded crack approach." In *Computational Modeling of Concrete Structures*, H. Mang, N. Bicanic and R. de Borst, eds., Pineridge Press, Swansea, pp. 343–352.

Lubliner, J. (1986) "Normality rules in large-deformation plasticity." *Mech. Mater.*, **5**, 29–34.

Lundborg, N. (1967) "Strength-size relation of granite." *Int. J. Rock Mech. Min. Sci.*, **4**, 269–272.

MacGregor, J. G. and Gergely, P. (1977) "Suggested revisions to ACI code – Clauses dealing with shear in beams." *ACI J.*, **74**(10), 493–500.

Mai, Y.-W. (1991) "Fracture and fatigue of non-transformable ceramics: The role of crack-interface bridging." In *Fracture Processes in Concrete, Rock and Ceramics*, J. G. M. van Mier, J. G. Rots and A. Bakker, eds., E & FN Spon, London, pp. 3–26.

Maji, A. K. and Shah, S. P. (1988) "Process zone and acoustic emission measurement in concrete." *Exp. Mech.*, **28**, 27–33.

Malvern, L. E. (1969) *Introduction to the Mechanics of a Continuous Medium*, Prentice-Hall, Englewood Cliffs, New Jersey.

Mandelbrot, B. B., Passoja, D.E. and Paullay, A. (1984) "Fractal character of fracture surfaces of metals." *Nature*, **308**, 721–722.

Mariotte, E. (1686) *Traité du mouvement des eaux*, Posthumously edited by M. de la Hire, Engl. transl. by J.T. Desvaguliers, London (1718), p. 249. (Also *Mariotte's collected works*, 2nd ed., The Hague (1740).)

Martha, L. F., Llorca, J., Ingraffea, A. R. and Elices, M. (1991) "Numerical simulation of crack initiation and propagation in an arch dam." *Dam Eng.*, **2**(3), 193–213.

Marti, P. (1980) *Zur Plastischen Berechnung von Stahlbeton*. Bericht No. 104, Institute für Baustatik und Konstruktion, ETH, Zürich.

Marti, P. (1985) "Basic tools of reinforced concrete beam design." *ACI J.*, **82**(1), 46–56. (Discussion **82**(6), 933–935.)

Marti, P. (1989) "Size effect in double-punch tests on concrete cylinders." *ACI Mater. J.*, **86**(6), 597–601.

Massabò, R. (1994) *Mechanismi di Rottura nei Materiali Fibrorinforzati*. Doctoral thesis. Dottorato di Ricerca in Ingegneria Strutturale, Politecnico di Torino, Torino, Italia.

Maturana, P., Planas, J. and Elices, M. (1990) "Evolution of fracture behaviour of saturated concrete in the low temperature range." *Eng. Fract. Mech.*, **35**(4-5), 827–834.

Mazars, J. (1981) "Mechanical damage and fracture of concrete structures." In *Advances in Fracture Research, Preprints 5th. Int. Conf. Fracture*, Vol. 4, D. François, ed., Pergamon Press, Oxford, pp. 1499–1506.

Mazars, J. (1984) *Application de la Mécanique de l'Endomagement au Comportement Non-Linéaire et à la Rupture du Béton de Structures*. Doctoral thesis. Université de Paris 6.

Mazars, J. (1986) "A model for a unilateral elastic damageable material and its application to concrete." In *Fracture Toughness and Fracture Energy of Concrete*, F. H. Wittmann, ed., Elsevier, Amsterdam, pp. 61–71.

McHenry, D. (1943) "A new aspect of creep in concrete and its application to design." *Proc. ASTM*, **43**, 1069–1086.

McKinney, K. R. and Rice, R. W. (1981) "Specimen size effects in fracture toughness testing of heterogeneous ceramics by the notch beam method." In *Fracture Mechanics Methods for Ceramics, Rocks, and Concrete*, S. W. Freiman and E. R. Fuller Jr., eds., American Society for Testing and Materials, Philadelphia, pp. 118–126. (ASTM Special Technical Publication No. 745.)

McMullen, A. E. and Daniel, H. R. (1975) "Torsional strength of longitudinally reinforced beams containing an opening." *ACI J.*, **72**(8), 415–420.

Melan (1932) "Der spannungzustand der durch eine einzelkraft im innern beanspruchten halbschiebe." *2 Angew. Math. Mech*, **12**(6).

Meyer, C. and Okamura, H., eds. (1986) *Finite Element Analysis of Reinforced Concrete Structures*, ASCE, New York.

van Mier, J. G. M. (1984) *Strain-Softening of Concrete Under Multiaxial Loading Conditions.* Doctoral thesis. De Technische Hogeschool Eindhoven, The Netherlands.

van Mier, J. G. M. (1986) "Multiaxial strain-softening of concrete; Part I: Fracture; Part II: Load histories." *Mater. Struct.*, **19**(111), 179–200.

van Mier, J. G. M. and Vervuurt, A. (1995) "Micromechanical analysis and experimental verification of boundary rotation effects in uniaxial tension tests on concrete." In *Fracture of Brittle Disordered Materials: Concrete, Rock, Ceramics*, G. Baker and B. L. Karihaloo, eds., E & FN Spon, London, pp. 406–420.

van Mier, J. G. M., Nooru-Mohamed, M. B. and Schlangen, E. (1991) "Experimental analysis of mixed mode I and II behavior of concrete." In *Analysis of Concrete Structures by Fracture Mechanics*, L. Elfgren and S. P. Shah, eds., Chapman and Hall, London, pp. 32–43.

van Mier, J. G. M., Schlangen, E. and Vervuurt, A. (1996) "Tensile cracking in concrete and sandstone: Part 2 - Effect of boundary rotations." *Mater. Struct.*, **29**, 87–96.

van Mier, J. G. M., Vervuurt, A. and Schlangen, E. (1994) "Boundary and size effects in uniaxial tensile tests: A numerical and experimental study." In *Fracture and Damage in Quasibrittle Structures*, Z. P. Bažant, Z. Bittnar, M. Jirásek and J. Mazars, eds., E & FN Spon, London, pp. 289–302.

Mihashi, H. (1983) "A stochastic theory for fracture of concrete." In *Fracture Mechanics of Concrete*, F. H. Wittmann, ed., Elsevier Science Publishers, Amsterdam, pp. 301–339.

Mihashi, H. (1992) "Material structure and tension softening properties of concrete." In *Fracture Mechanics of Concrete Structures*, Z. P. Bažant, ed., Elsevier, London, pp. 239–250.

Mihashi, H. and Izumi, M. (1977) "Stochastic theory for concrete fracture." *Cement Concrete Res.*, **7**, 411–422.

Mihashi, H. and Wittmann, F. H. (1980) "Stochastic approach to study the influence of rate of loading on strength of concrete." *Heron*, **25**(3).

Mihashi, H. and Zaitsev, J. W. (1981) *Statistical Nature of Crack Propagation.* Report to RILEM TC 50-FMC.

Mikhlin, S. G. (1964) *Integral Equations*, Pergamon Press, Oxford.

Miller, R. A., Shah, S. P. and Bjelkhagen, H. (1988) "Measurement of crack profiles in mortar using laser holographic interferometry." *Exp. Mech.*, **28**(4), 388–394.

Mindess, S. (1983) "The application of fracture mechanics to cement and concrete: A historical review." In *Fracture Mechanics of Concrete*, F. H. Wittmann, ed., Elsevier Science Publishers, Amsterdam, The Netherlands, pp. 1–30.

Mindess, S. and Shah, S. P., eds. (1986) *Proc. MRS Symp. No. 64 on Cement Based Composites: Strain Rate Effect on Fracture*, Materials Research Society.

Mindess, S., Lawrence, F. V. and Kesler, C. E. (1977) "The J-integral as a fracture criterion for fiber reinforced concrete." *Cement Concrete Res.*, **7**, 731–742.

von Mises, R . (1936) "La distribution de la plus grande de *n* valeurs." *Rev. Math. Union Interbalcanique*, **1**, 1.

Mitchell, D. and Collins, M. P. (1974) "Diagonal compression field theory – a rational model for structural concrete in pure torsion." *ACI J.*, **71**(8), 346–408.

Modéer, M. (1979) *A Fracture Mechanics Approach to Failure Analyses of Concrete Materials.* Report No. TVBM-1001, Division of Building Materials, Lund Institute of Technology, Lund, Sweden.

Mori, T. and Tanaka, K. (1973) "Average stress in matrix and average elastic energy of materials with misfit inclusions." *Acta Metall.*, **21**, 571–574.

Mörsch, E. (1922) *Der Eisenbetonbau — Seine Theorie und Anwendung*, Vol. 1, 5th edition, Wittwer, Stuttgart. (Reinforced Concrete Construction—Theory and Application.)

Mosolov, A. B. and Borodich, F. M. (1992) "Fractal fracture of brittle bodies under compression." *Doklady Akademii Nauk.*, **324**(3), 546–549. (In Russian.)

Mueller, H. K. and Knauss, W. G. (1971) "Crack propagation in a linearly viscoelastic strip." *J. Appl. Mech.-T. ASME*, **38**, 483–488.

Mühlhaus, H.-B. and Aifantis, E. C. (1991) "A variational principle for gradient plasticity." *Int. J. Solids Struct.*, **28**, 845–858.

Mulmule, S. V., Dempsey, J. P. and Adamson, R. M. (1995) "Large-scale *in-situ* ice fracture experiments. Part II: Modeling aspects." In *Ice Mechanics 1995*, J. P. Dempsey and Y. D. S. Rajapakse, eds., The American Society of Mechanical Engineers, New York, pp. 129–146. (AMD-Vol. 207, ASME Summer Meeting, Los Angeles, CA.)

Mura, T. (1987) *Micromechanics of Defects in Solids*, 2nd edition, Martinus Nijhoff Publishers, Dordrecht.

Murakami, Y. (1987) *Stress Intensity Factors Handbook*, Pergamon Press, Oxford.

Nallathambi, P. and Karihaloo, B. L. (1986a) "Determination of specimen- size independent fracture toughness of plain concrete." *Mag. Concrete Res.*, **38**(135), 67–76.

Nallathambi, P. and Karihaloo, B. L. (1986b) "Stress intensity factor and energy release rate for three-point bend specimen." *Eng. Fract. Mech.*, 25(3), 315–321.

Naus, D. J. (1971) *Applicability of Linear-Plastic Fracture Mechanics to Portland Cement Concretes.* Doctoral thesis. University of Illinois at Urbana-Champaign.

Naus, D. J. and Lott, J. L. (1969) "Fracture toughness of portland cement concretes." *ACI J.*, **66**, 481–498.

Nemat-Nasser, S. and Obata, M. (1988) "A microcrack model of dilatancy in brittle material." *J. Appl. Mech.-T. ASME*, **55**, 24–35.

Nesetova, V. and Lajtai, E. Z. (1973) "Fracture from compressive stress concentration around elastic flaws." *Int. J. Rock Mech. Min. Sci.*, **10**, 265–284.

Newman Jr., J. C. (1971) *An Improved Method of Collocation for the Stress Analysis of Cracked Plates with Various Shaped Boundaries.* Technical Note No. TN D-6376, NASA.

Nielsen, K. E. C. (1954) "Effect of various factors on the flexural strength of concrete test beams." *Mag. Concrete Res.*, **15**, 105–114.

Nielsen, M. P. and Braestrup, N. W. (1975) *Plastic Shear Strength of Reinforced Concrete Beams.* Techn. Report No. 3, Bygningsstatiske Meddelesler (Vol. 46).

Nixon, W. F. (1996) "Wing crack models of the brittle compressive failure of ice." *Cold Reg. Sci. Technol.*, **24**, 41–55.

Noghabai, K. (1995a) *Splitting in Concrete in the Anchoring Zone of Deformed Bars.* Graduate thesis. Division of Structural Engineering, Luleå University of Technology, Luleå, Sweden.

Noghabai, K. (1995b) "Splitting of concrete covers – a fracture mechanics approach." In *Fracture Mechanics of Concrete Structures*, F. H. Wittmann, ed., Aedificatio Publishers, Freiburg, Germany, pp. 1575–1584.

Nuismer, R. J. (1975) "An energy release rate criterion for mixed mode fracture." *Int. J. Fracture*, **11**, 245–250.

Ogden, R. W. (1984) *Non-linear elastic deformations*, Ellis Horwood, Ltd. and John Wiley & Sons, Chichester, U.K.

Oglesby, J. J. and Lamackey, O. (1972) *An Evaluation of Finite Element Methods for the Computation of Elastic Stress Intensity Factors.* Report No. No. 3751, NSRDC.

Ohgishi, S., Ono, H., Takatsu, M. and Tanahashi, I. (1986) "Influence of test conditions on fracture toughness of cement paste and mortar." In *Fracture Toughness and Fracture Energy of Concrete*, F. H. Wittmann, ed., Elsevier Science, Amsterdam, The Netherlands, pp. 281–290.

Ohtsu, M. and Chahrour, A. H. (1995) "Fracture analysis of concrete based on the discrete crack model by the boundary element method." In *Fracture of Brittle Disordered Materials: Concrete, Rock, Ceramics*, G. Baker and B. L. Karihaloo, eds., E & FN Spon, London, pp. 335–347.

Oliver, J. (1989) "A consistent characteristic length for smeared cracking models." *Int. J. Numer. Meth. Eng.*, **28**, 461–474.

Oliver, J. (1995) "Modeling strong discontinuities in solid mechanics via strain softening constitutive equations." *Monograph CIMNE*, 28.

Olsen, P. C. (1994) "Some comments on the bending strength of concrete beams." *Mag. Concrete Res.*, **46**, 209–214.

Ortiz, M. (1985) "A constitutive theory for the inelastic behaviour of concrete." *Mech. Mater.*, 4, 67–93.

Ortiz, M. (1987) "An analytical study of the localized failure modes in concrete." *Mech. Mater.*, **6**, 159–174.

Ottosen, N. S. (1977) "A failure criterion for concrete." *J. Eng. Mech. Div.-ASCE*, **103**(4), 527–535.

Ouchterlony, F. (1975) *Concentrated Loads Applied to the Tips of a Symmetrically Cracked Wedge.* Report No. DS-1975:3, Swedish Dectonic Research Foundation.

Owen, D. R. J. and Hinton, E. (1980) *Finite Elements in Plasticity: Theory and Practice*, Pineridge Press, Swansea, U.K.

Ožbolt, J. and Bažant, Z. P. (1991) "Cyclic microplane model for concrete." In *Fracture Processes in Concrete, Rock and Ceramics*, J. G. M. van Mier, J. G. Rots and A. Bakker, eds., E & FN Spon, London, pp. 639–650.

Ožbolt, J. and Bažant, Z. P. (1992) "Microplane model for cyclic triaxial behavior of concrete and rock." *J. Eng. Mech.-ASCE*, **118**(7), 1365–1386.

Ožbolt, J. and Bažant, Z. P. (1996) "Numerical smeared fracture analysis: Nonlocal microcrack interaction approach." *Int. J. Numer. Meth. Eng.*, **39**, 635–661.

Ožbolt, J. and Eligehausen, R. (1995) "Size effect in concrete and reinforced concrete structures." In *Fracture Mechanics of Concrete Structures*, Vol. 1, F. H. Wittmann, ed., Aedificatio Publishers, Freiburg, Germany, pp. 665–674.

Palmer, A. C. and Sanderson, T. J. O. (1991) "Fractal crushing of ice and brittle solids." *Philos. T. Roy. Soc. A*, **443**, 469–477.

Pan, Y. C., Marchertas, A. H. and Kennedy, J. M. (1983) "Finite element analysis of blunt crack propagation, a modified J-integral approach." In *Transactions of the Seventh International Conference on Structural Mechanics in Reactor Technology*, North-Holland, New York, pp. 235–292.

Pande, G. N. and Sharma, K. G. (1981) "Implementation of computer procedures and stress-strain laws in geotechnical engineering." In *Proc. Symp. on Implementation of Computer Procedures and Stress-Strain Laws in Geotechnical Engineering.*, C. S. Desai and S. K. Saxena, eds., Acorn Press, Durham, N.C., pp. 575–590.

Pande, G. N. and Sharma, K. G. (1982) *Multi-Laminate Model of Clays—A Numerical Evaluation of the Influence of Rotation of the Principal Stress Axis.* Report, Dept. of Civil Engrg., University College of Swansea, Swansea, U.K.

Pande, G. N. and Xiong, W. (1982) "An improved multi-laminate model of jointed rock masses." In *Proc. Int. Sym. on Numerical Models in Geomechanics*, R. Dungar, G. N. Pande and G. A. Studder, eds., Balkema, Rotterdam, pp. 218–226.

Paris, P. C. and Erdogan, F. (1963) "Critical analysis of propagation laws." *J. Basic Eng.*, 85, 528–534.

Paris, P. C., Gomez, M. P. and Anderson, W. E. (1961) "Rational analytic theory of fatigue." *Trends Eng.*, **13**(1).

Park, R. and Paulay, T. (1975) *Reinforced Concrete Structures*, John Wiley & Sons, New York.

Pastor, J. Y. (1993) *Fractura de Materiales Cerámicos Estructurales Avanzados.* Doctoral thesis. Facultad de Ciencias Físicas, Dep. de Ciencia de Materiales, Univeridad Complutense de Madrid, Ciudad Universitaria, 28040 Madrid, Spain. ('Fracture of Advanced Structural Ceramics', in Spanish.)

Pastor, J. Y., Guinea, G., Planas, J. and Elices, M. (1995) "Nueva expresión del factor de intensidad de tensiones para la probeta de flexión en tres puntos." *Anales de Mecánica de la Fractura*, **12**, 85–90. ('A new expression for the stress intensity factor of a three-point bend specimen', in Spanish.)

Paul, B. (1968) "Macroscopic criteria for plastic flow and brittle fracture." In *Fracture – An Advanced Treatise*, Vol. 2, H. Liebowitz, ed., Academic Press, New York, pp. 313–496. (Chapter 4.)

Peirce, F. T. (1926) "Tensile strength of cotton yarns. V.—The weakest link theorems on the strength of long and composite specimens." *J. Textile Inst.*, **17**, T355–368.

Perdikaris, P. C. and Calomino, A. M. (1989) "Kinetics of crack growth in plain concrete." In *Fracture of Concrete and Rock*, S. P. Shah and S. E. Swartz, eds., Springer-Verlag, New York, pp. 64–69.

Petersson, P.-E. (1981) *Crack Growth and Development of Fracture Zone in Plain Concrete and Similar Materials.* Report No. TVBM-1006, Division of Building Materials, Lund Institute of Technology, Lund, Sweden.

Petrovic, J. J. (1987) "Weibull statistical fracture theory for the fracture of ceramics." *Metall. Trans. A*, **18**, 1829–1834.

Phillips, D. V. and Binsheng, Z. (1993) "Direct tension tests on notched and un-notched plain concrete specimens." *Mag. Concrete Res.*, **45**, 25–35.

Pietruszczak, S. and Mróz, Z. (1981) "Finite element analysis of deformation of strain-softening materials." *Int. J. Numer. Meth. Eng.*, **17**, 327–334.

Pijaudier-Cabot, G. and Bažant, Z. P. (1987) "Nonlocal damage theory." *J. Eng. Mech.-ASCE*, **113**(10), 1512–1533.

Pijaudier-Cabot, G. and Bažant, Z. P. (1988) "Dynamic stability analysis with nonlocal damage." *Comput. Struct.*, **29**(3), 503–507.

Pijaudier-Cabot, G. and Bažant, Z. P. (1991) "Cracks interacting with particles or fibers in composite materials." *J. Eng. Mech.-ASCE*, **117**(7), 1611–1630.

Planas, J. (1992) Untitled letter. Privately communicated comment to Z. P. Bažant, Northwestern University, July 13.

Planas, J. (1993) *A Note on the Effect of Specimen Self Weight on the Effective Crack Extension Measurement by the Compliance Method.* Report No. 93-jp02, Departamento de Ciencia de Materiales, ETS de Ingenieros de Caminos, Universidad Politécnica de Madrid, Ciudad Universitaria sn. 28040 Madrid, Spain.

Planas, J. (1995) *Crack growth in a n elastic medium with random crack growth resistance.* Report No. 95-jp03, Departamento de Ciencia de Materiales, ETS de Ingenieros de Caminos, Universidad Politécnica de Madrid, Ciudad Universitaria sn. 28040 Madrid, Spain.

Planas, J. and Bažant, Z. P. (1997) *Statistics of crack growth based on random R-curves.* Report No. 97-jp02, Departamento de Ciencia de Materiales, ETS de Ingenieros de Caminos, Universidad Politécnica de Madrid, Ciudad Universitaria sn. 28040 Madrid, Spain.

Planas, J. and Elices, M. (1986a) "Towards a measure of G_F: An analysis of experimental results." In *Fracture Toughness and Fracture Energy of Concrete*, F. H. Wittmann, ed., Elsevier, Amsterdam, pp. 381–390.

Planas, J. and Elices, M. (1986b) "Un nuevo método de análisis del comportamiento de una fisura cohesiva en Modo I." *Anales de Mecánica de la Fractura*, **3**, 219–227.

Planas, J. and Elices, M. (1989a) "Size effect in concrete structures: Mathematical approximations and experimental validation." In *Cracking and Damage, Strain Localization and Size Effect*, J. Mazars and Z. P. Bažant, eds., Elsevier Applied Science, London, pp. 462–476.

Planas, J. and Elices, M. (1989b) "Conceptual and experimental problems in the determination of the fracture energy of concrete." In *Fracture Toughness and Fracture Energy: Test Methods for Concrete and Rock*, H. Mihashi, H. Takahashi and F. H. Wittmann, eds., Balkema, Rotterdam, pp. 165–181.

Planas, J. and Elices, M. (1990a) "Fracture criteria for concrete: Mathematical approximations and experimental validation." *Eng. Fract. Mech.*, **35**, 87–94.

Planas, J. and Elices, M. (1990b) "Anomalous structural size effect in cohesive materials like concrete." In *Serviceability and Durability of Construction Materials*, Vol. 2, B. A. Suprenant, ed., American Society of Civil Engineers (ASCE), New York, pp. 1345–1356.

Planas, J. and Elices, M. (1990c) "The approximation of a cohesive crack by effective elastic cracks." In *Fracture Behaviour and Design of Materials and Structures*, Vol. 2, D. Firrao, ed., Engineering Materials Advisory Services Ltd. (EMAS), Warley, West Midlands, U.K., pp. 605–611.

Planas, J. and Elices, M. (1991a) "Nonlinear fracture of cohesive materials." *Int. J. Fracture*, **51**, 139–157.

Planas, J. and Elices, M. (1991b) "Asymptotic analysis of cohesive cracks and its relation with effective elastic cracks." In *Toughening Mechanisms in Quasi-Brittle Materials*, S. P. Shah, ed., Kluwer Academic Publishers, Dordrecht, pp. 189–202.

Planas, J. and Elices, M. (1991c) "The influence of specimen size and material characteristic size on the applicability of effective crack models." In *Fracture Processes in Concrete, Rock and Ceramics*, J. G. M. van Mier, J. G. Rots and A. Bakker, eds., E & FN Spon, London, pp. 375–385.

Planas, J. and Elices, M. (1991d) *On the Bazant-Herrmann Approximation to the Stress Intensity Factor in Single Edge Notched Beams.* Report No. 91-jp03, Departamento de Ciencia de Materiales, ETS de Ingenieros de Caminos, Universidad Politécnica de Madrid, Ciudad Universitaria sn. 28040 Madrid, Spain.

Planas, J. and Elices, M. (1992a) "Asymptotic analysis of a cohesive crack: 1. Theoretical background." *Int. J. Fracture*, **55**, 153–177.

Planas, J. and Elices, M. (1992b) "Shrinkage eigenstresses and structural size-effect." In *Fracture Mechanics of Concrete Structures*, Z. P. Bažant, ed., Elsevier Applied Science, London, pp. 939–950.

Planas, J. and Elices, M. (1993a) "Asymptotic analysis of a cohesive crack: 2. Influence of the softening curve." *Int. J. Fracture*, **64**, 221–237.

Planas, J. and Elices, M. (1993b) "Drying shrinkage effect on the modulus of rupture." In *Creep and Shrinkage of Concrete*, Z. P. Bažant and I. Carol, eds., E & FN Spon, London, pp. 357–368.

Planas, J., Corres, H., Elices, M. and Chueca, R. (1984) "Thermal deformation of loaded concrete during thermal cycles from 20 C to –165 C." *Cement Concrete Res.*, **14**, 639–644.

Planas, J., Elices, M. and Guinea G. V. (1992) "Measurement of the fracture energy using three-point bend tests: 2. Influence of bulk energy dissipation." *Mater. Struct.*, **25**, 305–312.

Planas, J., Elices, M. and Guinea, G. V. (1993) "Cohesive cracks versus nonlocal models: Closing the gap." *Int. J. Fracture*, **63**, 173–187.

Planas, J., Elices, M. and Guinea, G. V. (1994) "Cohesive cracks as a solution of a class of nonlocal models." In *Fracture and Damage of Quasibrittle Structures*, Z. P. Bazant, Z. Bittnar, M. Jirásek and J. Mazars, eds., E & FN Spon, London, pp. 131–144.

Planas, J., Elices, M. and Guinea, G. V. (1995) "The extended cohesive crack." In *Fracture of Brittle Disordered Materials: Concrete, Rock and Ceramics*, G. Bakker and B. L. Karihaloo, eds., E & FN Spon, London, pp. 51–65.

Planas, J., Elices, M. and Ruiz, G. (1993) "The equivalent elastic crack: 2. X-Y equivalences and asymptotic analysis." *Int. J. Fracture*, **61**, 231–246.

Planas, J., Elices, M. and Toribio, J. (1989) "Approximation of cohesive crack models by R-CTOD curves." In *Fracture of Concrete and Rock, Recent Developments*, S. P. Shah, S. E. Swartz and B. Barr, eds., Elsevier Applied Science, London, pp. 203–212.

Planas, J., Guinea, G. V. and Elices, M. (1994a) *SF-1. Draft Test Method for Flexural Strength and Elastic Modulus of Notched Concrete Beams Tested in Three-Point Bending.* Report No. 94-jp02, Departamento de Ciencia de Materiales, ETS de Ingenieros de Caminos, Universidad Politécnica de Madrid, Ciudad Universitaria sn. 28040 Madrid, Spain. (Contribution to the Japan Concrete Institute International Collaboration Project on Size Effect in Concrete Structures.)

Planas, J., Guinea, G. V. and Elices, M. (1994b) *SF-2. Draft Test Method for Linear Initial Portion of the Softening Curve of Concrete.* Report No. 94-jp03, Departamento de Ciencia de Materiales, ETS de Ingenieros de Caminos, Universidad Politécnica de Madrid, Ciudad Universitaria sn. 28040 Madrid, Spain. (Contribution to the Japan Concrete Institute International Collaboration Project on Size Effect in Concrete Structures.)

Planas, J., Guinea, G. V. and Elices, M. (1995) "Rupture modulus and fracture properties of concrete." In *Fracture Mechanics of Concrete Structures*, Vol. 1, F. H. Wittmann, ed., Aedificatio Publishers, Freiburg, Germany, pp. 95–110.

Planas, J., Guinea, G. V. and Elices, M. (1996) *Basic Issues on Nonlocal Models: Uniaxial Modeling.* Report No. 96-jp03, Departamento de Ciencia de Materiales, ETS de Ingenieros de Caminos, Universidad Politécnica de Madrid, Ciudad Universitaria sn. 28040 Madrid, Spain.

Planas, J., Guinea, G. V. and Elices, M. (1997) "Generalized size effect equation for quasibrittle materials." *Fatigue Fract. Eng. Mater. Struct.*, **20**(5), 671–687.

Planas, J., Ruiz, G. and Elices, M. (1995) "Fracture of lightly reinforced concrete beams: Theory and experiments." In *Fracture Mechanics of Concrete Structures*, Vol. 2, F. H. Wittmann, ed., Aedificatio Publishers, Freiburg, Germany, pp. 1179–1188.

Plesha, M. E. and Aifantis, E. C. (1983) "On the modeling of rocks with microstructure." In *Proc. 24th U.S. Symp. Rock Mech.*.

Post-Tensioning Institute (1988) *Design and Construction Specifications for Segmental Concrete Bridges.* Final Report, Post-Tensioning Institute, Phoenix, Arizona.

Priddle, E. K. (1976) "High cycle fatigue crack propagation under random and constant amplitude loadings." *Int. J. Pres. Ves. Pip.*, **4**, 89–117.

Prandtl, L. (1904) "Uber die Flüssigkeitsbewebung bei sehr kleiner Reibung." In *Verhandlungen, III. Int. Math.-Kongr.*, Heidelberg, Germany.

Prat, P. C. and Bažant, Z. P. (1997) "Tangential stiffness of elastic materials with systems of growing or closing cracks." *J. Mech. Phys. Solids*, **45**(4), 611–636; wth Addendum and Errata **45**(8), 1419–1420.

Press, W. H., Teukolsky, S. A., Vetterling, W. T. and Flannery, B. P. (1992) *Numerical Recipes in C*, Cambridge University Press, New York.

Primas, R. J. and Gstrein, R (1994) *ESIS TC Round Robin on Fracture Toughness.* EMPA Report No. 155'088, Swiss Federal Laboratories for Material Testing And Research (EMPA). (Draft Nov. 1994.)

Pugh, E. M. and Winslow, G. H. (1966) *The Analysis of Physical Measurements*, Addison-Wesley, Reading, MA.

Rashid, Y. R. (1968) "Analysis of prestressed concrete pressure vessels." *Nucl. Eng. Des.*, **7**(4), 334–355.

Reagel, F. V. and Willis, T. F. (1931) "The effect of dimensions of test specimens on the flexural strength of concrete." *Public Roads*, **12**, 37–46.

Reece, M. J., Guiu, F. and Sammur M. F. R. (1989) "Cyclic fatigue crack propagation in alumina under direct tension-compression loading." *J. Am. Cera. Soc.*, **72**, 348–352.

Reich, R. Červenka, J. and Saouma, V. (1994) "Merlin: A computational environment for 2D/3D discrete fracture analysis." In *Computational Modeling of Concrete Structures*, H. Mang, N. Bicanic and R. de Borst, eds., Pineridge Press, Swansea, pp. 999–1008.

Reineck, K.-H. (1991) "Model for structural concrete members without transverse reinforcement." In *Proc. IABSE Colloquium on Structural Concrete*, Stuttgart, pp. 643–648. (IABSE Report Vol. 62.)

Reinhardt, H. W. (1981a) "Masstabeinfluss bei schubversuchen im licht der bruchmechanik." *Beton und Stahlbetonbau*, **7**, 19–21. ("Size Effect in Shear Tests in the Light of Fracture Mechanics". In German.)

Reinhardt, H. W. (1981b) "Similitude of brittle fracture of structural concrete." In *Proc. IABSE Colloquium on Advances in Mechanics of Reinforced Concrete*, pp. 201–210.

Reinhardt, H. W. (1982) "Length influence on bond shear strength of joints in composite concrete slabs." *Int. J. Cement Compos. Lightweight Concrete*, **4**(3), 139–143.

Reinhardt, H. W. (1984) "Fracture mechanics of fictitious crack propagation in concrete." *Heron*, **29**(2), 3–42.

Reinhardt, H. W. (1992) "Bond of steel to strain-softening concrete taking account of loading rate." In *Fracture Mechanics of Concrete Structures*, Z. P. Bažant, ed., Elsevier Applied Science, London, pp. 809–820.

Reinhardt, H. W. and Cornelissen, H. A. W. (1984) "Post-peak cyclic behavior of concrete in uniaxial and alternating tensile and compressive loading." *Cement Concrete Res.*, **14**(2), 263–270.

Reinhardt, H. W. and van der Veen, C. (1992) "Splitting failure of a strain-softening material due to bond stresses." In *Application of Fracture Mechanics to Reinforced Concrete*, A. Carpinteri, ed., Elsevier Applied Science, London, pp. 333–346.

Rektorys, K. (1969) *Survey of Applicable Mathematics*, Kluwer Acad. Publ., Dordrecht. (Also Iliffe Books Ltd., London, 1969.)

Rice, J. R. (1968a) "A path independent integral and the approximate analysis of strain concentrations by notches and cracks." *J. Appl. Mech.-T. ASME*, **35**, 379–386.

Rice, J. R. (1968b) "Mathematical analysis in the mechanics of fracture." In *Fracture – An Advanced Treatise*, Vol. 2, H. Liebowitz, ed., Academic Press, New York, pp. 191–308.

Rice, J. R. (1970) "On the structure of stress-strain relations for time-dependent plastic deformation of metals." *J. Appl. Mech.-T. ASME*, **37**, 728–737.

Rice, J. R. (1988) "Elastic fracture concepts for interfacial cracks." *J. Appl. Mech.-T. ASME*, **55**, 98–103.

Rice, J. R. and Levy, N. (1972) "The part-through surface crack in an elastic plate." *J. Appl. Mech.-T. ASME*, **39**, 185–194.

Rice, J. R. and Rosengren, G. F. (1968) "Plane strain deformation near a crack tip in a power law hardening material." *J. Mech. Phys. Solids*, **16**, 1–12.

Rice, J. R. and Sih, G. C. (1965) "Plane problem of cracks in dissimilar media." *J. Appl. Mech.-T. ASME*, **32**(2), 418–425.

Riedel, H. (1989) "Recent advances in modelling creep crack growth." In *Advances in Fracture Research*, Vol. 2, K. Salama, K. Ravi-Chandar, D. M. R. Taplin and P. Rama Rao, eds., Pergamon Press, Oxford, pp. 1495–1523.

RILEM (1985) "Determination of the fracture energy of mortar and concrete by means of three-point bend tests on notched beams." *Mater. Struct.*, **18**, 285–290. (RILEM Draft Recommendation, TC 50-FMC Fracture Mechanics of Concrete.)

RILEM (1990a) "Determination of fracture parameters (K^s_{Ic} and $CTOD_c$) of plain concrete using three-point bend tests." *Mater. Struct.*, **23**, 457–460. (RILEM Draft Recommendation, TC 89-FMT Fracture Mechanics of Concrete–Test methods.)

RILEM (1990b) "Size-effect method for determining fracture energy and process zone size of concrete." *Mater. Struct.*, **23**, 461–465. (RILEM Draft Recommendation, TC 89-FMT Fracture Mechanics of Concrete–Test methods.)

Ritter, W. (1899) "Die bauweise hennebique." *Schweiz. Bauzeitung Zürich*, **33**(7), 59–61.

Rocco, C. G. (1996) *Influencia del Tamaño y Mecanismos de Rotura del Ensayo de Compresión Diametral.* Doctoral thesis. Dep. Ciencia de Materiales, Universidad Politecnica de Madrid, ETS de Ingenieros de Caminos, Ciudad Universitaria, 28040 Madrid, Spain. ('Size-Dependence and Fracture Mechanisms in the Diagonal Compression Splitting Test', in Spanish.)

Rocco, C., Guinea, G. V., Planas, J. and Elices, M. (1995) "The effect of the boundary conditions on the cylinder splitting strength." In *Fracture Mechanics of Concrete Structures*, F. H. Wittmann, ed., Aedificatio Publishers, Freiburg, Germany, pp. 75–84.

Rodriguez-Ortiz, J. M. (1974) *Study of Behavior of Granular Heterogeneous Media by Means of Analogical and Mathematical Discontinuous Models.* Doctoral thesis. Universidad Politécnica de Madrid, 28040-Madrid, Spain.

Roelfstra, P. E. (1988) *Numerical Concrete.* Doctoral thesis. Laboratoire de Matériaux de Construction, Ecole Polytéchnique Féderale de Lausanne, Lausanne, Suisse.

Roelfstra, P. E. and Wittmann, F. H. (1986) "Numerical method to link strain softening with failure of concrete." In *Fracture Toughness and Fracture Energy of Concrete*, F. H. Wittmann, ed., Elsevier Science, Amsterdam, pp. 163–175.

Roelfstra, P. E., Sadouki, H. and Wittmann, F. H. (1985) "Le béton numérique." *Mater. Struct.*, **18**, 327–335.

Rokugo, K., Iwasa, M., Suzuki, T. and Koyanagi, W. (1989) "Testing methods to determine tensile strain softening curve and fracture energy of concrete." In *Fracture Toughness and Fracture Energy: Test Methods for Concrete and Rock*, H. Mihashi, H. Takahashi and F. H. Wittmann, eds., Balkema, Rotterdam, pp. 153–163.

Rolfe, S. T. and Barsom, J. M. (1987) *Fracture and Fatigue Control in Structures*, 2nd edition, Prentice-Hall, Englewood Cliffs, NJ.

Rooke, D. P. and Cartwright, D. J. (1976) *Compendium of Stress Intensity Factors*, Her Majesty's Stationary Office, London.

Rosati, G. and Schumm, C. (1992) "Modelling of local bar-to-concrete bond in reinforced concrete beams." In *Proc. Int. Conf. on Bond in Concrete – From Research to Practice*, Vol. 3, A. Skudra and R. Tepfers, eds., pp. 34–43.

Roscoe, R. A. (1952) "The viscosity of suspensions of rigid spheres." *Brit. J. Appl. Phys.*, **3**, 267–269.

Rosen, B. W. (1965) "Mechanics of composite strengthening." In *Fiber Composite Materials*, Chapter 3, Am. Soc. for Metals Seminar.

Ross, C. A. and Kuennen, S. T. (1989) "Fracture of concrete at high strain-rates." In *Fracture of Concrete and Rock: Recent Developments*, S. P. Shah, S. E. Swartz and B. Barr, eds., Elsevier Applied Science, London, pp. 152–161.

Ross, C. A., Thompson, P. Y. and Tedesco, J. W. (1989) "Split-Hopkinson pressure-bar tests on concrete and mortar in tension and compression." *ACI Mater. J.*, **86**(5), 475–481.

Rossi, P. and Richer, S. (1987) "Numerical modeling of concrete cracking based on a stochastic approach." *Mater. Struct.*, **21**, 3–12.

Rossi, P. and Wu, X. (1992) "Probabilistic model for material behavior analysis and appraisement of concrete structures." *Mag. Concrete Res.*, **44**, 271–280.

Rossmanith, H. P., ed. (1993) *Fracture and Damage of Concrete and Rock*, E & FN Spon, London.

Rots J. G. (1988) *Computational Modeling of Concrete Fracture.* Doctoral thesis. Delft University of Technology, Delft, The Netherlands.

Rots, J. G. (1989) "Stress rotation and stress locking in smeared analysis of separation." In *Fracture Toughness and Fracture Energy, Test Methods for Concrete and Rock*, H. Mihashi, H. Takahashi and F. H. Wittmann, eds., Balkema, Rotterdam, pp. 367–382.

Rots, J. G. (1992) "Simulation of bond and anchorage: Usefulness of softening fracture mechanics." In *Application of Fracture Mechanics to Reinforced Concrete*, A. Carpinteri, ed., Elsevier Applied Science, London, pp. 285–306.

Rots, J. G., Nauta, P., Kusters, G. M. A. and Blauwendraad, J. (1985) "Smeared crack approach and fracture localization in concrete." *Heron*, **30**(1), 1–48.

Ruiz, G. (1996) *El Efecto de Escala en Vigas de Hormigón Débilmente Armadas y su Repercusión en los Criterios de Proyecto.* Doctoral thesis. Dep. Ciencia de Materiales, Universidad Politecnica de Madrid, ETS de Ingenieros de Caminos, Ciudad Universitaria, 28040 Madrid, Spain. ('Size Effect in Lightly Reinforced Concrete Beams and its Repercussion on Design Criteria', in Spanish.)

Ruiz, G. and Planas, J. (1994) "Propagación de una fisura cohesiva en una vigas de hormigón debilmente armadas: modelo de la longitud efectiva de anclaje." *Anales de Mecánica de la Fractura*, **11**, 506–513.

Ruiz, G. and Planas, J. (1995) "Estudio experimental del efecto de escala en vigas debilmente armadas." *Anales de Mecánica de la Fractura*, **12**, 446–451.

Ruiz, G., Planas, J. and Elices, M. (1993) "Propagación de una fisura cohesiva en vigas de hormigón debilmente armadas." *Anales de Mecánica de la Fractura*, **10**, 141–146.

Ruiz, G., Planas, J. and Elices, M. (1996) "Cuantía mínima en flexión: Teoría y normativa." *Anales de Mecánica de la Fractura*, **13**, 386–391.

Rüsch, H. (1960) "Researches toward a general flexural theory for structural concrete." *ACI J.*, **57**(1), 1–28.

Russ, J. C. (1994) *Fractal Surfaces*, Plenum Press, New York.

Sabnis, G. M. and Mirza, S. M. (1979) "Size effects in model concretes?" *J. Struct. Div.-ASCE*, **106**, 1007–1020.

Saenz. L. P. (1964) "Discussion of 'Equation for stress-strain curve of concrete' by P. Desay and S. Krishnan." *ACI J.*, **61**, 1229–1235.

Saleh, A. L. and Aliabadi, M. H. (1995) "Crack growth analysis in concrete using boundary element method." *Eng. Fract. Mech.*, **51**, 533–545.

Sallam, S. and Simitses, G. J. (1985) "Delamination buckling and growth of flat, cross-ply laminates." *Compos. Struct.*, **4**, 361–381.

Sallam, S. and Simitses, G. J. (1987) "Delamination buckling of cylindrical shells under axial compression." *Compos. Struct.*, **8**, 83–101.

Sammis, C. G. and Ashby, M. F. (1986) "The failure of brittle porous solids under compressive stress state." *Acta Metall.*, **34**(3), 511–526.

Sanderson, T. J. O. (1988) *Ice Mechanics Risks to Offshore Structures*, Graham and Trotman, Boston.

Saouma, V. E., Ayari, M. L. and Boggs, H. (1989) "Fracture mechanics of concrete gravity dams." In *Fracture of Concrete and Rock*, S. P. Shah and S. E. Swartz, eds., Springer-Verlag, New York, pp. 311–333.

Saouma, V. E., Barton, C. C. and Gamaleldin, N. E. (1990) "Fractal characterization of fracture surfaces in concrete." *Eng. Fract. Mech.*, **35**, 47–53.

Saouma, V. E., Broz, J. J., Brühwiler, E. and Ayari, M. L. (1990) *Fracture Mechanics of Concrete Dams, Vols. I, II, and III.* Reports submitted to the Electric Power Research Institute, Department of Civil Engineering, University of Colorado, Boulder, CO.

Saouma, V. E., Broz, J. J., Brühwiler, E. and Boggs, H. L. (1991) "Effect of aggregate and specimen size on fracture properties of dam concrete." *J. Mater. Civil Eng.*, **3**(3), 204–218.

Sayers, C. M. and Kachanov, M. (1991) "A simple technique for finding effective elastic constants of cracked solids for arbitrary crack orientation statistics." *Int. J. Solids Struct.*, **27**(6), 671–680.

Scanlon, A. (1971) *Time Dependent Deflections of Reinforced Concrete Slabs.* Doctoral thesis. Univ. of Alberta, Edmonton, Canada.

Schapery, R. A. (1975a) "A theory of crack initiation and growth in viscoelastic media I. Theoretical development." *Int. J. Fracture*, **11**, 141–159.

Schapery, R. A. (1975b) "A theory of crack initiation and growth in viscoelastic media II. Approximate methods of analysis." *Int. J. Fracture*, **11**, 369–388.

Schapery, R. A. (1975c) "A theory of crack initiation and growth in viscoelastic media III. Approximate methods of analysis." *Int. J. Fracture*, **11**, 549–562.

Schijve, J. (1979) "Four lectures on fatigue crack growth." *Eng. Fract. Mech.*, **11**, 167–221.

Schlaich, J., Schafer, K. and Jannewein, M. (1987) "Toward a consistent design for structural concrete." *J. Prestressed Concrete Inst.*, **32**(3), 75–150.

Schlangen, E. (1993) *Experimental and Numerical Analysis of Fracture Processes in Concrete.* Doctoral thesis. Delft University of Technology, Delft, The Netherlands.

Schlangen, E. (1995) "Computational aspects of fracture simulations with lattice models." In *Fracture Mechanics of Concrete Structures*, F. H. Wittmann, ed., Aedificatio Publishers, Freiburg, Germany, pp. 913–928.

Schlangen, E. and van Mier, J. G. M. (1992) "Shear fracture in cementitious composites, Part II: Numerical simulations." In *Fracture Mechanics of Concrete Structures*, Z. P. Bažant, ed., Elsevier Applied Science, New York, pp. 671–676.

Schulson, E. M. (1990) "The brittle compressive fracture of ice." *Acta Metall. Mater.*, **38**, 1963–1976.

Schulson, E. M. and Nickolayev, O. Y. (1995) "Failure of columnar saline ice under biaxial compression: failure envelopes and the brittle-to-ductile transition." *J. Geophys. Res.*, **100**(B11), 22383–22400.

Şener, S. (1992) "Bond splice tests." In *FIP'92 Symposium*, G. Tassi, ed., Hungarian Scientific Society of Building, Budapest, pp. 357–362.

Şener, S., Bažant, Z. P. and Becq-Giraudon, E. (1997) *Sizew effect in failure of lap splice of reinforcing bars in concrete beams.* Report, Northwestern University, Evanston, IL.

Serrano, A. A. and Rodriguez-Ortiz, J. M. (1973) "A contribution to the mechanics of heterogeneous granular media." In *Proc. Symp. Plasticity and Soil Mech.*.

Shah, S. P. and John, R. (1986) "Strain rate effects on mode I crack propagation in concrete." In *Fracture Mechanics and Fracture Energy of Concrete*, F. H. Wittmann, ed., Elsevier, Amsterdam, pp. 453–465.

Shah, S. P. and McGarry, F. J. (1971) "Griffith fracture criterion and concrete." *J. Eng. Mech. Div.-ASCE*, **97**, 1663–1676.

Shetty, D. K., Rosenfield, A. R. and Duckworth, W. H. (1986) "Mixed mode fracture of ceramics in diametrical compression." *J. Am. Ceram. Soc.*, **69**(6), 437–443.

Sidoroff, F. (1974) "Un modéle viscoélastique non linéaire avec configuration intermédiaire." *J. de Mécanique,* **13**, 679–713.

Sih, G. C. (1973) *Handbook of Stress Intensity Factors for Researchers and Engineers*, Lehigh University, Bethlehem, PA.

Sih, G. C. (1974) "Strain energy density factor applied to mixed mode crack problems." *Int. J. Fracture,* **10**, 305–322.

Simo, J. C. (1988) "A framework for finite strain elastoplasticity based on maximum plastic dissipation and the multiplicative decomposition." *Comput. Meth. Appl. Mech. Eng.,* **66**, 199–219. (Also **68**, 1–31.)

Simo, J. C. and Oliver, J. (1994) "A new approach to the analysis and simulation of strong discontinuities." In *Fracture and Damage in Quasibrittle Structures*, Z. P. Bažant, Z. Bittnar, M. Jirásec and J. Mazars, eds., E & FN Spon, London, pp. 25–39.

Simo, J. C. and Ortiz, M. (1985) "A unified approach to finite deformation elasto-plasticity based on the use of hyperelastic constitutive equations." *Comput. Meth. Appl. Mech. Eng.,* **49**, 177–208.

Simo, J. C. and Rifai, S. (1990) "A class of mixed assumed strain methods and the method of incompatible nodes." *Int. J. Numer. Meth. Eng.,* **29**, 1595–1638.

Simo, J. C., Oliver, J. and Armero, F. (1993) "An analysis of strong discontinuities induced by strain-softening in rate-independent inelastic solids." *Comput. Mech.,* **12**, 227–296.

Sinha, B. P., Gerstle, K. H. and Tulin, L. G. (1964) "Stress-strain relations for concrete under cyclic loading." *ACI J.,* **62**(2), 195–210.

Slepyan, L. I. (1990) "Modeling of fracture of sheet ice." *Izvestia AN SSSR, Mekhanika Tverdogo Tela,* **25**(2), 151–157.

Smith, C. W. and Kobayashi, A. S. (1993) "Experimental fracture mechanics." In *Handbook of Experimental Mechanics*, 2nd edition, A. S. Kobayashi, ed., VCH Publishers and Society for Experimental Mechanics (SEM), pp. 905–968.

Smith, E. (1995) "Recent research on the cohesive zone description of an elastic softening material." In *Fracture of Brittle Disordered Materials: Concrete, Rock, Ceramics*, G. Baker and B. L. Karihaloo, eds., E & FN Spon, London, pp. 450–463.

Sneddon, I. N. (1946) "The distribution of stress in the neighbourhood of a crack in an elastic solid." *Philos. T. Roy. Soc. A,* **187**, 229–260.

Sneddon, I.N. and Lowengrub, M. (1969) *Crack Problems in the Classical Theory of Elasticity*, John Wiley & Sons, New York.

So, K. O. and Karihaloo, B. L. (1993) "Shear capacity of longitudinally reinforced beams – A fracture mechanics approach." *ACI Struct. J.,* **90**, 591–600.

Sok, C., Baron, J. and François, D. (1979) "Mécanique de la rupture appliquée au béton hydraulique." *Cement Concrete Res.,* **9**, 641–648.

Sozen, M. A., Zwoyer, E. M. and Siess, C. P. (1958) "Strength in shear of beams without web reinforcement." *Bulletin Eng. Experiment Station,* **452**, 1–69.

Spencer, A. J. M. (1971) "Theory of invariants." In *Continuum Physics, 1 –Mathematics*, A. Cemal Eringen, ed., Academic Press, New York, pp. 239–353.

Srawley, J. E. (1976) "Wide range stress intensity factor expressions for ASTM E-399 standard fracture toughness specimens." *Int. J. Fracture,* **12**, 475–476.

Steif, P. S. (1984) "Crack extension under compressive loading." *Eng. Fract. Mech.,* **20**, 463–473.

Strang, G. (1980) *Linear Algebra and Its Applications*, 2nd edition, Academic Press, New York.

Stroh, A. N. (1957) "A theory of the fracture of metals." *Adv. Phys., Philos. Mag. Suppl.,* **6**, 418–65.

Stroud, A. H. (1971) *Approximate Calculation of Multiple Integrals*, Prentice-Hall, Englewood Cliffs, NJ.

Suidan, M. and Schnobrich, W. C. (1973) "Finite element analysis of reinforced concrete." *J. Struct. Div.-ASCE,* **99**(10), 2109–2122.

Suo, Z. and Hutchinson, J. W. (1989) "Sandwich test specimens for measuring interface crack toughness." *Mater. Sci. Eng. A,* **107**, 135–143.

Suresh, S. (1991) *Fatigue of Materials*, Cambridge University Press, Cambridge.

Swartz, S. E. and Go, C. G. (1984) "Validity of compliance calibration to cracked concrete beams in bending." *Exp. Mech.,* **24**(2), 129–134.

Swartz, S. E. and Refai, T. M. E. (1989) "Influence of size effects on opening mode fracture parameters for precracked concrete beams in bending." In *Fracture of Concrete and Rock*, S. P. Shah and S. E. Swartz, eds., Springer-Verlag, New York, pp. 242–254.

Swartz, S. E. and Taha, N. M. (1990) "Mixed-mode crack propagation and fracture in concrete." *Eng. Fract. Mech.,* **35**(1-3), 137–144.

Swartz, S. E. and Taha, N. M. (1991) "Crack propagation and fracture of plain concrete beams subjected to shear and compression." *ACI Struct. J.,* **88**(2), 177–196.

Swartz, S. E., Hu, K. K. and Jones, G. L. (1978) "Compliance monitoring of crack growth in concrete." *J. Eng. Mech. Div.-ASCE,* **104**, 789–800.

Swartz, S. E., Hu, K. K., Fartash, M. and Huang, C. M. J. (1982) "Stress intensity factors for plain concrete in bending – Prenotched versus precracked beams." *Exp. Mech.,* **22**(11), 412–417.

Swenson, D. V. and Ingraffea, A. R. (1991) "The collapse of the Schoharie Creek bridge: A case study in concrete fracture mechanics." *Int. J. Fracture,* **51**(1), 73–92.

Tada, H., Paris, P. C. and Irwin, G. R. (1973) *The Stress Analysis of Cracks Handbook*, Del Research Corporation, Hellertown, PA.

Tada, H., Paris, P. C. and Irwin, G. R. (1985) *The Stress Analysis of Cracks Handbook*, Paris Productions, Saint Louis, MO.

Tandon, S., Faber, K. T., Bažant, Z. P. and Li, Y.-N. (1995) "Cohesive crack modeling of influence of sudden changes in loading rate on concrete fracture." *Eng. Fract. Mech.,* **52**(6), 987–997.

Tang, T., Shah, S. P. and Ouyang, C. (1992) "Fracture mechanics and size effect of concrete in tension." *J. Struct. Eng.-ASCE,* **118**(11), 3169–3185.

Taylor, G. I. (1938) "Plastic strain in metals." *J. Inst. Metals,* **62**, 307–324.

Tepfers, R. (1973) *A Theory of Bond Applied to Overlapped Tensile Reinforcement Splices for Deformed Bars.* Doctoral thesis. Division of Concrete Structures, Chalmers University of Technology, Göteborg, Sweden.

Tepfers, R. (1979) "Cracking of concrete cover along anchored deformed reinforcing bars." *Mag. Concrete Res.,* **31**(106), 3–12.

Thouless, M. D., Hsueh, C. H. and Evans, A. G. (1983) "A damage model of creep crack growth in polycrystals." *Acta Metall.,* **31**(10), 1675–1687.

Thürlimann, B. (1976) *Shear Strength of Reinforced and Prestressed Concrete Beams, CEB Approach.* Technical Report, E. T. H. Zürich.

Timoshenko, S. (1956) *Strength of Materials*, Van Nostrand, New York.

Timoshenko, S. and Goodier, J. N. (1951) *Theory of Elasticity*, 2nd edition, McGraw-Hill, New York.

Tippett, L. H. C. (1925) "On the extreme individuals and the range of samples taken from a normal population." *Biometrika,* **17**, 364–387.

Triantafyllidis, N. and Aifantis, E (1986) "A gradient approach to localization of deformation. I. Hyperelastic materials." *J. Elasticity,* **16**, 225–237.

Tschegg, E. Kreuzer, H. and Zelezny, M. (1992) "Fracture of concrete under biaxial loading — Numerical evaluation of wedge splitting test results." In *Fracture Mechanics of Concrete Structures*, Z. P. Bažant, ed., Elsevier Applied Science, London, pp. 455–460.

Uchida, Y., Kurihara, N., Rokugo, K. and Koyanagi, W. (1995) "Determination of tension softening diagrams of various kinds of concrete by means of numerical analysis." In *Fracture Mechanics of Concrete Structures*, Vol. 1, F. H. Wittmann, ed., Aedificatio Publishers, Freiburg, Germany, pp. 17–30.

Uchida, Y., Rokugo, K. and Koyanagi, W. (1992) "Application of fracture mechanics to size effect on flexural strength of concrete." *Proceedings of JSCE, Concrete Engineering and Pavements,* (442), 101–107.

Ulfkjær, J. P. and Brincker, R. (1993) "Indirect determination of the σ–w relation of HSC through three-point bending." In *Fracture and Damage of Concrete and Rock*, H. P. Rossmanith, ed., E & FN Spon, London, pp. 135–144.

Ulfkjær, J. P., Brincker, R. and Krenk, S. (1990) "Analytical model for complete moment-rotation curves of concrete beams in bending." In *Fracture Behavior and Design of Materials and Structures*, Vol. 2, D. Firrao, ed., Engineering Materials Advisory Services Ltd. (EMAS), Warley, West Midlands, U.K., pp. 612–617.

Ulfkjær, J. P., Hededal, O., Kroon, I. and Brincker, R. (1994) "Simple application of fictitious crack model in reinforced concrete beams — analysis and experiments." In *Size Effect in Concrete Structures*, H. Mihashi, H. Okamura and Z. P. Bažant, eds., E & FN Spon, London, pp. 281–292.

Vakulenko, A. A. and Kachanov, M. (1971) "Continuum theory of medium with cracks." *Mech. Solids,* **6**, 145–151.

Valente, S. (1995) "On the cohesive crack model in mixed-mode conditions." In *Fracture of Brittle Disordered Materials: Concrete, Rock and Ceramics*, G. Bakker and B. L. Karihaloo, eds., E & FN Spon, London, pp. 66–80.

Vardoulakis, I. (1989) "Shear banding and liquefaction in granular materials on the basis of Cosserat continuum theory." *Ingenieur-Archiv,* **59**, 106–113.

Varga, R. S. (1962) *Matrix Iterative Analysis*, Prentice-Hall, Englewood Cliffs, NJ.

van der Veen, C. (1991) "Splitting failure of reinforced concrete at various temperatures." In *Fracture Processes in Concrete, Rock and Ceramics*, J. G. M. van Mier, J. G. Rots and A. Bakker, eds., E & FN Spon, London, pp. 629–638.

da Vinci, L. (1500s) *—see* The Notebooks of Leonardo da Vinci *(1945), Edward McCurdy, London (p. 546); and* Les Manuscrits de Léonard de Vinci, *transl. in French by C. Ravaisson-Mollien, Institut de France (1881-91), Vol. 3.*.

Wagner, H. (1929) "Ebene blechwandträger mit sehr dünnem stegblech." *Z. Flugtechnik Motorluftschifffahr,* **20**, 8–12.

Walker, S. and Bloen, D. L. (1957) "Studies of flexural strength of concrete–Part 3: Effects of variations in testing procedures." *ASTM Proc.,* **57**, 1122–1139.

Walraven, J. C. (1978) *The Influence of Depth on the Shear Strength of Lightweight Concrete Beams Without Shear Reinforcement.* Stevin Laboratory Report No. 5-78-4, Delft University of Technology, Delft, The Netherlands.

Walsh, P. F. (1972) "Fracture of plain concrete." *Indian Concrete J.,* **46**(11), 469–470 and 476.

Walsh, P. F. (1976) "Crack initiation in plain concrete." *Mag. Concrete Res.,* **28**, 37–41.

Wawrzynek, P. A. and Ingraffea, A. R. (1987) "Interactive finite element analysis of fracture processes: An integrated approach." *Theor. Appl. Fract. Mech.,* **8**, 137–150.

Wecharatana, M. (1986) "Specimen size effect on non-linear fracture parameters in concrete." In *Fracture Toughness and Fracture Energy of Concrete*, F. H. Wittmann, ed., Elsevier Science, Amsterdam, pp. 437–440.

Wecharatana, M. and Shah, S. P. (1980) *Resistance to Crack Growth in Portland Cement Composites.* Report, Department of Material Engineering, University of Illinois at Chicago Circle, Chicago, IL.

Weibull, W. (1939) "A statistical theory of the strength of materials." *Proc. Royal Swedish Academy of Eng. Sci.,* **151**, 1–45.

Weibull W. (1949) "A statistical representation of fatigue failures in solids." *Proc. Roy. Inst. of Techn.,* (27).

Weibull, W. (1951) "A statistical distribution function of wide applicability." *J. Appl. Mech.-T. ASME,* **18**, 293–297.

Weibull W. (1956) "Basic aspects of fatigue." In *Proc. Colloquium on Fatigue*, Springer–Verlag.

Weihe, S. and Kröplin, B. (1995) "Fictitious crack models: A classification approach." In *Fracture Mechanics of Concrete Structures*, F. H. Wittmann, ed., Aedificatio Publishers, Freiburg, Germany, pp. 825–840.

Wells, A. A. (1963) "Application of fracture mechanics at and beyond general yielding." *Brit. Weld. J.,* **10**, 563–570.

Willam, K., Bićanić, N. and Sture, S. (1986) "Composite fracture model for strain-softening and localised failure of concrete." In *Computational Modelling of Reinforced Concrete Structures*, E. Hinton and D. R. J. Owen, eds., Pineridge Press, Swansea, pp. 122–153.

Willam, K., Pramono, E. and Sture, S. (1989) "Fundamental issues of smeared crack models." In *Fracture of Concrete and Rock*, S. P. Shah and S. E. Swartz, eds., Springer Verlag, New York, pp. 142–157.

Williams, M. L. (1952) "Stress singularities resulting from various boundary conditions in angular corners of plates in extension." *J. Appl. Mech.-T. ASME,* **19**, 526–528.

Wilson, W. K. (1966) Untitled. In *Plane Strain Crack Toughness Testing*, Brown, W. F. and J. E Srawley, eds., American Society for Testing and Materials, Philadelphia, pp. 75–76. (Contribution to Discussion, ASTM Special Technical Publication No. 410.)

Wilson, W. K. (1971) *Crack Tip Finite Elements for Plane Elasticity.* Report No. 71-1E7-FM-PWR-P2, Westinghouse.

Wiss, A.N. (1971) *Application of Fracture Mechanics to Cracking in Concrete Beams.* Doctoral thesis. University of Washington.

Wiss, Janney, Eltsner Associates, Inc. and Mueser Rutledge Consulting Engineers (1987) *Collapse of the Thruway Bridge at Schoharie Creek.* Final Report submitted to the New York State Thruway Authority, Wiss, Janney, Eltsner Associates, Inc. and Mueser Rutledge Consulting Engineers, Albany, New York.

Wittmann, F. H., ed. (1983) *Fracture Mechanics of Concrete*, Elsevier, Amsterdam.

Wittmann, F. H. and Zaitsev, Y. V. (1981) "Crack propagation and fracture of composite materials such as concrete." In *Advances in Fracture Research, Preprints 5th. Int. Conf. Fracture*, Vol. 5, D. François, ed., Pergamon Press, Oxford, pp. 2261–2274.

Wittmann, F. H., Roelfstra, P. E. and Kamp, C. L. (1988) "Drying of concrete: an application of the 3L-approach." *Nucl. Eng. Des.,* **105**, 185–198.

Wittmann, F. H., Roelfstra, P. E., Mihashi, H., Huang, Y. Y., Zhang, X. H. and Nomura, N. (1987) "Influence of age of loading, water-cement ratio, and rate of loading on fracture energy of concrete." *Mater. Struct.,* **20**, 103–110.

Wittmann, F. H., Rokugo, K., Brühwiler, E., Mihashi, H. and Simonin, P. (1988) "Fracture energy and strain softening of concrete as determined by means of compact tension specimens." *Mater. Struct.,* **21**, 21–32.

Wright, P. J. F. (1952) "The effect of the method of test on the flexural strength of concrete." *Mag. Concrete Res.,* **11**, 67–76.

Wu, X-R. and Carlsson A. J. (1991) *Weight Functions and Stress Intensity Factor Solutions*, Pergamon Press, Oxford.

Wu, Z. S. and Bažant, Z. P. (1993) "Finite element modeling of rate effect in concrete fracture with influence of creep." In *Creep and Shrinkage of Concrete*, Z. P. Bažant and I. Carol, eds., E & FN Spon, London, pp. 427–432.

Xi, Y. and Bažant, Z. P. (1992) "Markov process model for random growth of crack with R-curve." In *Fracture Mechanics of Concrete Structures*, Z. P. Bažant, ed., Elsevier Applied Science, London, pp. 179–182.

Xi, Y. and Bažant, Z. P. (1993) "Continuous retardation spectrum for solidification theory of concrete creep." In *Creep and Shrinkage of Concrete*, Z. P. Bažant and I. Carol, eds., E & FN Spon, London, pp. 225–230.

Yankelevsky, D. Z. and Reinhardt H. W. (1989) "Uniaxial behaviour of concrete in cyclic tension." *J. Struct. Eng.-ASCE,* **115**(1), 166–182.

Yin, W.-L., Sallam, S., and Simitses, G. J. (1986) "Ultimate axial capacity of a delaminated beam-plate." *AIAA J.,* **24**(1), 123–128.

Young , T. (1807) *A course of lectures on natural philosophy and the mechanical arts*, Vol. 1, , London. (p. 144.)

Yuan, Y. Y., Lajtai, E. Z. and Ayari, M. L. (1993) "Fracture nucleation from a compression-parallel finite-width elliptical flaw." *Int. J. Rock Mech. Min. Sci.,* **30**(7), 873–876.

Yuzugullu, O. and Schnobrich, W. C. (1973) "A numerical procedure for the determination of the behavior of a shear wall frame system." *ACI J.,* **70**(7), 474–479.

Zaitsev, Y. V. (1985) "Inelastic properties of solids with random cracks." In *Mechanics of Geomaterials: Rocks, Concretes, Soils*, Z. P. Bažant,, ed., John Wiley & Sons, Chichester, New York, pp. 89–128.

Zaitsev, Y. V. and Wittmann, F. H. (1974) "Verformung und Bruchvorgang poröser Baustoffe unter kurzzeitiger Belastung und unter Dauerlast." *Deutscher Ausschuss für Stahlbeton,* (232), 65–145.

Zaitsev, Y. V. and Wittmann, F. H. (1981) "Simulation of crack propagation and failure of concrete." *Mater. Struct.,* **14**, 357–365.

Zech, B. and Wittmann, F. H. (1977) "A complex study on the reliability assessment of the containment of a PWR, Part II. Probabilistic approach to describe the behavior of materials." In *Trans. 4th Int. Conf. on Structural Mechanics in Reactor Technology*, H, T. A. Jaeger and B. A. Boley, eds., European Communities, Brussels, pp. 1–14.

Zhang, C.-Y. and Karihaloo, B.L. (1992) "Stability of a crack in a linear viscoelastic tension-softening material." In *Fracture Mechanics of Concrete Structures*, Z. P. Bažant, ed., Elsevier Applied Science, London, pp. 155–162.

Zhou, F. P. (1992) *Time-Dependent Crack Growth and Fracture in Concrete.* Report No. TVBM-1011, Division of Building Materials, Lund University, Lund, Sweden.

Zhou, F. P. (1993) "Cracking analysis and size effect in creep rupture of concrete." In *Creep and Shrinkage of Concrete*, Z. P. Bažant and I. Carol, eds., E & FN Spon, London, pp. 407–412.

Zhou, F. P. and Hillerborg, A. (1992) "Time-dependent fracture of concrete: Testing and modelling." In *Fracture Mechanics of Concrete Structures*, Z. P. Bažant, ed., Elsevier Applied Science, London, pp. 906–911.

Zienkiewicz, O. C. and Pande, G. N. (1977) "Time-dependent multi-laminate model of rocks—A numerical study of deformation and failure of rock masses." *Int. J. Numer. Anal. Meth. Geomech.,* **1**, 219–247.

Zubelewicz, A. (1980) *Contact Element Method.* Doctoral thesis. Technical University of Warsaw, Warsaw, Poland. (In Polish.)

Zubelewicz, A. (1983) "Proposal of a new structural model for concrete." *Archiwum Inzynierii Ladowej,* **29**, 417–429. (In Polish.)

Zubelewicz, A. and Bažant, Z. P. (1987) "Interface element modeling of fracture in aggregate composites." *J. Eng. Mech.-ASCE,* **113**, 1619–1630.

Zubelewicz, A. and Mróz, Z. (1983) "Numerical simulation of rockburst processes treated as problems of dynamic instability." *Rock Mech. Rock Eng.,* **16**, 253–274.

Reference Citation Index

Spencer (1971), 236
Srawley (1976), 50, 115
Steif (1984), 298
Strang (1980), 514
Stroh (1957), 389
Stroud (1971), 532
Suidan and Schnobrich (1973), 237
Suo and Hutchinson (1989), 379
Suresh (1991), 429–431
Swartz and Go (1984), 103, 113, 432
Swartz and Refai (1989), 113, 147
Swartz and Taha (1990), 377
Swartz and Taha (1991), 377
Swartz, Hu and Jones (1978), 103, 112, 113, 432
Swartz, Hu et al. (1982), 103, 113
Swenson and Ingraffea (1991), 375
Tada, Paris and Irwin (1973), 50, 51
Tada, Paris and Irwin (1985), 49, 70, 119, 121, 161, 202, 287, 302, 352, 354
Tandon et al. (1995), 429
Tang, Shah and Ouyang (1992), 117, 296
Taylor (1938), 528
Tepfers (1973), 370
Tepfers (1979), 370
Thürlimann (1976), 335
Thouless, Hsueh and Evans (1983), 395
Timoshenko (1956), 27
Timoshenko and Goodier (1951), 79, 281
Tippett (1925), 438
Triantafyllidis and Aifantis (1986), 489
Tschegg, Kreuzer and Zelezny (1992), 165
Uchida et al. (1995), 171, 271
Uchida, Rokugo and Koyanagi (1992), 268, 282
Ulfkjær and Brincker (1993), 171
Ulfkjær et al. (1994), 356, 357
Ulfkjær, Brincker and Krenk (1990), 356
Vakulenko and Kachanov (1971), 562
Valente (1995), 174
Vardoulakis (1989), 489
Varga (1962), 514
van der Veen (1991), 370
Wagner (1929), 343
Walker and Bloen (1957), 280
Walraven (1978), 329
Walsh (1972), 16, 18, 102, 103, 111, 248
Walsh (1976), 102, 103, 111
Wawrzynek and Ingraffea (1987), 174
Wecharatana (1986), 170
Wecharatana and Shah (1980), 248
Weibull (1939), 10, 280, 437, 438, 441
Weibull (1949), 438
Weibull (1951), 437, 441
Weibull (1956), 438
Weihe and Kröplin (1995), 165
Wells (1963), 116
Willam, Bićanić and Sture (1986), 248
Willam, Pramono and Sture (1989), 248
Williams (1952), 86
Wilson (1966), 39
Wilson (1971), 62
Wiss (1971), 366
Wiss, Janney et al. (1987), 375
Wittmann (1983), 5
Wittmann and Zaitsev (1981), 298
Wittmann, Roelfstra and Kamp (1988), 550
Wittmann, Roelfstra et al. (1988), 168
Wittmann, Rokugo et al. (1987), 171, 271
Wright (1952), 280, 290
Wu and Bažant (1993), 385–387, 404, 425–427
Wu and Carlsson (1991), 55, 73
Xi and Bažant (1992), 438, 470
Xi and Bažant (1993), 408
Yankelevsky and Reinhardt (1989), 434
Yin, Sallam, and Simitses (1986), 60
Young (1807), 437
Yuan, Lajtai and Ayari (1993), 298, 379
Yuzugullu and Schnobrich (1973), 237
Zaitsev (1985), 298
Zaitsev and Wittmann (1974), 438
Zaitsev and Wittmann (1981), 298
Zech and Wittmann (1977), 438, 441, 458
Zhang and Karihaloo (1992), 373
Zhou (1992), 387–389, 424
Zhou (1993), 388, 424
Zhou and Hillerborg (1992), 387–389, 424
Zienkiewicz and Pande (1977), 528
Zubelewicz (1980), 551
Zubelewicz (1983), 551
Zubelewicz and Bažant (1987), 551, 552
Zubelewicz and Mróz (1983), 551

Index